frontiers | Research Topics

Ethological dynamics in diorama environments

Edited by
Toshiyuki Nakagaki, Audrey Dussutour, Takuji Ishikawa and Laurence Wilson

Published in
Frontiers in Cell and Developmental Biology
Frontiers in Ecology and Evolution

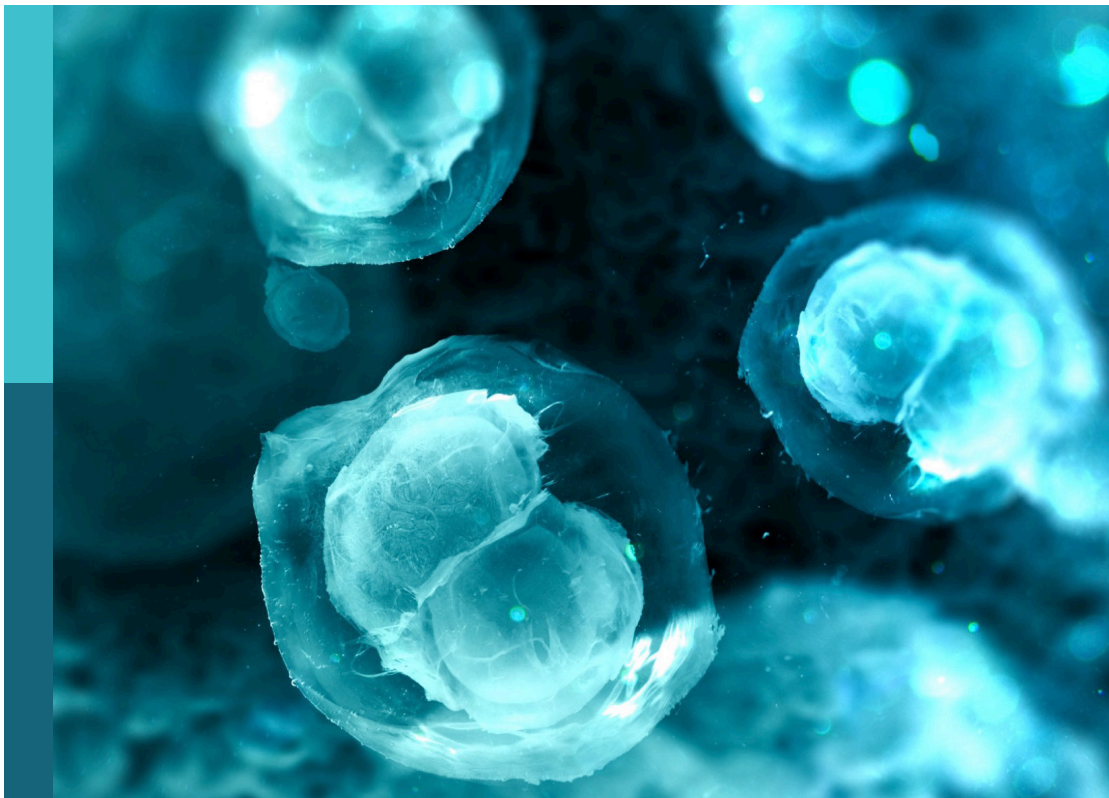

ISSN 1664-8714
ISBN 978-2-8325-4310-8
DOI 10.3389/978-2-8325-4310-8

About Frontiers

Frontiers is more than just an open access publisher of scholarly articles: it is a pioneering approach to the world of academia, radically improving the way scholarly research is managed. The grand vision of Frontiers is a world where all people have an equal opportunity to seek, share and generate knowledge. Frontiers provides immediate and permanent online open access to all its publications, but this alone is not enough to realize our grand goals.

Frontiers journal series

The Frontiers journal series is a multi-tier and interdisciplinary set of open-access, online journals, promising a paradigm shift from the current review, selection and dissemination processes in academic publishing. All Frontiers journals are driven by researchers for researchers; therefore, they constitute a service to the scholarly community. At the same time, the *Frontiers journal series* operates on a revolutionary invention, the tiered publishing system, initially addressing specific communities of scholars, and gradually climbing up to broader public understanding, thus serving the interests of the lay society, too.

Dedication to quality

Each Frontiers article is a landmark of the highest quality, thanks to genuinely collaborative interactions between authors and review editors, who include some of the world's best academicians. Research must be certified by peers before entering a stream of knowledge that may eventually reach the public - and shape society; therefore, Frontiers only applies the most rigorous and unbiased reviews. Frontiers revolutionizes research publishing by freely delivering the most outstanding research, evaluated with no bias from both the academic and social point of view. By applying the most advanced information technologies, Frontiers is catapulting scholarly publishing into a new generation.

What are Frontiers Research Topics?

Frontiers Research Topics are very popular trademarks of the *Frontiers journals series*: they are collections of at least ten articles, all centered on a particular subject. With their unique mix of varied contributions from Original Research to Review Articles, Frontiers Research Topics unify the most influential researchers, the latest key findings and historical advances in a hot research area.

Find out more on how to host your own Frontiers Research Topic or contribute to one as an author by contacting the Frontiers editorial office: frontiersin.org/about/contact

Ethological dynamics in diorama environments

Topic editors

Toshiyuki Nakagaki — Hokkaido University, Japan

Audrey Dussutour — UMR5169 Centre de Recherches sur la Cognition Animale (CRCA), France

Takuji Ishikawa — Tohoku University, Japan

Laurence Wilson — University of York, United Kingdom

Citation

Nakagaki, T., Dussutour, A., Ishikawa, T., Wilson, L., eds. (2024). *Ethological dynamics in diorama environments*. Lausanne: Frontiers Media SA.

doi: 10.3389/978-2-8325-4310-8

Table of contents

05 Editorial: Ethological dynamics in diorama environments
Toshiyuki Nakagaki, Audrey Dussutour, Laurence Wilson and Takuji Ishikawa

07 Biological benefits of collective swimming of sperm in a viscoelastic fluid
Shiva Phuyal, Susan S. Suarez and Chih-Kuan Tung

18 Switching of behavioral modes and their modulation by a geometrical cue in the ciliate *Stentor coeruleus*
Syun Echigoya, Katsuhiko Sato, Osamu Kishida, Toshiyuki Nakagaki and Yukinori Nishigami

31 Long-time behavior of swimming *Euglena gracilis* in a heterogenous light environment
Kazuki Muku, Hiroshi Yamashita, Touya Kamikubo, Nobuhiko J. Suematsu and Makoto Iima

39 Calaxin is required for asymmetric bend initiation and propagation in sperm flagella
Kogiku Shiba, Shoji A. Baba, Eiji Fujiwara and Kazuo Inaba

50 Bioconvection pattern of *Euglena* under periodical illumination
Nobuhiko J. Suematsu, Hiroshi Yamashita and Makoto Iima

55 Strain, cell density, and nutrient condition affect patterns of diurnal vertical migration and superoxide production in a red-tide alga
Tomoyuki Shikata, Saho Kitatsuji and Koki Yuasa

65 Squirmer hydrodynamics near a periodic surface topography
Kenta Ishimoto, Eamonn A. Gaffney and David J. Smith

78 Positive selection on ADAM10 builds species recognition in the synchronous spawning coral *Acropora*
Masaya Morita, Seiya Kitanobo, Shun Ohki, Kogiku Shiba and Kazuo Inaba

90 Emergence of a *Euglena* bioconvection spot controlled by non-uniform light
Hiroshi Yamashita, Touya Kamikubo, Kazuki Muku, Nobuhiko J. Suematsu, Shunsuke Izumi and Makoto Iima

97 A cell membrane model that reproduces cortical flow-driven cell migration and collective movement
Katsuhiko Sato

111 Foraging strategies of fungal mycelial networks: responses to quantity and distance of new resources
Yu Fukasawa and Kaho Ishii

119 Three-dimensional architecture and assembly mechanism of the egg-shaped shell in testate amoeba *Paulinella micropora*
Mami Nomura, Keisuke Ohta, Yukinori Nishigami, Takuro Nakayama, Kei-Ichiro Nakamura, Kenjiro Tadakuma and Josephine Galipon

134 Random walk and cell morphology dynamics in *Naegleria gruberi*
Masahito Uwamichi, Yusuke Miura, Ayako Kamiya, Daisuke Imoto and Satoshi Sawai

151 CatSper mediates not only chemotactic behavior but also the motility of ascidian sperm
Taiga Kijima, Daisuke Kurokawa, Yasunori Sasakura, Michio Ogasawara, Satoe Aratake, Kaoru Yoshida and Manabu Yoshida

164 Relation between learning process and morphology of transport tube network in plasmodium of *Physarum polycephalum*
Emiri Yoneoka and Atsuko Takamatsu

frontiers | Frontiers in Cell and Developmental Biology

TYPE Editorial
PUBLISHED 05 January 2024
DOI 10.3389/fcell.2023.1347957

OPEN ACCESS

EDITED AND REVIEWED BY
Vladimir S. Mashanov,
Wake Forest University, United States

*CORRESPONDENCE
Toshiyuki Nakagaki,
nakagaki@es.hokudai.ac.jp

RECEIVED 01 December 2023
ACCEPTED 14 December 2023
PUBLISHED 05 January 2024

CITATION
Nakagaki T, Dussutour A, Wilson L and Ishikawa T (2024), Editorial: Ethological dynamics in diorama environments. *Front. Cell Dev. Biol.* 11:1347957. doi: 10.3389/fcell.2023.1347957

Editorial: Ethological dynamics in diorama environments

Toshiyuki Nakagaki[1]*, Audrey Dussutour[2,3], Laurence Wilson[4] and Takuji Ishikawa[5]

[1]Research Institute for Electronic Science, Hokkaido University, Sapporo, Hokkaido, Japan, [2]UMR5169 Centre de Recherches Sur La Cognition Animale (CRCA), Toulouse, Midi-Pyrénées, France, [3]Université Toulouse III Paul Sabatier, Toulouse, Occitanie, France, [4]School of Physics, Engineering and Technology, University of York, York, United Kingdom, [5]Department of Biomedical Engineering, Graduate School of Biomedical Engineering, Tohoku University, Sendai, Japan

KEYWORDS

cell movement, biomechanics, protist, bio-fluid dynamics, cell behavior, sperm, cilia a flagella, collective motion

Editorial on the Research Topic
Ethological dynamics in diorama environments

Introduction to the scope of this Research Topic

Exploring behavioral smartness of single cells in their natural habitats is interesting as many such habitats are highly variable in space and time. We can observe that ciliates typically move around the complicated shape (in the scale of their body length) of sedimentary materials on pond beds, and these in turn are dynamic environments: water flows; cells encounter both predators and prey; and temperature, chemicals and light levels all fluctuate. Hence, the environment where they are living is complex, and they need to behave responsively.

Environmental responses are often highly adapted and pragmatic, even when the environment appears bafflingly complex to the human eye. The behavioral complexity of single cells are often unknown or ignored, while unicellular organisms express subtle and nuanced responses. Here we throw light on the behavioral abilities of single cells, and begin to unpick their underlying mechanisms.

For such studies, we propose a few key points of methodology. The first point is to well-design an experimental setup of a complex environment. We name such artificial environments as 'diorama environment', where organisms can show their potential abilities. Diorama environments, for example, may mimic some of the complexity of natural habitats, or may be a sequence of experimental stimulation that is designed to test the ability of learning including habituation and conditioning. The second point is to formulate a mathematical (mechanical) model to describe the smart behavior in its complex environment. The third point is, if possible, to extract the algorithm (or heuristics) of information processing for the behavior under focus. The term 'ethological dynamics' we propose here refers to the model equations that involve algorithms of cellular information processing for smart behavior. As the Research Topic described here is in its infancy, we hope that this Research Topic will be recognized and shared more widely in the future.

Editorial summary of fifteen contributed papers

Cell movement can be roughly divided into two types: swimming by cilia and crawling by pseudopodia. We begin with ciliary swimming. A typical adaptive behavior observed in a diorama environment is 'switching of behavioral modes and their modulation by a geometrical cue in the ciliate *Stentor coeruleus*' (Echigoya et al.). In this study, designing a swimming space with a specific shape revealed *Stentor*'s ability to distinguish the space shapes. Spatial inhomogeneity is common nature of environment and, in a heterogeneous light environment, 'long-time behavior of swimming *Euglena gracilis*' was reported (Muku et al.).

The regulation of ciliary beating that leads to ciliary swimming are being studied as Shiba et al. reported that 'Calaxin is required for asymmetric bend initiation and propagation in sperm flagella', and Kijima et al. reported that 'CatSper mediates not only chemotactic behavior but also the motility of ascidian sperm'. Based on an understanding about molecular mechanism, a mechanical model of ciliary swimming can be formulated. Ishimoto et al. investigated 'squirmer hydrodynamics near a periodic surface topology'. Microbial hydrodynamics is a necessary tool for elucidating mechanisms for adaptive behavior in swimming microorganisms.

Regarding amoeboid movement, Nomura et al. reported a remarkable ability of pseudopod movement: 'three-dimensional architecture and assembly mechanism of the egg-shaped shell in testate amoeba *Paulinella micropora*'. This paper shows that the pseudopods are able to complete the complex operating procedures that construct the amoeba's shell.

The possibility of learning and memory in a single cell has been the subject of debate since many years ago, and Yoneoka et al. reported 'relation between learning process and morphology of transport tube network in plasmodium of *Physarum polycephalum*'.

In free locomotion of *Naegleria gruberi*, 'random walk and cell morphology dynamics' in the absence of directional cues was characterized by a detailed and careful analysis (Uwamichi et al.), deepening our understanding of intrinsic movements that help to formulate amoeboid movement. Sato reported 'a cell membrane model that reproduced cortical flow-driven cell migration and collective movement'. This simplified and elegant model recreates observed mechanical behavior without the need for detailed assumptions about the cell biology.

Next, we pay attention to collective motions of cells that are common in natural habitats. One of the most impressive phenomena is the algal 'red tide'; Shikata et al. reported that 'strain, cell density, and nutrient condition affect patterns of diurnal vertical migration and superoxide production in a red-tide alga'. At a smaller scale in the laboratory, similar collective motions called bio-convection were studied in heterogeneous environments. Rich patterns of convection spots were found in micro-alga under non-uniform light or periodic illumination, described in 'emergence of a *Euglena* bioconvection spot controlled by non-uniform light' (Yamashita et al.), and 'bioconvection pattern of *Euglena* under periodic illumination' (Suematsu et al.).

Collective swimming can be observed during fertilization in mammals when a large amount of sperm swims in the mucus layer within the reproductive tract. Phuyal et al. focused on 'biological benefits of collective swimming of sperm in a viscoelastic fluid'.

Intermediate crowdedness - more than single cell and less than collective motion - is found when many species of reef-building coral show simultaneous spawning and ejaculation at a once-a-year event of their life cycle. In there, very many sperms and eggs move up to the surface of water and the sperms swim toward one of eggs under the perturbation of water waves. To initiate study on the behavior of sperm in this environment, Morita et al. reported, at a first step of study, that 'positive selection on ADAM10 builds species recognition in the synchronous spawning coral *Acropora*'.

In multicellular organisms, the optimal foraging ability of fungal mycelial networks is clearly demonstrated in a diorama environment as Fukasawa and Ishii reported in 'foraging strategies of fungal mycelial networks: responses to quantity and distance of new resources'.

We hope that these fifteen contributed papers will be helpful in understanding the ethological dynamics in diorama environments, and that more research on this Research Topic will be conducted in the future.

Author contributions

TN: Writing–original draft. AD: Writing–review and editing. LW: Writing–review and editing. TI: Writing–review and editing.

Funding

The author(s) declare financial support was received for the research, authorship, and/or publication of this article. This work was supported by the grant-in-aid MEXT Kakenhi NO. 21H05303.

Conflict of interest

The authors declare that the research was conducted in the absence of any commercial or financial relationships that could be construed as a potential conflict of interest.

Publisher's note

frontiers | Frontiers in Cell and Developmental Biology

TYPE Original Research
PUBLISHED 22 September 2022
DOI 10.3389/fcell.2022.961623

OPEN ACCESS

EDITED BY
Takuji Ishikawa,
Tohoku University, Japan

REVIEWED BY
Kyosuke Shinohara,
Tokyo University of Agriculture and Technology, Japan
Toru Hyakutake,
Yokohama National University, Japan

*CORRESPONDENCE
Chih-Kuan Tung,
ctung@ncat.edu

SPECIALTY SECTION
This article was submitted to Evolutionary Developmental Biology, a section of the journal Frontiers in Cell and Developmental Biology

RECEIVED 05 June 2022
ACCEPTED 26 August 2022
PUBLISHED 22 September 2022

CITATION
Phuyal S, Suarez SS and Tung C-K (2022), Biological benefits of collective swimming of sperm in a viscoelastic fluid.
Front. Cell Dev. Biol. 10:961623.
doi: 10.3389/fcell.2022.961623

Biological benefits of collective swimming of sperm in a viscoelastic fluid

Shiva Phuyal[1,2], Susan S. Suarez[3] and Chih-Kuan Tung[1]*

[1]Department of Physics, North Carolina A&T State University, Greensboro, NC, United States, [2]Applied Science and Technology PhD Program, North Carolina A&T State University, Greensboro, NC, United States, [3]Department of Biomedical Sciences, Cornell University, Ithaca, NY, United States

Collective swimming is evident in the sperm of several mammalian species. In bull (*Bos taurus*) sperm, high viscoelasticity of the surrounding fluid induces the sperm to form dynamic clusters. Sperm within the clusters swim closely together and align in the same direction, yet the clusters are dynamic because individual sperm swim into and out of them over time. As the fluid in part of the mammalian female reproductive tract contains mucus and, consequently, is highly viscoelastic, this mechanistic clustering likely happens *in vivo*. Nevertheless, it has been unclear whether clustering could provide any biological benefit. Here, using a microfluidic *in vitro* model with viscoelastic fluid, we found that the collective swimming of bull sperm in dynamic clusters provides specific biological benefits. In static viscoelastic fluid, clustering allowed sperm to swim in a more progressive manner. When the fluid was made to flow in the range of 2.43–4.05 1/sec shear rate, clustering enhanced the ability of sperm to swim upstream. We also found that the swimming characteristics of sperm in our viscoelastic fluid could not be fully explained by the hydrodynamic model that has been developed for sperm swimming in a low-viscosity, Newtonian fluid. Overall, we found that clustered sperm swam more oriented with each other in the absence of flow, were able to swim upstream under intermediate flows, and better withstood a strong flow than individual sperm. Our results indicate that the clustering of sperm can be beneficial to sperm migrating against an opposing flow of viscoelastic fluid within the female reproductive tract.

KEYWORDS

sperm motility, collective dynamics, rheotaxis, female reproductive tract, viscoelastic fluid

Introduction

Collective swimming of sperm is widespread in mammalian species such as in cattle (Woolley et al., 2009; Nosrati et al., 2015; Tung et al., 2017), mice (Moore et al., 2002; Fisher and Hoekstra, 2010; Qu et al., 2021), opossums (Rodger and Bedford, 1982; Moore and Taggart, 1995), guinea pigs (Martan and Shepherd, 1973; Flaherty et al., 1993), and sheep (Creppy et al., 2013; David et al., 2015). Collective motion of sperm exists in various forms, including motile trains, massal motility, pairs, and dynamic clusters (Schoeller

et al., 2020; Tung and Suarez, 2021). So far, the emergence of collective motion in mammalian sperm can be attributed to factors such as physical attachment (Moore and Taggart, 1995; Moore et al., 2002; Fisher et al., 2014), high concentrations of sperm (Schoeller et al., 2020), and viscoelasticity of the fluid in which sperm swim (Tung et al., 2017). For example, in the wood mouse (*Apodemus sylvaticus*), the sperm head has a hook that physically attaches to another sperm head or flagellum, resulting in motile sperm trains (Moore et al., 2002). These trains can be composed of hundreds to thousands of sperm, and they swim faster than individually swimming sperm. Several sperm with their heads conjoined together are also found to swim at a higher speed (Fisher and Hoekstra, 2010). In these cases of sperm physically attached to each other, the collective movement offers the advantage of moving sperm more quickly. Meanwhile, some collective dynamics of sperm do not require physical attachment between sperm. For example, massal motility is seen in undiluted samples of semen, where thousands to millions of sperm swim together to form mass wave-like motions in the fluid (Creppy et al., 2015). Sperm caught up in the wavelike motions have been associated with increased fertility outcomes (David et al., 2015), while the mechanism for such enhancement has remained unknown.

We previously reported dynamic clustering of bull sperm in a medium that mimics the viscoelasticity of some fluids in the female tract (Tung et al., 2017). Bull sperm in dynamic clusters are not physically attached to each other. When in a dynamic cluster, the sperm swim closely to each other and align in the same direction. Sperm freely leave and join various clusters over time (Tung et al., 2017). Unexpectedly, we found that the swimming speeds of sperm in clusters were not faster than the speeds of individually swimming sperm (Tung et al., 2017), leaving how this clustering behavior benefits sperm migration in the female tract unclear. Nevertheless, there may be other ways in which dynamic clustering may provide an advantage to migrating sperm in the female reproductive tract. In this study, we examined the progressivity of clustered sperm and the ability of sperm to swim against a flow of highly viscoelastic fluid, which occurs in the female reproductive tract (Suarez and Pacey, 2006; Lai et al., 2009; Suarez, 2016; Li et al., 2021).

Viscoelasticity occurs when a fluid contains components much larger than the solvent molecules, such as long polymers dissolved in water. A typical fluid that lacks viscoelasticity, such as a simple saline solution in water, does not retain a shape of its own, but rather acquires the shape of its container. Its viscosity is constant and independent of a stress applied upon the fluid. In contrast, the elasticity of a viscoelastic fluid, such as mucus that fills part of the female reproductive tract (Suarez and Pacey, 2006; Riley and Lauga, 2014; Li et al., 2021), varies depending on the stress applied on the fluid. Viscoelastic fluid also has a tendency to return to its previous shape within a short time scale when a stress is released (Barnes et al., 1989). *In vivo*, viscoelastic fluid flows in some parts of the female reproductive tract, such as mucus in the cervix, and sperm are required to swim against flows of viscoelastic fluid in order to fertilize the eggs (Suarez, 2016). Most previous studies of how fluid flow orients sperm migration or produces rheotaxis (swimming against a flow) (Bukatin et al., 2015; Zhang et al., 2016) have focused more on the flow of low-viscosity medium (Miki and Clapham, 2013; Tung et al., 2014, 2015a). Here, we aimed to examine how bull sperm, which have similar dimensions as human sperm, swim under flows of highly viscoelastic fluid, particularly whether sperm undergo rheotaxis to move against flows of viscoelastic fluid. We tested the hypothesis that *clustering of bull sperm increases the progressivity and rheotactic capabilities of sperm swimming in viscoelastic fluids.*

We used a previously developed microfluidic model (Tung et al., 2015a) that contains channels filled with a fluid that simulates the viscoelasticity of cervical mucus of cows in estrus (the fertile period of the bovine hormonal cycle). A syringe pump was used to provide well-controlled rates of fluid flow. It has been established that sperm swim in circular trajectories near a solid surface (Friedrich et al., 2010; Tung et al., 2015a), so we used the trajectory curvature of individual vs. clustered bull sperm under no flow as a quantitative tool to examine the progressivity of sperm movement. Further, we compared the responses of clustered vs individually swimming sperm in the presence of various rates of fluid flows.

Materials and methods

Media preparation

Tyrode Albumin Lactate Pyruvate (TALP) medium (Parrish et al., 1988) was prepared as a standard medium for bovine sperm. TALP medium is comprised of 99 mM NaCl, 10 mM HEPES free acid, 3.1 mM KCl, 0.39 mM NaH_2PO_4, 25 mM $NaHCO_3$, 25.4 mM sodium lactate, 2 mM $CaCl_2$, 1.1 mM $MgCl_2$, 1 mM of sodium pyruvate, 5 mg/L of Gentamycin and 6 g/L of Bovine Serum Albumin (BSA). The final pH of the TALP medium was titrated to 7.42 with 1 N NaOH. Viscoelastic fluid was prepared by dissolving 0.7% of long-chain polyacrylamide (LC-PAM, 5–6 MDa) in TALP and with gentle magnetic stirring and alternating between room temperature and refrigeration for approximately 5 h, or until no clumps were observed within the fluid. This 0.7% PAM solution has comparable rheology to estrous bovine cervical mucus (Tung et al., 2015b). In preparation for experiments, the media were incubated at 38.5°C (bovine core body temperature) under 5% CO_2 in humidified air for at least 2 h prior to adding sperm.

Bovine sperm sample preparation

Frozen bovine semen provided by Genex Cooperative, Inc. (Ithaca, NY, United States) was extended in OptiXcell and transferred to 0.5 ml plastic straws (50 million sperm/straw) using their standard procedures (Kaproth et al., 2005). The straws were stored in liquid nitrogen. For sperm sample preparation, the straws were thawed in a 37°C water bath for 30 s. The thawed fluid was then centrifuged through two layers (40% and 80%) of Bovipure in Bovidilute solution, Spectrum Technologies, Inc., Healdsburg, CA, United States) at 300 x g for 10 min. Next, after removing the supernatant, the pellet was diluted in 3 ml of TALP and centrifuged at 300 x g for 3 min. The supernatant was removed and the sperm pellet was resuspended in 20 μL TALP medium and incubated at 38.5 °C under 5% CO_2 in humidified air. All the experiments were carried out independently using the two frozen semen straws from three different bulls.

Microfluidic device fabrication

Silicon master mold fabrication was performed using the microfluidic design adapted from a previously developed microfluidic device (Tung et al., 2014). The silicon master consisted of a channel 4 cm long, 2.47 mm wide, and 120 μm deep. The description of our microfluidic device setup can be found in Supplementary Figure S3. The casting of microfluidic devices in polydimethylsiloxane (PDMS) was as follows: 10: 1 base to curing agent mixture of PDMS (SLYGARD 184 Silicone Elastomer kit, Dow Corning, Midland, MI, United States) were poured onto the fabricated silicon master, followed by degassing the PDMS mixture in an evacuated desiccator chamber for 30 min and curing at 65°C for 1 h. To make a sperm seeding port and a fluid input port, respectively, a 2 mm hole and a 1 mm hole were made in the PDMS pieces using Sklar Tru-Punch disposable biopsy punches (Sklar, West Chester, PA, United States). The PDMS pieces were bonded to glass slides using oxygen plasma cleaner (HARRICK PLASMA, PDC-32G, Ithaca, NY, United States) in a high RF power setting for 60 s. The microfluidic device channel was filled with viscoelastic 0.7% PAM in TALP medium and was equilibrated at 38.5 °C under 5% CO_2 in humidified air before performing experiments.

Addition of sperm to device

Two straws of frozen bovine semen (50 million sperm/straw) from one bull were used in each experiment. The sperm were prepared as described above. An aliquot of 5 µl sperm suspension was seeded 2–3 times to populate the device chamber. Sperm were allowed to swim out of the suspension into the viscoelastic medium for 30–45 min. Then videos were made of sperm swimming 3–5 mm from the seeding port, close to the center of the 2.47 mm wide channel. In this region of the channel, the sperm concentration was 2.95–5.54 million sperm/ml. Note that sperm were predominantly found on the channel surfaces, as expected, instead of being uniformly distributed.

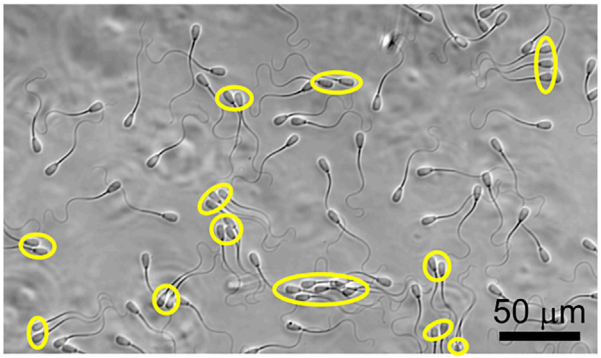

FIGURE 1
Coexistence of individually swimming and clustered sperm. Clustered sperm are labeled with yellow ovals.

Flow ranges and experimental setup

Tubing (ETT-24, Weico Wire & Cable) connected to a 1 ml syringe (BD, Franklin Lakes, NJ, United States) was inserted into the 1 mm fluid inlet port of a microfluidic device filled with 0.7% PAM viscoelastic fluid and the device was placed in an on-stage environmentally controlled chamber (operated by OKO-Touch) heated to 38.5 °C and humidified to 65% on a Nikon Eclipse inverted microscope. Then, 5 μl sperm suspension was seeded 2–3 times into the 2 mm seeding port, and the device was incubated for 30–45 min on the stage to allow sperm time to swim into the polymer solution until the sperm count was similar to that in Figure 1. This procedure was used to maintain the rheological properties of the polymer solution. Next, the syringe pump (KDS-230, KD Scientific, Holliston, MA, United States) was used to provide flow rates ranging from 0 to 5 μl/min (equivalent to 0–13.5 1/s shear rates). The syringe pump was kept running for ≈60 s to establish a stable fluid flow condition during the experiment. Each experiment lasted 2–2.5 h.

Analysis of sperm orientation and trajectory curvature

An Andor Zyla digital video camera and 20x objective (S Plan Fluor ELWD) were used to record phase-contrast images of sperm swimming on the lower surface of the microfluidic device

chamber under a range of fluid flow rates. NIS Element BR software was used to control recording at 6.67 frames/sec and to view image files. The duration of each recorded video was 1 min. The recordings were used to compare movements of individually swimming sperm with those of sperm in clusters. To analyze sperm orientation at a given moment, all sperm in one still image were manually tracked using the straight-line tracking tools in ImageJ software. All sperm within a frame were tracked, and once sperm orientation reached a steady-state, several frames were analyzed to improve statistics.

To analyze individually swimming sperm trajectories, each sperm was manually tracked for 3.6 s using the Manual Tracking plugin in ImageJ and the tracks were plotted using MATLAB. For clustered sperm, one sperm out of each cluster of 2-4 sperm was manually tracked for 3.6 s, as described for individual sperm. This selection of small clusters was made for technical practicalities. First of all, we needed a trajectory to be long enough to see if it is curved or not. However, since sperm were not bound to each other in our dynamic clusters, they were free to dissociate from the cluster to become individual during the period being tracked. We found that sperm in clusters of more than 4 sperm often left the clusters in less than 3.6 s therefore could not be part of the analysis. The curvature of each trajectory was determined by fitting location data points (x, y) in to a circle (defined as $x^2 + y^2 + ax + by + c = 0$) to compute the radius of curvature by using the "fitnlm" function of MATLAB. The coordinate for the center of each circle was $(h, k) = (-a/2, -b/2)$ and the radius (R) was given by $R = \sqrt{(h^2 + k^2 - c)}$. To get all points on the circumference of the circle, we used the parametric equation of a circle defined as: $(X, Y) = (R\cos\theta + h, R\sin\theta + k)$, where $\theta = atan2(y - k, x - h)$, where atan2 is a MATLAB function for arc tangent (https://www.mathworks.com/matlabcentral/answers/559322-fitting-a-circle-with-fitnlm#comment_924827).

Analysis of sperm clustering and responses to a flow

Two sperm were defined as swimming within the same cluster when their head orientations were within 20° and the sperm were separated by less than 17.5 μm. This definition was consistent with previous work Tung et al. (2017). The overall behaviors were not sensitive to the exact definition. When we assessed videos of sperm swimming in a flow, some sperm swam upstream, some swam downstream, some were pushed back, and some were swept downstream. Each classification was made based on 80 consecutive frames (12 s) of the videos, and only live sperm cells were counted during the analysis. We categorized sperm as swimming downstream when they were swimming in the direction of the flow (Figure 5B, Supplementary Video S2) throughout the 12 s long video. Sperm were considered to be swept away when they initially swam against the fluid flow and their orientation changed toward downstream during the 12 s video (Figure 5C, Supplementary Video S3). Sperm were considered to be pushed back (Figure 5A, Supplementary Video S1) when they were not moving forward over the course of the 80 frames while maintaining upstream orientation. We chose this definition of pushed back to avoid repeated measurements of the same sperm. Since swimming downstream, swept downstream, or pushed back sperm were not moving forward against a flow, they would be jointly referred to as "failing in rheotaxis". In each individual or clustered category, the percentages of rheotaxis failure were calculated by adding downstream swimming, swept downstream, and pushed back sperm, and dividing by the total individual or clustered sperm.

Statistical analysis

All error bars denote standard errors of the mean (SEM) unless otherwise noted. p-values less than 0.05 were considered to be statistically significant. The differences in histogram distribution were calculated using the two-sample Kolmogorov Smirnov (K-S) test. A t-test was performed in Excel to detect differences between the means, and a two proportion z-test was conducted to find differences between two proportions. All data were analyzed using MATLAB software unless otherwise noted.

Results

In the absence of a flow, the swimming of clustered sperm was more directional than that of individually swimming sperm

In Figure 1, we show the co-existence of individually swimming and clustered sperm, and compared the swimming trajectories of individually swimming and clustered sperm when there is no flow in Figures 2A,B. Note that, since roughly half of the sperm were found in clusters and the other half were found swimming individually at a given moment, the analyses on the two populations were obtained from the same videos. The majority of the clustered sperm comprised 2-4 cells, and each trajectory was 3.60 s long. The swimming track length of individually swimming sperm (Figure 2A) appeared to extend slightly further than the track length of clustered sperm (Figure 2B), which was verified by statistical analysis in Supplementary Figure S1 ($p < 0.05$ by two tailed t-test). This is in agreement with a previous study that clustered sperm on average swim at a slower speed than individual sperm (Tung et al., 2017).

Clustered sperm trajectories appeared to be more straight than those from individually swimming counterparts. To verify this, we computed radius of curvature (R) for each trajectory through curve fitting (Figure 2C inset), and then compared the distributions from

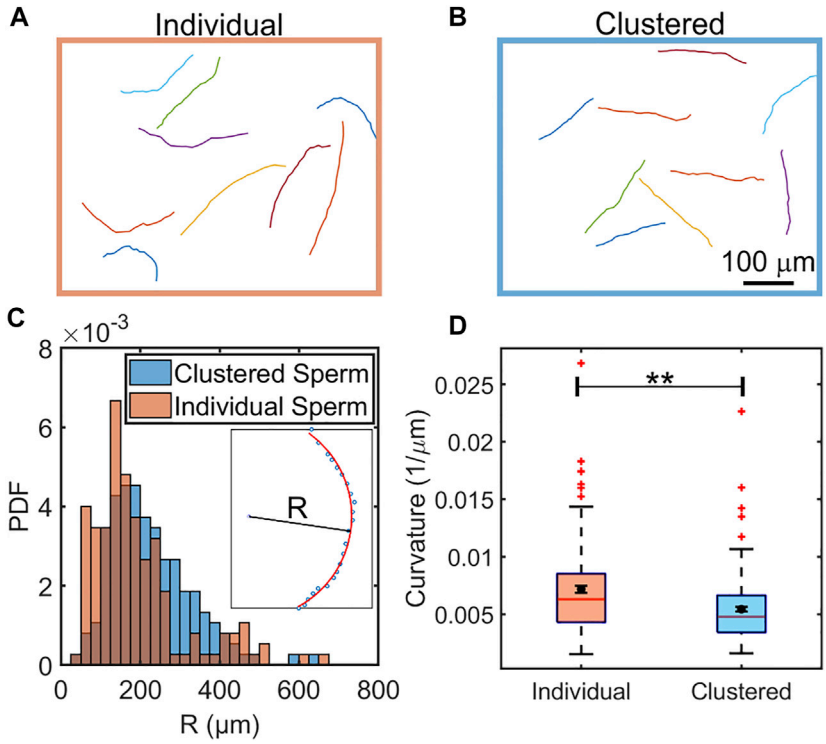

FIGURE 2
Comparison of swimming trajectories of individual **(A)** and clustered **(B)** sperm in the absence of flow. N = 9 sample trajectories, each sampled at 6.67 Hz and for 3.60 s. The distributions of radii of curvature of clustered (blue) and individual (orange) sperm from 150 trajectories each **(C)**. Inset: Calculation of the R was performed by fitting a trajectory to a partial circle using MATLAB. **(D)**, Box plot comparison of curvature of individual and clustered sperm. The means are shown by a black dot. The box plot shows the median, 25%, and 75% quartiles; whiskers show the smallest and largest data within 1.5 interquartile ranges below 25% and above 75% quartiles respectively; data beyond the whiskers are outliers and shown by +. N = 150 trajectories each sampled at 6.67 Hz and for 3.60 s. Error bars represent standard errors of the mean (SEM) and **indicates $p < 0.01$.

the two populations (Figure 2C). We found that the two distributions of the radius of curvature (R) were significantly different ($p < 0.001$ by two sample K-S test). Likewise, the mean and median of the trajectory curvatures ($1/R$) of clustered sperm were also found to be less than those of individually swimming sperm ($p < 0.01$ by two tailed t-test), as shown in a box plot (Figure 2D). The comparison of radii of curvature (R) and the logarithm of radii ($\ln R$) were likewise significantly different ($p < 0.01$ for R and $p < 0.001$ for $\ln R$ by two tailed t-test), as shown in Supplementary Figure S2. We concluded that, in a viscoelastic fluid, clustering enables sperm to swim straighter (more progressively) than when sperm swim individually.

Emergence of sperm rheotaxis in a highly viscoelastic fluid differed from that of sperm in a low-viscosity fluid

Emergence of rheotaxis in sperm has been quantitatively explained by a hydrodynamic model (Kantsler et al., 2014; Tung et al., 2015a), so we examined whether a similar mechanistic model applies when sperm swim in a flow of highly viscoelastic fluid. Similar to sperm rheotaxis in a low-viscosity medium, sperm swam upstream within certain flow rates in a high-viscoelastic fluid, as shown in Figure 3A. However, some of the trajectories shown in Figure 3A were harder to reconcile with the existing mechanistic model (Tung et al., 2015a). According to the existing model, when sperm swim close to a solid interface in a flow, the broad sperm head experiences more hydrodynamic resistance than the narrow sperm tail. This causes the tail to swing around toward the downstream direction, thereby orienting the sperm to swim upstream. Under this model, sperm exhibit curved trajectories when swimming toward a downstream direction (while turning toward upstream), while upstream swimming sperm exhibit linear trajectories while swimming near a wall (Tung et al., 2015a). In the highly viscoelastic fluid, we observed linear upstream swimming trajectories. However, in contrast to the model, we also found sperm swimming downstream in linear trajectories in the highly viscoelastic fluid (Figure 3A). Whereas the number of these unexplained trajectories was not high (3 out of 50), their existence indicated that modifications are needed to the

mechanistic model in order to account for linear downstream swimming. Note that, in our microfluidics device, nearly all sperm swim close to surfaces soon after they are introduced into the channel and we were tracking sperm that were swimming close to the bottom surface of the channel.

It has been understood that the onset of upstream swimming occurs in a low-viscosity fluid when a flow exceeds a certain threshold flow rate (Tung et al., 2015a). After the onset, the upstream trajectories become linear. We also show here that, unlike in low-viscosity fluid, there is no clear onset of the emergence of upstream swimming in highly viscoelastic fluid.

Figure 3B illustrates the average sperm orientation under various flow rates for clustered, individual, and all sperm. In the absence of flow, sperm appeared to swim in all directions in Figure 3D. We calculated the average sperm orientation by assigning a unit vector to the direction of each sperm, and then averaged the component of presumed upstream direction $\langle S_x \rangle$ and the component in the perpendicular direction $\langle S_y \rangle$. When there was no flow, $\langle S_x \rangle = 0.03 \pm 0.01$ (mean ± SEM, N = 3,033), which agreed with the expectation of random orientation. $\langle S_x \rangle$ gradually and steadily increased with a flow rate from 0.3 to 1.2 μl/min.

From the sperm trajectories in Figures 2A,B, we found sperm orientation turned in both clockwise (CW) and counter-clockwise (CCW) directions (viewed from above), which was also a departure from what has been seen in low-viscosity medium (Miki and Clapham, 2013; Kantsler et al., 2014; Tung et al., 2015a). Applying the existing mechanistic model (Tung et al., 2015a), once sperm locked into the upstream (x) direction, we would anticipate seeing them swimming in either direction (±y) perpendicular to the flow. Indeed, upstream trajectories were found on both upper and lower quadrants to the left side of Figure 3A. Further, when we computed $\langle S_y \rangle$, all values were close to 0 (Figure 3C).

Clustered sperm exhibited better rheotactic responses than individual sperm

It has been known that rheotaxis response occurs within a specific range of flow speeds, as few sperm orient upstream under a weak flow, and most are swept away by a strong flow (El-Sherry et al., 2014; Tung et al., 2014; Zaferani et al., 2018; Ataei et al., 2021). We found that, under a flow rate expected to induce rheotaxis, clustered sperm exhibited a stronger rheotactic response than individually swimming sperm. First, as the flow rate increased to 0.9 and 1.1 μL/min (Figure 3B), it could be seen that clustered sperm were more oriented against the flow than were individual sperm ($p < 0.0001$ by two tailed t-test). To further illustrate the effects, three measures were used to make this comparison: probability distribution of sperm orientation, upstream components of sperm orientation, and percentage of sperm oriented upstream. We also compared these three measures against no flow as a control to show that the differences found between clustered and individual swimming sperm were results of the externally applied flow. In the absence of flow, the orientation angle distributions in clustered and individual sperm were nearly flat and similar ($p > 0.05$ by two sample K-S test (Figure 4A). In contrast, at 1.5 μl/min flow, the orientation angle distribution of clustered sperm showed a more pronounced peak in the upstream direction ($\theta = 0^{\circ}$) than orientation of individual sperm ($p < 0.0001$ by two sample K-S test, Figure 4B).

In the absence of flow, clustered and individual sperm showed means and medians of S_x that were close to 0 and only slightly different ($p = 0.0434$ by two tailed t-test, Figure 4C). Here, the differences in the statistics of S_x between clustered and individual sperm with no flow arose from the larger variability of data among clustered sperm. In the case of individual sperm statistics, $S_x = 0$ is obtained from averaging across sperm of all orientations. In the case of clustered sperm, each cluster had several sperm oriented in the same direction, therefore several fold more sperm were required to achieve the same level of accuracy as achieved for individually swimming sperm. When we analyzed all the sperm from the same frame, which led to similar numbers of individual and clustered sperm, the mean for clustered sperm fluctuated more than within the individual sperm (Figure 4A). The means and medians of S_x with a 1.5 μL/min flow rate in clustered and individual sperm showed significant differences between them ($p < 0.0001$ by two tailed t-test, Figure 4D). These results showed that clustered sperm were more oriented against the flow than individual sperm. Likewise, under no flow, the percentages of sperm swimming to the left (that is, the upstream direction in the device when a flow is applied) were 47 ± 1% (mean ± SEM) for individual sperm vs. 46 ± 1% for clustered sperm ($p > 0.05$ by two proportion z-test, Figure 4E), which was close to 50% of the ideal value when sperm are uniformly distributed in all directions. The percentages of upstream swimming with a 1.5 μL/min flow was 58 ± 1% for individual sperm and 82.1 ± 0.9% for clustered sperm ($p < 0.0001$ by two proportion z-test, Figure 4F). All of the above results show that clustered sperm responded to an intermediate flow by swimming against the flow better than individually swimming sperm.

Clustering reduced the numbers of sperm swept downstream by strong flows

We examined whether clustering protects sperm from being swept downstream by a strong flow. We categorized three types of sperm behaviors when they failed to swim into a strong flow of viscoelastic fluid: (1) sperm that were pushed back by the flow while maintaining upstream orientation (Figure 5A), (2) sperm that swam in the downstream direction (Figure 5B), or (3) sperm

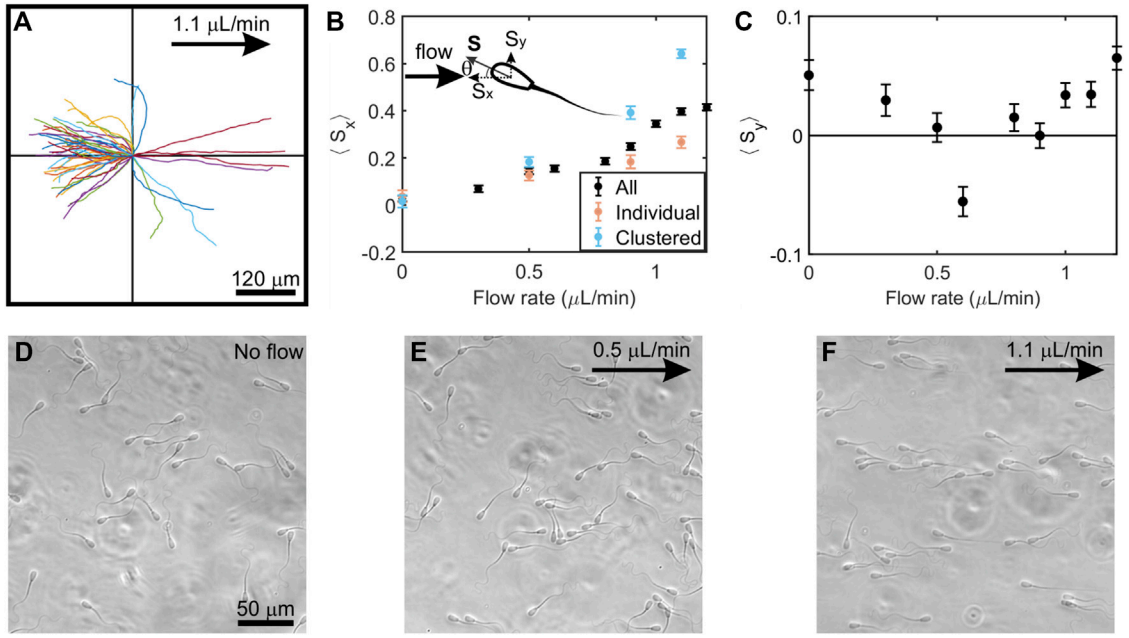

FIGURE 3
Behavior of sperm swimming in a low-speed flow of viscoelastic fluid. **(A)**, In a 1.1μl/min flow, sperm showed linear trajectories when swimming both upstream (upper and lower left quadrants) and downstream (upper and lower right quadrants) (N = 50 trajectories; each trajectory is 4.5 s long) **(B)**, The vector mean of the orientation of all sperm, clustered, and individual sperm along the x-axis ($\langle S_x \rangle$) at increasing flow rates. Upper left: schematic of sperm head orientation denoted by a unit vector **S**, where θ is the angle to the x-axis. S_x and S_y is an orientation of sperm along the x-axis and y-axis respectively. $\langle S_x \rangle = 0$ implies random swimming along the x-axis while $\langle S_x \rangle = 1$ implies perfect alignment of sperm in x-axis. **(C)**, The vector means of the orientation of all sperm along the y-axis ($\langle S_y \rangle$) at increasing flow rates. Three experiments (n = 3) from semen samples of three bulls were carried out, and each point represents N ≈ 800–1,100 tracked sperm cells. Each data point in the figure denotes the mean of three experiments and error bars represent the standard errors of the mean. **(D)**, **(E)**, **(F)**, Photo micrographs (264 × 264 μm) of sperm swimming at no flow, 0.5 μL/min, and 1.1 μL/min, respectively. Flows are applied toward the positive x-direction and denoted by an arrow.

that changed orientation from upstream into downstream as they were swept downstream (Figure 5C). Here, we compared the percentages of sperm exhibiting one of the three behaviors that failed in rheotaxis between clustered and individually swimming sperm under a strong flow of 1.5–5.0 μL/min flow rates (or 4.05–13.5 1/sec shear rates) within a time interval of 12 s. Note that we did not observe sperm being swept downstream or pushed back under a flow below 1.5 μl/min.

Figure 5D shows the percentages of pushed back sperm. Unsurprisingly, the percentage increased as the flow rate increased. We did not observe significant differences between clustered and individual sperm. Figure 5E shows the percentages of individual vs. clustered sperm exhibiting downstream swimming. The percentage of individual sperm swimming downstream (range, 23–29%) was significantly greater than that of clustered sperm (range, 4–9%) ($p < 0.0001$ by two proportion z-test), suggesting that clustering promoted sperm upstream orientation under a strong flow. Figure 5F shows the percentages of sperm swept downstream by strong flows. At each flow rate, the percentages of clustered sperm that were swept downstream were significantly lower than those of individual sperm ($p < 0.001$ by two proportion z-test), indicating that clustering protected sperm from being swept downstream.

Combining all three types of failure to undergo rheotaxis (pushed back, downstream swimming, and swept downstream) in Figure 5G, at each flow rate, we found that clustered sperm had roughly a 20% lower rate of failing ($p < 0.0001$ by two proportion z-test). Overall, these results suggested that clustering protects sperm from being moved downstream by fluid flow.

Discussion

Our results support our hypothesis that clustering of bull sperm increases the progressivity and rheotactic capabilities of sperm swimming in viscoelastic fluids. This indicates that clustering benefits sperm migrating to the egg in the female reproductive tract. Here, we identified the benefits of clustering under three different flow ranges. In the absence of flow, clustering enabled sperm to swim more progressively. Under an intermediate flow that induced upstream swimming, clustering oriented sperm to achieve better rheotactic

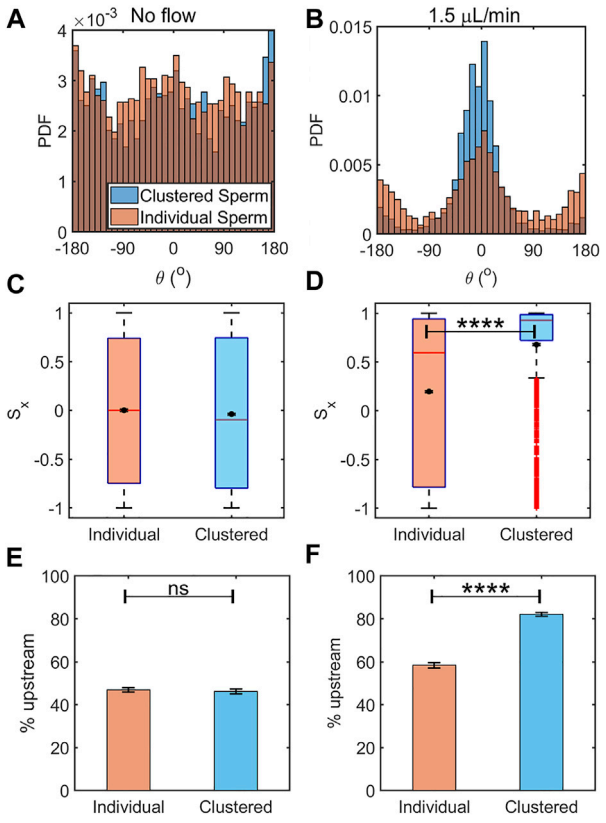

FIGURE 4
Clustered sperm exhibited greater rheotactic responses than individual sperm. Histogram of orientation angle between the clustered and individual sperm in the absence of flow **(A)** (N ≈ 2,800 cells for each) and under an intermediate flow rate of 1.5 μL/min **(B)** (N ≈ 2,900 cells for each). Box plot along with mean of the sperm upstream orientation component (S_x) under no flow **(C)** and an intermediate flow rate of 1.5 μl/min **(D)**. The means are shown by a black dot. The box plot shows the median, 25%, and 75% quartiles; whiskers show smallest and largest data within 1.5 interquartile ranges below 25% and above 75% quartiles respectively; data beyond the whiskers are outliers and shown by +. Percentages of sperm oriented upstream, individual vs. clustered sperm under no flow **(E)** (N ≈ 4,300 cells) and flow rate of 1.5 μL/min **(F)** (N ≈ 3,500 cells). The error bars represent the standard errors of the mean (SEM), ns: not significant, and ****: $p < 0.0001$).

responses. Under a strong flow that was capable of moving sperm downstream, clustering provided protection for sperm from being carried downstream by the flow. Our results predict that clustered sperm are more likely to swim upstream and are more aligned than individual sperm against flows *in vivo*.

Furthermore, we showed that the current mechanistic model for the emergence of upstream swimming of sperm (Tung et al., 2015a) requires modification in order to account for the behavior of sperm in a flow of a highly viscoelastic fluid. Specifically, in highly viscoelastic fluid, we found a lack of a distinct onset of rheotaxis in sperm. The absence of a distinct onset in upstream swimming could be explained by the variability in sperm circular trajectories in highly viscoelastic fluid. Some sperm in highly viscoelastic fluid swam in linear trajectories, which would cause the onset of upstream swimming to be 0. In low viscosity medium, the origin of the onset of upstream swimming is from circular trajectories of sperm (Tung et al., 2015a). The constant turning that leads to the circular trajectories prevents sperm from aligning against the flow. The flow alignment needs to be strong enough to break this circling in order to lock sperm into a consistently upstream direction. Without the circular trajectory in the first place, any flow alignment is sufficient to orient sperm upstream. Combined with the fact that clustered sperm exhibited more linear (less curved) trajectories than individual sperm, upstream swimming was also triggered more readily for clustered than individual sperm. The above observations can be explained well by the existing mechanistic models (Kantsler et al., 2014; Tung et al., 2015a). However, we also found that, in highly viscoelastic medium, a few sperm swam downstream in linear trajectories. A possible explanation derives from the observations is as follows. Sperm in highly viscoelastic fluid propel themselves via planar flagellar beating (Tung et al., 2017; Walker et al., 2020), while, sperm in low-viscosity fluid commonly rotate along the long axis while swimming. Sperm are also known to swim much closer to a solid surface in a highly viscoelastic fluid than in low viscosity fluid (Nosrati et al., 2015). Altogether, the two-dimensional beating and the closeness of the sperm flagellum to the wall may result in the tail experiencing similar or higher hydrodynamic resistance than that experienced by the head, thereby interrupting the turning of head-to-tail orientation that leads to the curved trajectory. More studies on the hydrodynamic interaction between the sperm head/tail and a solid interface will be needed in order to better understand this phenomenon.

Regarding the linearity (progressivity) of clustered sperm trajectories, it has been known that mouse sperm in the genus *Peromyscus*, which cluster by attaching head-to-head, swim with greater linearity than do individually swimming sperm (Fisher et al., 2014). At the same time, it has been shown that flagellar synchronization can be observed among 2-4 sperm with their heads conjoined together (Woolley et al., 2009), which has been found to enhance swimming velocity over that of individually swimming sperm. Likewise, opossum sperm (*Monodelphis domestica*) physically attach head-to-head to form pairs that swim straighter than individual sperm, and that paired sperm swim efficiently in highly viscous fluids (Moore and Taggart, 1995). Here, we showed that bull sperm swimming collectively without physically attaching to one another are affected similarly as sperm that attach physically to each other. This suggests that enhancement of sperm movement progressivity through collective dynamics may be widely observed across different species, but has not yet been recognized because it is a more subtle behavior than sperm physically joining to one another. The mechanistic understanding of this enhancement remains to

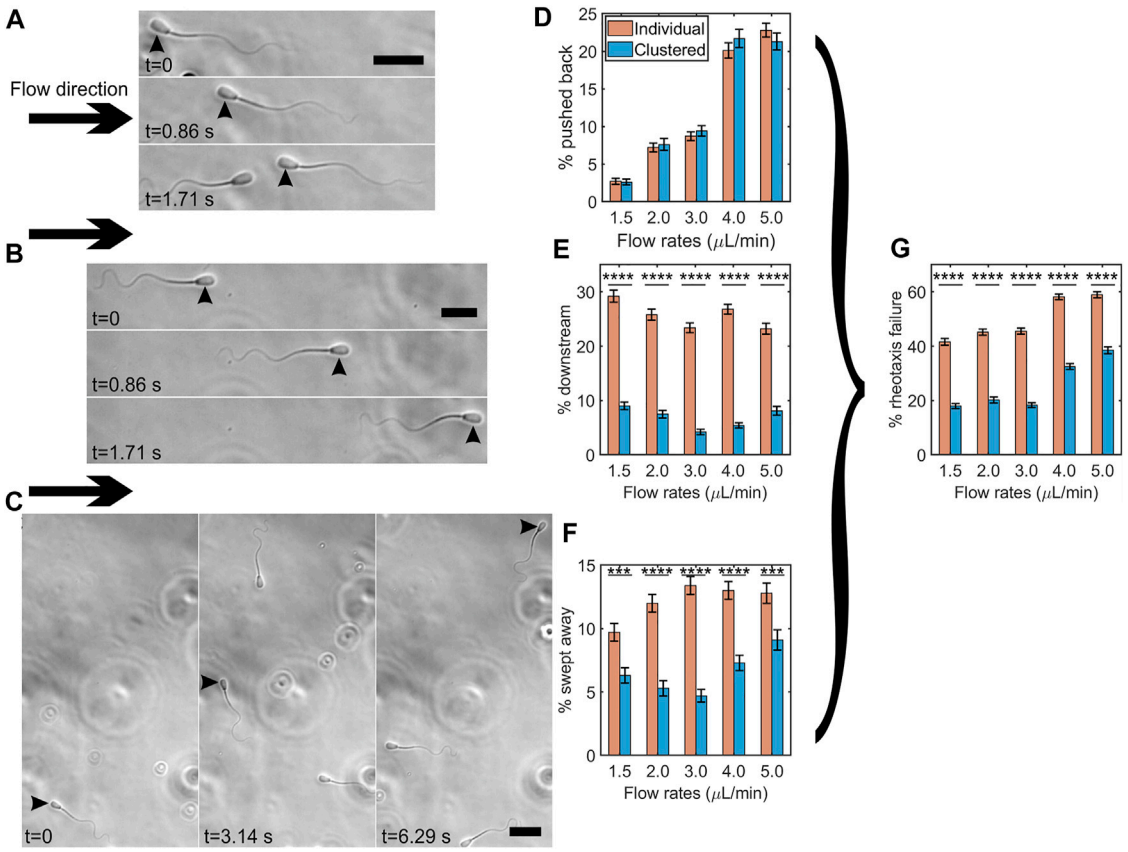

FIGURE 5
Clustering protected sperm from being swept downstream by a strong flow. Time lapse montage of bovine sperm being pushed back **(A)**, swimming downstream **(B)**, and being swept away **(C)** under a flow of 5.0 μl/min. Flow direction is shown by arrows and the sperm showing the specific behavior is indicated by arrowheads. Scale bar = 25 μm. Percentages of individual vs. clustered sperm being pushed back **(D)**, swimming downstream **(E)**, and being swept away under different flow rates **(F)**. Percentages of individual vs. clustered sperm undergoing rheotaxis failure under different flow rates **(G)**. The error bars represent the standard error of the mean (SEM, N ≈ 3,200–4,300 cells per bar), ***: $p < 0.001$, and ****: $p < 0.0001$. (p = 0.91, 0.64, 0.42, 0.21, and 0.30 for 1.5, 2.0, 3.0, 4.0, and 5.0 μl/min respectively for the % of pushed-back sperm by two proportion z-test).

be understood, although it is useful to point out that opossum sperm swimming collectively exhibit lower amplitude flagellar bends than individually swimming sperm (Moore and Taggart, 1995), which may lead to less directional change over each beat cycle, therefore a more progressive trajectory. It has also been reported that the directional fluctuation of a cluster of *Peromyscus* mouse sperm is less than that of individual sperm (Fisher et al., 2014), resulting in greater linearity of clustered sperm trajectories.

Results in this study highlight the significance of studying sperm motility in a fluid environment that resembles the mucus sperm naturally encounter in the female reproductive tract (Lai et al., 2009; Tung et al., 2015b). Our results predict that clustered sperm have a better chance to swim upstream and are more aligned than individual sperm against the flow *in vivo*. Although there is strong evidence that rheotaxis provides an effective guiding mechanism for mammalian sperm (Miki and Clapham, 2013; Kantsler et al., 2014; Tung et al., 2015b; Zhang et al., 2016), it has also been known that flows stronger than what sperm can overcome exist *in vivo* (Overstreet and Cooper, 1978). While microgrooves in microfluidic devices that mimic microgrooves in the wall of the cervix have been found to protect bull sperm from being swept downstream by a strong flow (Tung et al., 2014), such microgrooves are not ubiquitous throughout the mammalian female reproductive tract. For example, the endometrium of the mammalian uterus typically lack microgrooves, even though strong flows exist due to muscle contraction (Overstreet and Cooper, 1978; Tung and Suarez, 2021). While comparing the percentages of rheotaxis failure between clustered and individual sperm at different flow rates, we found that individual sperm failed in rheotaxis more often than the clustered sperm, indicating that clustered sperm are better positioned to remain swimming against a strong flow.

The strength of the rheotactic response has been related to male fertility. Human sperm from samples showing greater positive rheotaxis were demonstrated to have more normal morphology and better genomic quality (De Martin et al., 2017; Ataei et al., 2021; Sharma et al., 2022). Recently, it was reported that rheotaxis success of bull sperm was positively correlated with bull fertility (Yaghoobi et al., 2022). Similarly, it has been observed that the selection of rheotactic *Mus musculus* mouse sperm *in vitro* increased fertilization success and quality of early embryonic development (Romero-Aguirregomezcorta et al., 2021). Given our results indicating that clustered sperm have improved rheotactic responses, it would be worth investigating the relationship between clustering of sperm in viscoelastic medium to other types of assessments of male fertility. In addition, whether the directional movement of sperm through collective swimming selects certain genetic traits remains to be seen, although it is interesting to point out that some motility features have been linked to advantages such as DNA integrity (Nosrati et al., 2014; Riordon et al., 2019).

From cervix to oviduct, the fluid that fills the female reproductive tract is viscoelastic in nature (Tung et al., 2015b; Striggow et al., 2020); therefore, sperm encounter the mechanical environment required for forming dynamic clusters *in vivo* (Tung et al., 2017). The other requirement for clustering is a high concentration of sperm, such as concentrations found in semen (Tung et al., 2017; Schoeller et al., 2020). During coitus in humans and cattle, the male deposits semen in the anterior vagina at the entrance to the cervix, where sperm quickly enter viscoelastic cervical mucus flowing out of the cervical canal (Sobrero and MacLeod, 1962). In cattle, it has been documented that the cervical walls are lined with microgrooves that provide preferential pathways for sperm to pass through the cervix into the uterus (Mullins and Saacke, 1989). These pathways also shield sperm from the fastest outflow of mucus, which occurs in the center of the main cervical canal. Because dynamic clustering of sperm enhances rheotaxis of sperm, we propose that clustering assists bull sperm in swimming upstream through the outflow of cervical mucus until they reach the microgrooves (Tung et al., 2015b). Dynamic clustering may also assist sperm upstream swimming in other species and in other regions of the female tract, such as the uterotubal junction that connects the uterus to the oviduct.

Our findings indicate that collective swimming is beneficial for sperm migration, even without the physical attachment of sperm to each other. Compared to individually swimming sperm, we found that clustered sperm show better progressivity during no flow, better rheotactic behavior during an intermediate flow, and more protection against a strong flow. These results elucidate the importance of collective swimming in sperm migration against viscoelastic fluid flow within the female reproductive tract. In addition, this information is useful for designing methods and microfluidics devices for selecting sperm for *in vitro* fertilization.

Data availability statement

The original contributions presented in the study are included in the article/Supplementary Material, further inquiries can be directed to the corresponding author.

Author contributions

C-KT and SS conceived the experiments; SP conducted the experiments; SP and C-KT analysed the results. All authors contributed to the writing of the manuscript.

Funding

This work is supported by the National Institutes of Health (NIH) grant R15HD095411 to C-KT.

Acknowledgments

Bovine semen was kindly provided by Genex Cooperative (later known as URUS Group) at Ithaca, NY. The fabrication was performed using the Joint School of Nanoscience and Nanoengineering (JSNN, NSF ECCS-2025462, Greensboro, NC) and the Chapel Hill Analytical and Nanofabrication Laboratory (CHANL, NSF ECCS-2025064, Chapel Hill, NC).

Conflict of interest

The authors declare that the research was conducted in the absence of any commercial or financial relationships that could be construed as a potential conflict of interest.

Publisher's note

Supplementary material

The Supplementary Material for this article can be found online at: https://www.frontiersin.org/articles/10.3389/fcell.2022.961623/full#supplementary-material

References

Ataei, A., Lau, A., and Asghar, W. (2021). A microfluidic sperm-sorting device based on rheotaxis effect. *Microfluid. Nanofluidics* 25, 52–10. doi:10.1007/s10404-021-02453-8

Barnes, H. A., Hutton, J. F., and Walters, K. (1989). *An introduction to rheology, vol. 3*. Amsterdam, Netherlands: Elsevier. doi:10.1016/B978-0-444-87469-6.50010-X

Bukatin, A., Kukhtevich, I., Stoop, N., Dunkel, J., and Kantsler, V. (2015). Bimodal rheotactic behavior reflects flagellar beat asymmetry in human sperm cells. *Proc. Natl. Acad. Sci. U. S. A.* 112, 15904–15909. doi:10.1073/pnas.1515159112

Creppy, A. K., Plouraboué, F., Praud, O., and Viel, A. (2013). Collective motility of sperm in confined cells. *Comput. Methods Biomech. Biomed. Engin.* 16, 11–12. doi:10.1080/10255842.2013.815899

Creppy, A., Praud, O., Druart, X., Kohnke, P. L., and Plouraboué, F. (2015). Turbulence of swarming sperm. *Phys. Rev. E Stat. Nonlin. Soft Matter Phys.* 92, 032722. doi:10.1103/PhysRevE.92.032722

David, I., Kohnke, P., Lagriffoul, G., Praud, O., Plouarboué, F., Degond, P., et al. (2015). Mass sperm motility is associated with fertility in sheep. *Anim. Reprod. Sci.* 161, 75–81. doi:10.1016/j.anireprosci.2015.08.006

De Martin, H., Cocuzza, M. S., Tiseo, B. C., Wood, G. J., Miranda, E. P., Monteleone, P. A., et al. (2017). Positive rheotaxis extended drop: A one-step procedure to select and recover sperm with mature chromatin for intracytoplasmic sperm injection. *J. Assist. Reprod. Genet.* 34, 1699–1708. doi:10.1007/s10815-017-1024-1

El-Sherry, T. M., Elsayed, M., Abdelhafez, H. K., and Abdelgawad, M. (2014). Characterization of rheotaxis of bull sperm using microfluidics. *Integr. Biol.* 6, 1111–1121. doi:10.1039/c4ib00196f

Fisher, H. S., Giomi, L., Hoekstra, H. E., and Mahadevan, L. (2014). The dynamics of sperm cooperation in a competitive environment. *Proc. Biol. Sci.* 281, 20140296. doi:10.1098/rspb.2014.0296

Fisher, H. S., and Hoekstra, H. E. (2010). Competition drives cooperation among closely related sperm of deer mice. *Nature* 463, 801–803. doi:10.1038/nature08736

Flaherty, S. P., Swann, N. J., Primakoff, P., and Myles, D. G. (1993). A role for the wh-30 protein in sperm-sperm adhesion during rouleaux formation in the Guinea pig. *Dev. Biol.* 156, 243–252. doi:10.1006/dbio.1993.1073

Friedrich, B. M., Riedel-Kruse, I. H., Howard, J., and Jülicher, F. (2010). High-precision tracking of sperm swimming fine structure provides strong test of resistive force theory. *J. Exp. Biol.* 213, 1226–1234. doi:10.1242/jeb.039800

June Mullins, K., and Saacke, R. G. (1989). Study of the functional anatomy of bovine cervical mucosa with special reference to mucus secretion and sperm transport. *Anatomical Rec.* 225, 106–117. doi:10.1002/ar.1092250205

Kantsler, V., Dunkel, J., Blayney, M., and Goldstein, R. E. (2014). Rheotaxis facilitates upstream navigation of mammalian sperm cells. *Elife* 3, e02403. doi:10.7554/eLife.02403

Kaproth, M., Rycroft, H., Gilbert, G., Abdel-Azim, G., Putnam, B., Schnell, S., et al. (2005). Effect of semen thaw method on conception rate in four large commercial dairy heifer herds. *Theriogenology* 63, 2535–2549. doi:10.1016/j.theriogenology.2004.11.001

Lai, S. K., Wang, Y.-Y., Wirtz, D., and Hanes, J. (2009). Micro-and macrorheology of mucus. *Adv. Drug Deliv. Rev.* 61, 86–100. doi:10.1016/j.addr.2008.09.012

Li, G., Lauga, E., and Ardekani, A. M. (2021). Microswimming in viscoelastic fluids. *J. Newt. Fluid Mech.* 297, 104655. doi:10.1016/j.jnnfm.2021.104655

Martan, J., and Shepherd, B. A. (1973). Spermatozoa in rouleaux in the female Guinea pig genital tract. *Anat. Rec.* 175, 625–629. doi:10.1002/ar.1091750309

Miki, K., and Clapham, D. E. (2013). Rheotaxis guides mammalian sperm. *Curr. Biol.* 23, 443–452. doi:10.1016/j.cub.2013.02.007

Moore, H. D., and Taggart, D. (1995). Sperm pairing in the opossum increases the efficiency of sperm movement in a viscous environment. *Biol. Reprod.* 52, 947–953. doi:10.1095/biolreprod52.4.947

Moore, H., Dvorakova, K., Jenkins, N., and Breed, W. (2002). Exceptional sperm cooperation in the wood mouse. *Nature* 418, 174–177. doi:10.1038/nature00832

Nosrati, R., Driouchi, A., Yip, C. M., and Sinton, D. (2015). Two-dimensional slither swimming of sperm within a micrometre of a surface. *Nat. Commun.* 6, 8703–8709. doi:10.1038/ncomms9703

Nosrati, R., Vollmer, M., Eamer, L., San Gabriel, M. C., Zeidan, K., Zini, A., et al. (2014). Rapid selection of sperm with high dna integrity. *Lab. Chip* 14, 1142–1150. doi:10.1039/C3LC51254A

Overstreet, J., and Cooper, G. (1978). Sperm transport in the reproductive tract of the female rabbit: I. The rapid transit phase of transport. *Biol. Reprod.* 19, 101–114. doi:10.1095/biolreprod19.1.101

Parrish, J., Susko-Parrish, J., Winer, M., and First, N. (1988). Capacitation of bovine sperm by heparin. *Biol. Reprod.* 38, 1171–1180. doi:10.1095/biolreprod38.5.1171

Qu, Y., Chen, Q., Guo, S., Ma, C., Lu, Y., Shi, J., et al. (2021). Cooperation-based sperm clusters mediate sperm oviduct entry and fertilization. *Protein Cell.* 1, 810–817. doi:10.1007/s13238-021-00825-y

Riley, E. E., and Lauga, E. (2014). Enhanced active swimming in viscoelastic fluids. *EPL Europhys. Lett.* 108, 34003. doi:10.1209/0295-5075/108/34003

Riordon, J., Tarlan, F., You, J. B., Zhang, B., Graham, P. J., Kong, T., et al. (2019). Two-dimensional planar swimming selects for high dna integrity sperm. *Lab. Chip* 19, 2161–2167. doi:10.1039/C9LC00209J

Rodger, J., and Bedford, J. (1982). Separation of sperm pairs and sperm—Egg interaction in the opossum, didelphis virginiana. *J. Reprod. Fertil.* 64, 171–179. doi:10.1530/jrf.0.0640171

Romero-Aguirregomezcorta, J., Laguna-Barraza, R., Fernández-González, R., Štiavnická, M., Ward, F., Cloherty, J., et al. (2021). Sperm selection by rheotaxis improves sperm quality and early embryo development. *Reproduction* 161, 343–352. doi:10.1530/REP-20-0364

Schoeller, S. F., Holt, W. V., and Keaveny, E. E. (2020). Collective dynamics of sperm cells. *Philos. Trans. R. Soc. Lond. B Biol. Sci.* 375, 20190384. doi:10.1098/rstb.2019.0384

Sharma, S., Kabir, M. A., and Asghar, W. (2022). Selection of healthy sperm based on positive rheotaxis using a microfluidic device. *Analyst* 147, 1589–1597. doi:10.1039/D1AN02311J

Sobrero, A. J., and MacLeod, J. (1962). The immediate postcoital test. *Fertil. Steril.* 13, 184–189. doi:10.1016/S0015-0282(16)34447-8

Striggow, F., Medina-Sánchez, M., Auernhammer, G. K., Magdanz, V., Friedrich, B. M., and Schmidt, O. G. (2020). Sperm-driven micromotors moving in oviduct fluid and viscoelastic media. *Small* 16, 2000213. doi:10.1002/smll.202000213

Suarez, S. S. (2016). Mammalian sperm interactions with the female reproductive tract. *Cell. Tissue Res.* 363, 185–194. doi:10.1007/s00441-015-2244-2

Suarez, S. S., and Pacey, A. (2006). Sperm transport in the female reproductive tract. *Hum. Reprod. Update* 12, 23–37. doi:10.1093/humupd/dmi047

Tung, C.-k., Ardon, F., Fiore, A. G., Suarez, S. S., and Wu, M. (2014). Cooperative roles of biological flow and surface topography in guiding sperm migration revealed by a microfluidic model. *Lab. Chip* 14, 1348–1356. doi:10.1039/c3lc51297e

Tung, C.-k., Ardon, F., Roy, A., Koch, D. L., Suarez, S. S., and Wu, M. (2015a). Emergence of upstream swimming via a hydrodynamic transition. *Phys. Rev. Lett.* 114, 108102. doi:10.1103/PhysRevLett.114.108102

Tung, C.-k., Hu, L., Fiore, A. G., Ardon, F., Hickman, D. G., Gilbert, R. O., et al. (2015b). Microgrooves and fluid flows provide preferential passageways for sperm over pathogen tritrichomonas foetus. *Proc. Natl. Acad. Sci. U. S. A.* 112, 5431–5436. doi:10.1073/pnas.1500541112

Tung, C.-k., Lin, C., Harvey, B., Fiore, A. G., Ardon, F., Wu, M., et al. (2017). Fluid viscoelasticity promotes collective swimming of sperm. *Sci. Rep.* 7, 3152–3159. doi:10.1038/s41598-017-03341-4

Tung, C.-K., and Suarez, S. S. (2021). Co-adaptation of physical attributes of the mammalian female reproductive tract and sperm to facilitate fertilization. *Cells* 10, 1297. doi:10.3390/cells10061297

Walker, B. J., Phuyal, S., Ishimoto, K., Tung, C.-K., and Gaffney, E. A. (2020). Computer-assisted beat-pattern analysis and the flagellar waveforms of bovine spermatozoa. *R. Soc. Open Sci.* 7, 200769. doi:10.1098/rsos.200769

Woolley, D. M., Crockett, R. F., Groom, W. D., and Revell, S. G. (2009). A study of synchronisation between the flagella of bull spermatozoa, with related observations. *J. Exp. Biol.* 212, 2215–2223. doi:10.1242/jeb.028266

Yaghoobi, M., Azizi, M., Mokhtare, A., Javi, F., and Abbaspourrad, A. (2022). Rheotaxis quality index: A new parameter that reveals male mammalian *in vivo* fertility and low sperm dna fragmentation. *Lab. Chip* 22, 1486–1497. doi:10.1039/d2lc00150k

Zaferani, M., Cheong, S. H., and Abbaspourrad, A. (2018). Rheotaxis-based separation of sperm with progressive motility using a microfluidic corral system. *Proc. Natl. Acad. Sci. U. S. A.* 115, 8272–8277. doi:10.1073/pnas.1800819115

Zhang, Z., Liu, J., Meriano, J., Ru, C., Xie, S., Luo, J., et al. (2016). Human sperm rheotaxis: A passive physical process. *Sci. Rep.* 6, 23553–23558. doi:10.1038/srep23553

frontiers | Frontiers in Cell and Developmental Biology

TYPE Original Research
PUBLISHED 01 November 2022
DOI 10.3389/fcell.2022.1021469

OPEN ACCESS

EDITED BY
Helena Soares,
Fac. Ciências Universidade de Lisboa, Portugal

REVIEWED BY
Wallace Marshall,
University of California, San Francisco, United States
Anne-Marie Tassin,
Centre National de la Recherche Scientifique (CNRS), France
Judith Van Houten,
University of Vermont, United States

*CORRESPONDENCE
Yukinori Nishigami,
nishigami@es.hokudai.ac.jp

SPECIALTY SECTION
This article was submitted to Evolutionary Developmental Biology, a section of the journal Frontiers in Cell and Developmental Biology

RECEIVED 17 August 2022
ACCEPTED 17 October 2022
PUBLISHED 01 November 2022

CITATION
Echigoya S, Sato K, Kishida O, Nakagaki T and Nishigami Y (2022), Switching of behavioral modes and theirmodulation by a geometrical cue in theciliate *Stentor coeruleus*. *Front. Cell Dev. Biol.* 10:1021469. doi: 10.3389/fcell.2022.1021469

Switching of behavioral modes and their modulation by a geometrical cue in the ciliate *Stentor coeruleus*

Syun Echigoya[1], Katsuhiko Sato[1,2], Osamu Kishida[3], Toshiyuki Nakagaki[1,2] and Yukinori Nishigami[1,2]*

[1]Graduate School of Life Science, Hokkaido University, Sapporo, Japan, [2]Research Institute for Electronic Science, Hokkaido University, Sapporo, Japan, [3]Field Science Center for Northern Biosphere, Tomakomai Experimental Forest, Hokkaido University, Tomakomai, Japan

Protists ubiquitously live in nature and play key roles in the food web chain. Their habitats consist of various geometrical structures, such as porous media and rigid surfaces, affecting their motilities. A kind of protist, *Stentor coeruleus,* exhibits free swimming and adhering for feeding. Under environmental and culture conditions, these organisms are often found in sediments with complex geometries. The determination of anchoring location is essential for their lives. However, the factors that induce the behavioral transition from swimming to adhering are still unknown. In this study, we quantitatively characterized the behavioral transitions in *S. coeruleus* and observed the behavior in a chamber with dead ends made by a simple structure mimicking the environmental structures. As a result, the cell adheres and feeds in narrow spaces between the structure and the chamber wall. It may be reasonable for the organism to hide itself from predators and capture prey in these spaces. The behavioral strategy for the exploration and exploitation of spaces with a wide variety of geometries in their habitats is discussed.

KEYWORDS

geometrical cue, ciliates, *Stentor*, spatial exploration, behavioral transition, protists

1 Introduction

Animal navigation is widely observed in nature. For example, birds perform homing behaviors (Landreth and Ferguson, 1967) that have been actively studied in neuroscience (Capaldi et al., 1999), and ants explore the locations of food, which can be explained by simple algorithms such as cellular automata (Deneubourg et al., 1990). Even in bacteria and protists, a navigation ability is required to survive, and their habitats consist of diverse microscopic structures that affect their behaviors. Indeed, the behavioral responses of these organisms have been studied in various microspace geometries: porous media (Bhattacharjee and Datta, 2019), rigid surfaces (Kantsler et al., 2013; Ohmura et al., 2018, 2021), dead ends (Kunita et al., 2014), corners (Théry et al., 2021), interstices between inclined plates (Ishikawa and Kikuchi, 2018) and confined areas (Beppu et al., 2017, 2021;

Ostapenko et al., 2018; Bentley et al., 2021). From these studies, it was determined that cell behaviors change in response to the geometrical structures of living spaces.

A kind of protist, namely, ciliates, live in various natural environments, such as fresh water and even the deep sea (Hausmann et al., 2002; Lynn, 2017). These organisms play key roles in the food web chain in the hydrosphere (Sanders and Wickham, 1993; Lynn, 2008). Many kinds of ciliates *Vorticella* (Sleigh and Barlow, 1976), *Opercularia* (Sládecek, 1981; Hartmann et al., 2007) and *Stentor* (Tartar, 1961) anchor to underwater surfaces and consume bacteria, small ciliates and small detritus. Alternatively, they are preyed upon by large multicellular organisms. Thus, their behaviors play an important role in ecosystems in their habitats (Sherr and Sherr, 2002).

Stentor is a large single-celled organism (0.5–1 mm) belonging to the phylum Ciliophora in the order Heterotrichida (Adl et al., 2019); this organism has been well studied for wound healing and regeneration (Tartar, 1961; Blauch et al., 2017; Marshall, 2021; Zhang et al., 2021). The entire body surface of *Stentor* is covered in cilia for swimming. On the edge of the oral region (peristome), the cilia are also tightly packed (membranelle), i.e., two or three rows of cilia (20–25 cilia in each row (Randall and Jackson, 1958)). The membranelles are components of a ring-like oral structure (membranellar band). The membranelles collectively beat and stir the fluid to generate a feeding vortex (Maupas, 1888), which brings food to the oral apparatus.

Stentor exhibits free swimming. They become sessile once attached to the structures such as dead leaves and twig duckweed, *Spirogyra* mats and dead cattail leaves (Tartar, 1961). Switching its motility may depend on the intra- and extracellular conditions. Light affects their behaviors; that is, a negative photoresponse can be caused by the colored pigment stentorin under the near cell surface (Tartar, 1961; Song et al., 1980a, 1980b; Iwatsuki and Song, 1989; Iwatsuki, 1992). Recently, Trinh et al. reported that "complex decision-making" in *Stentor* (Dexter et al., 2019) relates to intracellular conditions (Trinh et al., 2019).

In their behavior, *Stentor* mainly exhibits three shape states: a droplet, a cone and a trumpet (Tartar, 1961). In free swimming, the cell forms a cone shape; on the other hand, trumpet-shaped cells slowly swim or attach to substances for feeding. Mechanical and electrical stimuli produce a quick contraction from cone or trumpet shapes to droplet shapes as an avoidance behavior. During the adherence process, the *Stentor* anchors to a surface using an adherent structure (holdfast) at the posterior end, in which mucus is secreted (Andrews, 1945). The determination of anchoring location is essential for capturing prey and hiding from predators. However, it is still unclear what external cues induce the behavioral change from swimming to adhering. In this study, we quantitatively evaluated the effect of extracellular structures on *Stentor*'s behavior.

2 Materials and methods

2.1 Cell cultures

S. coeruleus was collected from the pond at Tomakomai located Hokkaido, Japan (42.67°N, 141.59°W) and was maintained in a 96-well cell culture plate (TR5003, TrueLine, United States; 6.4 mm diameter) containing filtered pond water using a Millex 0.22 μm fileter (Merck Millipore, Burlington, MA, United States) at room temperature in the dark. We placed *Cryptomonas paramecium* into the culture plate as the *Stentor*'s feed, which was axenically grown in a CHM medium [0.1% $CH_3COONa{\cdot}3H_2O$, 0.1% "Lab-Lemco" powder (Oxoid L29) in Milli-Q water; The pH 6.9 ± 0.1 with 1 N NaOH] was adjusted under light-dark conditions (12 h:12 h) at room temperature every three or 4 days. We transferred *C. paramecium* to a fresh CHM medium every week.

In the experiments using chambers with/without structure, cells were collected from the Shiribetsu River located in Hokkaido, Japan (42.81°N, 140.69°W) and cultured at 25°C in a 6 cm diameter plastic dish containing modified Peters' solution (0.55 mM $CaCl_2$, 0.15 mM $MgSO_4$, 0.15 mM K_2CO_3 and 0.75 mM Na_2CO_3, adjusted pH 7.4 ± 0.1 with 1 N HCl) in the dark (de Terra, 1966) with one wheat grain (MRP-706, Marukan, Osaka, Japan). The cells were transferred into a fresh medium to maintain the cultures every 2–3 weeks. The difference in the strain was not significant in our experiment (detailed in Supplementary Figure S1).

2.2 Observation of the shape transitions of the cell

Before the observations, we washed the cells in fresh pond water twice and starved them for 3 days. Prior to transferring a cell into an observation chamber, we washed the cell with fresh pond water again and equilibrated it for over 20 min. The observation chamber was made of a silicon sheet (244-6012-03, HAGITEC Co., Ltd., Chiba, Japan; 0.2 mm depth, 5 mm inner diameter) and covered by a cover slip (Supplementary Figure S2). Cell behavior was observed by an inverted microscope IX73 (Olympus, Tokyo, Japan) equipped with a PLANPO X1.25 objective (Olympus, Tokyo, Japan). Images were recorded by using a CMOS camera (ORCA-Flash4.0 v2, Hamamatsu Photonics, Hamamatsu, Japan) with an exposure time of 5.0 ms and a frame rate of 10 frames per second (fps) under a brightness field using weak 700 nm light (M700L4, Thorlabs, New Jersey, United States) to reduce the photoresponse effects (Song et al., 1980a, 1980b; Iwatsuki, 1992; Song, 1999).

We used 14 cells to measure the swimming speed and the cell length over 25 min after placing them in the chamber. We recorded each cell for 24.7 ± 3.4 min (SD, 14 cells, maximum

32.0 min, minimum 18.6 min, total 345.1 min: Supplementary Figure S3). To measure the duration time of each shape transition and the diameter of the swimming trajectory in the trumpet shape, we recorded the cell behaviors and analyzed the data (Supplementary Figure S4). Because of the very low frequency at the droplet state, we recorded the behaviors of the cells in the droplet state by adding an external mechanical stimulus to obtain a transition vector and conducted computational classification of the cell state (Supplementary Figure S4).

Due to the speed of the contraction from the trumpet shape to the droplet shape, we recorded the contractions of eight cells by the high-speed camera FASTCAM Mini AX50 (Photron, Tokyo, Japan) at 2,000 fps and an exposure time of 1/2,000 s. Images were collected by using the IX73 microscope with a UNLPlan X10 (Olympus, Tokyo, Japan) objective under 700 nm light.

When we observed the shape transitions from the trumpet shape to the droplet shape, we added an external stimulus by striking the chamber using a tweezer (Meister 0-SA, Rubis, Switzerland).

2.3 Image analyses and measurements of the center of the cell, swimming speed, cell length and swimming trajectory

First, we analyzed the data containing no external stimulus. We cutoff sequential images to several sections (2,000–5,000 frames) and obtained each background image by calculating the local median intensity. Then, the sequential images subtracted from each background were subjected to Gaussian blurring (radius = 1.1 pixels), and binary images were acquired using the MaxEntropy threshold algorithm (Kapur et al., 1985). After that, we obtained the centers C_i: $\boldsymbol{r}_i = (x_i, y_i)$ (mm) of the cells at the ith frame. To measure the cell length, we obtained the length $l_i(\theta)$ from the center of the cell to the edge by converting images to polar coordinates by 2° each (Supplementary Figure S5). The cell length L_i was defined by $L_i = l_i(\theta_1) + l_i(\theta_2)$, where $l_i(\theta_1)$ and $l_i(\theta_2)$ are the top two local maxima of $l_i(\theta)$, and θ_1 and θ_2 denote the directions of the anterior and posterior directions, respectively (Supplementary Figure S5).

Instantaneous swimming speeds $s_i = |\boldsymbol{v}_i|$ were calculated from the center of the cell C_i, defined by $\boldsymbol{v}_i = 0.5\,[(\boldsymbol{r}_{i+1} - \boldsymbol{r}_{i-1}) \cdot \mathrm{fps}]$ (mm/s). Because of the difficulties of obtaining the shape and the center of the cell due to the thin posterior region and the fusing to the air bubble, we obtained a smoothed time series of the cell length L'_i and speed s'_i from the median values for ± 5 s (50 frames) for displaying the overview of behaviors; ± 3 s (30 frames) for obtaining the time duration from cone to trumpet; and ± 1 s (10 frames) for obtaining the time duration from droplet to cone and from droplet to trumpet.

In the contraction process from trumpet to droplet by adding an external mechanical stimulus, we manually extracted three points of the posterior end (P) and two edges of the oral apparatus, OA_1 and OA_2, due to defocusing in striking. Then, we calculated the middle point (M) between OA_1 and OA_2. After that, the cell length L was determined as the distance of the MP.

2.4 The estimation of the frequencies of each cell state

To obtain an overview of the behaviors and compare them with the computational classification of the cell states (see Section 2.6), we divided the behaviors into three states (droplet, cone and trumpet) with reference to Tartar's descriptive classification (Tartar, 1961). Then, we obtained the frequency of the cell states and the distributions of the cell length and swimming speed at each state. The normalized length $\tilde{L}$ and speed $\tilde{s}$ were obtained by calculating the averaged length L_0 and speed s_0 in each free-swimming cell in the cone state for 10 s (the parameters were the same in all experiments). The normalized values at the ith frame defined by $\tilde{L}_i = L'_i/L_0$, $\tilde{s}_i = s'_i/s_0$, where L'_i and s'_i were the median values for ± 5 s (the parameter was the same in all experiments) with regard to the length L and speed s, respectively. Exceptionally, the average length and speed in 1 sample in the gel chamber with a structure were determined to be $L_0 = 0.5$ and $s_0 = 0.9$ because most of the state in this cell was adhesion, and we could not extract averaged values at the swimming state. The bin width was 0.03 (normalized).

All image analyses were conducted by using Python 3.7.1 (https://www.python.org/) and ImageJ/Fiji (Schindelin et al., 2012).

2.5 Obtaining the vector field of the behavioral transition of the cell

We described the behaviors of cells in a 2D state field. The field consists of the normalized length $\tilde{L}$ and speed $\tilde{s}$ (averaged values were calculated from the data for ± 10 s). A dot $\boldsymbol{S}_i$: $(\tilde{L}_i, \tilde{s}_i)$ and a trajectory connecting those dots in the field represent the cell state at frame i and the sequential behavior of a cell, respectively. To obtain these data, we used ± 5 s median values. When a cell remained in the same state, these dots and trajectories accumulated in a region. To derive the directions of the trajectories, we defined the transition vector field of behavioral transition $\boldsymbol{v}_i$, defined by $\boldsymbol{v}_i = \boldsymbol{S}_{i+1} - \boldsymbol{S}_{i-1}$. To obtain smoothed vectors, we calculated the averaged vector in ± 5 s.

Then, we derived the vector field of the transition of the cell state, and we divided the state field into a grid pattern at regular interval 0.1 (normalized). We calculated the median vector in a grid. We eliminated the vector in the grid less than 0.05%.

2.6 The computational classification of cellular states in the state field

We eliminated the transition periods (±15 s of droplet state, ±60 s of cone state, ±30 s of trumpet state) to classify the steady states of the cells computationally. Hierarchical cluster analysis was carried out to divide the cell states into three clusters using the "AgglomerativeClustering" function included in the "sklearn.cluster" library in Python (Pedregosa et al., 2011). The parameters used in the clustering method were the number of clusters ("$n_{clusters}$"): 3, "affinity": Euclidean, "linkage": complete. Downsampling was applied to the data points (±5 s median values) by 10-increment sampling due to the limitation of the computational memory.

2.7 Measurements of the swimming trajectory and evaluation of the diameter of the local swimming trajectory in the trumpet shape

The swimming trajectories were obtained from the centers of the cell C_i. To compare the trajectories of a cell in the cone state (swimming) and in the trumpet state (rotating), we extracted 400 frames (40 s) of sequential images from each swimming state (20 sections, 14 cells) and sequential images from each trumpet state (2502 ± 901 frames (SD, 20 sections); maximum 4435 frames; minimum 1111 frames; 14 cells).

The evaluation of the diameter of the local swimming trajectory in trumpet shape was conducted from each lap trajectory extracted from the trajectory in the rotating state (133 sections, 11 cells). The diameters of each trajectory were calculated by the maximum distance of the position (Supplementary Figure S6).

2.8 Estimations of the characteristic time of the shape transitions

From the obtained time series of cell length L_i, we estimated the characteristic time of duration for the shape transitions. First, we obtained a smoothed time series of cell length L'_i from the median (following the above). The starting points of each shape transition were decided at the cross point of the line before the transition and after the transition (from cone to trumpet), the point of the minimum length from the contraction to after 20 s (from droplet to cone or trumpet) and the point at which external stimuli were added (from trumpet to droplet).

The duration times of each cell deformation were estimated from the deformation rate var $\varepsilon(t)$ by fitting the following exponential functions. The deformation rate was defined as $\varepsilon(t) = [L(t)-L_0]/L_0$, where L_0 is the cell length at the starting time of shape transitions in elongation or at the final state in contraction (t = 40 ms). In elongation, the rate was determined by calculating the averaged length for 10 s before each transition. To determine the duration times of each transition τ, the least-squares method (in Python using the package scipy. optimize.curve_fit) was conducted using the following function:

$$\varepsilon(t) = A \cdot \left(1 - \exp\left(-t/\tau\right)\right)$$

In the contraction process, we used the mechanical model of the damped harmonic oscillator to model the contraction process in *Vorticella convallaria* (Moriyama et al., 1998). The model included the viscous resistance around the cell. The least-squares method was conducted by using the following function:

$$\varepsilon(t) = B_1 \cdot \left(\exp\left(-t/\tau_1\right)\right) + B_2 \cdot \left(\exp\left(-t/\tau_2\right)\right).$$

The standard deviation of the time series of the strain was calculated for ±1 s in the elongations or ±0.5 ms in the contraction.

In the derivation of the correlation of the cell length and swimming speed, we calculated the normalized values by the maximum value of the speed in the transition is 1, and we defined the length at that time as 1. We fitted these values by power laws in two sections (1–1.25 and 1.25–1.45 about normalized length).

2.9 Preparation of the chambers made by agar to compare of two shapes

The observation chambers were obtained by mold casting in two processes: the preparation of prime molds made by polydimethylsiloxane (PDMS) and the formation of a gel chamber by pouring the agarose gel into PDMS prime molds. We made two kinds of chambers. One is the chamber (diameter 5 mm, depth 0.3 mm) with a disk-like structure (diameter 2.5 mm), and the another is the chamber (diameter 5 mm, depth 0.3 mm) without any structure (Supplementary Figure S7).

The prime mold data were designed by Fusion 360 software (Autodesk, California, United States). The data were sent to a CAMM-3 Model PNC-3200 milling machine (Roland DG Corporation, Hamamatsu, Japan) by MODELA Player Version 3.7 (Roland DG Corporation, Hamamatsu, Japan), and prime molds were made by cutting a ZW-100 (Roland DG Corporation, Hamamatsu, Japan). Cutting involved three processes: surface cutting, rough cutting and finish cutting. Each cutting parameter is shown in Supplementary Table S1. The parameters in surface cutting and rough cutting were the same. For rough cutting and finish cutting of the chamber with structure, we used the micro end mill, MHRH230 φ0.2 × 2 (NS TOOL, Tokyo, Japan). In other processes, the end mill 2CEM-G-2.5D-2 (MonotaRO, Hyogo Japan) was used.

PDMS was prepared by mixing the prepolymer and the curing agent of the SYLGARD™184 silicone elastomer kit

(Dow Corporate, Michigan, United States) in a 10:1 (weight: weight) ratio. The mixture was mixed for 20–30 min by plastic stick by hand. After that, it was vacuum-degassed for approximately 1 h. The mixture was poured into molds and vacuum-degassed again for approximately 1 h. Then, PDMS prime chambers covering a glass slide were horizontally kept at 25°C. After 48 h, the PDMS prime chambers were removed from the molds.

Prior to obtaining the observation chambers, the surface of the PDMS chamber was washed with ethanol and Milli-Q water and sonicated in reverse osmosis water. These processes were repeated three times or more. Then, the surface was rinsed with Milli-Q water. After drying, the surface was coated with plasma (PC-400T, STREX, Osaka, Japan) for 10–20 s for hydrophilization.

The mixture of the 2% (weight per volume) agarose (PrimeGel™ Agarose LE 1–20K, Takara Bio, Shiga, Japan) medium that melted the fresh modified Peters' solution was poured into PDMS molds and covered by a cover slip to flatten the agar chambers. After 2–3 min, the cover slip was vertically removed, and the agar chambers were withdrawn from the PDMS prime mold. If we could not remove the agar chambers by the above methods, then the chamber was removed by sonication using the ultrasonic cleaner US-5KS (SND, Nagano, Japan) containing reverse osmosis water.

2.10 The observation method in the chamber with/without a structure

Prior to the observations, we washed the cells in a fresh medium twice and starved them for several hours. Then, we placed the gel chambers on a cover slip, and the surface of the chambers was wetted by the medium and covered on a glass slip with a plasma coating (20 s). After that, a glass slide on the chamber was slid until a swimming arena appeared, and the cell was transferred into the chamber from the edge of the glass slide by using a pipette tip. Its inside was coated with the 2% 2-methacryloyloxyethyl phosphorylcholine (MPC) polymer Lipidure® CM5206 (NOF Corporation, Tokyo, Japan) in ethanol (weight per volume) to prevent the cell surface from adhering to the inside of a tip. In this operation, most of the cell quickly contracted due to external stimuli or hydrophilicity of the gel chambers; however, the cell swam after several seconds. Last, we slowly slid the cover slip to cover the observation chamber.

The behaviors were observed by using a stereomicroscope SZX16 (Olympus, Tokyo, Japan) equipped with a C-Mount Adaptor 0.5X, U-TV0.5XC-3 (Olympus, Tokyo, Japan) and a CMOS camera, ORCA-spark C11440-36U (Hamamatsu Photonics, Hamamatsu, Japan). The exposure time was 50 ms at 4 fps. A 2 × 2 binning scheme under a dim white brightness field, filtered by a red right pass plate for approximately 40 min, was utilized. The quantum sensor MQ-610 (Apogee Instruments, Utah, United States) could not detect the observation light due to weakness [<1 μmol s^{-1} m^{-2} ~ 0.2 W/m^2 (650 nm)]. Less than 0.2 W/m^2 red light has little influence on the phototactic behavior (Song et al., 1980a).

2.11 The analyses of behavioral changes in the chamber with/without a structure

We obtained the behavioral data (center of the cell, swimming speed and cell length) according to Section 2.3. The different points were the obtained background images (using sequential images for 15 min by calculating local maximum intensity), the parameter of the Gaussian blur [radius = 0.5 (pixels)] and the threshold algorithm [triangle methods (Zack et al., 1977)]. When we could not acquire the exact cell position automatically, we manually excluded the noise and dust and prepared the threshold of the circularity or 4 pixel opening process (due to the high circularity of the cell compared with dust). After that, we obtained the position by the automatic method according to Section 2.3. To estimate the cell length, we converted the polar coordinate by 1° each. These acquired time series of length and speed are shown in Supplementary Figures S8, S9.

To calculate the local staying frequency in chambers, we divided the quasi-2D physical fields by 36 mm^2 (6 mm × 6 mm) at regular intervals of 56 × 56 grids. Then, the probability density $p(x_i, y_j)$ in each grid was obtained from the number of observed centers of the cells in each grid. $p(x_i, y_j)$ was normalized as

$$\iint_{-3}^{3} p(x, y)\mathrm{d}x\mathrm{d}y = 1$$

Adhesive spots of the cells, duration times and the directions of anterior end adherence were manually extracted from the sequential images. Crescent areas are defined as the region within 1 mm from the tip of the crescent. We did not count the cells staying for less than 10 s as adhesion. All statistical analyses were conducted in Python 3.7.1 using the "scipy.stat" package version 1.1.0.

3 Results

3.1 Cell behaviors in free swimming

After placing them in the chamber, we recorded the behavior of the cells in a quasi-2D disk chamber to perform quantitative measurements of the swimming speed and the cell length over 25 min. The cell exhibits three kinds of shape and behavioral transitions between these states (droplet, cone and trumpet) (Figure 1A). These shapes and transitions are consistent with the previous description (Tartar, 1961). In our experiments, some cells change their states frequently (Figure 1B, Cell A), while others take

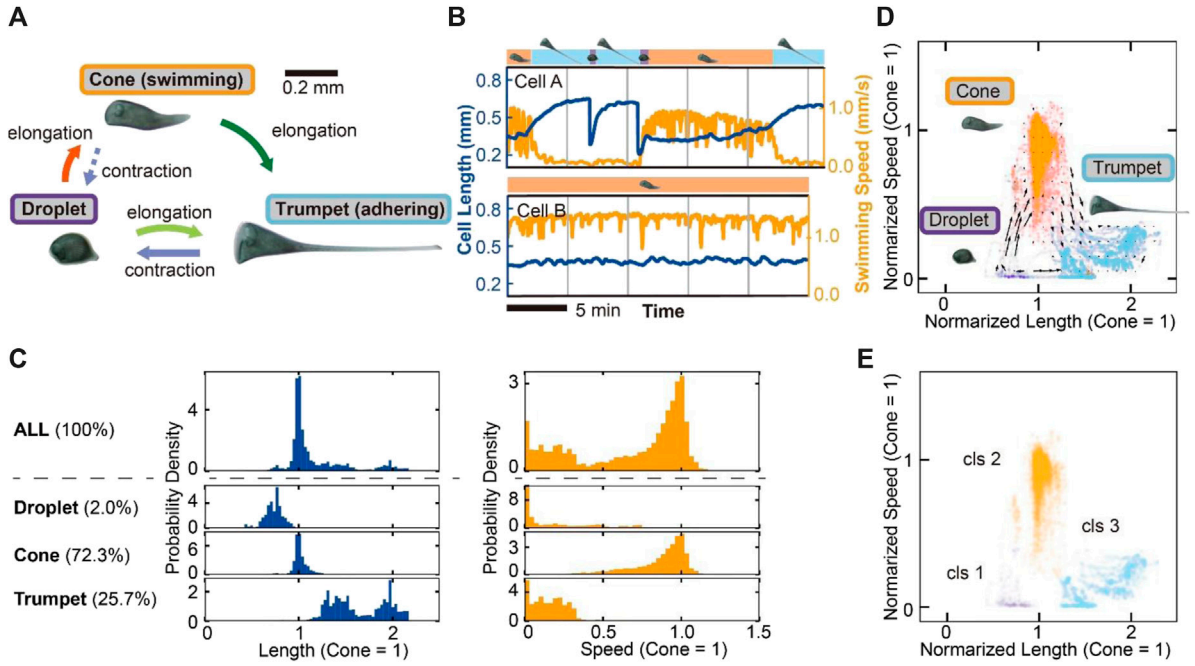

FIGURE 1
Three modes and transitions of *S. coeruleus* and the variety of behavioral modes in the quasi-2D disk chamber. **(A)** Schematic images of the cell states and the transitions. The cell takes three shapes (droplet, cone and trumpet). The cell elongates or contracts between these states, corresponding to each arrow. In the shape transition from cone to trumpet, the switching behavior occurs from swimming to adhering to a substrate. **(B)** The time series of cell length (blue line) and swimming speed (orange line). The graph displays the behaviors of two cells (Cell A, B). The cell states are shown on the top of each graph. Cell A often experiences a shape transition; on the other hand, Cell B remains in a swimming cone state for a longer observation time. **(C)** The frequency of the cell state and the distributions of the cell length and speed in each state. Each state was manually divided (droplet, 2.0%; cone, 72.3%; trumpet, 25.7%). The distributions of the length and the speed were normalized by calculating averaged values in the cone state. The length in the droplet is shorter than that in the cone. On the other hand, the length in the trumpet shape is higher than that in the cone. Swimming speed is separated into two regions, the swimming state (cone) and the adhering or lower swimming state (droplet and trumpet). **(D)** The transition vector of the cells. The dots represent the cell states in the 2D field containing the cell length and speed at time points. The speed and length are normalized by cone = 1. The dots were manually classified into three by cell state Tartar's classification (droplet, purple; cone, orange; trumpet, light blue). **(E)** Hierarchical clustering of the steady cell states. The dots in the 2D state field are divided into three clusters. The computational clustering is similar to manual classification **(D)**.

the steady cone state (Figure 1B, Cell B). There is a variation in the frequency of changing the states among those cells in this situation (Supplementary Figure S3). In the following analyses, we used the behavioral data containing these states. In our observation, cone-shaped cells and trumpet-shaped cells are observed in 72.3% and 25.7% of cells, respectively. Droplet-shaped cells are rarely observed in 2.0% (Figure 1C, Supplementary Figures S13A,B). The distributions of normalized length in each state (cone = 1) are distributed to three regions (Figure 1C). Cone-shaped cells perform free swimming, and droplets and trumpet-shaped cells mostly adhere or swim slowly. Then, we plotted the behavioral data in Figure 1C on the 2D state field. Figure 1D shows that the plots mainly form three clusters corresponding to each state. The vectors in the 2D field represent the velocity of the behavioral change. The graph allows the cell states and transitions in Figure 1A to be evaluated quantitatively and describes the behavioral flows between the cell states. Because two transitions from droplet to trumpet and from trumpet to droplet go through the same path toward mutually opposite directions in the state field, the velocities with respect to the behavioral changes are canceled and underestimated. Hierarchal clustering analysis, which connects the nearest clusters or dots repeatedly and makes several clusters, is conducted on the dots in the steady cell states (Figure 1E). When the computational clustering divides the cell state into three, the result corresponds to the classification in manual clustering (Figures 1D,E).

3.2 Shape transitions of the cells

To characterize the behavioral transitions accompanied by the shape deformations in Figures 1A,D, we measured the time series of the cell length and estimated the duration times in each shape deformation (Figure 2). The duration time of each transition was estimated by exponential fitting to the averaged time series of the deformation rate. Because the contraction process from cone to droplet was observed only three times in

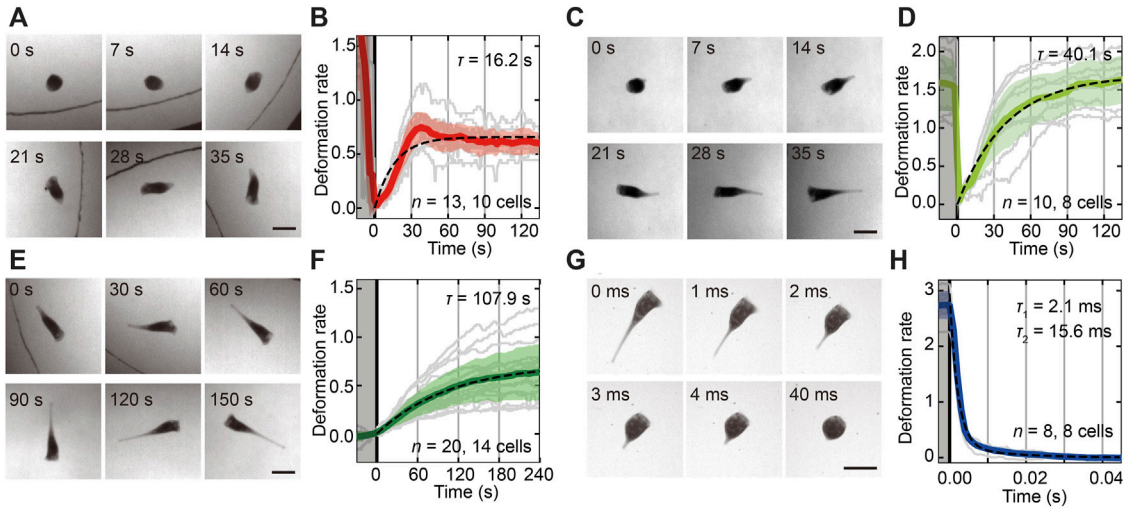

FIGURE 2
The shape transitions between the cell states and the estimation of each duration time of the transitions. **(A,C,E,G)** Sequential images of the shape transitions from droplet to cone **(A)**, from droplet to trumpet **(C)**, from cone to trumpet **(E)** and from trumpet to droplet **(G)**. The time is shown at the upper left in each image. The beginning time of the shape transition is adjusted at 0 s. In the transitions from droplet to cone **(A)** and cone to trumpet **(E),** the cell moves actively. The black curved line in **(A)** and **(E)** represents the boundary of the chamber. All bars are 0.2 mm. **(B,D,F,H)** The time series of shape deformation rates in each transition from droplet to cone **(B)**, from droplet to trumpet **(D)**, from cone to trumpet **(F)** and from trumpet to droplet **(H)**. The gray regions represent the sections before each transition. The colored solid lines are a time series of the averaged deformation rate. Individual data and the standard deviation of the rate are shown by gray lines and transparent colored regions, respectively. The duration times are estimated by exponential fitting to the averaged deformation rate represented as black dashed lines. These characteristic times are 16.2 ± 0.2 s (SD, n = 13, 10 cells) from droplet to cone **(A,B)**, 40.1 ± 0.51 s (SD, n = 10, eight cells) from droplet to trumpet **(C,D)**, and 107.9 ± 1.47 s (SD, n = 20, 14 cells) from cone to trumpet **(E,F).** The duration time from trumpet to droplet **(G,H)** is estimated at 2.1 ± 0.51 ms and 15.6 ± 2.3 ms (SD, n = 8, eight cells).

total recording time (over 6 h), the process was eliminated from the analysis. Therefore, the *Stentor* almost takes the droplet shape caused by the contraction of the trumpet shape. Then, the contracted droplet cell becomes cone shaped and swims away (Figure 2A) or becomes trumpet shaped again (Figure 2C). Additionally, the duration times are 16.2 ± 0.2 s (SD, n = 13, 10 cells, Figure 2B) and 40.1 ± 0.51 s (SD, n = 10, eight cells, Figure 2D). Figure 2E shows another elongation process from cone to trumpet, and the duration time was 107.9 ± 1.47 s (SD, n = 20, 14 cells, Figure 2F). The contractile process from trumpet to droplet is very quick, more than ten thousand times faster than other transitions (Figure 2G). In the contraction process, the two-mode exponential function (Moriyama et al., 1998) fits well [2.1 ± 0.51 ms and 15.6 ± 2.3 ms (SD, n = 8, eight cells, Figure 2H)] with the averaged deformation rate rather than the function with a single time scale (details in Supplementary Figure S10).

3.3 Behavioral switching from swimming to adhering

In this section, we focus on the transition from cone to trumpet (Figures 2E,F) related to the determination of the adhering location. In the transition, the swimming speed of the cell decreases, accompanied by increasing cell length (Figures 3A,B). The correlation between the length and speed of the cell shows a negative correlation, and two kinds of relationships are observed in the transition by scaling methods ($s \sim l^{-6.3}$ and $s \sim l^{0.2}$, Figure 3B). In the behavioral transition, the swimming trajectory changed from straight forward to rotating (Figure 3C, Supplementary Video S1). The trajectories in the swimming and trumpet states are shown in Figures 3D,E. The true diameter of the trajectory in the free-swimming cone state could not be measured because the cone-shaped cell usually swims in a straight trajectory and the swimming is affected by the chamber's wall due to the restriction of the observation area. The diameter of the rotating trajectory of the trumpet cell (Figure 3E) is distributed at 1.4 ± 0.3 mm (SD, n = 133, 11 cells, Figure 3F). The parameters of the beating forms of the membranellar band are different between the cone state and trumpet state (Supplementary Figure S11).

3.4 The influence of a structure on behaviors in an arena

In nature, *Stentor* elongates and adheres to a better location for better living conditions. In these processes, the

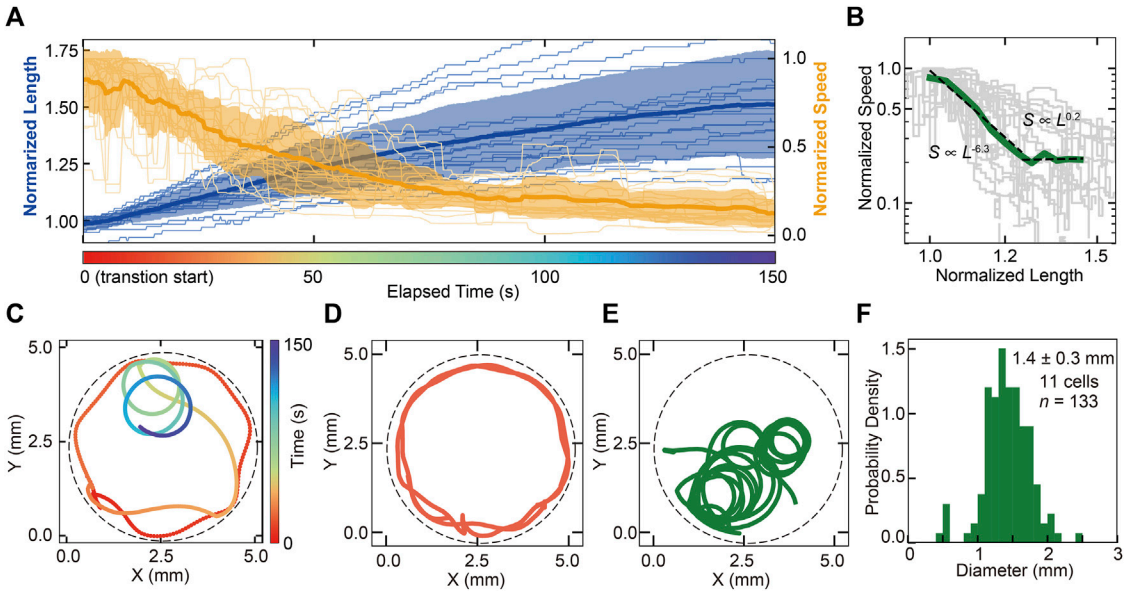

FIGURE 3
The processes of behavioral switching from swimming (cone shaped) to adhering (trumpet shaped). **(A)** Time series of the cell length (blue line) and swimming speed (orange line) of the cell in the transition from cone to trumpet (Figures 2E,F). Averaged lines are represented as solid bold lines, and individual data are represented as solid thin lines. Standard deviations of values for each cell at a time point are the transparent regions. These values are normalized by Cone = 1. It shows the negative correlation between the cell length and swimming speed. **(B)** The correlation between cell length and speed. The green solid line represents the average speed. Gray lines are individual transition data, and averaged data are fitted by power laws. The characteristic factors of the law are −6.3 in the range of 1–1.25 (normalized length) and 0.2 in the range of 1.25–1.45 (normalized length). **(C)** The trajectory of a cell in the behavioral transition from swimming to adhering. As the cell elongates, the cell becomes locally rotating. The color represents elapsed time from the beginning of the transition. The dashed line represents the wall of the chamber. **(D,E)** The comparison between the swimming trajectories at swimming steady state and steady rotating state. **(F)** The distribution of the swimming pass diameter in the steady rotating state. The diameter was 1.4 ± 0.3 mm (SD, n = 133, 11 cells).

cell obtains some information about the outer environment. To determine where they tend to adhere, we focused on the geometry in the outer swimming environment and observed their behaviors in the quasi-2D gel chambers to encourage cell adhesion with/without the structure (Figure 4A).

The structure in the chamber causes a change in the frequency of the cell states. In the chamber without the structure (control), the cell mainly takes the cone state in 74.1%, and trumpet and droplet states are observed for 22.4% and 3.5%, respectively (Figure 4B). However, in the chamber with the structure, the cell mainly takes a trumpet shape in 72.4% and a droplet shape in 10.7%. Cone-shaped cells were observed in only 16.9% (Figure 4B). In the chamber with the structure, trumpet- and droplet-shaped cells mostly adhere, and swimming cells often collide with the structure. Thus, a distribution of lower swimming speeds is often observed (Supplementary Figure S12A,C). The averaged each state have significant differences in Welch's t-test (p = 0.0026 in droplet, $p = 6.3 \times 10^{-7}$ in cone, $p = 2.0 \times 10^{-6}$ in trumpet, Figure 4C). The geometry in the outer environment affects the modulation of their states.

The 2D color maps in Figures 4D,E represent the averaged probability densities of the cell's position in each chamber. In the quasi-2D chamber without a structure, the probability density is uniformly distributed along the wall (Figure 4D). On the other hand, the cell frequently stays in the locations between the wall and the structure, which are termed the crescent areas (in the orange area in Figure 4A) (Figure 4E). Except for adhering, existence frequencies were 614.9 ± 136.6 s/mm^2 (SE, n = 12, 12 cells) in crescent and 43.4 ± 11.1 s/mm^2 (SE, n = 12, 12 cells) in other regions. Welch's t-test was applied to the values, revealing a significant difference between them (p = 0.0015, Figure 4F). It shows the increase of the presence in the crescent areas.

Our experiment suggests that the cell tends to stay in and adhere to the crescent areas. Figure 4G displays the positions and duration times of adhesion in 12 cells. All 12 cells adhere to substrate in the chamber with the structure. Though two cells did not adhere to the crescent areas, the others (10 cells) exhibited switching behavior from swimming to adhesion (from cone to trumpet) in crescent areas. In the 10 cells, 9 cells maintained their feeding (trumpet state) with the oral structure directed to the opposite side of the dead end (Figures 4G,H,L). Although the adhering frequency in crescent areas (28.0 events/mm^2) increases

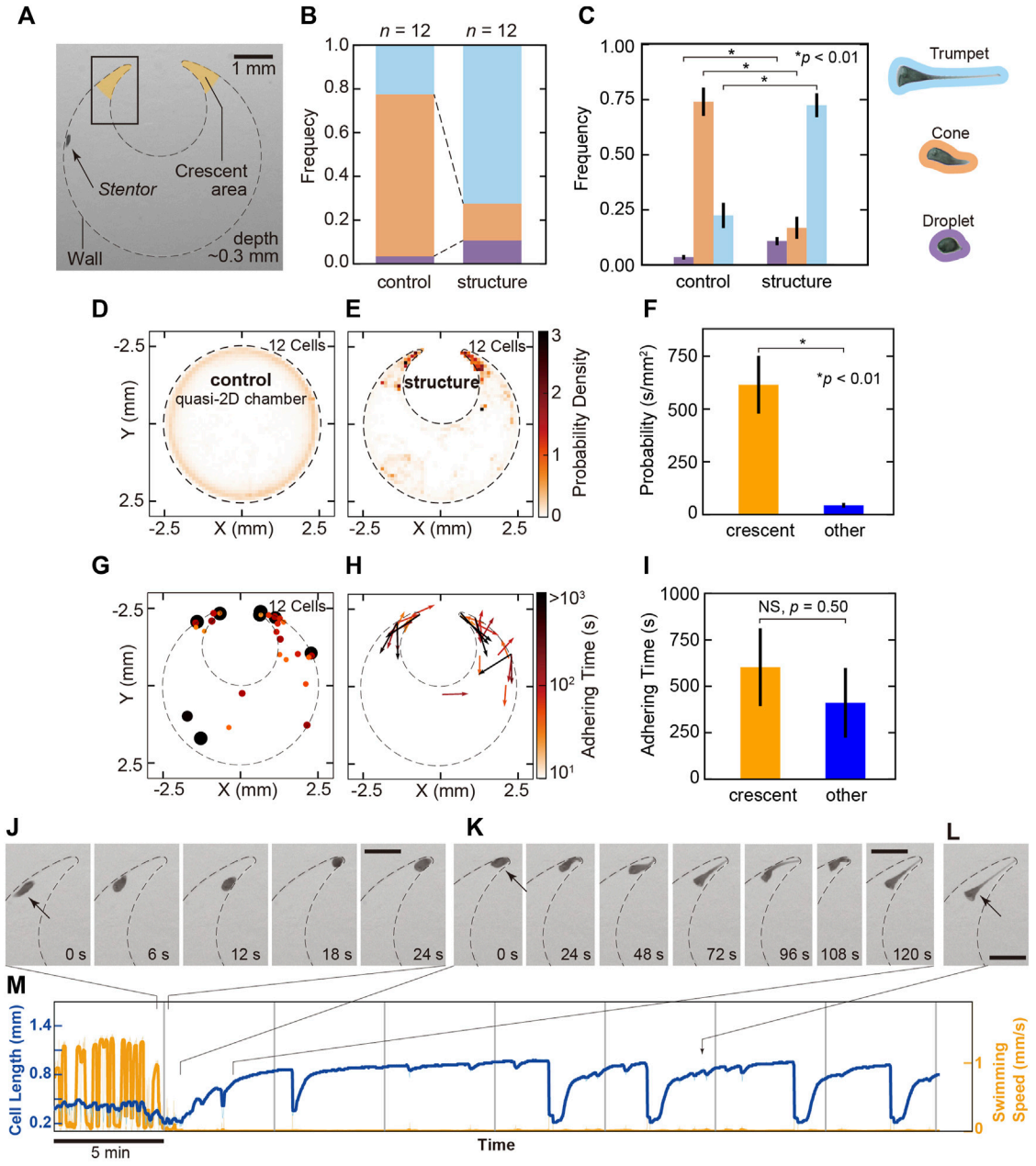

FIGURE 4
The behavioral change in swimming to adhesion in the crescent areas. **(A)** Image of the geometry of the gel chamber with the structure in the experiments. The dashed line represents the wall of the chamber. Crescent areas are indicated as two orange regions. The depth of the chamber is 0.3 mm. **(B)** The frequency of the cell states in the gel chamber with/without the structure. In the chamber without the structure (control), the cell mainly takes the cone state in 74.1% (orange), and trumpet (light blue) and droplet (purple) states are observed in 22.4% and 3.5%, respectively. In the chamber with the structure, the cell mainly takes a trumpet shape in 72.4% and a droplet shape in 10.7%. Cone-shaped cells are observed in only 16.9% of cells. **(C)** The difference in the probability of three states in the simple chamber and in the chamber with structure. The colors correspond with each state indicated in **(B)**. This bar plot exhibits the probability of cell states in the simple chamber and the chamber with structure. The cone shape was dominant in the simple chambers, but the trumpet type was dominant in the chambers containing structures. The probability of the cell states was tested by Welch's *t*-test, revealing significant differences between the chamber with/without structure ($p = 0.0026$ in droplet; $p = 6.3 \times 10^{-7}$ in cone; $p = 2.0 \times 10^{-6}$ in trumpet). The bars are standard errors (12 cells). **(D,E)** 2D maps of the probability density observed in the cells in each chamber. **(F)** The comparison of presence probability within the crescent areas and other regions. Except for adhering, presence probabilities are 614.9 ± 136.6 s/mm² (SE, $n = 12$, 12 cells) in crescent and 43.4 ± 11.1 s/mm² (SE, $n = 12$, 12 cells) in other regions. The difference is statistically significant in Welch's *t*-test. Black bars are standard errors. **(G)** The locations and duration times of adhesion in the cell. The color and size of the dots represent the duration of the adhesion. The color bar represents the logarithmic adherence time scale. **(H)** The directions of the cell in the adhesive state. The color and length of the vectors represent the adhering time in one direction. **(I)** The comparison of adhering time prior to the detachment within the crescent areas and other regions. Ten cells adhered in crescent areas (18 events) and 7 cells adhered in other regions (13 events) in

(*Continued*)

FIGURE 4 (Continued)
observed 12 cells (31 events). Averaged adhering times prior to detachment are 603.0 ± 209.2 s (SE, n = 18, 10 cells) in the crescent areas and 411.2 ± 187.1 s (SE, n = 13, seven cells) in other regions. Welch's t-test revealed that they did not have a significant difference (p = 0.50). Black bars are standard errors. **(J–L)** Typical sequential images of the process from swimming to adhesion in the crescent area [in the rectangle in **(A)**]. **(J)** Before the cell adheres, the cell enters the crescent area. **(K)** Adhesive cells become trumpet-shaped from cone-shaped cells. **(L)** The cell adheres and feeds in the crescent area. The direction of the anterior end directs toward the opposite side to the dead end. All bars are 0.5 mm. **(M)** Time series of the cell length and swimming speed in the process from swimming to adhesion at the crescent area. Images in **(J)**–**(L)** represent the sections in the graph.

compared to the one in other regions (0.9 events/mm^2), the difference between adhering times per cell prior to the detachment were not significant in Welch's t-test [603.0 ± 209.2 s (SE, n = 18, 10 cells) in crescent areas and 411.2 ± 187.1 s (SE, n = 13, seven cells) in other regions; p = 0.50; Figure 4I].

Figures 4J–L shows typical sequential images of the adhesion processes in the crescent area (Supplementary Video S2). First, the cell encounters the crescent area and goes back and forth (Figure 4J). Then, the posterior shortly elongates and contacts the wall. The cell sometimes swims backward. Then, the posterior region adheres to the substrate and elongates over 1–2 min (Figure 4K). In this process, we can sometimes observe the bending behavior (sequential images from 96 to 120 s in Figure 4K). Although contraction and elongation between the trumpet and droplet occur, the cell typically remains adherent at the same location for more than 35 min (Figure 4M, Supplementary Figure S9).

Modulation of their states is affected by the structure in an arena. In the crescent areas, the cell not only stays frequently but also switches its behavior and adheres for a long time with its oral structure directed to the opposite side of the dead end.

4 Discussion

Protists perform some behavioral modulations according to their surrounding environments. The ciliate *Stentor* exhibits changing shape and motility, and several studies have shown the complexity of these behavioral transitions (Jennings, 1906; Wood, 1969b; Dexter et al., 2019; Trinh et al., 2019). The environmental information around the cell affects the behavioral transitions. Here, we quantitatively evaluated the behaviors of *S. coeruleus* and then measured the characteristic durations of their behavioral transitions. Considering the swimming speed and cell length, the cell states are computationally classified into three states, consistent with the previous descriptive classification of the three states (Tartar, 1961). Among those three states, we revealed that *S. coeruleus* has 4 transition processes accompanied by each characteristic duration time. Previously, the durations time from droplet to trumpet and trumpet to droplet have been estimated by qualitative observations, and our results are consistent with their reports (Wood, 1969a; Kristensen et al., 1974). The contraction process in *S. coeruleus* from trumpet to droplet contributes to the contractile filaments, myoneme (Randall and Jackson, 1958; Huang and Pitelka, 1973). The contraction time in *Vorticella convallaria* (Moriyama et al., 1998), which also uses a similar contractile filament, the spasmoneme (Lynn, 2008) is almost the same as that in *S. coeruleus*. In this paper, we also characterized the duration of the elongation processes from droplet to cone and from cone to trumpet. The elongation processes are associated with the sliding of microtubule ribbons in the km-fibers (Randall and Jackson, 1958; Huang and Pitelka, 1973). In our study, the duration times of each elongation were different. This means that the question of whether all three elongation processes relate to sliding in the km-fibers is still open.

In the transition from cone to trumpet, we found a negative correlation between the cell length l and swimming speed s with the power laws $s \sim l^{-6.3}$ and $s \sim l^{0.2}$ (Figure 3B). Hydrodynamically, in a moving sphere (radius r) with the same energy, the swimming speed is proportional to r^{-1} by Stokes law. We found that the exponent between observed length and speed is different from that derived from the stokes law. It is considered that the difference in the relationship between our experiment and the theory is derived from the difference in the ciliary waveforms between the cone state and the trumpet state (Supplementary Figure S11, Supplementary Video S3).

The changes in swimming speed and trajectory in *S. coeruleus* play crucial roles in exploring feeding location. In microorganisms, the modulations induced by taxis-caused chemical substances, light and flows have been well studied experimentally and mathematically (Wan and Jékely, 2021). In *Stentor*, photoresponse (Song et al., 1980a; Song et al., 1980b; Iwatsuki, 1992), external mechanical stimuli (Wood, 1969b) and chemical avoidance responses (Jennings, 1906; Dexter et al., 2019; Trinh et al., 2019) have been reported previously. The behaviors of microorganisms are strongly influenced by extracellular geometries (Kantsler et al., 2013; Kunita et al., 2014; Beppu et al., 2017; Beppu et al.,2021; Ishikawa and Kikuchi, 2018; Nishigami et al., 2018; Ohmura et al., 2018; Ohmura et al., 2021; Ostapenko et al., 2018; Bhattacharjee and Datta, 2019; Bentley et al., 2021; Okuyama et al., 2021; Théry et al., 2021) corresponding to mud, dead leaves or other varieties of sediments in their habitats. In our study, we evaluated the effect of a structure on behavioral transition. In the chamber with the crescent areas, the probability density of the cell's position at

the crescent areas is higher, and the cell becomes more adherent than the cells at other locations. Although the frequency of presence except for adhering had a significant difference, adhering time per cell prior to detachment did not have a significant difference. These statistical analyses indicated that the bias to adhere to the crescent was dominated by an increase in adhesion than a decrease in detachment.

Previously, a directional swimming organism such a *Chlamydomonas* accumulates the corner in the geometrical chamber, and the phenomenon has been described as a theoretical model (Théry et al., 2021). Although the cell accumulates in the corner without changing the behavioral state (Mondal et al., 2021), we revealed that *S. coeruleus*, which is frequently found in a free-swimming form (Reynierse and Walsh, 1967), tended to adhere to the chamber with the structure, and the behavioral change promoted accumulation in the crescent areas. The anterior end of the cell faces the opposite side of the dead end. Hydrodynamically, *S. coeruleus*, which belongs to the puller-like swimmer in the squirmer model, tends to swim away from the wall (Lighthill, 1952; Blake, 1971; Lauga and Powers, 2009). When the posterior region of the cell, which secretes a sticky substance, attaches to a substrate (Andrews, 1945), the cell directs the anterior toward the opposite side of the dead end; this plays a role in positive feeding efficiency.

Moreover, it is known that the *Stentor* causes two feeding vortices at the left and right sides of the oral apparatus on a focal plane (Maupas, 1888). Proximity to the attachment surface or substrate causes vortex flow near the sessile filter feeders, *Vorticella* and *Opercularia,* generating feeding currents around the oral apparatus similar to *Stentor* (Liron and Blake, 1981; Hartmann et al., 2007; Pepper et al., 2010, 2013). The feeding efficiency influenced by the feeding vortex depends on the environmental situations and theoretical definitions. The eddies contribute to decreasing the long-term feeding efficiency defined by the clearance rate (the volume of nutrient water crossed per time) due to recirculation when we consider that there is no nutrient in the flow processed the oral region once (Liron and Blake, 1981; Hartmann et al., 2007; Pepper et al., 2013, 2021). On the other hand, when we modeled that the organisms probabilistically capture prey, the vortex array contributes to the positive efficiency of their feedings because the recirculation allows an increase in feeding chances of starfish larvae (Gilpin et al., 2017). Additionally, vortex flow enhances the mixing and transport of substances, i.e., nutrients and wastes, around the cell (Mondal et al., 2021). Combining our results and these reports, we determined that *S. coeruleus* adheres to narrow areas not only by avoiding being the prey of potential predators but also by capturing prey and mixing nutrients around the cell.

How organisms perceive the narrowness and shape of space is an interesting future topic. Two possibilities are discussed here: 1) the interaction between the flow in the narrow space and the ciliary beating that causes it, 2) the concentration of some chemical secretions (due to suppression of diffusion by narrow space). The *Stentor* swims by moving their cilia to move the water around the body. Ciliary beating is modulated in response to the reaction force cilia receive from water. This modulation is the interaction of the cilia with the surrounding flow of water (Brumley et al., 2015; Wan et al., 2020). In a narrow space, the surrounding flow changes, so it may react to the change in the flow field around the body (Liron and Blake, 1981; Pepper et al., 2010). Sensing a geometric shape may also be possible in principle since the flow field pattern changes with the spatial shape. In other words, it is a mechanism that can be called *hydrodynamic sensing* for spatial shape. On the other hand, the second possibility is *chemical diffusion sensing*. The *Stentor* secretes various chemical substances, such as signal substances and excretory substances (Andrews, 1945, 1946; Miyake et al., 2001). These chemicals move away from the body by diffusion and advection if the space is sufficiently open. However, in a narrow space, these outflows are suppressed, and the concentration becomes high. This change in a chemical concentration may be a cue for the organism to switch the swimming behavior.

The above two effects do not have to be mutually exclusive, and both may work as possible. Alternatively, in a narrow space where the flow tends to stagnate, bacteria and other microorganisms are likely to grow, and it is possible that the *Stentor* will react to it. In any case, the ability of *Stentor* to perceive the narrowness and shape of space simply by moving around in space, in other words, without perceiving the overall shape from a bird's-eye view, is surprising in terms of the information processing ability of living things.

Data availability statement

The raw data supporting the conclusion of this article will be made available by the authors, without undue reservation.

Author contributions

SE, KS, TN, and YN contributed to conceptualizing the research and designing the experiments. SE, YN, and OK performed the experiments. SE acquired and analyzed the data. SE wrote the draft of the manuscript. SE, KS, OK, TN, and YN contributed to manuscript revision and read and approved the submitted version.

Funding

This research was supported by JSPS KAKENHI Grant Numbers, JP16H06280 (TN), JP21H05308 (YN), JP21H05310 (TN), JP19KK0180 (YN), and JP20K03871 (KS). A part of this

study was supported by the "Dynamic Alliance for Open Innovation Bridging Human, Environment and Materials" of the Ministry of Education, Culture, Sports, Science and Technology of Japan (TN, KS, and YN), the JSPS Core-to-Core Program, A. Advanced Research Networks (YN), the Project of Junior Scientist Promotion in Hokkaido University (YN), Photo-Excitonix Project in Hokkaido University (TN), Hokkaido University Support Program for Frontier Research (YN), Global Station for Soft Matter at Hokkaido University (KS, TN and YN), the Sasakawa Scientific Research Grant from The Japan Science Society Grant No. 2021-6029 (SE), and the establishment of university fellowships towards the creation of science technology innovation, Grant Number JPMJFS2101 (SE).

Acknowledgments

We thank Takuji Ishikawa and Kenta Ishimoto for helpful discussions and comments from theoretical aspects. We also thank Taku Morimoto and the Division of Technical Staffs in the Research Institute for Electronic Science, Hokkaido University for supporting the fabrication technique.

Conflict of interest

The authors declare that the research was conducted in the absence of any commercial or financial relationships that could be construed as a potential conflict of interest.

Publisher's note

Supplementary material

The Supplementary Material for this article can be found online at: https://www.frontiersin.org/articles/10.3389/fcell.2022.1021469/full#supplementary-material

References

Adl, S. M., Bass, D., Lane, C. E., Lukeš, J., Schoch, C. L., Smirnov, A., et al. (2019). Revisions to the classification, nomenclature, and diversity of eukaryotes. *J. Eukaryot. Microbiol.* 66, 4–119. doi:10.1111/jeu.12691

Andrews, E. A. (1946). Ingestion organs in folliculinids and in stentors. *J. Morphol.* 79, 419–444. doi:10.1002/jmor.1050790304

Andrews, E. A. (1945). Stentor's anchoring organs. *J. Morphol.* 77, 219–232. doi:10.1002/jmor.1050770206

Bentley, S. A., Anagnostidis, V., Schlogelhofer, H. L., Gielen, F., and Wan, K. Y. (2021). Phenotyping single-cell motility in microfluidic confinement. bioRxiv [preprint]. doi:10.1101/2021.12.24.474109

Beppu, K., Izri, Z., Gohya, J., Eto, K., Ichikawa, M., and Maeda, Y. T. (2017). Geometry-driven collective ordering of bacterial vortices. *Soft Matter* 13, 5038–5043. doi:10.1039/c7sm00999b

Beppu, K., Izri, Z., Sato, T., Yamanishi, Y., Sumino, Y., and Maeda, Y. T. (2021). Edge current and pairing order transition in chiral bacterial vortices. *Proc. Natl. Acad. Sci. U. S. A.* 118, e2107461118. doi:10.1073/PNAS.2107461118

Bhattacharjee, T., and Datta, S. S. (2019). Bacterial hopping and trapping in porous media. *Nat. Commun.* 10, 2075–2110. doi:10.1038/s41467-019-10115-1

Blake, J. R. (1971). A spherical envelope approach to ciliary propulsion. *J. Fluid Mech.* 46, 199–208. doi:10.1017/S002211207100048X

Blauch, L. R., Gai, Y., Khor, J. W., Sood, P., Marshall, W. F., and Tang, S. K. Y. (2017). Microfluidic guillotine for single-cell wound repair studies. *Proc. Natl. Acad. Sci. U. S. A.* 114, 7283–7288. doi:10.1073/pnas.1705059114

Brumley, D. R., Polin, M., Pedley, T. J., and Goldstein, R. E. (2015). Metachronal waves in the flagellar beating of *Volvox* and their hydrodynamic origin. *J. R. Soc. Interface* 12, 20141358. doi:10.1098/rsif.2014.1358

Capaldi, E. A., Robinson, G. E., and Fahrbach, S. E. (1999). Neuroethology of spatial learning: The birds and the bees. *Annu. Rev. Psychol.* 50, 651–682. doi:10.1146/annurev.psych.50.1.651

de Terra, N. (1966). Culture of stentor coeruleus on colpidium campylum. *J. Protozool.* 13, 491–492. doi:10.1111/j.1550-7408.1966.tb01947.x

Deneubourg, J. L., Aron, S., Goss, S., and Pasteels, J. M. (1990). The self-organizing exploratory pattern of the argentine ant. *J. Insect Behav.* 3, 159–168. doi:10.1007/BF01417909

Dexter, J. P., Prabakaran, S., and Gunawardena, J. (2019). A complex hierarchy of avoidance behaviors in a single-cell eukaryote. *Curr. Biol.* 29, 4323–4329.e2. doi:10.1016/j.cub.2019.10.059

Gilpin, W., Prakash, V. N., and Prakash, M. (2017). Vortex arrays and ciliary tangles underlie the feeding-swimming trade-off in starfish larvae. *Nat. Phys.* 13, 380–386. doi:10.1038/nphys3981

Hartmann, C., Özmutlu, Ö., Petermeier, H., Fried, J., and Delgado, A. (2007). Analysis of the flow field induced by the sessile peritrichous ciliate *Opercularia asymmetrica*. *J. Biomech.* 40, 137–148. doi:10.1016/j.jbiomech.2005.11.006

Hausmann, K., Hülsmann, N., Polianski, I., Schade, S., and Weitere, M. (2002). Composition of benthic protozoan communities along a depth transect in the eastern Mediterranean Sea. *Deep Sea Res. Part I Oceanogr. Res. Pap.* 49, 1959–1970. doi:10.1016/S0967-0637(02)00095-X

Huang, B., and Pitelka, D. R. (1973). The contractile process in the ciliate, *Stentor coeruleus*: I. The role of microtubules and filaments. *J. Cell. Biol.* 57, 704–728. doi:10.1083/jcb.57.3.704

Ishikawa, T., and Kikuchi, K. (2018). Biomechanics of *Tetrahymena* escaping from a dead end. *Proc. Biol. Sci.* 285, 20172368. doi:10.1098/rspb.2017.2368

Iwatsuki, K., and Song, P. (1989). The ratio of extracellular Ca^{2+} to K^{+} ions affects the photoresponses in *Stentor coeruleus*. *Comp. Biochem. Physiol. A Comp. Physiol.* 92, 101–106. doi:10.1016/0300-9629(89)90749-4

Iwatsuki, K. (1992). *Stentor coeruleus* shows positive photokinesis. *Photochem. Photobiol.* 55, 469–471. doi:10.1111/j.1751-1097.1992.tb04264.x

Jennings, H. S. (1906). *Behavior of the lower organisms*. New York: Columbia University Press. doi:10.1037/10817-000

Kantsler, V., Dunkel, J., Polin, M., and Goldstein, R. E. (2013). Ciliary contact interactions dominate surface scattering of swimming eukaryotes. *Proc. Natl. Acad. Sci. U. S. A.* 110, 1187–1192. doi:10.1073/pnas.1210548110

Kapur, J. N., Sahoo, P. K., and Wong, A. K. C. (1985). A new method for gray-level picture thresholding using the entropy of the histogram. *Comput. Vis. Graph. Image Process.* 29, 273–285. doi:10.1016/0734-189X(85)90125-2

Kristensen, B. I., Nielsen, L. E., and Rostgaard, J. (1974). Variations in myoneme birefringence in relation to length changes in *Stentor coeruleus*. *Exp. Cell. Res.* 85, 127–135. doi:10.1016/0014-4827(74)90222-5

Kunita, I., Kuroda, S., Ohki, K., and Nakagaki, T. (2014). Attempts to retreat from a dead-ended long capillary by backward swimming in *Paramecium*. *Front. Microbiol.* 5, 270. doi:10.3389/fmicb.2014.00270

Landreth, H. F., and Ferguson, D. E. (1967). Newt orientation by sun-compass. *Nature* 215, 516–518. doi:10.1038/215516a0

Lauga, E., and Powers, T. R. (2009). The hydrodynamics of swimming microorganisms. *Rep. Prog. Phys.* 72, 096601. doi:10.1088/0034-4885/72/9/096601

Lighthill, M. J. (1952). On the squirming motion of nearly spherical deformable bodies through liquids at very small Reynolds numbers. *Commun. Pure Appl. Math.* 5, 109–118. doi:10.1002/cpa.3160050201

Liron, N., and Blake, J. R. (1981). Existence of viscous eddies near boundaries. *J. Fluid Mech.* 107, 109–129. doi:10.1017/S0022112081001699

Lynn, D. H. (2017). "Ciliophora," in *Handbook of the protists* (Switzerland: Springer International Publishing AG), 679–730. doi:10.1007/978-3-319-28149-0

Lynn, D. H. (2008). *The ciliated Protozoa*. 3rd ed. Dordrecht: Springer Netherlands. doi:10.1007/978-1-4020-8239-9

Marshall, W. F. (2021). Regeneration in *Stentor coeruleus*. *Front. Cell. Dev. Biol.* 9, 753625–753713. doi:10.3389/fcell.2021.753625

Maupas, E. (1888). Recherches experimentales sur la multiplication des infusoires cilies. *Arch. Zool. Exp. Gen.* 46, 498–516. Available at: https://www.biodiversitylibrary.org/bibliography/79165.

Miyake, A., Harumoto, T., and Iio, H. (2001). Defence function of pigment granules in *Stentor coeruleus*. *Eur. J. Protistol.* 37, 77–88. doi:10.1078/0932-4739-00809

Mondal, D., Prabhune, A. G., Ramaswamy, S., and Sharma, P. (2021). Strong confinement of active microalgae leads to inversion of vortex flow and enhanced mixing. *eLife* 10, 676633–e67723. doi:10.7554/eLife.67663

Moriyama, Y., Hiyama, S., and Asai, H. (1998). High-speed video cinematographic demonstration of stalk and zooid contraction of *Vorticella convallaria*. *Biophys. J.* 74, 487–491. doi:10.1016/S0006-3495(98)77806-3

Nishigami, Y., Ohmura, T., Taniguchi, A., Nonaka, S., Manabe, J., Ishikawa, T., et al. (2018). Influence of cellular shape on sliding behavior of ciliates. *Commun. Integr. Biol.* 11, 15066666–e1506675. doi:10.1080/19420889.2018.1506666

Ohmura, T., Nishigami, Y., Taniguchi, A., Nonaka, S., Ishikawa, T., and Ichikawa, M. (2021). Near-wall rheotaxis of the ciliate *Tetrahymena* induced by the kinesthetic sensing of cilia. *Sci. Adv.* 7, eabi5878. doi:10.1126/sciadv.abi5878

Ohmura, T., Nishigami, Y., Taniguchi, A., Nonaka, S., Manabe, J., Ishikawa, T., et al. (2018). Simple mechanosense and response of cilia motion reveal the intrinsic habits of ciliates. *Proc. Natl. Acad. Sci. U. S. A.* 115, 3231–3236. doi:10.1073/pnas.1718294115

Okuyama, K., Nishigami, Y., Ohmura, T., and Ichikawa, M. (2021). Accumulation of *Tetrahymena pyriformis* on interfaces. *Micromachines* 12, 1339. doi:10.3390/mi12111339

Ostapenko, T., Schwarzendahl, F. J., Böddeker, T. J., Kreis, C. T., Cammann, J., Mazza, M. G., et al. (2018). Curvature-guided motility of microalgae in geometric confinement. *Phys. Rev. Lett.* 120, 068002. doi:10.1103/PhysRevLett.120.068002

Pedregosa, F., Varoquaux, G., Gramfort, A., Michel, V., Thirion, B., Grisel, O., et al. (2011). Scikit-learn: Machine learning in Python. *J. Mach. Learn. Res.* 12, 2825–2830. Available at: https://scikit-learn.org/stable/about.html#citing-scikit-learn.

Pepper, R. E., Riley, E. E., Baron, M., Hurot, T., Nielsen, L. T., Koehl, M. A. R., et al. (2021). The effect of external flow on the feeding currents of sessile microorganisms. *J. R. Soc. Interface* 18, 20200953. doi:10.1098/rsif.2020.0953

Pepper, R. E., Roper, M., Ryu, S., Matsudaira, P., and Stone, H. A. (2010). Nearby boundaries create eddies near microscopic filter feeders. *J. R. Soc. Interface* 7, 851–862. doi:10.1098/rsif.2009.0419

Pepper, R. E., Roper, M., Ryu, S., Matsumoto, N., Nagai, M., and Stone, H. A. (2013). A new angle on microscopic suspension feeders near boundaries. *Biophys. J.* 105, 1796–1804. doi:10.1016/j.bpj.2013.08.029

Randall, J. T., and Jackson, S. F. (1958). Fine structure and function in *Stentor polymorphus*. *J. Biophys. Biochem. Cytol.* 4, 807–830. doi:10.1083/jcb.4.6.807

Reynierse, J. H., and Walsh, G. L. (1967). Behavior modification in the protozoan *Stentor* re-examined. *Psychol. Rec.* 17, 161–165. doi:10.1007/BF03393700

Sanders, R. W., and Wickham, S. A. (1993). Planktonic protozoa and metazoa: Predation, food quality and population control. *Mar. Microb. Food Webs* 7, 197–223. Available at: http://hdl.handle.net/11858/00-001M-0000-000F-E43A-E.

Schindelin, J., Arganda-Carreras, I., Frise, E., Kaynig, V., Longair, M., Pietzsch, T., et al. (2012). Fiji: An open-source platform for biological-image analysis. *Nat. Methods* 9, 676–682. doi:10.1038/nmeth.2019

Sherr, E. B., and Sherr, B. F. (2002). Significance of predation by protists in aquatic microbial food webs. *Ant. Van Leeuwenhoek* 81, 293–308. doi:10.1023/A:1020591307260

Sládecek, V. (1981). Indicator value of the genus Opercularia (ciliata). *Hydrobiologia* 79, 229–232. doi:10.1007/BF00006317

Sleigh, M. A., and Barlow, D. (1976). Collection of food by *Vorticella*. *Trans. Am. Microsc. Soc.* 95, 482. doi:10.2307/3225140

Song, P.-S., Häder, D.-P., and Poff, K. L. (1980a). Phototactic orientation by the ciliate, *Stentor coeruleus*. *Photochem. Photobiol.* 32, 781–786. doi:10.1111/j.1751-1097.1980.tb04055.x

Song, P.-S., Häder, D.-P., and Poff, K. L. (1980b). Step-up photophobic response in the ciliate, *Stentor coeruleus*. *Arch. Microbiol.* 126, 181–186. doi:10.1007/BF00511225

Song, P.-S. (1999). Photosensory signal transduction in *Stentor coeruleus*. *J. Photoscience* 6, 37–45.

Tartar, V. (1961). *The biology of* Stentor. New York: Pergammon Press. doi:10.5962/bhl.title.7444

Théry, A., Wang, Y., Dvoriashyna, M., Eloy, C., Elias, F., and Lauga, E. (2021). Rebound and scattering of motile: *Chlamydomonas* algae in confined chambers. *Soft Matter* 17, 4857–4873. doi:10.1039/d0sm02207a

Trinh, M. K., Wayland, M. T., and Prabakaran, S. (2019). Behavioural analysis of single-cell aneural ciliate, *Stentor roeseli*, using machine learning approaches. *J. R. Soc. Interface* 16, 20190410. doi:10.1098/rsif.2019.0410

Wan, K. Y., Hürlimann, S. K., Fenix, A. M., McGillivary, R. M., Makushok, T., Burns, E., et al. (2020). Reorganization of complex ciliary flows around regenerating *Stentor coeruleus*. *Philos. Trans. R. Soc. Lond. B Biol. Sci.* 375, 20190167. doi:10.1098/rstb.2019.0167

Wan, K. Y., and Jékely, G. (2021). Origins of eukaryotic excitability. *Philos. Trans. R. Soc. Lond. B Biol. Sci.* 376, 20190758. doi:10.1098/rstb.2019.0758

Wood, D. C. (1969a). Electrophysiological studies of the protozoan, *Stentor coeruleus*. *J. Neurobiol.* 1, 363–377. doi:10.1002/neu.480010402

Wood, D. C. (1969b). Parametric studies of the response decrement produced by mechanical stimuli in the protozoan, *Stentor coeruleus*. *J. Neurobiol.* 1, 345–360. doi:10.1002/neu.480010309

Zack, G. W., Rogers, W. E., and Latt, S. A. (1977). Automatic measurement of sister chromatid exchange frequency. *J. Histochem. Cytochem.* 25, 741–753. doi:10.1177/25.7.70454

Zhang, K. S., Blauch, L. R., Huang, W., Marshall, W. F., and Tang, S. K. Y. (2021). Microfluidic guillotine reveals multiple timescales and mechanical modes of wound response in *Stentor coeruleus*. *BMC Biol.* 19, 63–17. doi:10.1186/s12915-021-00970-0

frontiers | Frontiers in Cell and Developmental Biology

TYPE Brief Research Report
PUBLISHED 20 February 2023
DOI 10.3389/fcell.2023.1133028

OPEN ACCESS

EDITED BY
Toshiyuki Nakagaki,
Hokkaido University, Japan

REVIEWED BY
Masatoshi Ichikawa,
Kyoto University, Japan
Itsuki Kunita,
University of the Ryukyus, Japan

*CORRESPONDENCE
Makoto Iima,
✉ iima@hiroshima-u.ac.jp

SPECIALTY SECTION
This article was submitted to Evolutionary Developmental Biology, a section of the journal Frontiers in Cell and Developmental Biology

RECEIVED 28 December 2022
ACCEPTED 08 February 2023
PUBLISHED 20 February 2023

CITATION
Muku K, Yamashita H, Kamikubo T, Suematsu NJ and Iima M (2023), Long-time behavior of swimming *Euglena gracilis* in a heterogenous light environment.
Front. Cell Dev. Biol. 11:1133028.
doi: 10.3389/fcell.2023.1133028

Long-time behavior of swimming *Euglena gracilis* in a heterogenous light environment

Kazuki Muku[1], Hiroshi Yamashita[2], Touya Kamikubo[3], Nobuhiko J. Suematsu[4,5] and Makoto Iima[2]*

[1]Department of Integrated Arts and Sciences, Hiroshima University, Higashihiroshima, Japan, [2]Graduate School of Integrated Sciences for Life, Hiroshima University, Higashihiroshima, Japan, [3]Department of Mathematics, Hiroshima University, Higashihiroshima, Japan, [4]Meiji Institute for Advanced Study of Mathematical Sciences(MIMS), Meiji University, Nakano, Japan, [5]Graduate School of Advanced Mathematical Sciences, Meiji University, Nakano, Japan

The cell motion of *Euglena gracilis* in homogeneous and heterogeneous light environments was analyzed. Homogeneous and heterogeneous environments were prepared, with only a red color or with a red circle surrounded by brighter white regions, respectively. In a heterogeneous environment, the cells move into the red circle. Swimming orbits at 1/25 s intervals for 120 s were analyzed. The speed distribution of the 1 s-averaged cell orbits in a homogeneous environment was different from that in a heterogeneous environment, where the faster swimming fraction was enhanced. The relationship between speed and curvature radius was analyzed using a joint histogram. Histograms for short timescale motion, constructed by 1 s-averaged orbits, suggest that the cell swimming curves are not biased, while those for long timescale motion, constructed by 10 s-averaged orbits, suggest that the cell swimming curves are biased in the clockwise direction. Furthermore, the curvature radius determines the speed, which does not seem to depend on the light environment. The mean squared displacement in a heterogeneous environment is larger than that in a homogeneous environment on a 1 s timescale. These results will be the basis for constructing a model for the long-time behavior of photomovement for light differences.

KEYWORDS

E. gracilis, diorama environment, heterogeneous light condition, long time scale orbit, curvature radius

1 Introduction

Many microorganisms swim using cilia and flagella or move by pseudopods to improved habitats, boosting their survival chances. Such motion is due to information processing by sensing external signals. Cell movements to their preferred surroundings are called *taxis*, including chemotaxis (chemical concentration), gravitaxis (gravity), and phototaxis (light intensity). Here, we focused on the photomovement of *Euglena gracilis* under heterogeneous light conditions.

E. gracilis, a model microorganism with a body length of 50 μm, swims using a single long flagellum outside the body. The paraflagellar body (PFB), a light-sensing organ of *E. gracilis*, senses light through a chemical, photo-activated adenyl cyclase (PAC), specifically by a step-up photophobic response (Iseki et al., 2002). The light-sensing system functions when *E. gracilis* swims by rotating its body along the long axis, causing the stigma (red spot)

on the PFB to change light intensity to perceive the light direction (Diehn, 1973; Kato and Shinomura, 2019). Because *E. gracilis* has a single PFB, it must process light information at a single point in the PFB.

In a heterogeneous environment, *E. gracilis* swims to a location with a specific light intensity (Giometto et al., 2015; Ogawa et al., 2016). Consequently, they require a method of information processing to detect heterogeneous light distribution.

To date, three types of photomovements of *E. gracilis* are known (Diehn, 1973): (a) phototaxis: swimming direction changes according to the light vector; (b) photokinesis: swimming speed dependency on the light intensity; and (c) photophobic reponse: cell motion changes due to the change in light intensity.

Photophobic response is a photomovement related to cell behavior in an environment with spatial light distribution. The action spectrum, or the change in motion caused by a change in light intensity at a specific wavelength, has been studied. Because the action spectrum for the abrupt increasing light intensity correlates well with the absorption spectra of PAC, PAC is thought to be related to a step-up photophobic response (Iseki et al., 2002). Recently, a polygonal cell orbit with a sudden increase in light intensity has been reported (Tsang et al., 2018). This behavior is suggested to sense the spatial light distribution with a similar 'run-and-tumble' mechanism of bacterial chemotaxis (e.g., *Escherichia coli*) (Berg, 1993; Tsang et al., 2018).

It is unclear whether this mechanism is valid in a more general light environment, thus cell motion in a heterogeneous environment should be analyzed in detail. We focused on the long-term behavior of cell motion, which has not been studied as intensively as individual swimming (Rossi et al., 2017; Giuliani et al., 2021) or euglenoid motion (Noselli et al., 2019). When the randomness of the cell motion is focused on, the mean squared displacement (MSD) can be an indicator. For an active Brownian particle, which has a constant speed with the direction defined by Brownian motion (Marchetti et al., 2016), the exponent depends on the timescale; the behavior is ballistic (MSD ~ t^2) for shorter times than the characteristic timescale, called persistence, and diffusive for longer times (MSD ~ t^1). A similar transition has been reported for the orbit due to the 'run-and-tumble' motion observed in *E. coli* (Solon et al., 2015) and the Lévy walk model (Zaburdaev et al., 2015).

For *E. gracilis* motion, the exponent of MSD has been reported 1.89 (Ogawa et al., 2017); the cell motion after a sudden change in light intensity gives various exponents for shorter timescales of less than 10 s (Tsang et al., 2018), suggesting that the cell motion behavior depends on the spatial or temporal light change; however, the relationship between the exponent and the orbit in physical space is not fully understood. Particularly, *E. gracilis* cell motion adapted to heterogeneous light intensities has not been studied. Because there are several timescales for adaptation to environmental change (Ozasa et al., 2019), we expect that swimming behavior will change with the heterogeneous environment.

Here, we investigated the motion of *E. gracilis* in a spatially heterogeneous but stationary manner. We prepared homogeneous and heterogeneous environments and smoothed orbits to eliminate short-time helical motions owing to swimming details. The speed histograms for these environments were different. The orbits' shape was characterized by the curvature radius and the local speed; their functional relationships were determined. Additionally, MSD exponents in these environments differed.

2 Materials and methods

The experimental setup is shown in Figure 1A. The suspension container was illuminated from below by a small DLP projector with LED light source (PicoCube X, Felicross); the light field was prepared by the projection pattern generated on a PC through a white plastic sheet to diffuse light.

A suspension container was prepared using a silicone plate of 0.5 mm thickness with a circular hole D = 40 mm in diameter, sandwiched between a 100 mm × 100 mm glass plate and a 50 mm × 75 mm glass plate to generate a cylinder (D = 40 mm in diameter and 0.5 mm in thickness; Figure 1B).

The suspensions were prepared as follows: *E. gracilis* (Figure 2C) was pre-cultured in Koren-Hutner medium for 2–4 weeks with continuous light illumination. The cells were then inoculated into 2 g L^{-1} HYPONeX solution with periodic light illumination (15 h bright light, 9 h dark). After 10–30 days of culture in HYPONeX aqueous solution, the suspensions were used for each experiment between the circadian time (CT) 8–12 h. The HYPONeX culture was diluted to 2.35 × 10^4 cells mL^{-1} and sealed in a container. The volume fraction of the cell was O (10^{-4}), where O (10^a) means "order of magnitude of 10^a".

We performed two experiments (Experiments A and B).

In Experiment A, the temporal change in cell density under a heterogeneous light environment was quantitatively measured under a light field with two different intensity regions (Figure 1D).

Two patterns were prepared. Pattern 1 had a red filled circle of diameter D; the color was defined by RGB = (255, 64, 64) (denoted as 'red' hereafter). Pattern 2 had a smaller red filled circle of diameter d = 10 mm, and the outside color was defined by RGB = (255, 255, 255) ('white'). Because *E. gracilis* does not recognize red color, the color difference between them consists of green and blue elements; the red element was included for image analysis. The photoflux density (PFD) of the projected colors was 18.7 μmol m^{-2} s^{-1} (838 LUX) for red and 53.2 μmol m^{-2} s^{-1} (3252 LUX) for white, based on an average of 240 measurements with an exposure time of 500 μs using a spectrometer (MK350S Premium, UPRtek). Because the container diameter is equal to the diameter of Pattern 1, it provides a homogeneous light environment in the container, whereas Pattern 2 provides a heterogeneous light environment. Because the red region has an amount of light intensity, the light intensity difference is not analogous to the step-up light condition (Tsang et al., 2018; Ozasa et al., 2019).

The experimental system was kept motionless in dark conditions for 1 h before illumination with Pattern 1 for 10 min (State A) and then with Pattern 2 for 60 min. During illumination, the cells in the entire region were photographed every 5 min using a digital camera (Nikon Z7 II) with a macro lens (Nikkor Z 50 mm f/1.8 S). The focal depth was approximately 0.375 mm.

The whole region was divided to nine sub-regions A_k (k = 1, . . . , 9) defined by

$$A_k = \left\{ (x, y) \mid \left(r_{k-1}^2 \le x^2 + y^2 < r_k^2 \right), \qquad r_k = \frac{2k}{9}\frac{d}{2}, \quad 1 \le k \le 9 \right\} \tag{1}$$

10.3389/fcell.2023.1133028

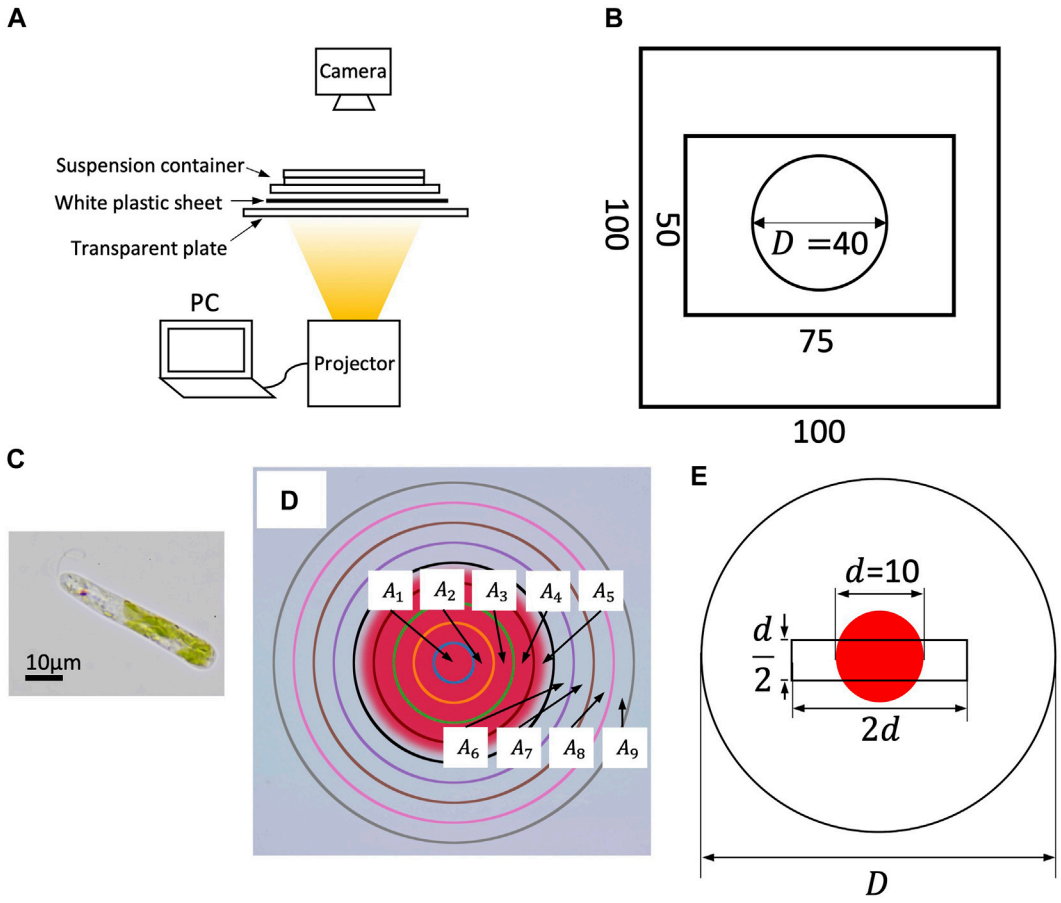

FIGURE 1
(A) Experimental setup. **(B)** Dimensions of suspension container. A silicone plate with 0.5 mm thickness is sandwiched between two rectangular glass plates. The suspension is put inside the circle (cylinder). **(C)** An image of *E. gracilis*. **(D)** Sub-regions for cell counting. **(E)** The search region of orbit analysis (a $d/2 \times 2d$ rectangle).

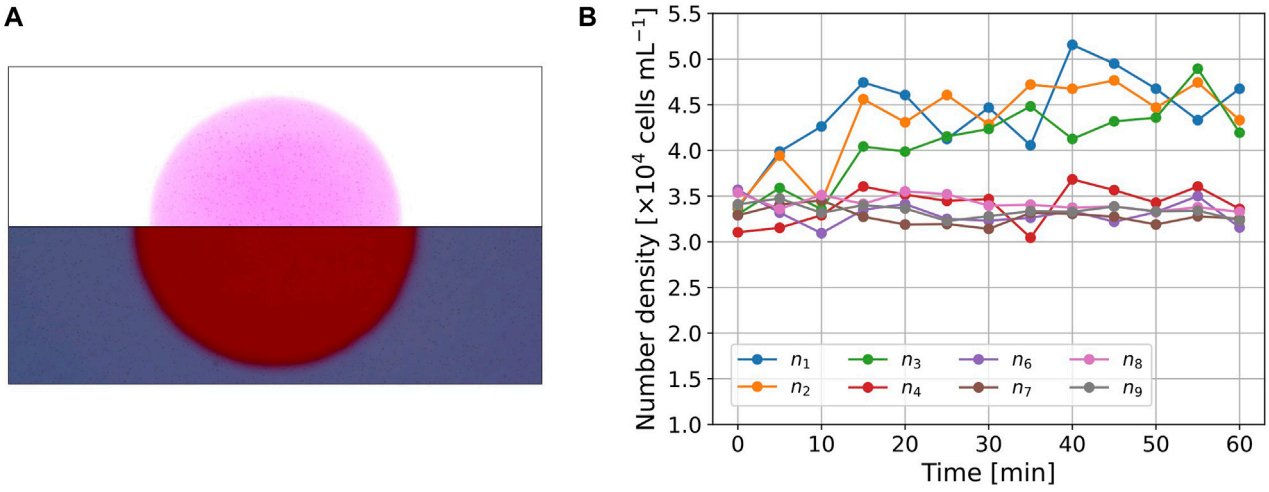

FIGURE 2
(A) Images of the cell distribution (t =30 min). The picture was divided into upper and lower parts, both of which were modified independently to visualize the cells for presentation purposes. **(B)** Time series of number density $n_k(t)$ in the subregions.

(Figure 1D). Here, A_5 includes the boundary of the circle, where the cell number was not counted because of non-uniform contrast. The largest area A_9 has diameter $2d$, half that of D. Therefore, we assumed that the counted cell number was not affected by the sidewall. The cell number in the sub-region A_k was counted by image analysis using ImageJ. The image was converted to an 8-bit black-and-white image and binarized with a threshold to count the number. The threshold values for the red circle and that for the outside region were adjusted such that the cell number densities at $t = 0$ were at a same level. The number density in subregion A_k at time t is denoted by $n_k(t)$.

In Experiment B, cell orbits were recorded. The experimental procedure was the same as that in Experiment A, until State A. After State A, in a homogeneous light environment, the culture was illuminated with Pattern 1 for 30 min before recording the orbit for 120 s at a rate of 25 fps. In a heterogeneous light environment, the same experiment was performed using Pattern 2. Each experiment was performed twice in each of the two environments.

We selected all the moving cells at $t = 0$ inside the search region, a $d/2 \times 2d$ rectangle, at the center of the container in both environments. The rectangle contains both red and white regions of Pattern 2; the areas for both colors are approximately equivalent (Figure 1E). All cells inside the search region were tracked at 1/25 s intervals using a computer digital tracking software (DIPP-Motion, DITECT) in both environments.

MSD of the orbit $\boldsymbol{X}(t)$ was defined as.

$$\mathrm{MSD}(t) = \langle \Delta X(t)^2 \rangle, \tag{2}$$

$$\Delta X(t)^2 = |\boldsymbol{X}(t) - \boldsymbol{X}(0)|^2, \tag{3}$$

where $\langle \cdot \rangle$ denotes the ensemble average and $\Delta X(t)^2$ is the squared displacement.

To exclude short-time motion such as helical orbit and measuring noises, and obtain an orbit with a long timescale, a moving average was performed. We use the term 'T − sec averaged orbit' for the orbit data after the moving average for the time interval of T s, $\int_{t-T/2}^{t+T/2} \boldsymbol{X}(t')dt'$.

3 Results

3.1 Cell density in a heterogeneous environment

Figure 2A shows a snapshot of the picture (t = 30 min) in Experiment A. The images were divided into upper and lower parts, and their brightness and contrast were independently modified to clearly show the cells in both regions. The cell number density inside the circle was larger than that outside the circle. The cells near the boundary could not be clearly detected owing to spatial changes in light intensity. Thus, we omitted the cell number data for A_5, $n_5(t)$, which contains the boundary. The initial cell number density was above that of the suspension because the cells accumulate due to negative phototaxis.

For quantitative analysis, $n_k(t)$ was measured, as shown in Figure 2B. The values of $n_k(t)$ $(1 \le k \le 3)$, which correspond to the region inside the circle, show an increase in the initial interval $0 \le t \le 30$ min and maintain larger values in the interval $30 < t < 60$ min. The values of $n_4(t)$ are also the cell number densities inside the circle, but the initial value, $n_4(0)$, is smaller than the other values of $n_k(0)$ $(k \ne 4)$. The values of $n_4(t)$ showed a slight increase on average, but the trend was clearly smaller than the values of $n_k(t)$ $(1 \le k \le 3)$. The cell density for the outer region, $n_k(t)$ $(6 \le k \le 9)$, maintained similar values throughout the entire time interval $0 \le t \le 60$ min, and the trend throughout the measurement period was almost constant or slightly decreased.

In Experiment A, we conclude that the cells of *E. gracilis* moves to red region in this setup and a balance between photomovement due to spatial light difference and the diffusion achieved after t = 30 min.

3.2 Cell orbit analysis

3.2.1 Orbital characteristics in homogeneous and heterogeneous light environments

Among all the moving cells in the search region, some disappeared or adhered to the upper glass before reaching the prescribed measured time (120 s). The tracked individuals were categorized as follows: (I) swimming individuals that went out of the focal plane or were adhered before the measurement time ended; (II) swimming individuals that stayed inside the focal plane until the measurement time. In a homogeneous environment, there were 79 orbits ((I) 14, (II) 65). In a heterogeneous environment, there were 81 orbits ((I) 30, (II) 51). Because the focus depth was smaller than the depth of the container, the motion of the disappeared cells was more three-dimensional. To test whether the difference in motion is related to the environment, we performed Fisher's exact test for the cell numbers in categories (I) and (II) with the null hypothesis that "The cell motions are independent of the environments," which was rejected at the 1% level (p = 0.00779), implying that the heterogeneous environment is related to the vertical cell motion, although the gradient of the light intensity is horizontal. In the following analysis, we focus on the orbits in category (II) to examine horizontal cell motion in different environments.

3.2.2 Orbit and speed distribution

The orbits of *E. gracilis* obtained in Experiment B are shown in Figure 3A (homogeneous environment) and Figure 3B (heterogeneous environment). In Figure 3A, all orbits' initial position was shifted to the origin because of homogeneity. In this figure, the orbits of the spatial scale from $O(10^3)$ to $O(10^4)$ μm are visible; many orbits consist of straight or curved parts and occasional direction changes, although some orbits change direction more randomly. In Figure 3B, the orbits in a heterogeneous environment are shown in the laboratory frame. The grey circle indicates the boundary of the red region.

The distributions of the local speed for the 1 s-averaged orbit are shown in Figure 3C (homogeneous environment) and Figure 3D (heterogeneous environment). The faster swimming fraction in a heterogeneous environment was enhanced. To confirm this difference, we sampled the orbits inside the red region in a heterogeneous environment (Figure 3D, solid lines); however, the distribution was clearly different from the distribution in Figure 3C.

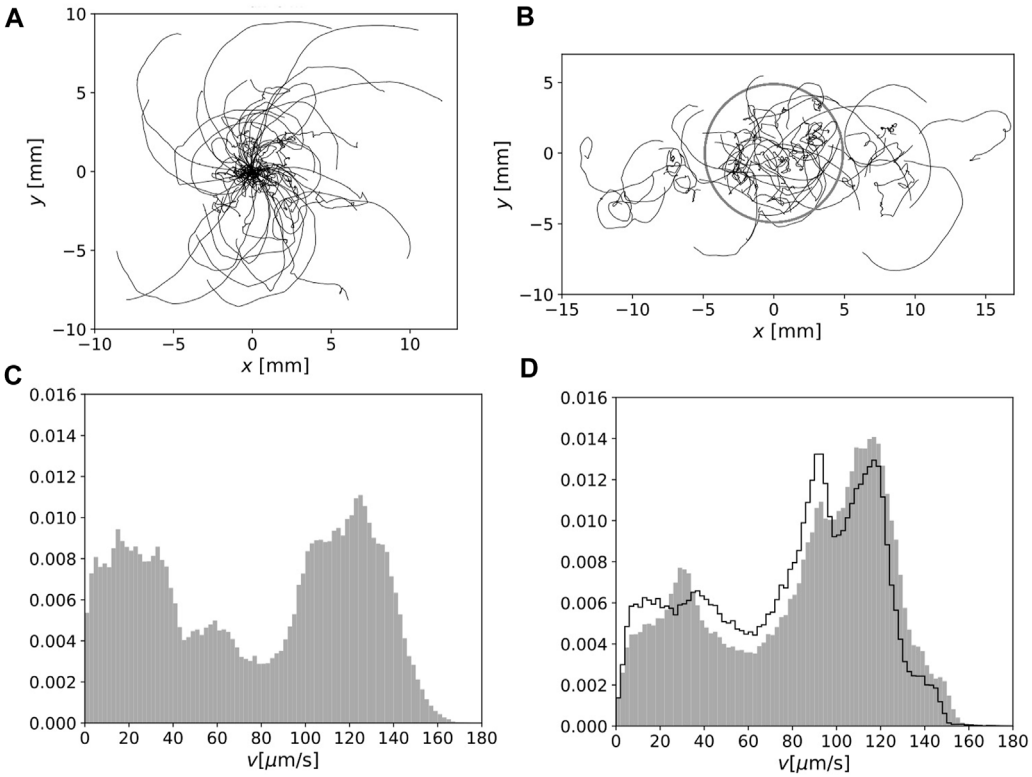

FIGURE 3
(A) Cell motion for 120 s in homogeneous environment. The initial positions were set at the origin. **(B)** As in **(A)** but under heterogeneous light conditions in the laboratory frame. The boundary of the red region is indicated by a grey circle. **(C)** Normalized speed distribution for 1 s-averaged orbits in a homogeneous environment. **(D)** As in **(C)** but in a heterogeneous environment. The normalized distribution of the speed of the orbits inside the red region is also indicated by the solid lines.

3.3 Long-time behavior: Analysis for moving-averaged orbit

3.3.1 Joint distribution of speed and curvature radius

Figure 4A and Figure 4B show joint distributions of speed v and curvature radius R for the 1 s-averaged orbits in homogeneous and heterogeneous environments, respectively. The distribution is symmetric with respect to the v-axis, suggesting that the orbit curve direction has no bias at this timescale. Although the density is biased to the faster speed region for heterogeneous environment, the values of R that give the peak of distribution for fixed v did not show significant differences in either environment.

Figures 4C,D each show similar joint distributions in Figures 4A,B, but for the 10 s-averaged orbits. The range of R in these figures extends to values much larger than those in Figures 4A,B. We note that the curvature radius is defined by local information (swimming speed and acceleration) alone, but the curvature radius of the moving time-averaged orbit contains large-scale shape information.

In this case, the distribution is clearly biased toward negative R, suggesting that the (large-scale) orbit curve direction is predominantly clockwise. The peak value at $v = 120\,\mu$m is given in $R \simeq 1000\,\mu$m, which is of the same order as the curvature radius of the orbits in Figures 3A,B. Interestingly, the value of R that gives the peak for a fixed v, does not show a significant difference between the two environments. However, in a heterogeneous environment, the speed distribution is shifted to the faster region, and thus, the orbit in the clockwise direction is predominant (*cf.* Figures 3A,B).

3.3.2 MSD

Figure 4E shows the MSDs in the homogeneous and heterogeneous environments. These were divided by t^2 to clearly show the difference from the ballistic orbit (MSD ~ t^2). In the long range of the timescale, $0.2 < t < 40$ s, the values of MSD in a heterogeneous environment are greater than those in a homogeneous environment, which is consistent with the speed distribution in a heterogeneous environment having a greater peak in the fast regime. The differences in the MSD curves outside the range nearly overlapped. For orbits in a homogeneous environment, the MSD shows a power-law region in the range $t < 4$. A fit line using the data in $0.4 < t < 4$ with an exponent of 1.92 was drawn. A power-law region observed in the heterogeneous environment in $0.4 < t < 4$ was close to ballistic, and a fit line using the same data range with an exponent of 1.98 was drawn. In both environments, the MSD deviates from t^2, and the exponent seems to decrease over a large timescale ($t > 10$).

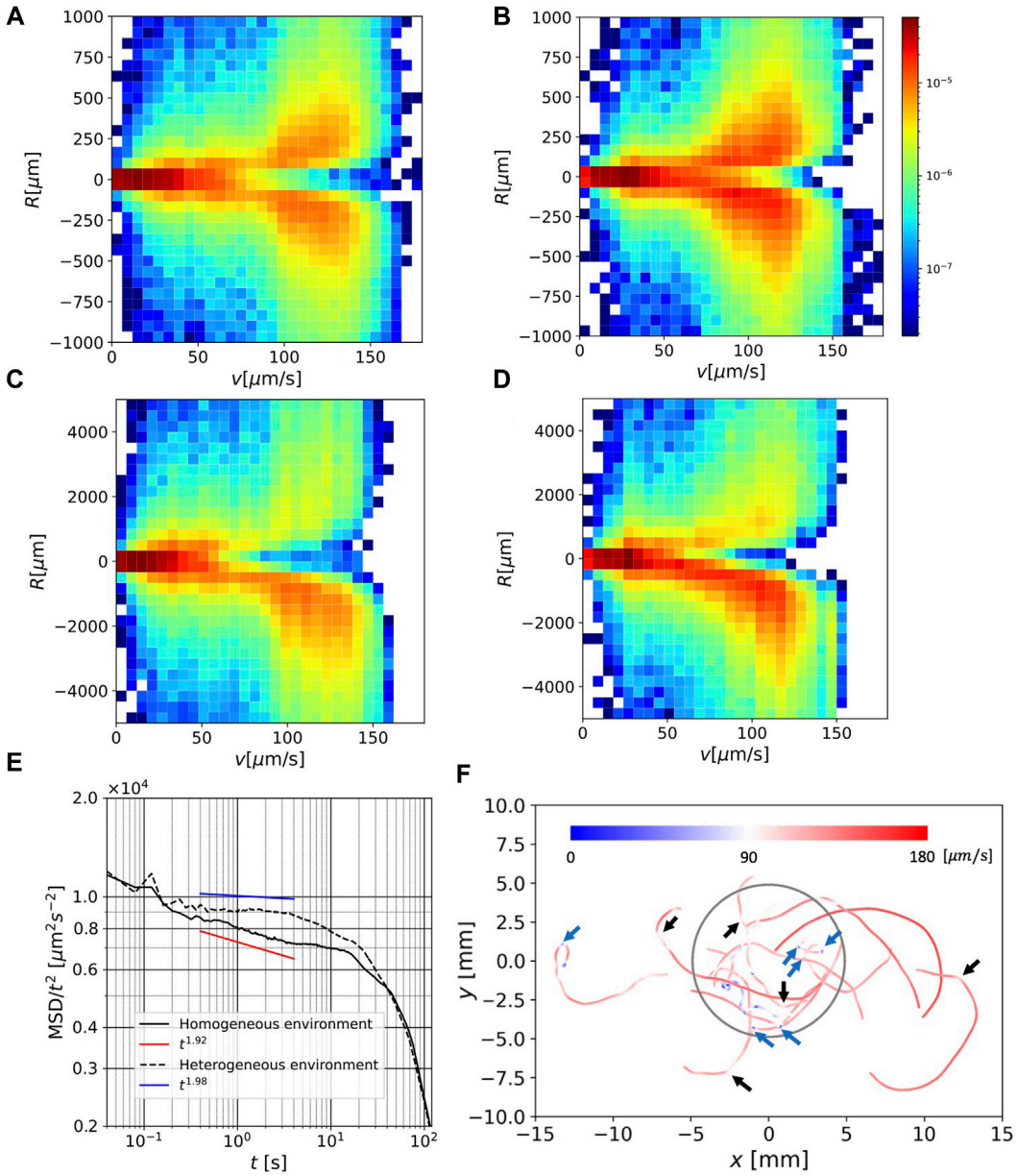

FIGURE 4
(A) Joint distribution of speed v and curvature radius R for 1 s-average orbit in a homogeneous environment. **(B)** As in **(A)** but in a heterogeneous environment.**(C)** As in **(A)**, but for 10 s-average orbit. **(D)** As in **(C)** but in a heterogeneous environment. **(E)** MSDs for all orbits under homogeneous and heterogeneous conditions. **(F)** Selected 5 s-average orbits in a heterogeneous environment, colored by local speed. The blue parts indicate speeds less than 90 μm/s and the red parts indicate speeds larger than 90 μm/s.

3.3.3 Orbit shape and speed

Figure 4F shows the 5 s-averaged orbits in a heterogeneous environment, selected on the condition $X(120)^{\frac{1}{2}} > 5 \times 10^3 \mu$m. The average time was chosen so that the difference between MSDs in the two environments was most distinct (c.f. Figure 4E), and the critical displacement length was determined by approximating MSD at t = 120 s. The orbit was colored with the local speed, red ($v > v_c$) and blue ($v < v_c$), where v_c = 90 μm/s.

Most of the large-scale curves of the radius $O(10^3) - O(10^4)$ μm are colored red, which indicates moving with a large curvature radius is characterized by a fast-swimming speed. This is consistent with the fact that a fast swimming speed is related to a large curvature radius (Figure 4D). This speed persistence is also consistent with the MSD, which exhibits a ballistic region.

Another interesting feature is the occasional quick change in swimming direction at a slow speed. Several significant directional changes on this spatial scale are indicated by blue arrows, and mild but apparent directional changes are indicated by black arrows. Although the light intensity changes at the boundary of the red region in a heterogeneous environment, no distinct orbital characteristics are observed near the boundary (Figure 3B; Figure 4F).

4 Discussion: How *E. gracilis* swims for longer-time scale in a heterogeneous environment

For *E. gracilis*, the time to swim for the circle diameter is approximately 10^2 s, which is longer than the adaptation timescale for the step-down photophobic responses, 20 s (Matsunaga et al., 1998), and of the same order of the relaxation time for the polygonal orbit after a sudden change in light intensity, ~ 120 s (Tsang et al., 2018). Considering that a swimming orbit can cross a circle with a shorter path, our experimental setup allowed microorganisms to experience successive changes in the environment with the same order of adaptation time. In this sense, this experimental setup provides a "diorama environment", an artificial condition to find potential adaptability in *E. gracilis*. As shown in Figure 3D, heterogeneous light condition is not simple superposition of two homogeneous illuminations with different light intensities.

Our orbit analysis suggests that orbits in a heterogeneous environment tend to be off the focus depth (Section 3.2.1), in other words, the cell motion in a heterogeneous environment is more three dimensional than that in homogeneous environment. The analysis of all individuals in the search region suggests that the speed distribution in a heterogeneous environment is different from that in a homogeneous environment (Figure 3).

The curvature radius of the orbit R, is strongly related to the local speed v for a long timescale (both the 1 s and 10 s timescales; Figures 4A–D), which is longer than the periods during helical trajectories by Rossi et al. (2017). This is consistent with the fact that single-flagellar swimming of *E. gracilis* restricts swimming behavior. The steering system of *E. gracilis* adapted to various environments, which is an important element in constructing the adaptation algorithm, should be sufficiently simple.

In view of the algorithm, the result that the bias of the swimming direction depends on the timescale is interesting. These results lead us to hypothesize that *E. gracilis* has a long timescale steering algorithm in which the curvature radius of orbit determined by speed. For swimming, the steering direction can be both clockwise and counterclockwise for a short timescale (1 s) but clockwise alone for a long timescale (10 s). These swimming behaviors appear to be the same in both environments. Non-etheless, the environmental difference leads to a difference in the 1 s scale orbit characteristics in the MSD.

In the long timescales ($0.2 < t < 40$), the MSD in a heterogeneous environment takes larger values than in a homogeneous environment (Figure 4E). In a homogeneous environment, the orbit had a power-law range, where it was close to ballistic but contained small randomness (the exponent was approximately 1.92), which is consistent with that of a previous study (Ogawa et al. (2017)). In a heterogeneous environment, the orbit had a ballistic range (the exponent was close to 1.98). These results allowed us to propose a hypothesis that the cells may use a strategy to search for a more favorable environment (darker region) by enhancing MSD in a heterogeneous environment. However, this remains an open question. For very long timescales ($t > 40$), the MSD deviates from (semi-) ballistic behavior, and the behavior is more diffusive. These differences may reflect the different behaviors of *E. gracilis* in different environments.

Figure 4F shows that the speed in straight or large-scale ($O(10^3)\mu$m) curved parts in orbit is fast, whereas the speed during direction change between these parts is slow. Such switching strategy reminds us of the 'run-and-tumble' algorithm for *E. coli* (Berg, 1993), where chemotaxis is achieved by switching between straight swimming and random direction change during an increasing or decreasing favorable chemical concentration, respectively. In our environment, however, the light gradient occurred in a narrow region, and we did not observe characteristic behavior near the boundary (Figure 3B; Figure 4F).

The results suggest that long-term and large-scale behavior is different from short-term and small-scale behavior, which can be related to the sudden change in light intensity. The photomovement of individuals under a spatial light gradient has been investigated by Ogawa et al. (2017); however, long-time orbits in heterogeneous media have not been analyzed.

For instance, a transition from ballistic to diffusive behavior observed in some theoretical models (Solon et al., 2015; Zaburdaev et al., 2015; Marchetti et al., 2016) may provide additional information for the algorithm for *E. gracilis* motion in a heterogeneous environment, especially for the spatial scale of heterogeneity. Further investigation for this is warranted.

5 Conclusion

We analyzed the cell motion of *E. gracilis* in homogeneous and heterogeneous light environments, where a heterogeneous light environment was prepared by a red circle region. The spatiotemporal cell number density showed that the cells moved into the red region. In the equilibrium state, in which the cell motion due to light difference balances with the diffusive motion, we tracked the cell motion to reveal that the speed distribution for the 1 s-averaged cell orbits in both environments showed a difference in that the high-speed fraction becomes greater in a heterogeneous environment. The joint histograms for the speed and curvature radius of the orbits in a short timescale (1 s-averaged) and long timescale (10 s-averaged) orbits were compared. The orbits in the short timescale provide a symmetric distribution of the curvature radius at a given speed in all speed regimes in both light environments. In the long timescale, the distribution of the curvature radius is strongly biased in the clockwise direction in the faster speed regime in both light environments. Power law exponent of MSD in a homogeneous environment was observed in the timescales $t \sim 1$ s and agreed with previous measurements by Ogawa et al. (2017). The MSD in the heterogeneous environment showed an almost ballistic regime at the same timescale. At this timescale, the MSD in a heterogeneous environment is larger than that in a homogeneous light environment.

Here, we demonstrated quantitative differences in long-time swimming behavior in a heterogeneous environment. The detailed algorithm for searching and moving to the favorite (red) region may

be determined in the future and compared with known algorithms, such as the 'run-and-tumble' mechanism.

Data availability statement

The raw data supporting the conclusion of this article will be made available by the authors, without undue reservation.

Author contributions

MI supervised the study and wrote the manuscript. The experiments were designed by MI, KM, HY, and NS and performed by KM, HY, and TK. The results were discussed by all the authors.

Funding

This work was partially supported by KAKENHI (21H05311).

Acknowledgments

The authors appreciate Prof. Shunsuke Izumi at Hiroshima University for providing *E. viridis* for preliminary comparison.

Conflict of interest

The authors declare that the research was conducted in the absence of any commercial or financial relationships that could be construed as a potential conflict of interest.

Publisher's note

References

Berg, H. C. (1993). *Random walks in Biology paperback*. Princeton University Press.

Diehn, B. (1973). Phototaxis and sensory transduction in Euglena. *Science* 181, 1009–1015. doi:10.1126/science.181.4104.1009

Giometto, A., Altermatt, F., Maritan, A., Stocker, R., and Rinaldo, A. (2015). Generalized receptor law governs phototaxis in the phytoplankton Euglena gracilis. *Proc. Natl. Acad. Sci.* 112, 7045–7050. doi:10.1073/pnas.1422922112

Giuliani, N., Rossi, M., Noselli, G., and DeSimone, A. (2021). How Euglena gracilis swims: Flow field reconstruction and analysis. *Phys. Rev. E* 103, 023102. doi:10.1103/PhysRevE.103.023102

Iseki, M., Matsunaga, S., Murakami, A., Ohno, K., Shiga, K., Yoshida, K., et al. (2002). A blue-light-activated adenylyl cyclase mediates photoavoidance in Euglena gracilis. *Nature* 415, 1047–1051. doi:10.1038/4151047a

Kato, S., and Shinomura, T. (2019). Eyespot structure and its function in photobehaviors of phytoflagellate. *PLANT Morphol.* 31, 3–9. doi:10.5685/plmorphol.31.3

Marchetti, M. C., Fily, Y., Henkes, S., Patch, A., and Yllanes, D. (2016). Minimal model of active colloids highlights the role of mechanical interactions in controlling the emergent behavior of active matter. *Curr. Opin. Colloid and Interface Sci.* 21, 34–43. doi:10.1016/j.cocis.2016.01.003

Matsunaga, S., Hori, T., Takahashi, T., Kubota, M., Watanabe, M., Okamoto, K., et al. (1998). Discovery of signaling effect of UV-B/C light in the extended UV-A/blue-type action spectra for step-down and step-up photophobic responses in the unicellular flagellate alga Euglena gracilis. *Protoplasma* 201, 45–52. doi:10.1007/bf01280710

Noselli, G., Beran, A., Arroyo, M., and DeSimone, A. (2019). Swimming *Euglena* respond to confinement with a behavioral change enabling effective crawling. *Nat. Phys.* 15, 496–502. doi:10.1038/s41567-019-0425-8

Ogawa, T., Izumi, S., and Iima, M. (2017). Statistics and stochastic models of an individual motion of photosensitive alga Euglena gracilis. *J. Phys. Soc. Jpn.* 86, 074401. doi:10.7566/jpsj.86.074401

Ogawa, T., Shoji, E., Suematsu, N. J., Nishimori, H., Izumi, S., Awazu, A., et al. (2016). The flux of Euglena gracilis cells depends on the gradient of light intensity. *PLOS ONE* 11, e0168114. doi:10.1371/journal.pone.0168114

Ozasa, K., Won, J., Song, S., Shinomura, T., and Maeda, M. (2019). Phototaxis and photo-shock responses of Euglena gracilis under gravitaxis. *Algal Res.* 41, 101563. doi:10.1016/j.algal.2019.101563

Rossi, M., Cicconofri, G., Beran, A., Noselli, G., and DeSimone, A. (2017). Kinematics of flagellar swimming in Euglena gracilis: Helical trajectories and flagellar shapes. *Proc. Natl. Acad. Sci.* 114, 13085–13090. doi:10.1073/pnas.1708064114

Solon, A. P., Cates, M. E., and Tailleur, J. (2015). Active brownian particles and run-and-tumble particles: A comparative study. *Eur. Phys. J. Special Top.* 224, 1231–1262. doi:10.1140/epjst/e2015-02457-0

Tsang, A. C. H., Lam, A. T., and Riedel-Kruse, I. H. (2018). Polygonal motion and adaptable phototaxis via flagellar beat switching in the microswimmer Euglena gracilis. *Nat. Phys.* 14, 1216–1222. doi:10.1038/s41567-018-0277-7

Zaburdaev, V., Denisov, S., and Klafter, J. (2015). Lévy walks. *Rev. Mod. Phys.* 87, 483–530. doi:10.1103/revmodphys.87.483

frontiers | Frontiers in Cell and Developmental Biology

TYPE Original Research
PUBLISHED 16 March 2023
DOI 10.3389/fcell.2023.1136404

OPEN ACCESS

EDITED BY
Takuji Ishikawa,
Tohoku University, Japan

REVIEWED BY
Ritsu Kamiya,
Chuo University, Japan
Jean-Ju Lucia Chung,
Yale Medicine, United States

*CORRESPONDENCE
Kogiku Shiba,
kogiku@shimoda.tsukuba.ac.jp

SPECIALTY SECTION
This article was submitted to Evolutionary Developmental Biology, a section of the journal Frontiers in Cell and Developmental Biology

RECEIVED 03 January 2023
ACCEPTED 08 March 2023
PUBLISHED 16 March 2023

CITATION
Shiba K, Baba SA, Fujiwara E and Inaba K (2023), Calaxin is required for asymmetric bend initiation and propagation in sperm flagella.
Front. Cell Dev. Biol. 11:1136404.
doi: 10.3389/fcell.2023.1136404

Calaxin is required for asymmetric bend initiation and propagation in sperm flagella

Kogiku Shiba[1]*, Shoji A. Baba[2], Eiji Fujiwara[3] and Kazuo Inaba[1]

[1]Shimoda Marine Research Center, University of Tsukuba, Shimoda, Japan, [2]Ochanomizu University, Otsuka, Japan, [3]Documentary Channel Co. Ltd., Tsurugashima, Japan

Regulation of waveform asymmetry in flagella is critical for changes in direction when sperm are swimming, as seen during the chemotaxis of sperm towards eggs. Ca^{2+} is an important regulator of asymmetry in flagellar waveforms. A calcium sensor protein, calaxin, is associated with the outer arm dynein and plays a key role in the regulation of flagellar motility in a Ca^{2+}-dependent manner. However, the underlying mechanism of regulating asymmetric waves by means of Ca^{2+} and calaxin remains unclear. To clarify the calaxin-dependent mechanism for generating Ca^{2+}-dependent asymmetric flagellar waveforms, we analyzed the initial step of flagellar bend formation and propagation in the sperm of the ascidian *Ciona intestinalis*. Our experiment used demembranated sperm cells, which were then reactivated by UV flash photolysis of caged ATP under both high and low Ca^{2+} concentrations. Here, we show that initial bends in the flagella are formed at the base of the sperm and propagate towards the tip during waveform generation. However, the direction of the initial bend differed between asymmetric and symmetric waves. When a calaxin inhibitor (repaglinide) was applied, it resulted in the failure of asymmetric wave formation and propagation. This was because repaglinide had no effect on initial bend formation, but it significantly inhibited the generation of the subsequent bend in the reverse direction. Switching of dynein sliding activity by mechanical feedback is crucial for flagellar oscillation. Our results suggest that the Ca^{2+}/calaxin mechanism plays an important role in the switching of dynein activity from microtubule sliding in the principal bend into the suppressed sliding in the reverse bend, thereby allowing the sperm to successfully change direction.

KEYWORDS

dynein, caged ATP, calcium ion, cilia, sperm motility

1 Introduction

Changes in the bending pattern of cilia and flagella are important for the regulation of cell movement and extracellular fluid flow (Inaba, 2015). In particular, the waveform of the sperm flagellum is composed of two bends: a principal bend (P-bend) and a reverse bend (R-bend) (Goldstein, 1977; Brokaw, 1979; Gibbons and Gibbons, 1980; Inaba and Shiba, 2018). When the radii of curvature of the two opposite flagellar bends are almost the same, sperm cells generate symmetric waveforms and swim straight. However, when the radius of curvature of the P-bend is much larger than that of the R-bend, sperm cells generate highly asymmetric waveforms, resulting in circular movements. The regulation of asymmetry in sperm flagellar waveforms is critical for changes in sperm swimming direction, as seen during sperm chemotaxis towards the eggs (Miller, 1985; Yoshida and Yoshida, 2011; Wachten et al., 2017).

Ca^{2+} plays a key role in the regulation of asymmetry in flagellar waveforms. For instance, the flagellar waveforms in demembranated models of sea urchin sperm cells change from symmetric to asymmetric with increasing Ca^{2+} concentrations (Brokaw, 1979; Gibbons and Gibbons, 1980). Such a change is implied in egg fertilization, as Ca^{2+} bursts induce highly asymmetric waveforms during sperm chemotaxis, thereby inducing the turning of sperm towards the egg in both ascidians and sea urchins (Bohmer et al., 2005; Wood et al., 2005; Shiba et al., 2008; Guerrero et al., 2010). However, much of the Ca^{2+}-dependent mechanism that spatiotemporally regulates the formation and propagation of asymmetric waves remains unknown.

We previously identified a Ca^{2+}-binding axonemal protein, calaxin, in the sperm of the ascidian *Ciona intestinalis* (recently renamed *C. intestinalis* type A or *Ciona robusta*). Calaxin is a member of the neuronal calcium sensor (NCS) family and directly interacts with the outer arm dynein on all nine doublet microtubules from the base to the tip of the flagellum (Mizuno et al., 2009). Inhibition of calaxin with the specific NCS inhibitor, repaglinide, suppresses the propagation of asymmetric flagellar waveforms required for chemotactic turn; however, a transient increase in intracellular Ca^{2+} during the turning movement normally still occurs (Mizuno et al., 2012). Although this suggests an important role of calaxin in the regulation of asymmetric flagellar bending, it is not completely understood how calaxin contributes to the formation and regulation of asymmetric waves. Calaxin homologs are well conserved among metazoans and some fungi (Inaba, 2015). Recent structural study using cryoelectron microscopy have identified the precise location of calaxin near outer dynein arms within the bovine respiratory cilia (Gui et al., 2021), suggesting the critical role of calaxin on dynein regulation and ciliary and flagellar motility.

Flagellar bending is associated with the coordination of microtubule sliding by multiple axonemal dyneins. The switching of dynein activity across the axoneme is thought to be controlled through the regulation of the central pair (CP) and radial spoke (RS) (Sale, 1986; Hayashi and Shingyoji, 2008; Lin and Nicastro, 2018). Mutual activation of opposite dyneins across the central pair in the axoneme induces flagellar oscillations (Lindemann and Lesich, 2010; Inaba, 2011; Lindemann, 2011; Shingyoji, 2013; Lin and Nicastro, 2018). The propagation of asymmetric flagellar waves is regulated in a Ca^{2+}- dependent manner. In fact, Ca^{2+}-binding proteins, including centrin and calmodulin, along with calmodulin-binding proteins, are localized as components of some inner arm dyneins or of the CP/RS (Smith and Yang, 2004; Wargo et al., 2005; Yamamoto et al., 2013; Zhao et al., 2019). The aim of our study is to determine how the Ca^{2+} sensor of the outer arm dynein, calaxin, contributes to the propagation of asymmetric waves.

To this end, we performed experiments using caged ATP to capture instantaneous images of the initial process for the formation and propagation of asymmetric waves and examined the effects of a calaxin inhibitor on these steps. We show that calaxin is not required for the formation of an initial P-bend at the flagellar base but is indispensable for the regulation of R-bend in the reverse direction. Our results suggest that Ca^{2+}/calaxin promotes the formation, growth and propagation of asymmetric flagellar waves by attenuating dynein-driven microtubule sliding in the reverse bend *via* mechanical feedback from the adjacent P-bend.

2 Materials and methods

2.1 Materials

The ascidian *C. intestinalis* (type A; also called *C. robusta*) was collected from Onagawa Bay near the Onagawa Field Research Center, Tohoku University or obtained from the National BioResource Project for *Ciona* (http://marinebio.nbrp.jp/). Animals were kept in aquaria under constant light for accumulation of gametes without spontaneous spawning. Semen samples were collected by dissecting the sperm duct and kept on ice until use.

2.2 Chemical and solutions

Ca^{2+}-free sea water (CFSW) contained 478.2 mM NaCl, 9.39 mM KCl, 48.27 mM $MgCl_2$, 2.5 mM EGTA and 10 mM Hepes-NaOH (pH 8.0). Sperm demembranation solution contained 0.2 M potassium acetate, 1 mM $MgSO_4$, 2.5 mM EGTA, 20 mM Tris-acetate (pH 7.8), 0.04% Triton X-100 and 1 mM DTT. Pre-incubation buffer contained 0.15 M potassium acetate, 2 mM $MgSO_4$, 2.5 mM EGTA, 39 μM (pCa10) or 2.51 mM (pCa5) $CaCl_2$, 50 mM Tris-HCl (pH8.0) and 1 mM DTT. Reactivation solution was the same as pre-incubation buffer but with 2 mM ATP. Free Ca^{2+} concentration was assessed by CALCON (http://www.bio.chuo-u.ac.jp/nano/calcon.html). Caged ATP was purchased from Dojindo (Kumamoto, Japan) dissolved in Pre-incubation buffer. Repaglinide was purchased from Sigma-Aldrich (St Louis, MO) and dissolved in dimethyl sulfoxide (DMSO). Theophylline from Sigma-Aldrich was dissolved in CFSW. Other reagents were of analytical grades.

2.3 Preparation of demembranated sperm

Demembranation and reactivation of *C. intestinalis* sperm were performed as described previously with some modifications (Mizuno et al., 2012). Semen was suspended in 100 volumes of CFSW containing 1 mM theophylline in CFSW to activate motility and incubated for 5 min at 25°C. Sperm were demembranated with 10 volumes of demembranation solution incubated for 3 min at 25°C. Demembranated sperm were kept for several minutes in pre-incubation buffer with or without 1 mM caged ATP until use. Demembranated sperm incubated with caged ATP were reactivated by UV irradiation. Demembranated sperm without caged ATP were reactivated with the same volume of the reactivation buffer containing 0.1–2 mM Mg-ATP (Final Mg-ATP concentrations were 0.05–1 mM). DMSO (control) or Repaglinide was added to the demembranation solution, pre-incubation buffer and reactivation buffer. DMSO concentration was kept below 0.5% in all experiments.

2.4 Experimental system

Movements of demembranated sperm incubated with caged ATP were observed under an inverted microscope with phase

optics (IX71, Olympus, Tokyo, Japan) with a ×20 objective and recorded with a high-speed CCD camera (HAS220, Detect, Tokyo, Japan). Flagellar waveforms were captured using a red-LED (Edison 3WStar, Taipei, Taiwan) and a laboratory-made LED stroboscopic illumination system synchronized with the exposure signals from the high-speed camera. Images were taken at a frame rate of 200 fps with 0.2 msec pulse from the red LED. A UV-LED (NS365L-3SVR, 365 nm, Nitride Semiconductors, Tokushima, Japan) was used for the photolysis of caged ATP. A mercury lamp in the lamp house of the microscope was replaced by a laboratory-made LED holder with UV-LED. A laboratory-made LED controller generated a 150 msec pulse for UV irradiation and triggered a recording cue signal on the high-speed camera (HAS220) which enables to record images 0.25 s before and 2.25 s after UV irradiation. To measure the flagellar beat frequency of sperm reactivated with Mg-ATP, flagellar waveforms were observed under an upright microscope with phase optics (BX51, Olympus) with a ×20 objective and recorded with a high-speed CCD camera (HAS-D3, Detect) at 500 fps.

2.5 Analysis of flagellar waveforms

The flagellar beat frequency and the flagellar curvature were analyzed using Bohboh software (Bohbohsoft, Tokyo, Japan). Individual images of sperm flagella were tracked automatically, and their curvatures calculated based on the method of Baba and Mogami (1985). Pseudocolor-maps of the flagellar curvature along the distance and time were created using by gnuplot 5.0 (http://www.gnuplot.info/).

2.6 Statistical analysis

All experiments were repeated at least three times with three different specimens. Data is expressed as means ± SE. Statistical significance was calculated using Student's t-test; $p < 0.05$ was considered significant.

3 Results

To elucidate the mechanism underlying the formation and propagation of asymmetric flagellar waves, we performed experiments using caged ATP to capture initial bend formation and subsequent propagation. Specifically, *Ciona* sperm were demembranated with Triton X-100 and incubated with 1 mM of caged ATP. Reactivation of motility was induced by UV flash photolysis of caged ATP. This method released the ATP from its caged compound within a few seconds by a UV flash (McCray et al., 1980; Goldman et al., 1982). To record the changes in sperm flagellar waveforms upon the UV flashing, we used a phase-contrast microscope with a red LED for illumination and captured the images using a high-speed camera, to which the LED pulse was synchronized. UV flashes were applied through the objective lens by a UV LED located in the lamp house.

After the UV flashing, we estimated the concentration of ATP released from caged ATP by measuring the flagellar beat frequency. The beat frequency of demembranated sperm, which had been reactivated with 1 mM of caged ATP and a 150 ms UV flash was estimated to be approximately 10 Hz (Figure 1A). Notably, sperm beat frequency did not significantly differ between solutions with low (10^{-10} M Ca^{2+}; pCa10) and high (10^{-5} M Ca^{2+}; pCa5) Ca^{2+} concentrations. In this study we used two different concentrations of Ca^{2+} to observe typical asymmetric and symmetric flagellar waves during chemotactic turn. To estimate the concentration of ATP release from caged ATP, we measured the beat frequency of demembranated sperm that were reactivated by various concentrations of Mg-ATP (Figure 1B). The flagellar waveform became more asymmetric at pCa5 than at pCa10, but no significant difference was observed in the beat frequency between two Ca^{2+} conditions within the range of 0.05–1 mM Mg-ATP present. From the calibration curve, we estimated that approximately ~0.1 mM of ATP was released under these conditions by the photolysis of caged ATP.

Next, we analyzed the process for the formation and propagation of flagellar waveforms upon ATP release. Low and high Ca^{2+} concentrations induced symmetric and asymmetric waveforms, respectively (Brokaw, 1979; Gibbons and Gibbons, 1980; Inaba and Shiba, 2018). By using photolysis for the controlled induction of dynein-microtubule sliding, we captured the initial process of bend formation and propagation of symmetric and asymmetric waves. All the regions of the flagellum from the base to the tip were examined under a microscope, and it was observed that the formation and propagation of flagellar bends occurred in one plane without any helical configuration (Figure 2; Figure 3).

Ascidian spermatozoa reactivated under low Ca^{2+} concentrations form a slightly asymmetric waveform and swim in a circle with a large radius. On the other hand, sperm reactivated at higher Ca^{2+} concentrations form a highly asymmetrical waveform, resulting in a circular motion with a small radius (Brokaw, 1987). In our experimental system using caged ATP, ATP release by photolysis at pCa10 induced the formation of the initial bend at the base of the flagellum 100–150 ms after the UV flash (Figure 2A; Table 1, Supplementary Video S1). As the bend propagated towards the flagellar tip, the formation of a second bend started to grow within 200 ms. Responses with similar time courses were observed in the formation and propagation of flagellar waves at pCa5, although the curvature of the initial bend was larger than that of the second bend (Figure 2B; Table 1, Supplementary Video S1).

We measured the curvatures along the flagellum, when flagellar oscillation was completely induced 200 ms after UV irradiation. We obtained the maximum and minimum flagellar curvatures in one flagellar beat cycle. In this study the bend showing the larger or smaller absolute value of curvature was defined as the P-bend or R-bend, respectively. We confirmed that the bend with larger curvature corresponded to the bend outside the sperm swimming path, which was originally defined the P-bend (Gibbons and Gibbons, 1972; Brokaw, 1979; Shingyoji, 2013). The curvature of the P-bend was plotted as a positive value and that of the R-bend was plotted as a negative value (Figures 2A, B bottom). Notably, we found that the initial bends of sperm reactivated at pCa10 consisted mostly of R-bends (Figure 2A). In contrast, the initial bends formed in the sperm reactivated at pCa5 were almost exclusively P-bends (Figure 2B). These results suggest that the initial bends are formed at the base in both symmetric and asymmetric waves but their

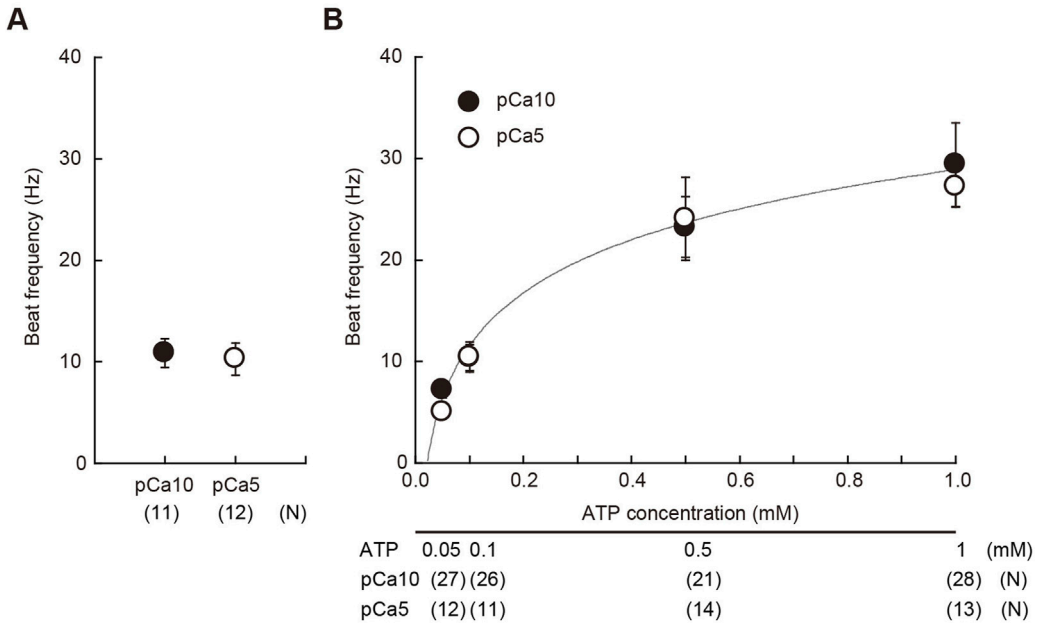

FIGURE 1
Estimation of the concentration of ATP released from caged ATP. **(A)** Beat frequency of demembranated *Ciona* sperm incubated with 1 mM caged ATP and reactivated by a 150 ms UV flash. N = 11 (pCa10), and N = 12 (pCa5). **(B)** Beat frequency of demembranated and reactivated *Ciona* sperm by various concentrations of Mg-ATP in the absence of caged ATP. Closed and open circles show Ca^{2+} concentrations in the reactivation solutions at pCa10 and pCa5, respectively. N = 13–28 from three different experiments. Values are expressed as mean ± S.D.

directions are different depending on the high and low Ca^{2+} concentrations.

We previously showed that calaxin is an important factor that regulates the propagation of asymmetric waveforms (Mizuno et al., 2012). Therefore, we next examined the role of calaxin in the formation, growth, and propagation of a bend during the initial generation of asymmetric flagellar waves. We used an inhibitor of the NCS family proteins, repaglinide (Okada et al., 2003), as a calaxin inhibitor since it specifically binds to calaxin and inhibits sperm chemotaxis in *Ciona* sperm flagella (Mizuno et al., 2012). Demembranated sperm cells were incubated with caged ATP and repaglinide and irradiated with UV light to induce ATP release. The process of initial bend formation and propagation was recorded at both low and high Ca^{2+} concentrations. At pCa10, both the initial and the second bends were formed normally; however, such formation occurred a little later (~250 ms) upon repaglinide treatment when compared to that in the control (Figure 3A; Table 1, Supplementary Video S1). Moreover, the maximum curvature after UV flashing was significantly smaller in the flagella of repaglinide-treated sperm than in those of untreated sperm (Table 1). In contrast, at pCa5 in the presence of repaglinide, an initial bend was formed but did not propagate to the flagellar tip (Figure 3B, Supplementary Video S2). The flagellum continued to vibrate at a high frequency with an overall constant waveform (Supplementary Video S2). The flagellum never formed the second bend, representing a state apparently similar to the quiescent pattern that was previously reported in sea urchin sperm (Goldstein, 1979; Gibbons and Gibbons, 1980), although it might not be comparable because the latter case is observed under the condition of pCa3 and 1 mM ATP. The failure of flagellar bend propagation at the caged ATP induced activation were observed in nearly 30% of the sperm treated by repaglinide at pCa5 (Supplementary Figures S1). We have also checked the bend formation pattern in reactivated sperm by 0.1 mM and 1 mM ATP in the presence and absence of repaglinide at pCa5. As previously reported, sperm reactivated with 1 mM ATP showed waveforms attenuated by repaglinide treatment, but most sperm oscillated and showed no abnormal wave propagation. On the other hand, about 8% of the sperm reactivated with 0.1 mM ATP showed abnormal propagation after treatment with repaglinide (Supplementary Figures S1, S2).

Next, we quantified the direction of the initial bend under low and high Ca^{2+} conditions. We assigned the P- and R-bend by comparing of the curvatures of the two bends at 200 ms after UV photolysis. At low concentrations of Ca^{2+}, 90.9% of the initial bend that formed upon the UV flash was observed in the reverse direction. In contrast, 81.9% of the initial bend was in the principal direction at high Ca^{2+} concentrations. The first bend direction formed in the flagella showed the same trend in the presence of repaglinide in low Ca^{2+} conditions (Figure 4). Since the flagellar wave did not oscillate in the presence of repaglinide at pCa5, it was not possible to determine the exact bend direction. However, since the curvature of the unilateral bend was as large as the P-bend formed at pCa5 in the absence of repaglinide, we assumed that the bend formed in the presence of repaglinide at pCa5 was a P-bend. These results indicate that the direction of the initial bend depends on Ca^{2+} and is unaffected by calaxin inhibition.

To better understand of the process of flagellar bend formation, the changes in flagellar curvature were plotted against time and distance from the flagellar base in a three-dimensional (3D) graph

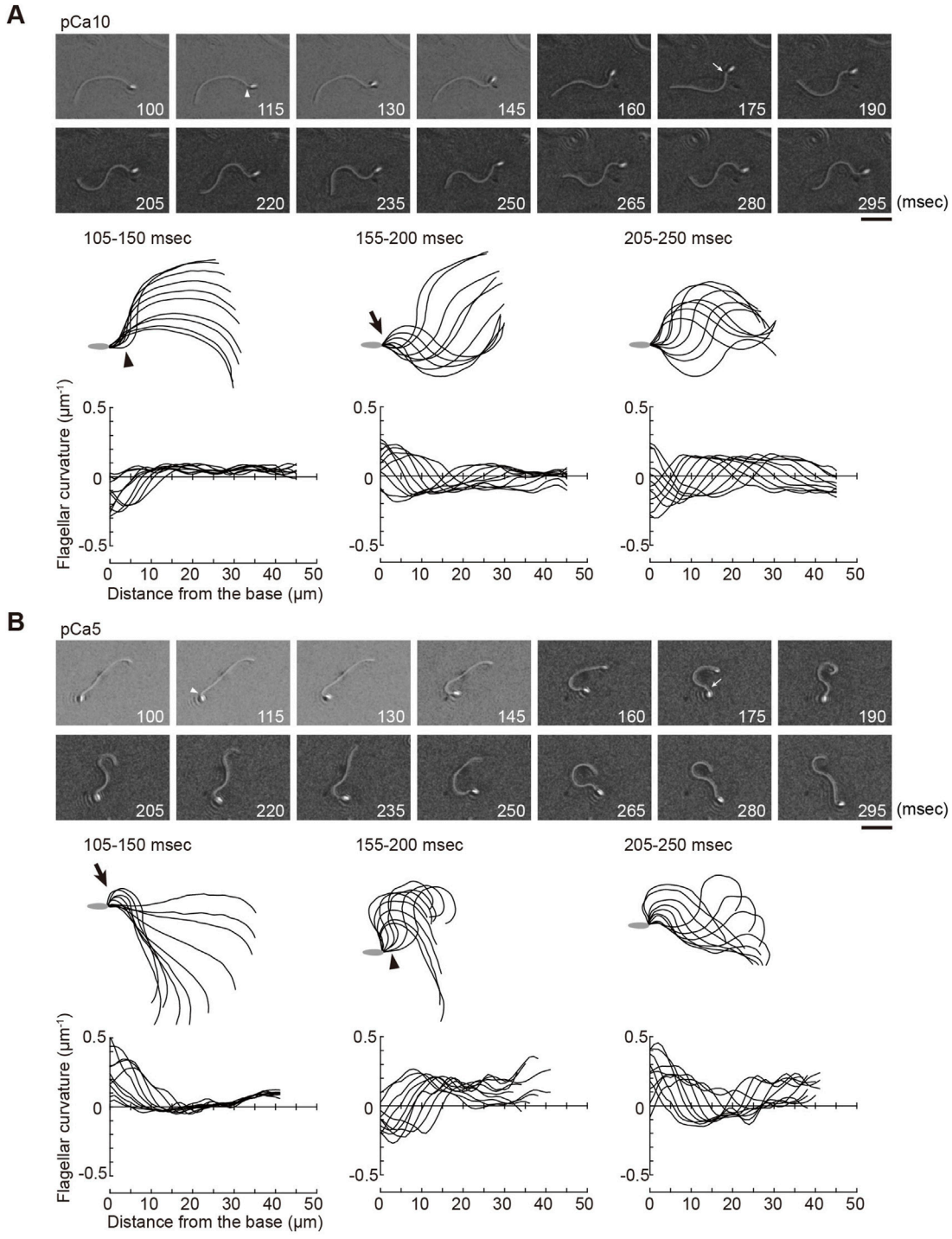

FIGURE 2
Generation of symmetric and asymmetric flagellar waveforms in *Ciona* sperm by photolytic release of caged ATP. Sperm cells were demembranated and incubated in the reactivation solution with caged ATP at low (pCa10; **(A)**) or high (pCa5; **(B)**) Ca^{2+} concentrations. Release of ATP was triggered by UV flash. Upper panel: sequential images of sperm flagellar waveforms at 15 ms-intervals from 100 ms after the UV flash. Arrow heads and arrows indicate the initial bend and the second bend, respectively. Scale bar, 20 μm. Middle panel: overwritten images of demembranated sperm at 5 ms intervals during the periods of time (105–250 ms) after release of ATP. Arrow heads and arrows indicate the initial bend and the second bend, respectively. Lower panel: changes of flagellar curvature occurring 105–250 ms after the UV flash are plotted against the distance from the base of flagellum. Ten waveforms produced at 50 ms are overwritten. Symmetric and asymmetric waveforms were generated in low calcium concentrations (pCa10, **(A)**) and high calcium concentrations (pCa10, **(B)**), respectively. One typical sperm example from the all experiments at least three times with three different specimens was shown.

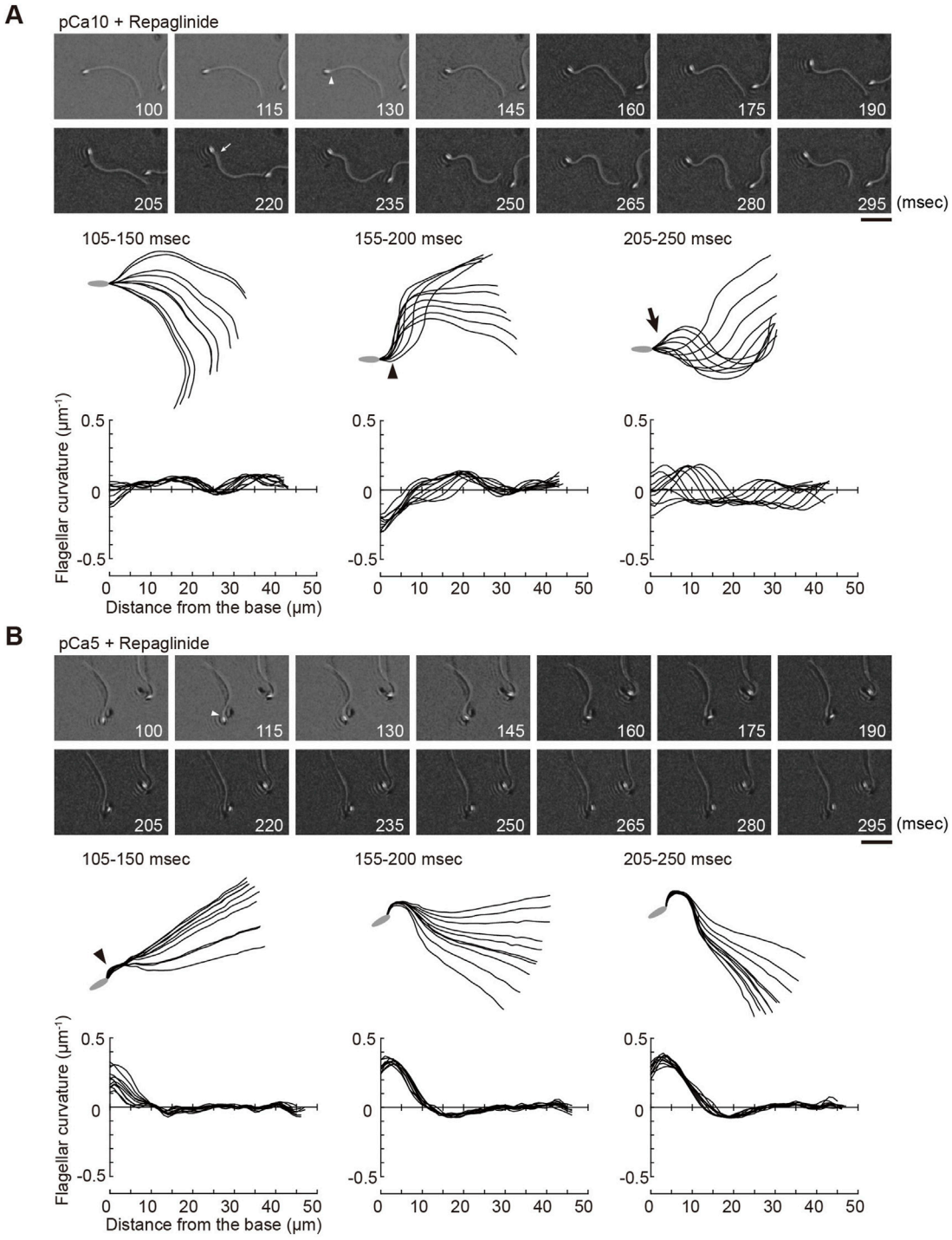

FIGURE 3
Effect of a calaxin inhibitor on the formation and propagation of asymmetry waveforms induced by photolytic release of caged ATP at high calcium concentrations. Sperm cells were demembranated and incubated in the reactivation solution with caged ATP at low (pCa10; **(A)**) or high (pCa5; **(B)**) Ca^{2+} concentrations with 150 μM repaglinide. Release of ATP was triggered by UV flash. Upper panel: sequential images of sperm flagellar waveforms at 15 ms-intervals from 100 ms after the UV flash. Arrow heads and arrows indicate the initial bend and the second bend, respectively. Scale bar, 20 μm. Middle panel: overwritten images of demembranated sperm at 5 ms intervals during the periods of time (105–250 ms) after release of ATP. Arrow heads and arrows indicate the initial bend and the second bend, respectively. Lower panel: changes of flagellar curvature occurring 105–250 ms after the UV flash are plotted against the distance from the base of flagellum. Ten waveforms produced at 50 ms are overwritten. One typical sperm example from the all experiments at least three times with three different specimens was shown.

TABLE 1 Properties of flagellar bends generated by the photolysis of caged ATP.

	DMSO (control)		Repaglinide	
	pCa10	pCa5	pCa10	pCa5
Maximum curvature (μm^{-1})	0.211 ± 0.006††	0.320 ± 0.021**	0.127 ± 0.016***	0.279 ± 0.025*
Curvature of initial bend (μm^{-1})	−0.164 ± 0.011	0.279 ± 0.020	−0.111 ± 0.037	0.185 ± 0.028†
Time by initial bend formation (ms)	139.00 ± 4.56	138.33 ± 5.23	190.00 ± 9.67***	168.13 ± 12.68
Beat period (ms)	75.00 ± 4.69†	88.89 ± 3.75*	81.11 ± 3.75	16.62 ± 1.21

Values are means ± S.E. N = 5–10. Flagellar bending was analyzed from successive 50 waveforms at 5 ms intervals. The curvature was determined at 5 μm from the base. *Significant at $p < 0.05$, **$p < 0.01$ or ***$p < 0.001$ (Student's t-test) as compared with DMSO, at pCa10. †Significant at $p < 0.05$, ††$p < 0.01$ or †††$p < 0.001$ (Student's t-test) as compared with DMSO, at pCa5. Curvature of initial bend was compared between DMSO, and Repaglinide only.

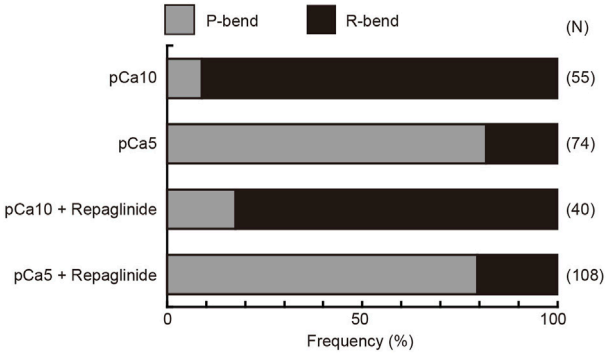

FIGURE 4
Preference for the direction of initial bend in the generation of symmetric and asymmetric flagellar waveforms. The relative frequencies of principal (P) and reverse (R) bends are shown for the initial bends formed after activation of demembranated *Ciona* sperm. Sperm was reactivated by photolysis of caged ATP in low (pCa10) or high (pCa5) Ca^{2+} concentrations in the presence of 0.5% DMSO (control) or 150 μM repaglinide. In both control and repaglinide-treated sperm, the formation of flagellar bends started with R-bends at pCa10, whereas it started with P-bends at pCa5. The number in brackets represents the number of observed spermatozoa in three different experiments.

(Figure 5). At pCa10, R-bends were generated at the flagellar base and propagated to the tip, followed by the generation and propagation of P-bends (Figure 5A). In contrast, P-bend formation preceded R-bend generation at pCa5 (Figure 5B). Repaglinide had little effect on the overall pattern of bend formation at pCa10, although the propagation of the R-bend proceeded more slowly and, consequently, the formation of the second bend (P-bend) was delayed (Figure 5C; Table 1). Conversely, at pCa5, repaglinide did not inhibit the generation of P-bends at the flagellar base but suppressed both the propagation and the subsequent formation of the R-bends. Under these conditions, P-bends were completely formed about ~150 ms after UV flashing and maintained a constant curvature for up to 325 ms (Figure 5D). Although the P-bend propagation was inhibited, the high-frequency vibration of the flagellum was observed (Supplementary Video S2; Figure 5D, right). The curvature of the P-bend oscillated with a periodicity of 5–40 ms and a frequency of 75.14 ± 7.49 Hz (N = 6) (Asterisks in Figure 5D and Table 1).

4 Discussion

Coordinated activation or inactivation of dyneins within the nine sets of doublet microtubules along the flagella control the proper formation and oscillation of flagellar bends (Inaba, 2011; King, 2018; Lin and Nicastro, 2018). The switching of dynein activity across the axoneme is particularly important for the oscillation of the sperm flagellar waveform. In sea urchin, starfish and mammalian sperm, the relationship between the directions of two opposite bends and the number of doublet microtubules with activated dyneins is understood (Sale, 1986; Mohri et al., 1987; Kanous et al., 1993; Lesich et al., 2014; Lin and Nicastro, 2018; Shingyoji, 2018) (Figure 6A). The formation of P-bends and R-bends is induced *via* the active sliding of microtubules by dyneins on doublet 7 and 3, termed P- and R-sliding, respectively (Figure 6A). We could not specify the doublet number of active dyneins in *Ciona* sperm, because of the lack of any markers observed in the axonemes of sea urchin and mammalian sperm. However, considering the structural conservation of the central apparatus throughout eukaryotic evolution (Carbajal-Gonzalez et al., 2013; Zhao et al., 2019; Leung et al., 2021) and the common effects of calaxin depletion in *Ciona* and mouse sperm (Mizuno et al., 2012; Sasaki et al., 2019), it is plausible that dyneins responsible for the P- and R-sliding would also be those on doublet 7 and 3 in *Ciona* sperm. In this study we developed a microscopic illumination system using caged ATP to capture the moment of the first bend formation. This experimental system allowed us to observe the formation and propagation of flagellar waveforms without physical disturbances such as fluid flow and mechanical stimuli (Vernon and Woolley, 1994; Tani and Kamimura, 1998; Hayashi and Shingyoji, 2008). Using this system, we found that in *Ciona* sperm, the first bend of the waves at low and high Ca^{2+} concentrations, formed at the proximal region of the flagellum, was predominantly an R-bend and P-bend respectively (Figures 2, 3). We assessed P and R bends according to the original definition (Gibbons and Gibbons, 1972; Brokaw, 1979; Shingyoji, 2013); the P-bend is the one with the larger curvature and the R-bend with a smaller curvature. Based on this definition, the first bend of symmetric waves that was formed at the proximal region of the flagellum at low Ca^{2+} was assigned as an R-bend (Figure 4). The second bend subsequently formed at the base with a larger curvature and was thus assigned as a P-bend. Following the propagation of the R-bend towards the flagellar tip, a P-bend was formed at the base of the flagellum under low Ca^{2+} conditions,

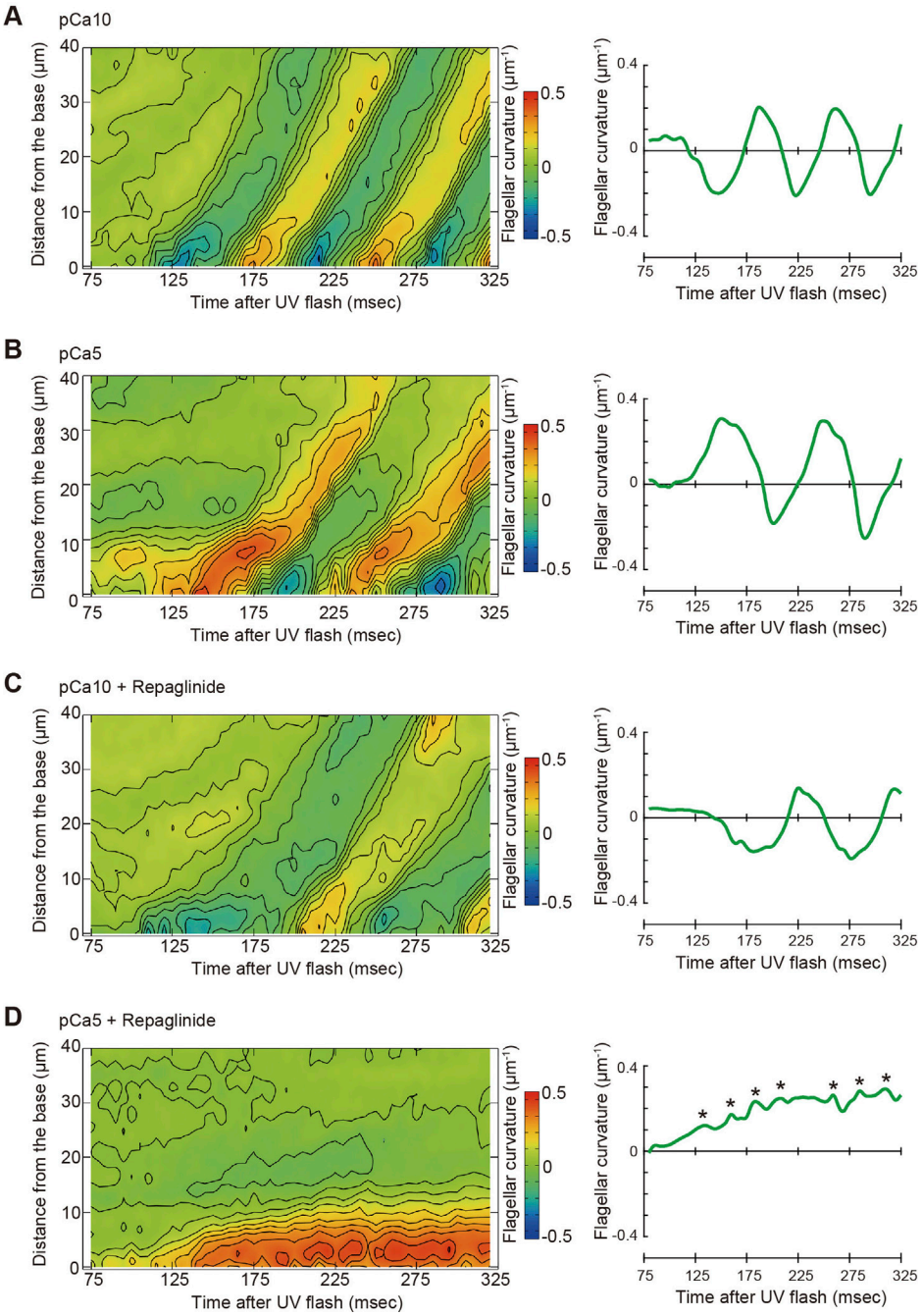

FIGURE 5
Pseudocolor maps showing spatiotemporal changes of the flagellar curvature. Left panels: the flagellar curvature of demembranated *Ciona* sperm was plotted against the distance from the base and time after the UV flash by pseudocolor mapping. Right panels: the flagellar curvature at 5 μm from the base was plotted against time after the UV flash. Sperm was reactivated through photolysis of caged ATP in low pCa10; **(A, C)** or high pCa5; **(B, D)** Ca^{2+} concentrations in the presence of 0.5% DMSO control; **(A, B)** or 150 μM repaglinide **(C, D)**.

presumably by switching the active dyneins to those located on the opposite side of the axoneme (Figure 6B, left). In contrast, high Ca^{2+} concentrations specifically suppresses R-sliding, resulting in waveform asymmetry (Nakano et al., 2003). Using caged ATP, we showed that *Ciona* sperm first formed a P-bend at the proximal region of the flagellum under high Ca^{2+} conditions, followed by its propagation toward the tip. Subsequently, the attenuated R-bend formed at the flagellar base (Figures 2, 3), suggesting that high Ca^{2+} suppresses R-sliding in *Ciona* spermatozoa (Figure 6B, right).

There is no clear reason for R-sliding priority in the bend formation at Low Ca^{2+}. In sea urchin sperm, a sudden increase in ATP induces bend formation and propagation (Goldstein, 1979; Tani and Kamimura, 1998). Demembranated sperm models with

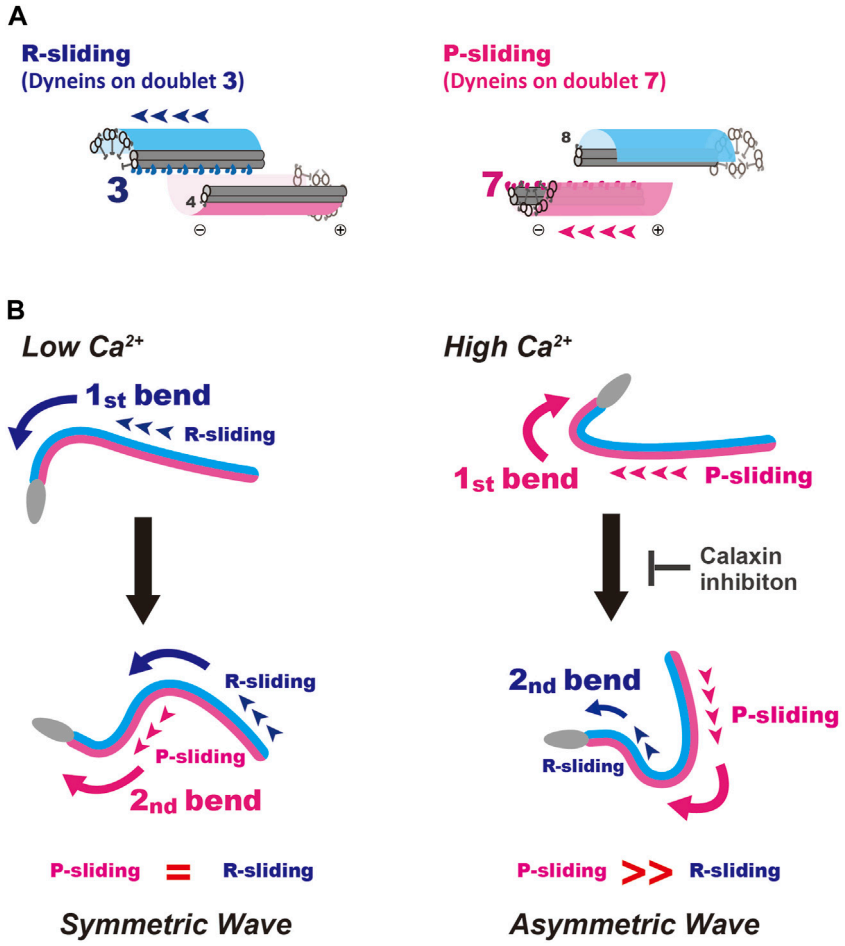

FIGURE 6
A model for the formation and propagation of the first bend and second bend in symmetric and asymmetric sperm flagellar waves. **(A)** Schematic representation for the R- and P-sliding in relation to the number of active dynein on doublet microtubule. Based on the studies of sea urchin and mammalian sperm. The formation of P-bends and R-bends is induced by the activation of dyneins on doublet 7 and 3, respectively. **(B)** A putative mechanism for initial bend formation and its propagation under low and high Ca^{2+} conditions are shown. Left, formation of a symmetric wave under low Ca^{2+} conditions. The first bend is formed by R-sliding. In turn, this R-bend induces switching of active dynein to that on the opposite side across the axoneme, resulting in P-sliding to form a P-bend. Right, generation of an asymmetric wave under high Ca^{2+} conditions. P-bend is first formed by P-sliding. In turn, this P-bend induces the switching of active dynein to that on the opposite side across the axoneme and generates suppressed R-sliding to form a R-bend with smaller curvature, resulting in the propagation of an asymmetric wave. A calaxin inhibitor, repaglinide, suppresses the generation of R-bend, possibly by inhibiting the mechanical transmission from P- to R-sliding.

straight flagella initially generate reverse bends (Tani and Kamimura, 1998), which coincides with our data. However, whether the initial bend starts from the P- or R-bend appears to depend on the mechanical state of the axonemes before ATP application (Goldstein, 1979). The flagella of demembranated sperm are not straight but show one large bend. This bend propagates from the formation of the initial bend (R-bend) until the distal region of the flagellum. However, bend initiation at the base is not always from the R-bend at low Ca^{2+} levels; 10%–20% flagella showed P-bend initiation at the base under the same Ca^{2+} conditions (Figure 4), indicating that the first bend formed at the base of the flagellum is equivocal.

We previously demonstrated by an *in vitro* motility assay using purified microtubules and outer arm dynein that dynein-mediated microtubule sliding was suppressed by calaxin under high Ca^{2+} conditions (Mizuno et al., 2012). This property of calaxin is essential for the propagation of asymmetric waveforms (Mizuno et al., 2012). Our present study, however, indicated the formation of the first P-bend was not affected by repaglinide under high Ca^{2+} conditions (Figure 3B), suggesting that calaxin activity is not involved in the P-sliding (Figure 6B, right). Instead, the flagellum never formed R-bend and maintained quiescence waveform (Figure 3B and Figure 5D). Therefore, calaxin is thought to be essential for the formation and propagation of R-sliding, but not for those of P-bend (Figure 6B, right). This limited participation of calaxin in the R-sliding is consistent with the observation that the R-bend propagates more slowly in the presence of repaglinide under low Ca^{2+} conditions (Figure 5C).

The mechanisms of the calaxin function in two aspects of asymmetric flagellar waves are yet unknown. First is the mechanism why the P-sliding normally occurs under high Ca^{2+} conditions, regardless of the presence or absence of repaglinide (Figure 3). Since calaxin is associated with outer arm dyneins on all nine doublet

microtubules (Mizuno et al., 2009), there must be a mechanism mediating the acceleration of P-sliding by doublet 7 dynein or suppression of R-sliding by doublet 3 dynein in Ca^{2+}-dependent but calaxin-independent manner. It is possible that the activity of inner arm dyneins regulated by CP/RS might affect the activity of outer arm dyneins through the regulatory protein complex connected to both the inner and outer dynein arms (Heuser et al., 2009; Pigino et al., 2011; Yamamoto et al., 2013; Oda et al., 2014). Second is the mechanism for the inhibition of R-sliding by repaglinide under high Ca^{2+} conditions. It was expected that the release of calaxin-dependent inhibition of dyneins would facilitate microtubule sliding as shown in vitro motility assay (Mizuno et al., 2012). However, repaglinide completely inhibited the formation of the R-bend and P-bend propagation, resulting in the quiescence arrest of a flagellum. Therefore, it is likely that calaxin does not simply suppress the sliding but is rather involved in the sliding at reduced velocity. This is supported by previous study (Mizuno et al., 2012) showing that R-bend formation at high Ca^{2+} (pCa5) is not inhibited in repaglinide treated sperm activated by 1 mM ATP, but propagates with attenuation. Capturing the first bend formation induced by low (0.1 mM) ATP in this study might emphasize the role of calaxin in the bend switching in flagella. The inhibition of R-sliding by repaglinide suggests that the bend formed by P-sliding at the proximal region cannot induce switching from P-sliding by doublet 7 dynein to R-sliding by doublet 3 dynein. Calaxin might be regulated by mechanical load and act a role in the generation of R-sliding in asymmetric wave by the release of calaxin-dependent inhibition of dyneins. In fact, the application of mechanical stimulations is shown to induce bend propagation in sea urchin sperm (Eshel et al., 1991; Izawa and Shingyoji, 2020). Further studies on the calaxin-mediated regulation of outer arm dyneins will shed light on this "low-gear" state sliding during the propagation of an asymmetric flagellar wave.

Data availability statement

The original contributions presented in the study are included in the article/Supplementary Material, further inquiries can be directed to the corresponding author.

Author contributions

KS and KI designed and performed the research; KS, EF, and SB developed the experimental system; KS and SB analyzed the results; KS and KI wrote the manuscript. All authors have read and approved the final version of the manuscript for publication.

Funding

This work was supported by Grants-in-Aid for Scientific Research from the Japan Society for the Promotion of Science 19K06592 and 16K07337 to KS and 17H01440 to KI, from the Ministry of Education, Culture, Sports, Science and Technology, Japan for Innovative Areas 15H01201 to KI, for Grant-in-Aid for Transformative Research Areas 21H05304 to KS, and by Narishige Zoological Science Award to KS.

Acknowledgments

We thank Drs Satoe Aratake, Reiko Yoshida, Manabu Yoshida, Yutaka Satou and other staff at Misaki Marine Biological Station, Grad Schl of Sci, University of Tokyo and in Lab of Dev Genomics, Grad Schl of Sci, Kyoto University, who distribute *Ciona* under the National BioResource Project, AMED, Japan. We are grateful to all the staff members of Onagawa Field Center, Graduate School of Agricultural Science, Tohoku University and International Coastal Research Center, University of Tokyo for supplying *Ciona*.

Conflict of interest

Author EF is employed by Documentary Channel Co. Ltd.

The remaining authors declare that the research was conducted in the absence of any commercial or financial relationships that could be construed as a potential conflict of interest.

Publisher's note

Supplementary material

The Supplementary Material for this article can be found online at: https://www.frontiersin.org/articles/10.3389/fcell.2023.1136404/full#supplementary-material

References

Baba, S. A., and Mogami, Y. (1985). An approach to digital image analysis of bending shapes of eukaryotic flagella and cilia. *Cell Motil.* 5, 475. doi:10.1002/cm.970050605

Bohmer, M., Van, Q., Weyand, I., Hagen, V., Beyermann, M., Matsumoto, M., et al. (2005). Ca2+ spikes in the flagellum control chemotactic behavior of sperm. *EMBO J.* 24, 2741. doi:10.1038/sj.emboj.7600744

Brokaw, C. J. (1979). Calcium-induced asymmetrical beating of triton-demembranated sea urchin sperm flagella. *J. Cell Biol.* 82, 401–411. doi:10.1083/jcb.82.2.401

Brokaw, C. J. (1987). Regulation of sperm flagellar motility by calcium and cAMP-dependent phosphorylation. *J. Cell Biochem.* 35, 175–184. doi:10.1002/jcb.240350302

Carbajal-Gonzalez, B. I., Heuser, T., Fu, X., Lin, J., Smith, B. W., Mitchell, D. R., et al. (2013). Conserved structural motifs in the central pair complex of eukaryotic flagella. *Cytoskelet. Hob.* 70, 101. doi:10.1002/cm.21094

Eshel, D., Shingyoji, C., Yoshimura, K., Gibbons, I. R., and Takahashi, K. (1991). Evidence for an inequality in the forces that generate principal and reverse bends in sperm flagella. *J. Cell Sci.* 100, 213. doi:10.1242/jcs.100.1.213

Gibbons, B. H., and Gibbons, I. R. (1980). Calcium-induced quiescence in reactivated sea urchin sperm. *J. Cell Biol.* 84, 13–27. doi:10.1083/jcb.84.1.13

Gibbons, B. H., and Gibbons, I. R. (1972). Flagellar movement and adenosine triphosphatase activity in sea urchin sperm extracted with triton X-100. *J. Cell Biol.* 54, 75–97. doi:10.1083/jcb.54.1.75

Goldman, Y. E., Hibberd, M. G., Mccray, J. A., and Trentham, D. R. (1982). Relaxation of muscle fibres by photolysis of caged ATP. *Nature* 300, 701–705. doi:10.1038/300701a0

Goldstein, S. F. (1977). Asymmetric waveforms in echinoderm sperm flagella. *J. Exp. Biol.* 71, 157–170. doi:10.1242/jeb.71.1.157

Goldstein, S. F. (1979). Starting transients in sea urchin sperm flagella. *J. Cell Biol.* 80, 61–68. doi:10.1083/jcb.80.1.61

Guerrero, A., Wood, C. D., Nishigaki, T., Carneiro, J., and Darszon, A. (2010). Tuning sperm chemotaxis. *Biochem. Soc. Trans.* 38, 1270–1274. doi:10.1042/BST0381270

Gui, M., Farley, H., Anujan, P., Anderson, J. R., Maxwell, D. W., Whitchurch, J. B., et al. (2021). De novo identification of mammalian ciliary motility proteins using cryo-EM. *Cell* 184, 5791–5806.e19. doi:10.1016/j.cell.2021.10.007

Hayashi, S., and Shingyoji, C. (2008). Mechanism of flagellar oscillation-bending-induced switching of dynein activity in elastase-treated axonemes of sea urchin sperm. *J. Cell Sci.* 121, 2833–2843. doi:10.1242/jcs.031195

Heuser, T., Raytchev, M., Krell, J., Porter, M. E., and Nicastro, D. (2009). The dynein regulatory complex is the nexin link and a major regulatory node in cilia and flagella. *J. Cell Biol.* 187, 921–933. doi:10.1083/jcb.200908067

Inaba, K. (2015). Calcium sensors of ciliary outer arm dynein: Functions and phylogenetic considerations for eukaryotic evolution. *Cilia* 4, 6. doi:10.1186/s13630-015-0015-z

Inaba, K., and Shiba, K. (2018). Microscopic analysis of sperm movement: Links to mechanisms and protein components. *Microsc. (Oxf)* 67, 144–155. doi:10.1093/jmicro/dfy021

Inaba, K. (2011). Sperm flagella: Comparative and phylogenetic perspectives of protein components. *Mol. Hum. Reprod.* 17, 524–538. doi:10.1093/molehr/gar034

Izawa, Y., and Shingyoji, C. (2020). Mechanical induction of oscillatory movement in demembranated, immotile flagella of sea urchin sperm at very low ATP concentrations. *J. Exp. Biol.* 223, jeb225797, doi:10.1242/jeb.225797

Kanous, K. S., Casey, C., and Lindemann, C. B. (1993). Inhibition of microtubule sliding by Ni2+ and Cd2+: Evidence for a differential response of certain microtubule pairs within the bovine sperm axoneme. *Cell Motil. Cytoskelet.* 26, 66–76. doi:10.1002/cm.970260107

King, S. M. (2018). Turning dyneins off bends cilia. *Cytoskelet. Hob.* 75 372–381. doi:10.1002/cm.21483

Lesich, K. A., Depinho, T. G., Dionne, B. J., and Lindemann, C. B. (2014). The effects of Ca2+ and ADP on dynein switching during the beat cycle of reactivated bull sperm models. *Cytoskelet. Hob.* 71, 611–627. doi:10.1002/cm.21196

Leung, M. R., Roelofs, M. C., Ravi, R. T., Maitan, P., Henning, H., Zhang, M., et al. (2021). The multi-scale architecture of mammalian sperm flagella and implications for ciliary motility. *EMBO J.* 40. e107410. doi:10.15252/embj.2020107410

Lin, J., and Nicastro, D. (2018). Asymmetric distribution and spatial switching of dynein activity generates ciliary motility. *Science* 360, eaar1968, doi:10.1126/science.aar1968

Lindemann, C. B. (2011). Experimental evidence for the geometric clutch hypothesis. *Curr. Top. Dev. Biol.* 95, 1–31. doi:10.1016/B978-0-12-385065-2.00001-3

Lindemann, C. B., and Lesich, K. A. (2010). Flagellar and ciliary beating: The proven and the possible. *J. Cell Sci.* 123, 519–528. doi:10.1242/jcs.051326

Mccray, J. A., Herbette, L., Kihara, T., and Trentham, D. R. (1980). A new approach to time-resolved studies of ATP-requiring biological systems; laser flash photolysis of caged ATP. *Proc. Natl. Acad. Sci. U. S. A.* 77, 7237–7241. doi:10.1073/pnas.77.12.7237

Miller, R. L. (1985). Demonstration of sperm chemotaxis in echinodermata - asteroidea, holothuroidea, ophiuroidea. *J. Exp. Zoology* 234, 383–414. doi:10.1002/jez.1402340308

Mizuno, K., Padma, P., Konno, A., Satouh, Y., Ogawa, K., and Inaba, K. (2009). A novel neuronal calcium sensor family protein, calaxin, is a potential Ca(2+)-dependent regulator for the outer arm dynein of metazoan cilia and flagella. *Biol. Cell* 101, 91–103. doi:10.1042/BC20080032

Mizuno, K., Shiba, K., Okai, M., Takahashi, Y., Shitaka, Y., Oiwa, K., et al. (2012). Calaxin drives sperm chemotaxis by Ca^{2+}-mediated direct modulation of a dynein motor. *Proc. Natl. Acad. Sci. U. S. A.* 109, 20497–20502. doi:10.1073/pnas.1217018109

Mohri, H., Mohri, T., and Okuno, M. (1987). Topographical relationship between the axonemal arrangement and the bend direction in starfish sperm flagella. *Cell Motil. Cytoskelet.* 8, 76–84. doi:10.1002/cm.970080111

Nakano, I., Kobayashi, T., Yoshimura, M., and Shingyoji, C. (2003). Central-pair-linked regulation of microtubule sliding by calcium in flagellar axonemes. *J. Cell Sci.* 116, 1627–1636. doi:10.1242/jcs.00336

Oda, T., Yanagisawa, H., Yagi, T., and Kikkawa, M. (2014). Mechanosignaling between central apparatus and radial spokes controls axonemal dynein activity. *J. Cell Biol.* 204, 807–819. doi:10.1083/jcb.201312014

Okada, M., Takezawa, D., Tachibanaki, S., Kawamura, S., Tokumitsu, H., and Kobayashi, R. (2003). Neuronal calcium sensor proteins are direct targets of the insulinotropic agent repaglinide. *Biochem. J.* 375, 87–97. doi:10.1042/BJ20030376

Pigino, G., Bui, K. H., Maheshwari, A., Lupetti, P., Diener, D., and Ishikawa, T. (2011). Cryoelectron tomography of radial spokes in cilia and flagella. *J. Cell Biol.* 195, 673–687. doi:10.1083/jcb.201106125

Sale, W. S. (1986). The axonemal axis and Ca2+-induced asymmetry of active microtubule sliding in sea urchin sperm tails. *J. Cell Biol.* 102, 2042–2052. doi:10.1083/jcb.102.6.2042

Sasaki, K., Shiba, K., Nakamura, A., Kawano, N., Satouh, Y., Yamaguchi, H., et al. (2019). Calaxin is required for cilia-driven determination of vertebrate laterality. *Commun. Biol.* 2, 226. doi:10.1038/s42003-019-0462-y

Shiba, K., Baba, S. A., Inoue, T., and Yoshida, M. (2008). Ca2+ bursts occur around a local minimal concentration of attractant and trigger sperm chemotactic response. *Proc. Natl. Acad. Sci. U. S. A.* 105, 19312–19317. doi:10.1073/pnas.0808580105

Shingyoji, C. (2013). Measuring the regulation of dynein activity during flagellar motility. *Methods Enzymol.* 524, 147–169. doi:10.1016/B978-0-12-397945-2.00009-3

Shingyoji, C. (2018). "Regulation of dynein-driven ciliary and flagellar movement," in *Dyneins: Structure, Biology and disease* Editor S. M. KING 2nd Edition ed (Amsterdam, Netherlands: Elsevier BV).

Smith, E. F., and Yang, P. (2004). The radial spokes and central apparatus: Mechano-chemical transducers that regulate flagellar motility. *Cell Motil. Cytoskelet.* 57, 8–17. doi:10.1002/cm.10155

Tani, T., and Kamimura, S. (1998). Reactivation of sea-urchin sperm flagella induced by rapid photolysis of caged ATP. *J. Exp. Biol.* 201, 1493–1503. doi:10.1242/jeb.201.10.1493

Vernon, G. G., and Woolley, D. M. (1994). Direct evidence for tension development between flagellar doublet microtubules. *Exp. Cell Res.* 215, 390–394. doi:10.1006/excr.1994.1357

Wachten, D., Jikeli, J. F., and Kaupp, U. B. (2017). Sperm sensory signaling. *Cold Spring Harb. Perspect. Biol.* 9, a028225. doi:10.1101/cshperspect.a028225

Wargo, M. J., Dymek, E. E., and Smith, E. F. (2005). Calmodulin and PF6 are components of a complex that localizes to the C1 microtubule of the flagellar central apparatus. *J. Cell Sci.* 118, 4655–4665. doi:10.1242/jcs.02585

Wood, C. D., Nishigaki, T., Furuta, T., Baba, S. A., and Darszon, A. (2005). Real-time analysis of the role of Ca(2+) in flagellar movement and motility in single sea urchin sperm. *J. Cell Biol.* 169, 725–731. doi:10.1083/jcb.200411001

Yamamoto, R., Song, K., Yanagisawa, H. A., Fox, L., Yagi, T., Wirschell, M., et al. (2013). The MIA complex is a conserved and novel dynein regulator essential for normal ciliary motility. *J. Cell Biol.* 201, 263–278. doi:10.1083/jcb.201211048

Yoshida, M., and Yoshida, K. (2011). Sperm chemotaxis and regulation of flagellar movement by Ca2+. *Mol. Hum. Reprod.* 17, 457–465. doi:10.1093/molehr/gar041

Zhao, L., Hou, Y., Picariello, T., Craige, B., and Witman, G. B. (2019). Proteome of the central apparatus of a ciliary axoneme. *J. Cell Biol.* 218, 2051–2070. doi:10.1083/jcb.201902017

frontiers | Frontiers in Cell and Developmental Biology

TYPE Perspective
PUBLISHED 17 March 2023
DOI 10.3389/fcell.2023.1134002

OPEN ACCESS

EDITED BY
Toshiyuki Nakagaki,
Hokkaido University, Japan

REVIEWED BY
Min Wu,
Yale University, United States
Seiji Takagi,
Future University Hakodate, Japan

*CORRESPONDENCE
Nobuhiko J. Suematsu,
suematsu@meiji.ac.jp

SPECIALTY SECTION
This article was submitted to Evolutionary Developmental Biology, a section of the journal Frontiers in Cell and Developmental Biology

RECEIVED 29 December 2022
ACCEPTED 06 March 2023
PUBLISHED 17 March 2023

CITATION
Suematsu NJ, Yamashita H and Iima M (2023), Bioconvection pattern of *Euglena* under periodical illumination.
Front. Cell Dev. Biol. 11:1134002.
doi: 10.3389/fcell.2023.1134002

Bioconvection pattern of *Euglena* under periodical illumination

Nobuhiko J. Suematsu[1,2]*, Hiroshi Yamashita[3] and Makoto Iima[3]

[1]Graduate School of Advanced Mathematical Sciences, Meiji University, Tokyo, Japan, [2]Meiji Institute for Advanced Study of Mathematical Sciences (MIMS), Meiji University, Tokyo, Japan, [3]Graduate School of Integrated Life Sciences, Hiroshima University, Higashihiroshima, Japan

Microorganisms respond to environmental conditions and often spontaneously form highly ordered convection patterns. This mechanism has been well-studied from the viewpoint of self-organization. However, environmental conditions in nature are usually dynamic. Naturally, biological systems respond to temporal changes in environmental condition. To elucidate the response mechanisms in such a dynamic environment, we observed the bioconvection pattern of *Euglena* under periodical changes in illumination. It is known that *Euglena* shows localized bioconvection patterns under constant homogeneous illumination from the bottom. Periodical changes in light intensity induced two different types of spatiotemporal patterns: alternation of formation and decomposition over a long period and complicated transition of pattern over a short period. Our observations suggest that pattern formation in a periodically changing environment is of fundamental importance to the behavior of biological systems.

KEYWORDS

bioconvection pattern, microorganisms, periodical environment, fluidic pattern, photosensitivity

1 Introduction

Microorganisms respond to environmental physicochemical conditions, such as chemical concentration (Colombetti and Diehn, 1978), gravity (Lebert and Häder, 1996), and light intensity (Diehn, 1969; Diehn, 1973; Creutz et al., 1978; Hader, 1987). Swimming microorganisms spontaneously generate macroscopic convection patterns originating from a response called "taxis" (Pedley et al., 1988; Hill and Pedley, 2005; Bees, 2020). When the environmental conditions prompt the organisms to swim upward, the cell density near the water surface increases and a top-heavy condition is generated. Once this unstable distribution is broken owing to fluctuation, the microorganisms settle locally and sink down owing to their own weight. Thereafter, upward swimming recommences, and the collective behavior of the population results in a spontaneous convection pattern. This phenomenon is known as "bioconvection."

Euglena is a microorganism that responds to light intensity (Ogawa et al., 2016; Tsang et al., 2018; Noselli et al., 2019; Ozasa et al., 2019; Muku et al., 2023) and is known to form a localized bioconvection pattern under strong illumination from the bottom of the culture medium (Suematsu et al., 2011; Shoji et al., 2014). Usually, light strength is constant in time and homogeneous in space in experiments. However, in nature, the environmental conditions are neither constant nor homogeneous. Therefore, the response of bioconvection patterns to dynamic non-uniform illumination will yield a greater understanding of how microorganisms adapt to periodical changes in environmental conditions.

10.3389/fcell.2023.1134002

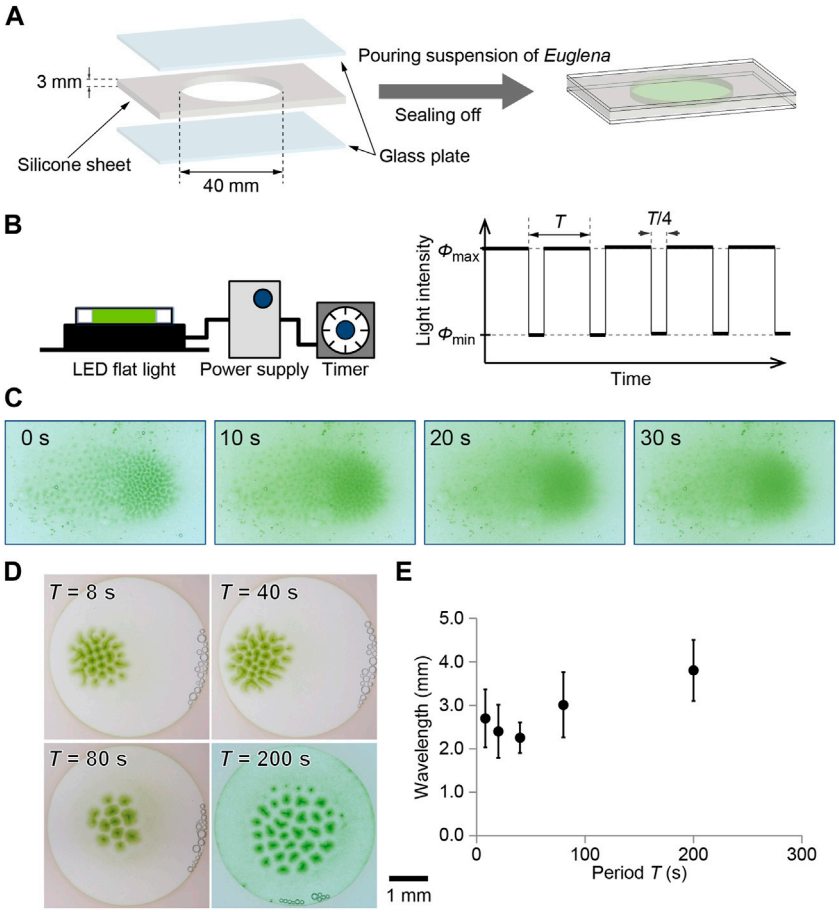

FIGURE 1
Illustration for **(A)** sample preparation and **(B)** temporal change in light illumination. A culture of *Euglena* was encapsulated using glass plates, where a silicone sheet was used as a spacer. The sample was illuminated from the bottom using flat light whose intensity was controlled with the *Arduino*. The light intensity was periodically changed between 0 and 3000 lx, where three quarters was bright and one quarter was dark. **(C)** Decomposition process of bioconvection pattern after stopping the illumination from the bottom. **(D)** Bioconvection pattern generated with temporal change in light intensity. The time periods were 8, 20, 40, 80, and 200 s. The snapshots obtained at 60 min are shown here for each period. **(E)** Characteristic wavelength for each pattern depending on the period. The snapshots obtained at 60 min were analyzed for each period.

Here, we suggest temporally periodic illumination as the next simplest condition after constant uniform illumination. The bioconvection of *Euglena* was observed under spatially homogeneous illumination, whose light intensity changed periodically over time. With a long period rather than forming a pattern, bioconvection alternates formation and decomposition. By contrast, a complex spatiotemporal behavior was observed under a short period of flashing illumination. Based on our experimental observations, we suggest one of the response mechanisms of microorganisms to the periodically changing environmental conditions.

2 Experimental setup

Euglena gracilis was cultured in Koren–Hutner (KH) solution for 1 week (Koren and Hutner, 1967) and then inoculated into HYPONeX aqueous solution to observe bioconvection. The culture was diluted to the desired cell density and then placed in the dark for 1 h before use for bioconvection observation. The cell density was adjusted to 1.0×10^6 cells/mL. All incubation processes were performed under 28°C and light conditions with 14 h bright and 10 h dark.

The HYPONeX culture was soaked in a custom-made container in which a silicone sheet with a circular hole was placed on a glass plate and covered with another glass plate (Figure 1A). As a result, the culture solution was shielded into the hole of the silicone sheet with a thickness of 3 mm and diameter of 40 mm.

A bioconvection pattern was observed under temporally changing illumination intensity. A flat-light panel (LED Flat Light, Aitec System Co., Ltd., Japan) was connected to a controller (Arduino UNO). The light intensity changed between 0 lx (ϕ_{min}) and 3000 lx (ϕ_{max}) with periods (T) of 8, 20, 40, 80, and 200 s, where the period of bright was $3T/4$ and of dark was $T/4$ (Figure 1B). The experiments curried out under room temperature, which was 24°C. Snapshots were captured using a digital camera (Eos Kiss X8, Canon, Japan). Images were analyzed using ImageJ (NIH, United States) on PC.

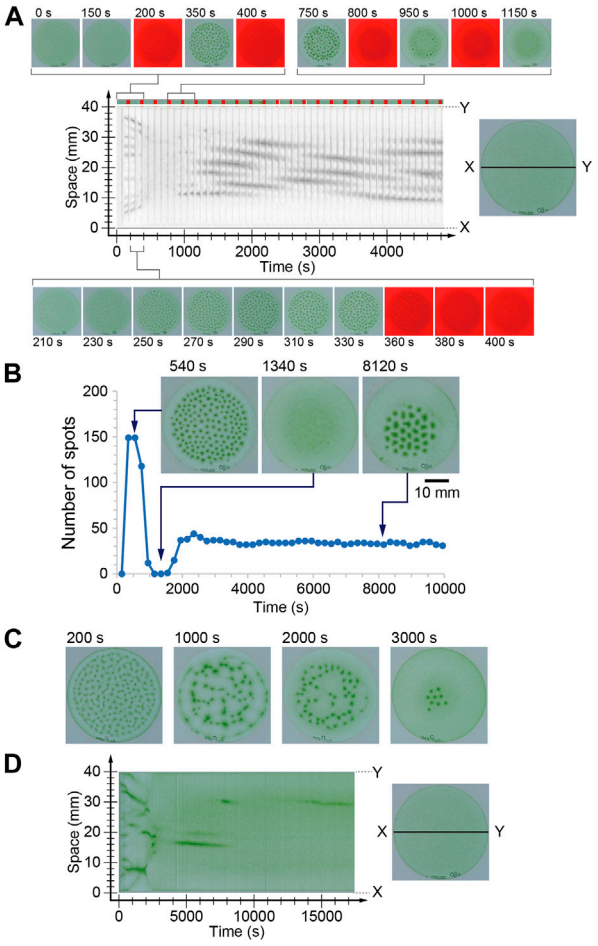

FIGURE 2
(A, B) Time series of the number of spots under the periodical illumination (200 s in the period). The space-time diagram in **(A)** was indicated gray scale image of red color. The dark periods are indicated in red on the color bar at the top of space-time diagram. **(C, D)** Time evolution of the bioconvection pattern under periodical changing light intensity whose period was 20 s.

3 Results

3.1 Relaxation time for pattern formation and decomposition

The initial homogeneous distribution of cells became unstable under homogeneous illumination from the bottom, and then a convection pattern, which looked like a collection of spots, was formed approximately 300 s after beginning the illumination. The spots were generated almost entirely in the space at the initial stage and shifted slightly toward the center of the container. Finally, the spots gathered and formed a localized pattern (Suematsu et al., 2011). Once the formation of the localized pattern was complete, it was stable and was maintained for more than 1 h as long as the illumination was maintained.

To maintain this pattern, illumination from the bottom is necessary. If the light stops, the pattern is quickly dispersed within 30 s (Figure 1C). The time scale was 30 s, such that the pattern decomposition was faster than the formation process.

3.2 Temporal change illumination

With illumination, the homogeneous cell density distribution in the container started to fluctuate, and spot-shaped dense green regions gradually formed. After 60 min, the pattern approached a stationary state (Figure 1D). Even though the total amount of light illuminated to *Euglena* was the same, the stationary pattern depended strongly on the period of temporal illumination (Figure 1D). To estimate the characteristic wavelength of the localized pattern, neighboring spots were defined using Voronoi analysis and the distances between neighboring spots were measured. As a result, the average of the distances decreased with the period up to 40 s and then increased for more than 80 s (Figure 1E).

In the case of a long period of 200 s, alternation between the pattern formation and decomposition processes was clearly observed during the initial three cycles. However, the next five cycles failed to form an ordered spot pattern. In these cycles, cells kept gathering, but the convection pattern was not completely formed. Thus, the spots or faint gathering spots collapsed during the dark period. However, the gathering at the center of the container progressed slightly, and convection pattern formation and decomposition were observed again (Figure 2A). This alternation was observed for more than 40 cycles and the spatial wavelength of the pattern was almost constant. At this time, decomposition was also observed during the dark period, but the pattern did not completely disappear. As a result, a stable pattern change in the oscillation was achieved (Supplemental Movie S1). To demonstrate this process, the number of spots was counted just before turning off the illumination for each period. The number suddenly increased in the initial two and three cycles and drastically decreased to zero in the next three cycles. Subsequently, the number increased again and approached 35 (Figure 2B).

The characteristic behavior was observed during transients of the pattern under temporal change illumination for 20 s in the period (Supplemental Movie S2). Under constant light, spots were generated at random positions and gathered monotonically. In the case of 20 s periodic light, the initial spot generation occurred similar to that observed under constant illumination (Figure 2C, 200 s). However, the spots were arranged in a network structure, which was very different from the localized pattern observed under constant illumination (Figure 2C, 1,000 s). Furthermore, the spots shifted toward random directions (Figure 2C, 2000 s), almost all spots disappeared, and several spots only survived locally (Figure 2C, 3000 s). At this time, the brightness of convection spots was a little brighter than that observed in the spots under constant illumination. Furthermore, the number of spots was nine, which was roughly one-fifth that of constant illumination. These results indicate that several cells swam in the region without convection. This was also quite different from the commonly observed convection pattern of *Euglena*. Usually, approximately all the cells gather in the convection region, and there are fewer cells in the region without convection.

4 Discussion

The convection pattern originated from the negative phototaxis of *Euglena*, which induced upward swimming of cells. The gathering of cells at the top of the culture lead to a density instability.

Consequently, downward flows occurred at these times. Therefore, the downward flow appeared as a green spot when viewed from above. Once the illumination from the bottom stopped, the driving force was lost, and the pattern disappeared during a few tens of seconds. The wavelength of bioconvection pattern once decreased and then increased with increasing the period of the light intensity oscillation (Figure 1E). In addition, the temporal evolution of the pattern strongly depended on the period of external oscillatory illumination (Figure 2).

The swimming speed of the cells was approximately 100 μm/s and the depth of the container was 3 mm. Therefore, more than 30 s was required to reach the top. However, cells often change their direction. Therefore, it might take several hundred seconds to gather the cells at the top and induce convection. The period of 200 s of external light was comparable to the period of upward swimming of the cell. Based on this speculation, the disappearance of the spots in the initial stage (Figure 2A) was induced due to the lack of a driving force for the long period case.

In the initial two or three cycles, the cells were sensitive to illumination because they were cultured in the dark before starting the experiments. Therefore, convection spots were generated in a short time. However, illumination for several hundred seconds induced adaptation of the cells; thus, the sensitivity was slightly weakened. Owing to the weakness of the light sensitivity, the gathering at the top also slowed. As a result, the cells might fail to fulfill the convection-inducing condition for 150 s illumination. Accordingly, the convection pattern disappeared. On the other hand, the lateral gathering of the cells occurred slowly, as could be seen in the space-time diagram (Figure 2A). By increasing the local cell density, gathering at the top could be easily overcome. Hence, after several cycles, a convection pattern appeared again in the localized region. In this time, the wavelength of the pattern became longer than that in constant illumination. This result is expected because of diffusion during long dark period, which decreased the local cell density resulting in long wavelength pattern.

In the case of the shorter period of 20 s, the cells experienced both high and low relative intensity during upward swimming. Although the detailed mechanism is still under investigation, the characteristic behavior observed in the convection patterns may originate from the alternation between upward swimming and random motion. It is known that *Euglena* shows tumbling behavior when the light intensity suddenly increases. Therefore, the upward swimming cells start to swim in a random direction while the light intensity is decreasing, and then tumble in response to a sudden increase in light intensity. On the other hand, downward moving cells experience gradual increase in intensity owing to the shading effect (Vincent and Hill, 1996; Ghorai and Hill, 2005). Notably, some of the cells can respond to strong light and others fail to respond to it and show tumbling. This complicated situation generates a characteristic time evolution of convection pattern, as shown in Figure 2D. Furthermore, the wavelength became slightly shorter than that observed under constant light illumination (Figure 1E). It might originate from failure to deformation of the pattern because of short dark period (5 s), which was shorter than the period to disappearing the pattern (Figure 1C). Uncovering the detailed mechanism of those characteristic observations is a topic for the future works. In addition, with period 8 s, a similar complicated pattern formation was observed on one of the three experiments. Thus, the threshold value of the period was not clear for observing the complicated pattern formation.

Finally, under short-period light, the convection pattern is expected to approach to that observed under constant illumination, in which the convection spots monotonically gathered and formed localized pattern. Because the cells cannot perceive the oscillation but feel an effective constant illumination with a time-averaged intensity under fast oscillation. This is also the future works.

5 Conclusion

In this study, we demonstrated one of the simplest setups for self-organized behavior in a temporally changing environment. If the oscillation period was similar in order of time scale for pattern formation behavior, non-trivial characteristic patterns appeared. In our study, the characteristic time was the upward swimming period, which comprised several tens of seconds. Taking a scientific approach to dissect a complex dynamical system behavior, the setup and environmental conditions are typically simplified. As such, it remains important to devise more complicated experimental models to understand these underlying mechanisms. Nevertheless, our work provides a first step toward understanding the spatiotemporal pattern formation of biological systems exposed to periodical environmental fluctuations. Our preliminary experiments clearly showed that a slight change in environmental conditions often induces unexpected and interesting behaviors. We should consider the effect of such a minimally complicated condition as a diorama of more notably complicated natural dynamical systems.

Data availability statement

The original contributions presented in the study are included in the article/Supplementary Material, further inquiries can be directed to the corresponding author.

Author contributions

NJS supervised the investigation and performed experiments and analyses. MI and HY discussed the underlying mechanisms and conducted the analyses. In addition, the story of the paper is discussed with all the authors.

Funding

This research was supported by JSPS KAKENHI Grant No. 21H05311.

Acknowledgments

The authors appreciate the contribution of Mr. Yuya Kumagai in his preliminary experiments.

Conflict of interest

The authors declare that the research was conducted in the absence of any commercial or financial relationships that could be construed as a potential conflict of interest.

Publisher's note

All claims expressed in this article are solely those of the authors and do not necessarily represent those of their affiliated organizations, or those of the publisher, the editors and the reviewers. Any product that may be evaluated in this article, or claim that may be made by its manufacturer, is not guaranteed or endorsed by the publisher.

Supplementary material

The Supplementary Material for this article can be found online at: https://www.frontiersin.org/articles/10.3389/fcell.2023.1134002/full#supplementary-material

References

Bees, M. A. (2020). Advances in bioconvection. *Annu. Rev. Fluid Mech.* 52, 449–476. doi:10.1146/annurev-fluid-010518-040558

Colombetti, G., and Diehn, B. (1978). Chemosensory responses toward oxygen in *Euglena gracilis*. *J. Protozool.* 25, 211–217. doi:10.1111/j.1550-7408.1978.tb04398.x

Creutz, C., Colombetti, G., and Diehn, B. (1978). Photophobic behavioral responses of *Euglena* in a light intensity gradient and the kinetics of photoreceptor pigment interconversions. *Photochem. Photobiol.* 27, 611–616. doi:10.1111/j.1751-1097.1978.tb07653.x

Diehn, B. (1969). Action spectra of the phototactic responses in *Euglena*. *Biochim. Biophys. Acta.* 177, 136–143. doi:10.1016/0304-4165(69)90073-7

Diehn, B. (1973). Phototaxis and sensory transduction in *Euglena*. *Science* 181, 1009–1015. doi:10.1126/science.181.4104.1009

Ghorai, S., and Hill, N. A. (2005). Penetrative phototactic bioconvection. *Phys. Fluids.* 17, 074101. doi:10.1063/1.1947807

Hader, D. P. (1987). Polarotaxis, gravitaxis and vertical phototaxis in the green flagellate, Euglena gracilis. Euglena gracilis. *Arch. Microbiol.* 147, 179–183. doi:10.1007/BF00415281

Hill, N. A., and Pedley, T. J. (2005). *Bioconvection. Fluid Dyn. Res.* 37, 1–20. doi:10.1016/j.fluiddyn.2005.03.002

Koren, L. E., and Hutner, S. H. (1967). High yield media for photosynthesizing *Euglena gracilis*. *Z. J. Protozool.* 14, 17.

Lebert, M., and Häder, D. P. (1996). How *Euglena* tells up from down. *Nature* 379, 590. doi:10.1038/379590a0

Muku, K., Yamashita, H., Kamikubo, T., Suematsu, N. J., and Iima, M. (2023). Long-time behavior of swimming Euglena gracilis in a heterogenous light environment. *Front. Cell Dev. Biol.* 11, 1133028. doi:10.3389/fcell.2023.1133028

Noselli, G., Beran, A., Arroyo, M., and DeSimone, A. (2019). Swimming *Euglena* respond to confinement with a behavioral change enabling effective crawling. *Nat. Phys.* 15, 496–502. doi:10.1038/s41567-019-0425-8

Ogawa, T., Shoji, E., Suematsu, N. J., Nishimori, H., Izumi, S., Awazu, A., et al. (2016). The flux of euglena gracilis cells depends on the gradient of light intensity. *PLoS ONE* 11, e0168114. doi:10.1371/journal.pone.0168114

Ozasa, K., Won, J., Song, S., Shinomura, T., and Maeda, M. (2019). Phototaxis and photo-shock responses of *Euglena gracilis* under gravitaxis. *Algal Res.* 41, 101563. doi:10.1016/j.algal.2019.101563

Pedley, T. J., Hill, N. A., and Kessler, J. O. (1988). The growth of bioconvection patterns in a uniform suspension of gyrotactic micro-organisms. *J. Fluid Mech.* 195, 223–237. doi:10.1017/s0022112088002393

Shoji, E., Nishimori, H., Awazu, A., Izumi, S., and Iima, M. (2014). Localized bioconvection patterns and their initial state dependency in Euglena gracilis suspensions in an annular container. *J. Phys. Soc. Jpn.* 83, 043001. doi:10.7566/JPSJ.83.043001

Suematsu, N. J., Awazu, A., Izumi, S., Noda, S., Nakata, S., and Nishimori, H. (2011). Localized bioconvection of euglena caused by phototaxis in the lateral direction. *J. Phys. Soc. Jpn.* 80, 064003–064008. doi:10.1143/JPSJ.80.064003

Tsang, A. C. H., Lam, A. T., and Riedel-Kruse, I. H. (2018). Polygonal motion and adaptable phototaxis via flagellar beat switching in the microswimmer Euglena gracilis. *Nat. Phys.* 14, 1216–1222. doi:10.1038/s41567-018-0277-7

Vincent, R. V., and Hill, N. A. (1996). Bioconvection in a suspension of phototactic algae. *J. Fluid Mech.* 327, 343–371. doi:10.1017/S0022112096008579

frontiers | Frontiers in Cell and Developmental Biology

TYPE Original Research
PUBLISHED 13 April 2023
DOI 10.3389/fcell.2023.1134227

OPEN ACCESS

EDITED BY
Toshiyuki Nakagaki,
Hokkaido University, Japan

REVIEWED BY
Encarnacion Diaz Santos,
Spanish National Research Council (CSIC), Spain
Gianfranco Santovito,
University of Padua, Italy

*CORRESPONDENCE
Tomoyuki Shikata,
shikatatomoyuki@gmail.com

RECEIVED 30 December 2022
ACCEPTED 05 April 2023
PUBLISHED 13 April 2023

CITATION
Shikata T, Kitatsuji S and Yuasa K (2023), Strain, cell density, and nutrient condition affect patterns of diurnal vertical migration and superoxide production in a red-tide alga.
Front. Cell Dev. Biol. 11:1134227.
doi: 10.3389/fcell.2023.1134227

Strain, cell density, and nutrient condition affect patterns of diurnal vertical migration and superoxide production in a red-tide alga

Tomoyuki Shikata[1]*, Saho Kitatsuji[1] and Koki Yuasa[2]

[1]Fisheries Technology Institute, Japan Fisheries Research and Education Agency, Nagasaki, Goto, Japan, [2]Fisheries Technology Institute, Japan Fisheries Research and Education Agency, Hiroshima, Hatsukaichi, Japan

A red tide occurs when cell densities of autotrophic microalgae and some heterotrophic protists increase dramatically and thereby change the color of the sea. Red tides sometimes have negative impacts on human activities, such as fisheries and tourism. Most red-tide flagellates display diurnal vertical migration (DVM) in which cells normally migrate upward during the day and downward at night. This behavior promotes active growth, due to the effective acquisition of nutrients and light, as well as population density increase and cell aggregation. However, the factors and their interactions influencing DVM remain to be clarified, such that no algorithm exists that can precisely simulate the DVM pattern and the development of a red tide in the field. *Chattonella* marina complex (hereafter *Chattonella*) is a representative microalga of harmful red tides and some previous studies has suggested that *Chattonella*'s DVM plays important roles in development of a red tide. *Chattonella* can produce a large amount of superoxide ($\bullet O_2^-$), which is responsible for the regulation of various physiological processes as well as its toxicity against microorganisms and animals. In the present study, we examined the effects of strain, growth phase, cell density, and nutrient deficiency on the pattern of DVM. In addition, we also measured the $\bullet O_2^-$ level in most experiments to assess the relationship between DVM and $\bullet O_2^-$ production. Some strains displayed clear DVM, whereas others aggregated at the surface all day in a fixed condition. Strains' DVM patterns did not show a relationship with $\bullet O_2^-$ production. Moreover, the DVM became less clear at high cell density and in nitrogen- or phosphorus-depleted conditions. Although a previous study reported that the $\bullet O_2^-$ production rate increased during the light period and decreased during the dark period, regardless of cell density, the diurnal pattern of $\bullet O_2^-$ became less clear at a higher cell density in a *Chattonella* strain used in the present study. Our findings indicate that DVM and $\bullet O_2^-$ production by a *Chattonella* population composed of various strains can change across developmental phases and environmental conditions. This characteristic may produce adaptability in species and increase the chances of a massive population increase.

KEYWORDS

circadian rhythm, diversity, flagellate, harmful algal bloom, interstrain difference, marine phytoplankton, raphidophyte, swimming

1 Introduction

In marine environments, cell densities of autotrophic microalgae and some heterotrophic protists increase and thereby change the color of the sea—a biological phenomenon known as a red tide. Some red tides negatively impact fisheries and tourism (Sellner et al., 2003), and the impacts of harmful red tides on coastal systems have increased in recent decades (Gobler, 2020). Techniques for mitigating damages in the fish culture industry have been suggested (Kim, 2006; Balaji-Prasath et al., 2022), with precautionary field interventions such as early harvesting, restricting fish feeding, and transport of fish cages into zones free of red tides being the most practical (Kim, 2006). To boost the effectiveness of these precautionary interventions, accurate forecasting of the arrival of a red tide at fishing grounds is necessary. Forecasting based on numerical models is challenging because the densification and expansion of a red tide are influenced by various factors, including biological, chemical, and physical processes (McGillicuddy, 2010; Davidson et al., 2016).

In most cases, the outbreak of a red tide in a marine area requires three steps. First is the appearance of cells in the area due to the transport of cells from other marine areas, growth of surviving cells at quite low density, and excystment. Next is the growth step, in which the cell division rate exceeds the loss rate. The third step is aggregation, which occurs due to physical and biological processes. Various environmental factors influence each of the three steps. As compared to the aggregation process, the growth and life-history stages (including excystment) of red-tide algae have been more thoroughly studied and reported (e.g., Granéli and Turner, 2006).

Most flagellates causing red tides display diurnal vertical migration (DVM) in which cells normally migrate upward during the day and downward at night (Kamykowski, 1995). DVM contributes greatly to the aggregation step (Lai and Yin, 2014) and likely to the growth step as well, as the process offers many ecological benefits to flagellates, such as nutrient acquisition at a wider range of depths, the ability to control the amount of light received for photosynthesis, and escape from predators (Smayda, 1997; Harvey and Menden-Deuer, 2011; Bollens et al., 2012).

Among red-tide flagellates, the DVM pattern follows the photoperiod and appears to be controlled by an endogenous clock (Roenneberg et al., 1989; Shikata et al., 2015), whereas the timing of change in swimming direction and swimming speed differ among species (Kamykowski, 1995; Shikata et al., 2015). Some studies indicated that even if the dominant species is the same across a marine area, DVM patterns can differ among places and days (Katano et al., 2014; Shikata et al., 2020). Previous studies revealed that the DVM pattern is influenced by external environmental factors such as temperature (Heaney and Eppley, 1980), salinity (Jephson et al., 2011), light (Ault, 2000), and nutrient concentrations (Heaney and Eppley, 1980). Based on their different swimming speeds, Bearon et al. (2004) postulated that DVM patterns differ among strains in a flagellate species.

Although numerical simulation models considering physical processes have been developed (Berdalet et al., 2014), no algorithm can precisely simulate DVM patterns of a red-tide algae in the field. This deficiency exists because few studies have assessed both the physical and biological processes underlying DVM, including the physiological responses to various environmental factors, and the biological parameters impacting DVM patterns remain to be clarified for each red tide flagellate.

The raphidophyte *Chattonella marina* complex (hereafter called *Chattonella*) is distributed in warm marine coastal areas around the world and has caused tremendous damage to fisheries (Imai and Yamaguchi, 2012). Reflecting these threats, a large amount of information on *Chattonella* has been gathered, particularly with regard to its growth physiology, life cycle, and interaction with other microorganisms. Field data collected before and after *Chattonella* red tides are also available for designing laboratory experiments and validating numerical models using biological parameters. In addition, studies on the DVM of *Chattonella* have been conducted as well. A field experiment using a mesocosm revealed that *Chattonella* could reach a depth of 7.5 m during DVM, and its migration speed was 0.8 m h^{-1} both upward and downward (Watanabe et al., 1995). *Chattonella* can sense weak UV and blue light, allowing it to cue its DVM to the day–night cycle (Shikata et al., 2013). Negative phototaxis was observed under a monochromatic light with UV and blue components, but the response disappeared by mixing light with longer wavelengths (Shikata et al., 2016). Although one report has noted chemotaxis toward inorganic phosphate (Ikegami et al., 1995), we also observed a clear DVM in *Chattonella* without a vertical gradient of phosphate concentration (Shikata et al., 2015). Therefore, the DVM pattern may be regulated mainly by the endogenous clock that synchronizes the photoperiod and switches between positive and negative geotaxis in *Chattonella*. However, low salinity in the upper layers arrests the upward migration of *Chattonella* (Katano et al., 2014; Shikata et al., 2014), and a field study of DVM showed that cell density in the water column might also affect DVM (Sakaguchi et al., 2017). These findings indicate that there are also factors inhibiting the DVM pattern regulated by the endogenous clock.

Chattonella can produce a large amount of superoxide ($\bullet O_2^-$) in the cell membrane and excrete it from the cell. This $\bullet O_2^-$ and hydrogen peroxide has antimicrobial activity and is a candidate toxin related to fish mortality (Oda et al., 1992), as the level of $\bullet O_2^-$ is highly correlated with toxicity to aquacultured fishes in seawater that contains *Chattonella* cells (Shikata et al., 2021). Ichthyotoxicity can disappear within a short period and only live *Chattonella* cells can kill fishes; ruptured cells and culture supernatant have no toxicity to fish (Matsusato and Kobayashi, 1974; Ishimatsu et al., 1996; Shen et al., 2010). These characteristics correspond with chemical unstableness of $\bullet O_2^-$. The amount of $\bullet O_2^-$ production is influenced by nutrient and light intensity conditions; nutrient deficiency and strong light can increase the production (Yuasa et al., 2020a; b). Moreover, *Chattonella* exhibits different $\bullet O_2^-$ production rates in the light and dark periods (Kim et al., 2005; Yuasa et al., 2020a). These results suggest that $\bullet O_2^-$ may be responsible for regulating various physiological processes with circadian rhythms.

In the present study, we examined the effects of strain, growth phase, cell density, and nutrient deficiency—factors scarcely addressed thus far—on the DVM pattern in *Chattonella*. In most experiments, we also simultaneously measured the $\bullet O_2^-$ level to investigate the potential synchronous patterns of DVM and $\bullet O_2^-$ production in this flagellate species.

TABLE 1 ***Chattonella*** **strains used in the present study. All strains were isolated from Japanese coastal areas. In cell shape, the length:width ratio of** ***Chattonella antiqua*****-like cells are larger than** ***Chattonella marina*****-like cells (Shikata et al., 2021).**

Strain name	Year collected	Origin	Contamination status	Shape[1)]	Ichthyotoxicity[1)]	References
NIES-1	1978	Harima-nada	Axenic	*C. antiqua*-like	High	1)
OP27	2010	Ariake Sea	Xenic	*C. antiqua*-like[2)]	High	3)
Ago03	2013	Ago Bay	Xenic	*C. marina*-like	High	1)
Ago04	2013	Ago Bay	Xenic	*C. marina*-like	Low	1)
3KGY	2010	Yatsushiro Sea	Axenic	*C. antiqua*-like	Medium	1)

[1)] Shikata et al. (2021); [2)] Akita et al. (2022); [3)] Wada et al. (2018).

2 Materials and methods

2.1 Culture of strains

Five clonal strains of *Chattonella* were used in this study. The dates and locations for the isolation of these strains are listed in Table 1. Two strains were axenic, and the others were not. The strains were subcultured in 50-mL Erlenmeyer flasks containing 25 mL of modified SWM-3 medium (Shikata et al., 2011) with a salinity of 32 psu at 25°C under 150 μmol photons m^{-2} s^{-1} of white fluorescent irradiation on a 12:12-h light:dark cycle (light period, 06:00 to 18:00 local time [LT]). The photosynthetic photon flux density in the incubator was measured with a Quantum Scalar Laboratory PPFD sensor (QSL-2101, Biospherical Instruments Inc., San Diego, CA, United States).

2.2 Monitoring DVM with a cylindrical aquarium

A cylindrical aquarium was used as a culture vessel to monitor DVM (Shikata et al., 2014). The aquarium (inner diameter, 5 cm; height, 90 cm) was made of acrylic, with nine sampling ports (diameter, 13 mm) at intervals of 10 cm, starting from the bottom. Each port was plugged with a silicone-rubber stopper. The aquarium was placed in a temperature-controlled room (25°C) and capped with a disc-shaped LED lamp (daylight color; INREDA, Spot-light LED, Inter IKEA Systems B.V., The Netherland). The light intensity at the surface was 250 μmol photons m^{-2} s^{-1}.

On the day prior to each experiment, we added modified SWM-3 medium and a cell suspension at 17:00–18:00 LT. The total volume of the medium and the cell suspension was adjusted to 1.6 L, and the final water depth in the aquarium was about 85 cm. Each experiment was initiated at 09:00 LT, and at 3-h intervals 5 mL of the cell suspension was sampled from the water surface or from each sampling port. Then a syringe and a needle were used to refill the aquarium from the surface and bottom sampling ports with 25 mL of fresh medium.

Yamaguchi et al. (1991) reported that the cell densities of *Chattonella* are positively correlated with *in vivo* fluorescence. Therefore, to determine the vertical distribution of cells, we measured the *in vivo* fluorescence (Brand et al., 1981) of the sample at each depth by using a fluorometer (Model 10-AU; Turner Designs, Sunnyvale, CA, United States). Cell densities were calculated using a standard curve for each strain, although only cell densities at the surface and bottom were counted under a light microscope (Eclipse TS-100; Nikon Co., Tokyo, Japan). For sample collection during the dark period, we used a red LED flashlight (peak wavelength, 630 nm) for illumination, because red light has little effect on the DVM pattern of *Chattonella* (Shikata et al., 2013).

2.3 Monitoring DVM with a digital camera system

The system described by Shikata et al. (2016) was also used for monitoring DVM. A rectangular acrylic chamber (base: 1 cm wide × 5 cm long) containing 25 mL of cell suspension (depth, 5 cm) was held by a clamp. Each sample was illuminated by a white LED from above; the photon flux density at the water surface was adjusted to 150 μmol photons m^{-2} s^{-1}.

A monochromatic, digital, charge-coupled device camera (Pixelfly, PCO AG, Kelheim, Germany) was used to photograph the sample from the side. A long pass filter (cut off wavelength of <800 nm; LX-903, Mitsubishi Layon Co. Ltd., Tokyo, Japan) was mounted in front of the camera lens. The samples were illuminated by an infrared LED (peak wavelength, 850 nm; Pi Photonics Inc., Shizuoka, Japan) from behind, and the camera captured the light scattered by the cells. Each sample was time-lapse photographed every 15 min for 66 h (from day 0 at 18:00 to day 2 at 12:00 LT) to obtain raw data for determining the DVM. The devices that composed the system were operated in a temperature-controlled (25°C) dark room.

In the digital images, the cell density in each area is roughly reflected by its brightness. Since the brightness of a pixel in the 8-bit image is represented by 256 (2^8) steps of gray values, we first read the gray values of pixels at respective areas of cell suspension using ImageJ software (http://rsbweb.nih.gov/ij/) to evaluate vertical profiles of the cells. The surface accumulation ratios were then calculated as the common logarithm of the ratio of the average of gray values in the surface layer (0–0.75 cm) and the bottom layer (2.50–3.00 cm). Because *Chattonella* generally migrated between the surface and bottom under most experimental light conditions, the time series of surface accumulation ratios was used to represent the DVM pattern and cell accumulation. High and low ratios were recorded

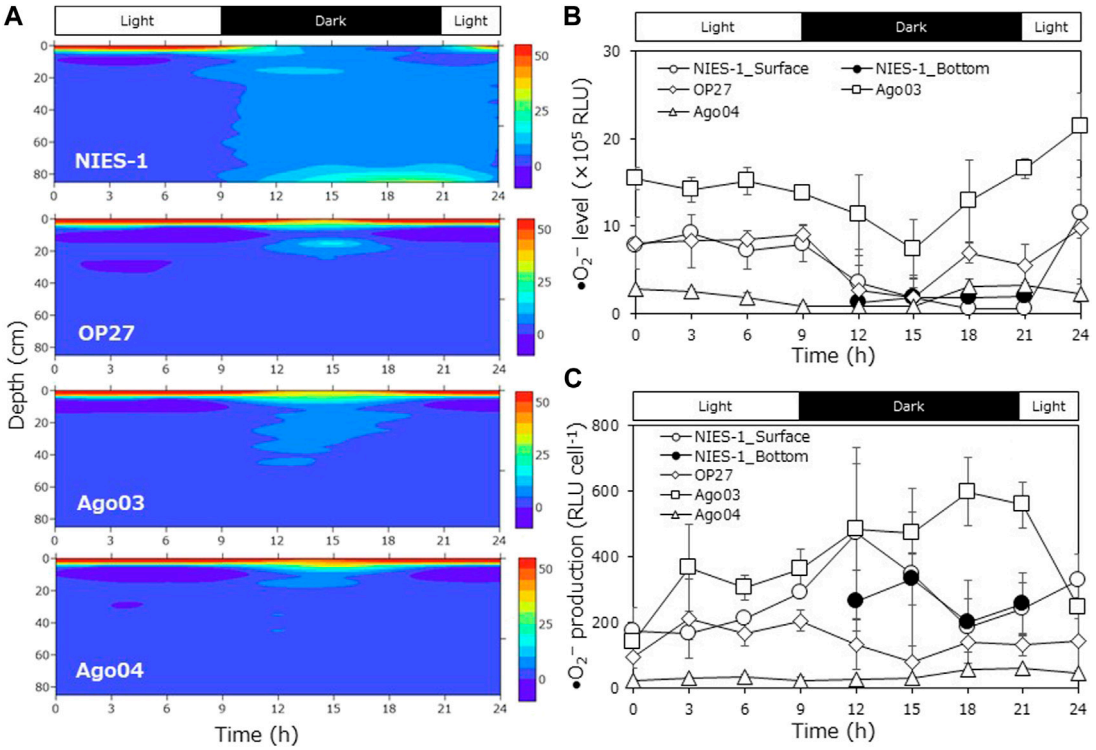

FIGURE 1
Diurnal vertical migration of different *Chattonella* strains in the cylindrical aquarium. **(A)** Time-course variations in the cell accumulation percentage at each depth layer (average of triplicate measurements), **(B)** time-course variations in superoxide ($\bullet O_2^-$) level (relative luminescence units: RLU), and **(C)** $\bullet O_2^-$ production ($\bullet O_2^-$ level per cell) of *Chattonella* strains at the surface or bottom layer (only dark periods of NIES-1) in the cylindrical aquarium. $\bullet O_2^-$ level was measured by a chemiluminescence method. Each bar represents the mean ± SD of three biological replicates.

when most cells were swimming upward and downward, respectively.

2.4 $\bullet O_2^-$ detection

$\bullet O_2^-$ was detected using the chemiluminescence reagent L-012 (FUJIFILM Wako Pure Chemical Corp., Osaka, Japan) (Nishinaka et al., 1993). The resultant chemiluminescence was monitored for 30 s using a luminometer (AB-2270 Luminescencer Octa, ATTO Corp., Tokyo, Japan). The $\bullet O_2^-$ levels in cultures were calculated by subtracting the chemiluminescence measured in the presence of 200 U of bovine superoxide dismutase (SOD; FUJIFILM Wako Pure Chemical Corp.) from the measured chemiluminescence.

2.5 Statistical analyses

The data were tested for homogeneity of variances using Levene's test. When variances were homogeneous, we used one-way analysis of variance and multiple comparisons with Tukey's honestly significant difference (HSD) test to assess the differences in *Chattonella* biological parameters among treatments. Data not showing homogeneous variances were log-transformed, and a Levene's test was performed once again. When the variances were not homogeneous even after log-transformation, we used the Dunnet T3 test. All analyses were performed with IBM SPSS Statistics Desktop Version 19.0 for Windows (IBM Japan, Tokyo, Japan), with $p < 0.05$ indicating a significant difference.

3 Results

3.1 Patterns of DVM and superoxide production in different *Chattonella* strains

We observed DVM in four strains of *Chattonella* (NIES-1, OP27, Ago03, and Ago04) using the cylindrical aquarium. Approximately equal amounts of cells (~3.0×10^5 cells) at the late logarithmic growth phase (late log phase; $1.5–3.0 \times 10^4$ cells mL^{-1}) were injected into the aquarium. The vertical cell distribution at each time was represented by the cell accumulation ratio (%), calculated as the cell abundance at a sampling depth layer divided by the sum of cell abundances at all sampling depth layers. Average cell densities in the water column over the observation periods ranged from 2.5×10^2 to 6.1×10^2 cells mL^{-1} in the four strains (Supplementary Figure S1). It was a common trend among strains that average cell abundance in the water column gradually decreased until the middle of the dark period and then recovered. A decline in the average cell abundance might have been caused by the aggregation of cells among sampling ports, whereas an increase might have been caused by sampling and

cell division, because most *Chattonella* cells divide during the latter half of the dark period (Nemoto and Furuya, 1985).

The strain NIES-1 displayed clear DVM (Figure 1A). Most cells started downward migration at the transitional period from light to dark (at 9 h from the start time), and a portion of the cells reached the bottom during the dark period. Maximum cell accumulation ratios at the bottom were 34.6% ± 11.7% (average ±SD). Thereafter, cells rapidly migrated to the surface at the transitional period from dark to light (at 21–24 h). The cell accumulation ratio at the surface varied from 4.7% ± 1.6% to 82.0% ± 2.0% through the experimental period.

In the other strains, most cells also accumulated at the surface during the light period (Figure 1A). However, most cells continued to aggregate at the surface and scarcely reached the bottom during the dark period. Maximum cell accumulation ratios at the bottom were 2.8% ± 2.3% in OP27, 3.2% ± 1.9% in Ago03, and 0.7% ± 0.2% in Ago04; these values were significantly lower than that of NIES-1 (Turkey test; $p < 0.05$). The cell accumulation ratio at the surface ranged from 36.3% ± 1.5% to 98.6% ± 0.38% in OP27, from 36.0% ± 15.5% to 96.8% ± 0.6% in Ago03, and from 51.3% ± 6.3% to 98.2% ± 0.8% in Ago04 during the experimental period.

Levels of $\bullet O_2^-$ (relative luminescence units: RLU) and $\bullet O_2^-$ production (RLU cell^{-1}) both differed among strains (Figures 1B,C). Although levels of $\bullet O_2^-$ at the surface decreased during the dark period and then increased during the light period in all strains, the maximum $\bullet O_2^-$ production in Ago04 was significantly lower than rates in other strains (Turkey test after log-transformation; $p < 0.05$). In NIES-1 and OP27, $\bullet O_2^-$ production increased during the light period, peaked around the beginning of the dark period (9–12 h), and then decreased at the start of the light period (21 h). In Ago03 and Ago04, however, $\bullet O_2^-$ production increased during the dark period and peaked around the beginning of the light period (18–21 h). We also measured the $\bullet O_2^-$ production level at the bottom for only NIES-1 during a part of the dark period, but the value was similar to that at the surface.

3.2 Patterns of DVM and superoxide production in different growth phases and cell densities

We investigated the effects of culture growth phase and cell density on the DVM pattern within the cylindrical aquarium. The strain 4KGY was used in this experiment. Cultures at the early log phase (4.6×10^3 cells mL^{-1}) and late log phase (2.6×10^4 cells mL^{-1}) were prepared. The culture at the early log phase was injected into the aquarium. Average cell density in the water column over the observation period was 6.3×10^2 cells mL^{-1}. Next, cultures in the late log phase were inoculated into separate aquaria at three different doses (low cell density, LD; medium cell density, MD; high cell density, HD). Average cell densities in the water column in LD, MD, and HD over the observation period was 2.9×10^2 cells mL^{-1}, 1.3×10^3 cells mL^{-1}, and 2.1×10^4 cells mL^{-1}, respectively (Supplementary Figure S2). As in the interstrain comparison experiments, the average cell abundance in the water column gradually decreased until the middle of the dark period and then recovered (Supplementary Figure S2). In the HD treatment, a portion of the cells aggregated at the bottom just after cell inoculation, and we could not sample the aggregate due to its stickiness. The average cell density in the water column did not decrease during the experimental period, meaning the aggregate scarcely increased (Supplementary Figure S2).

Cells in the early log phase displayed clear DVM (Figure 2A). Most cells started downward migration at the transitional period from light to dark (at 9 h), and a portion of the cells reached the bottom during the dark period. The maximum cell accumulation ratio at the bottom during the dark periods was 24.3% ± 12.0%. The surface cell accumulation ratio ranged from 7.7% ± 1.5% to 91.0% ± 1.9% throughout the experimental period. As with early log phase culture, cells at the late log phase at the low or medium cell density also migrated downward during the dark period. However, the maximum cell accumulation ratio at the bottom during the dark period was lower than that of the early log phase culture: 12.1% ± 3.5% at LD and 7.3% ± 1.9% at MD, although no statistically significant differences were detected (Turkey test; $p = 0.304$ for LD, $p = 0.110$ for MD). The cells did not display clear DVM at HD; cells accumulated within the upper half of the aquarium or near the bottom all day. At HD, the maximum cell accumulation ratio at the surface over the experimental period was significantly lower than in the early growth phase culture and at the other cell densities (Turkey test; $p < 0.05$).

We measured the $\bullet O_2^-$ level at the depths where cells accumulated most (surface or bottom). At LD and MD, levels of $\bullet O_2^-$ decreased during the dark period and then increased during the light period (Figure 2B). $\bullet O_2^-$ production increased during the light period and peaked during the light period (6–9 h; Figure 2C). At HD, clear rhythms of $\bullet O_2^-$ level and $\bullet O_2^-$ production were not observed. The $\bullet O_2^-$ production was very low all day, and the maximum value was significantly lower than those in other conditions (Dunnet T3 after log-transformation; $p < 0.05$).

3.3 DVM patterns and superoxide production under different nutrient conditions

We investigated the effects of nutrient deficiency on the DVM pattern using the digital camera system. Although it is difficult to completely remove nutrients from the medium based on natural seawater, the growth of *Chattonella* strains in artificial medium is not good. Therefore, we adopted the digital camera system, which requires no exchange of medium, in this experiment. Axenic strain 4KGY was incubated in medium lacking $NaNO_3$ (N-depleted medium), lacking $NaH_2PO_4{\cdot}2H_2O$ (P-depleted medium), or containing all components (complete medium) for 5 days before the observation of DVM. The cell densities were ~2.0×10^4 cells mL^{-1} at the start of the experiment.

Cells displayed DVM under all nutrient conditions, but surface accumulation ratios under nutrient-depleted conditions were lower than in the complete medium treatment during the light period (Figure 3). There were significant differences in the maximum moving averages of the surface accumulation ratio measured at 3-h intervals between the nutrient-depleted media and the complete medium on both days (Dunnett T3; $p < 0.05$). Moreover, to investigate the effects of nutrients on $\bullet O_2^-$ production in different *Chattonella* strains, we incubated axenic strains NIES-1

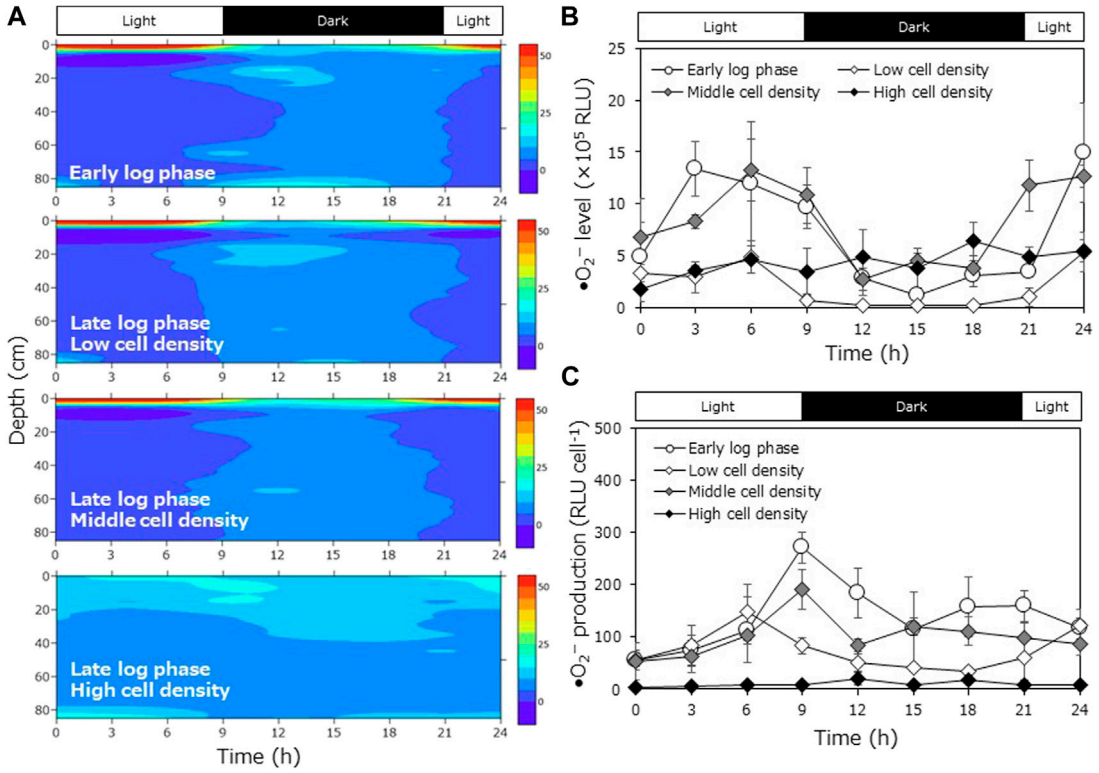

FIGURE 2
Diurnal vertical migration of *Chattonella* at different growth phases and cell densities in the cylindrical aquarium. **(A)** Time-course variations in the cell accumulation percentage at each depth (average of triplicate measurements), **(B)** time-course variations in superoxide ($\bullet O_2^-$) level (relative luminescence units: RLU), and **(C)** $\bullet O_2^-$ production ($\bullet O_2^-$ level per cell) of *Chattonella* at the surface or bottom layer in the cylinder aquarium. $\bullet O_2^-$ level was measured by a chemiluminescence method. Each bar represents the mean ± SD of three biological replicates.

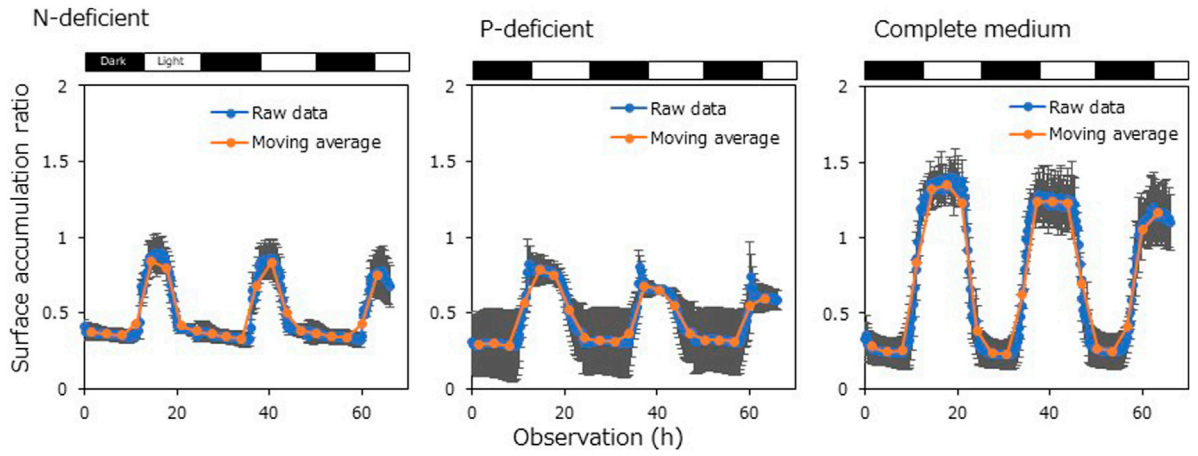

FIGURE 3
Diurnal vertical migrations of *Chattonella* at different degrees of nutrient deficiency observed by the digital camera system. Raw data and moving average at 3-h intervals are shown. Each bar represents the mean ± SD of four biological replicates.

and 4KGY in 50-mL Erlenmeyer flasks containing 25 mL of N-depleted medium, P-depleted medium, or complete medium and tracked the cell density and $\bullet O_2^-$ level for 9 days. Conditions of temperature and light were the same as in the subculture. Cells increased throughout the experimental period in the complete medium, but increases in cell densities stopped from day 5–7 under the nutrient-depleted conditions (Figure 4). The $\bullet O_2^-$ level in NIES-1 and 4KGY cultures peaked from days 5–7 under all

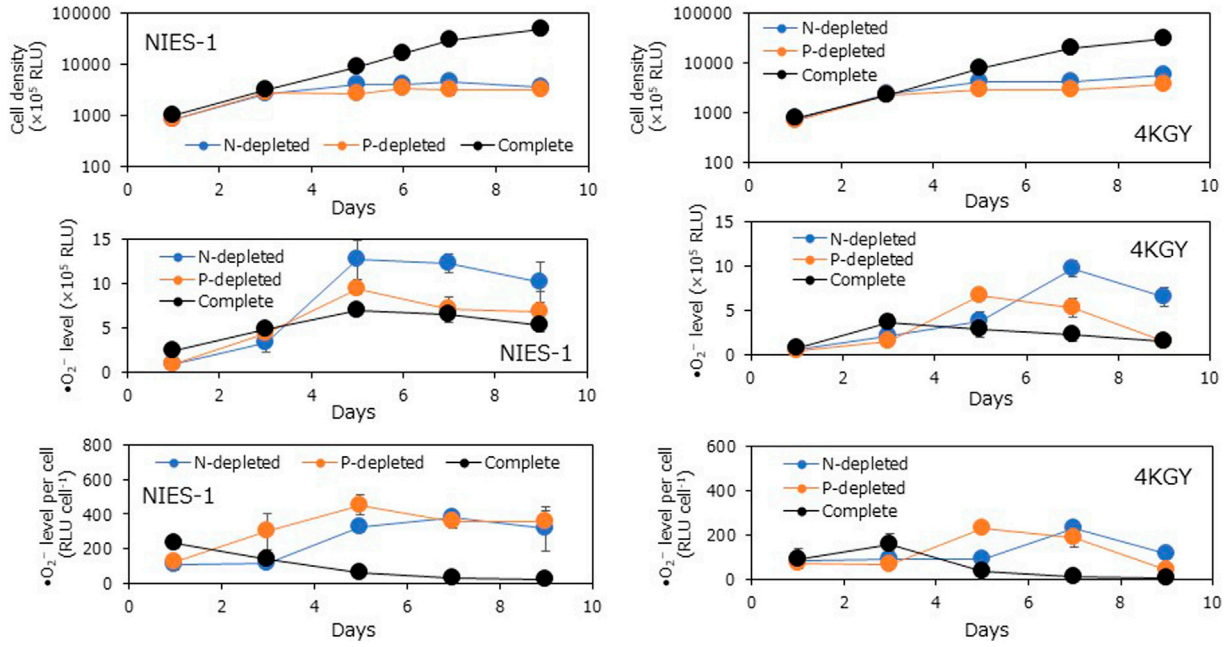

FIGURE 4
Time-course variations in cell density, superoxide ($\bullet O_2^-$) level (relative luminescence units: RLU), and $\bullet O_2^-$ production ($\bullet O_2^-$ level per cell) of two *Chattonella* strains at different degrees of nutrient deficiency. $\bullet O_2^-$ level was measured by a chemiluminescence method. Each bar represents the mean ± SD of three biological replicates.

conditions, but the maximum values under nutrient-depleted conditions were significantly higher than those in complete medium and that under N-depleted condition was significantly higher than that in P-depleted condition (Dunnet T3; $p < 0.05$). Production of $\bullet O_2^-$ by the two strains rapidly increased on day 5 under nutrient-depleted conditions, whereas it gradually decreased from day 1 in the complete medium. The maximum $\bullet O_2^-$ production by NIES-1 under nutrient-depleted conditions was significantly higher than that in complete medium (Dunnet T3; $p < 0.05$). For 4KGY, there were not statistically significant differences in the maximum $\bullet O_2^-$ production among nutrient conditions, but that under nutrient-depleted conditions was significantly higher than that in complete medium on day 5 (Turkey test; $p < 0.05$) and day 7 (Dunnet T3; $p < 0.05$). The maximum $\bullet O_2^-$ level and $\bullet O_2^-$ production of NIES-1 were significantly higher than those of 4KGY under each condition (Dunnet T3 after log-transformation; $p < 0.05$).

4 Discussion

Among investigations conducted under quiet conditions in enclosed coastal areas or in a mesocosm, there were differences in the depth reached by a *Chattonella* red tide at night (Watanabe et al., 1995; Araki et al., 2013; Sakurada et al., 2013; Katano et al., 2014; Sakaguchi et al., 2017). In previous laboratory studies using *Chattonella* strains NIES-1 and 3KGY, most *Chattonella* cells migrated to the surface of a vessel during the light periods and to the bottom during the dark periods (Kim et al., 2005; Shikata et al., 2014). Before the present study, however, we viewed flasks including *Chattonella* strains during the dark periods and found that some strains aggregated at the surface of the medium even during the night. The present study showed that some strains display clear downward migration during the dark periods, whereas others scarcely migrate under the same condition. Strains Ago03 and Ago04 were isolated from the same marine area during different years, and both displayed weak downward migration. Strains 4KGY used in the present study and 3KGY used in Shikata et al. (2014) were isolated from the same marine area on the same day. Compared to 4KGY (early log phase), 3KGY has higher surface accumulation ratios during the dark periods and accumulates at the bottom during the light periods in the same experimental setup, indicating that DVM in 3KGY has more entrainability. Although *Chattonella* shows variations in cell shape and toxicity among strains (Demura et al., 2009; Shikata et al., 2021), the relationship between their phenotypes (Table 1) and DVM pattern remains obscure. Our findings indicate that the strain composition of a *Chattonella* population may influence the vertical cell distribution at each time point in the field, although it is unclear what produced the interstrain differences in the DVM pattern.

Interstrain variation in the DVM pattern may contribute to species survival by decreasing the risk that all cells are exposed to a harmful environment at a certain depth. However, if only strains with a poor ability of downward migration survive, it is unclear whether the population could recover the ability. Moreover, the large diversity in DVM can inhibit densification of cells, leading to poorer competition with other microorganisms, such as antibiotic ability (Oda et al., 1992) and toxicity against other phytoplankters (Qiu et al., 2011; Fernández-Herrera et al., 2016). Therefore, the

strain composition of a *Chattonella* population may characterize the population dynamics in each marine area.

It is difficult to incubate some *Chattonella* strains at large volumes (>200 mL) in normal vessels such as an Erlenmeyer flask for days, although the reasons are unclear. Surprisingly, the present study revealed that strains OP27, Ago03, and Ago04, which can grow in large-scale incubation, displayed little downward migration. It is impossible to resuspend a cell pellet made by centrifugation of a *Chattonella* culture because the cells strongly adhere to each other at high cell density (Jenkinson et al., 2007). Although bioconvection occurs at the surface and mitigates densification during periods of upward migration, bioconvection does not occur at the bottom during periods of downward movement. Therefore, success in the large-scale incubation of *Chattonella* may be closely related to the ability of a strain to migrate downward.

Sakaguchi et al. (2017) reported that a red tide of *Chattonella* displays clear DVM when the average cell density is on the order of 10^3 cells mL^{-1} in the water column, whereas downward migration is scarcely observed when the average cell density is on the order of 10^4 cells mL^{-1} and nutrient concentrations are sufficient for *Chattonella* growth. Likewise, in the present study *Chattonella* cells scarcely displayed DVM when the average cell density in the water column (volume: 1.6 L) was more than 10^4 cells mL^{-1} (late log phase in Figure 2). Although the maximum cell density of *Chattonella* was normally on the order of 10^4 cells mL^{-1} even when the other conditions were suitable for growth, the growth phase at the time of the inoculation scarcely affected DVM patterns. Therefore, densification may hamper various physiological activities related to downward migration and growth, although the mechanism remains to be clarified. When the sample volume was small (25 mL), however, clear DVM was observed even on the order of 10^4 cells mL^{-1} (complete medium in Figure 3). In *Chattonella*, at greater incubation volume, the growth rate and maximum cell yield were lower. Thus, the effects of densification on physiological states may depend on the incubation volume in laboratory studies.

In various flagellate species, the depletion of nitrogen or phosphorus activates or inhibits DVM (Heaney and Eppley, 1980; Yuasa et al., 2018). We observed that the deficiency of nitrogen or phosphorus inhibited DVM in *Chattonella* with two axenic strains. Although the red-tide dinoflagellate *Karenia mikimotoi* aggregates at the surface all day under nitrogen-depleted conditions (Yuasa et al., 2018), we found that *Chattonella* sank more easily in nitrogen- or phosphorus-depleted conditions. In a Swedish fjord, the amount of *Chattonella* cells peaked in sediment traps deployed in deep layers (15 and 30 m depths) when a red tide of *Chattonella* was declining and nitrate concentrations in the surface layer (0–10 m depth) were low (Waite and Lindahl, 2006). In addition, DVM ceases under continuous darkness, whereas it persists under continuous red light, which acts on photosynthesis but scarcely shifts the phase of the DVM pattern (Shikata et al., 2015). Therefore, swimming would require energy from photosynthesis, which in turn requires light and nutrients, in *Chattonella*.

Kim et al. (2005) examined the relationship between the production of reactive oxygen species and DVM using the *Chattonella* strain NIES-1. They observed DVM similar to that recorded in the present study and found that $\bullet O_2^{--}$ production was high during the light period and that it decreased during the dark period in cell-aggregated layers (surface or bottom). Yuasa et al. (2020a) observed a similar diurnal pattern in $\bullet O_2^-$ production in the strain 4KGY. The present study also revealed a similar pattern of $\bullet O_2^-$ production in the strain OP27, but the DVM pattern of strains Ago03 and Ago04 was different from that of the other strains, with $\bullet O_2^-$ production increasing during the dark period. Interestingly, we noticed that characteristics of the cellular $\bullet O_2^-$ production pattern may be categorized by cell shape in *Chattonella* strains, as noted in strains with a *Chattonella antiqua*–like shape (NIES-1, 4KGY, OP27) and strains with a *C. marina*–like shape (Ago03, Ago04); the amount of $\bullet O_2^-$ production, however, is not categorized by cell shape among strains (Shikata et al., 2021). These findings imply that the DVM pattern may be independent of the $\bullet O_2^-$ production pattern because only the latter was categorized by cell shape.

Based on experiments using the strain NIES-1, Kim et al. (2004) suggested that the growth phase (or cell density) can affect the amount of $\bullet O_2^-$ production but has little effect on the diurnal pattern of $\bullet O_2^-$ production. The $\bullet O_2^-$ production rate had a maximum value during the exponential growth phase (low cell density) and subsequently decreased in the stationary phase (high cell density), but $\bullet O_2^-$ production increased during the light period and decreased during the dark period regardless of growth phases. However, the present study using strain 4KGY showed that the diurnal pattern of $\bullet O_2^-$ production was less clear at higher cell density (stationary phase).

Kim et al. (2004) reported that $\bullet O_2^-$ production was lower when nitrogen and phosphorus concentrations were low than when these nutrients were fully supplied in strain NIES-1. On the other hand, Yuasa et al. (2020a) reported that $\bullet O_2^-$ production is stimulated under nitrogen- or phosphorus-deficient conditions in the 4KGY strain. Therefore, the response of $\bullet O_2^-$ production to nutrient deficiency appears to depend on the strain. According to the reverification result in the present study, however, $\bullet O_2^-$ production was stimulated under nitrogen- or phosphorus-deficient conditions in both NIES-1 and 4KGY. Previous studies have suggested that the reducing power required for $\bullet O_2^-$ production in the cell membrane may originate from photosynthesis, based on inhibition of $\bullet O_2^-$ production by the administration of a photosynthetic inhibitor during the light period as well as the increase in $\bullet O_2^-$ production during the light period (Marshall et al., 2002; Yuasa et al., 2020b). Yuasa et al. (2020a) have reported that $\bullet O_2^-$ production under nitrogen- or phosphorus-deficient conditions increase during the dark period and the extracellular levels of $\bullet O_2^-$ under nutrient-deficient conditions are unaffected by the presence of an inhibitor of photosynthetic electron transport—indicating that pathways of $\bullet O_2^-$ production other than photosynthesis exist. However, the present study revealed that diurnal patterns of $\bullet O_2^-$ production differ among strains. Thus, there may be differences among strains with regard to the degree of dependence on each production pathway and sensitivity to environmental conditions such as cell density and nutrient availability.

In conclusion, our findings indicate that strain, cell density, and nutrient deficiency are factors that affect the DVM pattern and $\bullet O_2^-$ production in *Chattonella*. Moreover, our results suggest that the diurnal patterns of vertical migration and $\bullet O_2^-$ production may be

independently regulated, indicating that a *Chattonella* population can have cells with numerous combinations of DVM and $\bullet O_2^-$ production patterns. A great diversity of DVM and $\bullet O_2^-$ production in a population should increase the chances of acquiring nutrients and light and successfully competing against other microorganisms in the water column. Quantitative analyses using numerical models based on the information obtained in the present study are important future tasks.

Data availability statement

The original contributions presented in the study are included in the article/Supplementary Material, further inquiries can be directed to the corresponding author.

Author contributions

TS designed this study and data analyses; TS, SK, and KY conducted experiments. All authors have read and agreed to the published version of the manuscript.

Funding

This study was supported by JSPS KAKENHI Grant No. 21H05305 and a Grant-in-Aid from the Fisheries Agency of Japan.

Acknowledgments

We are grateful to Dr. Yukihiko Matsuyama for providing the culture strain OP27 of *Chattonella*.

Conflict of interest

The authors declare that the research was conducted in the absence of any commercial or financial relationships that could be construed as a potential conflict of interest.

Publisher's note

Supplementary material

The Supplementary Material for this article can be found online at: https://www.frontiersin.org/articles/10.3389/fcell.2023.1134227/full#supplementary-material

References

Akita, K., Yoshida, K., Noda, T., Chujo, T., Hotta, T., Shinoda, R., et al. (2022). Genetic parameter estimation for resistance to red tide raphidophyte *Chattonella antiqua* in Japanese yellowtail *Seriola quinqueradiata*. *Aquacul. Res.* 53, 4449–4459. doi:10.1111/are.15942

Araki, K., Matuoka, T., Morishita, T., and Kawasaki, S. (2013). Impacts of diel vertical migration of *Chattonella antique* (Raphidophyceae) on the benthic crustacean (*Penaeus japonicus*) in Ariake Bay. *Rep. Kumamoto Pref. Fish. Res. Cent.* 9, 13–18.

Ault, T. R. (2000). Vertical migration by the marine dinoflagellate *Prorocentrum triestinum* maximises photosynthetic yield. *Oecologia* 125, 466–475. doi:10.1007/s004420000472

Balaji-Prasath, B., Wang, Y., Su, Y. P., Hamilton, D. P., Lin, H., Zheng, L., et al. (2022). Methods to control harmful algal blooms: A review. *Environ. Chem. Lett.* 20, 3133–3152. doi:10.1007/s10311-022-01457-2

Bearon, R. N., Grünbaum, D., and Cattolico, R. A. (2004). Relating cell-level swimming behaviors to vertical population distributions in *Heterosigma akashiwo* (Raphidophyceae), a harmful alga. *Limnol. Oceanogr.* 49, 607–613. doi:10.4319/lo.2004.49.2.0607

Berdalet, E., McManus, M. A., Ross, O. N., Burchard, H., Chavez, F. P., Jaffe, J. S., et al. (2014). Understanding harmful algae in stratified systems: Review of progress and future directions. *Rev.Prog. Fut. Direct. Deep-Sea Res. II* 101, 4–20. doi:10.1016/j.dsr2.2013.09.042

Bollens, S. M., Quenette, J. A., and Rollwagen-Bollens, G. (2012). Predator-enhanced diel vertical migration in a planktonic dinoflagellate. *Mar. Ecol. Prog. Ser.* 447, 49–54. doi:10.3354/meps09467

Brand, L. E., Guillard, R. R. L., and Murphy, L. F. (1981). A method for the rapid and precise determination of acclimated phytoplankton reproduction rates. *J. Plankton Res.* 3, 193–201. doi:10.1093/plankt/3.2.193

Davidson, K., Anderson, D. M., Mateus, M., Reguera, B., Silke, J., Sourisseau, M., et al. (2016). Forecasting the risk of harmful algal blooms. *Harmful Algae* 53, 1–7. doi:10.1016/j.hal.2015.11.005

Demura, M., Noël, M. H., Kasai, F., Watanabe, M. M., and Kawachi, M. (2009). Taxonomic revision of *Chattonella antiqua, C. marina* and *C. ovata* (Raphidophyceae) based on their morphological characteristics and genetic diversity. *Phycologia* 48, 518–535. doi:10.2216/08-98.1

Fernández-Herrera, L. J., Band-Schmidt, C. J., López-Cortés, D. J., Hernández-Guerrero, C. J., Bustillos-Guzmán, J. J., and Núñez-Vázquez, E. (2016). Allelopathic effect of *Chattonella marina* var. *marina* (Raphidophyceae) on *Gymnodinium catenatum* (Dinophycea). *Harmful Algae* 51, 1–9. doi:10.1016/j.hal.2015.10.009

Gobler, C. J. (2020). Climate change and harmful algal blooms: Insights and perspective. *Harmful Algae* 91, 101731. doi:10.1016/j.hal.2019.101731

E. Granéli and J. T. Turner (Editors) (2006). *Ecology of harmful algae* (Berlin: Springer).

Harvey, E. L., and Menden-Deuer, S. (2011). Avoidance, movement, and mortality: The interactions between a protistan grazer and *Heterosigma akashiwo*, a harmful algal bloom species. *Limnol. Oceanogr.* 56, 371–378. doi:10.4319/lo.2011.56.1.0371

Heaney, S. I., and Eppley, R. W. (1980). Light, temperature and nitrogen as interacting factors affecting diel vertical migrations of dinoflagellates in culture. *J. Plankton Res.* 3, 331–344. doi:10.1093/plankt/3.2.331

Ikegami, S., Imai, I., Kato, J., and Ohtake, H. (1995). Chemotaxis towards inorganic phosphate in the red tide alga *Chattonella antiqua*. *J. Plankton Res.* 17, 1587–1591. doi:10.1093/plankt/17.7.1587

Imai, I., and Yamaguchi, M. (2012). Life cycle, physiology, ecology and red tide occurrences of the fish-killing raphidophyte *Chattonella*. *Harmful Algae* 14, 46–70. doi:10.1016/j.hal.2011.10.014

Ishimatsu, A., Sameshima, M., Tamura, A., and Oda, T. (1996). Histological analysis of the mechanisms of *Chattonella*-induced hypoxemia in yellowtail. *Fish. Sci.* 62, 50–58. doi:10.2331/fishsci.62.50

Jenkinson, I. R., Shikata, T., and Honjo, T. (2007). Modified ichthyoviscometer shows high viscosity in *Chattonella* culture. *Harmful Algae News* 35, 1–5.

Jephson, T., Fagerberg, T., and Carlsson, P. (2011). Dependency of dinoflagellate vertical migration on salinity stratification. *Aquat. Microb. Ecol.* 63, 255–264. doi:10.3354/ame01498

Kamykowski, D. (1995). Trajectories of autotrophic marine dinoflagellates. *J. Phycol.* 31, 200–208. doi:10.1111/j.0022-3646.1995.00200.x

Katano, T., Yoshida, M., Yamaguchi, S., Yoshino, K., Hamada, T., Koriyama, M., et al. (2014). Effect of nutrient concentration and salinity on diel vertical migration of

Chattonella marina (Raphidophyceae). *Mar. Biol. Res.* 10, 1007–1018. doi:10.1080/17451000.2013.879987

Kim, D., Watanabe, M., Nakayasu, Y., and Kohata, K. (2005). Changes in O_2^- and H_2O_2 production by *Chattonella antiqua* during diel vertical migration under nutrient stratification. *Aquat. Microb. Ecol.* 39, 183–191. doi:10.3354/ame039183

Kim, D., Watanabe, M., Nakayasu, Y., and Kohata, K. (2004). Production of superoxide anion and hydrogen peroxide associated with cell growth of *Chattonella antiqua*. *Aquat. Microb. Ecol.* 35, 57–64. doi:10.3354/ame035057

Kim, H. G. (2006). "Mitigation and controls of HABs," in *Ecology of harmful algae, ecological studies*. Editors E. Granéli and J. T. Turner (New York: Springer), 327–338.

Lai, Z., and Yin, K. (2014). Physical–biological coupling induced aggregation mechanism for the formation of high biomass red tides in low nutrient waters. *Harmful Algae* 31, 66–75. doi:10.1016/j.hal.2013.09.011

Marshall, J. A., Hovenden, M., Oda, T., and Hallegraeff, G. M. (2002). Photosynthesis does influence superoxide production in the ichthyotoxic alga *Chattonella marina* (Raphidophyceae). *J. Plankton Res.* 24, 1231–1236. doi:10.1093/plankt/24.11.1231

Matsusato, T., and Kobayashi, H. (1974). Studies on death of fish caused by red tide. *Bull. Nansei Reg. Fish. Res. Lab.* 7, 43–67.

McGillicuddy, D. J., Jr (2010). Models of harmful algal blooms: Conceptual, empirical, and numerical approaches. *J. Mar. Syst. J. Eur. Assoc. Mar. Sci. Tech.* 83, 105–107. doi:10.1016/j.jmarsys.2010.06.008

Nemoto, Y., and Furuya, M. (1985). Inductive and inhibitory effects of light on cell division in *Chattonella antiqua*. *Plant Cell Physiol.* 26, 669–674. doi:10.1093/oxfordjournals.pcp.a076956

Nishinaka, Y., Aramaki, Y., Yoshida, H., Masuya, H., Sugawara, T., and Ichimori, Y. (1993). A new sensitive chemiluminescence probe, L-012, for measuring the production of superoxide anion by cells. *Biochem. Biophys. Res. Commun.* 193, 554–559. doi:10.1006/bbrc.1993.1659

Oda, T., Ishimatsu, A., Shimada, M., Takeshita, S., and Muramatsu, T. (1992). Oxygen-radical-mediated toxic effects of the red tide flagellate *Chattonella marina* on *Vibrio alginolyticus*. *Mar. Biol.* 112, 505–509. doi:10.1007/bf00356297

Qiu, X., Yamasaki, Y., Shimasaki, Y., Gunjikake, H., Matsubara, T., Nagasoe, S., et al. (2011). Growth interactions between the raphidophyte *Chattonella antiqua* and the dinoflagellate *Akashiwo sanguinea*. *Harmful Algae* 11, 81–87. doi:10.1016/j.hal.2011.08.001

Roenneberg, T., Colfax, G. N., and Hastings, J. W. (1989). A circadian rhythm of population behavior in *Gonyaulax polyedra*. *J. Biol. Rhythm.* 4, 89–104. doi:10.1177/074873048900400208

Sakaguchi, M., Yamatogi, T., Hirae, S., Ishida, N., Hirano, K., and Aoki, K. (2017). Diurnal vertical migration of *Chattonella* spp. in mesocosm during a red tide in isahaya bay, nagasaki prefecture, Japan. *Bull. Plankton Soc. Jpn.* 64, 1–10.

Sakurada, K., Takahi, S., and Umemoto, T. (2013). Occuration and vertical migration of *Chattonella antiqua* in 2010 in yatsushiro sea. *Rep. Kumamoto Pref. Fish. Res. Cent.* 9, 85–90.

Sellner, K. G., Doucette, G. J., and Kirkpatrick, G. J. (2003). Harmful algal blooms: Causes, impacts and detection. *J. Ind. Microbiol. Biotechnol.* 30, 383–406. doi:10.1007/s10295-003-0074-9

Shen, M., Xu, J., Tsang, T. Y., and Au, D. W. (2010). Toxicity comparison between *Chattonella marina* and *Karenia brevis* using marine medaka (*Oryzias melastigma*): Evidence against the suspected ichthyotoxins of *Chattonella marina*. *Chemosphere* 80, 585–591. doi:10.1016/j.chemosphere.2010.03.051

Shikata, T., Kitatsuji, S., Abe, K., Onitsuka, G., Matsubara, T., Nakayama, N., et al. (2020). Vertical distribution of a harmful red-tide dinoflagellate, *Karenia mikimotoi*, at the decline stage of blooms. *J. Sea Res.* 165, 101960. doi:10.1016/j.seares.2020.101960

Shikata, T., Matsunaga, S., Iseki, M., Nishide, H., Higashi, S. I., Kamei, Y., et al. (2013). Blue light regulates the rhythm of diurnal vertical migration in the raphidophyte red-tide alga *Chattonella antiqua*. *J. Plankton Res.* 35, 542–552. doi:10.1093/plankt/fbt006

Shikata, T., Matsunaga, S., Kuwahara, Y., Iwahori, S., and Nishiyama, Y. (2016). Light spectrum regulates cell accumulation during daytime in the raphidophyte *Chattonella antiqua* causing noxious red tides. *J. Photochem. Photobiol. B Biol.* 160, 128–133. doi:10.1016/j.jphotobiol.2016.03.046

Shikata, T., Matsunaga, S., Nishide, H., Sakamoto, S., Onistuka, G., and Yamaguchi, M. (2015). Diurnal vertical migration rhythms and their photoresponse in four phytoflagellates causing harmful algal blooms. *Limnol. Oceanogr.* 60, 1251–1264. doi:10.1002/lno.10095

Shikata, T., Sakamoto, S., Onitsuka, G., Aoki, K., and Yamaguichi, M. (2014). Effects of salinity on diel vertical migration behavior in two red-tide algae, *Chattonella antiqua* and *Karenia mikimotoi*. *Plankton Benthos Res.* 9, 42–50. doi:10.3800/pbr.9.42

Shikata, T., Sakurada, K., Jomoto, Y., Oyama, N., Onji, M., Yoshida, M., et al. (2011). Growth dynamics of *Chattonella antiqua* in relation to nutrients in the Yatsushiro Sea. *Nippon. Suisan Gakk* 77, 40–52. doi:10.2331/suisan.77.40

Shikata, T., Yuasa, K., Kitatsuji, S., Sakamoto, S., Akita, K., Fujinami, Y., et al. (2021). Superoxide production by the red tide-producing *Chattonella marina* complex (Raphidophyceae) correlates with toxicity to aquacultured fishes. *Antioxidants* 10, 1635. doi:10.3390/antiox10101635

Smayda, T. J. (1997). Harmful algal blooms: Their ecophysiology and general relevance to phytoplankton blooms in the sea. *Limnol. Oceanogr.* 42, 1137–1153. doi:10.4319/lo.1997.42.5_part_2.1137

Wada, M., Takano, Y., Nagae, S., Ohtake, Y., Umezawa, Y., Nakamura, S., et al. (2018). Temporal dynamics of dissolved organic carbon (DOC) produced in a microcosm with red tide forming algae *Chattonella marina* and its associated bacteria. *J. Oceanogr.* 74, 587–592. doi:10.1507/endocrj.EJ17-0426

Waite, A. M., and Lindahl, O. (2006). Bloom and decline of the toxic flagellate *Chattonella marina* in a Swedish fjord. *Mar. Ecol. Prog. Ser.* 326, 77–83. doi:10.3354/meps326077

Watanabe, M., Kohata, K., Kimura, T., Takamatsu, T., Yamaguchi, S. I., and Ioriya, T. (1995). Generation of a *Chattonella antiqua* bloom by imposing a shallow nutricline in a mesocosm. *Limnol. Oceanogr.* 40, 1447–1460. doi:10.4319/lo.1995.40.8.1447

Yamaguchi, M., Imai, I., and Honjo, T. (1991). Effects of temperature, salinity and irradiance on the growth rates of the noxious red tide flagellates *Chattonella antiqua* and *C. marina* (Raphidophyceae). *Nippon. Suisan Gakk* 57, 1277–1284. doi:10.2331/suisan.57.1277

Yuasa, K., Shikata, T., Ichikawa, T., Tamura, Y., and Nishiyama, Y. (2020a). Nutrient deficiency stimulates the production of superoxide in the noxious red-tide-forming raphidophyte *Chattonella antiqua*. *Harmful Algae* 99, 101938. doi:10.1016/j.hal.2020.101938

Yuasa, K., Shikata, T., Kitatsuji, S., Yamasaki, Y., and Nishiyama, Y. (2020b). Extracellular secretion of superoxide is regulated by photosynthetic electron transport in the noxious red-tide-forming raphidophyte *Chattonella antiqua*. *J. Photochem. Photobiol. B Biol.* 205, 111839. doi:10.1016/j.jphotobiol.2020.111839

Yuasa, K., Shikata, T., Kuwahara, Y., and Nishiyama, Y. (2018). Adverse effects of strong light and nitrogen deficiency on cell viability, photosynthesis, and motility of the red-tide dinoflagellate *Karenia mikimotoi*. *Phycologia* 57, 525–533. doi:10.2216/17-61.1

frontiers | Frontiers in Cell and Developmental Biology

TYPE Original Research
PUBLISHED 13 April 2023
DOI 10.3389/fcell.2023.1123446

OPEN ACCESS

EDITED BY
Takuji Ishikawa,
Tohoku University, Japan

REVIEWED BY
On Shun Pak,
Santa Clara University, United States
William Uspal,
University of Hawaii at Manoa,
United States

*CORRESPONDENCE
Kenta Ishimoto,
ishimoto@kurims.kyoto-u.ac.jp

SPECIALTY SECTION
This article was submitted to Evolutionary Developmental Biology, a section of the journal Frontiers in Cell and Developmental Biology

RECEIVED 14 December 2022
ACCEPTED 15 March 2023
PUBLISHED 13 April 2023

CITATION
Ishimoto K, Gaffney EA and Smith DJ (2023), Squirmer hydrodynamics near a periodic surface topography. *Front. Cell Dev. Biol.* 11:1123446. doi: 10.3389/fcell.2023.1123446

Squirmer hydrodynamics near a periodic surface topography

Kenta Ishimoto[1]*, Eamonn A. Gaffney[2] and David J. Smith[3]

[1]Research Institute for Mathematical Sciences, Kyoto University, Kyoto, Japan, [2]Wolfson Centre for Mathematical Biology, Mathematical Institute, University of Oxford, Oxford, United Kingdom, [3]School of Mathematics, University of Birmingham, Birmingham, United Kingdom

The behaviour of microscopic swimmers has previously been explored near large-scale confining geometries and in the presence of very small-scale surface roughness. Here, we consider an intermediate case of how a simple microswimmer, the tangential spherical squirmer, behaves adjacent to singly and doubly periodic sinusoidal surface topographies that spatially oscillate with an amplitude that is an order of magnitude less than the swimmer size and wavelengths that are also within an order of magnitude of this scale. The nearest neighbour regularised Stokeslet method is used for numerical explorations after validating its accuracy for a spherical tangential squirmer that swims stably near a flat surface. The same squirmer is then introduced to different surface topographies. The key governing factor in the resulting swimming behaviour is the size of the squirmer relative to the surface topography wavelength. For instance, directional guidance is not observed when the squirmer is much larger, or much smaller, than the surface topography wavelength. In contrast, once the squirmer size is on the scale of the topography wavelength, limited guidance is possible, often with local capture in the topography troughs. However, complex dynamics can also emerge, especially when the initial configuration is not close to alignment along topography troughs or above topography crests. In contrast to sensitivity in alignment and topography wavelength, reductions in the amplitude of the surface topography or variations in the shape of the periodic surface topography do not have extensive impacts on the squirmer behaviour. Our findings more generally highlight that the numerical framework provides an essential basis to elucidate how swimmers may be guided by surface topography.

KEYWORDS

microswimming, low Reynolds number flow, cell motility, confinement, surface topography

1 Introduction

Ever since the studies of Robert Hooke and Antonie van Leeuwenhoek, it has been known that a drop of pond water contains countless microbes, many of which are motile, and indeed some can be lethal, such as *Naegleria fowleri*, the causative agent of amoebic meningitis. Even harmless motile microbes have attracted the attention of scientists for centuries, though more recently developments in nano- and micro-technology have also enabled fabrication of self-propelling artificial micro-robots and manipulation of their dynamics using microfluidic devices (Kherzi and Pumera, 2016). In laboratory experiments and observations, with both synthetic and biological swimmers, of the range of known control mechanisms, by far the most common is the influence of confining boundaries.

Nonetheless, the physical effects of walls on microswimmers can be subtle and have been extensively investigated theoretically, numerically, and experimentally in the past decade (Lauga and Powers, 2009; Elgeti et al., 2015). For instance, numerous biological microswimmers such as bacteria and sperm cells are known to accumulate near a flat wall boundary (Rothschild, 1963; Berke et al., 2008; Smith et al., 2009; Kantsler et al., 2013; Bianchi et al., 2017; Ohmura et al., 2018). Furthermore, motility near surfaces also has a functional role, for instance, biofilm formation and initial spread (Pratt and Kolter, 1998), as well as enhanced searching, which in turn is significant for fish egg fertilisation, where a sperm needs to enter the egg micropyle (Cosson et al., 2008). In addition, curved boundaries such as convex walls, corners, and obstacles are easily fabricated in microfluidic devices, which has motivated studies on the effects of such confinements both for biological microorganisms (Denissenko et al., 2012; Tung et al., 2014; Shum and Gaffney, 2015; Sipos et al., 2015; Ishimoto et al., 2016; Nosrati et al., 2016; Nishiguchi et al., 2018; Ostapenko et al., 2018; Rode et al., 2019; Yang et al., 2019) and artificial microswimmers (Takagi et al., 2014; Spagnolie et al., 2015; Liu et al., 2016; Yang et al., 2016; Wykes et al., 2017).

These curved boundaries and obstacles are typically larger than, or comparable to, the swimmer. If the structure on the wall boundary is smaller than the swimmer length scale, it may be considered a rough boundary instead of a completely flat surface. The impact of surface roughness has previously been considered *via* an asymptotically small amplitude of the surface topography in the presence of a spherical particle and a spherical microswimmer (Rad and Najafi, 2010; Assoudi et al., 2018), the so-called squirmer (Shaik and Ardekani, 2017).

The squirmer is a model microswimmer first proposed by Lighthill (1952) as a slightly deforming sphere and later corrected and used by Blake (1971) as a model of ciliate swimmers. This simple model is currently understood to provide qualitative predictions for a spherical biological microswimmer (Pedley, 2016; Pedley et al., 2016). In particular, a simplified version of the model, in which a rigid sphere can self-propel due to a given surface velocity slip profile, is known as the spherical tangential squirmer. This has been widely used as a simple mathematical model having a finite volume for studies on hydrodynamical aspects of microswimming such as nutrition uptake (Magar et al., 2003), cell–cell interactions (Ishikawa et al., 2006; Drescher et al., 2009), Janus particle motility (Spagnolie and Lauga, 2012; Ishimoto and Gaffney, 2013), collective dynamics (Evans et al., 2011; Zöttl and Stark, 2012; Delfau et al., 2016; Oyama et al., 2016), swimming in a non-Newtonian medium (Lauga, 2009; Zhu et al., 2012; Nganguia and Pak, 2018), and swimming near a wall (Llopis and Pagonabarraga, 2010; Spagnolie and Lauga, 2012; Ishimoto and Gaffney, 2013). The squirmer has also been studied in the context of confinement and obstacles such as the interior of a tube (Zhu et al., 2013), the presence of lattice-like multiple obstacles (Chamolly et al., 2017), or a curved and structured wall (Das and Cacciuto, 2019).

Investigations into the effects of small surface topography on microswimmers are, however, limited to the asymptotic analysis of rough surfaces or boundary features (Kurzthaler and Stone, 2021) such as curvatures with length scales that are much larger than those of the swimmer. The current study, therefore, aimed to bridge the gap between an asymptotically small amplitude of the surface roughness and large length scale curved boundaries. For periodic structures at this mesoscale, in particular, there is the prospect that the microswimmer may become oriented and guided by the surface, and we will numerically investigate the dynamics of a spherical tangential squirmer under these conditions. Such investigations are particularly motivated by recent studies of a colloidal microswimmer near a small surface topography (Simmchen et al., 2016), highlighting that a structured surface topography may be fabricated in a microfluidic device with the potential for utilisation in guiding microswimmers.

The very near-wall dynamics, at a separation of around 50 nm and less (Klein et al., 2003), typically depends on both hydrodynamic and steric interactions (Klein et al., 2003; Kantsler et al., 2013; Bianchi et al., 2017), and a short-range repulsive potential force is often utilised by modelling studies to ensure that simulated cells do not penetrate the walls (Spagnolie and Lauga, 2012). However, even a small difference in the repulsion function can alter swimmer behaviour (Lintuvuori et al., 2016; Ishimoto, 2017). Thus, in this initial study, we only focus on the hydrodynamic interactions and do not consider any additional steric interactions, contact mechanics, and charge effects.

This is motivated not only by the utility of the relative simplicity in this initial study but also for understanding the impact of hydrodynamic surface interactions where, despite these non-hydrodynamic forces, swimmer deposition is undesirable and thus of minimal interest, compared to topography guidance dynamics when deposition does not occur. It also entails that the results and conclusions of this study are not contingent on the details of contact mechanics and steric forces, which vary with surfaces and solutes (Klein et al., 2003). Thus, the numerical simulations are stopped just before the squirmer dynamics is influenced by the short-range dynamics on a very close surface approach. This short-range detail may be accommodated in later work together with many further refinements, such as incorporating more faithful representations of flagellated and ciliated swimmers (Ohmura et al., 2018; Ohmura et al., 2021).

The structure of this paper is as follows: Section 2 introduces the squirmer model and three different surface topographies. Section 3 discusses the numerical methods and their verifications. Section 4 presents the simulation results for the different surface topographies, followed by a discussion of the implications, in particular for microswimmer guidance *via* surface topography, in Section 5.

2 The squirmer

We consider the non-dimensional Stokes equations of the low Reynolds number flow, from which it follows for a velocity field $\boldsymbol{u}$ and a pressure field p that

$$\nabla p = \Delta \boldsymbol{u} \quad \text{and} \quad \nabla \cdot \boldsymbol{u} = 0. \tag{1}$$

We impose the no-slip boundary condition on the swimmer and the wall, together with the force and torque balance equations for a swimmer with negligible inertia.

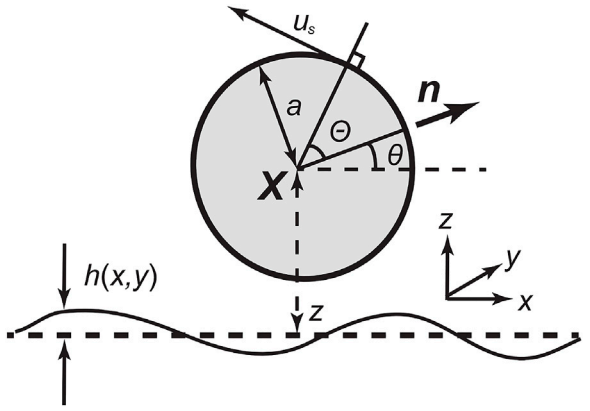

FIGURE 1
Schematic diagram of a spherical tangential squirmer, of radius $a = 1$, near a no-slip wall. Here, **X** denotes the centre of the spherical swimmer relative to a laboratory reference frame, with Cartesian coordinates (x, y, z) and $h(x, y)$ is the height of the surface above its average midplane (dashed) at $z = 0$. Furthermore, z is overloaded and also represents the height of the swimmer centre above the midplane, with an analogous overloading of x, y. Whether x, y, z refer to coordinates or the overloaded definition $\boldsymbol{X} = (x, y, z)$ for the location of the squirmer centre will be clear from context. The unit vector $\boldsymbol{n}$ gives the orientation of the swimmer, which makes an angle θ relative to the mid-plane of the surface topography, and Θ is the local polar angle of a point on the swimmer' surface relative to $\boldsymbol{n}$. The swimmer's motility is driven by an axisymmetric tangential velocity of its surface, of size u_s, and in the direction of increasing Θ, as detailed in the main text.

We first introduce the spherical tangential squirmer model. The no-slip boundary is imposed on a spherical swimmer of dimensionless radius $a = 1$, possessing an axisymmetric and tangential surface velocity (Ishikawa et al., 2006). The sphere centre is located at $\boldsymbol{X} = (x, y, z)$, and $\boldsymbol{n}$ denotes the unit vector of its orientation, as shown schematically in Figure 1, where coordinates, variables for the position of the squirmer centre, and the angles θ, Θ are defined using a diagram. Here, θ is the angle made by the swimming direction and the xy plane. In particular, $\Theta \in [0, \pi]$ denotes the polar angle relative to $\boldsymbol{n}$, and we impose an axisymmetric tangential velocity slip u_s on the squirmer, given by

$$u_s(\Theta) = \sum_{n=1}^{\infty} B_n V_n(\cos\Theta), \tag{2}$$

where V_n is a function derived from the Legendre polynomial $P_n(x)$ *via*

$$V_n(x) = \frac{2\sqrt{1-x^2}}{n(n+1)} \frac{dP_n(x)}{dx}. \tag{3}$$

The swimming velocity in free space is dictated by the first mode, with $\boldsymbol{U} = (2/3)B_1\boldsymbol{n}$ (Lighthill, 1952; Blake, 1971). We fix $B_1 = 3/2$ so that the squirmer swimming speed is set to be unity in free space, and we neglect the higher modes by setting $B_n = 0$ for $n \geq 3$ so that the swimmer is subsequently fully characterised by the squirmer parameter $\beta = B_2/B_1$ (Ishikawa et al., 2006). In particular, and following convention, the swimmer is denoted as a pusher when $\beta < 0$, a puller when $\beta > 0$, and a neutral swimmer when $\beta = 0$ (Evans et al., 2011). The second mode, associated with the parameter B_2, corresponds to the flow induced by the Stokes dipole. In particular, a cell with a trailing flagellum, such as an *E. coli* bacterium or a sperm cell, behaves as a pusher; cells with leading flagella, such as *Chlamydomonas* and *Leishmania* (Walker et al., 2019), are modelled as pullers; and cells possessing fore–aft symmetry, such as ciliates, behave as neutral swimmers (Evans et al., 2011).

Here, we focus on spherical tangential squirmers that swim stably near a flat surface. Thus, we consider puller squirmers with $\beta \gtrsim 5$, which are known to exhibit stable swimming near a flat surface (Ishimoto and Gaffney, 2013; Uspal et al., 2015). In particular, we examine their dynamics close to surfaces with structured topographies. The first of these topographies is a one-dimensional sinusoid defined by

$$h(x, y) = A\sin(kx), \tag{4}$$

where A is the amplitude and $k = 2\pi/\lambda$ is the wavenumber, with λ denoting the wavelength (Figure 2A). The second topography is given by the doubly periodic sinusoid.

$$h(x, y) = A\sin(kx)\sin(ky), \tag{5}$$

as depicted in Figure 2B, and the third is given by

$$h(x, y) = A[2\sin^2(kx)\sin^2(ky) - 1]. \tag{6}$$

This final topography is shown in Figure 2C and presents doubly periodic peaks with highest and lowest heights of $+A$ and $-A$, respectively, as in the previous two topographies. However, notably, the inter-peak wavelength is now halved, and the parameter $\lambda = 2\pi/k$ no longer represents the wavelength since the sinusoidal functions are squared in Eq. 6. Throughout this study of the doubly periodic topographies, we focus on cases that are symmetrical in switching the x and y-directions.

We consider both the surface of the squirmer and the wall surface topography denoted by S and W, respectively, with the boundary conditions of the Stokes equations given by no-slip conditions on both boundaries. The surface velocity of the squirmer, denoted $\boldsymbol{v}(\boldsymbol{x})$, can be described by combining the squirmer linear velocity $\boldsymbol{U}$ and angular velocity $\boldsymbol{\Omega}$, together with its tangential surface velocity, $\boldsymbol{u}_s$, of size given by Eq. 2 and in the axisymmetric tangential direction, as depicted in Figure 1. Hence, the no-slip condition entails the fluid velocity on the surface of the swimmer is given by

$$\boldsymbol{v}(\boldsymbol{x}) = \boldsymbol{U} + \boldsymbol{\Omega} \times (\boldsymbol{x} - \boldsymbol{X}) + \boldsymbol{u}_s(\boldsymbol{x}), \quad (\boldsymbol{x} \in S). \tag{7}$$

In contrast, the wall surface topography is assumed to be stationary, and we thus have

$$\boldsymbol{u}(\boldsymbol{x}) = \boldsymbol{0} \quad (\boldsymbol{x} \in W). \tag{8}$$

3 Numerical methods

3.1 Nearest-neighbour regularised Stokeslet method

The dynamics of the squirmer has been computed using the nearest-neighbour regularised Stokeslet method (nnRSM)

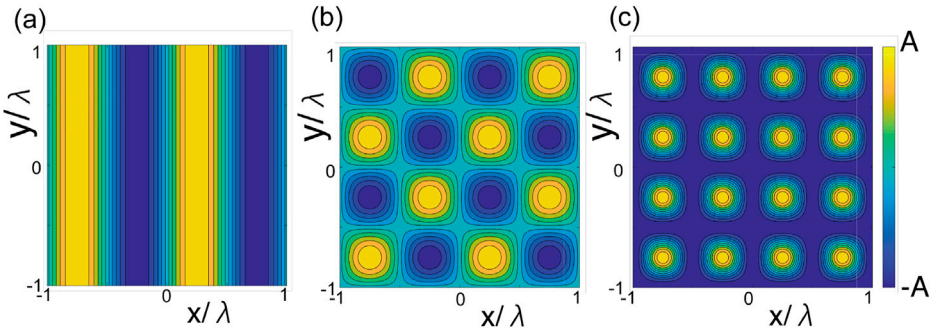

FIGURE 2
Illustrations of the surface topography functions $h(x, y)$ considered in this study. **(A)** Singly periodic sinusoidal wave topography, **(B)** doubly−periodic sinusoidal wave, and **(C)** doubly−periodic peaks, respectively, associated with Eqs 4–6. The maximum and minimum heights, $h(x, y)$, are $+A$ and $-A$ for all topographies.

(Gallagher and Smith, 2018; Smith, 2018), and the numerical simulations have been performed based on the MATLAB code accompanied by Gallagher and Smith (2018), as we now summarise. The Stokes flow boundary integral equations for the single-layer formulation are given by (Pozrikidis, 1992)

$$u_j(\boldsymbol{x}) = -\frac{1}{8\pi}\int_{S\cup W} S_{ij}(\boldsymbol{x},\boldsymbol{y}) f_i(\boldsymbol{y})\, dS_y. \tag{9}$$

Here, $f_i(\boldsymbol{y})$ denotes the components of the surface traction and the integral kernel S_{ij} is the Stokeslet, which exhibits an integrable singularity as $\boldsymbol{y} \to \boldsymbol{x}$, with the surface integral well-defined. For numerical tractability, Cortez introduced a regularised Stokeslet (Cortez, 2001), which is the exact divergence-free solution to the Stokes flow equations with a spatially smoothed point force, and then approximated the boundary integral (Cortez et al., 2005) *via*

$$u_j(\boldsymbol{x}) = -\frac{1}{8\pi}\int_{S\cup W} S^{\epsilon}_{ij}(\boldsymbol{x},\boldsymbol{y}) f_i(\boldsymbol{y})\, dS_y, \tag{10}$$

where S^{ϵ}_{ij} is the regularised Stokeslet and ϵ is the regularisation parameter. As the error in this approximation is $O(\epsilon)$, we recover the singular boundary integral once we take the limit of $\epsilon \to 0$. Following Cortez et al. (2005), we consider a regularised Stokeslet of the form,

$$S^{\epsilon}_{ij}(\boldsymbol{x},\boldsymbol{y}) = \left\{(r^2+2\epsilon^2)\delta_{ij} + r_i r_j\right\}\left(r^2+\epsilon^2\right)^{-3/2}, \tag{11}$$

where $\boldsymbol{r} = \boldsymbol{x} - \boldsymbol{y}$, $r = |\boldsymbol{r}|$, and δ_{ij} represent Kronecker's delta. The no-slip boundary conditions are simply given by enforcing $\boldsymbol{u}(\boldsymbol{x}) = \boldsymbol{v}(\boldsymbol{x})$ from Eqs. 7, 8 for boundary points in the integral Eq. 10. Since the squirmer is swimming freely, we also have the inertialess force and torque balance equations.

$$\int_S \boldsymbol{f}(\boldsymbol{x})\, dS_x = \boldsymbol{0}\,, \quad \int_S (\boldsymbol{x}-\boldsymbol{X})\times \boldsymbol{f}(\boldsymbol{x})\, dS_x = \boldsymbol{0}. \tag{12}$$

We then discretise the surface integrals (10), (12), by introducing the quadrature node positions $\boldsymbol{x}[n]$ and the associated weights $A[n]$ for the discretised surface point n (n = 1, . . ., N), where N is the total number of surface points. The aforementioned surface integrals contain the product of '$\boldsymbol{f}\, dS$' and we discretise the integral (Gallagher and Smith, 2018; Smith, 2018) *via*

$$\int \bullet\, f_j(\boldsymbol{x})\, dS_x \approx \sum_{n=1}^{N} \bullet\, g_j[n] A[n], \tag{13}$$

where the symbol, •, on the right-hand side, represents an arbitrary function of $\boldsymbol{x}$, evaluated at $\boldsymbol{x}[n]$, and $g_j[n] = f_j(\boldsymbol{x}[n])$.

Continuing with the framework of Smith (2018), we introduce a second surface discretisation, $\boldsymbol{x}[q]$, (q = 1, . . ., Q) which corresponds to a more refined discretisation than used for the surface traction, with $N \ll Q$, as illustrated in Figure 3. The regularisation error is $O(\epsilon)$, and this motivates taking relatively small values of ϵ in computations. The two discretisations enable an efficient numerical solution as the kernel, S^{ϵ}_{ij}, which can vary rapidly, and thus requires a finer discretisation, which would be inefficient if used for the surface traction, $\boldsymbol{f}$. In particular, the size of the dense linear system depends only on N, not Q. Thus, the cost of assembling the system is defined by $O(NQ)$, whereas the cost of the direct solver is defined by $O(N^3)$. Moreover, if the force and quadrature discretisations do not overlap, the quadrature error no longer diverges as $\epsilon \to 0$, and hence a less refined force discretisation in this framework is in general more accurate than if the two discretisations coincide (Gallagher et al., 2019).

The nearest-neighbour matrix, $\nu[q, n]$, is then defined separately for a swimmer and a wall as

$$\begin{cases} 1 & \text{if } n = \arg\min |\boldsymbol{x}[\hat{n}] - \boldsymbol{x}[q]| \ \ (\boldsymbol{x}[\hat{n}], \boldsymbol{x}[q] \in S) \\ 1 & \text{if } \ n = \arg\min |\boldsymbol{x}[\hat{n}] - \boldsymbol{x}[q]| \ \ (\boldsymbol{x}[\hat{n}], \boldsymbol{x}[q] \in W) \\ 0 & \text{otherwise,} \end{cases} \tag{14}$$

where arg min is the argument at which the minimum is attained over the set $\hat{n} \in \{1, \ldots, N\}$, and we use this matrix to interpolate the discretisation *via*

$$f_j(\boldsymbol{x}[q]) dS(\boldsymbol{x}[q]) \approx \sum_{n=1}^{N} \nu[q,n] g_i[n] A[n]. \tag{15}$$

Combining Eqs 13, 15 and noting the total number of the points for the finer discretisation Q, we have

$$\int \bullet(\boldsymbol{x})\, f_j(\boldsymbol{x})\, dS_x \approx \sum_{n=1}^{N} g_j[n] A[n] \sum_{q=1}^{Q} \bullet(\boldsymbol{x}[q])\, \nu[q,n]. \tag{16}$$

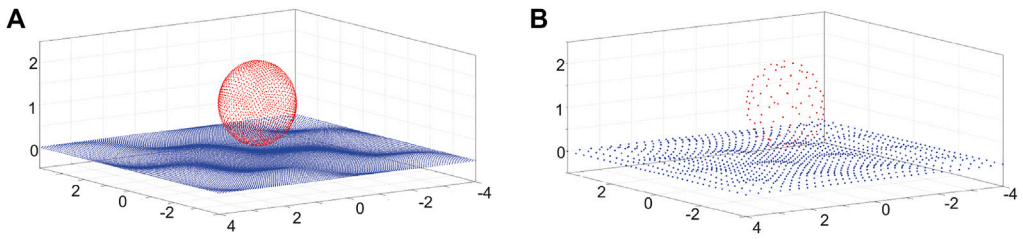

FIGURE 3
Illustration of the points representing the squirmer and surface topography, with the finer discretisation **(A)** used for the kernel and the coarser discretisation **(B)**, used for the surface traction. Discretisation points on the spherical squirmer surface are indicated by red dots. In contrast, blue discretisation points are shown for the doubly periodic surface topography of Figure 2B, with the size of the discretised surface given by $L = 8$ and the surface topography given by Eq. 5, as plotted in Figure 2B, with an amplitude of $A = 0.1$ and the wavelength given by $\lambda = 2$. Note that we here display the wall meshes after rescaling by the method described at the end of Section 3.

We use $\bullet(\boldsymbol{x}) = S^{\epsilon}_{ij}(\boldsymbol{x}', \boldsymbol{x})$ in Eq. 16 to discretise the boundary integral (10), and we use $\bullet(\boldsymbol{x}) = 1$ and $\bullet(\boldsymbol{x}) = \epsilon_{ijk}(x_k - X_k)$ in Eq. 13 for the force and torque balance relations (12), respectively.

In particular, to solve the squirmer trajectory, we first need to determine its velocity, $\boldsymbol{U}$, and angular velocity, $\boldsymbol{\Omega}$, which can then be integrated over time to determine the squirmer location and orientation. First, it should be noted that at a fixed point in time, the squirmer location and orientation are obtained from previous integration or from the initial conditions at the start of the simulation. Then, the discretisations of Eqs 10, 12, with $\boldsymbol{u} = \boldsymbol{v}$ eliminated in terms of $\boldsymbol{U}$, $\boldsymbol{\Omega}$, and the known $\boldsymbol{u}_s$ *via* Eqs. 2, 3, 7, 8, give $3N + 6$ constraints for the $3N + 6$ scalar unknowns associated with the unknown surface tractions at the N discretisation points and the unknowns $\boldsymbol{U}$, $\boldsymbol{\Omega}$. The resulting linear system is readily solved, provided that collocation points are unique, and we have a non-singular dense linear system that can be solved directly *via* standard methods.

As is the case for both singular and regularised versions of the boundary integral representation for flow around a constant volume body, the integral equation admits a gauge freedom $\boldsymbol{f} \to \boldsymbol{f} + \alpha\boldsymbol{m}$, where α is any constant and $\boldsymbol{m}$ is the surface normal pointing into the fluid (this can be observed by applying incompressibility and the divergence theorem to deduce that $\int_S S_{ij} m_i dS = 0$). In the absence of boundary conditions for traction, this freedom results in the pressure being determined only up to an additive constant in the exact problem. Discretisation results in an invertible matrix, and hence a unique (approximate) solution, because the discretised integral is no longer evaluated precisely to 0; moreover, the non-uniqueness of the continuum solution for the pressure is not dynamically important as it does not affect either the total force or moment on the swimmer.

3.2 Swimming in a free space

We first examine the numerical accuracy of the swimming velocity calculation for the squirmer in *free space*. The squirmer parameter is set to $\beta = 0$, and the exact swimming speed is $|\boldsymbol{U}| = 1$, as detailed in the previous section. We have fixed the regularisation parameter $\epsilon = 0.001$ and examined the impact of changing the discretisation refinement. In particular, with the total number of the points that form the squirmer surface given by $N = 6n_s^2$ and $Q = 6N_s^2$ for each discretisation (Gallagher and Smith, 2018; Smith, 2018), changes in both n_s and N_s have been examined. The results of Table 1 establish numerical parameters sufficient to obtain our desired relative error of around 1%. Finally, we also note that changes in β have not been observed to alter the swimming speed, as expected.

TABLE 1 Predictions for the free space swimmer speed. The exact speed is given by $|U| = 1$ and its numerical calculation is presented for refinements of both the discretisations used in the nearest–neighbour regularised Stokeslet method, where $N = 6n_s^2$ and $Q = 6N_s^2$.

ϵ	n_s	N_s	$\lvert U\rvert$
0.001	4	10	1.0135
0.001	4	12	1.0017
0.001	4	14	1.0073
0.001	4	16	1.0153
0.001	4	18	1.0048
0.001	5	10	1.0291
0.001	5	12	1.0079
0.001	5	14	1.0098
0.001	5	16	1.0113

3.3 Swimming near a wall

Hereafter, we set the squirmer discretisation parameters to be $(n_s, N_s) = (4, 18)$ and consider the squirmer near a no-slip wall. As previously studied by the boundary element method (Ishimoto and Gaffney, 2013), a strong puller tends to stably swim near a *flat* wall. We, therefore, choose $\beta = 7$ and set the initial location of the squirmer centre to be (0,0,1.15), with the initial orientation given by $\theta = -0.17\pi$, which is effectively the initial angle of attack relative to the mid-plane of the surface topography, as can be seen from Figure 1.

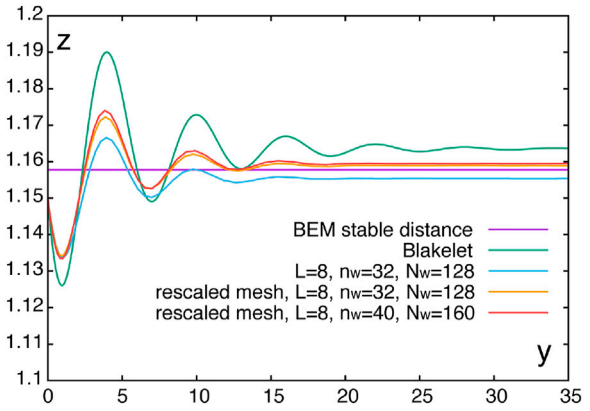

FIGURE 4
Swimming trajectories of the squirmer with a regularisation of ϵ = 0.001 and different discretisation parameters. Also plotted is the height of the stable fixed point obtained by the boundary element method using the singular Blakelet (Ishimoto and Gaffney, 2013), as labelled "BEM stable distance," and a trajectory using a regularised Blakelet with the nearest-neighbour regularised Stokeslet method, as labelled by "Blakelet."

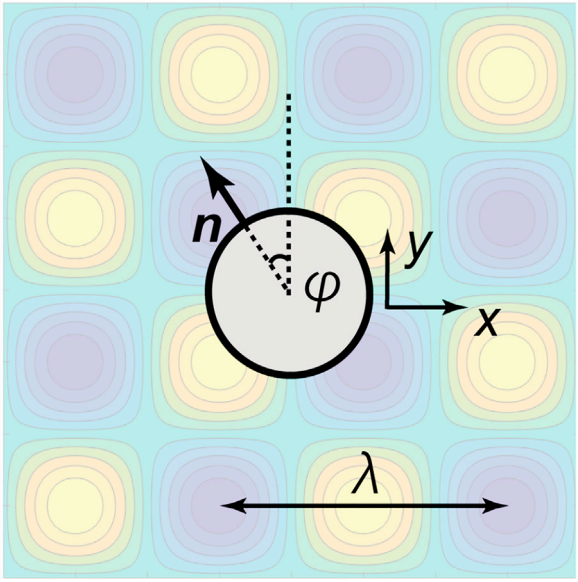

FIGURE 5
Bird's eye view of the squirmer above the doubly periodic surface topography of Eq. 5, as depicted in Figure 2B, with $\lambda = 4$. The angle φ is defined to be the angle of the x–y projection of the squirmer orientation vector $\boldsymbol{n}$ from the y-axis, as illustrated, and thus gives the direction of the squirmer in the x-y plane.

We first use the regularised Blakelet (Ainley et al., 2008) in the nearest-neighbour regularised Stokeslet method and compare the simulation result with the stable distance obtained *via* the boundary element method using the singular Blakelet (Ishimoto and Gaffney, 2013), with the latter providing the stable separation distance $z^* \approx 1.1578$. As shown in Figure 4, these predictions of these two algorithms are in reasonable agreement.

We then consider a wall that is captured by an explicit discretisation of its surface rather than by use of the Blakelet, as implemented in the sperm simulation of Gallagher and Smith (2018). The wall is given by the x-y plane and represented by the square with a length of L, with its centre at the location of the projection of the squirmer centre, $\boldsymbol{X}$, onto the plane $z = 0$. Each side contains n_w and N_w points with equal separations for surface traction and kernel discretisations, respectively (Gallagher and Smith, 2018; Smith, 2018). Hence, the number of points on the surface $S \cup W$ are given by $N = 6n_s^2 + n_w^2$ and $Q = 6N_s^2 + N_w^2$ for the surface traction and kernel discretisations, respectively. An example of a swimming trajectory is plotted in Figure 4.

We then rescale the wall points to resolve the squirmer–boundary hydrodynamic interaction more efficiently by using the function

$$f\colon [-1/2, 1/2] \to [-1/2, 1/2], \qquad f(x) = \frac{1}{2}\tan\left(\frac{\pi x}{2}\right). \tag{17}$$

The equally discretised square of unit length

$$\mathcal{S} = \{(x, y) \in [-1/2, 1/2] \times [-1/2, 1/2]\} \tag{18}$$

is mapped by this function, *via*

$$\{(f(x), f(y)); (x, y) \in \mathcal{S}\}, \tag{19}$$

and then dilated by the scale of L. The square obtained by this scheme more precisely represents the hydrodynamical interactions between the squirmer and the wall, as seen from the results labelled "rescaled" in Figure 4, which use this mapping. These trajectories in particular are sufficiently accurate for our purposes and very close to the prediction of the boundary element method (BEM) of the stable swimming height above the surface, which is exact to within discretisation error.

4 Results

In this section, we discuss the swimming trajectories of the squirmer near a surface with a structured periodic topography, as defined in Eqs. 4–6 and depicted in Figure 2. For all simulations presented, the initial height of the squirmer was fixed at $z = 1.2$, with the initial angle of attack given by $\theta = -0.17\pi$. Furthermore, initial squirmer centre location coordinates of $x = 0$, $y = 0$, are set together with squirmer parameters of $B_1 = 3/2$, $\beta = 7$, and a surface topography amplitude of $A = 0.1$, unless explicitly stated otherwise. Although the dynamics can change depending on the parameters and initial settings, we fix these variables to consider the stable behaviour and its modulation by surface topography, focussing on the impact of the initial orientation and topographic patterns. The surface topography wavelength and the initial orientation of the squirmer in the x–y plane, namely, φ in Figure 5, are thus varied extensively among the simulations and either stated or, in the case of φ, can otherwise be immediately inferred from the initial tangent angles of the trajectories in the presented plots.

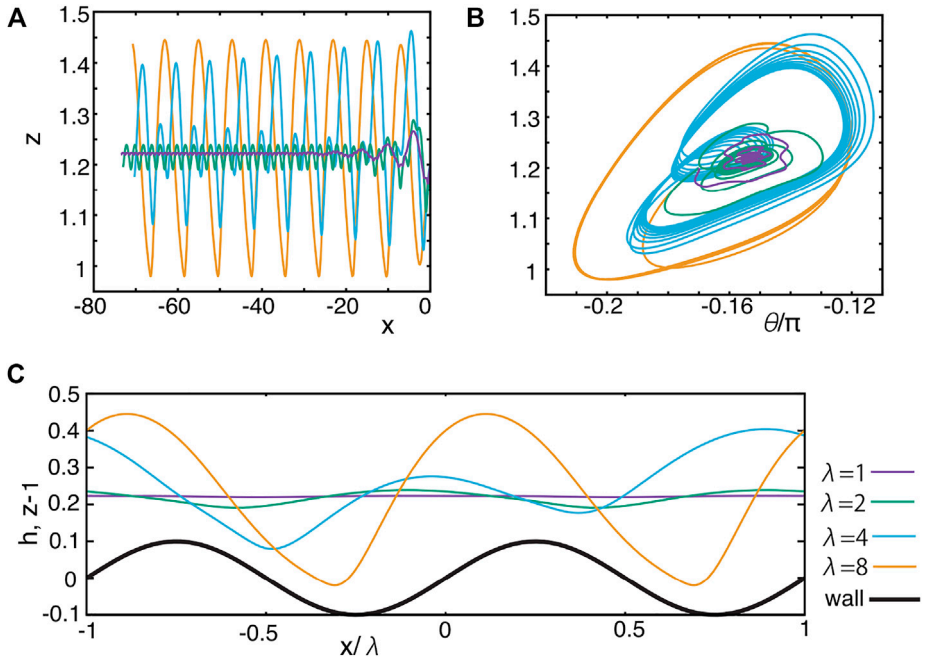

FIGURE 6
Dynamics of the squirmer swimming adjacent to the singly periodic sinusoidal topography of Eq. 4 and Figure 2A, with different wavelengths λ = 1, 2, 4, 8. The wave amplitude of the topography is fixed at A = 0.1. **(A)** Trajectories in the x–z plane. **(B)** Trajectories in the θ–z phase plane. **(C)** Horizontally rescaled and shifted z position for the last part of the simulation **(A)**, together with the topography function h.

4.1 Singly periodic sinusoidal topography

We start with the single-wave sinusoid topography given in Eq. 4 and Figure 2A. The initial location of the squirmer and the initial angle of attack are fixed at the simulation default initial values of $\boldsymbol{X}$ = (0, 0, 1.2) and $\theta = -0.17\pi$, as stated previously, while the initial orientation of the squirmer in the x–y plane has been initially considered in detail with $\varphi = 0.5\pi$ and then subsequently varied.

Thus, we first consider a squirmer swimming parallel to the wave vector of the sinusoidal topography or equivalently along the x-axis. Fixing the initial orientation relative to the x–y plane *via* $\varphi = 0.5\pi$, swimming trajectories in the x–z plane are plotted in Figure 6A for different surface topography wavelengths λ = 1, 2, 4, 8. Corresponding trajectories in the θ-z phase plane are shown in Figure 6B. When the wavenumber λ is smaller (λ = 1, 2), the squirmer attains stable oscillatory swimming, but the oscillation in the z-axis is smaller than the surface topography amplitude, A = 0.1, highlighting that the topography only perturbs the stable position associated with swimming near a flat wall. This may be observed in Figure 6C, where the z-dynamics for the last part of the oscillating motion obtained in Figure 6A are shown relative to a horizontally rescaled and shifted axis x/λ together with the surface topography function h. However, as the wavelength is increased to $\lambda = 4$, $\lambda = 8$, the oscillatory motion then transitions to an amplitude that is larger than that of the surface topography, as can be seen in Figure 6C. In addition, one can observe that, with λ = 4, the wavelength of the z-component oscillations in the trajectory need not match that of the underlying surface topography, though in contrast, these two wavelengths do match for the trajectories with λ = 2 and λ = 8. Although the problem converges to the locally flat wall case in the large wavelength limit, the locally flat approximation does not hold for the range of λ we have examined, as may be inferred from the oscillatory motion in Figure 6C.

We then consider the squirmer dynamics with different initial values of φ, and thus different initial orientations relative to the x–y plane, while once again varying the wavelength of the singly periodic topography. Figure 7 shows the predicted trajectories and the orientations for the case with the surface topography amplitude A = 0.1 and wavelength λ = 1, 2, 4, 8, while considering various values of φ, from 0 to 0.5π. From the figure, one can observe that the squirmer tends to swim either parallel or perpendicular to the direction of the well, which is aligned along the y-axis, though the orientation angle φ need not always necessarily match the direction of motion. For instance, some trajectories in Figure 7 follow the topographical crest by swimming in the direction of the positive y-axis, with the orientation angle, φ, remaining very close to the initial value rather than aligning with the y-axis, even after a long time. Also, some further trajectories are attracted towards the negative x-axis, without the orientation angle φ evolving to reflect this change in swimming direction. Hence, overall drifting, that is, a misalignment between the swimming direction and swimmer orientation, can be induced by the squirmer–topography hydrodynamic interaction.

Notably, the swimming dynamics associated with an initial orientation angle of $\varphi \approx 0.05$ with λ = 1, or $\varphi \approx 0.15$ with λ = 2, is unstable, and the trajectories evolve towards the stable orientations of φ = 0, as seen in Figures 7A, B. Here, the stable swimming along the y-axis is accompanied by hydrodynamic

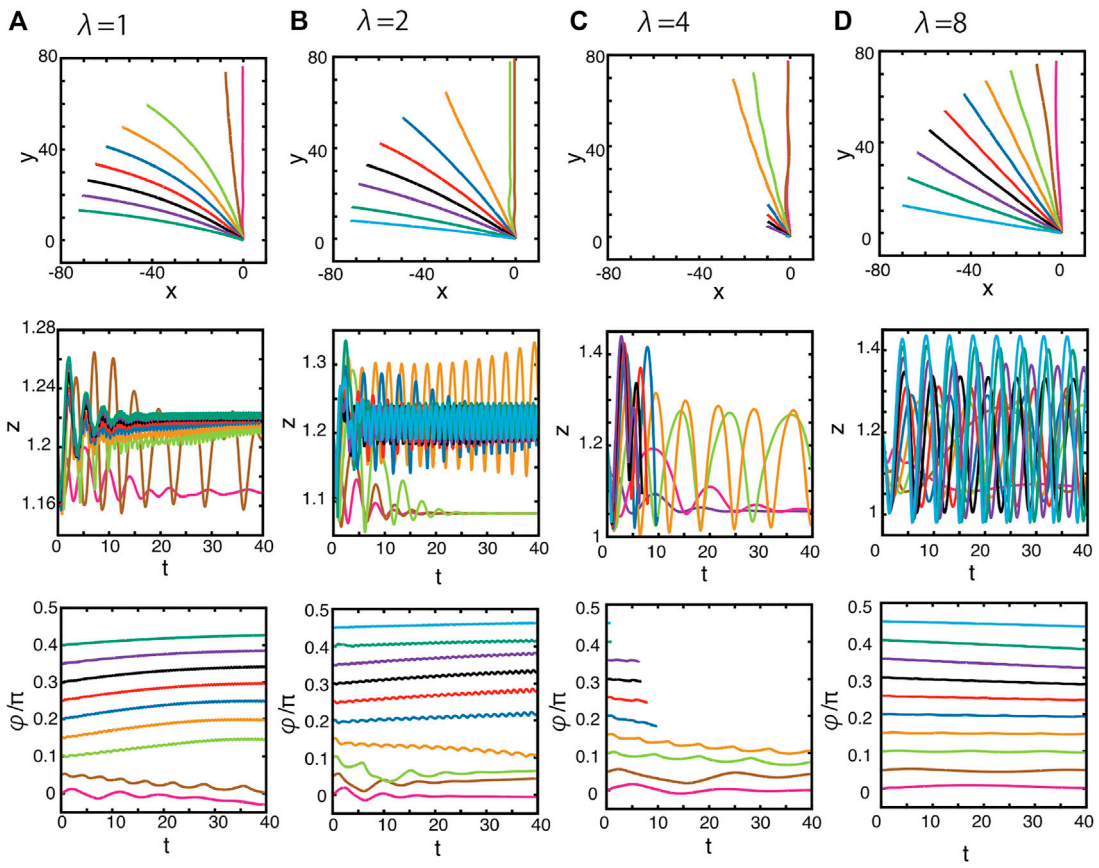

FIGURE 7
Dynamics of the squirmer near a surface with the singly periodic sinusoidal wave topography of Eq. 4 and Figure 2A. The surface topography amplitude is given by $A = 0.1$, and the wavelength is **(A)** $\lambda = 1$, **(B)** $\lambda = 2$, and **(C)** $\lambda = 4$, **(D)** $\lambda = 8$. (Top panels) the projections of the squirmer trajectories onto the x–y plane with different initial orientation angles, φ, as defined *via* Figure 5. These initial angles may be inferred from the initial tangents of the plotted projected trajectories. (Middle panels) the time evolution of the height of the centre of the squirmer, z. (Bottom panels) the time evolution of the orientation angle φ. Different colours index different initial values of the orientation angle, φ.

capturing, with the squirmer moving along a trough of the surface topography. Furthermore, in both cases, the z-dynamics attains a stable oscillatory motion, as may be observed in Figures 6A, B. In both cases, the qualitative aspects of these features are unaltered when the amplitude A is decreased, though the timescale for the reorientation along one of the axes becomes longer.

Analogously, an increase in the topography wavelength to the intermediate value of $\lambda = 4$ entails that swimming oblique to the troughs and peaks of topography can be observed, as seen in Figure 7C. However, at this wavelength, the squirmer concomitantly undergoes extensive oscillations in the z-direction. Furthermore, the squirmer enters the near vicinity of the surface (Figure 7C) once it is no longer oriented approximately along the y-axis. This requires a consideration of surface mechanics to proceed. More precisely, in practical applications, surface mechanics would become relevant and would need to be added to the model. This is outside the detailed scope of the study and, hence, we stop the numerical simulation, thus also avoiding the numerically unreasonable spatial resolutions required for the associated fine-scale hydrodynamics.

We further increase the wavelength of the sinusoidal topography to $\lambda = 8$, with trajectories presented in Figure 7D, which on projection to the x–y plane, are essentially straight, regardless of the initial orientation angle φ. Hence, at larger wavelengths, the squirmer swims with a direction that is unaffected by the surface. Furthermore, the z-dynamics of the squirmer trajectory become more oscillatory as the topography wavelength increases, as observed previously in Figure 6, unless the squirmer is captured in the trough along the y-axis, in which case the z-dynamics converges to a stable position.

More generally, all of these observations highlight that even with a surface topography amplitude of $A = 0.1$, which barely visible, as highlighted by Figure 3, the squirmer's behaviour is affected by the structured surface topography in a complex manner. In particular, the resulting trajectories are contingent on the details of the topography parameters and the squirmer orientation, especially once the topography wavelength is comparable to the squirmer size.

4.2 Doubly periodic sinusoidal topography

We now consider the squirmer dynamics near a surface with the doubly periodic wave topography, given by Eq. 5 and illustrated in Figure 2B. In the current setting, the topography breaks the

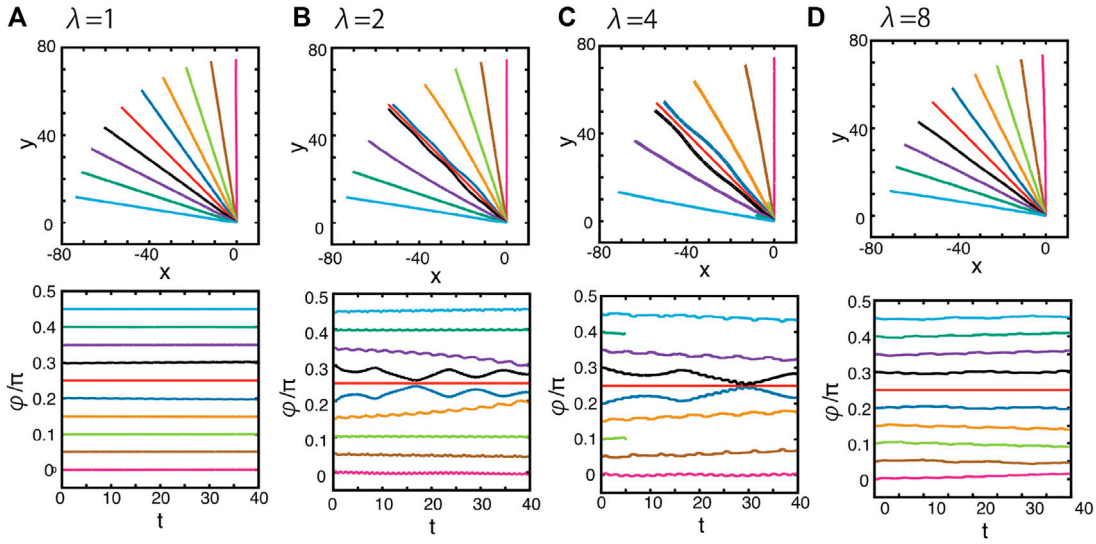

FIGURE 8
Dynamics of the squirmer near a surface with the doubly periodic sinusoidal wave topography of Eq. 5, as depicted in Figure 2B. The surface topography amplitude is given by $A = 0.1$, and the wavelength is **(A)** $\lambda = 1$, **(B)** $\lambda = 2$, **(C)** $\lambda = 4$, **(D)** $\lambda = 8$. (Top panels) the projections of the squirmer trajectories onto the x–y plane with different initial orientation angles, φ, as defined *via* Figure 5. These initial angles may be inferred from the initial tangents of the plotted projected trajectories. (Bottom panels) the time evolution of the orientation angle φ. Different colours index different initial conditions.

translational symmetry in the y-direction, and hence the trajectories now also depend on the value of the initial y position of the squirmer centre. We first consider the squirmer starting with an orientation $\varphi = 0.5\pi$ and an initial centre location coordinate of $y = \lambda/4$, with the other initial location coordinates and the initial angle of attack at the default values of $x = 0$, $z = 1.2$, and $\theta = -0.17\pi$. Then, the squirmer moves along the $-x$-axis with similar dynamics in the z-direction to that displayed in Figure 6. In particular, the dynamics in the z-direction are only slightly perturbed when $\lambda = 1, 2$ but display larger oscillations when $\lambda = 4, 8$.

We then consider variations in the initial squirmer orientation angle φ that, as previously, entails the trajectories are no longer constrained to two spatial dimensions. The surface topography amplitude remains fixed at $A = 0.1$, and the initial height, location, and attack angle are at default values, while we consider variation in the orientation angle φ and the topography wavelength, which here is still given by λ. When $\lambda = 1$ (Figure 8A), the trajectories are not affected by the surface topography, as the trajectories are straight when projected on to the x–y plane, and the angle φ is constant in time. However, in the simulation with the wavelength $\lambda = 2$ (Figure 8B), some trajectories with $\varphi \approx \pi/4$ are hydrodynamically captured near the bottom of the doubly periodic sinusoidal valley, whereas swimming outside of this region of initial orientation angles is not affected by the surface topography, as in the case of $\lambda = 1$.

These features can also be observed when we increase the wavelength to $\lambda = 4$ (Figure 8C). In contrast, for the larger wavelength of $\lambda = 8$, there is no evidence for an attracting trough of squirmer dynamics near the bottom of the topographic valley (Figure 8D). Together, these results highlight that the hydrodynamic attraction towards, and subsequently along, topographic valleys is not only limited but also only possible when the scale of the swimmer's diameter is comparable with the length scale of the surface topography.

We then move to consider the final surface topography of doubly periodic peaks as introduced by Eq. 6 and displayed in Figure 2C. Trajectories with straight line projections onto the x–y plane can be observed when the squirmer's initial location and orientation angle align along topography troughs or across topography crests. For example, given the default initial location of $\boldsymbol{X} = (0, 0, 1.2)$ and an initial orientation angle $\varphi = 0$, the squirmer swims with $\varphi = 0$ throughout time. In addition, these trajectories also exhibit nearly constant z-dynamics, though small z-oscillations are observed with amplitude $\lesssim 0.05$ due to the topography, and this oscillation is further diminished as the topography wavelength increases. Furthermore, with the default initial location and an initial value of $\varphi = 0.25\pi$, or with initial values of $\boldsymbol{X} = (0, \lambda/4, 1.2)$ and $\varphi = 0.5\pi$, straight line x–y projected trajectories are also observed. Furthermore, in the z-direction, the squirmer behaviour changes from small oscillatory perturbations to larger amplitude z-oscillations as the wavelength increases, in direct analogy to the examples considered in detail with the previous topographies.

For more general initial configurations of the squirmer, we have considered the three-dimensional behaviour of the resulting trajectories, with the simulation results plotted in Figure 9 for $\lambda = 2, 4, 8, 16$, observing the wavelength for this topography is $\lambda/2$, not λ. In the previous doubly periodic surface topography, swimming with the orientation angle $\varphi = \pi/4$ allowed the cell to move along a surface topography trough, noting that the prospect of drifting observed in the singly periodic topography of Figure 2A can be ruled out. In contrast, for the current case, an orientation of $\varphi = \pi/4$ moves across the surface topography peaks.

Again, the simulation results show that the squirmer is attracted by orientation angles corresponding to troughs in the surface

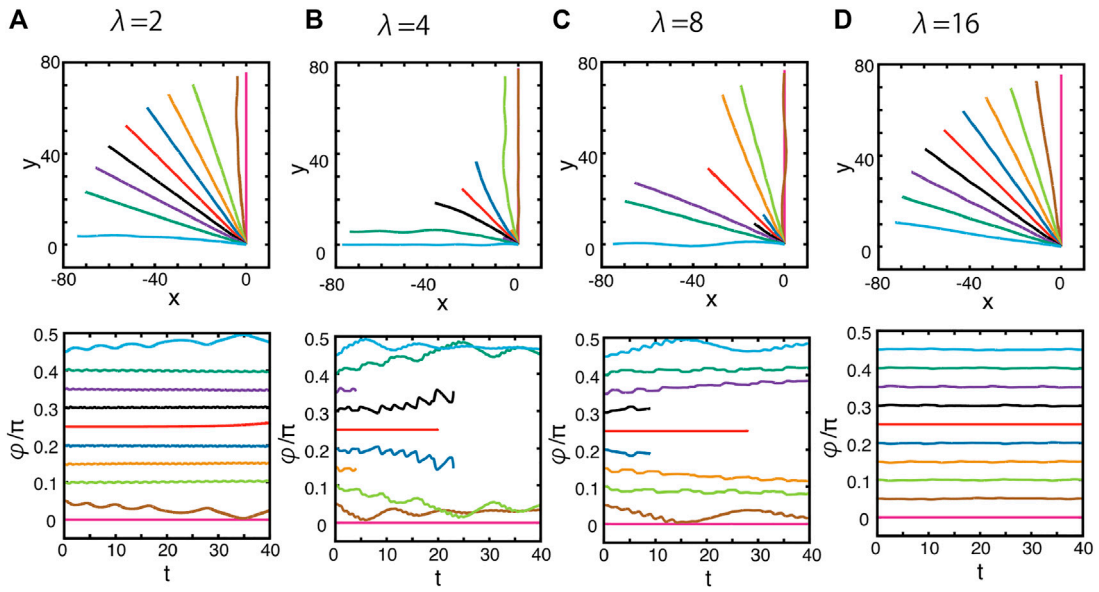

FIGURE 9
Dynamics of the squirmer near a surface with the doubly periodic sinusoidal wave topography of Eq. 6, as depicted in Figure 2C. The surface topography amplitude is given by $A = 0.1$, and the wavelength is unchanged from previous plots, but is no longer given by $\lambda = 2\pi/k$ where k is the wavenumber of the sinusoidal functions in Eq. 6, since these functions are squared. Hence, to preserve wavelength at 1, 2, 4, 8 length units in the respective columns, we take **(A)** $\lambda = 2$, **(B)** $\lambda = 4$, **(C)** $\lambda = 8$, and **(D)** $\lambda = 16$ on moving from left to right across the figure. (Top panels) the projections of the squirmer trajectories onto the x–y plane with different initial orientation angles, φ, as defined *via* Figure 5. These initial angles may be inferred from the initial tangents of the plotted projected trajectories. (Bottom panels) the time evolution of the orientation angle φ. Different colours index different initial conditions.

topography, which here are $\varphi = 0, \pi/2$, for example. Furthermore, such topographic attraction is realised when the squirmer diameter is close to the characteristic length scale of the surface modulation, as seen in Figures 9A–C. However, again for the parameter regimes of Figures 9B, C, the swimmer can approach very close to the surface, and the trajectory simulations are halted as detailed surface dynamics are outside the scope of the study. Finally, we note that once the surface topography wavelength is increased further, with $\lambda = 16$ as presented in Figure 9D, all projected trajectories are straight lines, and the orientation angle φ is constant in time. Hence, at these larger wavelengths, the surface–swimmer interactions no longer influence the guidance of the squirmer.

5 Discussion

In this paper, we have numerically investigated the hydrodynamics of a puller spherical tangential squirmer near a surface with a singly or doubly periodic structured topography. In particular, the amplitude of the surface topography was an order of magnitude less than the squirmer size and a wavelength on the scale of the squirmer size. The simulated squirmer is known to be attracted to a stable separation from a flat wall, and a mesh-free regularised Stokeslet boundary element numerical scheme was demonstrated to accurately capture the dynamics induced by the subtle hydrodynamic interactions between a spherical tangential squirmer and a flat wall.

When the wavelength of the sinusoidal surface topography is smaller than the squirmer size, the perpendicular dynamics of the swimmer trajectory is a small amplitude oscillatory perturbation from the constant stable swimming height associated with a flat boundary. However, as the wavelength of the surface topography is increased, the squirmer acquires larger vertical, z-direction, oscillations with a wavelength that matches that of the topography at very large surface topography wavelengths, but not always at intermediate values (Figure 6C).

Furthermore, the squirmer movement in the horizontal, x–y, plane has been observed to be highly dependent on the detailed geometrical properties of the surface topography. We first considered a singly periodic sinusoidal surface topography. When the wavelength of the surface topography (Eq. 4) is not significantly larger than the squirmer diameter ($\lambda < 4$), the horizontal squirmer motion reorientates towards one of two stable directions, i.e., parallel and perpendicular to the wavevector of the surface topography, as seen in Figure 7. Furthermore, drifting can sometimes be observed, whereby the direction of motion differs slightly from the orientation angle, φ, as noted in Figure 7, for example.

At intermediate wavelengths ($\lambda = 4$) the squirmer can approach the surface. The detailed subsequent behaviour would be contingent on the near-surface physics, the detailed study of which is beyond the scope of this study. Once the surface topography wavelength is further increased, with $\lambda = 8$ sufficient so that the wavelength is four times that of the squirmer diameter, we observed that the horizontal motion is that of straight lines and surface induced guidance of the squirmer in the horizontal plane is lost.

For the doubly periodic surface topographies, the squirmer had the tendency to be locally guided to swim along surface topography

troughs rather than over crests, though only when the squirmer diameter was comparable to the surface topography wavelength. However, such tendencies were weak and, at intermediate surface topography length scales, often accompanied by very close approaches to the surface where steric interactions would be important.

These qualitative features of the squirmer trajectories have also been observed when the squirmer parameter, $\beta = B_2/B_1$, from Eq. 2, was varied within the range that induced stable swimming in the vicinity of a flat wall. In addition, changing the sinusoidal surface topography to a sigmoidal topography to represent fabricated surface wells in microfluidic devices did not induce a significant change in the qualitative features of the swimming trajectories. In turn, this evidences that squirmer swimming behaviours are influenced mainly by the length scale of the surface topography. In addition, we have also observed that the swimmer behaviour can be complex, especially when the swimmer is not aligned along the surface topography troughs or above the surface topography crests, though a limited local guidance to swim along the surface topography troughs has also been common.

There are considerable numbers of studies focussing on microswimmer dynamics near non-trivial geometrical structures such as curved obstacles (Nishiguchi et al., 2018; Das and Cacciuto, 2019), bumps (Simmchen et al., 2016; Yang et al., 2019), and maze-like micro-devices (Denissenko et al., 2012; Tung et al., 2014), but the length scale of the surface topography in the current study features much finer surface structures. We also note that the transitional vertical behaviours in the z-direction, from perturbations of the stable swimming height for a flat wall to topography-following motion at very large surface topography wavelength, necessitate a consideration of the finite-size amplitude of the surface topography. In particular, such behaviours highlight that the dynamics examined in this study requires larger-scale physics beyond the effective boundary conditions (Sarkar and Prosperetti, 1996; Kunert et al., 2010; Luchini, 2013) based on a very small amplitude surface roughness.

In the context of representing biological microswimmers such as spermatozoa and bacteria, which are pusher swimmers rather than pullers, hydrodynamic stable swimming occurs for prolate pusher tangential squirmers, but not spherical squirmers (Ishimoto and Gaffney, 2013). Moreover, the hydrodynamic interactions strongly depend on the swimmer morphology and beating pattern (Smith et al., 2009; Shum et al., 2010; Ishimoto and Gaffney, 2014; Walker et al., 2019). In turn, this highlights that detailed numerical studies are required to explore the surface dynamics for both prolate squirmers and more realistic microbiological swimmers near non-trivial surface topographies, including the prospect of a ciliated epithelium, modelled as a dynamic periodic boundary (Smith et al., 2008).

Furthermore, contact dynamics are also experimentally known to be significant for boundary accumulation behaviours of microswimmers (Kantsler et al., 2013; Bianchi et al., 2017) and to vary extensively with solutes and surfaces (Klein et al., 2003). However, the current study does not consider the detailed surface dynamics in the region very close to the boundary since its scope considers universal hydrodynamic interactions, rather than the boundary behaviours for a specific swimmer, solute, and surface. Even with a simple short-range repulsion, the details of the repulsive force can alter the swimmer dynamics (Lintuvuori et al., 2016; Ishimoto, 2017), while the contact mechanics reflect the specific biological and physical features of the system under investigation. A further generalisation to be considered in artificial colloidal microswimmers is the impact of sedimentation and gyrotaxis due to swimmer density heterogeneity and density offset from the fluid (Das et al., 2020), as well as the chemical and physical mechanisms that drive the colloidal particle (Uspal et al., 2015). Also, the swirling squirmer characterised by a rotlet–dipole singularity is known to exhibit circular motion near a boundary (Ishimoto and Gaffney, 2013), and the impact of the surface topography on such a swimmer warrants future investigations.

In summary, this investigation has used the nearest neighbour regularised boundary element method (Gallagher and Smith, 2018) to numerically explore the hydrodynamic interactions between a spherical tangential squirmer and a spatially oscillating surface topography with an amplitude that is an order of magnitude less than the squirmer size. In particular, a squirmer was investigated that swam with very simple dynamics close to a flat boundary, relaxing to a stable distance from the wall, and swimming in the direction of its orientation in the horizontal plane. However, even with small amplitude surface topographies, this squirmer's dynamics has depended in a subtle and complex manner on the wavelength of the surface topography. We found that surface topographies could effect limited and local squirmer guidance towards topography troughs, in particular once the squirmer size is of the same order of magnitude as the surface topography wavelength. However, contact dynamics may also be induced at such wavelengths of the surface topography, especially if the initial squirmer orientation to the surface is not along topography crests or troughs. However, surface guided behaviours are robust to other aspects of the surface topography, such as reductions in the amplitude and changes in the shape of the surface topography waves. More generally, the framework enables these predictions to be made forming a basis for *in silico* experimentation of microorganisms and designing artificial micromachines.

Data availability statement

The raw data supporting the conclusions of this article will be made available by the authors without undue reservation. The data presented in this article is available from http://dx.doi.org/10.5287/ora-mzvppgob8.

Author contributions

KI, EG, and DS contributed to conception and design of the study. KI performed the numerical simulation. KI, EG, and DS analysed the data and wrote the manuscript.

Funding

KI acknowledges JSPS-KAKENHI (18K13456, 21H05309), JSPS Overseas Research Fellowship (29-0146), Kyoto University Hakubi Project, Kyoto University Supporting Program for Interaction-

Based Initiative Team Studies (SPIRITS), MEXT Leading Initiative for Excellent Young Researchers (LEADER), and JST, PRESTO Grant Number JPMJPR 1921, Japan. Elements of the numerical simulations were performed within the cluster computer system at the Research Institute for Mathematical Sciences (RIMS) and Institute for Information Management and Communication (IIMC), Kyoto University. DS acknowledges the EPSRC grant EP/N021096/1.

Acknowledgments

The authors are grateful to T. Montenegro-Johnson and M. T. Gallagher for fruitful discussions.

Conflict of interest

The authors declare that the research was conducted in the absence of any commercial or financial relationships that could be construed as a potential conflict of interest.

Publisher's note

All claims expressed in this article are solely those of the authors and do not necessarily represent those of their affiliated organizations, or those of the publisher, the editors, and the reviewers. Any product that may be evaluated in this article, or claim that may be made by its manufacturer, is not guaranteed or endorsed by the publisher.

References

Ainley, J., Durkin, S., Embid, R., Boindala, P., and Cortez, R. (2008). The method of images for regularized Stokeslets. *J. Comput. Phys.* 4227, 4600–4616. doi:10.1016/j.jcp.2008.01.032

Assoudi, R., Chaoui, M., Feuillebois, F., and Allouche, H. (2018). Motion of a spherical particle along a rough wall in a shear flow. *Z. Angew. Math. Phys.* 69, 112. doi:10.1007/s00033-018-1004-z

Berke, A. P., Turner, L., Berg, H. C., and Lauga, E. (2008). Hydrodynamic attraction of swimming microorganisms by surfaces. *Phys. Rev. Lett.* 101, 038102. doi:10.1103/PhysRevLett.101.038102

Bianchi, S., Saglimbeni, F., and Leonardo, R. D. (2017). Holographic imaging reveals the mechanism of wall entrapment in swimming bacteria. *Phys. Rev. X* 7, 011010. doi:10.1103/physrevx.7.011010

Blake, J. R. (1971). A spherical envelope approach to ciliary propulsion. *J. Fluid Mech.* 46, 199–208. doi:10.1017/s002211207100048x

Chamolly, A., Ishikawa, T., and Lauga, E. (2017). Active particles in periodic lattices. *New J. Phys.* 19, 115001. doi:10.1088/1367-2630/aa8d5e

Cortez, R., Fauci, L., and Medovikov, A. (2005). The method of regularized Stokeslets in three dimensions: Analysis, validation, and application to helical swimming. *Phys. Fluids* 17, 031504. doi:10.1063/1.1830486

Cortez, R. (2001). The method of regularized Stokeslets. *SIAM J. Sci. Comput.* 23, 1204–1225. doi:10.1137/s106482750038146x

Cosson, J., Groison, A.-L., Suquet, M., Fauvel, C., Dreanno, C., and Billard, R. (2008). Marine fish spermatozoa: Racing ephemeral swimmers. *Reproduction* 136, 277–294. doi:10.1530/REP-07-0522

Das, S., and Cacciuto, A. (2019). Colloidal swimmers near curved and structured walls. *Soft Matter* 15, 8290–8301. doi:10.1039/c9sm01432b

Das, S., Jalilvand, Z., Popescu, M. N., Uspal, W. E., Dietrich, S., and Kretzschmar, I. (2020). Floor- or ceiling-sliding for chemically active, gyrotactic, sedimenting janus particles. *Langmuir* 36, 7133–7147. doi:10.1021/acs.langmuir.9b03696

Delfau, J. B., Molina, J., and Sano, M. (2016). Collective behavior of strongly confined suspensions of squirmers. *EPL* 114, 24001. doi:10.1209/0295-5075/114/24001

Denissenko, P., Kantsler, V., Smith, D. J., and Kirkman-Brown, J. (2012). Human spermatozoa migration in microchannels reveals boundary-following navigation. *Proc. Natl. Acad. Sci. U. S. A.* 109, 8007–8010. doi:10.1073/pnas.1202934109

Drescher, K., Leptos, K. C., Tucval, I., Ishikawa, T., Pedley, T. J., and Goldstein, R. E. (2009). Dancing *volvox*: Hydrodynamic bound states of swimming algae. *Phys. Rev. Lett.* 102, 168101. doi:10.1103/PhysRevLett.102.168101

Elgeti, J., Winkler, R. G., and Gompper, G. (2015). Physics of microswimmers—single particle motion and collective behavior: A review. *Rep. Prog. Phys.* 78, 056601. doi:10.1088/0034-4885/78/5/056601

Evans, A. A., Ishikawa, T., Yamaguchi, T., and Lauga, E. (2011). Orientational order in concentrated suspensions of spherical microswimmers. *Phys. Fluids* 23, 111702. doi:10.1063/1.3660268

Gallagher, M. T., Choudhuri, D., and Smith, D. J. (2019). Sharp quadrature error bounds for the nearest-neighbor discretization of the regularized stokeslet boundary integral equation. *SIAM J. Sci. Comput.* 41, B139–B152. doi:10.1137/18m1191816

Gallagher, M. T., and Smith, D. J. (2018). Meshfree and efficient modeling of swimming cells. *Phys. Rev. Fluids* 3, 053101. doi:10.1103/physrevfluids.3.053101

Ishikawa, T., Simmonds, M. P., and Pedley, T. J. (2006). Hydrodynamic interaction of two swimming model micro-organisms. *J. Fluid Mech.* 568, 119–160. doi:10.1017/s0022112006002631

Ishimoto, K., Cosson, J., and Gaffney, E. A. (2016). A simulation study of sperm motility hydrodynamics near fish eggs and spheres. *J. Theor. Biol.* 389, 187–197. doi:10.1016/j.jtbi.2015.10.013

Ishimoto, K., and Gaffney, E. A. (2014). A study of spermatozoan swimming stability near a surface. *J. Theor. Biol.* 360, 187–199. doi:10.1016/j.jtbi.2014.06.034

Ishimoto, K., and Gaffney, E. A. (2013). Squirmer dynamics near a boundary. *Phys. Rev. E* 88, 062702. doi:10.1103/PhysRevE.88.062702

Ishimoto, K. (2017). Guidance of microswimmers by wall and flow: Thigmotaxis and rheotaxis of unsteady squirmers in two and three dimensions. *Phys. Rev. E* 96, 043103. doi:10.1103/physreve.96.043103

Kantsler, V., Dunkel, J., Polin, M., and Goldstein, R. E. (2013). Ciliary contact interactions dominate surface scattering of swimming eukaryotes. *Proc. Natl. Acad. Sci. U. S. A.* 110, 1187–1192. doi:10.1073/pnas.1210548110

Kherzi, B., and Pumera, M. (2016). Self-propelled autonomous nanomotors meet microfluidics. *Nanoscale* 8, 17415–17421. doi:10.1039/c6nr06665h

Klein, J., Clapp, A., and Dickinson, R. B. (2003). Direct measurement of interaction forces between a single bacterium and a flat plate. *J. Colloid Interface Sci.* 261, 379–385. doi:10.1016/S0021-9797(03)00095-X

Kunert, C., Harting, J., and Vinogradova, O. I. (2010). Random-roughness hydrodynamic boundary conditions. *Phys. Rev. Lett.* 105, 016001. doi:10.1103/PhysRevLett.105.016001

Kurzthaler, C., and Stone, H. A. (2021). Microswimmers near corrugated, periodic surfaces. *Soft matter* 17, 3322–3332. doi:10.1039/d0sm01782e

Lauga, E. (2009). Life at high Deborah number. *EPL* 86, 64001. doi:10.1209/0295-5075/86/64001

Lauga, E., and Powers, T. R. (2009). The hydrodynamics of swimming microorganisms. *Rep. Prog. Phys.* 72, 096601. doi:10.1088/0034-4885/72/9/096601

Lighthill, M. J. (1952). On the squirming motion of nearly spherical deformable bodies through liquids at very small Reynolds numbers. *Commun. Pure Appl. Math.* 5, 109–118. doi:10.1002/cpa.3160050201

Lintuvuori, J. S., Brown, A. T., Stratford, K., and Marenduzzo, D. (2016). Hydrodynamic oscillations and variable swimming speed in squirmers close to repulsive walls. *Soft Matter* 12, 7959–7968. doi:10.1039/c6sm01353h

Liu, C., Zhou, C., Wang, W., and Zhang, H. P. (2016). Bimetallic microswimmers speed up in confining channels. *Phys. Rev. Lett.* 117, 198001. doi:10.1103/PhysRevLett.117.198001

Llopis, I., and Pagonabarraga, I. (2010). Hydrodynamic interactions in squirmer motion: Swimming with a neighbour and close to a wall. *J. Non-Newt. Fluid Mech.* 165, 946–952. doi:10.1016/j.jnnfm.2010.01.023

Luchini, P. (2013). Linearized no-slip boundary conditions at a rough surface. *J. Fluid Mech.* 737, 349–367. doi:10.1017/jfm.2013.574

Magar, V., Goto, T., and Pedley, T. J. (2003). Nutrient uptake by a self-propelled steady squirmer. *Q. J. Mech. Appl. Math.* 56, 65–91. doi:10.1093/qjmam/56.1.65

Nganguia, H., and Pak, O. S. (2018). Squirming motion in a Brinkman medium. *J. Fluid Mech.* 855, 554–573. doi:10.1017/jfm.2018.685

Nishiguchi, D., Aranson, I. S., Snezhko, A., and Sokolov, A. (2018). Engineering bacterial vortex lattice via direct laser lithography. *Nat. Commun.* 9, 4486. doi:10.1038/s41467-018-06842-6

Nosrati, R., Graham, P. J., Liu, Q., and Sinton, D. (2016). Predominance of sperm motion in corners. *Sci. Rep.* 6, 26669. doi:10.1038/srep26669

Ohmura, T., Nishigami, Y., Taniguchi, A., Nonaka, S., Ishikawa, T., and Ichikawa, M. (2021). Near-wall rheotaxis of the ciliate tetrahymena induced by the kinesthetic sensing of cilia. *Sci. Adv.* 7, eabi5878. doi:10.1126/sciadv.abi5878

Ohmura, T., Nishigami, Y., Taniguchi, A., Nonaka, S., Manabe, J., Ishikawa, T., et al. (2018). Simple mechanosense and response of cilia motion reveal the intrinsic habits of ciliates. *Proc. Nat. Acad. Sci. U. S. A.* 115, 3231–3236. doi:10.1073/pnas.1718294115

Ostapenko, T., Schwarzendahl, F. J., Böddeker, T. J., Kreis, C. T., Cammann, J., Mazza, M. G., et al. (2018). Curvature-guided motility of microalgae in geometric confinement. *Phys. Rev. Lett.* 120, 068002. doi:10.1103/PhysRevLett.120.068002

Oyama, N., Molina, J. J., and Yamamoto, R. (2016). Purely hydrodynamic origin for swarming of swimming particles. *Phys. Rev. E* 93, 043114. doi:10.1103/PhysRevE.93.043114

Pedley, T. J., Brumley, D. R., and Goldstein, R. E. (2016). Squirmers with swirl: A model for volvox swimming. *J. Fluid Mech.* 798, 165–186. doi:10.1017/jfm.2016.306

Pedley, T. J. (2016). Spherical squirmers: Models for swimming micro-organisms. *IMA J. Appl. Math.* 81, 488–521. doi:10.1093/imamat/hxw030

Pozrikidis, C. (1992). *Boundary integral and singularity methods for linearized viscous flow*. Cambridge University Press.

Pratt, L., and Kolter, R. (1998). Genetic analysis of *Escherichia coli* biofilm formation: Roles of flagella, motility, chemotaxis and type I pili. *Mol. Microbiol.* 30, 285–293. doi:10.1046/j.1365-2958.1998.01061.x

Rad, S. H., and Najafi, A. (2010). Hydrodynamic interactions of spherical particles in a fluid confined by a rough no-slip wall. *Phys. Rev. E* 82, 036305. doi:10.1103/PhysRevE.82.036305

Rode, S., Elgeti, J., and Gompper, G. (2019). Sperm motility in modulated microchannels. *New J. Phys.* 21, 013016. doi:10.1088/1367-2630/aaf544

Rothschild, L. (1963). Non-random distribution of bull spermatozoa in a drop of sperm suspension. *Nature* 198, 381. doi:10.1038/200381b0

Sarkar, K., and Prosperetti, A. (1996). Effective boundary conditions for Stokes flow over a rough surface. *J. Fluid Mech.* 316, 223–240. doi:10.1017/s0022112096000511

Shaik, V. A., and Ardekani, A. M. (2017). Motion of a model swimmer near a weakly deforming interface. *J. Fluid Mech.* 824, 42–73. doi:10.1017/jfm.2017.285

Shum, H., and Gaffney, E. A. (2015). Hydrodynamic analysis of flagellated bacteria swimming in corners of rectangular channels. *Phys. Rev. E* 92, 063016. doi:10.1103/PhysRevE.92.063016

Shum, H., Gaffney, E. A., and Smith, D. J. (2010). Modelling bacterial behaviour close to a no-slip plane boundary: The influence of bacterial geometry. *Proc. R. Soc. A Math. Phys. Eng. Sci.* 466, 1725–1748. doi:10.1098/rspa.2009.0520

Simmchen, J., Katuri, J., Uspal, W. E., Popescu, M. N., Tasinkevych, M., and Sanchez, S. (2016). Topographical pathways guide chemical microswimmers. *Nat. Commun.* 7, 10598. doi:10.1038/ncomms10598

Sipos, O., Nagy, K., Leonardo, R. D., and Galajda, P. (2015). Hydrodynamic trapping of swimming bacteria by convex walls. *Phys. Rev. Lett.* 114, 258104. doi:10.1103/PhysRevLett.114.258104

Smith, D., Gaffney, E., Blake, J., and Kirkman-Brown, J. (2009). Human sperm accumulation near surfaces: A simulation study. *J. Fluid Mech.* 621, 289–320. doi:10.1017/s0022112008004953

Smith, D. J. (2018). A nearest-neighbour discretisation of the regularized stokeslet boundary integral equation. *J. Comput. Phys.* 358, 88–102. doi:10.1016/j.jcp.2017.12.008

Smith, D. J., Gaffney, E. A., and Blake, J. R. (2008). Modelling mucociliary clearance. *Respir. Physiol. Neurobiol.* 163, 178–188. doi:10.1016/j.resp.2008.03.006

Spagnolie, S. E., and Lauga, E. (2012). Hydrodynamics of self-propulsion near a boundary: Predictions and accuracy of far-field approximations. *J. Fluid Mech.* 700, 105–147. doi:10.1017/jfm.2012.101

Spagnolie, S. E., Moreno-Flores, G. R., Bartolo, D., and Lauga, E. (2015). Geometric capture and escape of a microswimmer colliding with an obstacle. *Soft Matter* 11, 3396–3411. doi:10.1039/c4sm02785j

Takagi, D., Palacci, J., Braunschweig, A. B., Shelley, M. J., and Zhang, J. (2014). Hydrodynamic capture of microswimmers into sphere-bound orbits. *Soft Matter* 10, 1784–1789. doi:10.1039/c3sm52815d

Tung, C.-K., Ardon, F., Fiore, A. G., Suarez, S. S., and Wu, M. (2014). Cooperative roles of biological flow and surface topography in guiding sperm migration revealed by a microfluidic model. *Lab. Chip* 14, 1348–1356. doi:10.1039/c3lc51297e

Uspal, W. E., Popescu, M. N., Dietrich, S., and Tasinkevych, M. (2015). Rheotaxis of spherical active particles near a planar wall. *Soft Matter* 11, 6613–6632. doi:10.1039/c5sm01088h

Walker, B. J., Wheeler, R. J., Ishimoto, K., and Gaffney, E. A. (2019). Boundary behaviours of l*eishmania mexicana*: A hydrodynamic simulation study. *J. Theor. Biol.* 462, 311–320. doi:10.1016/j.jtbi.2018.11.016

Wykes, M. S. D., Zhong, X., Tong, J., Adachi, T., Liu, Y., Ristroph, L., et al. (2017). Guiding microscale swimmers using teardrop-shaped posts. *Soft Matter* 13, 4681–4688. doi:10.1039/c7sm00203c

Yang, F., Qian, S., Zhao, Y., and Qiao, R. (2016). Self-diffusiophoresis of janus catalytic micromotors in confined geometries. *Langmuir* 32, 5580–5592. doi:10.1021/acs.langmuir.6b01214

Yang, J., Shimogonya, Y., and Ishikawa, T. (2019). Bacterial detachment from a wall with a bump line. *Phys. Rev. E* 99, 023104. doi:10.1103/PhysRevE.99.023104

Zhu, L., Lauga, E., and Brandt, L. (2013). Low-Reynolds-number swimming in a capillary tube. *J. Fluid Mech.* 725, 285–311. doi:10.1017/jfm.2013.225

Zhu, L., Lauga, E., and Brandt, L. (2012). Self-propulsion in viscoelastic fluids: Pushers vs. pullers. *Phys. Fluids* 24, 051902. doi:10.1063/1.4718446

Zöttl, A., and Stark, H. (2012). Hydrodynamics determines collective motion and phase behavior of active colloids in quasi-two-dimensional confinement. *Phys. Rev. Lett.* 108, 118101. doi:10.1103/PhysRevLett.112.118101

frontiers | Frontiers in Cell and Developmental Biology

TYPE Original Research
PUBLISHED 20 April 2023
DOI 10.3389/fcell.2023.1171495

OPEN ACCESS

EDITED BY
Takuji Ishikawa,
Tohoku University, Japan

REVIEWED BY
Ryusaku Deguchi,
Miyagi University of Education, Japan
John H. Henson,
Dickinson College, United States

*CORRESPONDENCE
Masaya Morita,
morita@lab.u-ryukyu.ac.jp

RECEIVED 22 February 2023
ACCEPTED 10 April 2023
PUBLISHED 20 April 2023

CITATION
Morita M, Kitanobo S, Ohki S, Shiba K and Inaba K (2023), Positive selection on ADAM10 builds species recognition in the synchronous spawning coral *Acropora*. *Front. Cell Dev. Biol.* 11:1171495. doi: 10.3389/fcell.2023.1171495

Positive selection on ADAM10 builds species recognition in the synchronous spawning coral *Acropora*

Masaya Morita[1]*, Seiya Kitanobo[1,2], Shun Ohki[3], Kogiku Shiba[2] and Kazuo Inaba[2]

[1]Sesoko Station, Tropical Biosphere Research Center, University of the Ryukyus, Nishihara, Japan, [2]Shimoda Marine Research Center, University of Tsukuba, Shimoda, Japan, [3]Department of Immunology, Graduate School of Biomedical and Health Sciences, Hiroshima University, Hiroshima, Japan

The reef-building coral *Acropora* is a broadcast spawning hermaphrodite including more than 110 species in the Indo-Pacific. In addition, many sympatric species show synchronous spawning. The released gametes need to mate with conspecifics in the mixture of the gametes of many species for their species boundaries. However, the mechanism underlying the species recognition of conspecifics at fertilization remains unknown. We hypothesized that rapid molecular evolution (positive selection) in genes encoding gamete-composing proteins generates polymorphic regions that recognize conspecifics in the mixture of gametes from many species. We identified gamete proteins of *Acropora digitifera* using mass spectrometry and screened the genes that support branch site models that set the "foreground" branches showing strict fertilization specificity. ADAM10, ADAM17, Integrin α9, and Tetraspanin4 supported branch-site model and had positively selected site(s) that produced polymorphic regions. Therefore, we prepared antibodies against the proteins of *A. digitifera* that contained positively selected site(s) to analyze their functions in fertilization. The ADAM10 antibody reacted only with egg proteins of *A. digitifera*, and immunohistochemistry showed ADAM10 localized around the egg surface. Moreover, the ADAM10 antibody inhibited only *A. digitifera* fertilization but not the relative synchronous spawning species *A. papillare*. This study indicates that ADAM10 has evolved to gain fertilization specificity during speciation and contributes to species boundaries in this multi-species, synchronous-spawning, and species-rich genus.

KEYWORDS

***Acropora coral*, ADAM10, positive selection, fertilization, species recognition, synchronous spawning**

1 Introduction

In sessile animals such as coral, gamete recognition is a trait associated with mate choice. Species recognition by gametes is crucial for synchronous spawning species, especially species-rich genera (Knowlton, 2000; Carlisle and Swanson, 2021). Gamete recognition (species- and self-recognition) provides a mechanism for mate choice to distinguish self from non-self and species identity in hermaphroditic species that broadcast gamete during multispecies spawning events. Mate choice is imperative for maintaining species boundaries and the fitness of descendants (Gowaty et al., 2007; Harrison and Larson,

2014; Ihle et al., 2015). The mechanism(s) of species- and self-recognition are essential for species boundaries (Willis et al., 2006). However, how gamete fertilizes with conspecifics of the other colonies is still unknown in the *Acropora* corals.

The coral *Acropora* is a broadcast-spawning hermaphrodite. Their gametes are fertilized in the water column after the release of a small package filled with sperm and eggs called "gamete bundles." In most species, gametes possess strict species recognition to mate with conspecifics after synchronous spawning among congeneric species ("multi-specific spawning") (Willis et al., 2006; Baird et al., 2009). Although species recognition is a prerequisite for reproductive isolation and species boundary in *Acropora* spp., the mechanism of species recognition is still unclear.

In *Acropora*, synchronous spawning behaviors provoke a risk of hybridization, and therefore, specific fertilization pathways are required for their species boundary. For example, sperm may swim toward eggs (Morita et al., 2006), but the cascades from gamete interaction with conspecifics to membrane fusion are still unknown. In contrast, gamete recognition proteins leading to adhering conspecific gametes are identified. For example, gamete recognition protein "binding" in sea urchins contributes to species-specific adhering. The bindin is under positive selection (Zigler et al., 2005), and genotypes of "bindin" evolved to obtain fertilization efficiency depending on the sperm concentration (Levitan et al., 2007). In addition, the genotypes of the "bindin" changed rapidly according to the fertilization condition due to changes in sea urchin population number (Levitan and Stapper, 2009). Lysin in the sperm of the broadcast-spawning marine invertebrate, abalone, is also involved in the gamete species recognition (Vacquier and Lee, 1993). Lysin is also under positive selection (Lee et al., 1995; Galindo et al., 2003), and interacts with the egg protein VERL (Galindo et al., 2002; Aagaard et al., 2010). The VERL shows coevolution with lysin (Clark et al., 2009). However, gamete proteins involved in *Acropora* fertilization have not been fully studied.

The integrin family of proteins is involved in cell–cell adhesion (Hynes, 1987; Arnaout et al., 2007). In *Acropora*, its involvement in sperm and egg interactions (Iguchi et al., 2007) and its divergence in terms of sequences and expression (Knack et al., 2008) have been reported. The ADAM family of disintegrins and metalloproteases includes ADAM2 (a "fertilin"), which is implicated in sperm–egg binding via integrin—ADAM binding (Evans, 2001; Merc et al., 2021). However, the function of integrins and ADAM in the fertilization of coral have not yet been investigated. Although integrin β1 is partly involved in fertilization in *Acropora*, the involvement of integrins in fertilization in mammalian species with an internal fertilization system is controversial (Miller et al., 2000; He et al., 2003; Barraud-Lange et al., 2007). For example, antibodies against integrins suppress fertilization (Barraud-Lange et al., 2007). Fertilization occurs in eggs (without the ZP) lacking integrin α6β1 (Miller et al., 2000), and the removal of the ZP layer indicates that integrin β1-knockout mice are not sterile (He et al., 2003).

Another family of candidate proteins with a role in sperm—egg interaction is that of the transmembrane tetraspanins. In mammals, the tetraspanin family members participate in primary sperm binding, gamete fusion, and polyspermy blocking (Jankovicova et al., 2020). Of the tetraspanins, the cluster of differentiation (CD9) is essential in the mouse gamete fusion and fertilization (Kaji et al., 2000; Miyado et al., 2000). CD9 participates in the formation of integrin α6β1/tetraspanin clusters in the plasma membrane, which are required for gamete fusion (Ziyyat et al., 2006). The other tetraspanins play many roles, such as sperm-to-egg binding in the ZP (CD9, CD81, and CD151) (Yanagimachi, 1994; Jin et al., 2011) and polyspermy blocking at the plasma membrane (CD9 and CD81) (Talbot and Dandekar, 2003; Ravaux et al., 2018). However, the presence and role of tetraspanins in *Acropora* have not been studied.

Although these proteins in mammals are involved in gamete binding at fertilization, the functions of the proteins in the coral *Acropora* are unknown. Released gametes must mate with conspecifics within the mixture of heterospecifics. In other words, gamete proteins for species recognition must be polymorphic to recognize conspecifics.

The extracellular region of proteins potentially underlies species recognition due to its interaction with other proteins localizing on the gamete's surface (Swanson and Vacquier, 2002; Palumbi, 2009; Carlisle and Swanson, 2021). The rapid evolution of the recognition sites is supposed to arise via a positive selection of specific codons in the extracellular region. The species-recognition sites are typically diverse, and many proteins are potentially involved in recognition. Taken together, the history of the species-recognition proteins reflects the speciation history of the coral *Acropora*.

In this study, gamete species-recognition proteins in the coral *Acropora* were explored. Proteins in sperm and eggs from *A. digitifera* were identified using mass spectrometry. The rates of molecular evolution of integrins, ADAMs, and tetraspanins from the identified proteins were analyzed to focus on the acquisition of species recognition. In the analyses, we set non-crossing species as those that acquired strict species recognition. Presumably, proteins in the non-crossing species have positively selected sites at the recognition region. The analyses indicated four proteins, ADAM10, ADAM17, tetraspanin 4, and integrin α9 that were candidates for the recognition proteins. The function(s) of the candidates in fertilization were investigated via antibody treatment. Although the positively selected sites in ADAM10 are supposed to be strong enough to be rigor species recognition in the more than 110 species in the coral *Acropora*, the inhibitory effect of the antibody was species-specific. Therefore, ADAM10 could be one of the gamete recognition proteins in the broadcast spawning coral *Aropora*.

2 Materials and methods

2.1 Coral

Acropora digitifera, *A. austera*, *A. tenuis*, and *A. papillare* were used for fertilization analyses. *A. tenuis* and *A. austera* spawn the same night, but the spawning time was earlier than the *A. digitifera*. *A. papillare* spawns closer to the *A. digitifera* and their gametes are compatible (Table 2). The other species, *A. intermedia*, *A. florida*, and *A. donei*, were used for RNA isolation and analysis of cDNA sequences of candidate genes. Published sequence data of 15 *Acropora* species were used, and species were re-sequenced when the registered sequences lacked parts of the open reading

frames (ORFs). All colonies were collected at Sesoko Island, Okinawa Prefecture, Japan.

2.2 Mass spectrometry (MS) analyses to identify integrins in Acropora

Eggs and sperm of *A. digitifera* were collected after spawning according to the previously described methods (Morita et al., 2006), and proteins in the eggs or sperm were analyzed with liquid chromatography-tandem MS at the Kazusa DNA Research Center (Ibaraki, Japan). To identify proteins, the genome information of *A. digitifera* was used. Approximately 2 g of eggs or 100 mg of sperm were used for the analyses.

2.3 Isolation of orthologs of the integrin, tetraspanin, and ADAM families

Orthoscope v1.5.1 for *Acropora* (http://yurai.aori.u-tokyo.ac.jp/orthoscope/Acropora.html) (Inoue and Satoh, 2019) was used to isolate orthologs. To isolate CD9 orthologs in *Acropora*, we used a fasta file of CD9 from *Homo sapiens* (NM_001769.4).

Phylogenetic trees of isolated ORF sequences were constructed using RaxML with a rapid bootstrap and general time reversible-gamma model (Stamatakis, 2006), and the sequences were aligned using MAFFT v. 7 (multiple alignment program for amino acid or nucleotide sequences) (https://mafft.cbrc.jp/alignment/server/) (Katoh et al., 2019). The aligned *phylip* files and the maximum likelihood (ML) tree files were used for molecular evolutionary analyses with CodeML (Yang, 1997).

2.4 Molecular evolutionary analysis of candidate genes

The relative rates of synonymous and non-synonymous substitutions in Integrins, Tetraspanins, and ADAMs were calculated using CodeML in PAML (Yang, 1997). Complete ORFs of functional genes from the isolated sequences in Orthoscope were used in the analyses. The codon site model (Model 8 vs. 7) was used, and then confirmed comparison between Model8 and 8a (Supplementary Figure S1), and Bayes empirical Bayes (BEB) analyses were used to detect positively selected sites in the candidate genes (Swanson et al., 2003; Yang et al., 2005).

Branch site analyses (model 2a) were conducted in candidate proteins setting non-crossing species as foreground branches (Yang et al., 2005; Zhang et al., 2005) (Supplementary Figure S1). If the ML model included a category of sites with non-synonymous/synonymous mutations (dN/dS > 1), positive selection likely acted on those sites along that specific lineage. Based on previous studies (Hatta et al., 1999; Fukami et al., 2003; Suzuki et al., 2016), we set non-crossing species (*A. digitifera*, *A. nasuta*, *A. accuminata*, *A. muricata*, *A. hyacinthus*, and *A. cytherea*) as the foreground and crossing species (*A. tenuis*, *A. yongei*, *A. intermedia,* and *A. florida*) as the background. Several species where species-specificity has not yet been identified (such as *A. selago*, *A. microphathalma*, *A. awi*) were set as background branches. In the null model, *dN/dS* of positively selected sites in the foreground was constrained to one. A likelihood ratio test was conducted with one degree of freedom. If the branch site model was supported, positively selected sites calculated from BEB analyses were checked.

We also did branch site analyses with aBSREL (http://www.datamonkey.org/absrel) using phylip file (Smith et al., 2015). We set non-crossing species as foreground branches at sites and run the analyses.

2.5 Synthesis of cDNA for construction of expression vectors

Fragments of coral for RNA extraction were collected by snorkeling 3–5 months prior to the predicted spawning month in June. Total RNA was extracted from fresh or preserved coral fragments using TRIzol reagent (Thermo Fisher, Waltham, MA, United States); cDNA was synthesized from the total RNA using SuperScript IV (Thermo Fisher, Waltham, MA, United States) with oligo dT primers.

2.6 TA cloning candidate gene cDNA

TA cloning was performed to isolate several genes from *A. papillare* and *A. donei*, whose sequences were not indetified. First, target sequences were amplified with ExTaq (Takara, Ohtsu, Japan) using several primers (Supplementary Table S1). The PCR products were ligated into the pGEM-T Easy Vector (Promega, Madison, WI, United States), which was then transformed into JM109 competent cells (Takara, Ohtsu, Japan). Plasmids were extracted, and cycle sequencing reactions were conducted using ABI BigDye Terminator version 3.1 and Cycle Sequencing Kits with T7 or SP6 primers, followed by capillary electrophoresis in an ABI 3730xl sequencer (Applied Biosystems, Foster City, CA, United States).

2.7 Antibody generation

We generated antibodies against the genes that were positively selected in *A. digitifera*. Proteins were expressed with the expression vector, pColdPros2, purified, and then the expressed proteins were used as antigens. To construct expression vectors, primers were designed to cover positively selected sites. The target region was amplified using Primstar HS (Takara, Otsu, Japan) and ligated into the vector after restriction enzyme treatment (XhoI/EcoRI) using the DNA Ligation Kit - Mighty Mix (Takara, Otsu, Japan). The ligated plasmid was subcloned into DH5α cells, and the plasmid was isolated. The isolated plasmid was again transformed into BL21 cells, which were then cultured at 37°C in Luria Bertani medium containing ampicillin until reaching OD_{600} of 0.5, and the expression was induced at 15°C in the presence of 1 mM isopropyl β-D-1-thiogalactopyranoside (IPTG) for 24 h. Expressed proteins were solubilized with 8 M urea and 2 M thiourea and dialyzed against 5 M urea overnight. The supernatant of the extract was applied to TALON resin (Takara,

TABLE 1 Identified ADAM-Integrin and tetraspanin family in sperm and egg proteins.

Integrins	Gene bank ID	Name of identified proteins	Sperm	Eggs	Codon site model						Branch site model				BEB selected sites	aBSREL
					model8	model8a	model7	ΔlnL	P	Number of BEB selected site	model2b	Null	ΔlnL	P		
	XP_015755972.1	PREDICTED: integrin beta-1-like [*Acropora digitifera*]		○	−3775.2	−3776.3	−3776.68	2.1	0.15	2 codon sites	−3776.3	−3776.3	0	1		
	XP_015777528.1	PREDICTED: integrin alpha-V-like [*Acropora digitifera*]		○	−3488	−3503.8	−3503.99	31.4	<0.0001*	4 codon sites	−3503.8	−3503.8	0	1		
	XP_015777540.1	PREDICTED: integrin alpha-PS1-like [*Acropora digitifera*]		○	−3300.3	−3312.8	−3313.28	25.1	<0.0001*	3 codon sites	−3312.8	−3312.8	0	1		
	XP_015750743.1	PREDICTED: integrin alpha-8-like [*Acropora digitifera*]		○	−1402.2	−1403.2	−1403.3	2	0.16		−1401.8	−1403.2	2.98	0.08		
	XP_015763542.1	PREDICTED: integrin-linked protein kinase-like [*Acropora digitifera*]	○	○	−740.1	−741.1	−742.89	1.96	0.16		−740.6	−740.6	0	1		
	XP_015757723.1	PREDICTED: calcium and integrin-binding protein 1-like [*Acropora digitifera*]		○	−402.1	−402.1	−402.09	0	1		−402.1	−402.1	0	1		
	XP_015777529.1	PREDICTED: integrin alpha-9-like, partial [*Acropora digitifera*]		○	−2635.8	−2670.5	−2670.58	69.4	<0.0001*	22 codon sites	−2698.2	−2712.1	27.89	<0.0001*	16S, 82M, 160F	positive slections in forregroud was not supported
	XP_015772241.1	PREDICTED: integrin beta-PS-like [*Acropora digitifera*]		○	−2334.3	−2335.9	−2336.26	3.19	0.073654301*	2 codon sites	−2335.5	−2335.8	0.6	0.44		
ADAMs																
	XP_015757289.1	PREDICTED: A disintegrin and metalloproteinase with thrombospondin motifs 6-like [*Acropora digitifera*]		○	−1719.3	−1721.5	−1721.76	4.25	0.039*		−1720	−1721.45	2.89	0.089		
	XP_015769952.1	PREDICTED: disintegrin and metalloproteinase domain-containing protein 12-like isoform X1 [*Acropora digitifera*]		○	−6259.9	−6277.2	−6277.32	34.5	<0.0001*	5 codon sites	−6277.2	−6277.2	0	1		
	XP_015758816.1	PREDICTED: A disintegrin and metalloproteinase with thrombospondin motifs 18-like [*Acropora digitifera*]		○	−2181.6	−2183.4	−2181.61	3.74	0.053		−2181.3	−2183.1	3.56	0.059		
	XP_015769077.1	PREDICTED: A disintegrin and metalloproteinase with thrombospondin motifs 6-like [*Acropora digitifera*]		○	−918.5	−920.8	−920.8	4.51	0.034*	1 codon site	−920.5	−920.5	0	1		
	XP_015778638.1	PREDICTED: disintegrin and metalloproteinase domain-containing protein 10-like [*Acropora digitifera*]	○	○	−2227.3	−2240.5	−2240.82	26.4	<0.0001*	2 codon sites	−2240.4	−2240.4	0	1		

(Continued on following page)

10.3389/fcell.2023.1171495

TABLE 1 (*Continued*) Identified ADAM-Integrin and tetraspanin family in sperm and egg proteins.

Integrins	Gene bank ID	Name of identified proteins	Sperm	Eggs	Codon site model						Branch site model				BEB selected sites	aBSREL
					model8	model8a	model7	ΔlnL	P	Number of BEB selected site	model2b	Null	ΔlnL	P		
	XP_015778639.1	PREDICTED: disintegrin and metalloproteinase domain-containing protein 10-like [*Acropora digitifera*]	▲	○	−3608.5	−3663.1	−3663.22	109.2	<0.0001*	15 cidin sites	−3270.3	−3277.9	15.21	<0.0001*	56R, 386D	Not supported
	XP_015765941.1	PREDICTED: disintegrin and metalloproteinase domain-containing protein 10-like, partial [*Acropora digitifea*]		○	−1960.9	−1964.7	−1964.71	7.61	0.0058*	1 codon site	−1964.7	−1964.7	0	1		
	XP_015780892.1	PREDICTED: ADAM 17-like protease [*Acropora digitifera*]		○	−2941.9	−2987.7	−2989.94	91.6	<0.0001	35 codon sites	−3329.8	−3333.4	7.4	0.0065*	103S	Not supported
Tetraspanins																
	XP_015766542.1	PREDICTED: tetraspanin-3-like [*Acropora digitifera*]		○	−817.2	−831.9	−832.27	29.6	<0.0001*	13 codon sites	−1496.7	−1497.9	2.33	0.126		
	XP_015766319.1	PREDICTED: tetraspanin-4-like [*Acropora digitifera*]	○	○	−743.9	−751.6	−751.65	15.5	<0.0001*	4 codon sites	−996.9	−1002.5	11.08	<0.0001*	191E	Supported in A.muricata
	XP_015756085.1	PREDICTED: tetraspanin-33-like [*Acropora digitifera*]	○	○	−116.09	−117.29	−117.3	2.41	0.12		−117.3	−117.3	0			
	XP_015764299.1	PREDICTED: tetraspanin-7-like [*Acropora digitifera*]	○	○	−1320.8	−1327.1	−1327.31	12.51	<0.0001*	2 codon site	−1327.1	−1327.1	0			
	XP_015759357.1	PREDICTED: CD63 antigen-like [*Acropora digitifera*]	○	○	−1349.5	−1365.9	−1365.92	32.8	<0.0001*	8 coden sites	−1365.7	−1365.7	0			
	not registrated	CD9		●	−1252.4	−1253.5	−1253.87	2.21	0.14		−1253.5	−1253.5	0			

▲: not detected in western blotting but identiferd in mass analyses.
●: not identified in mass analyses but detected in western blotting.

10.3389/fcell.2023.1171495

TABLE 2 Spawning synchronisms and gamete compatibility in the *Acropora* of the database of Orthoscope.

Species	Spawning	Spawning time	Gamete compatibility	
Acropora digitifera	June	21:40–22:30		*Acropora papillare* (not in the database) is compatible.
Acropora tenuis	June	19:20–19:40	[a]	*Acropora donei* (not in the database) is also compatible.
Acropora awi	unknown	unknown		
Acropora echinata	unknown	unknown		
Acropora nasuta	June	22:10–22:30		
Acropora gemmifera	June	22:10–22:40	[b]	
Acropora intermedia	June	22:20–22:40	[bc]	
Acropora florida	June	21:40–22:10	[bc]	
Acropora muricata	June	22:17–22:23		
Acropora yongei	June	19:30 (from Fukami et al., 2003)	[a]	
Acropora hyacinthus	June	22:20–22:40		
Acropora cytherea	June	22:20–22:40		
Acropora mircophthalma	unknown	unknown		
Acropora acuminata	June	22:10–22:30		
Acropora selago	unknown	unknown		

[a]Compatible each other.
[b]Compatible each other.
[c]Compatible each other.

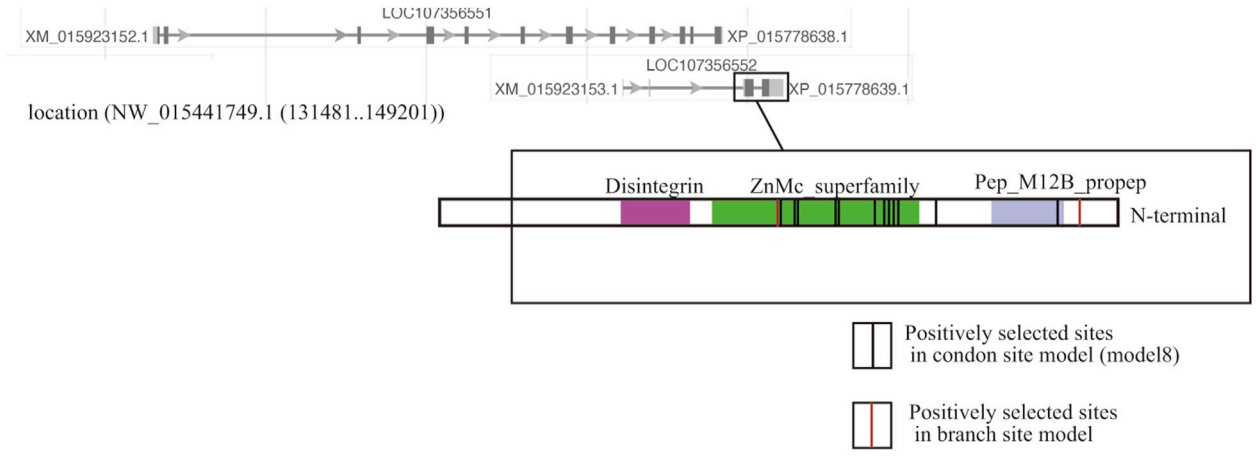

FIGURE 1
Localization of two copies of ADAM10 on the genome of the coral Acropora digitifera. Of the two ADAM10 sequences (XP_015778638.1, XP_015778639.1), the substitution rates of the several limited amino acid sites in one copy (XP_015778639.1) was accelerated. The red lines show codon sites in the Bayes empirical Bayes (BEB) analyses in the branch site model, and the black lines indicate the codon site model (Table 1).

Otsu, Japan). The resin was equilibrated with equilibration buffer (300 mM NaCl and 50 mM NaH_2PO_4, pH 7.4) and the proteins eluted with elution buffer (300 mM NaCl, 50 mM NaH_2PO_4, and 150 imidazole, pH 7.4). The purified proteins (3–5 mg) were dialyzed against phosphate-buffered saline, generating a polyclonal antibody. Antibody preparation was conducted at Biologica Co. (Nagoya, Japan). Antiserum was purified with Protein A, and IgG was eluted with 0.1 M glycine (pH 3.0). The eluted IgG with glycine was dialyzed with PBS. The IgG concentration was adjusted to 1.0 mg/mL with PBS.

2.8 Western blotting

Egg or sperm proteins were subjected to 7.5% or 10% acrylamide gel electrophoresis, and the separated proteins were transferred to

10.3389/fcell.2023.1171495

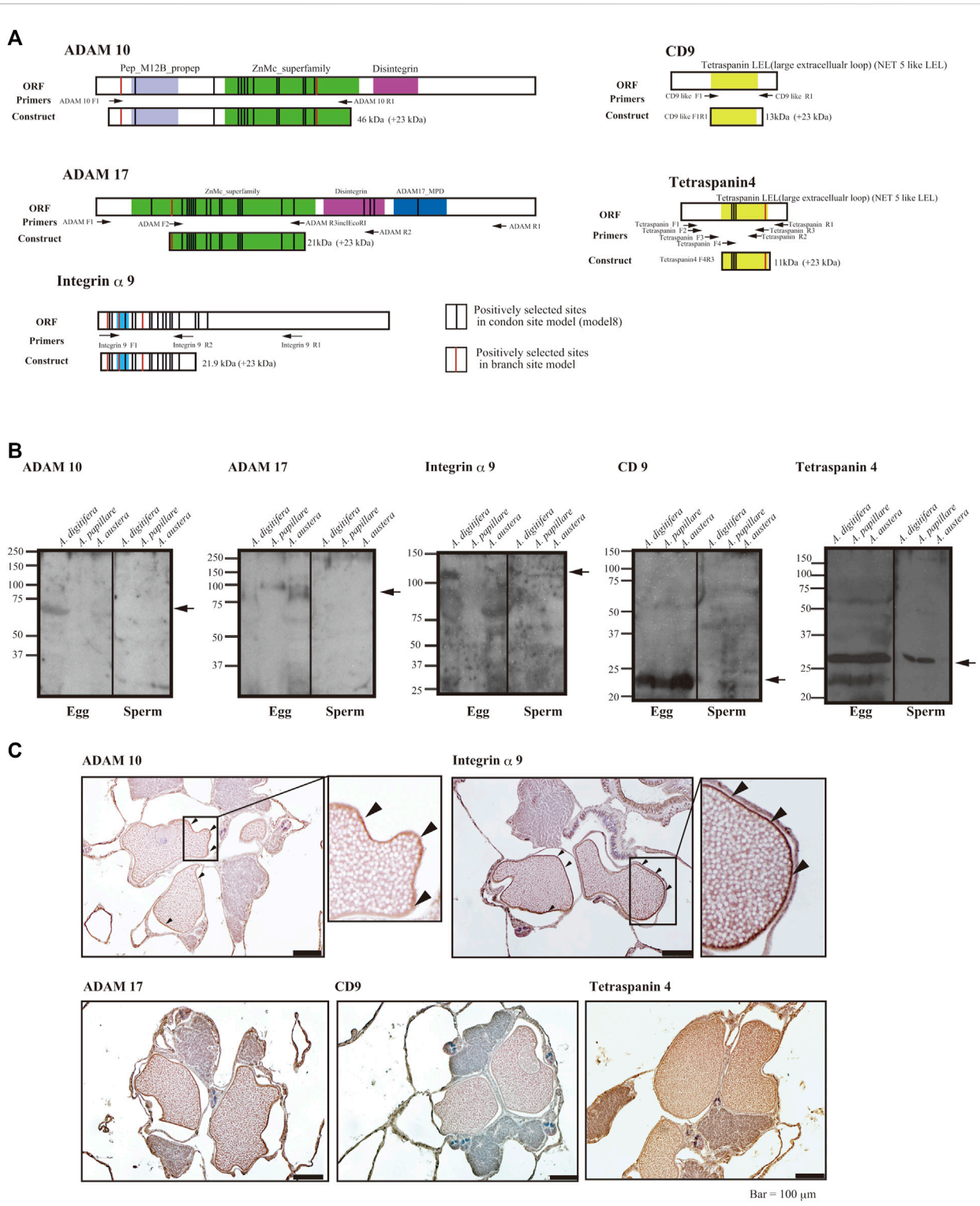

FIGURE 2
(A) Functional domains and positively selected sites of integrin α9, tetraspanins, ADAMs, and region(s) of antigen for antibody generation, **(B)** immunoblot analyses, and **(C)** immunohistology with the antibodies against sperm and eggs of the coral *Acropora*. **(A)** Functional domains of open reading frames, location of primers, and positively selected sites are indicated (red indicates the branch site model and black, the codon site model). Upper panels are hydropathy plots of deduced amino acid sequences. **(B)** Immunoblot analyses with eggs or sperm of *A. digitifera*, *A. papillare*, and *A. austera*. For tetraspanin 4 and CD9, 10% acrylamide gel was used to separate the proteins, and 7.5% gel was used for ADAMs and integrin α9. **(C)** Localization of ADAM10, ADAM17, Integrin α9, CD9, and Tetraspaning in about 1 week before the spawning of the coral *A. digitifera*. Arrowheads indicate the surface of oocytes. Bars = 100 μm.

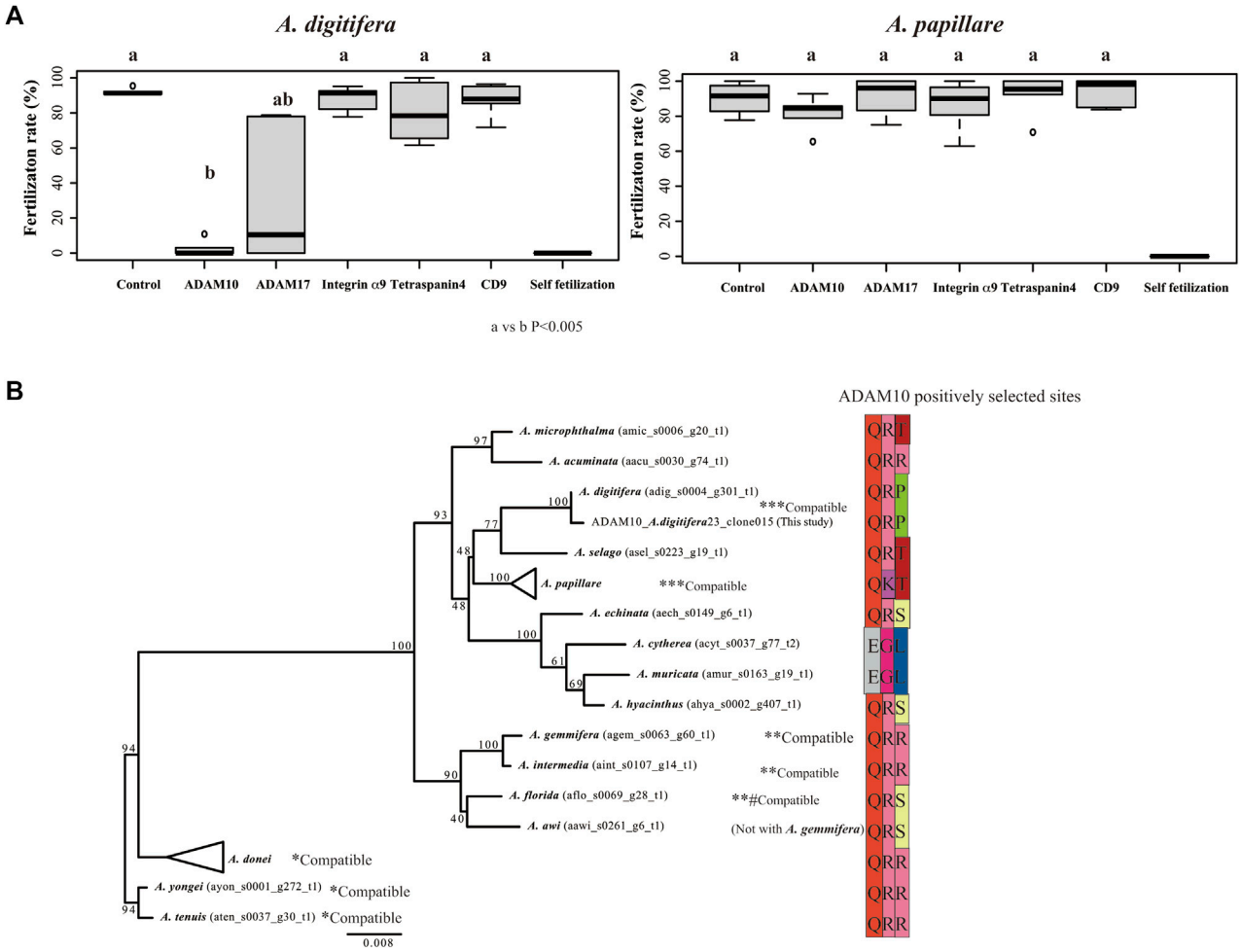

FIGURE 3
Fertilization ratio in the presence of antibodies against tetraspanins, integrin α9, and ADAMs. Fertilization in the presence of 10 μL of each antibody (1 mg/mL IgG) in 1 mL seawater (finally 10 μg/mL) was observed in gametes from *Acropora digitifera* and *A. papillare*. **(A)** Fertilization was conducted at 106 sperm/mL conditions, and the mixture of the gametes was finished within 2 h of spawning. Six crosses using gametes from three colonies of each species ($N = 6$; three colonies from both *A. digitifera* and *A. papillare*). Self-fertilization was used as a negative control. **(A)** or **(B)** indicates a significant difference (Wilcoxon rank sum test) **(B)** Maximum likelihood (ML) phylogenetic tree of *ADAM10* and sequences of positively selected sites (branch site analyses) among species. Gamete-compatible species are indicated with *, **, or ***.

polyvinylidene difluoride membranes. The membrane was then blocked with 5% (w/v) skim milk and Tris-base saline (TBS)-Tween (150 mM NaCl, 0.05% (v/v) Tween-20, 25 mM Tris-HCl, pH 7.4) overnight at 4°C. The first antibody reaction was carried out at 1/5,000–1/10,000 dilutions in the blocking solution for 1 h at room temperature (25–27°C), and the membrane was washed with TBS-Tween three times for 10 min each. Then, secondary antibody reactions of horseradish peroxidase (HRP)-labeled anti-rabbit immunoglobulin (Ig)G (Rockland, Limerick, PA, United States) were carried out at 1/20,000 dilution in the blocking solution for 1 h at room temperature. The membranes were again washed with TBS-Tween three times for 10 min each. Protein signals were detected using EzWestLumi Plus (ATTO, Tokyo, Japan).

2.9 Immunohistochemistry

Localizations of ADAM10 and Integrin α9 were examined 1 week before spawning according to the method of Morita et al. (2019). Fragments of the coral, *A. digitifera*, were fixed in Bouin's solution. After the skeletons were dissolved, tissues were embedded in paraffin and cut into 5-μm-thick sections. The sections were washed with 0.1 M phosphate-buffered saline (PBS), soaked in methanol containing 3% H_2O_2 for 15 min, and washed with PBS. The H_2O_2-treated slides were blocked with goat serum from a Histofine kit (Nichirei, Tokyo, Japan) overnight at 4°C. After blocking, the slides were incubated with an antibody against ADAM10 (1/2000 dilution) in PBS containing 1% (w/v) BSA at 4°C for 4 h, and then washed with PBS for 5 min, three times each. The slides were incubated with biotinylated secondary antibody from the Histofine kit for 15 min at room temperature and then washed with PBS. Streptavidin-horseradish peroxidase (HRP) was applied to the slides for 15 min at room temperature and washed with PBS. Peroxidase activity was visualized with 3,3′-diaminobenzidine (DAB) in a Tris-HCl (pH 7.6) buffer containing H_2O_2.

2.10 Fertilization experiments

Fertilization trials were carried out with eggs and sperm after spawning of *A. digitifera*, *A. austera*, and *A. papillare*. Eggs were incubated with filtered seawater (SW) with one of the developed antibodies (10 μL antibody (1 mg/mL)/1 mL SW) for 10 min at room temperature, and sperm concentration was adjusted to 10^6 sperm/mL with filtered seawater. Fertilization was confirmed by observing for developed embryos after 2.5–3 h. Fertilization rates were calculated from ratios of developed embryos and the total number of eggs.

2.11 Statistical analysis

Pairwise comparisons using Wilcoxon rank sum test was used to determine significant differences among treatments in fertilization experiments ($p < 0.05$). Bonferroni correction was carried out for multiple comparisons. R v. 4.0.1 was used for the analysis (Team, 2020).

3 Results

3.1 Integrin, ADAM, and tetraspanin expression in *Acropora* eggs and sperm

Mass Spectrometry (MS) analyses showed that several integrin and ADAM proteins were present in the eggs and sperm (Table 1). Integrin β1 was detected in eggs, and variables of integrin α and β-like (integrin α-X, -V, -9, -PS1, and β-PS) were also found. However, integrins were not found in the sperm. Several ADAM proteins were found in both sperm (ADAM7 and 10) and eggs (ADAM 6, 10, 12, 17, and 18). On the other hand, ADAM10 was detected only in the eggs by western analyses (see below). In addition, bindin, lysin, and VERL contributing gamete species recognitions in the sea urchin and abalone were not found.

Tetraspanins were found in eggs (tetraspanin 3, 4, 7, and 33) and sperm (tetraspanin 4, 7, and CD63). CD9 was not detected in either eggs or sperm; CD9 of *A. digitifera* is not registered in GenBank (https://www.ncbi.nlm.nih.gov/gene/); CD9 could not be identified due to lack of the data. However, CD9 of *Acropora* was obtained from Orthoscope, and cDNA of CD9 in *A. digitifera* was isolated. We prepared an antibody from the cDNA of *A. digitifera*, and the antibody reaction was observed corresponding to its mass. Therefore, CD9 is plausibly present in *Acropora* eggs.

3.2 Molecular evolution of integrins, ADAMs, and tetraspanins

Codon site analysis suggested several genes were positively selected among congeneric *Acropora* (Table 1). Most species whose genome information is available to show synchronous spawning and gamete compatibility are also identified, except for several species (Table 2). For example, *A. digitifera* does not show crossing among species in the database for Orthoscope. Branch site analyses were conducted to specify the correlation between the substitution rates of the several limited amino acid sites and species-specific fertilization. Of the integrins, ADAMs, and tetraspanins, four genes (*ADAM10*, *ADAM17*, *integrin α9*, and *tetraspanin 4*) had positively selected sites during the acquisition of fertilization specificity (Table 1). In contrast, aBSREL analyses support branch analyses only in *A. muricata* in the tetraspanin 4 (Table 1). *CD9* was subjected to strong purifying selection.

Two *ADAM10* sequences were detected (XP_015778638.1, XP_015778639.1), but only one *ADAM10* (XP_015778639.1) supported the branch-site model according to the species-specific fertilization mechanism. The loci of these two genes overlapped, but positive selection sites of *ADAM10* (XP_015778639.1) were localized on a distinctive region of the genome (Figure 1).

3.3 Involvement of the branch-site supported integrins, ADAMs, and tetraspanins in fertilization

We developed antibodies against the proteins (integrin α9, ADAM10, ADAM17, and tetraspanin 4), for which the substitution rates of the several amino acid sites had been accelerated according to species-specific fertilization traits. We prepared antibodies against the antigen of each protein containing the positively selected sites (Figure 2A). Immunoblotting using each antibody suggested that ADAMs, integrins α9, and CD9 were present only in the eggs, but tetraspanin4 was localized in both sperm and eggs (Figure 2B). All of the bands corresponded the expected molecular mass from CDs sequences (ADAM10; 68 kDa, ADAM17; 94 kDa, Integrin α9; 110 kDa, tetraspanin 4; 26 kDa, CD9; 28 kDa). In anti-ADAM10 and integrin α9 antibodies, antibodies reacted only with proteins in *A. digitifera* eggs (Figure 2B). Immunohistochemistry also showed that ADAM10 was localized on the surface of the oocytes (Figure 2C). ADAM17 localized both oocytes and strong signal was found on the surface of the oocytes like ADAM10 and integrin α9. CD9 were mainly found in the oocytes but tetraspanin 4 were stained many tissues including oocytes.

Of the candidates that mediated species-specific fertilization, only antibodies against ADAM10 strongly inhibited fertilization in *A. digitifera* (Figure 3A; vs. control, $p < 0.001$). ADAM17 slightly inhibited fertilization in *A. digitifera* (Figure 3A; vs. control, $p < 0.05$). Other antibodies against integrin α9, tetraspanin4, and CD9 did not inhibit fertilization in any tested species, including *A. papillare* (Figure 3A; $p > 0.05$). The positively selected sites of ADAM10 in *Acropora*, including *A. papillare*, were different (Figure 3B). As a control, we did intercross experiments between *A. digitifera* and *A. papillare*, showing intercrossing but not fully compatible (Supplementary Figure S2A). In the *A. austera*, we could succeed with experiments only with one combination. We thus could not conclude anything from the results (Supplementary Figure S2B). However, the fertilization was not suppressed with antibodies except CD9. The gametes of all colonies did not show self-fertilization as a negative control (Figure 3A).

4 Discussion

In this study, we examined the roles of integrins, ADAMs, and tetraspanins in *Acropora* fertilization. As shown in mammals, the

roles of ADAMs and integrins are controversial (e.g., Evans, 2001; He et al., 2003). Integrin β1 has been reported to be involved in *Acropora* fertilization (Iguchi et al., 2007). The other integrins, ADAMs, and tetraspanins were found in the gametes of *A. digitifera*. In the presence of antibodies against ADAM10, fertilization in *A. digitifera* was inhibited; ADAM10 may therefore be associated with fertilization in *A. digitifera*.

Although ADAM10 has not been reported to be involved in fertilization, our results suggest that ADAM10 is partly associated with gamete species recognition in *Acropora*. Fertilization-related ADAMs (ADAM2, ADAM9, ADAM12, ADAM15, and ADAM23) (Evans, 2001) interact with integrins (alpha4beta3, alpha9beta1) (Vjugina et al., 2009; Desiderio et al., 2010). The differences in the architecture of eggs between coral and mice suggest that the functions of ADAMs differ among species. For example, ADAMs and integrins are suggested to contribute to gamete interaction only when the ZP is present in the eggs (Evans et al., 1997). In *Acropora*, there is no ZP, and ADAM10 was found only in the eggs; the interacting integrins were not found in the sperm. Antibodies against integrin β1 slightly inhibit fertilization (Iguchi et al., 2007), and thus, the involvement of integrin β1 should be carefully considered. Overall, ADAM10 may interact with proteins other than integrins. Further studies are required to identify the protein(s) that interact with ADAM10.

The positively selected codon site in ADAM10 differs among species. Although the ADAM10 antibody specifically inhibited *A. digitifera* fertilization, only the two positively selected codon sites differed between *A. papillare* and *A. digitifera*. In addition, only two positively selected codon sites may be insufficient to determine their fertilization specificity for more than 20 synchronous species (Baird et al., 2021) or 110 extant species. Therefore, whether ADAM10 governs fertilization specificity among at least 20 synchronous spawning species is questionable. In addition, the feasibility of intercrossing between *A. digitifera* and *A. papillare* provokes the hypothesis that other gamete-composing proteins also play a role in species recognition.

Positive selections for species recognition might have arisen in many gamete protein genes in the Acropora spp. (Table 1; Morita et al., unpublished data). Specific codon sites are positively selected to generate polymorphic regions for recognition. Gamete compatibility is often congruent with rates of molecular evolution (Zigler et al., 2005). In addition, the risk of hybridization could influence the rates of molecular evolution. For example, the mixture of gametes from congeneric species could be associated with the risk of hybridization. The rates of codon evolution become slower when gamete interactions among heterospecifics are rare (Geyer et al., 2020).

The fertilization specificity and spawning synchronicity of several species (e.g., *A. awi* and *A. echinata*) used in this study are unknown. Thus, these species were not set as "foreground" for branch site analyses. For expedience, these species with unidentified fertilization specificity, such as *A. awi* and *A. echinate*, were set as background sequences. Due to the inclusion of these ambiguous species, the branch site analyses possibly underestimate the positively selected sites, and the robustness of the analyses needs to be considered carefully.

Coral is a basal animal, and its fertilization mechanisms are likely different from those in mammals, except for the plasma membrane fusion between sperm and egg. During the membrane fusion of sperm and eggs, CD9 functions as a strong determinant of fertilization in the mouse pathway (Miyado et al., 2008). Therefore, antibodies against CD9 were expected to suppress fertilization in all examined species. In contrast to our prediction, the CD9 antibody did not suppress fertilization. We developed an antibody against *A. digitifera* CD9 using its long extracellular loop (LEL) region, which is suggested to be involved in sperm–egg fusion (Umeda et al., 2020). It is also possible that antibodies against *A. digitifera* CD9 do not react with the functional site of CD9. In addition, small vesicles containing CD9 are released during membrane fusion between sperm and eggs in mice (Miyado et al., 2008; Barraud-Lange et al., 2012), but coral eggs are filled with wax esters (Harii et al., 2007), which are too rigid to form vesicles.

Another possibility is that CD9 does not underlie membrane fusion between sperm and eggs of the coral *Acropora*. The partner of CD9, EWI-2 protein with an Ig domain (Stipp et al., 2001), was not found in the eggs. Although EWI-2 protein has not been identified by MS analysis due to non-registration of EWI-2 cDNA, treatment with an anti-CD9 antibody against its LEL region was presumably insufficient to suppress the membrane fusion process if CD9 worked together with the EWI-2 complex. Our preliminary data found that proteins with IgG domains may be related to fertilization, but whether a protein–IgG complex interacts with CD9 and facilitates membrane fusion is unclear. To identify the differences between mammals and coral, the detailed pathway from sperm adhesion to membrane fusion should be investigated in *Acropora*.

The functions of the other tetraspanins are predicted to be different because differences in egg architecture are associated with differences in gamete adhesion pathways (e.g., Frolikova et al., 2019). Tetraspanins related to plasma membrane fusion (CD81 and CD151) were not found in the coral sperm. However, CD63, which functions as a primary adhesive of the cumulus cell layer in mammalian eggs, was found. In this study, we did not examine the role of CD63 because the positive selection of *CD63* was not supported (Table 1). CD63 in mouse sperm is implicated in sperm–egg interactions via integrins (Frolikova et al., 2019). Functional investigation of other tetraspanins (including CD63) is needed to identify the evolution and differentiation of fertilization mechanisms through speciation.

Among the identified gamete proteins, the rapid evolution of integrin α9, ADAMs, and tetraspanin 4 is supported by molecular evolutionary analysis. Functional modifications might occur in these proteins, and their functions are potentially not limited to fertilization. In this study, although the immunostaining implies these proteins may be present in the many tissues in the corals, we did not investigate the localization of these proteins in other tissues. Therefore, their localization and roles in different tissues are still unclear. Their functions could be diverse and potentially useful in many tissues. Indeed, the ADAM10 and 17 localize many tissues and function in many aspects, such as the embryonic development process (Harrison et al., 2021). Although the function of integrins and ADAMs are questionable, integrins α9 forms complex with could interact with CD9 in the mouse (Zhu and Evans, 2002). *Acropora* has experienced climate change and is surviving. The rapid evolution of the proteins is presumably associated with the tolerance/resilience of the corals. However, further study is required.

In conclusion, we examined the roles of integrins, ADAMs, and tetraspanins in fertilization. As a result of this study,

ADAM10 plausibly mediates species recognition. The ADAM10 antibody reacted only with *A. digitifera*, and thus, it still needs to be confirmed that ADAM10 governs species-specific fertilization in the other *Acropora* spp. In addition, positively selected sites in ADAM10 that arose during the acquisition of strict species recognition are limited. Overall, we predict more proteins are involved in species recognition, which is deeply associated with species boundaries in the coral *Acropora*.

Data availability statement

The datasets presented in this study can be found in online repositories. The names of the repository/repositories and accession number(s) can be found below: https://zenodo.org/deposit/6483451, 10.5281/zenodo.6483451.

Author contributions

MM conceived the study design, conducted all experiments, performed molecular evolutionary analyses, and wrote the paper. SK collected egg proteins for mass spectrometry analyses. KS and KI assisted in antibody preparation. All authors contributed critically to the drafts and gave final approval for publication.

Funding

This work was partly supported by the Project Foundation of the Tropical Biosphere Research Center of the University of the Ryukyus and JSPS KAKENHI (17K07414, 21H05304, and 22H02369 to MM; 21K15146 to SK).

Acknowledgments

We gratefully acknowledge the discursive inputs of Dr. K. Miyado and N. Kawano.

Conflict of interest

The authors declare that the research was conducted in the absence of any commercial or financial relationships that could be construed as a potential conflict of interest.

Publisher's note

All claims expressed in this article are solely those of the authors and do not necessarily represent those of their affiliated organizations, or those of the publisher, the editors and the reviewers. Any product that may be evaluated in this article, or claim that may be made by its manufacturer, is not guaranteed or endorsed by the publisher.

Supplementary material

The Supplementary Material for this article can be found online at: https://www.frontiersin.org/articles/10.3389/fcell.2023.1171495/full#supplementary-material

References

Aagaard, J. E., Vacquier, V. D., Maccoss, M. J., and Swanson, W. J. (2010). ZP domain proteins in the abalone egg coat include a paralog of VERL under positive selection that binds lysin and 18-kDa sperm proteins. *Mol. Biol. Evol.* 27, 193–203. doi:10.1093/molbev/msp221

Arnaout, M. A., Goodman, S. L., and Xiong, J. P. (2007). Structure and mechanics of integrin-based cell adhesion. *Curr. Opin. Cell Biol.* 19, 495–507. doi:10.1016/j.ceb.2007.08.002

Baird, A., Guest, J., and Willis, B. (2009). Systematic and biogeographical patterns in the reproductive biology of scleractinian corals. *Annu. Rev Ecol Evol Syst* 40, 551–571. doi:10.1146/annurev.ecolsys.110308.120220

Baird, A. H., Guest, J. R., Edwards, A. J., Bauman, A. G., Bouwmeester, J., Mera, H., et al. (2021). An Indo-Pacific coral spawning database. *Sci. Data* 8, 35. doi:10.1038/s41597-020-00793-8

Barraud-Lange, V., Chalas Boissonnas, C., Serres, C., Auer, J., Schmitt, A., Lefevre, B., et al. (2012). Membrane transfer from oocyte to sperm occurs in two CD9-independent ways that do not supply the fertilising ability of Cd9-deleted oocytes. *Reproduction* 144, 53–66. doi:10.1530/REP-12-0040

Barraud-Lange, V., Naud-Barriant, N., Saffar, L., Gattegno, L., Ducot, B., Drillet, A. S., et al. (2007). Alpha6beta1 integrin expressed by sperm is determinant in mouse fertilization. *BMC Dev. Biol.* 7, 102. doi:10.1186/1471-213X-7-102

Carlisle, J. A., and Swanson, W. J. (2021). Molecular mechanisms and evolution of fertilization proteins. *J. Exp. Zool. B Mol. Dev. Evol.* 336, 652–665. doi:10.1002/jez.b.23004

Clark, N. L., Gasper, J., Sekino, M., Springer, S. A., Aquadro, C. F., and Swanson, W. J. (2009). Coevolution of interacting fertilization proteins. *PLoS Genet.* 5, e1000570. doi:10.1371/journal.pgen.1000570

Desiderio, U. V., Zhu, X., and Evans, J. P. (2010). ADAM2 interactions with mouse eggs and cell lines expressing α4/α9 (ITGA4/ITGA9) integrins: Implications for integrin-based adhesion and fertilization. *PLoS One* 5, e13744. doi:10.1371/journal.pone.0013744

Evans, J. P. (2001). Fertilin beta and other ADAMs as integrin ligands: Insights into cell adhesion and fertilization. *Bioessays* 23, 628–639. doi:10.1002/bies.1088

Evans, J. P., Schultz, R. M., and Kopf, G. S. (1997). Characterization of the binding of recombinant mouse sperm fertilin alpha subunit to mouse eggs: Evidence for function as a cell adhesion molecule in sperm-egg binding. *Dev. Biol.* 187, 94–106. doi:10.1006/dbio.1997.8612

Frolikova, M., Valaskova, E., Cerny, J., Lumeau, A., Sebkova, N., Palenikova, V., et al. (2019). Addressing the compartmentalization of specific integrin heterodimers in mouse sperm. *Int. J. Mol. Sci.* 20, 1004. doi:10.3390/ijms20051004

Fukami, H., Omori, M., Shimoike, K., Hayashibara, T., and Hatta, M. (2003). Ecological and genetic aspects of reproductive isolation by different spawning times in *Acropora* corals. *Mar. Biol.* 142, 679–684. doi:10.1007/s00227-002-1001-8

Galindo, B. E., Moy, G. W., Swanson, W. J., and Vacquier, V. D. (2002). Full-length sequence of VERL, the egg vitelline envelope receptor for abalone sperm lysin. *Gene* 288, 111–117. doi:10.1016/s0378-1119(02)00459-6

Galindo, B. E., Vacquier, V. D., and Swanson, W. J. (2003). Positive selection in the egg receptor for abalone sperm lysin. *Proc. Natl. Acad. Sci. U. S. A.* 100, 4639–4643. doi:10.1073/pnas.0830022100

Geyer, L. B., Zigler, K. S., Tiozzo, S., and Lessios, H. A. (2020). Slow evolution under purifying selection in the gamete recognition protein bindin of the sea urchin Diadema. *Sci. Rep.* 10, 9834. doi:10.1038/s41598-020-66390-2

Gowaty, P. A., Anderson, W. W., Bluhm, C. K., Drickamer, L. C., Kim, Y. K., and Moore, A. J. (2007). The hypothesis of reproductive compensation and its assumptions about mate preferences and offspring viability. *Proc. Natl. Acad. Sci. U. S. A.* 104, 15023–15027. doi:10.1073/pnas.0706622104

Harii, S., Nadaoka, K., Yamamoto, M., and Iwao, K. (2007). Temporal changes in settlement, lipid content and lipid composition of larvae of the spawning hermatypic coral *Acropora tenuis*. *Mar. Ecol. Prog. Ser.* 346, 89–96. doi:10.3354/meps07114

Harrison, N., Koo, C. Z., and Tomlinson, M. G. (2021). Regulation of ADAM10 by the TspanC8 family of tetraspanins and their therapeutic potential. *Int. J. Mol. Sci.* 22, 6707. doi:10.3390/ijms22136707

Harrison, R. G., and Larson, E. L. (2014). Hybridization, introgression, and the nature of species boundaries. *J. Hered.* 105 (1), 795–809. doi:10.1093/jhered/esu033

Hatta, M., Fukami, H., Wang, W., Omori, M., Shimoike, K., Hayashibara, T., et al. (1999). Reproductive and genetic evidence for a reticulate evolutionary history of mass-spawning corals. *Mol. Biol. Evol.* 16, 1607–1613. doi:10.1093/oxfordjournals.molbev.a026073

He, Z., Brakebusch, C., Fässler, R., Kreidberg, J. A., Primakoffand Myles, D. G. (2003). None of the integrins known to be present on the mouse egg or to be ADAM receptors are essential for sperm–egg binding and fusion. *Dev. Biol.* 254, 226–237. doi:10.1016/s0012-1606(02)00043-x

Hynes, R. O. (1987). Integrins: A family of cell surface receptors. *Cell* 48, 549–554. doi:10.1016/0092-8674(87)90233-9

Iguchi, A., Marquez, L. M., Knack, B., Shinzato, C., Van Oppen, M. J., Willis, B. L., et al. (2007). Apparent involvement of a beta1 type integrin in coral fertilization. *Mar. Biotechnol. (NY)* 9, 760–765. doi:10.1007/s10126-007-9026-0

Ihle, M., Kempenaers, B., and Forstmeier, W. (2015). Fitness benefits of mate choice for compatibility in a socially monogamous species. *PLoS Biol.* 13, e1002248. doi:10.1371/journal.pbio.1002248

Inoue, J., and Satoh, N. (2019). Orthoscope: An automatic web tool for phylogenetically inferring bilaterian orthogroups with user-selected taxa. *Mol. Biol. Evol.* 36, 621–631. doi:10.1093/molbev/msy226

Jankovicova, J., Neuerova, Z., Secova, P., Bartokova, M., Bubenickova, F., Komrskova, K., et al. (2020). Tetraspanins in mammalian reproduction: Spermatozoa, oocytes and embryos. *Med. Microbiol. Immunol.* 209, 407–425. doi:10.1007/s00430-020-00676-0

Jin, M., Fujiwara, E., Kakiuchi, Y., Okabe, M., Satouh, Y., Baba, S. A., et al. (2011). Most fertilizing mouse spermatozoa begin their acrosome reaction before contact with the zona pellucida during *in vitro* fertilization. *Proc. Natl. Acad. Sci. U. S. A.* 108, 4892–4896. doi:10.1073/pnas.1018202108

Kaji, K., Oda, S., Shikano, T., Ohnuki, T., Uematsu, Y., Sakagami, J., et al. (2000). The gamete fusion process is defective in eggs of Cd9-deficient mice. *Nat. Genet.* 24, 279–282. doi:10.1038/73502

Katoh, K., Rozewicki, J., and Yamada, K. D. (2019). MAFFT online service: Multiple sequence alignment, interactive sequence choice and visualization. *Brief. Bioinform* 20, 1160–1166. doi:10.1093/bib/bbx108

Knack, B. A., Iguchi, A., Shinzato, C., Hayward, D. C., Ball, E. E., and Miller, D. J. (2008). Unexpected diversity of cnidarian integrins: Expression during coral gastrulation. *BMC Evol. Biol.* 8, 136. doi:10.1186/1471-2148-8-136

Knowlton, N. (2000). Molecular genetic analyses of species boundaries in the sea. *Hydrobiologia* 420, 73–90. doi:10.1023/a:1003933603879

Lee, Y. H., Ota, T., and Vacquier, V. D. (1995). Positive selection is a general phenomenon in the evolution of abalone sperm lysin. *Mol. Biol. Evol.* 12, 231–238. doi:10.1093/oxfordjournals.molbev.a040200

Levitan, D. R., and Stapper, A. P. (2009). Simultaneous positive and negative frequency-dependent selection on sperm bindin, a gamete recognition protein in the sea urchin *strongylocentrotus purpuratus*. *Evolution* 64, 785–797. doi:10.1111/j.1558-5646.2009.00850.x

Levitan, D. R., Terhorst, C. P., and Fogarty, N. D. (2007). The risk of polyspermy in three congeneric sea urchins and its implications for gametic incompatibility and reproductive isolation. *Evolution* 61, 2007–2014. doi:10.1111/j.1558-5646.2007.00150.x

Merc, V., Frolikova, M., and Komrskova, K. (2021). Role of integrins in sperm activation and fertilization. *Int. J. Mol. Sci.* 22, 11809. [Online]. doi:10.3390/ijms222111809

Miller, B. J., Georges-Labouesse, E., Primakoff, P., and Myles, D. G. (2000). Normal fertilization occurs with eggs lacking the integrin alpha6beta1 and is CD9-dependent. *J. Cell Biol.* 149, 1289–1296. doi:10.1083/jcb.149.6.1289

Miyado, K., Yamada, G., Yamada, S., Hasuwa, H., Nakamura, Y., Ryu, F., et al. (2000). Requirement of CD9 on the egg plasma membrane for fertilization. *Science* 287, 321–324. doi:10.1126/science.287.5451.321

Miyado, K., Yoshida, K., Yamagata, K., Sakakibara, K., Okabe, M., Wang, X., et al. (2008). The fusing ability of sperm is bestowed by CD9-containing vesicles released from eggs in mice. *Proc. Natl. Acad. Sci. U. S. A.* 105, 12921–12926. doi:10.1073/pnas.0710608105

Morita, M., Kitanobo, S., Nozu, R., Iwao, K., Fukami, H., and Isomura, N. (2019). Reproductive strategies in the intercrossing corals Acropora donei and A. tenuis to prevent hybridization. *Coral Reefs* 38, 1211–1223. doi:10.1007/s00338-019-01839-z

Morita, M., Nishikawa, A., Nakajima, A., Iguchi, A., Sakai, K., Takemura, A., et al. (2006). Eggs regulate sperm flagellar motility initiation, chemotaxis and inhibition in the coral *Acropora digitifera, A. gemmifera* and *A. tenuis*. *J. Exp. Biol.* 209, 4574–4579. doi:10.1242/jeb.02500

Palumbi, S. R. (2009). Speciation and the evolution of gamete recognition genes: Pattern and process. *Heredity* 102, 66–76. doi:10.1038/hdy.2008.104

Ravaux, B., Favier, S., Perez, E., and Gourier, C. (2018). Egg CD9 protein tides correlated with sperm oscillations tune the gamete fusion ability in mammal. *J. Mol. Cell Biol.* 10, 494–502. doi:10.1093/jmcb/mjy005

Smith, M. D., Wertheim, J. O., Weaver, S., Murrell, B., Scheffler, K., and Kosakovsky Pond, S. L. (2015). Less is more: An adaptive branch-site random effects model for efficient detection of episodic diversifying selection. *Mol. Biol. Evol.* 32, 1342–1353. doi:10.1093/molbev/msv022

Stamatakis, A. (2006). RAxML-VI-HPC: Maximum likelihood-based phylogenetic analyses with thousands of taxa and mixed models. *Bioinformatics* 22, 2688–2690. doi:10.1093/bioinformatics/btl446

Stipp, C. S., Kolesnikova, T. V., and Hemler, M. E. (2001). EWI-2 is a major CD9 and CD81 partner and member of a novel Ig protein subfamily. *J. Biol. Chem.* 276, 40545–40554. doi:10.1074/jbc.M107338200

Suzuki, G., Keshavmurthy, S., Hayashibara, T., Wallace, C. C., Shirayama, Y., Chen, C. A., et al. (2016). Genetic evidence of peripheral isolation and low diversity in marginal populations of the *Acropora hyacinthus* complex. *Coral Reefs* 35, 1419–1432. doi:10.1007/s00338-016-1484-2

Swanson, W. J., Nielsen, R., and Yang, Q. (2003). Pervasive adaptive evolution in mammalian fertilization proteins. *Mol. Biol. Evol.* 20, 18–20. doi:10.1093/oxfordjournals.molbev.a004233

Swanson, W. J., and Vacquier, V. D. (2002). The rapid evolution of reproductive proteins. *Nat. Rev. Genet.* 3, 137–144. doi:10.1038/nrg733

Talbot, P., and Dandekar, P. (2003). Perivitelline space: Does it play a role in blocking polyspermy in mammals? *Microsc. Res. Tech.* 61, 349–357. doi:10.1002/jemt.10348

Team, R. C. (2020). *R: A language and environment for statistical computing*. Vienna, Austria: R Foundation for Statistical Computing.

Umeda, R., Satouh, Y., Takemoto, M., Nakada-Nakura, Y., Liu, K., Yokoyama, T., et al. (2020). Structural insights into tetraspanin CD9 function. *Nat. Commun.* 11, 1606. doi:10.1038/s41467-020-15459-7

Vacquier, V. D., and Lee, Y. H. (1993). Abalone sperm lysin: Unusual mode of evolution of a gamete recognition protein. *Zygote* 1, 181–196. doi:10.1017/s0967199400001465

Vjugina, U., Zhu, X., Oh, E., Bracero, N. J., and Evans, J. P. (2009). Reduction of mouse egg surface integrin alpha9 subunit (ITGA9) reduces the egg's ability to support sperm-egg binding and fusion. *Biol. Reprod.* 80, 833–841. doi:10.1095/biolreprod.108.075275

Willis, B. L., Van Oppen, M. J. H., Miller, D. J., Vollmer, S. V., and Ayre, D. J. (2006). The role of hybridization in the evolution of reef corals. *Ann. Rev. Ecol. Evol. Syst.* 37, 489–517. doi:10.1146/annurev.ecolsys.37.091305.110136

Yanagimachi, R. (1994). "Mammalian fertilization," in *The physiology of reproduction*. Editors E. Knobil and J. D. Neill (NEW YORK: Raven Press), 189–317.

Yang, Z. (1997). Paml: A program package for phylogenetic analysis by maximum likelihood. *Bioinformatics* 13, 555–556. doi:10.1093/bioinformatics/13.5.555

Yang, Z., Wong, W. S., and Nielsen, R. (2005). Bayes empirical bayes inference of amino acid sites under positive selection. *Mol. Biol. Evol.* 22, 1107–1118. doi:10.1093/molbev/msi097

Zhang, J., Nielsen, R., and Yang, Z. (2005). Evaluation of an improved branch-site likelihood method for detecting positive selection at the molecular level. *Mol. Biol. Evol.* 22, 2472–2479. doi:10.1093/molbev/msi237

Zhu, X., and Evans, J. P. (2002). Analysis of the roles of RGD-binding integrins, alpha(4)/alpha(9) integrins, alpha(6) integrins, and CD9 in the interaction of the fertilin beta (ADAM2) disintegrin domain with the mouse egg membrane. *Biol. Reprod.* 66, 1193–1202. doi:10.1095/biolreprod66.4.1193

Zigler, K. S., Mccartney, M. A., Levitan, D. R., and Lessios, H. A. (2005). Sea urchin bindin divergence predicts gamete compatibility. *Evolution* 59, 2399–2404. doi:10.1554/05-098.1

Ziyyat, A., Rubinstein, E., Monier-Gavelle, F., Barraud, V., Kulski, O., Prenant, M., et al. (2006). CD9 controls the formation of clusters that contain tetraspanins and the integrin alpha 6 beta 1, which are involved in human and mouse gamete fusion. *J. Cell Sci.* 119, 416–424. doi:10.1242/jcs.02730

frontiers | Frontiers in Ecology and Evolution

TYPE Brief Research Report
PUBLISHED 20 April 2023
DOI 10.3389/fevo.2023.1132956

OPEN ACCESS

EDITED BY
Takuji Ishikawa,
Tohoku University, Japan

REVIEWED BY
Kenji Kikuchi,
Tohoku University, Japan
Azusa Kage,
Gakushuin University, Japan

*CORRESPONDENCE
Makoto Iima
✉ iima@hiroshima-u.ac.jp

RECEIVED 28 December 2022
ACCEPTED 03 April 2023
PUBLISHED 20 April 2023

CITATION
Yamashita H, Kamikubo T, Muku K, Suematsu NJ, Izumi S and Iima M (2023) Emergence of a *Euglena* bioconvection spot controlled by non-uniform light. *Front. Ecol. Evol.* 11:1132956. doi: 10.3389/fevo.2023.1132956

Emergence of a *Euglena* bioconvection spot controlled by non-uniform light

Hiroshi Yamashita[1], Touya Kamikubo[2], Kazuki Muku[3], Nobuhiko J. Suematsu[4,5], Shunsuke Izumi[1] and Makoto Iima[1]*

[1]Graduate School of Integrated Sciences for Life, Hiroshima University, Higashihiroshima, Japan, [2]Department of Mathematics, Hiroshima University, Higashihiroshima, Japan, [3]Department of Integrated Arts and Sciences, Hiroshima University, Higashihiroshima, Japan, [4]Graduate School of Advanced Mathematical Sciences, Meiji University, Nakano, Japan, [5]Meiji Institute for Advanced Study of Mathematical Sciences (MIMS), Meiji University, Nakano, Japan

Microorganisms possess taxes, which are the behavioral response to stimuli. The interaction between taxis and fluid dynamic instability leads to a macroscopic flow called bioconvection. In this study, we demonstrated that an isolated, single, three-dimensional bioconvection cell can exist within *Euglena* suspension. The isolated convection cell was named a "bioconvection spot." To reveal the formation of this bioconvection spot in a cylindrical container, position-control experiments were designed in a non-uniform light environment. Upon exposure of *Euglena* suspensions to varying light conditions with white and red regions, *Euglena* was determined to aggregate into the red (darker) region. This was attributed to its phototactic response of *Euglena*, causing its movement toward a darker environment and away from a strong light. Thus, the bioconvection spot was created by manipulating the local cell density of the suspension and the light environments. Using our experimental setup, we observed the structure of the spot and established that it radiated pulses of local cell densities of *Euglena*.

KEYWORDS

bioconvection, collective motion, microorganisms, plankton, *Euglena*, phototaxis, photo response

1. Introduction

Microorganisms can change their mode of locomotion by responding to various stimuli, such as chemicals (Berg, 1975), gravity (Häder et al., 2005), and light (Häder and Iseki, 2017). These behavioral responses are called taxes (Pedley and Kessler, 1992); these responses cause a macroscopic phenomenon called bioconvection. Wager (1911) reported net-like patterns that appeared within dense *Euglena* suspensions in various containers and demonstrated that variations in aggregation occurred when stimulated by external light targeted vertically down from the top. Platt (1961) considered the reasons for the onset of bioconvection patterns observed in various microorganisms; consequently, these bioconvections were not due to Rayleigh–Bénard thermal convections. The container's depth and the suspension's average cell density were determined to be important for the formation of this bioconvection. Additionally, Williams and Bees (2011) showed the time evolution of pattern formation of *Chlamydomonas* bioconvections in dense suspensions. *Chlamydomonas* bioconvection occurs due to three taxes (phototaxis, gyrotaxis, and gravitaxis) which are not completely independent. They showed variation in this time evolution depending on the intensity of light treatment from above and below the suspensions. Recently, Ramamonjy et al. (2022) demonstrated the

detailed interaction between phototaxis and bioconvection in *Chlamydomonas*.

This study focused on the bioconvection that was induced in a *Euglena* suspension due to negative phototaxis. *Euglena* is a well-known unicellular flagellate with a body length of approximately 50 μm and spindle-like shape. This flagellate moves forward by moving a single anterior flagellum (puller-type swimmer) (Ogawa et al., 2017; Rossi et al., 2017). *Euglena* is a photosynthetic microorganism with positive and negative phototaxis (Diehn, 1973). *Euglena* moves toward a weak light source (positive phototaxis) and away from a strong light source (negative phototaxis). When a strong light from below illuminates the diluted suspension of *Euglena*, it moves toward the top of the suspension due to the corresponding negative phototaxis. As a result, the local cell density of the microorganisms near the top of the suspension becomes higher. As the specific gravity of *Euglena* is greater than one, it causes an unstable stratification of mass density, where the top layer is heavier than bottom layer. In such a situation, Rayleigh–Taylor instability occurs, where a downward flow occurs from the top to the bottom of the suspension. In this process, *Euglena* is swept to the bottom layer by the downward flow. Additionally, simultaneous migration to the upper layer of suspension is maintained via the *Euglena*-dependent negative phototaxis. The balance between the microorganisms' upward and downward movements generates a macroscopic convective flow (bioconvection) in the suspension, as illustrated in Figure 1A.

Recent studies demonstrated that spatially-localized bioconvection can occur within dilute suspensions of *Euglena* (Suematsu et al., 2011; Shoji et al., 2014). Suematsu et al. (2011) revealed that bioconvection cells appeared when a *Euglena* suspension was illuminated by a strong light from below and spatially localized in a thin cylindrical container. Overall, the pattern of the localized bioconvection cells depends on the average cell density and container thickness. When the average cell density increases, the number of convection cells increases. However, the size of the bioconvection cells does not change, and there is no considerable change in the distance between the convection cells. This phenomenon differs from Rayleigh–Bénard thermal convection, in which the convection cells cover the entire container. Shoji et al. (2014) investigated the existence and behavioral characteristics of the bioconvection unit consisting of two convection rolls in an annular container with periodicity in a circumferential direction. They demonstrated a two-dimensional-like unit that maintained its structure and moved in a circumferential direction along the side wall. When two bioconvection units exist within a container, they can either merge with time or maintain a constant distance between them. The stable non-equilibrium states of the bioconvection unit in an annular container are similar to thermal convection in binary fluid mixtures (Bensimon et al., 1990; Watanabe et al., 2011, 2012). Nonetheless, the laws governing the motion of bioconvection units remain unknown. No prior study has investigated an isolated, single, three-dimensional bioconvection cell in a container such as a petri dish. Therefore, whether such a bioconvection cell can maintain its structure without other convection cells surrounding it is unclear.

Overall, we aimed to understand the localized bioconvection of *Euglena* and demonstrate the existence of an isolated, single, three-dimensional bioconvection cell, which was termed a "bioconvection spot." In this study, we established a "position-control" experiment method to generate a *Euglena*-dependent bioconvection spot in a container. In addition, we established that this bioconvection spot can exist alone, without a wall nearby, and maintain its corresponding structure via the position-control technique. Recently, Arrieta et al. (2019) reported a control method for the bioconvection plumes of *Chlamydomonas*. They controlled the local cell density of a dense *Chlamydomonas* suspension by LED illumination using optical fiber. Alternatively, time-varying non-uniform light fields were used in this study. Ogawa et al. (2016) observed the cell numbers of a *Euglena* suspension in a capillary laid horizontally, which had two regions illuminated with different light intensities from below. The cell number in each region was biased depending on the differences in the average intensity and the gap between the two light intensities. This indicated that *Euglena* exhibits lateral movements in response to light. By utilizing this response and exposing the suspension to a controlled light environment with bright and dark regions that changed temporally, we manipulated the local cell density of the *Euglena* suspension. As a result, the bioconvection spot would emerge at a specific location within the dilute suspension where the local cell density of *Euglena* reaches a high level, which was mediated by this indirect manipulation with light.

2. Materials and methods

Euglena gracilis strain Z (Figure 1B) was pre-cultured using Koren–Hunter medium with continuous light illumination. The cells were inoculated into a 2g/L HYPONeX aqueous solution with periodic light illumination at room temperature (20±1°C). The light period (4.27 μmol/m^2/s, 306 lx) was conducted between 7 a.m. to 10 p.m. (15 h light/9 h dark cycle). The average cell densities of the suspension were prepared by diluting the suspension extracted from the cell culture with a HYPONeX aqueous solution of the same concentration. The suspension was left in the darkroom for an hour before placing it on our experimental device. We conducted all experiments from 1 p.m. to 7 p.m. Figure 1C shows a schematic of the experimental setup used in this study. We used a projector (PicoCube X, Felicross Co. Ltd.) as the light source, and varying light conditions were projected onto a screen made of white polystyrene sheet (thickness: 0.2 mm). The light environment corresponded to a flip drawing controlled by an in-house Python program with library Pygame. The *Euglena* suspension was placed in a cylindrical acrylic container (40 mm in diameter and 5mm in thickness) with a top cover made of glass. This container was placed on the screen and observed from above using a digital single-lens reflex camera (Z 7II & NIKKOR Z 50 mm f/1.8 S, Nikon).

Euglena migrates away from strong light when the environment suddenly changes (Ogawa et al., 2016; Tsang et al., 2018). By exposing the *Euglena* suspension to an artificial, non-uniform light environment, we manipulated the local cell density of the *Euglena*

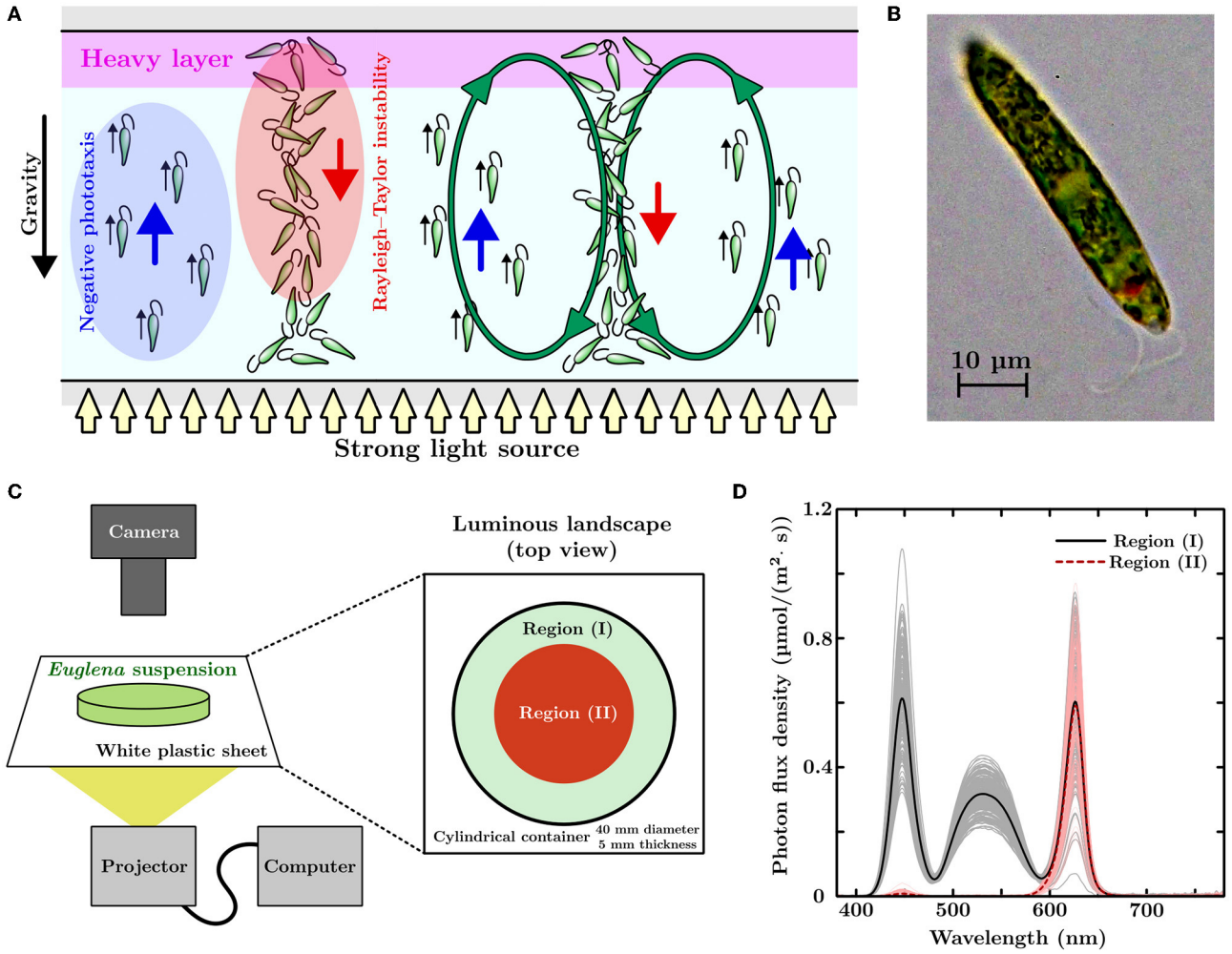

FIGURE 1
(A) Schematic of bioconvection. **(B)** Microscopic picture of *Euglena gracilis*. **(C)** Experimental setup and luminous landscape. A projector is adopted as the light source and used to illuminate a cylindrical container (diameter of 40 mm and thickness of 5 mm) containing a *Euglena* suspension. The non-uniform light environment has bright (I) and dark (II) regions. **(D)** Light brightness of each region in the luminous landscape. The black solid and red dashed lines represent the averaged profiles of photon flux density (PFD) for the white and red lights projected on the screen, respectively. Gray and bright-red lines represent PFD profiles for each measurement.

by utilizing this movements. As shown in Figure 1C, the artificial light environment had two regions, (I) and (II), with different light colors and brightness. Region (II) incorporated a darker color than that of region (I). The circle radius for region (II) was initially 20 mm (covering the whole region of the cylindrical container). The radius of this region decreased linearly with time until this region vanished after a specific designated time. The light intensity of the projected pattern fluctuated (50 Hz) due to refreshing the image. To obtain an average light brightness for each region, we measured the light 240 times using a spectrometer (MK350S Premium, UPRtek) with an exposure time of 500 μs. Figure 1D shows the profiles of photon flux density (PFD) for wavelengths from 380 nm to 780 nm. Black-solid and red-dashed lines represent the averaged PFD profiles of the light conditions that were projected in white and red colors, respectively. Gray and bright-red lines indicated the PFD profiles obtained using each measurement. The net light brightness, an integrated PFD with respect to wavelength, of the white and red regions was 55.4 μmol/m^2/s (3500 lx) and 15.6 μmol/m^2/s (695 lx), respectively.

The following image analysis was performed to quantify the relationship between *Euglena*-rich regions observed in a container and the average cell density of the suspensions. We extracted the *Euglena*-rich regions inside a container from the images of a whole region using an in-house Python program with library Pillow. We converted the images taken after region (II) vanished to 8bit-grayscale images; we then inverted the grayscale of these images. We eliminated the regions with bubbles in the images. Additionally, we set an image intensity threshold to 145 (57% of a maximum intensity on 8-bit grayscale) to extract the regions corresponding to the green haze. For all images, we utilized the same threshold value; therefore, the values in each image smaller than this threshold were considered noise and replaced with zero. We calculated the average image intensity of the converted images by dividing the sum of the image intensity of each pixel by the total number

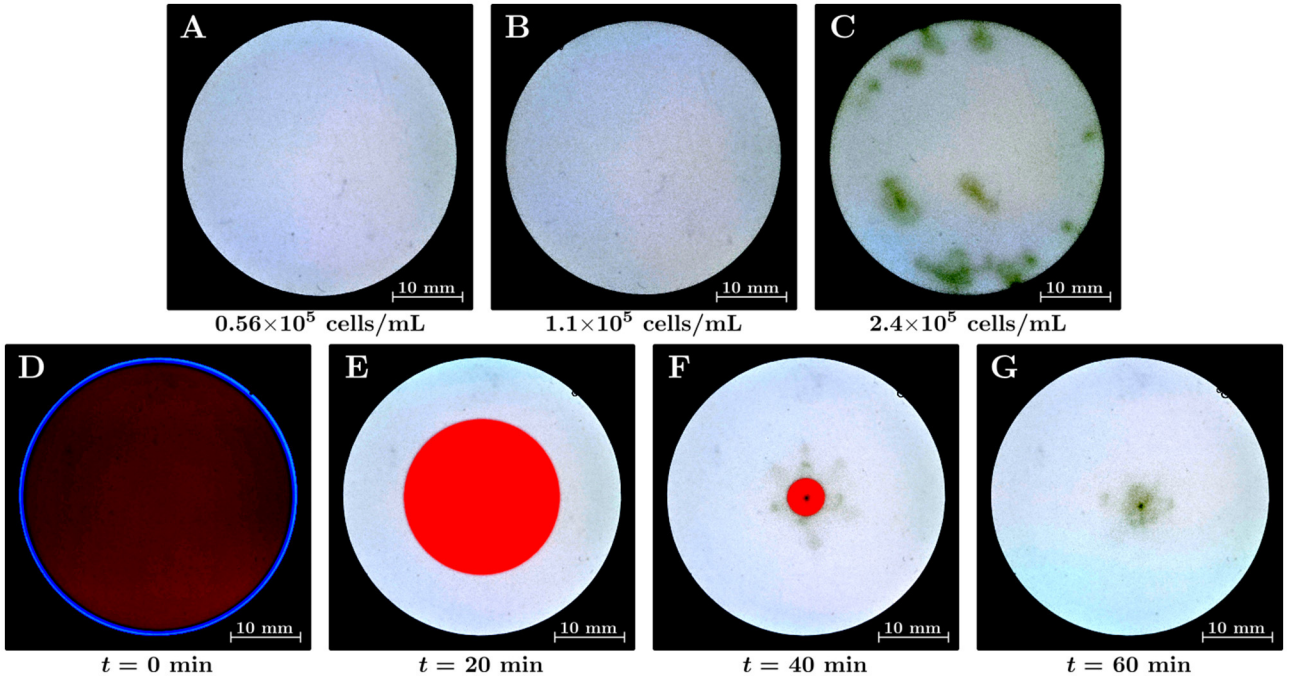

FIGURE 2
(A–C) *Euglena* bioconvection in a uniform light environment with varying average cell densities in the suspensions. The suspension is illuminated by white light over the whole region of the container from below. Snapshots are shown at $t = 15$ min. The average cell densities of the suspensions were **(A)** 0.56×10^5 cells/mL, **(B)** 1.1×10^5 cells/mL, and **(C)** 2.4×10^5 cells/mL. **(D–G)** The emergence of a bioconvection spot of *Euglena* by shrinking the red-light region (II). The duration time of the shrinking was 45 min; the average cell density of the suspension was 0.37×10^5 cells/mL.

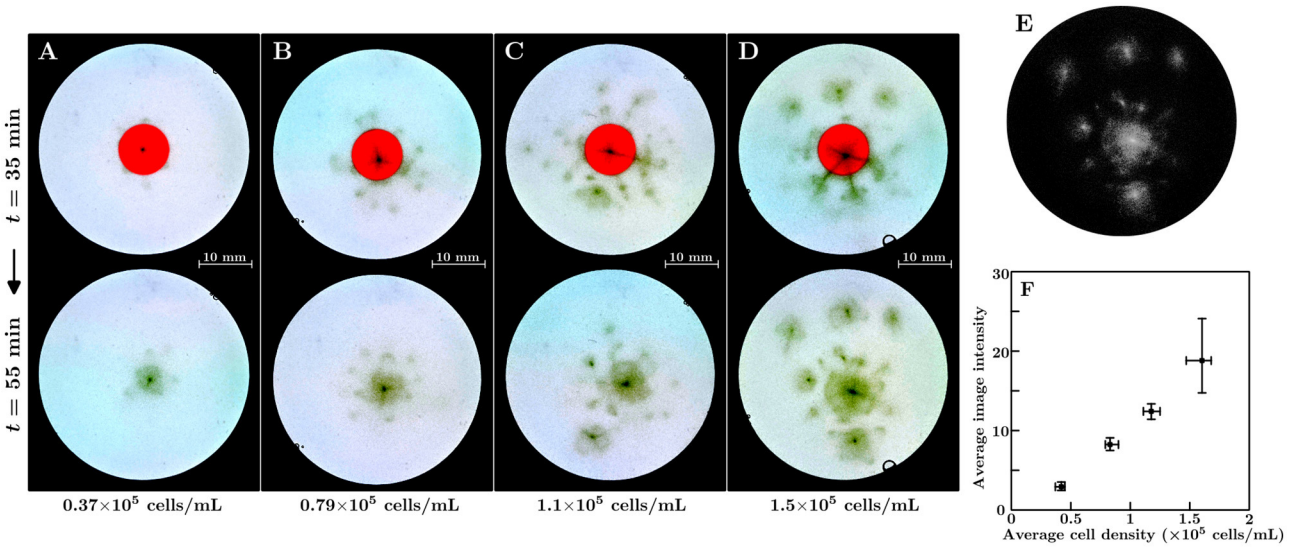

FIGURE 3
(A–D) Emergence of the bioconvection spot depends on the suspension's average cell density. The average cell density of the suspensions were as follows: **(A)** 0.37×10^5 cells/mL, **(B)** 0.79×10^5 cells/mL, **(C)** 1.1×10^5 cells/mL, and **(D)** 1.5×10^5 cells/mL. **(E)** Extraction of the dense regions in the container. The grayscale image corresponds to the lower panel of **(D)**. **(F)** The average image intensity of the extracted dense regions in the containers for the average cell density of suspension 10 min after region (II) vanished. Squares indicate mean values, and whiskers represent the minimum and maximum values.

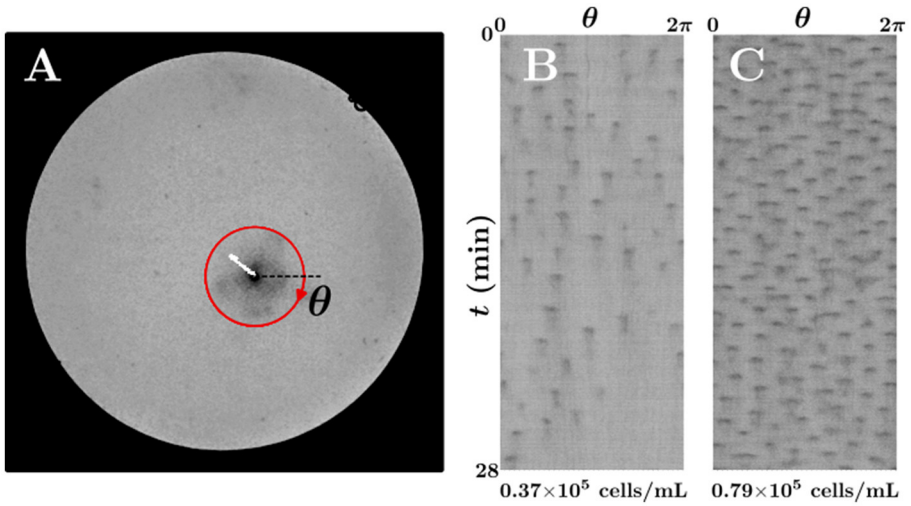

FIGURE 4
Time variations of the local cell density around the bioconvection spot. **(A)** Tracking of the spot center (white line). **(B, C)** Time variations of the image intensity along the red closed path in **(A)** for **(B)** 0.37×10^5 cells/mL and **(C)** 0.79×10^5 cells/mL suspensions.

of pixels inside the container. This average image intensity was used to represent the extent of pattern formation considering each degree of aggregation of the bioconvection cells induced within the container.

3. Results

3.1. Euglena bioconvection in uniform light

First, we analyzed the induction of *Euglena* bioconvection in a uniformly lit environment. *Euglena* suspensions of varying average cell densities were placed on the screen that was irradiated by white-colored light; then, we observed these suspensions for 30 min. The average cell densities in this study were 0.56×10^5, 1.1×10^5, and 2.4×10^5 cells/mL, as shown in Figures 2A–C, respectively. These figures correspond to snapshots taken at t = 15 min; the dark-green-colored haze in Figure 2 represents an area of high cell density. We observed the hazes from above at an angle and confirmed that the densest part of each green haze corresponded to the downward flow of the bioconvection. Figure 2C indicates that the green hazes were observed at various locations in the container, with bioconvection occurring for the 2.4×10^5 cells/mL suspension. The hazes in the central region correspond to bioconvection cells; in addition, we observed that a few hazes maintained their structure and remained close to the side wall. The bioconvection cells maintained their corresponding structure for at least 30 min; however, Figure 2C alone could not be used to determine whether these bioconvection cells can exist without interacting with other cells and/or the side walls. In contrast, the green haze was not observed for 1.1×10^5 cells/mL (Figure 1B) or 0.56×10^5 cells/mL (Figure 1A) suspensions. However, a bioconvection was observed in our experiments two out of five times for a suspension containing approximately 1×10^5 cells/mL.

3.2. Position-control experiments for the onset of bioconvection spot

We performed the position-control experiments for the emergence of a bioconvection spot using a non-uniform light environment (Figures 2D–G). The radius of region (II) decreased for 45 min, and the luminous area was gradually replaced by white light across the whole region. The average cell density of the suspension was 0.37×10^5 cells/mL. Figures 2D–G indicate the time variation of the suspension in the container: (D) at the initial state, (E) at t = 20 min, (F) at t = 40 min, and (G) at t = 60 min. The average cell density of the suspension was 0.37×10^5 cells/mL, which is more diluted than the case with no bioconvection in uniform light environment (0.56×10^5 cells/mL). We observed that a bioconvection spot emerged near the center of the container when region (II) gradually decreased in size (Figure 2F). This indicated that *Euglena* moved toward the inner side of region (II), and the local cell density inside the red region (II) became higher than that in the bright region (I). In a non-uniform stationary light environment with red and white lights, the cell density in the region illuminated by red light increases (Muku et al., 2023). The bioconvection spot maintained its structure for at least 30 min after region (II) vanished. The bioconvection spot radiates clusters of *Euglena* individuals, as pulses of local cell density, in various directions (Supplementary Movie S1).

Position-control experiments were performed with different average cell densities. The duration time of the shrinking was set to 45 min. Figures 3A–D show the corresponding results for the 0.37×10^5, 0.79×10^5, 1.1×10^5, and 1.5×10^5 cells/mL suspensions, respectively. The upper and lower parts of each figure represent snapshots taken before and after region (II) vanished. We determined that, in all suspensions, the bioconvection spot emerges at the region of the shrinking red light. However, as the average cell density increases, the bioconvection spots emerged at locations other than the target position before the region (II) vanishes. This

suggests that during the shrinking for the region (II), the local cell density in the central region becomes larger than the critical density for bioconvection.

Figure 3E shows the converted image of the lower part of Figure 3D. Figure 3F shows the average image intensities for the different average cell densities of the suspensions 10 min after region (II) vanished. A linear relationship was found between average intensity and average cell density. We performed experiments with various duration times of the shrinking for region (II) across the 15–60 min range. The average cell density of each suspension was set to $0.7–0.9\times10^5$ cells/mL. We determined that a bioconvection spot emerges at the shrinking region for all duration times tested. Even for the shortest duration time of the shrinking (15 min), we confirmed the onset of a bioconvection spot 11 out of 12 times.

Bioconvection spots in Figures 3A, B (Supplementary Movies S1, S2) were not stationary after region (II) vanishes; we determined that the pulses radiated from the spot were different regarding frequency. To characterize of the pulse radiation, we defined the spot center as the point of minimum intensity of the gray image to track the position of the bioconvection spot (Figure 4A). The white curve in Figure 4A corresponds to the trajectory of the spot center; the red circle is centered at the spot center, and the radius is 5 mm. Figures 4B, C show the intensity variations along the red closed path with respect to time, where $t = 0$ corresponds to 2 min after region (II) vanished. The darker area in the figure represents the area of high cell density. The number of pulses radiating from the center of a bioconvection spot per unit time differed in Figures 4B, C. During $0 \leq t \leq 28$ min, the total number of the radiated pulses was 55 and 150 in Figures 4B, C, respectively. Thus, the spot in the higher average cell density suspension of 0.79×10^5 cells/mL was determined to radiate more pulses.

4. Discussion

The occurrence of a bioconvection spot in *Euglena* suspension and the external light environment in this study may or may not exist in natural environment. Our experimental setups involved artificial environments designed to demonstrate that a bioconvection spot can maintain its structure alone. Further, they are used to test the behavior of the bioconvection spot, by which we can analyze the characteristics of collective motion. We call such a well-designed environment "diorama environment". We expect *Euglena*'s potential ability or adaptability that may be hidden in a complex natural environment can emerge using the diorama environment. This study could contribute to understanding microorganisms' behavioral characteristics and fluid dynamics. In an annular container, the behavior of *Euglena* bioconvection resembles that of thermal convection in binary fluid; nonetheless, their convection mechanisms are different. Overall, our position-control technique can be used for more controlled experiments, leading to an essential understanding of the dynamics of spatially localized structures.

Bioconvection did not always occur for the suspension with approximately 1×10^5 cells/mL in a uniformly lit environment. This implies that 1×10^5 cells/mL is close to the critical cell density required for bioconvection. We presumed the initial uniform distribution of cell density; however, the slight difference in initial distributions may contribute to the occurrence of bioconvection. In a uniformly lit environment, experiments for non-uniform initial distributions are difficult to conduct because of distribution control. To observe the induction of a bioconvection spot in a container, it is essential to perform position-control experiments, which manipulate the local cell density of the suspension.

We demonstrated the linear relationship between the average image intensity of bioconvection observed and the average cell density of the corresponding suspensions (Figure 3F). One factor for the linear relationship is that the number of spots increases as the suspension of average cell density increases (Figures 3B–D). However, the average image intensities differed in the suspensions of 0.37×10^5 cells/mL (Figure 3A) and 0.79×10^5 cells/mL (Figure 3B), nonetheless the number of a bioconvection spot formed was one in both suspensions. Figures 4B, C show that the spot observed in Figure 3B radiated more pulses than that in Figure 3A. These indicate that the spot in Figure 3B contains more microorganisms than that in Figure 3A. In addition, an upper limit on the number of cells in which a bioconvection spot can be constructed exists, because several bioconvection spots emerged in the higher average cell density suspension (Figures 3C, D). Considering the lower limit (the critical density for bioconvection), we suggest that the effective cell number range exists to maintain the bioconvection spot structure.

5. Conclusion

We established position-control experiments and determined that a bioconvection spot can exist independently and radiate pulses of local cell density. Moreover, we showed that the behavior of pulses changes depending on the average cell density of the suspension used. Our new experimental setup is expected to understand the localized bioconvection of *Euglena* and to reveal the behavioral characteristics of an isolated single three-dimensional bioconvection cell (bioconvection spot). For example, by using this setup, we can investigate the competition between the spots in events such as collision and coexistence. This can be conducted by generating two controlled bioconvection spots in a container that approach each other. In future studies, we will investigate the factors involved in the structural changes of bioconvection spots and aim to elucidate the mechanism of these radiated pulses and the laws of motion that govern them.

Data availability statement

The original contributions presented in the study are included in the article/Supplementary material, further inquiries can be directed to the corresponding author.

Author contributions

HY, NS, and MI conceptualized the research and designed the experimental setup. SI cultivated and provided *Euglena*. HY, TK, and KM conducted preliminary experiments to establish the experiments. HY performed the experiments, analyzed the data, and drafted the manuscript. All authors confirmed the manuscript and contributed to the revision. All authors contributed to the article and approved the submitted version.

Funding

This work was partially supported by JSPS KAKENHI (21H05311).

Acknowledgments

The authors thank Dr. Charles Fosseprez and Prof. Yukinori Nishigami at Hokkaido University for their helpful comments on the experimental setup and analyses.

Conflict of interest

The authors declare that the research was conducted in the absence of any commercial or financial relationships that could be construed as a potential conflict of interest.

Publisher's note

All claims expressed in this article are solely those of the authors and do not necessarily represent those of their affiliated organizations, or those of the publisher, the editors and the reviewers. Any product that may be evaluated in this article, or claim that may be made by its manufacturer, is not guaranteed or endorsed by the publisher.

Supplementary material

The Supplementary Material for this article can be found online at: https://www.frontiersin.org/articles/10.3389/fevo.2023.1132956/full#supplementary-material

References

Arrieta, J., Polin, M., Saleta-Piersanti, R., and Tuval, I. (2019). Light control of localized photobioconvection. *Phys. Rev. Lett.* 123, 158101. doi: 10.1103/PhysRevLett.123.158101

Bensimon, D., Kolodner, P., Surko, C. M., Williams, H., and Croquette, V. (1990). Competing and coexisting dynamical states of travelling-wave convection in an annulus. *J. Fluid Mech.* 217, 441–467. doi: 10.1017/S0022112090000799

Berg, H. C. (1975). Bacterial behaviour. *Nature* 254, 389–392. doi: 10.1038/254389a0

Diehn, B. (1973). Phototaxis and sensory transduction in E uglena. *Science* 181, 1009–1015. doi: 10.1126/science.181.4104.1009

Häder Häder, D.-P., and Iseki, M. (2017). *Photomovement in Euglena*. Cham: Springer International Publishing.

Häder, D.-P., Hemmersbach, R., and Lebert, M. (2005). "Gravity and the behavior of unicellular organisms," in *Developmental and Cell Biology Series*. Cambridge: Cambridge University Press.

Muku, K., Yamashita, H., Kamikubo, T., Suematsu, N. J., and Iima, M. (2023). Long-time behavior of swimming *Euglena gracilis* in a heterogenous light environment. *Front. Cell Dev. Biol.* 11, 1133028. doi: 10.3389/fcell.2023.1133028

Ogawa, T., Izumi, S., and Iima, M. (2017). Statistics and stochastic models of an individual motion of photosensitive alga *Euglena gracilis. J. Phys. Soc. Jpn* 86, 074401. doi: 10.7566/JPSJ.86.074401

Ogawa, T., Shoji, E., Suematsu, N. J., Nishimori, H., Izumi, S., Awazu, A., et al. (2016). The flux of *Euglena gracilis* cells depends on the gradient of light intensity. *PLoS ONE* 11, e0168114. doi: 10.1371/journal.pone.0168114

Pedley, T. J., and Kessler, J. O. (1992). Hydrodynamic phenomena in suspensions of swimming microorganisms. *Annu. Rev. Fluid Mech.* 24, 313–358. doi: 10.1146/annurev.fl.24.010192.001525

Platt, J. R. (1961). "bioconvection patterns" in cultures of free-swimming organisms. *Science* 133, 1766–1767. doi: 10.1126/science.133.3466.1766

Ramamonjy, A., Dervaux, J., and Brunet, P. (2022). Nonlinear phototaxis and instabilities in suspensions of light-seeking algae. *Phys. Rev. Lett.* 128, 258101. doi: 10.1103/PhysRevLett.128.258101

Rossi, M., Cicconofri, G., Beran, A., Noselli, G., and DeSimone, A. (2017). Kinematics of flagellar swimming in *Euglena gracilis*: helical trajectories and flagellar shapes. *Proc. Natl. Acad. Sci.* 114, 13085–13090. doi: 10.1073/pnas.1708064114

Shoji, E., Nishimori, H., Awazu, A., Izumi, S., and Iima, M. (2014). Localized bioconvection patterns and their initial state dependency in *Euglena gracilis* suspensions in an annular container. *J. Phys. Soc. Jpn.* 83, 043001. doi: 10.7566/JPSJ.83.043001

Suematsu, N. J., Awazu, A., Izumi, S., Noda, S., Nakata, S., and Nishimori, H. (2011). Localized bioconvection of *Euglena* caused by phototaxis in the lateral direction. *J. Phys. Soc. Jpn.* 80, 064003. doi: 10.1143/JPSJ.80.064003

Tsang, A. C. H., Lam, A. T., and Riedel-Kruse, I. H. (2018). Polygonal motion and adaptable phototaxis via flagellar beat switching in the microswimmer *Euglena gracilis. Nat. Phys.* 14, 1216–1222. doi: 10.1038/s41567-018-0277-7

Wager, H. W. T. (1911). On the effect of gravity upon the movements and aggregation of *Euglena viridis, Ehrb.*, and other micro-organisms. *Philos. Trans. R. Soc. B* 201, 333–390. doi: 10.1098/rstb.1911.0007

Watanabe, T., Iima, M., and Nishiura, Y. (2012). Spontaneous formation of travelling localized structures and their asymptotic behaviour in binary fluid convection. *J. Fluid. Mech.* 712, 219–243. doi: 10.1017/jfm.2012.413

Watanabe, T., Toyabe, K., Iima, M., and Nishiura, Y. (2011). Time-periodic traveling solutions of localized convection cells in binary fluid mixture. *Theor. Appl. Mech. Jpn.* 59, 211–219. doi: 10.11345/nctam.59.211

Williams, C. R., and Bees, M. A. (2011). A tale of three taxes: photo-gyro-gravitactic bioconvection. *J. Exp. Biol.* 214, 2398–2408. doi: 10.1242/jeb.051094

frontiers | Frontiers in Cell and Developmental Biology

TYPE Original Research
PUBLISHED 23 June 2023
DOI 10.3389/fcell.2023.1126819

OPEN ACCESS

EDITED BY
Namrata Gundiah,
Indian Institute of Science (IISc), India

REVIEWED BY
Takashi Miura,
Kyushu University, Japan
Rui Travasso,
University of Coimbra, Portugal

*CORRESPONDENCE
Katsuhiko Sato,
katsuhiko_sato@es.hokudai.ac.jp

RECEIVED 19 December 2022
ACCEPTED 30 May 2023
PUBLISHED 23 June 2023

CITATION
Sato K (2023), A cell membrane model that reproduces cortical flow-driven cell migration and collective movement. *Front. Cell Dev. Biol.* 11:1126819. doi: 10.3389/fcell.2023.1126819

A cell membrane model that reproduces cortical flow-driven cell migration and collective movement

Katsuhiko Sato*

Research Institute for Electronic Science, Hokkaido University, Sapporo, Japan

Many fundamental biological processes are dependent on cellular migration. Although the mechanical mechanisms of single-cell migration are relatively well understood, those underlying migration of multiple cells adhered to each other in a cluster, referred to as cluster migration, are poorly understood. A key reason for this knowledge gap is that many forces—including contraction forces from actomyosin networks, hydrostatic pressure from the cytosol, frictional forces from the substrate, and forces from adjacent cells—contribute to cell cluster movement, making it challenging to model, and ultimately elucidate, the final result of these forces. This paper describes a two-dimensional cell membrane model that represents cells on a substrate with polygons and expresses various mechanical forces on the cell surface, keeping these forces balanced at all times by neglecting cell inertia. The model is discrete but equivalent to a continuous model if appropriate replacement rules for cell surface segments are chosen. When cells are given a polarity, expressed by a direction-dependent surface tension reflecting the location dependence of contraction and adhesion on a cell boundary, the cell surface begins to flow from front to rear as a result of force balance. This flow produces unidirectional cell movement, not only for a single cell but also for multiple cells in a cluster, with migration speeds that coincide with analytical results from a continuous model. Further, if the direction of cell polarity is tilted with respect to the cluster center, surface flow induces cell cluster rotation. The reason why this model moves while keeping force balance on cell surface (i.e., under no net forces from outside) is because of the implicit inflow and outflow of cell surface components through the inside of the cell. An analytical formula connecting cell migration speed and turnover rate of cell surface components is presented.

KEYWORDS

force balance, surface flow, cell cluster migration, cell cluster rotation, analytical formula for cell migration, mechanical model

1 Introduction

Cellular migration is a key component of numerous biological processes, including the morphogenesis of multicellular organisms, wound healing, and cancer metastasis (Friedl and Gilmour, 2009; Scarpa and Mayor, 2016; Bodor et al., 2020). Consequently, elucidating the molecular and biophysical mechanisms that control cell movement can provide fundamental insight to enhance our understanding of these critical processes. Notably, although the mechanisms controlling single-cell migration are relatively well understood (Bodor et al.,

2020), those underlying multiple-cell migration, wherein cells adhere to each other and form a cluster, prior to undergoing unidirectional (Haas and Gilmour, 2006; Weijer, 2009; Haigo and Bilder, 2011; Montell et al., 2012; Kuwayama and Ishida, 2013; Pagès et al., 2022) and rotational motion (Founounou et al., 2021), referred to as cluster migration, remain unclear. One reason for this is that the phenomenon of cluster migration involves what is known as a many-body problem. That is, within cells, there are many forces related to cell movement, such as contraction forces coming from actomyosin, adhesion forces between cells, hydrostatic pressure from cytosol, and forces from adjacent cells; cell movement is a result of balance between these forces. Thus, whereas it is challenging to determine how cell membranes move under this force balance even for a single cell, it is even more difficult in the case of multiple cells, particularly when trying to understand how multiple cells coordinately move. In such complex scenarios, mechanical modeling approaches may be useful, given that these methods guarantee force balance for every element and hence, generate results that can be relied upon with some conviction.

Cell movements are mainly classified into one of two types (Callan-Jones and Voituriez, 2016). In mesenchymal migration, the cell attaches to a substrate at focal adhesions and extends its body at the leading edge by forming lamellipodia and filopodia (Innocenti, 2018). During this process, a retrograde flow of actin filaments is observed beneath the plasma membrane of the cell (Haas and Gilmour, 2006; Case and Waterman, 2015). The second type of cell movement is amoeboid migration; in this case, specific adhesion to the substrate is not necessarily required, but, nonspecific friction between the cell membrane and the surrounding matrix is thought to be sufficient for migration (Lämmermann et al., 2008; Reversat et al., 2020; O'Neill et al., 2018; Farutin et al., 2019). By contracting the rear part of the cell body via a force generated from the actomyosin meshwork under the plasma membrane, the cell increases hydrostatic pressure within the cytosol and produces blebs at the leading edge to extend its body forward (Paluch and Raz, 2013). During ameboid migration, cortical flow from front to rear is observed inside the cell, which is believed to play an important role in this process (Bergert et al., 2015). The shapes of cells undergoing each mode of migration are also different. That is, cells performing amoeboid migration are relatively rounded, whereas those engaging in mesenchymal migration are relatively elongated (Haas and Gilmour, 2006). Recent studies, however, have begun to suggest that this concept of cell movement involving two distinct migration modes is too limited and does not allow the rigorous classification of all cell movements (Bodor et al., 2020). Indeed, some cells exhibit both mesenchymal and amoeboid-like movement modes and plastically switch between these, depending on the environmental conditions (Bergert et al., 2012; Ruprecht et al., 2015). Thus, some investigators have initiated studies aimed at identifying shared universal mechanisms underlying all cell migration.

From a mechanical modeling viewpoint, a number of common features present in both the mesenchymal and amoeboid modes of migration can be identified. For example, bleb formation in amoeboid migration and lamellipodia formation in mesenchymal migration are similar, given that, in both cases, the membrane in the front region of the cell tends to expand. Mechanically, this behavior of the cell membrane at the leading edge is expressed by weak surface tension. Strong attachment between membrane and substrate in mesenchymal migration and nonspecific friction in amoeboid migration are also expressed by one parameter of a mechanical model. That is, strong attachment is expressed by a large friction coefficient value between membrane and substrate, whereas weak nonspecific friction is expressed by a small friction coefficient value. Moreover, in both modes, contractions at the trailing end of the cell membrane are expressed by a strong surface tension in that region. These observations highlight the common mechanistic features underlying all forms of cell migration. Further, in both migration modes, cortical flow beneath the plasma membrane is present and is thought to play an important role in cell movement (Bray and White, 1988; Salbreux et al., 2012). However, as noted above, because there are many forces within cells, even if we focus only on the cell membrane, it is very hard to anticipate how cell membranes move and how cells ultimately move eventually under these myriad forces. Therefore, to better understand the mechanical mechanisms underlying cell migration, mechanical models that appropriately express forces within the cells and keep these forces balanced at each point on the cell membrane are needed.

A number of mechanical models for cell migration that satisfy these conditions have been developed. For example, some groups have proposed excellent three-dimensional (3D) surface models, in which directed surface flow and cell division are reproduced (Mietke et al., 2019; Bächer et al., 2021; Okuda et al., 2022). However, 3D mechanical models require a long computational time and are not appropriate for dealing with multiple cells simultaneously. In 2D cases, cellular vertex models are frequently used for describing multiple cell dynamics, wherein cells are approximated by polygons, and cell boundaries between adjacent cells are represented by straight segments (Fletcher et al., 2014). This model have succeeded in explaining important phenomena in epithelial sheets (Farhadifar et al., 2007; Rauzi et al., 2008; Aigouy et al., 2010; Fletcher et al., 2014; Sato et al., 2015a). However, if we extend this 2D cellular vertex model and try to more precisely describe cell surface dynamics on the substrate, some problems arise. One minor problem is that because the cell boundary between adjacent cells is represented by a straight segment, the model does not appropriately express the curvature of the cell boundary. This can be overcome relatively easily, however, by adding vertices to split the straight segment into multiple segments.

If we try to extend the 2D cellular vertex model to deal with curved cell boundaries with multiple segments, the expression of frictional force can be a major problem. In the current vertex model, only the vertices of polygons experience friction forces from the surrounding objects (Fletcher et al., 2014). This means that if a cell boundary is divided into some number of segments to express its curvature more smoothly, the friction forces on the cell boundary can change depending on the number of segments. For example, let us consider the case where we represent a straight boundary between cells A and B in two ways. One is that the cell boundary is represented by one segment specified by vertices 1 and 2. The other is that we add a new vertex 3 to the segment 12 and split the segment into two segments (i.e., the cell boundary is now represented by two segments, segment 13 and segment 32). Then, we consider the case where the cell boundary shifts slightly. In that motion, the latter representation of the cell

boundary obviously experiences a larger friction force than the former representation if the friction coefficients are the same, because the latter representation has three vertices whereas the former representation has two vertices. Friction force on the cell boundary should not depend on discretization of the cell boundary, but instead, should satisfy a continuous limit (i.e., the frictional force is expressed by a quantity per unit length of the cell boundary). Recently a 2D continuous mathematical model has been proposed that successfully reproduces the adhesion-independent movement of a single cell confined in a 3D space under axisymmetric conditions (Jankowiak et al., 2020). However, this model can assess only one cell. To comprehensively investigate cell migration, mechanical models capable of treating multiple cells that adhere to each other and satisfying force balance on the cell surface are necessary.

Here, we present a 2D cell membrane model, in which cells on a substrate are represented by polygons, and various forces on the cell surface, including contraction forces from actomyosin, adhesion between cells, and hydrostatic pressure from the cytosol, are implemented and balanced on the surface at all times. This model is equivalent to a continuous model if the lengths of segments representing the cell surface are kept within an appropriate range, using defined replacement rules, as described below. Cell clusters are represented by allowing a common surface between adjacent cells. We show that if cells in this model have a polarity expressed by direction-dependent surface tension, this causes the cell surface to flow from front to rear, and that flow induces unidirectional cell movement, not only for a single cell but also for a cluster of cells. In addition, if the surface-tension polarities of cells within the cluster are tilted with respect to the center of the cluster, the clusters rotate around the cluster center. This mechanical model produces movement while keeping forces balanced on the cell surface due to the inflow and outflow of cell surface components from inside the cell. The relationship between cell migration speed and turnover rate of cell surface components is discussed in Section 3.5.

2 Model

2.1 The situations treated by the mechanical model

We consider situations where cells are on a substrate; some cells exist individually on the substrate, while other cells are attached to each other to form a cluster. We focus on the dynamics of the peripheries of the cells, which movements are determined by force balance on the cell boundaries. Each cell has a polarity, and depending on the direction of the polarity, each cell changes the strength of contraction force on the cell boundary. We are concerned with two setups of cell polarity. One is that there is a chemoattractant gradient in a definite direction on the substrate, say the x-direction, and all cells have polarity in the x direction (Sections 3.2–3.6). The other is that cells that form a cluster have different directions of polarity. To be specific, the direction of polarity of each cell tilts with respect to the center of the cluster (Section 3.7). This tilted polarity may be achieved by chance or by using chirality of the cells (Taniguchi et al., 2011; Tee et al., 2015; Wan et al., 2016). A characteristic point of our model is that force balance holds at any parts of the cell boundaries at any time.

2.2 Setup of the model

In our model, cells on a substrate are represented by polygons; specifically, the α-th cell is represented by a polygon that consists of N_α segments and N_α nodes (Figure 1A). The number N_α can differ from cell to cell and changes with time, based on the following rules: if the segment under consideration becomes longer than some critical length ℓ^*_{long}, it is split into two segments by creating a new node at the center of the segment, and if the segment under consideration becomes shorter than some critical length ℓ^*_{short}, it is replaced by a single node whose position is the center of the segment before the replacement (Figure 1B). Using appropriate ℓ^*_{long} and ℓ^*_{short} values, the surface of the cell becomes smooth enough, and the dynamics of this discretized model are consistent with those observed in continuous models, as shown in Figures 1C, 2B, C. When a cell adheres to an adjacent cell, the segments and nodes on the cell boundary are shared between the two cells; that is, they have the same segments and nodes at their boundary (Figure 1A). Quantities assigned to the cell boundary, such as surface tension and rigidity of the cell boundary, are obtained by considering each quantity on the surfaces of the two cells, as in the existing vertex models (Fletcher et al., 2014).

Cell boundaries experience two types of forces: one is the frictional forces that are expressed by the dissipation function given in Eq. 1, and the other is the mechanical forces that are expressed by a potential function U in Eq. 2. Frictional forces arise from both external and internal factors. When the segments comprising the cells move with respect to the substrate, each segment bears a frictional force from the substrate, whose strength is proportional to the length and velocity of the segment. The frictional coefficient can depend on the direction of movement relative to the direction of the segment; that is, when the segment moves parallel to the direction of the segment, the frictional coefficient is $\eta_\parallel$, whereas when the segment moves perpendicular to the direction of the segment, the frictional coefficient is $\eta_\perp$. In addition, it is assumed that each segment has an internal friction; when a segment shrinks or expands, a resistance force arises within the segment. The strength of the internal friction is proportional to the strain rate of the segment, with the friction coefficient μ. Elongation or shrinkage of the segment is assumed to be an affine transformation (i.e., the segment is homogeneously elongated or shrunken). Under these assumptions, we can calculate the dissipation function W, which gives the frictional forces on segments in terms of only the positions and velocities of nodes on the cell surfaces (see Supplementary Appendix A for details), as

$$W = \sum_{\langle ij \rangle} \left\{ \frac{\eta_\parallel^{(ij)} \ell_{ij}}{2} \left(\left(\dot{X}_{ij} \cos\theta_{ij} + \dot{Y}_{ij} \sin\theta_{ij} \right)^2 + \frac{\left(\dot{\ell}_{ij} \right)^2}{12} \right) + \frac{\eta_\perp^{(ij)} \ell_{ij}}{2} \left[\left(\dot{X}_{ij}{}^2 + \dot{Y}_{ij}{}^2 + \frac{\left(\dot{\ell}_{ij} \right)^2}{12} + \frac{\left(\dot{\theta}_{ij} \ell_{ij} \right)^2}{12} \right) - \left(\left(\dot{X}_{ij} \cos\theta_{ij} + \dot{Y}_{ij} \sin\theta_{ij} \right)^2 + \frac{\left(\dot{\ell}_{ij} \right)^2}{12} \right) \right] + \frac{\mu^{(ij)}}{2} \frac{\left(\dot{\ell}_{ij} \right)^2}{\ell_{ij}} \right\}. \tag{1}$$

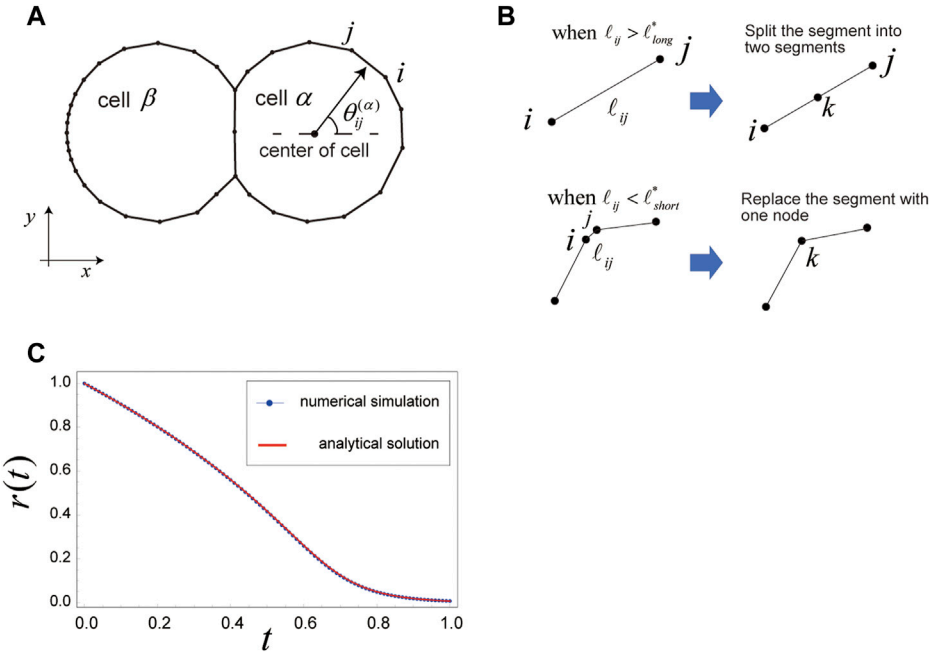

FIGURE 1
Setup for the two-dimensional (2D) cell membrane model of cell migration. **(A)** In this model, cells on a substrate are represented by polygons. If a cell adheres to an adjacent cell, the two cells share the segments and nodes on the joint boundary. The cell surface experiences various mechanical forces that are expressed by W and U in Eqs. 1, 2, respectively. These forces are balanced at all times on the cell surface, as shown in Eq. 3. **(B)** Replacement rules for cell boundary segments are as follows. When the length ℓ_{ij} of segment ij on a cell boundary exceeds a critical length, ℓ^*_{long}, the segment ij is split into two segments, ik and kj, at the next step, creating a new node k at the center of the previous segment ij. When ℓ_{ij} becomes less than a critical length, ℓ^*_{short}, the segment ij is replaced with a new node k, whose position is the center of the previous segment, ij. If appropriate lengths of ℓ^*_{long} and ℓ^*_{short} are chosen, the cell shape is kept smooth, and movement of the cell surface coincides with that observed under a continuous limit (e.g., Figures 2B, C). **(C)** Comparison between the numerical simulation and analytical solution for $r(t)$, where $r(t)$ is the radius of a circular cell that shrinks with constant surface tension $\gamma = 1$, and there are no constraints on area and perimeter of the cell. The parameters used here are as follows: $\eta = 1.0$, $\mu = 0.1$, $K = 0$, $K_p = 0$, $\kappa^{(ijk)} = 0$, and $\Delta t = 1/10000$. The initial configuration for the numerical simulation is a regular 40-sided polygon, with $r = 1$.

Here, ℓ_{ij} is the length of the segment that connects the ith and jth nodes; that is, $\ell_{ij} = |\mathbf{r}^{(i)} - \mathbf{r}^{(j)}|$, where $\mathbf{r}^{(i)} = (x_i, y_i)$ is the position of the ith node. $\mathbf{R}_{ij} = (X_{ij}, Y_{ij})$ is the position of the center of the segment ij, given by $\mathbf{R}_{ij} = (\mathbf{r}^{(i)} + \mathbf{r}^{(j)})/2$, and θ_{ij} is the angle between the x-axis and the vector from the i-th node to the j-th node. The dot over a quantity represents its time derivative, and the symbol $\langle ij \rangle$ under the summation symbol means that the sum is taken over all the segments in the system. Note that the sets of $\{\mathbf{R}_{ij}\}$, $\{\theta_{ij}\}$ and $\{\ell_{ij}\}$ are expressed by the set of positions of nodes, $\{\mathbf{r}^{(i)}\}$. Thus, as mentioned above, W is a function of $\{\mathbf{r}^{(i)}\}$ and $\{\dot{\mathbf{r}}^{(i)}\}$.

The frictional coefficients $\eta_{\parallel}^{(ij)}$, $\eta_{\perp}^{(ij)}$, and $\mu^{(ij)}$ in Eq. 1 can vary from segment to segment. However, our main objective is to show some simple applications of this model. We, therefore, kept these coefficients the same for every segment, such that $\eta_{\parallel}^{(ij)} = \eta_{\perp}^{(ij)} = \eta$ and $\mu^{(ij)} = \mu$ throughout this paper. Differentiating W in Eq. 1 with respect to the velocity the i-th node gives the frictional force $\mathbf{F}^{(i)}_{friction}$ on the i-th node as $\mathbf{F}^{(i)}_{friction} = -\partial W/\partial \dot{\mathbf{r}}^{(i)}$ (Landau and Lifshitz, 1976). Note that the dissipation function W in Eq. 1 considers the length dependence of the frictional force on the segment. Thus, even if a segment ij is divided into two segments, ik and kj, by adding a new node k, the total frictional forces on the segments ik and kj are the same as those on the segment ij before the division, provided movement of segments ik and kj is the same as that of segment ij. In this sense, the frictional force on the cell surface does not depend on the number of nodes on the cell surface and this model satisfies some continuous limits on the frictional forces.

The other mechanical forces on the cell surface, such as contraction forces coming from the actomyosin network beneath the plasma membrane and hydrostatic pressure from the cytosol, are represented by the following effective potential U, as follows:

$$U = \frac{K}{2}\sum_{\alpha}\left(A_\alpha - A_\alpha^{(0)}\right)^2 + \frac{K_p}{2}\sum_{\alpha}\left(L_\alpha - L_\alpha^{(0)}\right)^2 + \frac{1}{2}\sum_{\langle ijk\rangle}\kappa^{(ijk)}\left(\frac{\mathbf{r}^{(j)} - \mathbf{r}^{(i)}}{\ell_{ij}} - \frac{\mathbf{r}^{(k)} - \mathbf{r}^{(j)}}{\ell_{jk}}\right)^2 \frac{2}{\ell_{ij} + \ell_{jk}} + \sum_{\langle ij\rangle}\gamma_{ij}(t)\ell_{ij}, \tag{2}$$

where K, K_p, and $\kappa^{(ijk)}$ are non-negative constants. This form of U is quite similar to that given in existing vertex models (Farhadifar et al., 2007; Fletcher et al., 2014; Sato et al., 2015b), although it differs in the introduction of the third term, which represents the bending energy of cell membranes, and the form of $\gamma_{ij}(t)$, which expresses the strengh of surface tension on the cell membrane and is related to cell polarity.

The first term in Eq. 2 represents a pressure acting on the segments arising from the area difference between the current area of the cell, A_α, and its preferred constant value, $A_\alpha^{(0)}$. This

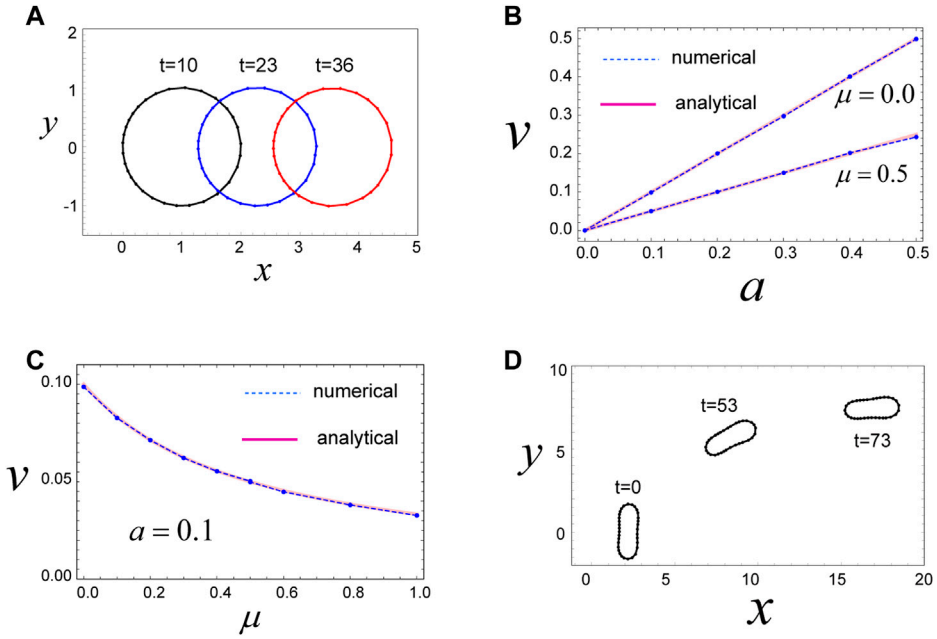

FIGURE 2
Mechanism for migration of a circular and non-circular cell. **(A)** A circular cell migrates in the x-direction due to the direction-dependent surface tension in Eq. 4, which generates a continuous flow of cell surface from front to rear. The cell movement is maintained as long as the cell has the polarity expressed by Eq. 4. Parameters used are as follows: $\mu = 0$, $\gamma_0 = 1.0$, $a = 0.1$, $\ell^*_{long} = 0.31$, $\ell^*_{short} = 0.12$, $K = 100$, $K_p = 0$, and $\kappa^{(ijk)} = 0$. **(B)** The steady speed v of circular cell movement as a function of a that represents the degree of polarization of the cell (see Eq. 4). The numerical results (dashed lines) and analytical results (red lines) show good agreement with one another, indicating that our discrete model, described by Eqs 1–3, coincides with a continuous model if we choose appropriate values for ℓ^*_{long} and ℓ^*_{short}. Parameters used are as follows: $\gamma_0 = 1.0$, $\ell^*_{long} = 0.31$, $\ell^*_{short} = 0.12$, $K = 100$, $K_p = 0$, and $\kappa^{(ijk)} = 0$. **(C)** The steady speed v of circular cell movement as a function of μ, which is the friction coefficient for internal friction of the cell surface, defined in Eq. 1. The analytical results (red curve) and numerical results (dashed curve) are in agreement with one another. Parameters used are as follows: $\gamma_0 = 1.0$, $a = 0.1$, $\ell^*_{long} = 0.31$, $\ell^*_{short} = 0.12$, $K = 100$, $K_p = 0$, and $\kappa^{(ijk)} = 0$. **(D)** A non-circular cell also migrates due to the direction-dependent surface tension in Eq. 4. In the final state, the long axis of the cell is aligned in the x-axis. Parameters used here are $\mu = 0$, $\gamma_0 = 0$, $a = 0.2$, $\ell^*_{long} = 0.4$, $\ell^*_{short} = 0.15$, $K = 1.0$, $K_p = 1.0$, $\kappa^{(ijk)} = 0.1$, and $L_0 = 0.25\,\pi$.

pressure can be interpreted as the hydrostatic pressure in the cytosol on the membrane of the cell. The α under the summation symbol indicates that the sum is taken over all cells in the system. The second term in Eq. 2 expresses the property that the cell tends to keep the perimeter length L_α at some preferable length $L_\alpha^{(0)}$. This term represents the tendency to conserve the amount of cell membrane (Fletcher et al., 2014; Sato, 2017). The third term in Eq. 2 expresses the bending energy of the membrane. The strength of the membrane against bending is characterized by the coefficient $\kappa^{(ijk)}$, such that, if $\kappa^{(ijk)}$ is large, the part of the membrane under consideration, expressed by segments ij and jk, is difficult to bend, and *vice versa*. The symbol $\langle ijk\rangle$ under the summation symbol indicates that the sum is taken over all pairs of segments that are connected and adjacent to each other. Lastly, the final term in Eq. 2 expresses the surface tension acting on the membrane, which is the result of both contraction forces from the actomyosin networks beneath the membrane and adhesion of the cell to outside objects, such as adjacent cells or substrate. Surface tension strength, expressed by γ_{ij}, is controlled by the cell via altered expression of proteins, such as myosin, actin, cadherin, and integrin. When contraction force is strong or adhesion is weak at segment ij, γ_{ij} becomes large, whereas when adhesion at segment ij is strong or contraction force is weak at segment ij, γ_{ij} becomes small.

Using this value of γ_{ij}, we can express the polarity of the cell. For example, consider the case where a cell has a polarity in the x-direction, and assume that the cell has a weak contraction force at the leading edge ($x > x_0$, where x_0 is the x-component of the position of the cell center) and a strong contraction force at the rear ($x < x_0$). This situation is expressed by letting the value of γ_{ij} depend on the relative position of the cell membrane with respect to the center of the cell. That is, a small value is assigned to γ_{ij} at the front of the cell, and a large value is assigned to γ_{km} at the rear. In this paper, we consider several cases with different assigned γ_{ij} values. If we accept the form of U given in Eq. 2, the total mechanical force $\mathbf{F}_U^{(i)}$ from U on the i-th node is given by $\mathbf{F}_U^{(i)} = -\partial U/\partial \mathbf{r}^{(i)}$.

In this model, we assume that the inertial force of the cell surface is negligible compared with the mechanical forces in question, and thus, all forces acting on the i-th node coming from U and W must be balanced at all times. That is,

$$-\frac{\partial W}{\partial \dot{\mathbf{r}}^{(i)}} - \frac{\partial U}{\partial \mathbf{r}^{(i)}}\bigg|_{\gamma_{jk}=\hat{\gamma}_{jk}} = 0 \tag{3}$$

holds for all i's at any given time. Here, the symbol $\gamma_{jk} = \hat{\gamma}_{jk}$ in the second term indicates that, after the derivative with respect to $\mathbf{r}^{(i)}$, each γ_{jk} in the second term is replaced by an explicit value $\hat{\gamma}_{jk}$, which is expressed as a function of $\{\mathbf{r}^{(i)}\}$ (Fletcher et al., 2014; Sato et al.,

2015b; Sato, 2017). This operation means that γ_{jk} obeys some other dynamics that are much faster than those of $\{\mathbf{r}^{(i)}\}$, such that γ_{jk} immediately reaches a value determined by $\{\mathbf{r}^{(i)}\}$ (Sato, 2017). If we accept that the dynamics of localization of molecules related to contraction, such as myosin, on the cell surface (tens of seconds) is much faster than that of cell membrane movement (a few minutes), this operation may be allowed. Eq. 3 gives the time evolution equations for $\{\mathbf{r}^{(i)}\}$.

2.3 Methods for numerical simulations

To numerically solve Eq. 3, we first nondimensionalize the variables and parameters appearing in the equation, using the following units: length, $\sqrt{A_0/\pi}$; time, $\eta/(K_0\sqrt{A_0/\pi})$; and energy, $K_0(A_0/\pi)^2$; where K_0 is a typical value of K solving for U in Eq. 2. Hereafter, we imply that the variables and parameters appearing in our model are nondimensionalized with the above units. For example, $A_0 = \pi$ and $\eta = 1$. We then numerically solve the nondimensionalized Eq. 3 for $\{\mathbf{r}^{(i)}\}$ by the Euler method, with the step size dt = 1/5000 or 1/10000. For each step, we further determine whether the length of each segment satisfies the replacement criteria $\ell^*_{long} < \ell_{ij}$ or $\ell^*_{short} > \ell_{ij}$. Any segments that satisfy either of these two conditions are replaced by the rules shown in Figure 1B.

3 Results

3.1 A case in which a circular cell isotropically shrinks with a constant surface tension

To test our model, we first determine whether the dissipation function W given in Eq. 1 appropriately expresses the frictional forces on the cell surface. For this we consider a case where a circular cell has a constant surface tension $\gamma = 1$ and no constraints on its area A and perimeter L; that is, we set $K = 0, K_p = 0$, and $\kappa^{(ijk)} = 0$ in Eq. 2. In this case, the circular cell shrinks with some speed, while maintaining its circular shape. The time series of the radius of the circular cell, $r(t)$, is analytically obtained (Supplementary Appendix B), resulting in $r(t) = \sqrt{\frac{\mu}{\eta} W_0\left(\frac{\eta}{\mu} e^{-\frac{2}{\mu}\left(\gamma_0 t - \left(\frac{\eta}{2} r_0^2 + \mu \log r_0\right)\right)}\right)}$, where $W_0(x)$ is the Lambert W function (the product logarithm) that satisfies $x = W_0(x)\, e^{W_0(x)}$ for $x > -1/e$. Comparing this analytical solution with the results of numerical simulation for Eq. 3 reveals good agreement (Figure 1C). Thus, we conclude that the friction force expressed by Eq. 1 appropriately expresses the frictional force experienced by the cell membrane, at least for this simple test case.

3.2 A circular cell migrates due to direction-dependent surface tension

Next, we investigate a more realistic case wherein the cell under consideration is circular with a constant area $A = A_0$ and has a polarity in the x-direction. Constant area of the cell is achieved by using the parameters $K \gg 1$, $K_p = 0$, and $\kappa^{(ijk)} = 0$ in Eq. 2, and cell polarity is expressed by the direction-dependent surface tension $\hat{\gamma}_{ij}$ in Eq. 3 as

$$\hat{\gamma}_{ij} = \gamma_0 - a\cos\theta^{(\alpha)}_{ij}, \tag{4}$$

where γ_0 is a positive constant, a is a non-negative constant, and $\theta^{(\alpha)}_{ij}$ is the angle between the x-axis and the vector connecting the center of cell α that contains segment ij and the center of segment ij (see Figure 1A). The value of a represents the degree of the polarity, such that, when $a = 0$, the cell is isotropic and has no polarity, whereas when $a > 0$, the cell boundary at a relatively large x has a weak surface tension, and the cell boundary at a relatively small x has a strong surface tension. Hereafter, we refer to the region of cell boundary at a relatively larger x as the "front" of the cell, and the region of the cell boundary at a relatively smaller x as the "rear" of the cell. If $a = 0$, the shape of the cell is circular due to the constant area and constant surface tension, γ_0, on the cell surface. In this simulation, we set a as a small positive value ($a \ll \gamma_0$), such that the circular shape of the cell is still retained.

We then examined the steady state of the cell with these model parameters. Numerical simulations reveal that the cell moves in the positive x-direction, with a constant speed, while keeping a circular shape in the steady state (Figure 2A). The driving force for this movement is the direction-dependent surface tension in Eq. 4 and the resulting cell surface flow from the front to the rear (Supplementary Movie S1). That is, in the front region of the cell, surface tension is relatively weak due to the parameters of Eq. 4, such that the surface in the front region tends to expand. In contrast, surface tension in the rear region of the cell is relatively strong, and hence, the surface in this region tends to shrink. This surface tension-dependent tendency of the cell surface to expand or shrink produces a flow of cell membrane, in which the front region is always expanding (in some sense, blebbing is continuously occurring in front of the cell), whereas the rear region is always shrinking (Supplementary Movie S1). These behaviors act as a source and sink of cell surface and yield a flow of cell surface from front to rear. In addition, within this system, there is a frictional force between the cell surface and the substrate. Thus, if the cell surface moves in some direction, the whole cell experiences forces that move it in the opposite direction, based on the action–reaction principle.

The velocity $\mathbf{V}$ of this cell movement resulting from the direction-dependent surface tension can be analytically calculated, by treating the cell as a continuous circular object (see Supplementary Appendix C for details). The result ist

$$\mathbf{V} = \left(a/\left(\eta R\left(1 + 2\mu/\left(\eta R^2\right)\right)\right), 0\right), \tag{5}$$

where R is the radius of the circular cell. We then compared this analytical solution with the cell speed obtained by numerically solving Eq. 3 and found that these values are in good agreement with each other (Figures 2B, C). This indicates that our discrete model described by Eqs. 1–3 can describe continuous cell surface dynamics if we choose appropriate values for parameters, such as ℓ^*_{long} and ℓ^*_{short}.

3.3 An elongated cell migrates due to direction-dependent surface tension

We further find that single-cell migration induced by direction-dependent surface tension, described in Eq. 4, occurs even when the cell shape is elliptical (Figure 2D). We

can model an elliptical-shaped cell using finite values for K_p and $\kappa^{(ijk)}$ in Eq. 2 and by ensuring the preferred cell perimeter L_0 is longer than that of a circle with the area A_0, $2\sqrt{\pi A_0}$. Overall, the mechanism for cell movement is basically the same as for circular cells, that is, the surface flows from front to rear due to direction-dependent surface tension, described in Eq. 4. In this simulation, we set the initial configuration of the cell, such that the long axis is aligned in the y-direction (Figure 2D; $t = 0$). Initially, up until $t = 8$, the elliptical cell moves in the x-direction, while keeping the short axis of the cell aligned with the x-axis. However, at around $t = 25$, the long body axis begins to incline toward the x-direction, and the direction of cell movement also begins to incline; that is, the cell has the y-component of velocity (Supplementary Movie S2). In the final stage, the long body axis is completely oriented to the x-axis, and the cell moves in the x-axis again. The final speed of the cell is faster than in the earlier stage, where the long axis of the cell is perpendicular to the x-axis. This simulation indicates that if the cell shape is elliptical and the direction of cell polarity is fixed in the x-axis, cell movement in which the short axis is oriented to the x-axis is slow and unstable, whereas cell movement in which the long body axis is oriented to the x-axis is fast and stable. In general, the parameters of Eq. 4 make cell movement fast if the long axis of the cell is directed in the direction of cell polarity. This property clearly appears in the next case, where the cell is sandwiched by two parallel walls.

3.4 A case in which a cell is sandwiched by two walls

Motivated by results from published experiments (Bergert et al., 2015; Liu et al., 2015; Sakamoto et al., 2022), we next examined the scenario in which a cell is sandwiched by two parallel walls. In this case, the wall is expressed using the potential $U_{wall}(y) = (y - d)\Theta(y - d) - (y + d)\Theta(-y - d)$, where d is one-half the distance between the walls, and $\Theta(x)$ is the Heaviside step function, defined as $\Theta(x) = 1$, for $x > 0$, and $\Theta(x) = 0$, for $x \leq 0$. By adding the terms $\sum_{all\ nodes\ i's} U_{wall}(y^{(i)})$ to Eq. 2, the cell surface close to the walls experiences a repulsive force from the wall potential. In this setup, the area of the cell is held constant as $A = A_0$, which is achieved with the same parameters as used for the simulation with a circular cell. Under these conditions, the cell also migrates in the x-direction in the steady state (Figure 3A), where the speed of the cell increases as d decreases (Figure 3B), consistent with published experimental results (Liu et al., 2015; Sakamoto et al., 2022). To demonstrate how and why cell speed increases with decreased d, we derive the analytical expression for the speed of the cell (see Supplementary Appendix C), which is given by

$$V_x = \frac{2}{\pi\eta d}\left(\int_0^{\pi/2} \sin\xi_1 \frac{d\gamma(\theta_{forward}(\xi_1))}{d\xi_1}\, d\xi_1 + \int_{\pi/2}^{\pi} \sin\xi_2 \frac{d\gamma(\theta_{backword}(\xi_2))}{d\xi_2}\, d\xi_2\right) + \frac{2\Delta\gamma}{\pi\eta d}, \tag{6}$$

where $\theta_{forward}(\xi_1) = \arctan\left(\frac{d\sin\xi_1}{d\cos\xi_1 + L_x}\right)$, $\theta_{backword}(\xi_2) = \arctan\left(\frac{d\sin\xi_2}{d\cos\xi_2 - L_x}\right)$, and $\Delta\gamma = \gamma(\pi - \theta_1) - \gamma(\theta_1) = 2aL_x/\sqrt{L_x^2 + d^2}$. The

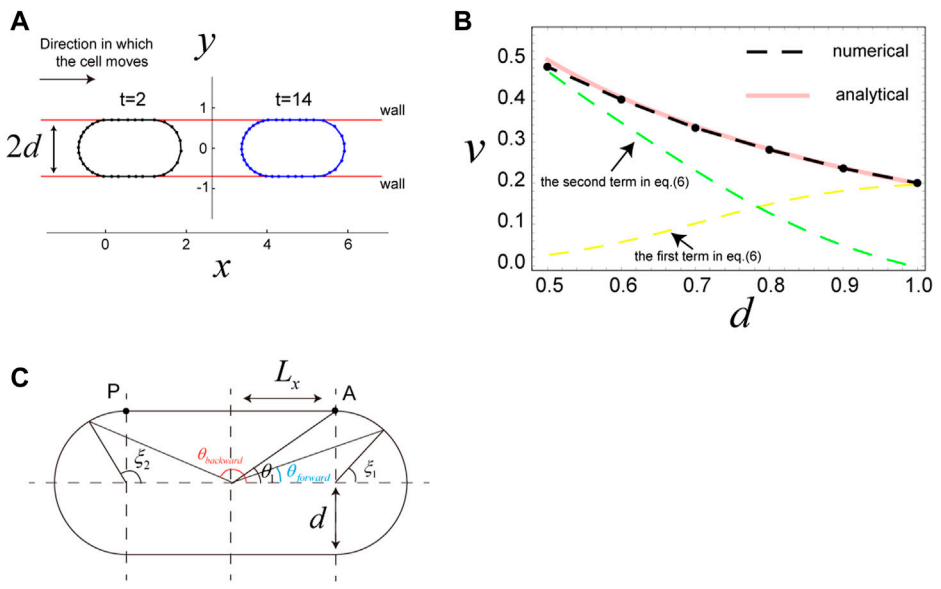

FIGURE 3
Migration of a cell sandwiched by two walls. **(A)** Snapshots of a cell sandwiched by two walls, which migrates in the x-direction due to surface flow resulting from the direction-dependent surface tension in Eq. 4. The distance between the two walls is $2d$; a decrease in d increases migration speed, v, of the cell (see panel B). Parameters used are as follows: $d = 0.7$, $\mu = 0$, $\gamma_0 = 1.0$, $a = 0.2$, $\ell^*_{long} = 0.31$, $\ell^*_{short} = 0.12$, $K = 100$, $K_p = 0$, and $\kappa^{(ijk)} = 0$. **(B)** The steady speed, v, of a cell sandwiched by walls as a function of d. The dashed black curve shows the numerical results, and the red curve represents the analytical results from Eq. 6, which are in good agreement. The yellow and green dashed curves are the first and second terms in Eq. 6, respectively. Parameters used here are the same as in panel A, except that d is varied. **(C)** Geometrical explanation of the quantities θ_1, $\theta_{forward}$, $\theta_{backword}$, ξ_1, and ξ_2 in Eq. 6.

angles $\theta_{forward}$, $\theta_{backward}$, ξ_1, and ξ_2 used here are defined as shown in Figure 3C. The values L_x and d are the half-length of the straight part of the cell and the radius of the circular part of the cell, respectively. Because the total area of the cell is kept at $A = A_0$, L_x and d are related as $4L_x d + \pi d^2 = A_0$.

Results from analytical expression Eq. 6 are in good agreement with the results of numerical simulations (Figure 3B). Thus, we use Eq. 6 to interpret the cell speed in this scenario. The first term in Eq. 6 is the contribution from surface flow on the two semicircles of the cell, and the second term is the contribution from surface flow on the straight parts of the cell. When d becomes small, the semicircles also become small, and the flow speed of cell surface along the semicircles becomes slow due to the surface tension gradient along the small semicircles. Thus, the first term in Eq. 6 becomes small when d decreases (Figure 3B, yellow dashed curve). In contrast, $\Delta\gamma$ in the second term in Eq. 6, which is the surface tension difference between the two edges of the straight parts of the cell (Figure 3C), increases with decreased d (see Eq. 4). Furthermore, d in the denominator of the second term in Eq. 6, which represents the resistance of the semicircle parts to the cell movement, also enlarges this term as the value of d decreases. Thus, the whole second term in Eq. 6 drastically increases when d decreases (Figure 3B, green dashed curve). The tendency that the migration speed v of the sandwiched cell increases with decrease in d appears even when we take a different setup of $\hat{\gamma}_{ij}$. For example, we consider the case where the surface tension is constantly increased along the cell surface form front to rear, in which the minimum and maximum surface tensions are kept to be constant, i.e., $\hat{\gamma}_{ij} = 0.8$ at the front and $\hat{\gamma}_{ij} = 1.2$ at the rear. These values are the same as those in the simulations in Figure 3B. The results of numerical simulations with this setup is given in Supplementary Figure S2, where as in Figure 3B v increases with decrease in d, while the d dependence of v is somewhat moderate compared to Figure 3B. This same tendency of v implies that the increase in v of the sandwiched cell with decrease in d may be a robust phenomena, as frequently observed in experiments (Bergert et al., 2015; Sakamoto et al., 2022).

3.5 Properties of surface flow-mediated cell migration

To better understand why and how cells move due to surface flow while keeping the forces balanced at all times, we surveyed the properties of cell movement observed in this model. Although these properties derived below are provided in a continuous form, it is not difficult to translate them into a discrete form. As noted above, our model neglects all inertia of the cell surface, so that the forces on any element of the cell surface are balanced at any time, and more importantly, the total force on the cell surface from the substrate must vanish at any time. Because the force on the cell surface from the external object—the substrate—is friction only, we have the following equality:

$$\int_\Omega \eta \mathbf{v}(\xi,t)\frac{\partial s(\xi,t)}{\partial \xi}d\xi = 0, \tag{7}$$

at any time t. Here, ξ is the material coordinate that is assigned to the element of cell surface under consideration and $s(\xi,t)$ is the counter length of the arc of cell surface between some reference point on the cell surface and the cell surface element specified by ξ at time t. Additionally, $\mathbf{v}(\xi,t)$ is the velocity of the surface element at ξ and t; Ω under the integral symbol indicates that the range of the integral is the whole cell surface. We then consider the situation where cell movement reaches a steady state, with cell velocity and cell shape constant in time, focusing on some time t_0 in this steady state. At $t = t_0$, we reassign the material coordinate ξ on the cell surface, such that ξ coincides with the counter length s; that is,

$$s(\xi,t_0) = \xi. \tag{8}$$

With this situation, let us consider the time evolution of the cell surface density, ρ. In general, ρ obeys the following time evolution equation

$$\partial\rho(\xi,t)/\partial t = -\left((\partial\mathbf{r}/\partial\xi)\cdot(\partial\mathbf{v}/\partial\xi)\right)/\left(\partial s/\partial\xi\right)^2\rho + J(\xi,t), \tag{9}$$

Where $\mathbf{r}(\xi,t)$ is the position vector of the surface element at ξ and t, and J is the flux of cell surface component from the cell inside to the cell surface per unit length. The derivation of Eq. 9 is shown in Supplementary Appendix D. In the steady state, ρ is constant in time, say $\rho = \rho_0$, and the time derivative $\partial\rho/\partial t$ is zero. Thus, from Eqs. 8, 9 we obtain

$$J(\xi,t_0) = \rho_0\,(\partial\mathbf{r}/\partial\xi)\cdot(\partial\mathbf{v}/\partial\xi), \tag{9.1}$$

which describes the relationship between J, $\mathbf{r}$, and $\mathbf{v}$ in the steady state. Because of the constant cell shape in the steady state, the total flux of the cell surface components must vanish at any time. Thus,

$$\int_\Omega J(\xi,t_0)d\xi = 0. \tag{10}$$

Interestingly, J in Eq. 9.1 is related to the cell migration velocity $\mathbf{V}$ in the steady state for the following reasons. In the steady state, the cell surface center of mass also moves with the same velocity $\mathbf{V}$. However, as indicated in Eqs. 7, 8, there is no net velocity of components on the cell surface, i.e., $\int_\Omega \mathbf{v}(\xi,t_0)d\xi = 0$. This implies that the shift in cell surface center of mass is, in fact, achieved by the inflow and outflow of cell surface components from inside the cell. Thus, the integral of the product of $J(\xi,t_0)$ and $\mathbf{r}(\xi,t_0)$ over the whole cell surface gives the transport rate of cell surface components through the inside of the cell. Dividing this quantity by the total amount of components on the cell surface, $\rho_0 L_{cell}$, yields the velocity of the cell surface center of mass. Therefore,

$$\mathbf{V} = \int_\Omega \mathbf{r}(\xi,t_0)J(\xi,t_0)d\xi/\rho_0 L_{cell}, \tag{11}$$

where L_{cell} is the cell perimeter in the steady state. Eq. 11 is interesting because this relation connects apparently different quantities, the cell migration velocity $\mathbf{V}$ and the turnover rate J of the cell surface. Indeed, we can confirm that Eqs. 7, 10, and 11 exactly hold for the circular cell migration case with $\mu = 0$ as shown below. From the analytical results given in Equation (C.16) in Supplementary Appendix C, $\mathbf{r}$ and $\mathbf{v}$ of the circular cell in the steady state are given as

$$\begin{aligned}\mathbf{r}(\xi) &= \left(\frac{a}{\eta R}t + R\cos\frac{\xi}{R}, R\sin\frac{\xi}{R}\right)\\ \mathbf{v}(\xi) &= \left(\frac{a}{\eta R} - \frac{2a}{\eta R}\left(\sin\frac{\xi}{R}\right)^2, \frac{2a}{\eta R}\sin\frac{\xi}{R}\cos\frac{\xi}{R}\right)\end{aligned}. \tag{12}$$

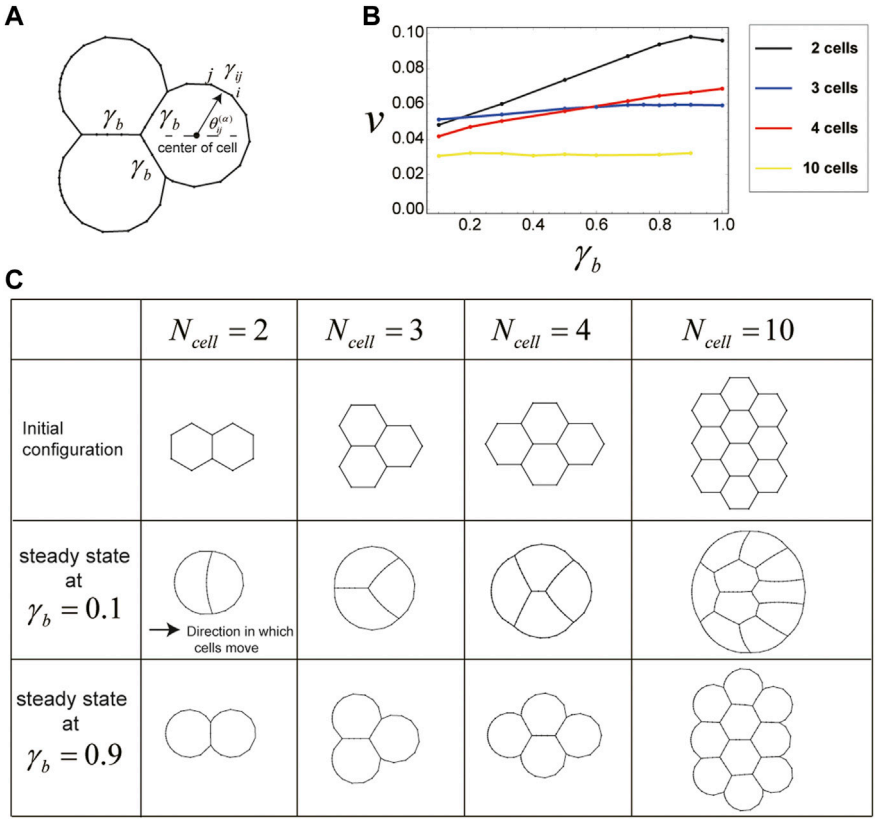

FIGURE 4
Cells in a cluster also migrate due to direction-dependent surface tension. **(A)** Setup for the surface tension of cells in a cluster. The boundaries between any two cells in the cluster have a constant surface tension γ_b, whereas the other cell surfaces, which are outside of the cluster, have the direction-dependent surface tension expressed by Eq. 4. **(B)** The steady speed v of cell cluster migration as a function of γ_b, for each cell number N_{cell}. When γ_b is increased, cluster migration speed also tends to increase. Parameters used here are as follows: $\mu = 0$, $\gamma_0 = 1.0$, $a = 0.1$, $\ell^*_{long} = 0.6$, $\ell^*_{short} = 0.08$, $K = 100$, $K_p = 0$, and $\kappa^{(ijk)} = 0$. **(C)** Shapes of cells in the cluster during steady state migration for each N_{cell} and γ_b.

From Eqs 9.1–12, we have

$$J = \rho_0 \frac{2a}{\eta R^2} \cos \frac{\xi}{R}. \tag{12.1}$$

Inserting Eqs. 12–12.1 into Eq 11 gives

$$\mathbf{V} = \left(\frac{a}{\eta R}, 0 \right), \tag{12.2}$$

where we have used $L_{cell} = 2\pi R$ and the fact that the range of ξ is $[0, 2\pi R]$. Eq. 12.2 coincides with Eq. 5 for the case of $\mu = 0$.

3.6 Multiple cells in a cluster also move via direction-dependent surface tension

The above simulations focus on migration of individual cells; however, cells often move together with other cells. Therefore, we next examined whether cell migration due to direction-dependent surface tension occurs even when multiple cells are attached to each other, forming a cluster. Specifically, we investigated the case where the number N_{cell} of cells on the substrate is $N_{cell} = 2, 3, 4, 10$ with some initial configuration in which the cells are attached to each other (Figure 4C). In these simulations, we have set the surface tension on the boundary between the cells to a constant value (*i.e.*, $\gamma = \gamma_b$), by assuming that the same type of cells is adhering to each other with some characteristic strength (Figure 4A). The other cell boundaries, which do not contact other cells, have the direction-dependent surface tension specified by Eq. 4. As in the case of single-cell migration investigated in Sections 3.2–3.4, each cell in this system keeps its area constant and has no constraint on its perimeter; that is, $K = 100$, $K_p = 0$, and $\kappa^{(ijk)} = 0$ in Eq. 2. Under these conditions, multiple cells move in the x-direction, while maintaining attachment between cells in the steady state (Figure 4C, Supplementary Movies S3–S10). Moreover, the mechanism of multiple-cell migration is basically the same as that of single-cell migration. That is, due to the direction-dependent surface tension of each cell, the surface of the cell cluster flows from front to rear, and this flow drives movement of the whole cluster.

The shape and velocity of the cluster during this movement depend on the value of γ_b. When γ_b decreases, the shape becomes round, and speed becomes slow (Figures 4B, C). The roundness of the cell cluster at small γ_b results from the constant area and lack of constraint on the perimeter of each

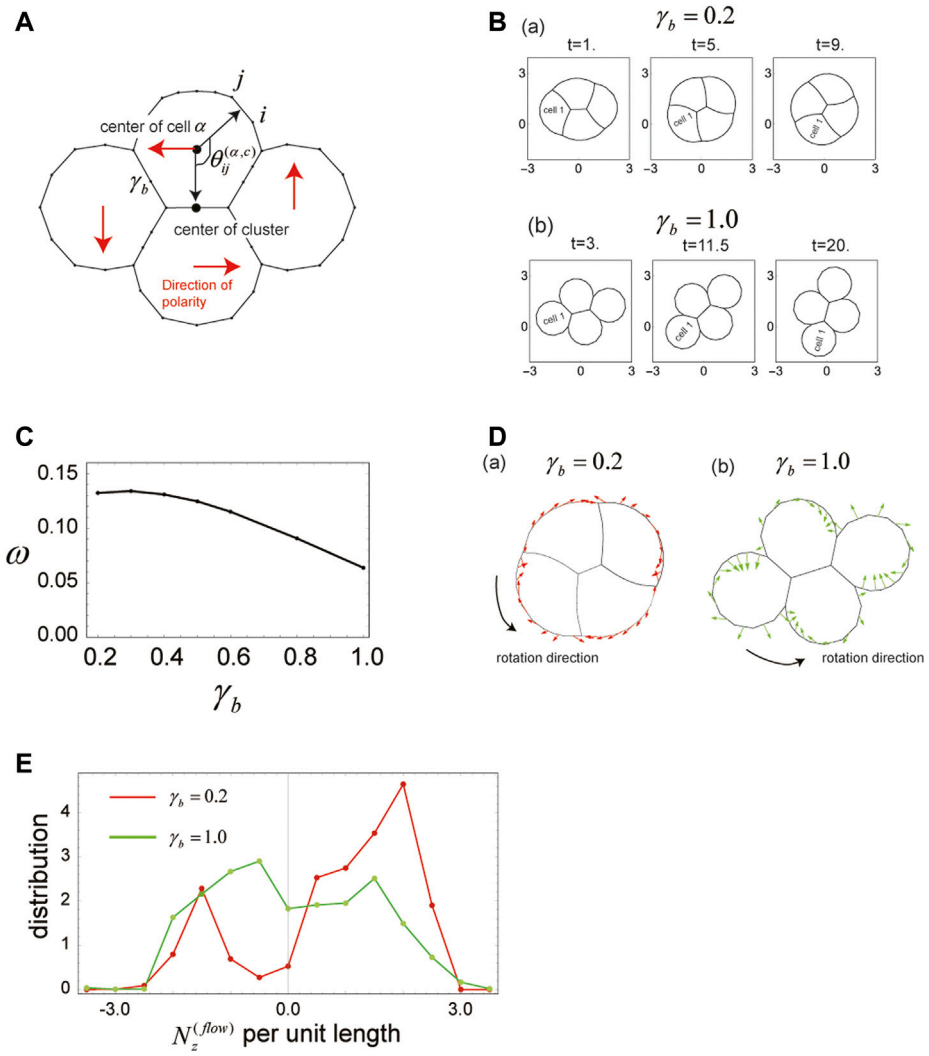

FIGURE 5
Cells in a cluster rotate when the polarity of each cell is tilted with respect to the cluster center. **(A)** Geometrical explanation of the angle $\theta_{ij}^{(a,c)}$ used in Eq. 13. Polarity of each cell in the cluster is indicated by the red arrow, which has a direction perpendicular to the vector from the cell center to the center of the cluster. **(B)** Snapshots of the cell cluster, rotating counterclockwise about the center of the cluster due to the direction-dependent surface tension in Eq. 13. Parameters used are as follows: $\mu = 0$, $\gamma_0 = 1.0$, $a = 0.1$, $\ell^*_{long} = 0.6$, $\ell^*_{short} = 0.08$, $K = 100$, $K_p = 0$, and $\kappa^{(ijk)} = 0$. In **B(a)**, $\gamma_b = 0.2$ and in **B(b)**, $\gamma_b = 1.0$. **(C)** The angular velocity, ω, of cluster rotation as a function of γ_b. **(D)** Velocities of the cell surface during rotation. **(a)** Red arrows indicate the cell surface velocities for $\gamma_b = 0.2$. **(b)** Green arrows indicate the cell surface velocities for $\gamma_b = 1.0$. The velocities for $\gamma_b = 0.2$ are oriented closer to the tangent of the cell surface, compared with those for $\gamma_b = 1.0$. **(E)** Distribution of the z-component of the torque generated by surface flow, which is induced by the direction-dependent surface tension in Eq. 13. When $\gamma_b = 0.2$, stronger torques that rotate the cluster more rapidly are generated, compared with the torques produced when $\gamma_b = 1.0$.

cell. Due to these parameters, when γ_b becomes small, boundaries between cells tend to extend, and the whole cell cluster behaves like one object. Further, because the cell cluster surface has a constant surface tension, γ_0, from Eq. 4, which reduces the cluster perimeter as much as possible under the constant area, $A_{cluster} = N_{cell}A_0$, the whole cluster is nearly a circle. In contrast, when γ_b becomes large, boundaries between cells tend to shrink, and outer cells within the cluster tend to be round, with the surface tension γ_0 (Figure 4C).

The slow cluster movement speed at small γ_b results from the roundness of the cell cluster. As shown in Sections 3.2–3.4, surface flow-induced cell migration, in general, becomes fast when the cell is elongated in the x-axis. This tendency is most evident in the case of a cell sandwiched by two walls, described in Section 3.4, where $\Delta\gamma$ in Eq. 6 acts as the driving force for movement. Similarly, in the case of cluster migration, the surface tension gradient along the cell surface (and the resultant flow of cell surface) is also the driving force for movement. Thus, if cells within the cluster are relatively elongated in the x-direction, the speed of cluster movement is relatively fast. However, when the cluster is round, such as for $N_{cell} = 2, 4$ and $\gamma_b = 0.1$ (Figure 4C), each cell in the cluster is relatively elongated in the y-axis, and thus, the driving forces are small, and the movement becomes slow.

3.7 Cell clusters rotate when cell direction is tilted with respect to the center of a cluster

To this point, we have examined only scenarios in which all cells on a substrate have the same direction of polarity (e.g., the x-direction). However, because clustered cells may also show distinct polarities, we next investigated the case wherein direction of polarity for individual cells within a cluster differs from cell to cell. In particular, we considered four cells comprising a cluster, in which each individual cell has a polarity that is directed perpendicular to the direction from the center of the cell to that of the cell cluster (Figure 5A). Surface tension for cells within this situation is expressed as

$$\hat{\gamma}_{ij} = \gamma_0 - a\cos\left(\theta_{ij}^{(\alpha,c)} - 3\pi/2\right), \tag{13}$$

where $\theta_{ij}^{(\alpha,c)}$ is the angle between the vector from the center of cell α that contains segment ij to the center of the cluster and the vector from the center of cell α to the center of segment ij (Figure 5A). The other parameters for this simulation are the same as those for cluster migration investigated in Section 3.6; that is, boundaries between cells within the cluster have a constant surface tension, $\gamma_{ij} = \gamma_b$, and each cell in the cluster keeps its area constant and has no constraint on its perimeter, with $K = 100$, $K_p = 0$, and $\kappa^{(ijk)} = 0$ in Eq. 2.

The initial configuration of the cell cluster is the same as in Figure 4C ($N_{cell} = 4$). Numerical simulations with the above parameters further indicate that each cell within the cluster continues to rotate counterclockwise around the center of the cluster while maintaining its attachments (Figure 5B; Supplementary Movies S11, S12). This rotation continues as long as each cell has the polarity established in Eq. 13, and the mechanism of movement is basically the same as observed for cluster migration and single-cell migration. That is, cells move due to the direction-dependent surface tension expressed by Eq. 13; the surface of the cell cluster moves clockwise, and this surface movement generates the driving force for rotational movement of the whole cluster. In this simulation, we set the polarities of the cells in the cluster with Eq. 13. However, in reality it may be more reasonable that the direction of cell polarity changes with time by following some other rules. One such rule is called the velocity alignment mechanism (Camley et al., 2014), in which cells align their polarity to their velocity. We incorporated this rule into our model and performed numerical simulations. The results show that for any initial directions of cell polarity, the cell polarities finally align such that the cluster of cells rotates (Supplementary Movies S13, S14). The direction of rotation depends on the initial distribution of cell polarities in the cluster. That is, the cell cluster rotates clockwise or counter clockwise depending on the initial distribution of cell polarities. Our system does not require cell confinement for this rotational motion, which is different from the results of previous studies (Camley et al., 2014).

As in the case of single-polarity cluster migration examined in Section 3.6, shape and rotational velocity of the cell cluster change with γ_b (Figures 5B, C). When γ_b is small, the cell cluster becomes round, and the angular velocity for the rotational movement of the cluster becomes large. The reasons for this cluster roundness are the same as those outlined in Section 3.6, that is, the whole cluster behaves like one object due to a lack of constraint on cell perimeter and small γ_b. In addition, the constant surface tension, γ_0, reduces cluster surface as much as possible under the constant whole area, $A_{cluster} = N_{cell}A_0$.

The faster rotation of the cell cluster at small γ_b originates from the velocity distribution of the cell cluster surface (Figure 5Da), and the reasons for this are as follows. First, cell boundaries within the cluster are classified into one of two types: 1) Cell boundaries that are located at the surface of the cluster and are associated with only one cell, referred to as the "outer cell boundaries" and 2) cell boundaries that are located within the cluster and form boundaries between two adjacent cells, referred to as "inner cell boundaries." During rotation of the cluster, the driving forces for cluster movement come from the flow of the outer cell boundaries, because only the outer cell boundaries have cell polarity, as indicated by Eq. 13. In the case of the round cluster ($\gamma_b = 0.2$; Figure 5Da), most velocities of the outer cell boundaries are directed in the tangent of the cluster surface, which comes from the monotonic decrease in surface tension along the surface. These velocities generate a large magnitude of torque compared with those present in the case of $\gamma_b = 1.0$ (see Figures 5D, E). Here, $N_z^{(flow)}$ is the z-component of the torque generated by the surface flow of the outer cell boundaries and is evaluated as $N_z^{(flow)} = -\eta\sum_{\langle ij\rangle_{outer}}((\mathbf{R}_{ij} - \mathbf{r}_c) \times (\dot{\mathbf{R}}_{ij} - \dot{\mathbf{r}}_c))_z \ell_{ij}$, where $\mathbf{r}_c$ is the position vector of the cluster center, and $\langle ij\rangle_{outer}$ indicates that the summation range is over all outer cell boundaries. $N_z^{(flow)}$ is balanced with the z-component of torque generated from frictional forces experienced by the inner cell boundaries, denoted by $N_z^{(friction)}$, and this balance determines the angular velocity, ω, of the cluster rotation. $N_z^{(friction)}$ is roughly expressed as $N_z^{(friction)} = -\zeta\omega$, where ζ is a coefficient given by $\zeta = \eta\sum_{\langle ij\rangle_{inner}}|\mathbf{R}_{ij} - \mathbf{r}_c|^2\ell_{ij}$. The ζ coefficient is almost constant in time because it is determined by the shape of the network of inner cell boundaries, which is also almost constant in time (see Supplementary Movies S11, S12). The torque balance on the cell surface gives $\omega = N_z^{(flow)}/\zeta$. Although both $N_z^{(flow)}$ and ζ increase with decreased γ_b (Supplementary Figure S1), the increase in ζ is more gentle than for $N_z^{(flow)}$, which results from the fact that the size of the network of inner cell boundaries does not change much with γ_b (see Figure 5B). Thus, the increase in $N_z^{(flow)}$, which occurs with decreased γ_b, increases the angular velocity ω.

4 Discussion

In this study, we have developed a 2D cell membrane model, described by Eqs 1–3, which shows that cells on a substrate migrate due to direction-dependent surface tension, represented by Eq. 4. Notably, this is true, not only for a single cell but also for multiple cells that adhere to one another and form a cluster. Moreover, if we change the direction of cell polarity within a cell cluster, such that polarity varies from cell to cell, as in Eq. 13, the cell cluster rotates due to direction-dependent surface tension. A key point of emphasis is that, because this model neglects any inertia of the cell surface and ensures that forces are balanced on the cell surface at all times, the total force exerted on each cell from outside objects, such as the substrate and neighboring cells, always vanishes. That is, the cell movement in this situation is, what we call, "force free", and this is driven by the inflow and outflow of cell membrane components from inside the cell, as discussed in Section 3.5.

Although this is a 2D model, it is expected that the cell movement we observe herein, namely, single-cell migration, cluster migration, and cluster rotation, may also be present in 3D models, because the mechanism of movement (i.e., direction-dependent surface tension) is likely applicable to 3D cases. Indeed, single-cell migration due to direction-dependent surface tension has been demonstrated in a previously published study (Okuda et al., 2022), for a spherical cell migrating with a constant velocity in 3D space. Thus, we anticipate that cluster migration and rotation will be shown in well-implemented 3D models.

We further expect this model may reveal relevant information for better understanding cell shape and cortical flow during cell movement in real-life situations. This is because, as previously emphasized, our model satisfies force balance on the cell membrane at all times, and hence, the cell shapes appearing in this model are the results of that force balance on cell surface during cell migration (e.g., see Figures 2D, 4C). Thus, if a parameter set in our model mimics the cell shapes and cell movement observed in experiments, we can expect which part of the cell experiences strong contractile forces and which part of the cell membrane has strong stiffness by looking at the experimental results. In addition, this mechanical model provides the speed of cell movement. Thus, with these properties we can address the relationship between cell shape and cell velocity, which is proposed in the existing works (Ohta and Ohkuma, 2009) by using a symmetry argument. We can examine the relationship between shape and speed of cells by the cell-level model. In addition, by regarding the segments in our model as the cortex in cells, we are able to investigate cortical flow within moving cells, as in previously published studies (Jankowiak et al., 2020). A key point of the present model is that due to the discreteness of this model, we can easily set the parameter values that specify key characteristics of the cells we are modeling. For example, we can change the strength of contractile and frictional forces, as well as the stiffness of the cortex, by changing γ_{ij}, η_{ij}, and $\kappa^{(ijk)}$ in space and time. For example, cells change its behaviors depending on the stiffness of the substrate (Durotaxis) (Lo et al., 2000). By setting up that the values of γ_{ij}, η_{ij}, and $\kappa^{(ijk)}$ depend on the stiffness of the substrate in some way in our model, we can investigate effects of the stiffness of the substrate on the cell movement from a subcellular level.

In our model, as already mentioned in Section 2.1, we focused on the dynamics of the cell peripheries. However, in many real-life cases, cells are attached to the substrate at some focal adhesions, and the two-dimensional flow of the cortex at the bottom region of the cells is also important for cell movement. Therefore, it would be a good strategy to extend the presented cortex model to a model that expresses the two-dimensional flow on the plane. This will be a target of future work. In addition, it has been observed that the plasma membrane and the cortex beneath the plasma membrane move separately during cell movement (Taniguchi et al., 2023). This observation implies that it is more realistic for a model of cell movement to describe the dynamics of two components, the plasma membrane and the cortex. This will also be a target of future research.

In the current remodeling rules for segments that represent cell boundaries, given in Section 2.2, the attachment and detachment of cells, which are important processes for considering more general movement of cells, are not described. In fact, by adding only some rules to the current setup, we can describe the attachment and detachment of cells. An example of it is as follows. When two separated cells are close to each other and the distance between some parts of two cell surfaces becomes shorter than some critical distance, then the parts of cell surfaces are merged and becomes one segment. This setup describes the attachment of two cells. In addition, when the common cell boundary between two adhered cells becomes shorter than some critical length, then the common cell boundary is split into two cell boundaries and two cell are separated. This situation represents the detachment of two cells. By introducing this rule into the current version, we can investigate more complex behaviors of cells on a substrate.

In the present paper, we have assumed that cell polarity is represented by the direction dependence of γ_{ij}. However, because the front and rear of a cell differ in regard to the stiffness of the cell surface and the strength of attachment to the substrate, it may be more plausible to model the situation in which cell polarity can change the cell stiffness, $\kappa^{(ijk)}$, as well as the friction coefficients, η_{ij} and μ_{ij}. By doing so, we may reproduce more realistic cell behaviors, such as blebbing (Paluch and Raz, 2013). We can also consider many variations of the form of $\hat{\gamma}_{ij}$. For example, since the position of nucleus in a cell plays an important role for cell dynamics (Moure and Gomez, 2020), it may be more realistic thet the value of $\hat{\gamma}_{ij}$ is determined by the relative position of the cortex to the nucleus.

In the present paper cell polarity was *a priori* given as in Eqs. 4, 13. But in reality, the direction of cell polarity dynamically changes with time depending on the environment surrounding the cell and the state of itself. Many possible ways for describing the time evolution of cell polarity have been proposed (Camley et al., 2014). By introducing proposed descriptions of cell polarity into our mechanical model and comparing the results obtained by the model to experiments, we might be able to determine which time evolution rule for cell polarity is most appropriate.

The phenomenon of cells migrating on a substrate, while forming a cluster, has been observed during development of the zebrafish lateral line (Haas and Gilmour, 2006; Lecaudey et al., 2008) and by the amoeba *Dictyostelium discoideum* (Hirose et al., 2011; Hayakawa et al., 2020). In addition, some clusters of epithelial cells were found to rotate 90° within an epithelial sheet during *Drosophila* eye development (Mlodzik, 1999; Mirkovic and Mlodzik, 2006; Jenny, 2010; Founounou et al., 2021). Although there are many possible explanations for such collective behavior (Haas and Gilmour, 2006; Lecaudey et al., 2008), it has been difficult to understand from a mechanistic standpoint, due to the many-body problem inherent in analyzing complex systems. In this regard, mechanical models are useful to better understand the forces that drive multi-cell behavior as noted in the Introduction, and the mechanism presented in this paper represents one possible explanation for such collective cell movement. By comparing experimental results, such as the spatial distribution of actomyosin and adhesion molecules in cells and observed cell shapes, with the results from our numerical simulations, we may uncover new insights into the complex patterns of cell movement observed in living systems.

Data availability statement

The original contributions presented in the study are included in the article/Supplementary Material, further inquiries can be directed to the corresponding author.

Author contributions

The author was the sole contributor of this work and approved the submitted version for publication.

Funding

This work was supported by a JSPS KAKENHI Grant Number JP20K03871, 23H04300 and 21H05310, the "Dynamic Alliance for Open Innovation Bridging Human, Environment and Materials" of the Ministry of Education, Culture, Sports, Science and Technology of Japan, and the Global Station for Soft Matter at Hokkaido University.

Acknowledgments

We would like to thank T. Nakagaki, H. Orihara, N. Nishigami, M. Nishikawa, M. Akiyama, M. Kimura, and Y. Tanaka for their valuable comments and discussions.

Conflict of interest

The author declares that the research was conducted in the absence of any commercial or financial relationships that could be construed as a potential conflict of interest.

Publisher's note

Supplementary material

The Supplementary Material for this article can be found online at: https://www.frontiersin.org/articles/10.3389/fcell.2023.1126819/full#supplementary-material

References

Aigouy, B., Farhadifar, R., Staple, D. B., Sagner, A., Röper, J. C., Jülicher, F., et al. (2010). Cell flow reorients the axis of planar polarity in the wing epithelium of Drosophila. *Cell.* 142(5), 773–786. doi:10.1016/j.cell.2010.07.042

Bächer, C., Khoromskaia, D., Salbreux, G., and Gekle, S. (2021). A three- dimensional numerical model of an active cell cortex in the viscous limit. *Front. Phys.* 9, 753230. doi:10.3389/fphy.2021.753230

Bergert, M., Chandradoss, S. D., Desai, R. A., and Paluch, E. (2012). Cell mechanics control rapid transitions between blebs and lamellipodia during migration. *Proc. Natl. Acad. Sci. U. S. A.* 109 (36), 14434–14439. doi:10.1073/pnas.1207968109

Bergert, M., Erzberger, A., Desai, R. A., Aspalter, I. M., Oates, A. C., Charras, G., et al. (2015). Force transmission during adhesion-independent migration. *Nat. Cell. Biol.* 17 (4), 524–529. doi:10.1038/ncb3134

Bodor, D. L., Pönisch, W., Endres, R. G., and Paluch, E. K. (2020). Of cell shapes and motion: The physical basis of animal cell migration. *Dev. Cell.* 52 (5), 550–562. doi:10.1016/j.devcel.2020.02.013

Bray, D., and White, J. G. (1988). Cortical flow in animal cells. *Science* 239 (4842), 883–888. doi:10.1126/science.3277283

Callan-Jones, A. C., and Voituriez, R. (2016). Actin flows in cell migration: From locomotion and polarity to trajectories. *Curr. Opin. Cell. Biol.* 38, 12–17. doi:10.1016/j.ceb.2016.01.003

Camley, B. A., Zhang, Y., Zhao, Y., Li, B., Ben-Jacob, E., Levine, H., et al. (2014). Polarity mechanisms such as contact inhibition of locomotion regulate persistent rotational motion of mammalian cells on micropatterns. *Proc. Natl. Acad. Sci. U. S. A.* 111 (41), 14770–14775. doi:10.1073/pnas.1414498111

Case, L. B., and Waterman, C. M. (2015)). Integration of actin dynamics and cell adhesion by a three-dimensional, mechanosensitive molecular clutch. *Nat. Cell. Biol.* 17 (8), 955–963. doi:10.1038/ncb3191

Farhadifar, R., Roper, J. C., Aigouy, B., Eaton, S., and Julicher, F. (2007). The influence of cell mechanics, cell-cell interactions, and proliferation on epithelial packing. *Curr. Biol.* 17, 2095–2104. doi:10.1016/j.cub.2007.11.049

Farutin, A., Étienne, J., Misbah, C., and Recho, P. (2019). Crawling in a fluid. *Phys. Rev. Lett.* 123 (11), 118101. doi:10.1103/PhysRevLett.123.118101

Fletcher, A. G., Osterfield, M., Baker, R. E., and Shvartsman, S. Y. (2014). Vertex models of epithelial morphogenesis. *Biophys. J.* 106, 2291–2304. doi:10.1016/j.bpj.2013.11.4498

Founounou, N., Farhadifar, R., Collu, G. M., Weber, U., Shelley, M. J., and Mlodzik, M. (2021). Tissue fluidity mediated by adherens junction dynamics promotes planar cell polarity-driven ommatidial rotation. *Nat. Commun.* 12 (1), 6974. doi:10.1038/s41467-021-27253-0

Friedl, P., and Gilmour, D. (2009). Collective cell migration in morphogenesis, regeneration and cancer. *Nat. Rev. Mol. Cel. Biol.* 10 (7), 445–457. doi:10.1038/nrm2720

Haas, P., and Gilmour, D. (2006)). Chemokine signaling mediates self-organizing tissue migration in the zebrafish lateral line. *Dev. Cell.* 10 (5), 673–680. doi:10.1016/j.devcel.2006.02.019

Haigo, S. L., and Bilder, D. (2011). Global tissue revolutions in a morphogenetic movement controlling elongation. *Science* 331 (6020), 1071–1074. doi:10.1126/science.1199424

Hayakawa, M., Hiraiwa, T., Wada, Y., Kuwayama, H., and Shibata, T. (2020). Polar pattern formation induced by contact following locomotion in a multicellular system. *Elife* 9, e53609. doi:10.7554/eLife.53609

Hirose, S., Benabentos, R., Ho, H. I., Kuspa, A., and Shaulsky, G. (2011). Self-recognition in social amoebae is mediated by allelic pairs of tiger genes. *Science* 333 (6041), 467–470. doi:10.1126/science.1203903

Innocenti, M. (2018). New insights into the formation and the function of lamellipodia and ruffles in mesenchymal cell migration. *Cell. Adh Migr.* 12 (5), 401–416. doi:10.1080/19336918.2018.1448352

Jankowiak, G., Peurichard, D., Reversat, A., Schmeiser, C., and Sixt, M. (2020). Modeling adhesion-independent cell migration. *Math. Models Methods Appl. Sci.* 30, 513–537. doi:10.1142/S021820252050013X

Jenny, A. (2010). Planar cell polarity signaling in the Drosophila eye. *Curr. Top. Dev. Biol.* 93, 189–227. doi:10.1016/B978-0-12-385044-7.00007-2

Kuwayama, H., and Ishida, S. (2013). Biological soliton in multicellular movement. *Sci. Rep.* 3, 2272. doi:10.1038/srep02272

Lämmermann, T., Bader, B. L., Monkley, S. J., Worbs, T., Wedlich-Söldner, R., Hirsch, K., et al. (2008). Rapid leukocyte migration by integrin-independent flowing and squeezing. *Nature* 453 (7191), 51–55. doi:10.1038/nature06887

Landau, L. D., and Lifshitz, E. M. (1976). "Mechanics," in *Course of theoretical physics*. 3rd edn. Volume 1 (Oxford: Butterworth- Heinemann).

Lecaudey, V., Cakan-Akdogan, G., Norton, W. H., and Gilmour, D. (2008). Dynamic Fgf signaling couples morphogenesis and migration in the zebrafish lateral line primordium. *Development* 135 (16), 2695–2705. doi:10.1242/dev.025981

Liu, Y. J., Le Berre, M., Lautenschlaeger, F., Maiuri, P., Callan-Jones, A., Heuzé, M., et al. (2015). Confinement and low adhesion induce fast amoeboid migration of slow mesenchymal cells. *Cell.* 160 (4), 659–672. doi:10.1016/j.cell.2015.01.007

Lo, C. M., Wang, H. B., Dembo, M., and Wang, Y. L. (2000). Cell movement is guided by the rigidity of the substrate. *Biophys. J.* 79 (1), 144–152. doi:10.1016/S0006-3495(00)76279-5

Mietke, A., Jülicher, F., and Sbalzarini, I. F. (2019). Self-organized shape dynamics of active surfaces. *Proc. Natl. Acad. Sci. U. S. A.* 116 (1), 29–34. doi:10.1073/pnas.1810896115

Mirkovic, I., and Mlodzik, M. (2006). Cooperative activities of drosophila DE-cadherin and DN-cadherin regulate the cell motility process of ommatidial rotation. *Development* 133 (17), 3283–3293. doi:10.1242/dev.02468

Mlodzik, M. (1999). Planar polarity in the Drosophila eye: A multifaceted view of signaling specificity and cross-talk. *EMBO J.* 18 (24), 6873–6879. doi:10.1093/emboj/18.24.6873

Montell, D. J., Yoon, W. H., and Starz-Gaiano, M. (2012)). Group choreography: Mechanisms orchestrating the collective movement of border cells. *Nat. Rev. Mol. Cell. Biol.* 13 (10), 631–645. doi:10.1038/nrm3433

Moure, A., and Gomez, H. (2020). Dual role of the nucleus in cell migration on planar substrates. *Biomech. Model. Mechanobiol.* 19 (5), 1491–1508. doi:10.1007/s10237-019-01283-6

O'Neill, P. R., Castillo-Badillo, J. A., Meshik, X., Kalyanaraman, V., Melgarejo, K., and Gautam, N. (2018). Membrane flow drives an adhesion-independent amoeboid cell migration mode. *Dev. Cell.* 46 (1), 9–22.e4. doi:10.1016/j.devcel.2018.05.029

Ohta, T., and Ohkuma, T. (2009). Deformable self-propelled particles. *Phys. Rev. Lett.* 102 (15), 154101. doi:10.1103/PhysRevLett.102.154101

Okuda, S., Sato, K., and Hiraiwa, T. (2022). Continuum modeling of non-conservative fluid membrane for simulating long-term cell dynamics. *Eur. Phys. J. E* 45, 69. doi:10.1140/epje/s10189-022-00223-0

Pagès, D. L., Dornier, E., de Seze, J., Gontran, E., Maitra, A., Maciejewski, A., et al. (2022). Cell clusters adopt a collective amoeboid mode of migration in confined nonadhesive environments. *Sci. Adv.* 8 (39), eabp8416. doi:10.1126/sciadv.abp8416

Paluch, E. K., and Raz, E. (2013). The role and regulation of blebs in cell migration. *Curr. Opin. Cell. Biol.* 25 (5), 582–590. doi:10.1016/j.ceb.2013.05.005

Rauzi, M., Verant, P., Lecuit, T., and Lenne, P. F. (2008). Nature and anisotropy of cortical forces orienting Drosophila tissue morphogenesis. *Nat. Cell. Biol.* 10, 1401–1410. doi:10.1038/ncb1798

Reversat, A., Gaertner, F., Merrin, J., Stopp, J., Tasciyan, S., Aguilera, J., et al. (2020). Cellular locomotion using environmental topography. *Nature* 582 (7813), 582–585. doi:10.1038/s41586-020-2283-z

Ruprecht, V., Wieser, S., Callan-Jones, A., Smutny, M., Morita, H., Sako, K., et al. (2015). Cortical contractility triggers a stochastic switch to fast amoeboid cell motility. *Cell.* 160 (4), 673–685. doi:10.1016/j.cell.2015.01.008

Sakamoto, R., Izri, Z., Shimamoto, Y., Miyazaki, M., and Maeda, Y. T. (2022). Geometric trade-off between contractile force and viscous drag determines the actomyosin-based motility of a cell-sized droplet. *Proc. Natl. Acad. Sci. U. S. A.* 119 (30), e2121147119. doi:10.1073/pnas.2121147119

Salbreux, G., Charras, G., and Paluch, E. (2012). Actin cortex mechanics and cellular morphogenesis. *Trends Cell. Biol.* 22 (10), 536–545. doi:10.1016/j.tcb.2012.07.001

Sato, K. (2017). Direction-dependent contraction forces on cell boundaries induce collective migration of epithelial cells within their sheet. *Dev. Growth Differ.* 59 (5), 317–328. doi:10.1111/dgd.12361

Sato, K., Hiraiwa, T., Maekawa, E., Isomura, A., Shibata, T., and Kuranaga, E. (2015). Left-right asymmetric cell intercalation drives directional collective cell movement in epithelial morphogenesis. *Nat. Commun.* 6, 10074. doi:10.1038/ncomms10074Refstyled

Sato, K., Hiraiwa, T., and Shibata, T. (2015). Cell chirality induces collective cell migration in epithelial sheets. *Phys. Rev. Lett.* 115, 188102. doi:10.1103/PhysRevLett.115.188102

Scarpa, E., and Mayor, R. (2016). Collective cell migration in development. *J. Cell. Biol.* 212 (2), 143–155. doi:10.1083/jcb.201508047

Taniguchi, A., Nishigami, Y., Kajiura-Kobayashi, H., Takao, D., Tamaoki, D., Nakagaki, T., et al. (2023). Light-sheet microscopy reveals dorsoventral asymmetric membrane dynamics of Amoeba proteus during pressure-driven locomotion. *Biol. Open* 12 (2), bio059671. doi:10.1242/bio.059671

Taniguchi, K., Maeda, R., Ando, T., Okumura, T., Nakazawa, N., Hatori, R., et al. (2011). Chirality in planar cell shape contributes to left-right asymmetric epithelial morphogenesis. *Science* 333 (6040), 339–341. doi:10.1126/science.1200940

Tee, Y. H., Shemesh, T., Thiagarajan, V., Hariadi, R. F., Anderson, K. L., Page, C., et al. (2015). Cellular chirality arising from the self-organization of the actin cytoskeleton. *Nat. Cell. Biol.* 17 (4), 445–457. doi:10.1038/ncb3137

Wan, L. Q., Chin, A. S., Worley, K. E., and Ray, P. (2016). Cell chirality: Emergence of asymmetry from cell culture. *Philos. Trans. R. Soc. Lond B Biol. Sci.* 371 (1710), 20150413. doi:10.1098/rstb.2015.0413

Weijer, C. J. (2009). Collective cell migration in development. *J. Cell. Sci.* 122 (Pt 18), 3215–3223. doi:10.1242/jcs.036517

frontiers | Frontiers in Cell and Developmental Biology

TYPE Original Research
PUBLISHED 24 August 2023
DOI 10.3389/fcell.2023.1244673

OPEN ACCESS

EDITED BY
Laurence Wilson,
University of York, United Kingdom

REVIEWED BY
Atsuko Takamatsu,
Waseda University, Japan
Yukinori Nishigami,
Hokkaido University, Japan

*CORRESPONDENCE
Yu Fukasawa,
yu.fukasawa.d3@tohoku.ac.jp

RECEIVED 22 June 2023
ACCEPTED 14 August 2023
PUBLISHED 24 August 2023

CITATION
Fukasawa Y and Ishii K (2023), Foraging strategies of fungal mycelial networks: responses to quantity and distance of new resources.
Front. Cell Dev. Biol. 11:1244673.
doi: 10.3389/fcell.2023.1244673

Foraging strategies of fungal mycelial networks: responses to quantity and distance of new resources

Yu Fukasawa* and Kaho Ishii

Laboratory of Forest Ecology, Graduate School of Agricultural Science, Tohoku University, Osaki, Miyagi, Japan

Fungal mycelial networks are essential for translocating and storing water, nutrients, and carbon in forest ecosystems. In particular, wood decay fungi form mycelial networks that connect various woody debris on the forest floor. Understanding their foraging strategies is crucial for complehending the role of mycelium in carbon and nutrient cycling in forests. Previous studies have shown that mycelial networks initiate migration from the original woody resource (inoculum) to a new woody resource (bait) if the latter is sufficiently large but not if it is small. However, the impact of energetic costs during foraging, such as the distance to the bait, has not been considered. In the present study, we conducted full-factorial experiments with two factors, bait size (4 and 8 cm^3) and distance from the inoculum (1 and 15 cm). An inoculum wood block, colonized by the wood decay fungus *Phanerochaete velutina*, was placed in one corner of a bioassay dish (24 cm × 24 cm) filled with unsterilized soil. Once the mycelium grew onto the soil to a distance >15 cm from the inoculum, a sterilized new bait wood block (of either size) was placed on the soil at one of the two distances to be colonized by the mycelia from the inoculum. After 50 days of incubation, the baits were harvested, and their dried weight was measured to calculate the absolute weight loss during incubation. The inoculum wood blocks were retrieved and placed on a new soil dish to determine whether the mycelium would grow out onto the soil again. If no growth occurred within 8 days of additional incubation, we concluded that the mycelium had migrated from the inoculum to the bait. The results showed that mycelia in inocula coupled with baits positioned 1 cm away migrated to the baits more frequently than those with baits positioned 15 cm away. A structural equation model revealed that bait weight loss (energy gain) and hyphal coverage on the soil (foraging cost) significantly influenced mycelial migration decisions. These findings suggest that fungal mycelia may employ their own foraging strategies based on energetic benefits.

KEYWORDS

foraging behaviour, hyphae, migration, soil microcosm, wood decay fungi

1 Introduction

Mycelial networks of fungi, which extend the litter-soil interface on the forest floor, play important roles in the forest ecosystem. In the case of decomposer fungi, mycelial networks connect numerous units of dead wood and leaf litter, contribute to the decomposition and mineralization of those plant tissues (Boddy, 1999). In the case of mycorrhizal fungi, mycelial

networks connect symbiotic tree roots, forming complex, interwoven common mycorrhizal networks (Simard et al., 1997). In both cases, mycelial networks facilitate the transfer of carbon (Wells et al., 1995; Simard et al., 1997), nutrients (Wells et al., 1990; Kiers et al., 2011), and even information (Johnson and Gilbert, 2015) across their expansive bodies, which can cover hundreds of hectares (Ferguson et al., 2003). Gaining a better understanding of the factors that affect the development of mycelial networks is crucial for predicting dynamics of forest ecosystems in a changing environment.

Resources for wood decay fungi are dead wood, which is unevenly distributed on the forest floor. Therefore, strategies for foraging for these dead woods, including which ones to colonize preferentially and when to leave old ones for new resources, are important for the optimal management not only of energy gain and survey cost but also of network structure, which is vital for efficient material transfer across mycelial networks (Fricker et al., 2017). Previous reports have shown that flexible behaviour of mycelial networks depends on the quantity and timing of resource addition, shedding light on their economic strategies. For example, mycelia of *Phanerochaete velutina*, a known basidiomycete species that forms mycelial "cords" (visible strand made of numerous parallel-running hyphae), completely leave old wood blocks after colonizing sufficiently large new wood blocks but do not abandon old ones if a new resource is small or the old ones are still nutritious (Fukasawa et al., 2020; Fukasawa and Kaga, 2021). This species also exhibits adaptive behaviour in response to grazing pressure from soil invertebrates by developing more highly-connected robust networks (Boddy et al., 2010), as well as in response to repeated artificial disturbances based on memory to minimize physical damage (Donnelly and Boddy, 1998). These results suggest that mycelial networks can also manage risk and cost when developing their networks. However, how a mycelium behaves when they faced with multiple issues simultaneously remains unclear. For example, what choices do they make when they encounter a large new resource (with significant benefits) far from their original location (involving substantial foraging costs), compared to a small new resource located much closer? Given the uneven and patchy distribution of dead wood on the forest floor, such situations are likely to be quite common. Nevertheless, few studies have explored fungal behaviour in multiple tasks.

In the field of behavioural ecology, which has mostly been developed to explain animal behaviour, optimal foraging strategies (OFS) are known to maximize net energetic gain by subtracting the costs associated with foraging activities (Davies et al., 2012). For individual motile organisms with clear individuality (e.g., animals), the time consumed for foraging is one of the most important factors determining the foraging cost (Krebs, 1973). On the other hand, for modular organisms such as plants, slime moulds, and fungi, which can flexibly enlarge their body size and shape but usually sessile, the distance (or spatial scale) to the resource could be an important factor determining the cost of their foraging activities (Dussutour et al., 2019; Zheng et al., 2022). Slime mould *Physarum polycephalum*, in particular, has been extensively studied for its ability to find the shortest and least stressful paths connecting multiple resources (Nakagaki et al., 2000a; Tero et al., 2010) and for its decision-making process on when to leave old resources (Latty and Beekman, 2009, 2015).

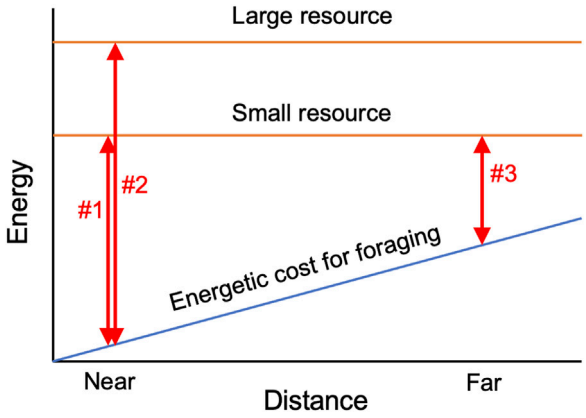

FIGURE 1
Schematic diagram explaining the hypothesis tested in the present study. Both the size and distance of the resource may impact the net energy gain (double-head arrows in the figure) by influencing the energetic cost of foraging. If the distance to the resources are equal, net energy gain might be mainly restricted by the size of the resource (comparison between arrow#1 and arrow#2), whereas if the distance to the resources are different, energetic cost for foraging might affect the difference in the net energy gain (comparison between arrow#1 and arrow#3).

Mathematical models have even been proposed to explain their adaptive behaviours (Tero et al., 2007; Lecheval et al., 2021; Hu et al., 2022). The Marginal Value Theorem (MVT) predicts that the optimal strategy for foragers is to leave patches when the instantaneous rate of return in the patch falls to the average of the returns that can be achieved in all the other patches within the environment (Latty and Beekman, 2015).

In contrast to slime moulds, the behavioural ecology of fungi is still in its infancy (Money, 2021), and their OFS has not been well explored in terms of balancing costs and benefits. Since hyphal production required to reach new resources is an energetic cost for fungi, finding a new resource located far from the original inoculum might be energetically more expensive than finding closer resources. Thus, a mycelium might be expected to obtain a larger net energy from closer resources compared to resources located far from the inoculum, assuming the size (or energetic value) of the new resources is equal (Figure 1). In fact, the size of the resource is important for mycelial decision-making, as mentioned above (Fukasawa et al., 2020), likely reflecting the difference in the amount of energy available from these resources. Regarding distance, we hypothesize that a mycelium will leave the inoculum and migrate to a new resource more frequently when the new resource is located closer to the inoculum, as the net energy gain from the new resource might be larger when it is closer (Figure 1).

The aim of this study was to evaluate the effects of the size and distance of new wood resources (baits) on the decision-making process of a fungal mycelium to migrate from an old inoculum to the bait. We hypothesized that larger and closer baits would induce more migration of the mycelium than smaller and farther baits because a mycelium can obtain more energy from the former set of baits compared to the latter set of baits per unit foraging effort, after subtracting the energetic cost. We used a soil dish microcosm and a saprotrophic cord-forming basidiomycete, *Phanerochaete velutina*

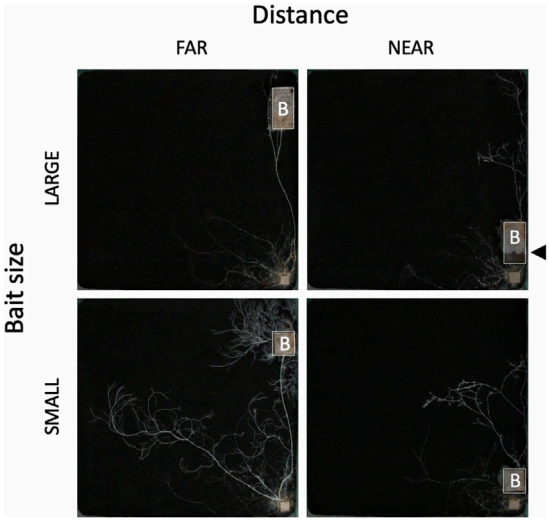

FIGURE 2
The effect of bait (B) size and distance on the development of *Phanerochaete velutina* mycelial systems originating from an inoculum wood block (small block at the bottom right corner). All photos were taken at the end of incubation period I. Bait size: 4 and 8 cm^3 for SMALL and LARGE, respectively. Bait distance: 15 and 1 cm for FAR and NEAR, respectively. The outline of the bait wood block is delineated by a white line for clarity. Note that in the LARGE-NEAR experiment (upper-right photo), mycelium colonization on the bait occurred from the side opposite the inoculum. Black arrowhead indicates the colonization front line of mycelium colonized from the side opposite to the inoculum.

(DC.) P. Karst., as a model system. This fungus is one of the most well-studied species in the research field of mycelial network behaviour (Boddy, 2009; Fukasawa et al., 2020; Fukasawa and Kaga, 2021). Absolute weight losses of the wood blocks (inoculum and bait) were measured as indices of energy gain, while hyphal coverage on the soil dish was measured as an index of the energetic cost for the mycelium during the foraging operation.

2 Materials and methods

2.1 Fungal culturing and inoculum preparation

Beech (*Fagus crenata*) wood was cut into blocks measuring 0.5 cm × 1 cm × 1 cm (0.5 cm^3) and dried at 70°C until the constant weight was achieved. The numbered blocks were soaked overnight in distilled water and then autoclaved at 121°C for 20 min. The autoclaving process was repeated three times with 1 day intervals to ensure sterilization. The sterilized wood blocks were placed on cultures of *P. velutina* (NBRC culture collection, #110184) grown on 0.5% malt extract agar (MEA; 5 g Lab M malt extract, 15 g Lab M agar no. 2) in non-vented 9 cm-diameter Petri dishes (1.5 cm thick). The plates were sealed with Parafilm® (Bemis Company Inc., Oshkosh, United States), and incubated in the dark at 20°C for 1 month before use. In total, 113 inoculum wood blocks were prepared in 11 Petri dishes, with 10–11 blocks in each dish. The whole experimental flow is shown in Supplementary Figure S1.

2.2 Microcosm preparation

Soil was collected from the top 10 cm (A layer) of a deciduous mixed forest dominated by *Quercus serrata* and *Larix kaempferi* in Kawatabi Field Science Center of Tohoku University, Miyagi, Japan (38°45′ N, 140°45′ E, 275 m a.s.l.). The soil was sieved on site using a 10 mm mesh, air-dried, sieved again through a 2 mm mesh, and frozen at −30°C for more than 48 h to kill soil invertebrates. The soil was then rehydrated with distilled water (70 mL for 130 g dried soil), transferred to 24 cm × 24 cm plastic bioassay dishes, smoothed and compacted to a depth of approximately 5 mm (approximately 200 g wet soil for each dish).

An inoculum wood block, from which surface mycelia and excess agar had been removed using a razor blade, was placed 1 cm from a corner of each dish. All dishes were incubated at 20°C in the dark in BioTRON (NK system, Osaka, Japan) for 50 days. This period is referred to as the pre-incubation period. Out of the total of 113 soil dishes with inoculum wood blocks, 40 dishes where mycelia had extended more than 15 cm from the inoculum wood block were selected for the downstream experiments. A new beech wood block (bait), prepared and sterilized as described above, was placed on each of the 40 dishes at two different distances from the inoculum: one at 1 cm (NEAR experiment) and the other at 15 cm (FAR experiment) away from the inoculum. Two sizes of bait wood blocks were used: 2 cm × 2 cm × 1 cm (4 cm^3, SMALL) and 2 cm × 4 cm × 1 cm (8 cm^3, LARGE). Thus, a total of four experiments were conducted (two distances × two bait sizes), with ten replicates for each experiment. The 73 inoculum wood blocks that were not used in the further incubation were harvested and dried at 70°C to a constant weight. The weight loss (%) of the inoculum wood blocks after the pre-incubation period was calculated using the following equation:

$$\textit{Weight loss}\ (\%) = \frac{\text{original dried weight} - \text{dried weight after preincubation period}}{\textit{original dried weight}} \times 100$$

The weight loss (%) data were used to create a regression line between weight loss (%) and hyphal coverage (cm^2) on the soil, which was measured as described later. Given the linear correlation between wood weight loss and hyphal coverage on soil (Fukasawa and Kaga, 2020), this regression line was used to estimate the weight loss (%) of the 40 inocula used for the further incubation experiment at the end of the pre-incubation period.

2.3 Microcosm incubation

All dishes were weighed after set-up, and their weight was monitored weekly to replace lost water by spraying distilled water evenly across the soil surface. The dishes were stacked in polythene bags to reduce water loss and were incubated at 20°C in the dark for 50 days in BioTRON (period I).

After period I, bait blocks were harvested, and their surface mycelia and soil were removed using a razor blade. The blocks were then dried at 70°C until a constant weight was achieved. Inoculum wood blocks were retrieved, scraped-off mycelia and soil on their surface, and placed centrally onto new soil dishes freshly prepared as described above but in smaller round dishes with a diameter of 14 cm and a thickness of 2.5 cm. In cases where the inoculum wood

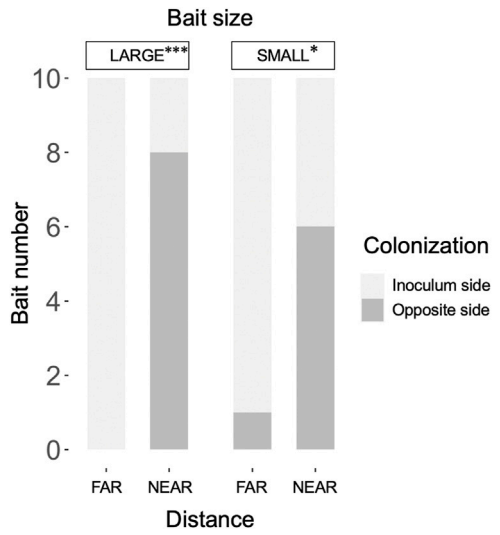

FIGURE 3
Frequency of hyphal colonization in LARGE and SMALL bait wood blocks, positioned at different distances from the inocula, from the side opposite the inoculum. The frequency was compared between the FAR and NEAR experiments (Fisher's exact test: *, $p < 0.05$; ***, $p < 0.001$).

blocks were too soft due to fungal decay activities, the soil under the blocks was cut out together with the blocks and transferred to the new dishes. The dishes were further incubated at 20°C in the dark for 8 days to check for mycelial regrowth from the inoculum (period II). If mycelial regrowth was not observed, it was recorded as migration from the inoculum to the bait.

During incubation period I, the dishes were randomly repositioned every 3 days to avoid possible effects of orientation and location within BioTRON on the direction of hyphal growth. After period II, the inoculum wood blocks were harvested, cleaned of surface mycelia and soil, and dried at 70°C to constant weight. The absolute weight loss (g) of the inoculum and bait wood blocks was calculated by subtracting the dried weight after the incubation period from the original dried weight of each wood block. We used the absolute weight loss of the wood blocks in the analyses as a proxy for the energy obtained by *P. velutina* from the wood blocks because the absolute weight loss is different between resource sizes even if the percentage weight loss is equal (Fukasawa and Kaga, 2020).

2.4 Image analysis

The dishes were photographed at the end of the pre-incubation period, every 3 days during incubation period I, and at the end of period II, using Canon EOS Kiss X10 camera, equipped with Canon EF-S18-55 mm F4-5.6 IS STM lens, mounted on a stand at a height of 52 cm, under the same light conditions to ensure consistency. The photo images at 24th day of period I were used to judge whether the mycelium colonized to the bait wood block from the inoculum side or from the opposite side (Supplementary Figure S2). The photo images at the end of period I were analyzed using ImageJ (National Institute of Health, United States) to evaluate the hyphal coverage on soil. The length of one side of the inoculum wood block (1 cm) was used as a calibration ruler. The edges of each soil dish and the wood blocks were removed by windowing, and the resulting images were converted to black (mycelia) and white (soil) using a manually set threshold. Hyphal coverage (cm^2) on the soil was used as a measure of hyphal biomass, representing the cost for *P. velutina*.

2.5 Statistical analysis

All analyses were performed using R 4.2.2 (R core team 2022). The normality of data distribution in each experiment was tested by Shapiro-Wilk test and equality of data variance across the experiments was tested by Bartlett test. Absolute weight losses of inoculum and bait were compared among the four experiments by Tukey-Kramer test because the data have normal distribution and equal variance across the experiments, whereas non-parametric Steel-Dwass test was employed for hyphal coverage at the end of period I due to lack of normality in one of the experiments. The frequency of mycelial migration from the inoculum to the bait wood blocks was compared between the two distance settings within experiments using same size of bait, employing Fisher's exact test.

The effects of bait size and the distance between the inoculum and bait on the absence of hyphal regrowth in period II (i.e., migration) were evaluated using a generalized linear model (GLM). A binomial distribution error was assumed, and a logit link function was used. The model did not include an interaction term of bait size and distance because our hypothetical scenario (Figure 1) predicts an interactive effect of resource size and distance on hyphal behaviour only when the distance is sufficiently large to make the cost for hyphal production larger than the energy available from resource. In this study, the hyphal production cost needed for resource survey might be much smaller than the energy available from the wood blocks, even in the FAR experiment, as hyphae grew out from the inoculum at one corner of the dish and reached the opposite side of the dish in most cases.

The indirect effects of bait size and distance on the absence of hyphal regrowth in period II (i.e., migration) through the weight losses of inoculum and bait wood blocks (energy benefit) and hyphal coverage (energy cost) were evaluated using structural equation modeling (SEM) with the lavaan package version 0.6-13 (Rosseel et al., 2023). Bait size and distance were set as the first-order variable, and the absolute weight losses of inoculum and bait wood blocks and hyphal coverage at the end of period I were set as the second-order variables. Link arrows pointed from lower- to higher-order variables, but the following links were removed from the model due to a lack of rationality: from bait size to inoculum weight loss, from distance to inoculum weight loss, and from distance to bait weight loss.

3 Results

The weight loss of the 73 unused (in incubation periods I and II) inoculum wood blocks at the end of the preincubation period was on

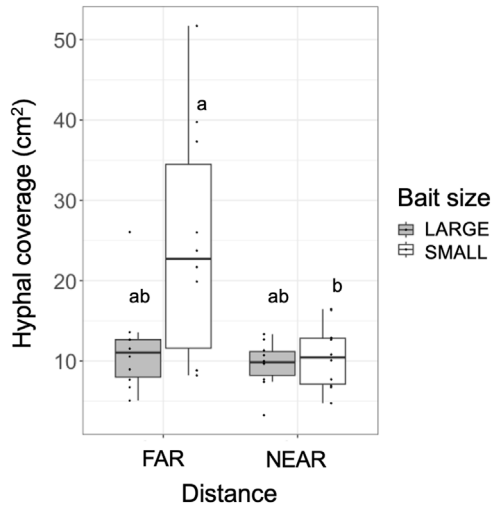

FIGURE 4
Hyphal coverage (cm^2) of mycelia extending from the inoculum wood block onto the soil at the end of incubation period I. Different letters on each box indicate significant ($p < 0.05$) differences among the four combinations of distance and bait (Steel-Dwass test, $N = 10$).

average (± standard error) 48.0% (±0.8%; range: 22.4%–60.9%). For the 40 used (in incubation periods I and II) inoculum wood blocks, the estimated weight loss at the end of the preincubation period (start of incubation period I) was on average 53.0% (±0.42%; range: 45.2%–58.2%), based on the regression line between weight loss and hyphal coverage (Supplementary Figure S3). Hyphae, grew out from the 40 inoculum wood blocks, successfully colonized on the baits regardless of their size and distance from inocula during incubation period I (Figure 2). Interestingly, in the FAR experiments, hyphal colonization on the bait started from the side facing the inoculum, whereas in the NEAR experiments, it frequently started from the opposite side of the bait (black arrowhead in Figures 2, 3). Hyphal coverage at the end of period I appeared to be larger in FAR compared to NEAR experiment in SMALL bait (Figure 4, Steel-Dwass test, $p = 0.04$, between FAR-SMALL and NEAR-SMALL experiments).

The absolute weight loss of the inoculum after the experiment (period II) was 0.163–0.237 g, representing 65%–92% of the original dried weight, and there were no significant differences across the experiments (Figure 5A). However, the absolute weight loss of the bait after period I was 0.054–0.429 g, representing 2.5%–14.2% of the original dried weight (Figure 5B). The weight loss of the bait was significantly lower in the NEAR-SMALL experiments compared with the other experiments (Figure 5B).

Mycelial migration from the inoculum to the bait (i.e., no regrowth from the inoculum in incubation period II) was observed more frequently in the NEAR experiments (8/10) than in the FAR experiments (3/10) with SMALL bait (Figure 6). However, there was no significant difference in migration frequency between the NEAR (6/10) and FAR (4/10) experiments with LARGE bait (Fisher's exact test, $p = 0.33$).

The results of the GLM indicated that the distance between the inoculum and bait significantly influenced migration occurrence (Table 1), with migration occurring more frequently when the distance was shorter. However the effect of bait size was not significant.

Structural equation modeling (SEM) analysis results revealed positive correlations between inoculum and bait weight losses and hyphal coverage (Figure 7). p-value of chi-square test > 0.05, comparative fit index (CFI) > 0.9, and root mean square error of approximation (RMSEA) < 0.1, indicated good model fit of the data. Additionally, bait weight loss was positively correlated with bait size. Hyphal coverage was positively correlated with the distance between the inoculum and bait, but negatively correlated with bait size. The occurrence of mycelial migration was negatively correlated with hyphal coverage. However, the direct effects of the factors, excluding hyphal coverage, on migration occurrence were not significant.

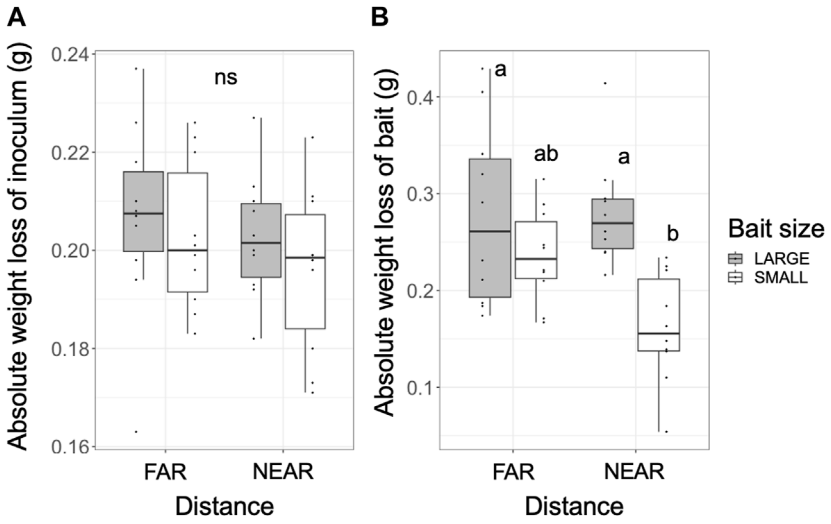

FIGURE 5
Absolute weight loss of the inoculum **(A)** after incubation period II and the bait **(B)** after incubation period I. Different letters on each box indicate significant ($p < 0.05$) differences among the four combinations of distance and bait (Tukey-Kramer, $N = 10$). ns, not significant.

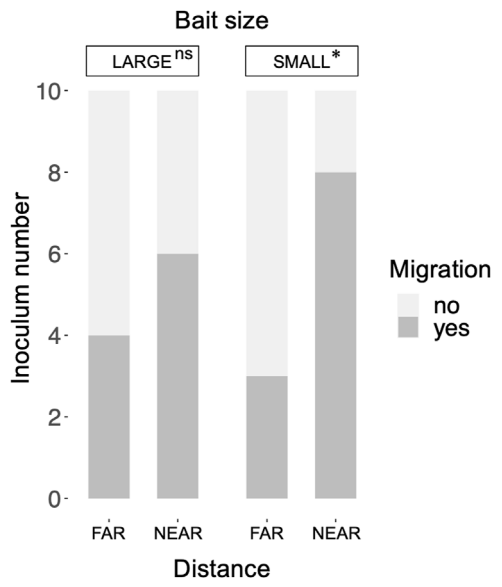

FIGURE 6
Frequency of mycelium migration in LARGE and SMALL bait wood blocks positioned at different distances from the inocula. Migration frequency was compared between the FAR and NEAR experiments (Fisher's exact test: *, $p < 0.05$; ns, not significant).

TABLE 1 GLM results explaining absence of hyphal regrowth in period II (i.g., migration) of mycelium from inoculum to bait wood block.

Factor	Estimate	S.E.	*Z* value	*p*-value
Bait size (SMALL)	0.229	0.678	0.338	0.7355
Distance (NEAR)	1.471	0.678	2.169	0.030

4 Discussion

SEM analysis results showed that when the bait was located far from the inoculum, there was an increase in hyphal coverage on the soil, which corresponded to a lower frequency of mycelial migration from the inoculum to the bait (Table 1 and Figure 7). This initial finding appears to support our hypothesis. However, we must exercise caution in discussing whether this is a result of high foraging costs associated with maintaining hyphae on the soil. Upon examining Figure 2, it seems that the increase in hyphal coverage in the FAR-SMALL experiment was not due to long connecting hyphae between the inoculum and bait but rather the secondary growth of foraging hyphae from the bait. This observation is further supported by the data from the LARGE experiments, where secondary growth of foraging hyphae was not observed, nor was there a difference in hyphal coverage between the NEAR-LARGE and FAR-LARGE experiments (Figure 4). Therefore, in the present study, the difference between the 1 and 15 cm distances from the inoculum to the bait may not have significantly affected the cost to maintaining hyphal connections between the inoculum and bait wood blocks. Instead, in the FAR-SMALL experiment, hyphal growth was also activated in a different direction without the presence of bait, suggesting that the inoculum serves as a hub for the established hyphal network (Figure 2). Conversely, such activation of hyphal growth in the direction without bait was not observed in other experiments. The reason for this difference becomes evident when examining the images of the NEAR experiment, shown in Figures 2, 3, where it is clear that hyphal colonization of the bait occurred from the side opposite the inoculum. In the present study, the hyphae of *P. velutina* were allowed to grow more than 15 cm from the inoculum before baiting, even in the NEAR experiment, to maintain uniform experimental conditions (excluding bait size and distance). Thus, in the NEAR experiment, the bait was placed on the basal part of the hyphal cord elongated from the inoculum. Therefore, the finding that hyphal colonization of the bait occurred from the side opposite the inoculum suggests that the main cytoplasmic body of the hyphae was located at its growing front, rather than in close proximity to the inoculum at the time of baiting.

Hyphae grow at their tips, where they exhibit strong directionality (Held et al., 2019). Particularly in a young growing colony, cytoplasmic flow, including nutrients, is concentrated toward the growing front, resulting in a larger nutrient content at this front than compared with the center of the colony (Tlalka et al., 2007). When a new bait is placed in close proximity to the inoculum (center) of such a growing colony, the majority of cytoplasm directed toward the growing front must reverse its flow to colonize the bait located at the center. This could explain why colonization of hyphae on large bait occurred from the side opposite the inoculum. For the same reason, colonization of NEAR baits may have taken more time than colonization of FAR baits, thereby delaying decomposition, especially on SMALL bait [although not statistically significant (Figure 5)]. These results suggest that the energy gain from bait may be greater in FAR experiments than in NEAR experiments. This contradicts our assumption that the net energy gain from a new resource would be larger when it is located closer.

If the migration of mycelium cannot be explained solely by the net energy gain from a new resource, an alternative explanation must be found. The foraging and migration behaviour of slime mould plasmodia have been studied extensively. Though unicellular, those organisms, have a superficially similar body design to fungal mycelia (Westerhoff et al., 2014; Boussard et al., 2021). Numerous studies on the model species *Physarum polycephalum* have revealed that plasmodia can optimize their network structure, connecting separately located multiple resources, by adjusting local cytoplasmic flow in response to the location, quantity, and quality of resources (Nakagaki et al., 2000b; Nakagaki and Guy, 2008). Similarly, previous studies on material transport within the mycelial network of *Phanerochaete velutina* have reported that nutrients, such as phosphorus, are transferred from the inoculum to bait wood blocks in relation to the size and quality of the bait (Fricker et al., 2017; Fukasawa et al., 2020). As demonstrated in the present SEM analysis, large bait reduced hyphal coverage on the soil and induced mycelial migration towards the bait. Furthermore, the migration decision of *P. velutina* mycelium was affected by the waiting time for the bait, i.e., the quality change of the original inoculum wood (Fukasawa and Kaga, 2021). If mycelium, as a modular organism, responds locally to these environmental stimuli (Itani et al., 2023), the NEAR experiment in the present study may have resulted in two separate parts of the mycelium responding to the bait, more or less, independently: the small part of the mycelium close to the original inoculum, and the larger spreading fans, including the growing front. Given that most of the nutrients are likely directed toward the growing front, the small part of the mycelium must respond to the new bait without a sufficient allocation of nutrients, which likely induces migration. Therefore, the difference in migration frequency observed in

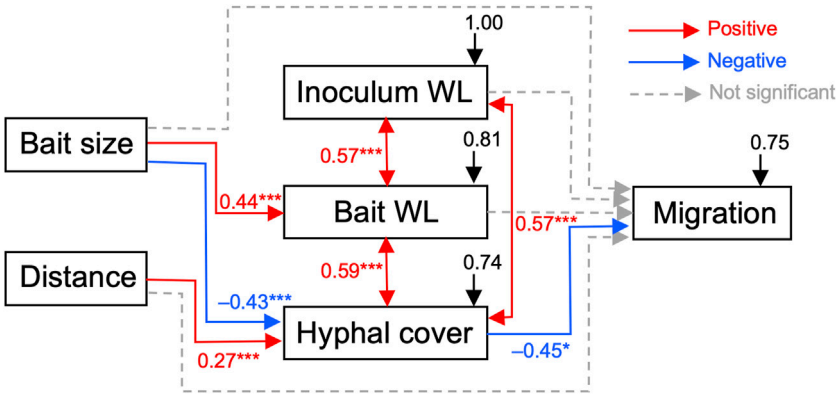

FIGURE 7
Results of structural equation modeling (SEM) showing potential causal relationships between bait size and distance, absolute weight losses of the inoculum and bait, hyphal coverage on the soil dish, and the presence of mycelial migration (p-value of Chi-square test = 0.262; comparative fit index [CFI] = 0.984; root mean square error of approximation [RMSEA] = 0.091; standardized root mean square residual [SRMR] = 0.09). Arrows represent causal pathways: red, blue, and dotted gray arrows indicate positive pathways, negative pathways, and non-significant pathways, respectively. *, $p < 0.05$; ***, $p < 0.001$. Numbers beside arrows represent path coefficients, taking values between −1 and 1, and difference from 0 indicates the strength of the relationship. Black arrows represent residual errors that arise in the prediction of the effects of unmeasured factors to the measured variables.

the present study could be attributed to the position of the new bait within a mycelial network that inherent possesses heterogeneity in its cytoplasm and nutrient distribution, rather than simply the distance between the inoculum and bait. A wood block on the soil (comprising both the inoculum and bait) serves as a carbon source for fungi, but it also functions as a base from which the fungi extend their hyphae into the soil to absorb nutrients. Hence, it might be more reasonable to position an old inoculum (a low-quality carbon source) far from the new bait, serving as a base (i.e., without migration), to facilitate the spread of hyphae into a larger area of soil, rather than keeping the old inoculum close to the new bait.

In the present study, we allowed the hyphae to grow more than 15 cm from the inoculum in all experiments before baiting to standardize the baiting time across the experiments. This resulted in a difference in the baiting position within the mycelium between the FAR and NEAR experiments. Bait was placed at the growing front of the hyphae in the FAR experiments, but it was positioned on the hyphal cord, far from the growing front, in the NEAR experiment. The initial hyphal elongation in both experiments may have reduced the difference in foraging costs between the FAR and NEAR experiments. To amplify the cost difference, an experimental approach could involve placing baits at the growing front of the mycelia in both FAR and NEAR experiments. However, this would introduce a difference in baiting time between the experiments, as hyphae takes 50 days to grow up to 15 cm. This difference in baiting time could potentially impact the quality of the inoculum and the nutrient status of the mycelium. On average, a 53% weight loss was estimated in the inocula during 50 days on the soil, with this result based on the regression line of 73 additional inocula not used in the baiting experiment. Overall, simultaneously unifying bait timing and distance from the inoculum across all experiments remains challenging.

The results of the present study reveal that the migration behaviour of *P. velutina* mycelia is influenced by bait size and its distance from the inoculum. Although the effect of bait size was not clear compared to previous study (Fukasawa et al., 2020), it might be attributable to the small difference in bait size in the present study. The results also suggest that the position of the bait within the mycelial network may play a crucial role in mycelial behaviour, rather than the distance between the inoculum and bait. To gain a deeper understanding of the foraging strategy of fungal mycelium, further microcosm experiments are warranted, focusing on mycelial behaviour in relation to the heterogeneity of resource utilization within a mycelium, particularly in systems involving multiple wood resources.

Data availability statement

The raw data supporting the conclusion of this article will be made available by the authors, without undue reservation.

Author contributions

YF: conceptualization, methodology, writing–original draft and review, supervision, funding acquisition. KI: methodology, writing–review. All authors contributed to the article and approved the submitted version.

Funding

The present study is financially supported by JSPS KAKENHI grant number 22H05669 to YF.

Acknowledgments

The authors thank Audrey Dussutour for suggesting related previous works on slime moulds.

Conflict of interest

The authors declare that the research was conducted in the absence of any commercial or financial relationships that could be construed as a potential conflict of interest.

Publisher's note

All claims expressed in this article are solely those of the authors and do not necessarily represent those of their affiliated organizations, or those of the publisher, the editors and the reviewers. Any product that may be evaluated in this article, or claim that may be made by its manufacturer, is not guaranteed or endorsed by the publisher.

Supplementary material

The Supplementary Material for this article can be found online at: https://www.frontiersin.org/articles/10.3389/fcell.2023.1244673/full#supplementary-material

References

Boddy, L., Hynes, J., Bebber, D. P., and Fricker, M. D. (2009). Saprotrophic cord systems: dispersal mechanisms in space and time. *Mycoscience* 50, 9–19. doi:10.47371/mycosci.myc50009

Boddy, L. (1999). Saprotrophic cord-forming fungi: meeting the challenge of heterogeneous environments. *Mycologia* 91, 13–32. doi:10.2307/3761190

Boddy, L., Wood, J., Redman, E., Hynes, J., and Fricker, M. D. (2010). Fungal network responses to grazing. *Fungal Genet. Biol.* 47, 522–530. doi:10.1016/j.fgb.2010.01.006

Boussard, A., Fessel, A., Oettmeier, C., Briard, L., Döbereiner, H-G., and Dussutour, A. (2021). Adaptive behaviour and learning in slime moulds: the role of oscillations. *Phil Trans. R. Soc. B* 376, 20190757. doi:10.1098/rstb.2019.0757

Davies, N. B., Krebs, J. R., and West, S. A. (2012). *An introduction to behavioural ecology*. New Jersey, USA: Wiley-Blackwell.

Donnelly, D. P., and Boddy, L. (1998). Repeated damage results in polarised development of foraging mycelial systems of *Phanerochaete velutina*. *FEMS Microbiol. Ecol.* 26, 101–108. doi:10.1111/j.1574-6941.1998.tb00496.x

Dussutour, A., Ma, Q., and Sumpter, D. (2019). Phenotypic variability predicts decision accuracy in unicellular organisms. *Proc. R. Soc. B* 286, 20182825. doi:10.1098/rspb.2018.2825

Ferguson, B. A., Dreisbach, T. A., Parks, C. G., Filip, G. M., and Schmitt, C. L. (2003). Coarse-scale population structure of pathogenic *Armillaria* species in a mixed-conifer forest in the Blue Mountains of northeast Oregon. *Can. J. For. Res.* 33, 612–623. doi:10.1139/x03-065

Fricker, M. D., Heaton, L. L. M., Jones, N. S., and Boddy, L. (2017). The mycelium as a network. *Microbiol. Spectr.* 5. FUNK-0033-2017. doi:10.1128/microbiolspec.FUNK-0033-2017

Fukasawa, Y., and Kaga, K. (2020). Effects of wood resource size and decomposition on hyphal outgrowth of a cord-forming basidiomycete, *Phanerochaete velutina*. *Sci. Rep.* 10, 21936. doi:10.1038/s41598-020-79058-8

Fukasawa, Y., and Kaga, K. (2021). Timing of resource addition affects the migration behavior of wood decomposer fungal mycelia. *J. Fungi* 7, 654. doi:10.3390/jof7080654

Fukasawa, Y., Savoury, M., and Boddy, L. (2020). Ecological memory and relocation decisions in fungal mycelial networks: responses to quantity and location of new resources. *ISME J.* 14, 380–388. doi:10.1038/s41396-019-0536-3

Held, M., Kaspar, O., Edwards, C., and Nicolau, D. V. (2019). Intracellular mechanisms of fungal space searching in microenvironments. *PNAS* 116, 13543–13552. doi:10.1073/pnas.1816423116

Hu, J., Gui, W., Heidari, A. A., Cai, Z., Liang, G., Chen, H., et al. (2022). Dispersed foraging slime mould algorithm: continuous and binary variants for global optimization and wrapper-based feature selection. *Knowledge-Based Syst.* 237, 107761. doi:10.1016/j.knosys.2021.107761

Itani, A., Masuo, S., Yamamoto, R., Serizawa, T., Fukasawa, Y., Takaya, N., et al. (2023). Local calcium signal transmission in mycelial network exhibits decentralized stress responses. *PNAS Nexus* 2, pgad012–10. doi:10.1093/pnasnexus/pgad012

Johnson, D., and Gilbert, L. (2015). Interplant signalling through hyphal networks. *New Phytol.* 205, 1448–1453. doi:10.1111/nph.13115

Kiers, E. T., Duhamel, M., Beesetty, Y., Mensah, J. A., Franken, O., Verbruggen, E., et al. (2011). Reciprocal rewards stabilize cooperation in the mycorrhizal symbiosis. *Science* 333, 880–882. doi:10.1126/science.1208473

Krebs, J. R. (1973). Behavioral aspects of predation. *Perspect. Ethol.* 1, 73–111.

Latty, T., and Beekman, M. (2009). Food quality affects search strategy in the acellular slime mould, Physarum polycephalum. *Behav. Ecol.* 20, 1160–1167. doi:10.1093/beheco/arp111

Latty, T., and Beekman, M. (2015). Slime moulds use heuristics based on within-patch experience to decide when to leave. *J. Exp. Biol.* 218, 1175–1179. doi:10.1242/jeb.116533

Lecheval, V., Larson, H., Burns, D. D. R., Ellis, S., Powell, S., Donaldson-Matasci, M. C., et al. (2021). From foraging trails to transport networks: how the quality-distance trade-off shapes network structure. *Proc. R. Soc. B* 288, 20210430. doi:10.1098/rspb.2021.0430

Money, N. P. (2021). Hyphal and mycelial consciousness: the concept of the fungal mind. *Fungal Biol.* 125, 257–259. doi:10.1016/j.funbio.2021.02.001

Nakagaki, T., and Guy, R. (2008). Intelligent behaviors of amoeboid movement based on complex dynamics of soft matter. *Soft Matter* 4, 57–67. doi:10.1039/b706317m

Nakagaki, T., Yamada, H., and Tóth, Á. (2000a). Maze-solving by an amoeboid organism. *Nature* 407, 470. doi:10.1038/35035159

Nakagaki, T., Yamada, H., and Ueda, T. (2000b). Interaction between cell shape and contraction pattern in the Physarum plasmodium. *Biophys. Chem.* 84, 195–204. doi:10.1016/s0301-4622(00)00108-3

R core team (2022). *R: A language and environment for statistical computing*. Vienna, Austria: The R foundation for statistical computing.

Rosseel, Y., Jorgensen, T. D., Rockwood, N., Oberski, D., Byrnes, J., Vanbrabant, L., et al. (2023). Package 'lavaan' version 0.6-13. Available at: https://lavaan.ugent.be.

Simard, S. W., Perry, D. A., Jones, M. D., Myrold, D. D., Durall, D. M., and Molina, R. (1997). Net transfer of carbon between ectomycorrhizal tree species in the field. *Nature* 388, 579–582. doi:10.1038/41557

Tero, A., Kobayashi, R., and Nakagaki, T. (2007). A mathematical model for adaptive transport network in path finding by true slime mold. *J. Theor. Biol.* 244, 553–564. doi:10.1016/j.jtbi.2006.07.015

Tero, A., Takagi, S., Saigusa, T., Ito, K., Bebber, D. P., Fricker, M. D., et al. (2010). Rules for biologically inspired adaptive network design. *Science* 327, 439–442. doi:10.1126/science.1177894

Tlalka, M., Bebber, D. P., Darrah, P. R., Watkinson, S. C., and Fricker, M. D. (2007). Emergence of self-organised oscillatory domains in fungal mycelia. *Fungal Genet. Biol.* 44, 1085–1095. doi:10.1016/j.fgb.2007.02.013

Wells, J. M., and BoddyEvans, L. R. (1995). Carbon translocation in mycelial cord systems of *Phanerochaete velutina* (DC: pers) parmasto. *New Phytol.* 129, 467–476. doi:10.1111/j.1469-8137.1995.tb04317.x

Wells, J. M., Hughes, C., and Boddy, L. (1990). The fate of soil-derived phosphorus in mycelial cord systems of *Phanerochaete velutina* and *Phallus impudicus*. *New Phytol.* 114, 595–606. doi:10.1111/j.1469-8137.1990.tb00430.x

Westerhoff, H. V., Brooks, A. N., Simeonidis, E., García-Contreras, R., He, F., Boogerd, F. C., et al. (2014). Macromolecular networks and intelligence in microorganisms. *Front. Microbiol.* 5, 379. doi:10.3389/fmicb.2014.00379

Zheng, X., Gao, Y., Wang, Y., XingZhao, F. M., and Gao, Y. (2022). Optimal foraging strategies in varying nutrient heterogeneity: responses of a stoloniferous clonal plant to patch pattern, size and quality. *Écoscience* 29, 221–232. doi:10.1080/11956860.2022.2048533

frontiers | Frontiers in Cell and Developmental Biology

TYPE Original Research
PUBLISHED 04 September 2023
DOI 10.3389/fcell.2023.1232685

OPEN ACCESS

EDITED BY
Laurence Wilson,
University of York, United Kingdom

REVIEWED BY
Fujio TSUMORI,
Kyushu University, Japan
Florian Raible,
University of Vienna, Austria

*CORRESPONDENCE
Mami Nomura,
mami_nomura_4p@sci.kj.yamagata-u.ac.jp

RECEIVED 01 June 2023
ACCEPTED 21 August 2023
PUBLISHED 04 September 2023

CITATION
Nomura M, Ohta K, Nishigami Y, Nakayama T, Nakamura K-I, Tadakuma K and Galipon J (2023), Three-dimensional architecture and assembly mechanism of the egg-shaped shell in testate amoeba *Paulinella micropora*.
Front. Cell Dev. Biol. 11:1232685.
doi: 10.3389/fcell.2023.1232685

Three-dimensional architecture and assembly mechanism of the egg-shaped shell in testate amoeba *Paulinella micropora*

Mami Nomura[1]*, Keisuke Ohta[2,3], Yukinori Nishigami[4,5], Takuro Nakayama[6], Kei-Ichiro Nakamura[2,3], Kenjiro Tadakuma[7,8] and Josephine Galipon[7,9,10,11]

[1]Faculty of Science, Yamagata University, Yamagata, Japan, [2]Division of Microscopic and Developmental Anatomy, Department of Anatomy, Kurume University School of Medicine, Kurume, Japan, [3]Advanced Imaging Research Center, Kurume University School of Medicine, Kurume, Japan, [4]Graduate School of Life Science, Hokkaido University, Sapporo, Japan, [5]Research Institute for Electronic Science, Hokkaido University, Sapporo, Japan, [6]Center for Computational Sciences, University of Tsukuba, Tsukuba, Japan, [7]Graduate School of Information Sciences, Tohoku University, Sendai, Japan, [8]Tough Cyberphysical AI Research Center, Tohoku University, Sendai, Japan, [9]Institute for Advanced Sciences, Keio University, Tsuruoka, Japan, [10]Graduate School of Media and Governance, Keio University, Fujisawa, Japan, [11]Graduate School of Science and Engineering, Yamagata University, Yonezawa, Japan

Unicellular euglyphid testate amoeba *Paulinella micropora* with filose pseudopodia secrete approximately 50 siliceous scales into the extracellular template-free space to construct a shell isomorphic to that of its mother cell. This shell-constructing behavior is analogous to building a house with bricks, and a complex mechanism is expected to be involved for a single-celled amoeba to achieve such a phenomenon; however, the three-dimensional (3D) structure of the shell and its assembly in *P. micropora* are still unknown. In this study, we aimed to clarify the positional relationship between the cytoplasmic and extracellular scales and the structure of the egg-shaped shell in *P. micropora* during shell construction using focused ion beam scanning electron microscopy (FIB-SEM). 3D reconstruction revealed an extensive invasion of the electron-dense cytoplasm between the long sides of the positioned and stacked scales, which was predicted to be mediated by actin filament extension. To investigate the architecture of the shell of *P. micropora*, each scale was individually segmented, and the position of its centroid was plotted. The scales were arranged in a left-handed, single-circular ellipse in a twisted arrangement. In addition, we 3D printed individual scales and assembled them, revealing new features of the shell assembly mechanism of *P. micropora*. Our results indicate that the shell of *P. micropora* forms an egg shape by the regular stacking of precisely designed scales, and that the cytoskeleton is involved in the construction process.

KEYWORDS

testate amoeba, shell formation, FIB-SEM, 3D reconstruction, 3D printer, *Paulinella*

1 Introduction

Algae and protist cellular structures are diverse, especially cell-covering structures, which vary widely in material and morphology from species to species (Preisig et al., 1994). Cell coverings in unicellular organisms supports the cytoplasm and protects the cell from dehydration and physical friction (Preisig et al., 1994). Finely formed cell coverings

composed of siliceous or calcium carbonate, such as those of diatoms and coccoliths, have been extensively studied. These coverings are formed in intracellular vesicles after cell division and are secreted by exocytosis to cover the cell (Taylor et al., 2017; Hildebrand et al., 2018). However, unlike diatoms, testate amoebae construct a shell of the same type as the mother cell in a mold-free space outside the cell, prior to cell division (Netzel, 1969). The shell constructed by this testate amoeba is identical to that of the mother cell, including the shape and position of the scales and spines (Netzel, 1969). The construction behavior of the testate amoeba, which constructs its shell in a space without mold, is similar to how animals such as humans and birds build houses and nests. However, it is clear that as a single-celled organism, the testate amoeba has a completely different system to construct their shell using the pseudopodia and associated cytoskeletons. How the unicellular testate amoeba manipulates extracellular components and constructs its shell remains unelucidated, and this mechanism remains highly intriguing from a cytological viewpoint.

Among the testate amoebae, Euglyphida harbor long and filose pseudopods that exit the shell aperture on one side and are used for locomotion and feeding (Meisterfeld, 2002; Adl et al., 2019). Euglyphids are found in a wide range of environments, including extremely cold climates (Smith, 1992; Santibáñez et al., 2011; Lara et al., 2016). Euglyphids form siliceous scales (parts of the shell) intracellularly and secrete them to construct an external shell (Meisterfeld, 2002; Adl et al., 2019). In particular, two photosynthetic species from the family Paulinellidae, *Paulinella micropora* and *Paulinella chromatophora*, are model organisms of interest to the research community because of the availability of type strains with fully sequenced genomes (Marin et al., 2005; Nomura et al., 2014; Nowack et al., 2016; Lhee et al., 2017; Matsuo et al., 2019; Lhee et al., 2021). In particular, the size of *P. micropora* is 12–17 μm, which is smaller than that of *P. chromatophora* (16–20 μm). Furthermore, the *P. micropora* NIES-4060 culture strain has the advantage of easy experimentation owing to its rapid growth (Nomura et al., 2014). Therefore, *P. micropora* is the model organism of choice to clarify the shell construction process in testate amoebae.

The *P. micropora* shell consists of approximately 50 slightly curved rectangular silica scales (Yoon et al., 2009; Nomura et al., 2014; Lhee et al., 2017). The scales arranged along the long axis of the shell are of varying sizes, with larger scales located towards the equator and smaller scales located at the posterior and aperture (Figure 1A). In addition, the posterior scales were decorated with ornaments, making it possible to distinguish approximately 10 longitudinally oriented scales from each other using scanning electron microscopy (SEM). Upon cell division, new scales are synthesized inside the mother cell and sequentially delivered to the template-free space outside the cell, which is followed by cell division (Kies, 1974; Nomura et al., 2014; Nomura and Ishida, 2016; Lhee et al., 2017). If larger scales are placed at the aperture or posterior side of the cell, or if smaller scales are placed in the middle, there will be a distance between adjacent scales, resulting in a hole or distortion of the shell shape. Therefore, if the scales are not placed in the correct position, an egg-shaped shell cannot be formed. The mechanism underlying the correct positioning of newly formed scales to form a similar egg-shaped shell for daughter cells remains unelucidated.

Previous studies have shown that *P. micropora* manipulates extracellular scales using a specialized thick pseudopodium extending from the maternal cytoplasm (Nomura et al., 2014; Nomura and Ishida, 2016). Time-lapse observations using optical microscopy further revealed that the scales are stacked in a left-handed helical manner, with the aperture of the mother cell side connected to the aperture of the daughter cell (Nomura et al., 2014). At this point, the thick pseudopodium extends from the mother cell to the shell under construction. The position and orientation of each scale is dynamically changed by the tips of the specialized thick pseudopodium and arranged to form an egg-shaped shell structure. Mitochondria, twisted microtubules, and the actin cytoskeleton present inside a specialized thick pseudopodium are involved in scale arrangement (Nomura and Ishida, 2016; Nomura and Ishida, 2017).

The detailed three-dimensional (3D) structure of the stable egg-shaped shell, 3D arrangement of the specialized thick pseudopodium observed during shell construction, and the precise arrangement of extracellular scales are not well understood. In this study, we analyzed the positioning of cytoplasm-derived specialized thick pseudopodium and extracellular scales during *P. micropora* shell construction, 3D morphology and architecture of the stable egg-shaped shell, and 3D shape of each individual scale using focused ion beam scanning electron microscopy (FIB-SEM) and 3D printing techniques. Our results show that the electron-dense cytoplasm intrudes extensively between the longitudinal sides of the scales that are about to be placed and those that have already been stacked in a cell undergoing shell construction. We also segmented each scale of *P. micropora* individually and plotted the position of its center of gravity, revealing that approximately 10 longitudinally aligned scales were arranged in a left-handed, single-circular ellipse and twisting arrangement.

2 Methods

2.1 Strains and culture conditions

Paulinella micropora strain NIES-4060 (MYN1) was maintained in modified Waris-H + Si medium (McFadden and Melkonian, 1986) where nutrients were reduced by half. The cultures were maintained at 20°C under a 12 h light/12 h dark cycle.

2.2 Specimen preparation for FIB-SEM

The 3D ultrastructure of the cells was analyzed using FIB-SEM tomography method (Miyazono et al., 2018). A 400 mL *P. micropora* culture was concentrated by centrifugation (1,000 × g, 5 min), and resuspended cells were washed with 5 mL of culture medium and fixed with 1 mL 4% glutaraldehyde and 0.75 mL 4% OsO_4 in culture medium at room temperature for 15 min. After five washes with Milli-Q water, the cell suspension was added into a culture dish (Ibidi, 81,166, Martinsried, Germany) coated with poly-L-lysine and left for 30 min to let the cells settle at the bottom of the dish. Samples were further fixed with 1.5% $K_4[Fe(CN)_6]\cdot 3H_2O$ and 2% OsO_4 in a 20 mM HEPES buffer for 30 min at 4°C and then washed five more

10.3389/fcell.2023.1232685

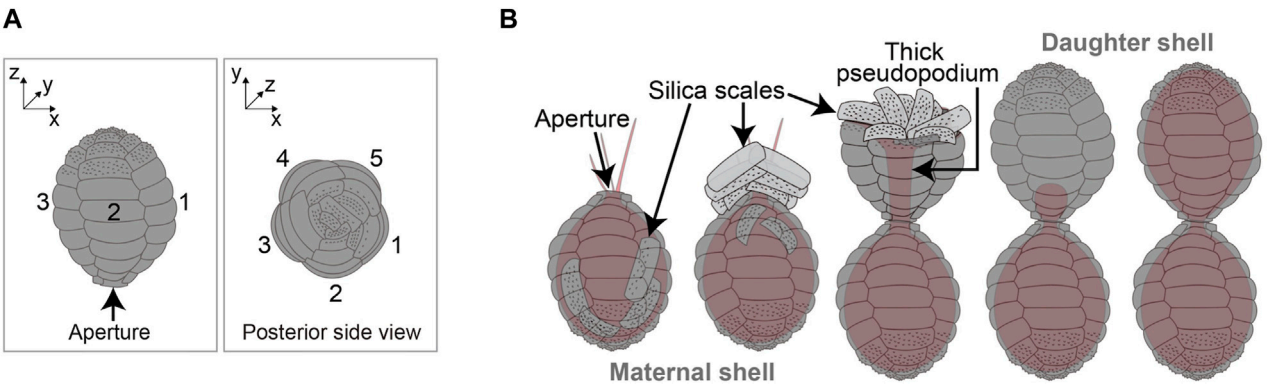

FIGURE 1
Shell architecture and its construction process of *Paulinella micropora*. **(A)** Viewing the shell of *P. micropora* from the posterior side of the cell, opposite from the aperture, reveals five rows of scales. Each scale is rectangular and curved. Each of the approximately 10 scales aligned along with the long axis has a different shape and can be distinguished from each other. **(B)** From left to right, the shell construction process in *P. micropora* is illustrated. *P. micropora* manipulates the extracellular scales to construct a new shell for one of the daughter cells with no extracellular template space. Cytoplasm and pseudopodia are represented in pale orange.

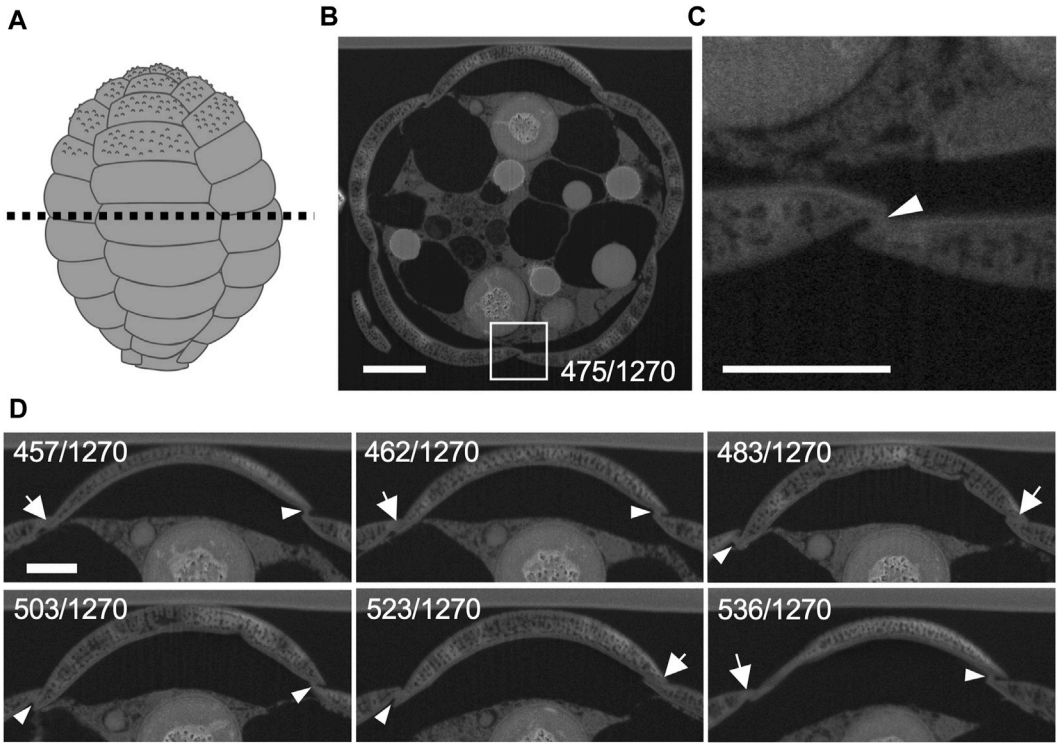

FIGURE 2
Organic material between silica scales observed by focused ion beam scanning electron microscopy (FIB-SEM). **(A)** Illustration of the shell of *Paulinella micropora*. **(B)** Cross section of the dotted line in **(A)**. The section from 1270 FIB-SEM scanning data is shown. **(C)** Enlarged view of the white boxed region in **(B)**. Organic cement material was observed between silica scales (arrowhead). **(D)** Sequential observation of the adhesion of the short sides of the scales to each other by the organic cement. Almost no organic cement is observed where the scales are tightly adhered to each other (arrows), and organic cement is observed on other adhesive surfaces (arrowheads). Scale bars: 2 μm in B, 1 μm in **(C)** and **(D)**.

times with Milli-Q water. The samples were then treated with 1% thiocarbohydrazide solution at 60°C for 1 h, washed five times with Milli-Q water, further reacted with 2% OsO_4 in Milli-Q water and again washed five times with Milli-Q water. The samples were then subjected to *en bloc* staining. The cells were incubated overnight with 4% uranyl acetate in distilled water. After three washes with Milli-Q water, the samples were immersed in Walton's lead aspartate solution and dehydrated in graded ethanol (20%, 50%, 70%, 80%, and 90%, twice in 100% for 5 min each), followed by infiltration with an epoxy resin mixture (EPON812; TAAB, Reading, England). The

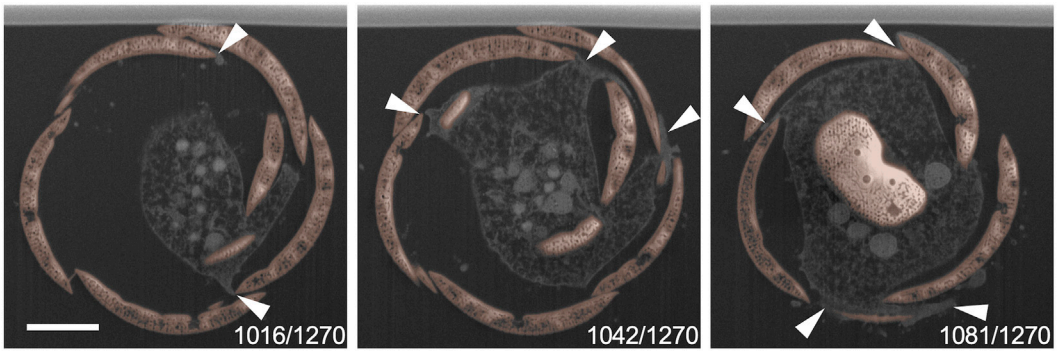

FIGURE 3
Cytoplasm elongates into the spaces between scales. The number in the lower right corner indicates which 1,270 focused ion beam scanning electron microscopy (FIB-SEM) scan data is represented. The smaller number indicates the mother cell side, and the larger number indicates the tip of the thick pseudopodia side. Each silica scale is individually segmented and labeled with different colors and the cytoplasm of a thick pseudopodium is an uncolored area. Arrowheads indicate cytoplasm that elongates towards between silica scales. Scale bar: 2 μm.

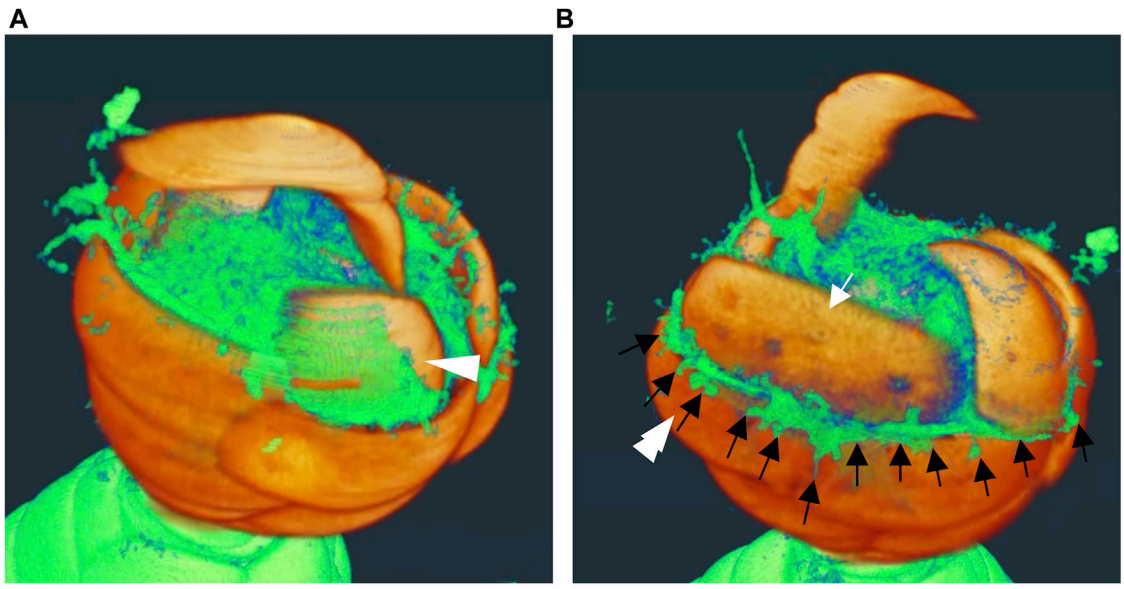

FIGURE 4
Three dimensional (3D) reconstructed images of daughter shell side during construction. These images are snapshots of the video shown in Supplemental movie 1. Areas other than the segmented scales on the side of the daughter shell are shown in yellow-green. **(A)** The scale indicated by the white arrowhead shows a well-covered appearance of the front edge of the thick pseudopodium. **(B)** Finely branched front edge of the thick pseudopodium (black arrow) extending outward and overflowing from the gap between the scale that has already been piled up (double white arrowheads) and the scale that is about to be piled up (white arrow).

resin was then polymerized at 65°C for 72 h. Following polymerization, the dishes were immersed in toluene to remove the bottom membrane, thus exposing the surface of the resin-embedded sample that had sunk to the bottom of the plastic dish. An inverted light microscope (CKX31, Olympus, Tokyo, Japan) was used to prepare a cell under shell construction, and a particular cell was cut from the flat frame because cells in the process of constructing new shells were rarely found. Target cells for 3D analysis were mounted on aluminum stubs glued with silver paste (Dotite D550; Fujikura Kasei, Tokyo, Japan). After plasma-coating the resin surface with osmium metal, the specimen was observed using an FIB-SEM (Quanta 3D FEG; FEI, Eindhoven, Netherlands). Serial stack images of the block were captured as previously described under the following conditions (Miyazono et al., 2018): The milling was performed using a gallium-ion beam at 30 kV and a beam current of 1 nA. The step size was set to 20 nm. Images were acquired at a landing energy of 2.5 keV. The milling and imaging cycles were repeated 1,000 times. Other acquisition parameters: Beam current = 51 pA, dwell time = 6 μs/pixel, image size = 2048 × 1768 pixels, and pixel size = 7.3 nm/pixel. The resulting

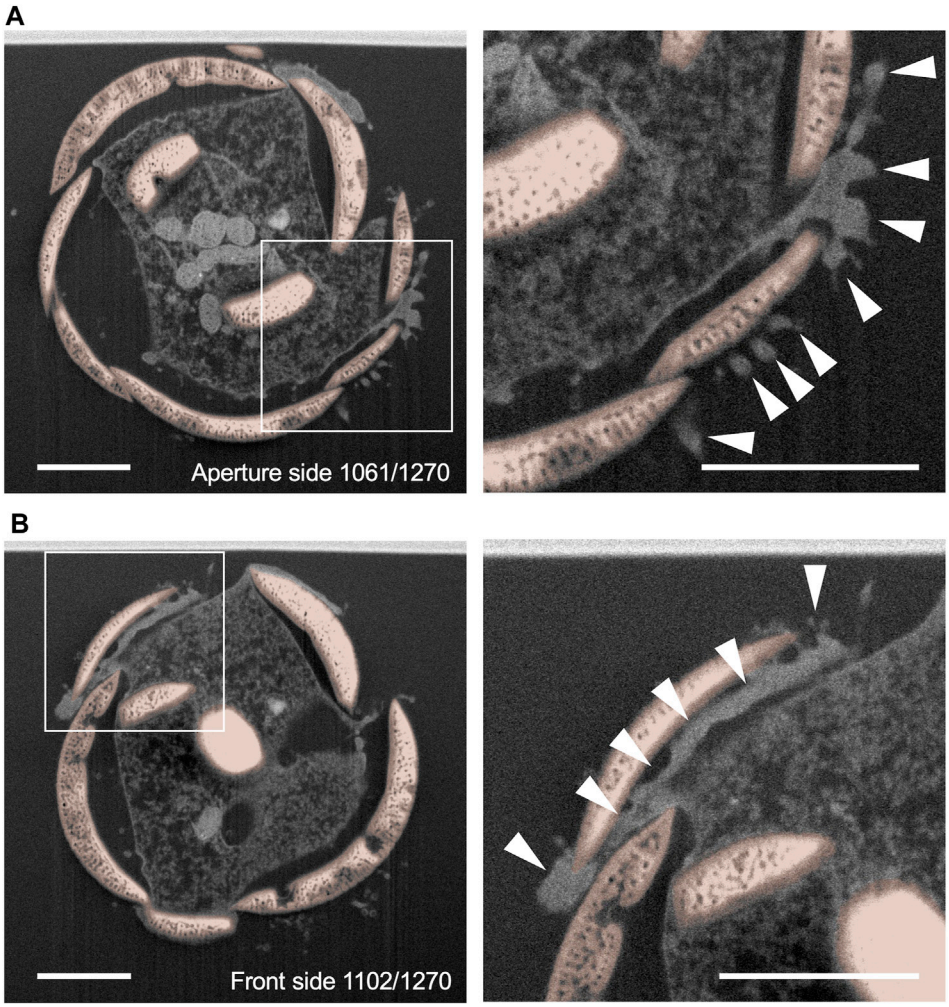

FIGURE 5
Single sections of the daughter shell side. **(A)** and **(B)** show a section of 1,270 focused ion beam scanning electron microscopy (FIB-SEM) scanning data. The smaller number indicates the aperture side, and the larger number indicates the posterior side of the daughter shell under construction. The right figure is an enlarged view of the area surrounded by squares in the left figure. Siliceous scales are shown in orange. The cytoplasm in the front edge of the thick pseudopodium which extends and intrudes between scales showed a high electron density (arrowheads). Scale bars: 2 μm.

image stacks were analyzed using Avizo 3D 2022.2 (FEI, Burlington, MA, United States).

2.3 Segmentation analysis and volume and centroid calculation of each scale

The silica scales and cytoplasm were manually and partially segmented automatically using Microscopy Image Browser (ver. 2.802, Belevich et al., 2016). The voxel size of the 52 segmented scales was adjusted by linear interpolation, and the data were meshed and exported in TIFF or STL format. To determine the centroid of each binarized scale, the positions of all scales were first adjusted from the overall cellular shape, such that the cell's long axis and *Z*-axis were parallel. Specifically, the images of all shells were projected onto a certain plane passing through the *Z*-axis, and this 2D projection was elliptically fitted. The locations of all the scales were rotated such that the elliptically fitted major and *Z*-axes were parallel. The images were then turned on their projection planes and projected onto a plane passing through the *z*-axis and intersecting the plane perpendicular to the plane. This 2D projection image was elliptically fitted, and all shell locations were rotated parallel to the long- and *z*-axes. This operation aligns the long axis of the cell along the *z*-axis. In this case, the scales on the posterior side of the mother shell had smaller Z values. The centroid and volume of each scale were determined using 3D ImageJ Suite (ver. 4.0.93, Ollion et al., 2013), a plugin for ImageJ.

2.4 3D printing

The STL files obtained in Section 2.3 were imported to Autodesk Fusion 360 (Autodesk, San Rafael, California, United States) with Netfabb Premium 2022 (Autodesk) and repaired using the automated repair function to correct wrongly

10.3389/fcell.2023.1232685

TABLE 1 Surface and contact area with the cytoplasm of each scale on the daughter shell side in the cell undergoing shell construction.

Scale	Surface area (μm²)	Contact area (μm²)
D1	10.470	0.000
D2	9.827	0.000
D3	8.692	0.000
D4	8.615	0.000
D5	8.459	0.000
D6	10.490	0.000
D7	11.044	0.017
D8	13.555	0.000
D9	15.002	0.000
D10	16.842	0.020
D11	18.165	0.017
D12	21.033	0.081
D13	21.876	0.069
D14	22.709	0.014
D15	23.345	0.026
D16	24.632	1.355
D17	24.796	1.087
D18	26.362	0.299
D19	26.857	1.972
D20	28.885	1.199
D21	27.313	2.277
D22	27.621	9.542
D23	28.885	28.885
D24	27.477	27.479
D25	28.988	0.050

oriented triangles and surfaces with zero thickness, which are problematic for 3D printing. To facilitate 3D printing, the scales were manually reoriented such that one of the thin sides faced the print bed. The final file was exported as a new STL file and converted to. g code using proprietary software provided with the following two types of printers: 1) Stereolithography (SLA) with the Formlabs Form 3 printer using Clear V4 resin with a layer height of 0.025 mm and default settings. After printing, the parts were washed in isopropanol, dried, and cured with an ANYCUBIC Wash & Cure Machine 2.0 (blue light 405 nm, 25 W) for 40 min (Figure 11A). 2) Fused Deposition Modeling (FDM) with the Agilista 3,100 using AR-M2 ink, high resolution settings; after printing, the parts were sonicated in 40°C water overnight using a 28 kHz ultrasonic bath (AU-80C, Aiwa Medical Industry Co., Tokyo, Japan) and washed in isopropanol for several hours before drying (Figures 11B, C).

3 Results

3.1 Whole-cell 3D imaging by FIB-SEM

FIB-SEM cuts a sample with an ion beam and scans its surface with an electron beam to continuously capture the cell structure with high resolution and ultimately constructs a 3D model. In this study, to understand the spatial arrangement of the thick pseudopodium extending from the maternal cytoplasm and the scales not yet placed, cells undergoing shell construction were selected from cell samples flat-embedded in resin under an optical microscope. FIB-SEM was then used to cut whole cells (20 nm each) approximately perpendicular to the cell long axis and capture images of the exposed surfaces ($n = 3$, Figure 2A). We succeeded in acquiring data with a resolution that enabled the identification of fine-scale structures and various organelles in all 3 cells in progress of shell construction (Figures 2B,C). In *P. micropora* transmission electron microscope (TEM) observations, cells were sectioned at right angles to the cell short axis, the long axis of the scales was placed at right angles to the cell long axis, and the long sides of the scales

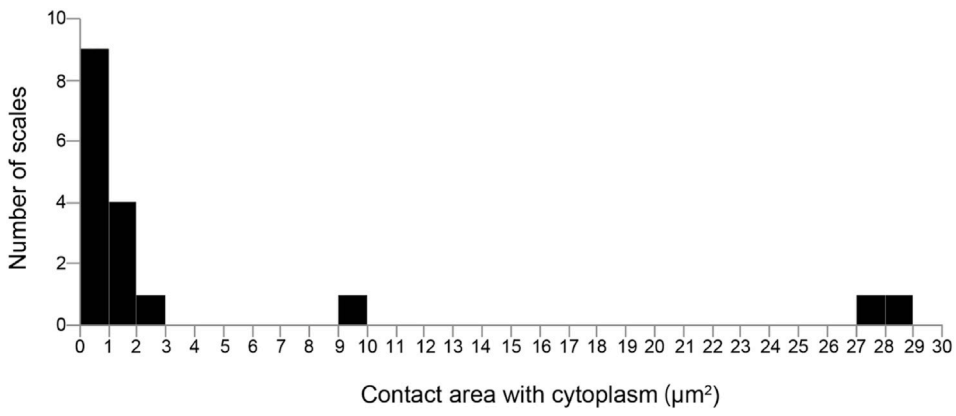

FIGURE 6
Distribution of the contact area with the cytoplasm. Most scales are only partially in contact with the cytoplasm.

10.3389/fcell.2023.1232685

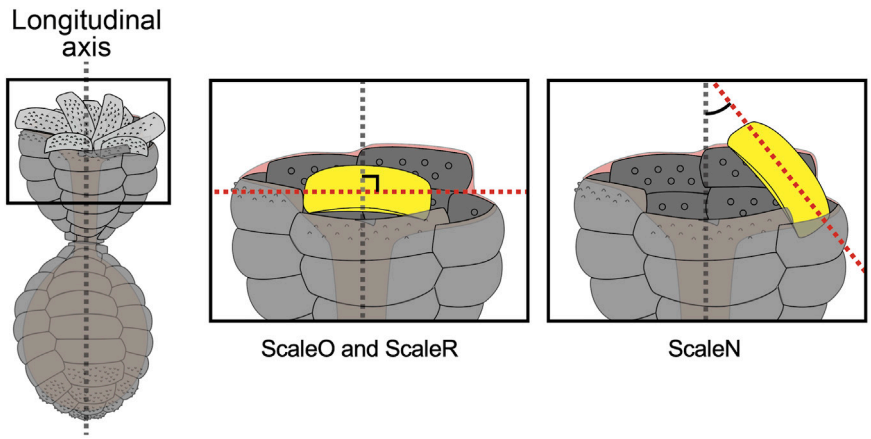

FIGURE 7
Relationship between scale arrangement and cytoplasmic contact area. The scales, most of whose surface area was in contact with the cytoplasm, were located near the center of the specialized thick pseudopodium and perpendicular to the long axis of the cell. Scale D22 was placed at the edge of the shell during construction and was located at an angle to the long axis of the cell.

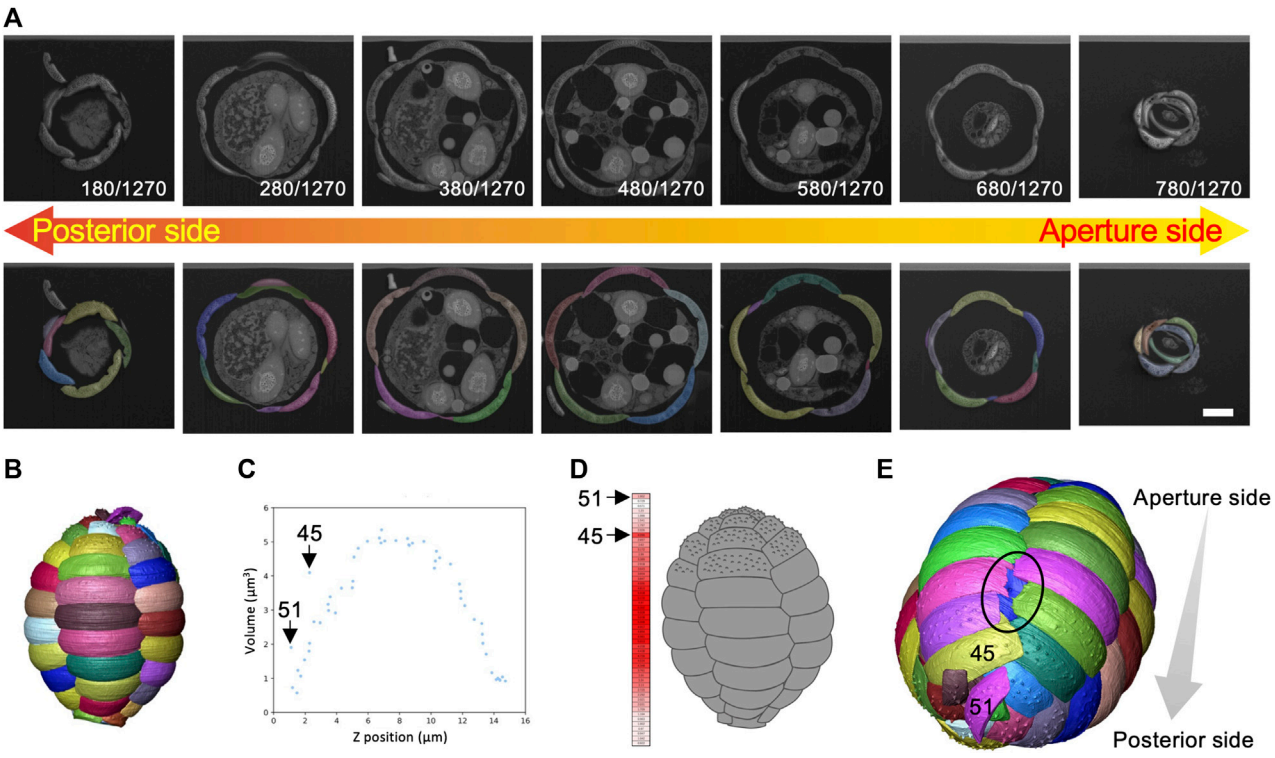

FIGURE 8
Segmentation analysis and calculation of volume and centroid of each scale. **(A)** There were 52 scales of this cell, each of which was segmented separately. Scale bar: 2 μm. **(B)** Three dimensional (3D) reconstructed image of the shell. **(C)** Graph of the volume of each scale placed along the long axis (*Z*-axis) of the shell. The volumes of Scale M45 and M51 are significantly larger than the surrounding scales. **(D)** Heat map of scale volume. Scales with larger volumes are shown in red and smaller scales are shown in white. Scale arrangement was disrupted at the posterior side of the shell. **(E)** Enlarged image of the posterior region of the 3D reconstructed image of the shell. The hole (black circled area) was caused by the misalignment of Scale M45 and M51. The blue-colored scale on the back side is visible. This hole is filled with organic cement (Supplementary Figures S2, S3; Supplementary Movie S4).

were attached to each other using organic cement (Nomura and Ishida, 2016). The results indicated that the long sides of the scales were attached to each other and the short sides were sequentially attached to each other by organic cement (Figures 2B–D, Supplementary Movie S1). Organic cement is particularly visible at gaps between scales (Figure 2D). In addition, the tips of

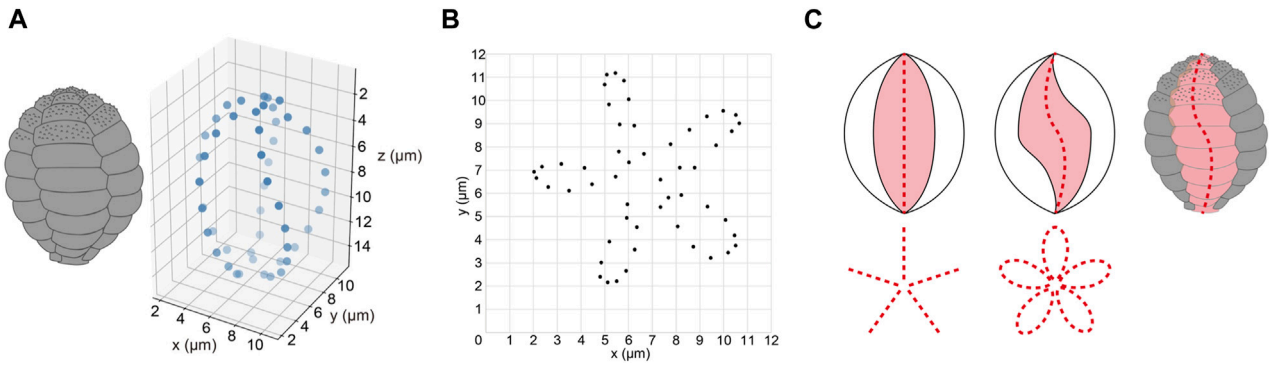

FIGURE 9
Position of the centroid of each scale in the shell. **(A)** Schematic diagram of the *Paulinella micropora* shell and the centroid of each scale plotted on three-dimensional coordinates. **(B)** XY plane coordinates plotted with the centroid of the scales. The centroids of the scales were arranged in a five-petal pattern. **(C)** The left figure is a schematic diagram of the case where the scales are aligned in a straight line along the long axis of the shell. The right figure is a schematic diagram of the case where the scales are aligned in an S-shape along the long axis of the shell.

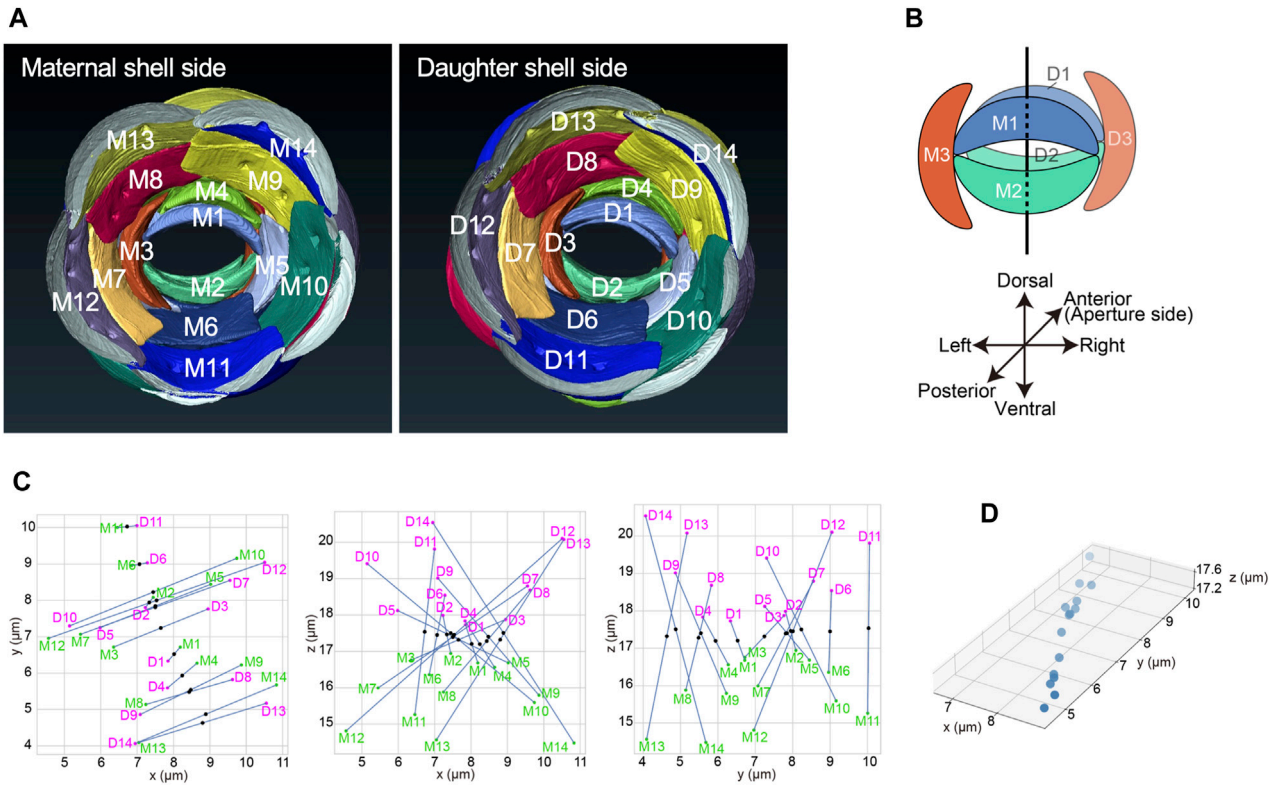

FIGURE 10
Spatial relationship between the mother and daughter shells. **(A)** Scale arrangement around each aperture of the mother and daughter shells, viewed from the posterior of each cell. Both the mother and daughter shells had the same scale arrangement. **(B)** The spatial relationship of the three scales that constitute each aperture of the mother and daughter shells, respectively. In this study, the side with the first scale is defined as dorsal, the side with the second scale is defined as ventral, and the side with the third scale is defined as left. **(C)** Scatter plots showing the positions of the centroids of scales M1-M14 (green) on the mother shell and scales D1-D14 (magenta) on the daughter shell. The midpoints between the centroids of the same numbered scales are also plotted (black). Plots are shown from left to right in the XY-plane, XZ-plane, and YZ-plane. **(D)** 3D plot of the midpoints of pairs of homologous scales in both shells shown in **(C)**. The midpoints between the centroids of each scale were plotted almost in a straight line, confirming that the scales of the mother and daughter shells are in line-symmetric positions.

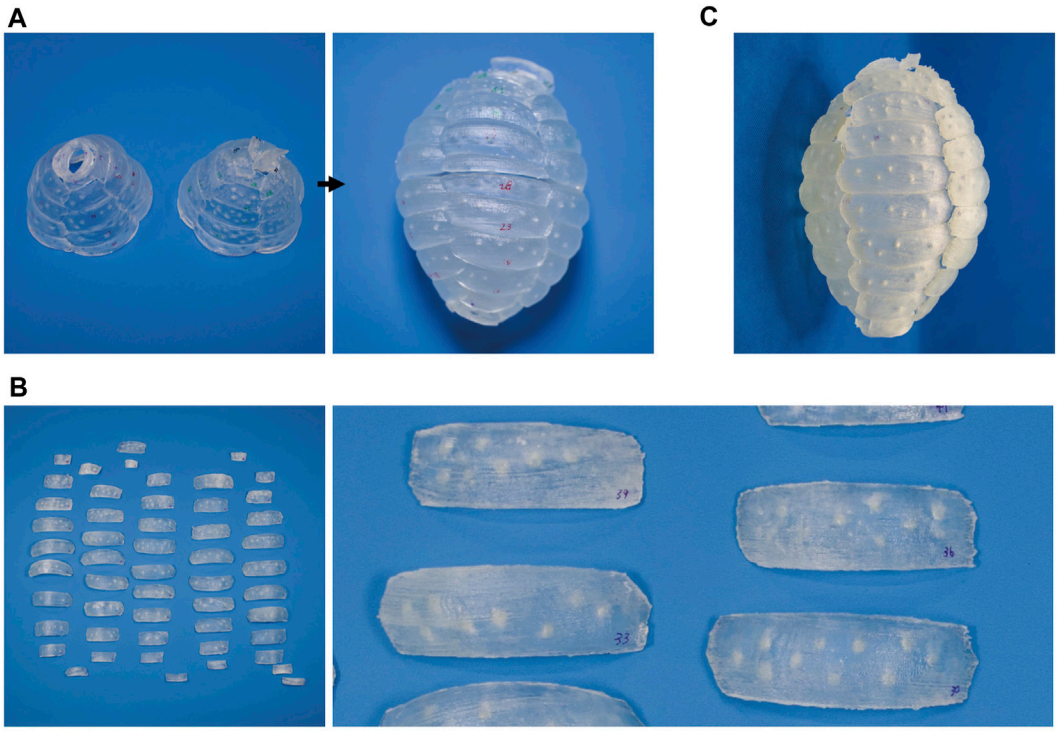

FIGURE 11
Three dimensional (3D)-printed *Paulinella micropora* shell. **(A)** The bisecting egg-shaped shell in the long axis direction was printed by 3D printer as a sample model. **(B)** 52 scales were individually printed. The figure on the right is an enlarged image of the printed scales. **(C)** The shell was assembled using 52 printed scales, following the sample model.

the specialized thick pseudopodium penetrated the joints between the short sides of the stacked scales at five locations on the daughter shell side (Figure 3).

Next, 3D reconstruction was performed to identify the spatial relationship between the cytoplasm of the thick pseudopodial tip and the extracellular scales. Only the scales on the daughter shell side were segmented as a single file and combined with other structures, including the cytoplasm of the thick pseudopodial tip (Figures 4, 5, Supplementary Movie S2). Some scales were tightly covered with a thick pseudopodial tip (Figure 4A). The peripheral region of the cytoplasm at the tip of the thick pseudopodium was finely branched (Figure 4B), and the electron density just beneath the cell membrane was high (Figure 5). These features were also observed in two of the 3 cells undergoing shell construction. All 3 cells for which FIB-SEM images were acquired in this study lacked the scales that would have piled up from this point on. In fact, we could not find a single scale with protruding ornamentation on the daughter shell side, which should be placed on the posterior side of the cell (opposite the aperture). This may be an artifact of fixation during electron microscopy sample preparation, and the impact of fixation, washing, and dehydration may have caused them to separate from the cell. Fragmented filose pseudopodia were observed extending to the tips of the thick pseudopodium, and the multiple scales to be piled may have been held by these filose pseudopodia (Figure 5).

To quantify the spatial relationship between the cytoplasm of the thick pseudopodial tip extending towards the daughter shell and the extracellular scales, segmentation analysis and calculation of the contact area were performed for the 25 scales in contact with the cytoplasm of the thick pseudopodial tip in a cell undergoing shell construction (Table 1). The frequency of the contact area of the thick pseudopodial tip with the cytoplasm in the cell undergoing shell construction is shown in Figure 6. In the cells analyzed in this study, 17 scales out of 25 were in contact with the cytoplasm of the pseudopodium, and in particular, Scale D23 and Scale D24 are found in contact over their entire surface, indicating that they were completely covered by the cytoplasm (Table 1). This pattern was also observed in two other cell types that did not undergo segmentation (Supplementary Figure S1). The remaining 15 scales were partially in contact with the cytoplasm, especially in areas where the already piled-up scales overlapped, and where the cytoplasm tended to elongate and contact the scales (Figure 3; Table 1). Of the scales that were partially in contact with the cytoplasm, Scale D22 had a large contact area 9.5 μm^2 in contact with the cytoplasm for a total surface area of the scale 27.6 μm^2, approximately one-third of the total surface area was in contact with the cytoplasm (Table 1; Figure 6). Unlike Scale D23 and D24, which were entirely covered with cytoplasm and perpendicular to the cell long axis, Scale D22 was located at the edge of the thick pseudopodium on the mother cell side, near the already piled-up scales and inclined towards the cell long axis (Figure 7). In two additional individuals that were not the subject of segmentation analysis, there were no scales with one-third of their surface area in contact with the cytoplasm, and we could not identify a trend.

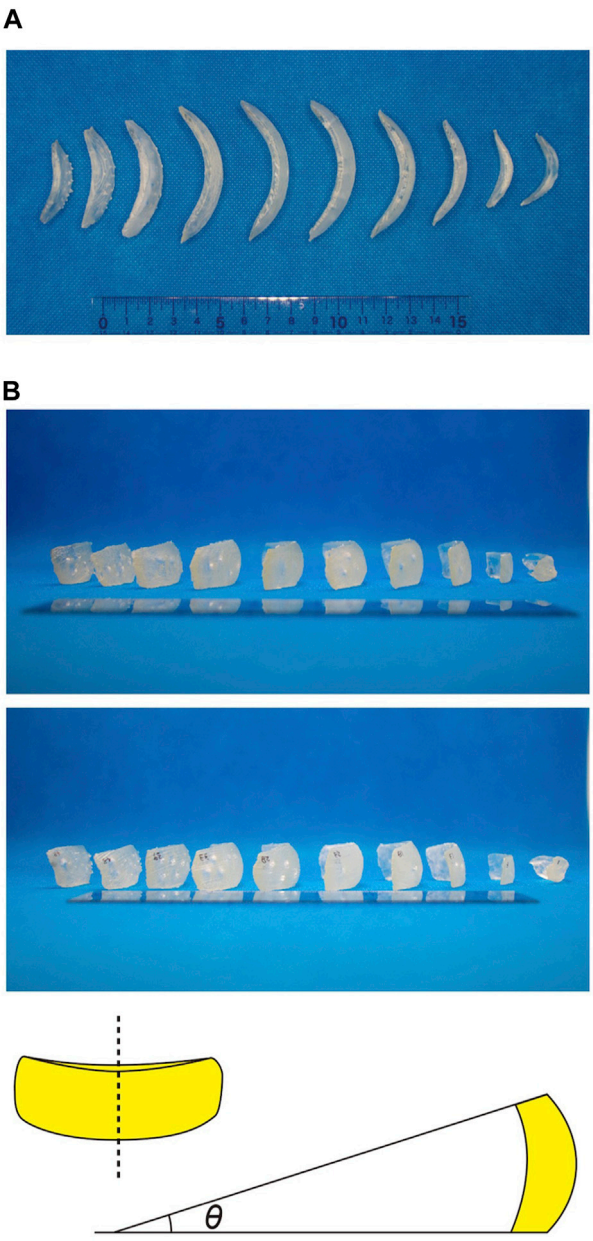

FIGURE 12
Characteristics of scales indicated by 3D printing. **(A)** The long sides of 10 scales aligned along the long axis of the shell were placed in the direction of gravity and photographed from above. **(B)** The scales are arranged as in **(A)**, photographed from the side. When the long sides of the scales were flipped up and down, the scales appeared to be slightly angled. In the illustration on the right, if the top and bottom of the long sides of the scales were angled at the top and bottom, it is expected that the angle θ formed by each tangent line would be important for the design of the egg-shaped shell.

3.2 Segmentation and 3D reconstruction of each scale

To understand the 3D morphology of the egg-shaped shell and the individual scales that construct the shell in *P. micropora*, a segmentation analysis was performed on each of the 52 scales in the maternal shell part of the FIB-SEM data and the scales were labeled in a left-handed helical direction, starting from the aperture (Figures 8A,B, Supplementary Movie S3). Although the *P. micropora* scales were originally highly porous, the interiors of the scales were filled during the segmentation process because the complexity of the structure increased, complicating analysis and 3D printing. The volume of each scale was calculated from the segmentation file, and the results were as expected, following a normal distribution with smaller volumes for the scales around the aperture and the posterior part of the shell and larger volumes for the scales in the middle layer (Figure 8C). However, the volume of Scale M45 and M51 showed outliers from the normal distribution, and when the scales were aligned in the *Z*-axis direction, the volume of Scales M45 and M51 were larger than those of the surrounding scales (Figure 8D). Furthermore, 3D reconstructed images revealed a hole in the posterior part of the shell, which was the result of a disrupted scale orientation (Figure 8E). This hole was filled with organic cement (Supplementary Figures S2, S3; Supplementary Movie S4).

To examine the architecture of the entire *P. micropora* shell, the centroid positions of the individual scales were calculated and plotted in the XYZ 3D space or in the XY plane, revealing a five-petal shape arrangement (Figures 9A,B). If the centroids of the scales aligned along the long axis of the cell were in a straight line, the lines would only extend radially in the XY-plane two-dimensional plot (Figure 9C). However, in this study, the petal-like arrangement of the centroid of the scales indicated that each row of scales was twisted approximately once (Figure 9C). That is, the centroids of the scales aligned along the long axis of the cell shifted. Conclusively, we established the entire architecture of the egg-shaped shell of *P. micropora* in three dimensions for the first time.

To elucidate the spatial relationship between the mother and daughter shell, the three-dimensional reconstruction of the scales of the daughter shell under construction was also performed via segmentation analysis. The scales were labeled in a left-handed helical order from the aperture side. Parts of the mother and daughter shells viewed from the inside of each are shown in Figure 10A (Supplementary Movie S5). The mother and daughter shells were found to be similar, and by aligning the orientations of the two shells, we confirmed that each pair of the corresponding scales had the same position (Figure 10A). The spatial relationship of the scales constituting the aperture of each of the mother and daughter shells, namely, Scales M1, M2, and M3 and Scales D1, D2, and D3, respectively, are shown in Figure 10B. We designated the spatial positions of scale numbers 1, 2, and 3, which constitute the aperture, as the anatomical dorsal, ventral, and left sides of the shell, respectively. The terms “dorsal” and “ventral” are traditionally used to describe the spatial axes of testate amoebae (e.g., Meisterfeld, 2002). Scales M1 and D1 appeared on the dorsal side, and Scales M2 and D2 appeared on the ventral side from the mother shell side, facing each other. Meanwhile, Scale M3 appeared on the left when viewed from the mother shell side, whereas Scale D3 appeared on the right (Figure 10B). For Scales M6 and D6 and Scales M11 and D11, these homologous scale pairs appeared on the ventral side when viewed from the mother shell side. Conversely, scales, including Scale M7 or M12 of the mother shell appeared on the left when viewed from the mother shell side, whereas Scale D7 or D12 of the daughter shell appeared on the right side when viewed from the mother shell side (Supplementary Movies S5, S6). Next, to accurately reveal the spatial relationship between the scales of the mother and daughter shell sides, the centroid positions of each scale in the mother and daughter shells were calculated, and used as a basis to

verify the positional relationship between homologous scales. Special attention was paid to the spatial relationship between the 14 scales of the daughter shell, Scales D1–D14, which presumably, were already placed in their position on the shell, and the corresponding scales on the mother shell side, Scales M1–M14 (Figure 10C). Plotting the midpoint between the centroids of the scales with the same number on the mother and daughter shell sides resulted in a nearly straight line in 3D space (Figures 10C,D). Furthermore, the spatial relationship between the mother and daughter shells in the other two individual cells for which segmentation analysis was not performed was verified by checking the arrangement of the scales at the apertures making reference to FIB-SEM image data. Thus, unlike the above individual cells, Scale M3 of the mother shell and Scale D3 of the daughter shell were positioned on the same left side when viewed from the mother shell side, and Scales M1 and D2, and Scales M2 and D1 were facing each other (Supplementary Figure S4). Additionally, the direction of the long axis of the elliptical aperture formed by the scales numbered 1 and 2 was almost the same in all the three pairs of mother and daughter shells examined (Supplementary Figures S4, S5).

3.3 3D printing of shell and scale characterization

3D printing represents a powerful tool to generate new research and development because it allows us to perform unique experiments that are difficult to perform *in silico*. To better understand the shell architecture of *P. micropora*, 3D printing was performed using segmentation files. First, to obtain an overall view of the shell of *P. micropora*, a file bisecting the egg-shaped shell in the long-axis direction was prepared, converted to an STL file, and 3D printed (Figure 11A). This sample model had an egg shape. The numbers labeled during segmentation were transcribed in the sample model and used as the reference model. Next, 52 scales were individually 3D printed at 10,000-fold the size of the reference model to allow for easy manipulation and visualization of each scale (Figure 11B). Approximately 10 scales aligned in the longitudinal direction of the cell, which have clearly different morphologies, and five horizontally aligned scales had slightly different numbers and positions of hollows on the dorsal side (cytoplasmic side), confirming that none of the printed scales had the same shape (Figure 11B). Finally, the labels from the segmentation file were transcribed onto these individually printed scales, and the shell was manually assembled by referring to the reference model. Using the transparent gel double-sided tape as an adhesive on the areas with organic cement observed in FIB-SEM, where the long and short sides of the scales were attached to each other, we succeeded in assembling a shell with a morphology representative of the reference model (Figure 11C). Similar to the behavior of *P. micropora*, it was easier to assemble them in order from the scales on the aperture side, and the shape was more stable as it approached an oval shape rather than a half-spherical shape.

4 Discussion

The testate amoeba *P. micropora* produces more than 50 differently designed scales within its cells, and once they commence shell assembly, it takes approximately 30 min to complete (Nomura et al., 2014). Although the shell-constructing behavior of testate amoebae, including *P. micropora* seems too complex for a unicellular organism and may appear to be a disadvantageous survival strategy, the study of this unique unicellular organism has the potential to reveal new cellular functions. However, many questions remain regarding the shell-constructing behavior of *P. micropora*, such as how the production of scales of different sizes is programmed, how they hold the secreted scales outside the cell, recognize or identify them by pseudopodia, how they can place specific scales in specific locations in a space without a template, when and at what time the placed scales are fixed with cement and glued to each other, how and when the cement is secreted, and when the scales adhere to each other. These questions remain unanswered because of limited observations of the shell-constructing behavior of *P. micropora*. Furthermore, studying the molecular mechanisms of *P. micropora* shell construction requires foundational information on the shell structure, such as the detailed 3D structure of the shell, spatial relationships between mother and daughter shells, and manner of the physical contact between the tips of the pseudopodium specialized for shell construction and the scales moved by them, all of which are currently lacking. In this study, we performed FIB-SEM analysis to understand the 3D architecture of the egg-shaped shell and its assembly in *P. micropora*. FIB-SEM, which cuts the sample surface with an ion beam and observes the exposed surface, is an innovative tool that allows the structural analysis of an entire protist cell with extremely high resolution, although it is inferior to TEM (Friedrichs et al., 2012; Gavelis et al., 2017; Xing et al., 2017; Hörning et al., 2020; Zgłobicka et al., 2021). Whole-cell analysis using FIB-SEM was performed on three *P. micropora* cells during shell construction.

4.1 Spatial relationship between the cytoplasm of the thick pseudopodial tip and the extracellular scales during shell construction

Although *P. micropora* cells undergoing shell construction have previously been observed by TEM (Nomura and Ishida, 2016), it is difficult to prepare several hundred ultrathin sections of an entire cell, and the positional relationship between extracellular scales and the specialized thick pseudopodium, which is unique to the shell construction process, has not yet been characterized in detail. The FIB-SEM results showed that, at high resolution, the tips of the specialized thick pseudopodium were spread out and in contact with the extracellular scales, as observed in previous studies using TEM (Figures 2, 3; Nomura and Ishida, 2016). Furthermore, by segmenting the scales and thick pseudopodial tips (cytoplasm) using FIB-SEM data and 3D reconstruction, we revealed that the electron-dense cytoplasm widely penetrates between the long sides of the scales that are about to be piled up and those that have already been arranged (Figures 4, 5). TEM observations during shell construction of *Euglypha acanthophora* and *Euglypha strigosa*, which belong to the same order as *P. micropora*, have shown electron-dense adhesion plaques (microfilaments) just beneath the cell membrane in contact with extracellular scales (Hedley and Ogden, 1974). The highly electron-dense structure observed

just beneath the cell membrane at the specialized thick pseudopodial tip in contact with the scale in shell-constructing *P. micropora* corresponds to the adhesion plaque previously reported in genus *E. acanthophora* and *E. strigosa*. Furthermore, indirect fluorescent antibody analysis of *P. micropora* during shell construction has suggested the presence of distributed actin in the tips of the specialized thick pseudopodium (Nomura and Ishida, 2017). In line with this, the highly electron-dense adhesion plaques observed in this study might be linked to the accumulation of actin filaments. Previous studies have reported that bundles of microtubules are arranged in a twisted manner within the specialized thick pseudopodium that extends into a constructing daughter shell, hinting at the potential involvement of microtubules in scale arrangement (Nomura and Ishida, 2016; 2017). Future research, for instance using specific inhibitors, is needed to determine if either of these cytoskeletal filaments is involved in the specialized thick pseudopodium formation. In addition, the cytoplasm that penetrates between the scales is thought to allow the scales to adhere to each other; however, owing to the low resolution compared to that of TEM, we were unable to identify vesicles containing organic cement within this cytoplasm (Figures 4, 5). However, given the results of TEM observations in a previous study, it was thought that organic cement was secreted from the cytoplasm that penetrated between the scales (Figures 4, 5; Nomura and Ishida, 2016). In addition, the scales to be stacked were held by the cytoplasm that had penetrated between the scales, and this cytoplasm was placed outside the shell (Figure 4B). To recover the cytoplasm that penetrated the outside of the shell, an appropriate amount of organic cement must be secreted at an appropriate time to hold the scales in place. In other words, the order and timing of the secretion of organic cement, placement of scales, and solidification rate of the organic cement were expected to have significant effects on the shell construction of *P. micropora*.

4.2 Contact area between scales and the cytoplasm indicates the stage of the scale migration process during shell construction

Contact area analysis between the specialized thick pseudopodium and the extracellular scales on the daughter shell side revealed three patterns: scales that were entirely covered with cytoplasm, scales that were approximately one-third covered, and scales that touched the cytoplasm only slightly (Figure 6; Table 1). The long sides of the scales that had the entire surface area in contact with the cytoplasm (Scale D23 and D24) were oriented almost perpendicular to the long axis of the cell and were located near the center of the shell during construction; a similar pattern was observed for the other two samples in which segmentation analysis was not performed (Figure 7). The greater the area of contact with the cytoplasm, the more likely it is that the cells will be able to control the orientation of the extracellular scales, and we can expect these scales to be placed in the proper position on the shell. In contrast, the scale with one-third of its entire surface area in contact with the cytoplasm (Scale D22) was positioned at an angle to the long axis of the cell and was located at the edge of the constructing shell. Although a larger contact area with the cytoplasm should allow for better control of scale orientation, Scale D22 was located closer to the tip of the thick pseudopodia than Scale D23 or D24, and in the neighborhood of the already piled-up scales, Scale D22 can also be expected to be placed in the proper position on the shell. In addition, the cytoplasm in contact with Scale D22 formed adhesion plaques, as described above, although the vesicles containing adhesion substances reported in a previous study could not be identified (Nomura and Ishida, 2016, Supplementary Figure S6). The adhesion plaques observed in *E. acanthophora* and *E. strigosa* were found inside the shell under construction, whereas the adhesion plaques observed in *P. micropora* in this study were found mainly outside the shell under construction (Figure 5; Hedley and Ogden, 1974). The shell architectures of *Euglypha* and *Paulinella* genera have the following differences: In the genus *Euglypha*, the size and shape of the scales are the same except for the aperture, and they are uniformly arranged; however, the orientation of the scales does not need to be precisely defined, as in the genus *Paulinella* (Hedley and Ogden, 1973; 1974; Hedley et al., 1974). In contrast, *Paulinella* has more than 10 different scale sizes and shapes that are roughly classified, each of which is placed in the appropriate position and direction to complete the egg-shaped shell (Johnson et al., 1988; Hannah et al., 1996; Nicholls, 2009; Lhee et al., 2017). Therefore, in the genus *Paulinella*, instead of a simple cytoplasm, they evolved to use a specialized thick pseudopodium and extend its front edge to the outside of the shell to assemble the egg-shaped shell. Thus, even among testate amoebae of the same order, Euglyphida, the shell construction strategy differed. The main principles of shell construction will be clarified in future studies that compare euglyphid species.

Scale D22, which was expected to be piled up, may have observed the moment of dynamic movement of scales. It is difficult to determine whether Scale D22 was able to capture the moment of shell construction or an artifact due to fixation because scales with approximately half of their surface area in contact with the cytoplasm were not observed in the 2 cells, except for the one whose contact area was analyzed in the present study. In a previous study performed using time-lapse video recordings, scales moved dynamically and quickly just before they are placed in a specific position (Nomura et al., 2014), and it is thought that the probability of successfully fixing multiple cells with appropriate timing is relatively low. In addition, the aforementioned adhesion plaque was observed just beneath the cell membrane in contact with Scale D22 (Supplementary Figure S6). Based on these results, it is highly likely that the cell in which segmentation analysis was performed among the 3 cells analyzed by FIB-SEM might have observed a moment of dynamic movement of the scales at the tip of the specialized thick pseudopodium. In the future, it will be necessary to quantify how the orientation of extracellular scales is changed by a specialized thick pseudopodium using confocal laser microscopy.

4.3 Architecture of the egg-shaped shell and spatial relationship between mother and daughter shell in *Paulinella micropora*

In this study, to examine the architecture of the entire complete shell of *P. micropora*, each scale was segmented

individually, and its centroid was calculated and plotted in the XY plane, which revealed that the centroid of the scales was arranged in a five-petal shape (Figure 9B). In the middle layer, where the radius of the *P. micropora* shell reaches its maximum, the large scales are arranged with their long side perpendicular to the shell's long axis, and the results of the present analysis indicate that the centroid of the large scales is located radially away from the center of the shell and that the radius of the shell is also increased. Centroids of approximately 10 scales aligned in the direction of the long axis of the shell did not overlap in a single row but were arranged in a left-handed ellipse around one round, indicating that these scales were arranged in a twisted manner. Considering approximately 10 scales aligned along the long axis direction of the shell as a single sheet, they formed a curved sheet structure, not an almond-shaped like a rugby ball (although a rugby ball has four sides, not five sides, like the shell of *P. micropora*) (Figure 9C). In other words, approximately 10 scales aligned in the longitudinal direction of the shell were arranged with their centroids not in a straight line but in a left-handed helical shape. When bricks are stacked on a building site, it is generally accepted that bricks aligned vertically in a straight line (stack bond) are weaker against external forces such as earthquakes; therefore, techniques have been developed to prevent the formation of stack bond patterns. Simulation studies have also investigated the influence of brick alignment on the structural vulnerability of brick walls (Drougkas et al., 2015). Similarly, the shell of *P. micropora* is expected to have a mechanically stable arrangement of left-handed helically oriented scales to prevent the formation of stacked bonds. This helical structure is also used in the cell coverings of other protists (Leadbeater et al., 2008; Hörning et al., 2020).

The cell segmentation analysis in this study revealed a hole in the posterior region of the shell filled with organic cement (Figure 8E). In the other 2 cells, for which no segmentation analysis was performed, the gaps were not as wide as those in this cell, although the organic cement increased in the posterior region of the shell (Supplementary Figure S7). In time-lapse video observations, the behavior of discarding one or two scales from the posterior side of a cell at the end of the shell construction process has been reported (Nomura et al., 2014). These findings suggest that the scales in the posterior region of the shell may be relatively flexible in changing positions and that the holes created by these changes are filled with organic cement. The amount of change that the cells can handle remains unknown; however, it is expected to depend on the amount of organic cement produced before or during shell construction and the size of the holes that can be filled. The identification of the organic cement and its dynamics during the shell construction process, as well as the behavior of *P. micropora* cells when shell construction is artificially inhibited, will help to elucidate the mechanism of shell construction and new cell functions.

The daughter shells under construction were presumed to have the same shape as the mother shells. We also presumed that they had line symmetry with the mother shells as they were facing the apertures of the mother shell during construction. To verify this assumption, we used the 3D modeled cell to examine the positional relationship between the homologous scales that constituted the mother and daughter shells. Thus, we found that the midpoint of the straight line passing through the centroids of two homologous scales existed almost on a straight line (Figure 10, Supplementary Movie S6). Further, when the daughter shell was rotated 180° around this line, it overlapped with the mother shell, confirming that there exists a two-fold symmetry between the mother and daughter shells, i.e., a line symmetric positional relationship between them (Figures 10B–D). The axis in this symmetry was roughly positioned on the contact surface of Scales M1 and D1 and Scales M2 and D2, constituting the apertures of the mother and daughter shells, respectively. It was also approximately horizontal to the dorsoventral axis and almost intersected perpendicularly with the left-right axis (Figure 10B). Further, we verified the positional relationship between the mother and daughter shells by examining the arrangement of the three scales constituting the aperture of the two shells using two additional individual cells that were not the subject of segmentation analysis. As a result, it was revealed that both cells had the mother and daughter shells in a line symmetry position, similar to the aforementioned cell. However, in these two individuals, Scale M3 of the mother shell and Scale D3 of the daughter shell were facing each other, and Scales M1 and M2 of the mother shell were facing Scales D2 and D1 of the daughter shell, respectively (Supplementary Figures S4, S5). Thus, it was found that the symmetry axis of these 2 cells was roughly parallel to the left-right axis, but not to the dorsoventral axis, unlike the symmetry axis of the first cell that was examined using its 3D model (Supplementary Figure S4). In this research, it is confirmed that in the shell construction process of *P. micropora*, the mother and daughter shells show line symmetry. Furthermore, the observed direction of the symmetry axis was not constant, and some cases roughly parallel to the dorsoventral axis and to the left-right axis were observed. Presently, owing to the limited number of observations, it is still inconclusive whether the symmetry axis of the shells during the shell construction process of *P. micropora* is always roughly parallel to the dorsoventral axis or the left-right axis. However, considering that various organelles, including the nucleus and chromatophores, move through the aperture connecting the mother and daughter shells during the cell division process (Nomura et al., 2014), it may be plausible that it always aligns in either of the two directions (i.e., roughly parallel to the dorsoventral or the left-right axis) where the aperture becomes widest. Regardless, more observations of shells under construction are needed in the future to verify this hypothesis.

4.4 3D printed model provided insight into the architecture and formation of the egg-shaped shell

Because of the small nature of unicellular organisms, it is necessary to use different types of microscopes to understand their cellular structure, and it is difficult to visualize the cell in its entirety. 3D printing, has been used in various fields,

including biomimetics (Shahrubudin et al., 2019). Here we show that it can also be applied to the study of single-celled organisms. By using a 3D printer to enlarge the morphology of microscopic single-celled organisms, we can better familiarize ourselves with their structures and possibly posit new research ideas. The architecture and construction process of the shell of the unicellular amoeba *P. micropora* remains unknown; however, there is no doubt that this phenomenon preserves the unknown potential of the cell. The 3D-printed shell of *P. micropora* is enlarged so that it can be physically held in hand, allowing for easier comparison of shapes than is possible with *in silico* comparative analysis using currently available programs. In this study, we performed 3D printing using data from the FIB-SEM segmentation analysis, printed the sample model and individual scales separately, and assembled the shell according to the sample model. This sample model and assembled shell had an egg shape, consistent with previously reported SEM observations (Figure 10; Yoon et al., 2009; Nomura et al., 2014; Lhee et al., 2017). Two new features of the egg-shaped shell structure of *P. micropora* were discovered. 1) The curvature of the scales is similar: After printing and re-checking the number and position of the depressions on the back of each scale, and the presence or absence of surface ornamentation, we confirmed that all the scales had different shapes. In contrast, the curvatures of the scales were almost equal, except for those at the aperture (Figure 12A). Because scales form just beneath the posterior cell membrane of the mother cell (Kies, 1974; Nomura and Ishida, 2016), the curvature of the mother shell likely represents a limiting factor. 2) Angled basal scale surfaces: The scales were curved and rectangular, and the basal surfaces of the upper and lower scales were attached to each other using organic cement. When the upper or lower sides of the scales were placed perpendicular to the direction of gravity, the angle formed by the short sides of each scales differed (Figure 12B). The upper and lower bottom surfaces of the scales are not parallel to each other; because of this angle, the scales gradually curve inward when piled up, forming the aforementioned egg shape. In the future, further quantification and simulation analysis based on FIB-SEM and segmentation results will help clarify how the scale features revealed by the 3D-printed scale model are involved in the construction of the shell. In addition, the shell model constructed from the 3D-printed scales would provide unique experimental opportunities that are difficult to perform *in silico*. For instance, by determining the elastic moduli of organic cement and individual scales and printing them, a shell model could be constructed to assess the structural stability of the *P. micropora* shell. Such insights from real-world experiments are expected to facilitate application to architectural engineering.

Data availability statement

The original contributions presented in the study are included in the article/Supplementary Material, further inquiries can be directed to the corresponding author.

Author contributions

MN designed the research; MN, KO, K-IN, KT, and JG performed the research; MN, KO, YN, TN, KT, and JG analyzed the data; MN drafted the manuscript. All authors contributed to the article and approved the submitted version.

Funding

This research was supported by JSPS KAKENHI Grant Numbers, 19H05367 (MN), 21H00359 (MN), 21K15131 (MN), 22H05670 (MN), 21H05308 (YN), and JP16H06280; Grant-in-Aid for Scientific Research on Innovative Areas—Platforms for Advanced Technologies and Research Resources "Advanced Bioimaging Support." A part of this study was supported by the Institute for Fermentation, Osaka (MN), and the Cooperative Research Program of the Network Joint Research Center for Materials and Devices (MN). The study was also supported in part by funds from Yamagata Prefecture and Tsuruoka City.

Acknowledgments

We thank Taku Demura of Nara Institute of Science and Technology (NAIST), Dr. Ken-ichi Kawaguchi of the University of Tokyo, Toshiyuki Nakagaki of Hokkaido University, Kentaro Nakano of University of Tsukuba and Yasushi Tamura of Yamagata University for helpful discussions, as well as student members of KT's group for help and advice on 3D printing.

Conflict of interest

The authors declare that the research was conducted in the absence of any commercial or financial relationships that could be construed as a potential conflict of interest.

Publisher's note

Supplementary material

The Supplementary Material for this article can be found online at: https://www.frontiersin.org/articles/10.3389/fcell.2023.1232685/full#supplementary-material

References

Adl, S. M., Bass, D., Lane, C. E., Lukeš, J., Schoch, C. L., Smirnov, A., et al. (2019). Revisions to the classification, nomenclature, and diversity of eukaryotes. *J. Eukaryot. Microbiol.* 66 (1), 4–119. doi:10.1111/jeu.12691

Belevich, I., Joensuu, M., Kumar, D., Vihinen, H., and Jokitalo, E. (2016). Microscopy image browser: A platform for segmentation and analysis of multidimensional datasets. *PLoS Biol.* 14 (1), e1002340. doi:10.1371/journal.pbio.1002340

Drougkas, A., Roca, P., and Molins, C. (2015). Numerical prediction of the behavior, strength and elasticity of masonry in compression. *Eng. Struct.* 90, 15–28. doi:10.1016/j.engstruct.2015.02.011

Friedrichs, L., Maier, M., and Hamm, C. (2012). A new method for exact three-dimensional reconstructions of diatom frustules. *J. Microsc.* 248 (2), 208–217. doi:10.1111/j.1365-2818.2012.03664.x

Gavelis, G. S., Wakeman, K. C., Tillmann, U., Ripken, C., Mitarai, S., Herranz, M., et al. (2017). Microbial arms race: ballistic "nematocysts" in dinoflagellates represent a new extreme in organelle complexity. *Sci. Adv.* 3 (3), e1602552. doi:10.1126/sciadv.1602552

Hannah, F., Rogerson, A., and Anderson, O. R. (1996). A description of *Paulinella indentata* n. sp. (filosea: euglyphina) from subtidal coastal benthic sediments. *J. Eukaryot. Microbiol.* 43 (1), 1–4. doi:10.1111/j.1550-7408.1996.tb02464.x

Hedley, R. H., Ogden, C. G., and Krafft, J. (1974). Observations on clonal cultures of *Euglypha acanthophora* and *Euglypha strigosa* (testacea: protozoa). *Bull. Br. Mus.* 26, 103–111.

Hedley, R. H., and Ogden, C. G. (1974). Adhesion plaques associated with the production of a daughter cell in *Euglypha* (Testacea; Potozoa). *Cell Tissue Res.* 153, 261–268. doi:10.1007/BF00226614

Hedley, R. H., and Ogden, C. G. (1973). Biology and fine structure of *Euglypha rotunda* (testacea: protozoa). *Bull. Br. Mus.* 25, 119–137.

Hildebrand, M., Lerch, S. J., and Shrestha, R. P. (2018). Understanding diatom cell wall silicification—Moving forward. *Front. Mar. Sci.* 5, 125. doi:10.3389/fmars.2018.00125

Hörning, M., Schertel, A., Schneider, R., Lemloh, M. L., Schweikert, M. R., and Weiss, I. M. (2020). Mineralized scale patterns on the cell periphery of the chrysophyte *Mallomonas* determined by comparative 3D Cryo-FIB SEM data processing. *J. Struct. Biol.* 209 (1), 107403. doi:10.1016/j.jsb.2019.10.005

Johnson, P. W., Hargraves, P. E., and Sieburth, J. M. (1988). Ultrastructure and ecology of *Calycomonas ovalis* wulff, 1919, (chrysophyceae) and its redescription as a testate rhizopod, *Paulinella ovalis* N. Comb. (Filosea: euglyphina). *J. Protozool. Res.* 35 (4), 618–626. doi:10.1111/j.1550-7408.1988.tb04160.x

Kies, L. (1974). Elektronenmikroskopische Untersuchungen an *Paulinella chromatophora* Lauterborn, einer Thekamobe mit blaugrunen Endosymbionten (Cyanellen). *Protoplasma* 80, 69–89. doi:10.1007/BF01666352

Lara, E., Roussel-Delif, L., Fournier, B., Wilkinson, D. M., and Mitchell, E. A. (2016). Soil microorganisms behave like macroscopic organisms: patterns in the global distribution of soil euglyphid testate amoebae. *J. Biogeogr.* 43 (3), 520–532. doi:10.1111/jbi.12660

Leadbeater, B. S., Henouil, M., and Berovic, N. (2008). Choanoflagellate lorica construction and assembly: the nudiform condition. II. *Acanthoeca spectabilis* ellis. *Protist* 159 (3), 495–505. doi:10.1016/j.protis.2008.03.001

Lhee, D., Lee, J., Ettahi, K., Cho, C. H., Ha, J. S., Chan, Y. F., et al. (2021). Amoeba genome reveals dominant host contribution to plastid endosymbiosis. *Mol. Biol. Evol.* 38 (2), 344–357. doi:10.1093/molbev/msaa206

Lhee, D., Yang, E. C., Im Kim, J., Nakayama, T., Zuccarello, G., Andersen, R. A., et al. (2017). Diversity of the photosynthetic *Paulinella* species, with the description of *Paulinella micropora* sp. nov. and the chromatophore genome sequence for strain KR01. *Protist* 168 (2), 155–170. doi:10.1016/j.protis.2017.01.003

Marin, B., Nowack, E. C., and Melkonian, M. (2005). A plastid in the making: evidence for a second primary endosymbiosis. *Protist* 156 (4), 425–432. doi:10.1016/j.protis.2005.09.001

Matsuo, M., Katahata, A., Tachikawa, M., Minakuchi, Y., Noguchi, H., Toyoda, A., et al. (2019). Large DNA virus promoted the endosymbiotic evolution to make a photosynthetic eukaryote. *bioRxiv[preprint]*. doi:10.1101/809541

McFadden, G. I., and Melkonian, M. (1986). Use of Hepes buffer for microalgal culture media and fixation for electron microscopy. *Phycologia* 25 (4), 551–557. doi:10.2216/i0031-8884-25-4-551.1

Meisterfeld, R. (2002). *Testate amoebae with filopodia.* The illustrated guide to the protozoa (ed. by J. J. Lee, G. F. Leedale, and P. Bradbury), pp. 1054–1084. Society of Protozoologists, Lawrence, Kansas, USA.

Miyazono, Y., Hirashima, S., Ishihara, N., Kusukawa, J., Nakamura, K. I., and Ohta, K. (2018). Uncoupled mitochondria quickly shorten along their long axis to form indented spheroids, instead of rings, in a fission-independent manner. *Sci. Rep.* 8, 350. doi:10.1038/s41598-017-18582-6

Netzel, H. (1969). Morphogenese und Fortpflanzung beschalter Amöben (Testacea). *IWF*, 1–13. doi:10.3203/IWF/C-1059

Nicholls, K. H. (2009). Six new marine species of the genus *Paulinella* (rhizopoda: filosea, or rhizaria: cercozoa). *J. Mar. Biol. Assoc. U.K.* 89 (7), 1415–1425. doi:10.1017/s0025315409000514

Nomura, M., and Ishida, K. (2016). Fine-structural observations on siliceous scale production and shell assembly in the testate amoeba *Paulinella chromatophora*. *Protist* 167 (4), 303–318. doi:10.1016/j.protis.2016.05.002

Nomura, M., and Ishida, K. (2017). Shell assembly of testate amoebae leads to new insight into eukaryotic cell potential. *Plant Morphol.* 29 (1), 47–51. (Written in Japanese). doi:10.5685/plmorphol.29.47

Nomura, M., Nakayama, T., and Ishida, K. I. (2014). Detailed process of shell construction in the photosynthetic testate amoeba *Paulinella chromatophora* (Euglyphid, Rhizaria). *J. Eukaryot. Microbiol.* 61 (3), 317–321. doi:10.1111/jeu.12102

Nowack, E. C., Price, D. C., Bhattacharya, D., Singer, A., Melkonian, M., and Grossman, A. R. (2016). Gene transfers from diverse bacteria compensate for reductive genome evolution in the chromatophore of *Paulinella chromatophora*. *Proc. Natl. Acad. Sci.* 113 (43), 12214–12219. doi:10.1073/pnas.1608016113

Ollion, J., Cochennec, J., Loll, F., Escudé, C., and Boudier, T. (2013). Tango: A generic tool for high-throughput 3D image analysis for studying nuclear organization. *Bioinformatics* 29 (14), 1840–1841. doi:10.1093/bioinformatics/btt276

Preisig, H. R., Anderson, O. R., Corliss, J. O., Moestrup, Ø., Powell, M. J., Roberson, R. W., et al. (1994). Terminology and nomenclature of protist cell surface structures. *Protoplasma* 181, 1–28. doi:10.1007/bf01666386

Santibáñez, P. A., Kohshima, S., Scheihing, R. A., Silva, R., Jaramillo, M. J. I., Labarca, P. P. J., et al. (2011). First record of testate amoebae on glaciers and description of a new species *Puytoracia jenswendti* nov. sp. (Rhizaria, Euglyphida). *Acta Protozool.* 50 (1). 10.4467/16890027AP.11.001.0001.

Shahrubudin, N., Lee, T. C., and Ramlan, R. J. P. M. (2019). An overview on 3D printing technology: technological, materials, and applications. *Procedia Manuf.* 35, 1286–1296. doi:10.1016/j.promfg.2019.06.089

Smith, H. G. (1992). Distribution and ecology of the testate rhizopod fauna of the continental Antarctic zone. *Polar Biol.* 12, 629–634. doi:10.1007/bf00236985

Taylor, A. R., Brownlee, C., and Wheeler, G. (2017). Coccolithophore cell biology: chalking up progress. *Annu. Rev. Mar. Sci.* 9, 283–310. doi:10.1146/annurev-marine-122414-034032

Xing, Y., Yu, L., Wang, X., Jia, J., Liu, Y., He, J., et al. (2017). Characterization and analysis of *Coscinodiscus* genus frustule based on FIB-SEM. *Prog. Nat. Sci. Mat. Int.* 27 (3), 391–395. doi:10.1016/j.pnsc.2017.04.019

Yoon, H. S., Nakayama, T., Reyes-Prieto, A., Andersen, R. A., Boo, S. M., Ishida, K., et al. (2009). A single origin of the photosynthetic organelle in different *Paulinella* lineages. *BMC Evol. Biol.* 9 (1), 98–11. doi:10.1186/1471-2148-9-98

Zgłobicka, I., Gluch, J., Liao, Z., Werner, S., Guttmann, P., Li, Q., et al. (2021). Insight into diatom frustule structures using various imaging techniques. *Sci. Rep.* 11 (1), 14555. doi:10.1038/s41598-021-94069-9

frontiers | Frontiers in Cell and Developmental Biology

TYPE Original Research
PUBLISHED 01 November 2023
DOI 10.3389/fcell.2023.1274127

OPEN ACCESS

EDITED BY
Toshiyuki Nakagaki,
Hokkaido University, Japan

REVIEWED BY
Makoto Iima,
Hiroshima University, Japan
Kenta Ishimoto,
Kyoto University, Japan

*CORRESPONDENCE
Satoshi Sawai,
cssawai@mail.ecc.u-tokyo.ac.jp

RECEIVED 07 August 2023
ACCEPTED 09 October 2023
PUBLISHED 01 November 2023

CITATION
Uwamichi M, Miura Y, Kamiya A, Imoto D and Sawai S (2023), Random walk and cell morphology dynamics in *Naegleria gruberi*.
Front. Cell Dev. Biol. 11:1274127.
doi: 10.3389/fcell.2023.1274127

Random walk and cell morphology dynamics in *Naegleria gruberi*

Masahito Uwamichi[1], Yusuke Miura[1], Ayako Kamiya[2], Daisuke Imoto[3] and Satoshi Sawai[1,4]*

[1]Graduate School of Arts and Sciences, The University of Tokyo, Tokyo, Japan, [2]Graduate School of Medicine, The University of Tokyo, Tokyo, Japan, [3]Second Department of Forensic Science, National Research Institute of Police Science, Chiba, Japan, [4]Research Center for Complex Systems Biology, Universal Biology Institute, The University of Tokyo, Tokyo, Japan

Amoeboid cell movement and migration are wide-spread across various cell types and species. Microscopy-based analysis of the model systems *Dictyostelium* and neutrophils over the years have uncovered generality in their overall cell movement pattern. Under no directional cues, the centroid movement can be quantitatively characterized by their persistence to move in a straight line and the frequency of re-orientation. Mathematically, the cells essentially behave as a persistent random walker with memory of two characteristic time-scale. Such quantitative characterization is important from a cellular-level ethology point of view as it has direct connotation to their exploratory and foraging strategies. Interestingly, outside the amoebozoa and metazoa, there are largely uncharacterized species in the excavate taxon Heterolobosea including amoeboflagellate *Naegleria*. While classical works have shown that these cells indeed show typical amoeboid locomotion on an attached surface, their quantitative features are so far unexplored. Here, we analyzed the cell movement of *Naegleria gruberi* by employing long-time phase contrast imaging that automatically tracks individual cells. We show that the cells move as a persistent random walker with two time-scales that are close to those known in *Dictyostelium* and neutrophils. Similarities were also found in the shape dynamics which are characterized by the appearance, splitting and annihilation of the curvature waves along the cell edge. Our analysis based on the Fourier descriptor and a neural network classifier point to importance of morphology features unique to *Naegleria* including complex protrusions and the transient bipolar dumbbell morphologies.

KEYWORDS

***Naegleria*, persistent random walk, cell migration, cell shape analysis, pseudopodium, cell polarity**

1 Introduction

Combinatorial use of persistent motion and reorientation is a common feature found in cell movement. Be it bacterial swimming or amoeboid crawling, persistent movement allows cells to gain most distance in one preferred direction so as to facilitate efficient escape from hazards or conversely attraction to nutrients. Reorientation on the other hand is not only required to adjust direction of persistent movement but also to facilitate cells to randomly explore and survey uncertain extracellular environments (Viswanathan et al., 1999; Bartumeus et al., 2002). In *E. coli* bacteria, the cell movement consists of a period of

straight run interrupted by a stall or "tumble" where flagellar rotation reverses and cells reorient in random directions. The frequency of tumbling is regulated through a chemosensory system so as to provide orientation bias towards an attractant or away from a repellent. The exact nature of such motility pattern determines how well *E. coli* cells disperse (Taktikos et al., 2013). In the amoeboid movement, pseudopodal protrusions enriched in branched F-actin networks (Pollard, 2007) are formed transiently and can guide cells in different orientations. In addition, a confined region of the plasma membrane needs to retract in order to realize net displacement. In many cell types, cortical F-actin that is crosslinked with myosin II is enriched in such contractile membrane regions (Chi et al., 2014). Persistent movement arises when a cell has mono-polarity meaning that it has a single dominating leading edge and a retracting trailing end. The occurrence and location of these organizational events along the plasma membrane determine the sequential appearance of plasma membrane protrusions and rear retractions, ultimately influencing the direction, speed, and duration of cell movements.

Quantitative time-series analyses of cell displacement and cell shape change are important for explicit characterization of random cell motion. In many cases, cell displacement can be approximated as a particle obeying persistent random walk. Phenomenologically, the simplest form of differential equation that describes such stochastic dynamics is the Langevin equation (Dunn and Brown, 1987; Selmeczi et al., 2005; Selmeczi et al., 2008)

$$\frac{d\vec{v}(t)}{dt} = -\beta\vec{v}(t) + \sigma\vec{\xi}_t \quad (1)$$

where $\vec{v}$ is the velocity vector, β is the decay rate, σ is the noise strength, and $\vec{\xi}_t$ is 2D white Gaussian noise. Random walk of *E. coli* can be approximated by Brownian motion having a short-term memory. In eukaryotic crawling, cell trajectories of fibroblast cells (Gail and Boone, 1970) and endothelial cells (Stokes et al., 1991) are also consistent with this simple persistent random walk model. In many other cell types, random walk includes memory that depends on the velocity and orientation which can be described by modifications to the above model (Takagi et al., 2008; Li et al., 2011). There are also random walk statistics called Lévy-walk with step lengths that follows a long tail (power-law) distribution (Viswanathan et al., 1999). There, the Mean Square Displacement (MSD) essentially diverges and the trajectories are characterized by self-similarity of the step lengths (Reynolds, 2010; Reynolds and Ouellette, 2016). Because Lévy-walk has very small probability of revisiting the same location, it is thought to arise in systems such as bird foraging that require an efficient search strategy. At the cellular-level, effector T-cells (Harris et al., 2012) and swarming bacteria have been reported to exhibit Lévy-flight like statistics (Ariel et al., 2015; Huo et al., 2021).

To date, quantitative understanding of random walk behavior of amoeboid cells is limited to data from a handful of cell-types; these are mostly timelapse microscopy images of cultured metazoan cells and amoebozoa *Dictyostelium*. From microbial ethology and evolutionary biology perspectives, however, we should note that amoeboid movement is found not only in animals, fungi and amoebozoans (Prostak et al., 2021) but also in largely uncharacterized species in the excavate taxon Heterolobosea namely *Naegleria* spp. and the slime mold acrasids (Brown et al., 2012). The ancestors of the opisthokont lineage and *Naegleria* diverged more than a billion years ago (Parfrey et al., 2011). Knowing the details of motility characteristics in *Naegleria* should help us understand the common design of the motility trait that is either deeply conserved across taxa or acquired independently by strong selective advantages.

Among members of genus *Naegleria*, non-pathogenic *Naegleria gruberi* (hereafter refer to as *N. gruberi*) is the better characterized species whose genome has been sequenced (Fritz-Laylin et al., 2010). In its amoebic phase, *N. gruberi* grows and divides by feeding on bacteria through phagocytosis (Fulton, 1970). Under low electrolyte conditions, it quickly shifts to the non-feeding flagellated state by rapid *de novo* synthesis of microtubules (Walsh, 2007). In the amoebic state, the overall cell cortex is enriched in F-actin with marked accumulation around membrane ruffles (Velle and Fritz-Laylin, 2020). An early work using reflection interference microscopy has revealed that *N. gruberi* adhere and form discrete dot-like contacts to non-treated glass surfaces and migrate (Preston and King, 1978). These so-called "focal contacts" leave behind footprints of membrane residues on the glass substrate as the cells crawl away (Preston and King, 1978). With the advent of genomics and molecular cell biology, it has become clear that *N. gruberi* possess the essential side-branching nucleator of F-actin—the Arp2/3 complex and its activators WASP and SCAR (Fritz-Laylin et al., 2017; Velle and Fritz-Laylin, 2020; Prostak et al., 2021). Inhibition of Formin reduces directional persistence, and inhibition of the Arp2/3 complex reduces the cell speed (Velle and Fritz-Laylin, 2020). *N. gruberi* also has Myosin II (Sebé-Pedrós et al., 2014) and a potential orthologue of Integrin beta (Morales et al., 2022), although whether they exist in other groups in Excavata is unclear (Velle and Fritz-Laylin, 2019).

While the above works indicate likely similarity of actin-dependent processes involved in cell crawling in an evolutionary distant eukaryote, quantitative characterization of the cell-level motility pattern is so far lacking. Do *N. gruberi* cells exhibit persistent random walk behavior? What is the characteristic time scale of persistence and reorientation if any? How similar are their movements compared to the well-studied systems such as *Dictyostelium* and immune cells? In this report, we performed quantitative analysis on cell movements and shape change of *N. gruberi*. Our analysis demonstrates that *N. gruberi* cells exhibit persistent random walk driven by a large morphology change that involves appearance, splitting and annihilation of uniquely complex pseudopodium protrusions.

2 Results

2.1 An overview of cell movement and cell morphology

To quantitate the movement of *N. gruberi* on a two-dimensional flat surface, we performed phase contrast time-lapse microscopy. A non-coated glass coverslip was employed as a cell substrate throughout this study. Figure 1A shows representative phase contrast images of *N. gruberi* in liquid growth media (*Materials and Methods*). The cells under our culture condition exhibited one

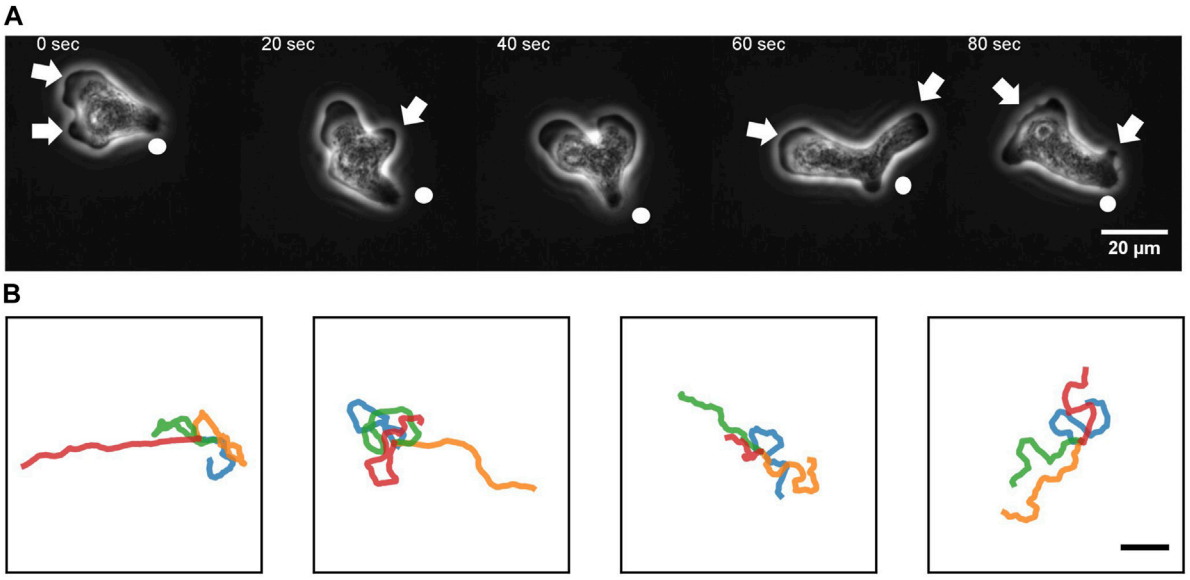

FIGURE 1
An overview of *N. gruberi* movement. **(A)** Representative phase contrast images from a time-series of a migrating *N. gruberi* cell. Arrows: protruding edges. Circles: a bud-like rear structure ("uroid"). **(B)** First 360 s of randomly selected centroid trajectories. 4 trajectories are separately shown for visibility. Scale bar: 100 μm.

or more hyaline protrusions that appeared dark in phase contrast images (Figure 1A arrows). In the example shown, protrusions extended along the glass surface for 15–50 s and the one that became dominant (i.e. the leading edge) extended in the direction of the overall cell movement (Figure 1A, 0 s). Marked cytoplasmic streaming from the center of the cell towards these extensions was observed (Supplementary Movie S1). A new protrusion appeared and extended first in the lateral direction (Figure 1A 20 s, 60 s arrow) and steered towards the front. It was then bent sideway before being retracted (Figure 1A 40 s, 80 s). Duration of the pseudopod extension/retraction cycle varied between 15–50 s (Supplementary Figure S1; Supplementary Movie S2). Concomitant reversal of cytoplasmic streaming was observed during retraction of pseudopods. A small bud-like bulge at the trailing end of a cell which we shall refer to as "uroid" appeared as a residue of a retracted pseudopod that was retained for an extended period of time (Figure 1A white circle). The uroid contained thin filopodia-like projections as described earlier (Preston and King, 1978).

Under our culture condition, the cells appeared to re-orient in random directions at irregular timing. We performed long time cell tracking by employing an automated stage that was programmed to track target cells (see Methods). Figure 1B shows representative cell trajectories obtained from the automated tracking. The trajectories consisted of a period of straight movement that lasted for about 30–200 s and a time period of relative low displacement and re-orientation (Figure 1B). The movement is thus, at surface, akin to the run-and-tumble behavior of *E. coli*. There was a close link between the run/re-orientation dynamics with the cell shape. During a straight run, cells took a fan-like shape (Figure 2A; Supplementary Movie S3). The tail remained narrow while the front was occupied by a broad lamellipodia that expanded then split into branches of pseudopods (Figure 2A, 0–16 s). These bifurcating protrusions often fused to restore a large lamellar extension (Figure 2A, 20 s). On the other hand, cells re-oriented when the bifurcated protrusions remained separate. In most cases, the uroid persisted during front splitting and thus the cells took a Y- or trident shape (Figure 2B; Supplementary Movie S4). There were also cases where the uroid disappeared in Y-shaped cells (Figure 2C; Supplementary Movie S5). The two fronts expanded in the opposing directions and gave rise to a transient "dumbbell-like" bipolar morphology (Figure 2C, 70 s). After 10 s, one end shrunk and became the uroid while the other end became the next front (Figure 2C, 80 s). There was little centroid displacement during this period which lasted for about 40 s.

2.2 Random walk statistics

To characterize the random-walk statistics, we quantified the mean square displacement (MSD) and the instantaneous speed defined by the centroid displacement in 1 s time interval from trajectories of $N = 10$ cells (Figure 3). Even with the help of automated stage tracking, fast movement of *N. gruberi* made it difficult to track cells for long time duration before they come close to the edge of the plate or collided with one another. Thus, to obtain MSD, single trajectories were each divided into sub-trajectories of 100–3,600 s time-window and treated as independent data samples (Figure 3A). The slope of the MSD from the individual trajectories was 1.5–2.0, where the mean and standard deviation are 1.77 and 0.08 (Figure 3B; Supplementary Figure S2A). The time-dependency of the MSD indicates that the random walk of *N. gruberi* falls somewhere between pure Brownian (exponent of 1) and ballistic (constant velocity) motion (exponent of 2). Figure 3C and

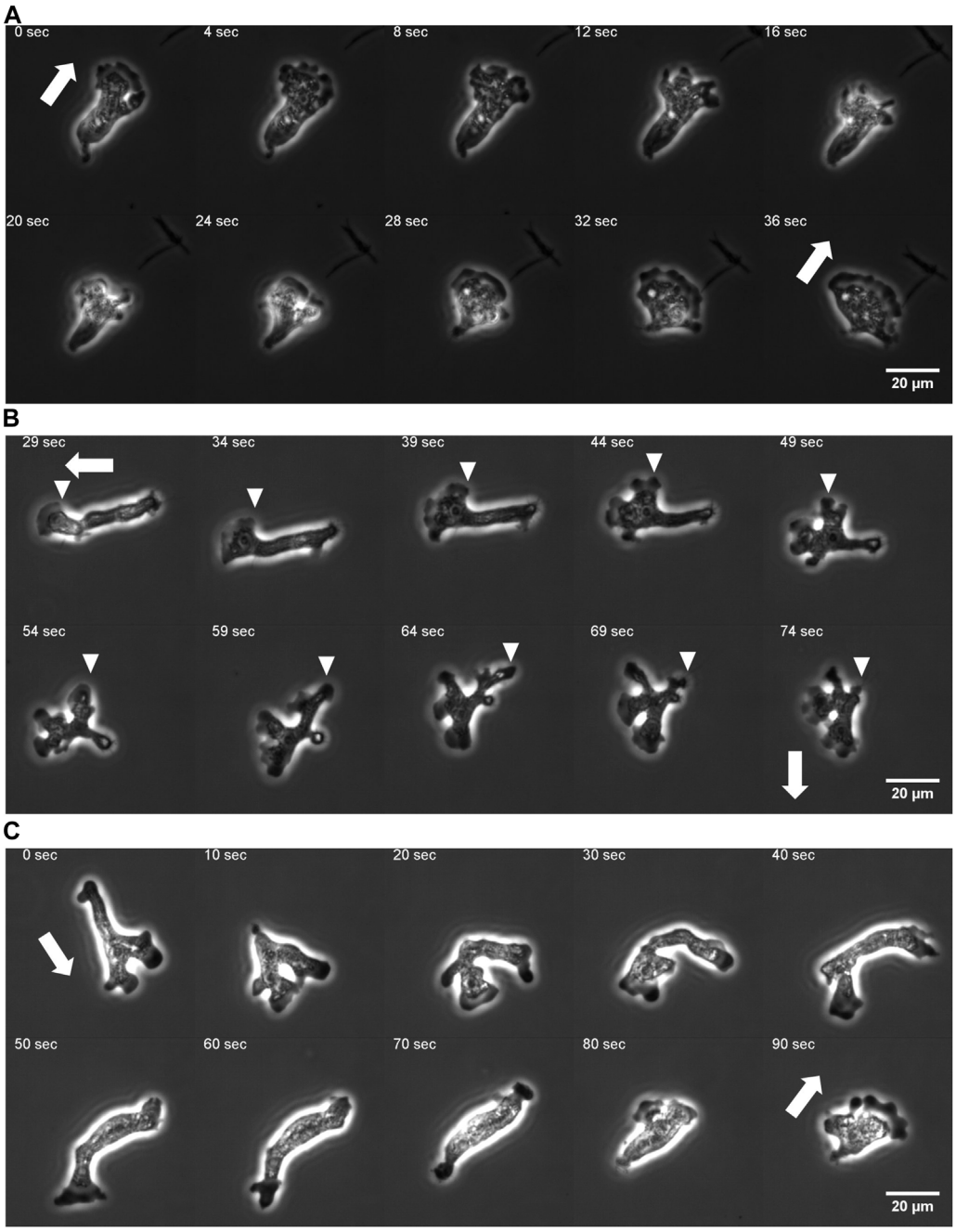

FIGURE 2
Protrusion dynamics and the cell shape change. **(A)** A fan-shaped cell with front splitting during a persistent run. **(B)** Front splitting followed by reorientation (curvature kymograph for the sequence is shown in Figure 5A). **(C)** Dumbbell shape arise after front splitting and disappearance of the uroid (curvature kymograph for the sequence is shown in Supplementary Figure S4E). Arrows: orientation of centroid movement. Inverted triangles: propagating curvature waves.

Supplementary Figures S2B–F show the distribution of the instantaneous velocity. The distribution followed 2-dimensional Gaussian with zero-mean and standard deviation of 51 μm/min (0.86 μm/s) (Figure 3C, Supplementary Figures S2B–F). This feature is distinct from *Dictyostelium* random motility which is non-Gaussian (Takagi et al., 2008). The median of the absolute speed was 60 μm/min (1.0 μm/s) which is close to the average speed reported in earlier literatures (King et al., 1981; Thong and Ferrante, 1986).

The temporal auto-correlation of the centroid speed (velocity auto-correlation; VAC) (Supplementary Figure S2G) shows, on average, that there are two characteristic decay times that cross over at around 10 s (Figure 3D). By assuming that VAC follows the sum of two exponential function (Selmeczi et al., 2005) with velocity $\vec{v}$:

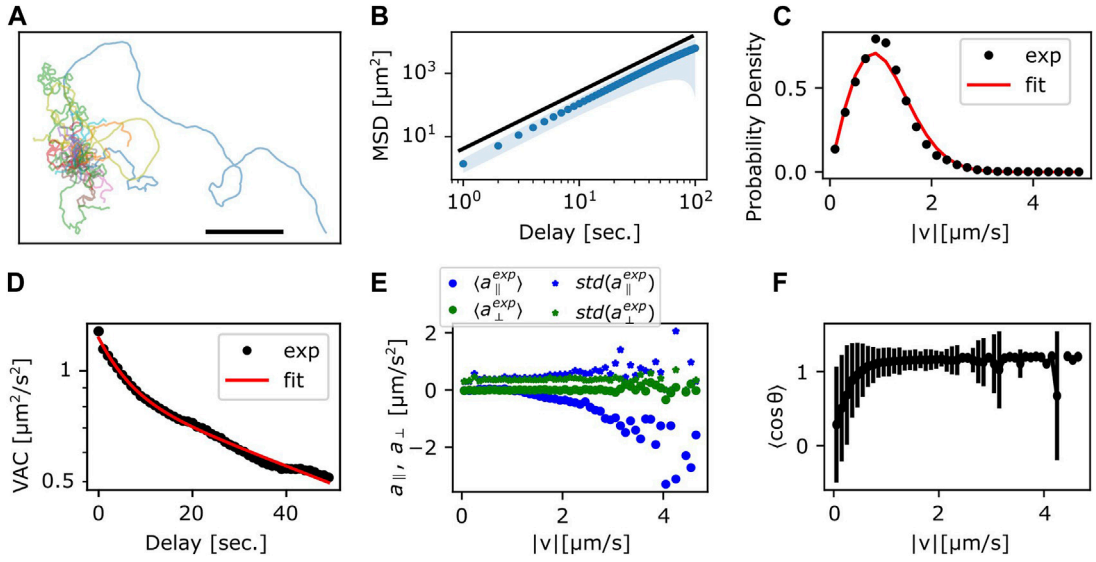

FIGURE 3
Statistics of the centroid movement. **(A)** The trajectories used for detailed analysis (N = 35). The origin is set at the initial position. Scale bar: 500 μm. **(B)** The ensemble averaged MSD. Red solid curve line: exponent 1.8, which is the result of fitting the ensemble averaged MSD. Shaded region: standard deviation. **(C)** Probability distribution of $|\vec{v}|$. Red solid curve: a fitting curve from a 2-dimensional isotropic Gaussian distribution with a standard deviation of 0.86 μm/s. **(D)** The ensemble averaged VAC. Red solid curve: the sum of two exponential functions (Eq. 2). **(E)** Acceleration parallel (blue) and orthogonal (green) to the velocity. The binned average (circle) and the standard deviation (star). **(F)** Persistence of displacement orientation in a unit time step. Cosine of the angle change θ in the velocity in 1 s interval. The binned average (circles) and the standard deviation (error bars).

$$\langle \vec{v}(t+\tau)\cdot\vec{v}(t)\rangle_t = \Phi_1 e^{-\frac{\tau}{T_1}} + \Phi_2 e^{-\frac{\tau}{T_2}} \tag{2}$$

we obtained decay time T_1 and T_2 of approximately 6 s and 90 s, respectively, where the weight Φ_1 and Φ_2 are 0.36 μm²/s² and 0.87 μm²/s² (Figure 3D Red curve). Based on the Bayesian information criterion (BIC) (Schwarz, 1978), two exponential functions gave the lowest value compared to one or three (Supplementary Figure S2H). When the length of time sequence chosen for the analysis was doubled from 50 s to 100 s, deviation of the parameter values was within an order of magnitude (Supplementary Figure S2H magenta curve). Decay time T_2 of approximately 90 s was also evident from the time derivative of VAC (Supplementary Figure S2I).

To check for orientational preference in the memory, we plotted the relationship between velocity and acceleration (change in $\vec{v}$ in 1 s interval) (Supplementary Figures S2J, K). The mean acceleration orthogonal ($a_\perp$) to the velocity was near zero regardless of $|v|$ (Figure 3E; green circle) with non-zero variance (Figure 3E green stars) which suggests that the orientation of *N. gruberi* has no apparent left-right asymmetry. On the other hand, the mean acceleration parallel ($a_\parallel$) to the velocity was near zero at small velocity then decreased towards the negative at large velocities (Figure 3E). The standard deviation (Figure 3E; blue stars) increased somewhat at high $|v|$, however rarity of these fast step events prevented us from obtaining reliable averages. These features of acceleration are similar to those reported for *Dictyostelium* (Takagi et al., 2008). The negative acceleration parallel to the migration direction at high $|v|$ implies that the cells do not maintain high $|v|$ during re-orientation. Accordingly, when we plot reorientation angle θ as a function of $|v|$ (Figure 3F) we see that most of re-orientation occurs below $|v|$ = 1 μm/sec. Above 1 μm/s the cells are moving in a straight line; i.e. cosθ = 1.

2.3 Generalized Langevin equation

To gain further insights on the specifics of the random walk statistics, it is instructive to compare the data with the behavior of simple idealized equations. The velocity auto-correlation that follows the sum of two exponential indicates that random walk dynamics cannot be captured simply by the Ornstein-Uhlenbeck process (Eq. 1) which only has a single exponent (Dunn and Brown, 1987). A straight-forward and minimal extension to Eq. 1 is to include additional memory with the decay rate γ as an integral in the form of generalized Langevin-equation (Selmeczi et al., 2005)

$$\frac{d\vec{v}(t)}{dt} = -\beta\vec{v}(t) + \alpha^2\int_{-\infty}^{t} e^{-\gamma(t-t')}\vec{v}(t')dt' + \sigma\vec{\xi}_t \tag{3}$$

Here, α is the strength of memory effect, and $\vec{\xi}_t$ is a normalized Gaussian white noise that satisfies $\langle\vec{\xi}_t\rangle = 0, \langle\vec{\xi}_t\vec{\xi}_{t'}^{\mathrm{T}}\rangle = \begin{pmatrix}1&0\\0&1\end{pmatrix}\delta(t-t'), \langle\,\rangle$ is an ensemble average and $\delta(t)$ is the delta function, σ is the noise strength (Selmeczi et al., 2005). By introducing

$$\vec{V}(t) = \alpha\int_{-\infty}^{t} e^{-\gamma(t-t')}\vec{v}(t')dt' \tag{4}$$

the equation of motion becomes

$$\frac{d\vec{v}(t)}{dt} = -\beta\vec{v}(t) + \alpha\vec{V}(t) + \sigma\vec{\xi}_t \tag{5a}$$

$$\frac{d\vec{V}(t)}{dt} = \alpha\vec{v}(t) - \gamma\vec{V}(t) \tag{5b}$$

Based on the values of T_1, T_2, Φ_1, Φ_2 obtained above, we calculated the parameter values of the generalized Langevin

TABLE 1 Parameters for the generalized Langevin equation. The experimental data were fitted with the analytical VAC (Eq. 29).

	α [s^{-1}]	β [s^{-1}]	γ [s^{-1}]	σ [$\mu m \cdot s^{-3/2}$]	σ_X [μm]
GLE	0.0741	0.116	0.0641	0.266	0
GLE w/positional uncertainty	0.0741	0.116	0.0641	0.266	0.155

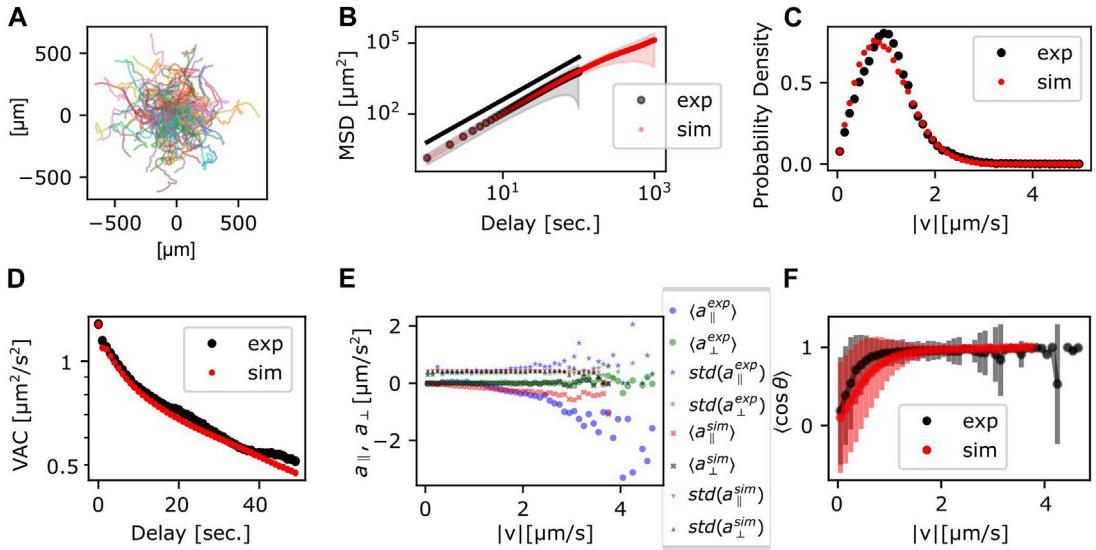

FIGURE 4
Statistics of the persistent random walker trajectories. **(A)** Simulated trajectories. **(B)** MSD; the ensemble average (circle) and the standard deviation (shade) (red). Experimental data (black) are duplicated from Figure 3B for comparison. **(C,D)** Probability distribution of $|\vec{v}|$ **(C)** and VAC **(D)** (red). Experimental data from Figures 3C, D (black) are duplicated for comparison. **(E)** Acceleration, parallel (red) and orthogonal (black) to the velocity. The average (cross mark) and the standard deviation (triangle). Blue and green markers show the experimental data in Figure 3E. **(F)** The average of cos θ (red circle) and the standard deviation (red error bar). Experimental data from Figure 3F (black circle and error bar) are duplicated for comparison.

equation (Eqs 5a, b) from the analytically obtained VAC at the steady state (see Eq. 29).

Trajectories, the MSD and the VAC were obtained by numerically calculating Eqs 5a, b with the parameters obtained above (Table 1). The individual trajectories consist of combination of persistent movement and turns (Figure 4A). The slope of MSD had mean and standard deviation of 1.80 ± 0.06, which matched well with the experimental data (Figure 4B). The distribution of $|v|$ showed a single peak that was slightly smaller compared to the experimental data (Figure 4C). The median was 56 μm/min (0.94 μm/s) in the simulation, which matched well with 60 μm/min in the experiment. The velocity autocorrelation consists of two slopes that crossed over at around 10 s (Figure 4D red), which was similar to the crossover in the experimental data (Figure 4D black). Velocity dependence of acceleration also matched well with the experimental data (Figure 4E). On the other hand, the range of cell speed at which turning occurred in the simulations was somewhat broader (0–1.2 μm/s) compared to the real cell (0–0.8 μm/s) (Figure 4F). While the MSD and the VAC characteristics were well captured by the memory effect described in Eq. 3, deviation from the model became evident when comparing autocorrelation separately for the centroid movement (absolute velocity $|\vec{v}|$) and the orientation ($\vec{v}/|\vec{v}|$) (Supplementary Figure S3). In the experimental data, it is only the autocorrelation of the orientation $\vec{v}/|\vec{v}|$ not $|\vec{v}|$ that showed two decay times (Supplementary Figure S3A, B). In the generalized Langevin-equation, the velocity and the orientation share the same time scales, and thus the autocorrelation of both the orientation $\vec{v}/|\vec{v}|$ and $|\vec{v}|$ decayed with the two exponents (Supplementary Figures S3C, D).

2.4 Cell shape dynamics

Rather than pursuing extensions of the particle-based formalism such as those that treat the two timescales separately (Li et al., 2008; Takagi et al., 2008), we sought to more directly characterize cell reorientation by analyzing the cell shape dynamics. Based on binarized cell mask images and a boundary tracking algorithm (Nakajima et al., 2016; see also Supplementary Figure S4A), 500 points along the edge of cell masks were tracked in the laboratory frame for the local curvature and the normal velocity (Figure 5A, B; see also Supplementary Figures S4B, D, F for another sample). A protruding edge can be seen as a positive local-maximum in the curvature (Figure 5A yellow regions). The advancing front of a cell can be discerned by its positive velocity (Figure 5B, yellow regions), and the trailing uroid by the negative velocity (Figure 5B, blue regions). At the cell front, a new protrusion frequently appeared to split off from a pre-existing protrusion (Figures 5A, B white

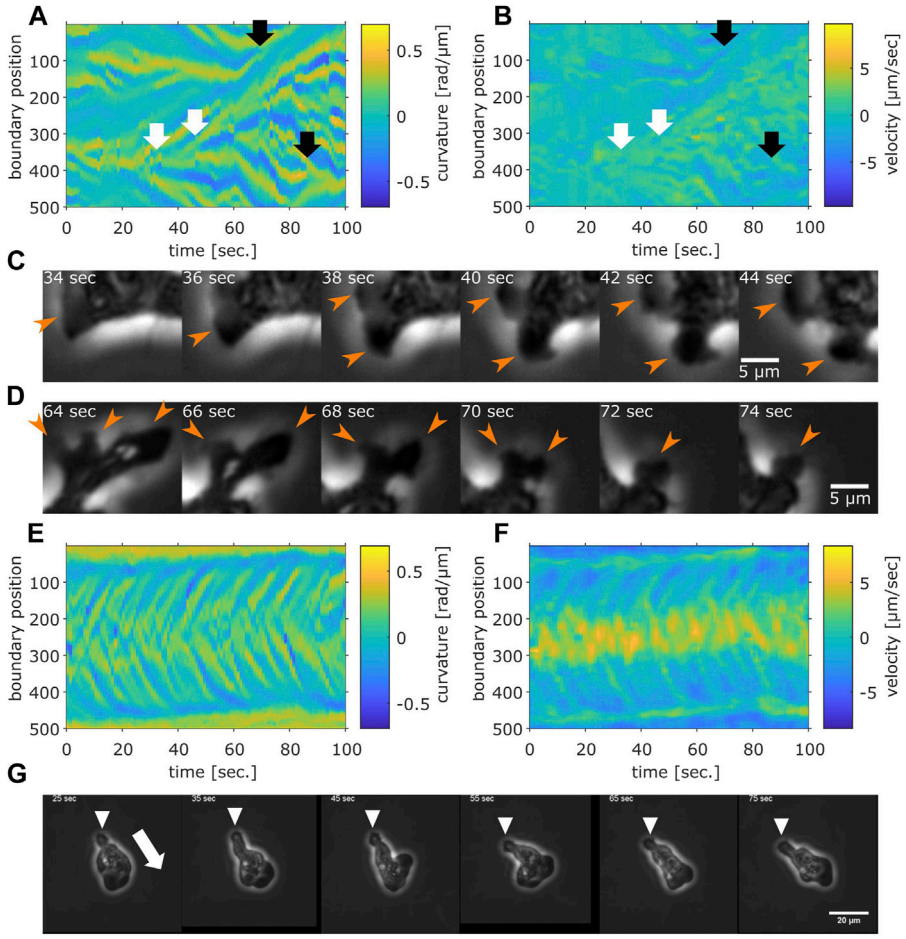

FIGURE 5
Cell boundary analysis. **(A,B)** The curvature **(A)** and the normal velocity **(B)** of the cell boundary taken from a representative cell exhibiting random walk. White arrows: splitting. Black arrows: pair annihilation. **(C,D)** Magnified view of a subsection in **(A,B)**. Orange arrows indicate protrusions that split **(C)** or annihilated **(D)**. **(E,F)** The curvature **(E)** and the normal velocity **(F)** of the boundary taken from a cell with high persistence. **(G)** Snapshots of the cell analyzed in **(E,F)**. The white arrow: the direction of the centroid movement. The inverted triangles mark the uroid.

arrows). These appeared in the kymograph as branching positive curvature regions that propagated rearward until they were annihilated at or near the uroid (Figures 5A, B black arrows). The sequence of curvature wave dynamics represents well the shape dynamics as seen in the snapshots (Figures 5C, D orange arrows; see also Figure 2B white arrows for a protrusion from split to annihilate).

The curvature wave dynamics are surprisingly similar to those obtained for *Dictyostelium* and neutrophil-like HL60 cells (Driscoll et al., 2012; Imoto et al., 2021) with a noticeable difference that splitting was more frequent and thus numerous. The other difference compared to *Dictyostelium* and HL60 cells is the occasional and transient appearance of dumbbell-like shape (Supplementary Figures S4C, E, G; Supplementary Movie S5). When it appears, the centroid velocity orientation showed discontinuous change (Supplementary Figure S4C, black arrow). In the kymograph representation, a dumbbell-like cell shape appears as two or three stable curvature waves (Supplementary Figure S4E, black arrow). Most positions had zero velocity (Supplementary Figure S4G, black arrow), indicating stalling of cell shape change. These observations indicate that as the dumbbell shape appeared, the cell stopped and randomized its orientation. There were also rare cases where the cell maintained mono-polarity for an extended period of time (Figures 5E–G; Supplementary Movie S6; see Supplementary Figure S5 for additional samples). There, new curvature waves emerged frequently and traveled fast before disappearing at the tail (Figure 5E). The position where curvature waves appeared always showed positive velocity, while the positions where curvature waves disappeared showed negative velocity (Figures 5E, F). These patterns in the kymograph correspond well with the observation of fast curvature waves that propagate from the advancing cell front and disappear at the uroid (Figure 5G).

A further analysis showed a close relationship between the curvature wave and the centroid movements. The protruding and the retracting membrane regions can be identified as positive curvature regions with positive (Figure 6A, white dots) or negative (Figure 6A black dots) velocity respectively. The orientation of the normal vector at the protruding region showed high correlation with the direction of centroid velocity (Figure 6B blue). The retracting regions oriented in the opposite

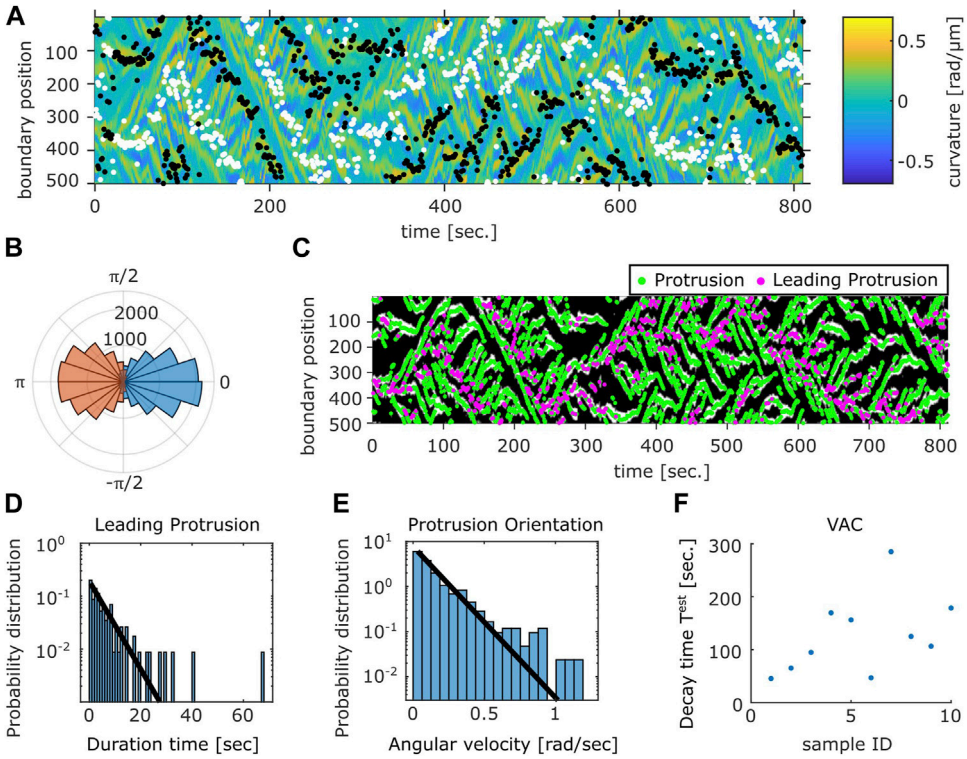

FIGURE 6
Relation between the membrane protrusions and the centroid velocity angle. **(A)** The protruding front (white) and the retracting rear (black) detected from the velocity kymograph are overlaid on top of the curvature kymograph (see Methods). **(B)** The angular histogram of the protruding front (blue) and the retracting rear (orange) relative to the cell orientation as determined by the centroid velocity. **(C)** The position of protrusive regions ("curvature waves;" green). The region that co-extended most closely in the direction of the cell centroid motion ("leading protrusion;" magenta). The binarized mask of the protrusion region (white) obtained from the curvature kymograph is shown in the background. **(D)** Duration time histogram of the leading protrusion (magenta in (C)). **(E)** Histogram of the angular velocity in the protrusion orientation [the vector normal to the cell contour at positions indicated in green in **(C)**]. Solid lines are exponential fit to the data **(D,E)**. **(F)** Estimated VAC decay time T^{est} for the representative data.

directions which appeared somewhat broader in distribution (Figure 6B orange). To further analyze the dynamics of the curvature wave, high curvature regions (Figure 6C white) at each time frame were assigned as individual protrusions (Figure 6C green). While there were multiple protrusions in the protruding region, a dominant leading edge can be detected from identifying a single protrusion whose normal vector angle was the closest to that of the centroid velocity (Figure 6C magenta). Once a curvature wave became the leading edge, it remained so for about 2.8 s as measured from its average lifetime (Figure 6D). Another interesting feature of the membrane extensions is that they gave birth to secondary pseudopods or were steered to other directions. The typical angular velocity associated with this dynamic was 0.1 rad/s (Figure 6E). Together with the two timescales of decay (Supplementary Figure S3B), these behaviors indicate that the centroid velocity angle by itself follows 1D persistent random walk. From experimentally obtained parameters of the leading edge lifetime (2.8 s) and the angular velocity 0.1 rad/s, the 1D model (see *Materials and Methods*, *Cell Boundary Analysis* section) yielded decay time of 142 s on average which matched well with the experimental data (Figure 6F).

2.5 Fourier-based morphology space analysis

To obtain a quantitative morphometry, we chose by eye 21 representative mask images each for the 3 shapes; fan-shape, split and dumbbell (Supplementary Figure S6A) and calculated the Fourier power spectrum of the cell edge coordinates and their principal components were calculated (see *Materials and Methods*). We found that the first two principal components were sufficient to obtain well separated clusters that represented the shape class (Figure 7A). All cell masks analyzed were distributed within a confined domain in the $PC1_{fourier}$ -$PC2_{fourier}$ space (Supplementary Figure S6B). The fan-shaped data were located at a low $PC1_{fourier}$ and high $PC2_{fourier}$ region (Figure 7A circles). The split-shape were found in the low $PC1_{fourier}$—low $PC2_{fourier}$ region (Figure 7A asterisks). The dumbbell-shape was located at high $PC1_{fourier}$ and high $PC2_{fourier}$ (Figure 7A triangles). To see what shape features the principal components represented, we reverse calculated an artificial form by obtaining Fourier spectrum as a product of synthetic principal component vector to the eigen vector matrix composed of the basis of Fourier spectrum (see Methods). In brief, $PC1_{fourier}$ indicated the aspect ratio i.e., elongation, $PC2_{fourier}$ the head width, $PC3_{fourier}$ the rear steepness (Supplementary Figure

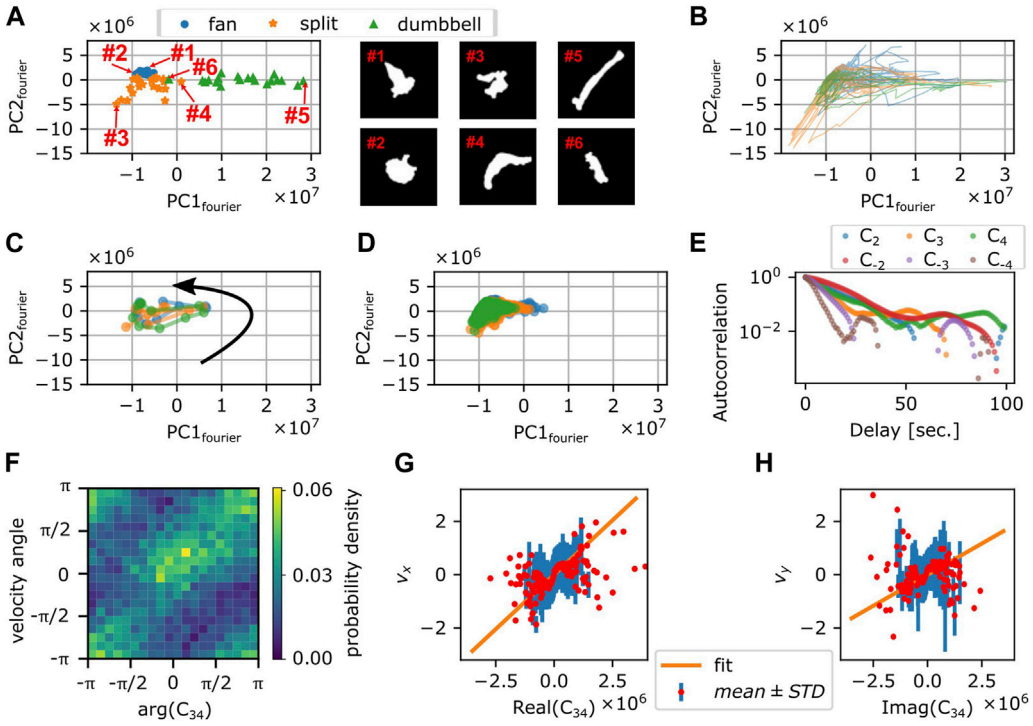

FIGURE 7
Fourier analysis of the cell contour. **(A)** Principal component space ($PC1_{fourier}$, $PC2_{fourier}$) obtained from 63 manually selected binarized snapshots (left panel). Representative cell masks (right panels). **(B)** Time series in $PC1_{fourier}$-$PC2_{fourier}$ space from 3 representative timelapse sequences (colors). The time spent in the negative $PC1_{fourier}$ region per total trajectory time was 676 s/814 s (blue), 287 s/382 s (orange), and 459 s/578 s (green). **(C)** Time evolution of $PC1_{fourier}$ and $PC2_{fourier}$ of 10 s around a large turn that involves transition to the dumbbell shape (3 representative events; colors). Black arrow indicates the direction of time evolution. **(D)** Time evolution of $PC1_{fourier}$ and $PC2_{fourier}$ during persistent migration. Colors indicate different time series [duration: 269 s (blue), 1,039 s (orange), or 3,600 s (green)]. **(E)** Autocorrelation of C_n ($n = \pm 2, \pm 3, \pm 4$). The decay rate: 12.2 (C_2), 18.0 (C_{-2}), 8.9 (C_3), 7.6 (C_{-3}), 10.6 (C_4), and 4.4 (C_{-4}) seconds. **(F)** Distribution of angles of centroid velocity and C_{34}. **(G,H)** The x- **(G)** and y-components **(H)** of centroid velocity plotted against real **(G)** and imaginary **(H)** parts of C_{34}. Red circles and blue bars indicate average and standard deviation of centroid velocity binned with the value of C_{34}. Orange lines indicate the result of fitting with linear proportionality.

S6C). Here, the main contribution to PC1 were from the wave number 1 and −1 with coefficients of 0.68 and 0.73. For PC2, the contribution from wave number 1, −1, 2, and 3 was 0.62, −0.59, −0.49, −0.12, respectively. Contribution from other modes was small with coefficients less than 0.03.

How the cell shape changed during turning can be analyzed by tracking the time sequence in the $PC1_{fourier}$—$PC2_{fourier}$ space. Figure 7B shows three independent samples of re-orienting cells. Here, cells were mainly located in the negative $PC1_{fourier}$ region with occasional visits to the positive $PC1_{fourier}$ region. This is consistent with the above observation that cells took fan- or branched-shape (negative $PC1_{fourier}$) in addition to rare occurrence of dumbbell-shape (positive $PC1_{fourier}$). Figure 7C shows three independent samples of the dumbbell-shape forming cells. The counter-clockwise circular trajectories in the $PC1_{fourier}$—$PC2_{fourier}$ space signify a transition from the fan-shape to splitting then to the dumbbell-shape. On the other hand, Figure 7D shows three independent trajectories that remained in the negative PC1 region for extended period of time. These cells at least during the time window of observation fluctuated between the fan-shape and the bifurcating fingers. There was no clear relationship between the morphometry state ($PC1_{fourier}$, $PC2_{fourier}$) and the cell speed (Supplementary Figures S7A, B). There was, however, negative correlation between the centroid speed and the rate of state transition $d\{PC1_{fourier}\}/dt$ but not with $d\{PC2_{fourier}\}/dt$ (Supplementary Figures S7C, D). As the former relation was seen in the negative direction $d\{PC1_{fourier}\}/dt$ <0, it signifies that cells accelerate when recovering from dumbbell-shape.

Besides the rate of state transition in the principal components, there should be a direct relationship between the Fourier components C_n themselves and the centroid movement. Autocorrelation analysis showed that the decay rates for C_{-3}, C_3, and C_4 were 7.6, 8.9, and 10.6 s, respectively (Figure 7E) and thus matched most closely to the short decay time of VAC. As for the centroid velocity itself, according to the deformation tensor-based theory of cell movement (Ohta et al., 2016), it should be proportional to $C_{nm} \equiv \dot{C}_{-n}C_m - C_{-n}\dot{C}_m$ where $-n + m = 1$. More specifically, C_{nm} is a complex number whose absolute value $|C_{nm}|$ and the angle arg (C_{nm}) are expected to be proportional to the speed and the velocity angle of the centroid respectively. In NIH3T3 cells, it has been shown that velocity is proportional to the elongation C_{-2} and triangular C_3 modes of deformation multiplied by their time derivatives; i.e. $C_{23} = \dot{C}_{-2}C_3 - C_{-2}\dot{C}_3$ (Ebata et al., 2018). However, in *N. gruberi*, we found little correlation between C_{23} and the centroid velocity (Supplementary Figures S7E–G). Instead, we

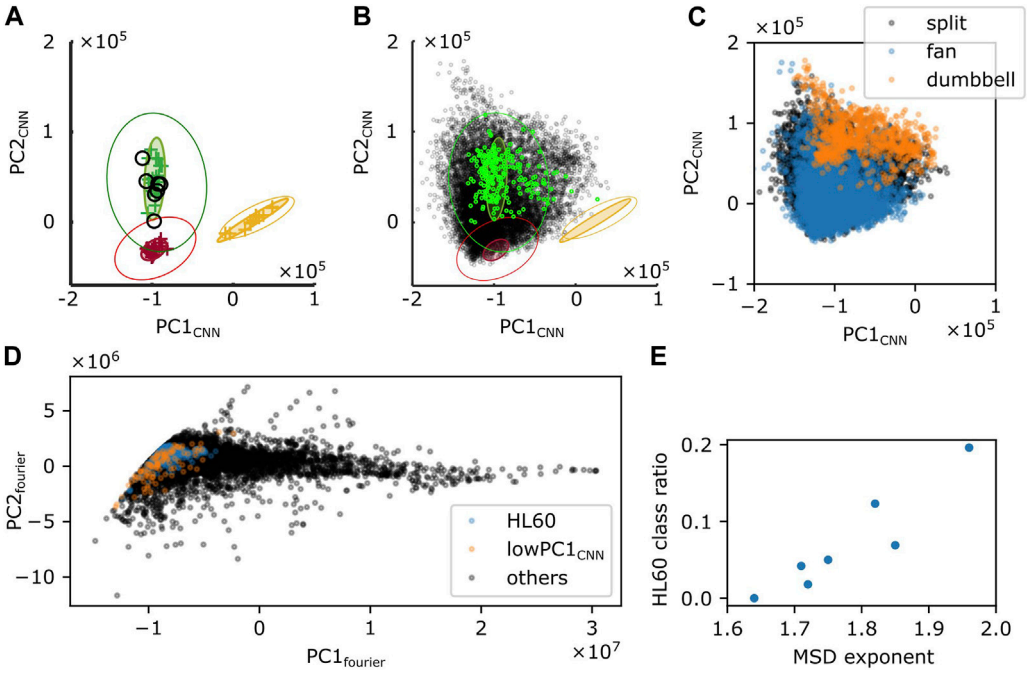

FIGURE 8
Shape analysis by a CNN-based classifier. **(A,B)** Time-average **(A)** or snapshot **(B)** of $PC1_{CNN}$ and $PC2_{CNN}$ from N. gruberi images (black) were superimposed on the $PC1_{CNN}$ -$PC2_{CNN}$ phase space of *D. discoideum* (green), HL60 (red), and fish keratocyte (yellow). **(C)** Snapshot data in (B; black) was classified into split (black), fan (blue) or dumbbell (orange) based on $PC1_{fourier}$ and $PC2_{fourier}$. **(D)** $PC1_{fourier}$ and $PC2_{fourier}$ of HL60-like (blue), cells with $PC1_{CNN}$ lower than -1.6×10^6 (orange), or the other cells (black) classified with CNN. **(E)** Ratio of frames whose shape was classified as HL60 in deep leaning-based classification.

found that it was $C_{34} = \dot{C}_{-3}C_4 - C_{-3}\dot{C}_4$ that correlated highly with the centroid velocity angle (Figure 7F) and x- and the y-component of the centroid velocity (Figures 7G, H). The difference between *Naegleria* and NIH3T3 may be attributed to the fact that *Naegleria* has many pseudopods that are complex in shape as analyzed below.

2.6 Deep learning-based morphology analysis

To further investigate the cell shape characteristics, we employed a convolutional neural network that was previously trained to classify cell shapes based on similarity to *Dictyostelium*-like, HL60-like, or fish keratocyte-like shapes (Imoto et al., 2021). While the method is not suited to track shape change over time due to discrete change in the morphometry space that is sometimes introduced by uncertainty in the cell orientation during mask alignment, it has an advantage of providing an objective morphometry that is independent of known feature basis. On average, Naegleria was classified as *Dictyostelium*-like (high $PC1_{cnn}$, low $PC2_{cnn}$) (Figure 8A). This was natural as it has been shown to pick up branching shapes that are elongated overall in the migrating direction (Imoto et al., 2021). We noticed substantial variability, however, in the individual cell shapes (Figure 8B; black) that exceeded those normally observed in *Dictyostelium* (Figure 8B; green). Shapes that deviated in the $PC1_{cnn}$ direction were mapped to dumbbell-like domain in the Fourier descriptor-based morphometry (Figure 8C; orange). Those that deviated towards low $PC1_{cnn}$ were mapped to the domain that showed numerous pseudopods (Figure 8D; orange). Datapoints that fell at or near the HL60-like domain (low $PC1_{cnn}$, low $PC2_{cnn}$) were mostly fan-like (Figure 8C; blue; Figure 8D; blue) and their occurrence per timeseries showed positive correlation with the MSD exponent (Figure 8E). This is consistent with the notion that more mono-polarized the cells are, the more ballistic the cell trajectories become.

3 Discussion

In this report, we analyzed movements of *N. gruberi* cells by quantifying their speed, directionality, and shape change. The locomotive speed of *N. gruberi* cells was around 60 μm/min, which is similar to that reported in early literatures (King et al., 1981; Thong and Ferrante, 1986). It is substantially larger in magnitude compared to that of fibroblast ~0.4–1.0 um/min (Welf et al., 2012; Passucci et al., 2019), and even larger compared to fast migrating cells such as vegetative *Dictyostelium* 5 μm/min (Li et al., 2008), and neutrophils 17 μm/min (Hartman et al., 1994). Despite the large speed difference, we found common features between *N. gruberi* and other cell types whose random motility have previously been characterized. The exponent of MSD was approximately 1.8 meaning that the random walk is non-Fickian and non-ballistic at least at surface. Stronger deceleration at higher velocity implies non-ballistic movement, where the non-memory term, i.e., fluctuating components plays a dominant role in determining the next move. Similar exponent is known in

MDCK cells (Dieterich et al., 2008), A549 cancer cells (Kwon et al., 2019) hematopoietic progenitor cells (Partridge et al., 2022), and T cells (Jerison and Quake, 2020). Of particular note is that the time-scale where such exponent was observed for *N. gruberi* was about 10–100 s which is within the order of magnitude required for a cell to move one cell-body length. This seems also to be the case for MDCK cells where the exponent of 1.8 was observed at much longer time-scale of 4–20 min with corresponding length scale 4 μm–20 μm. All in all, our data combined with the observations above from earlier literatures suggest that the time scale at which cells move in a straight line is the major determinant of cells' displacement.

The other common feature found in this study was the presence of two characteristic decay time in the VAC (Selmeczi et al., 2008). For *N. gruberi*, these were $T_1 = 6$ and $T_2 = 90$ s, which are in the same order of magnitude as that of *Dictyostelium* in the vegetative ($T_1 = 5.2$ and $T_2 = 228$ s) and the starved ($T_1 = 11$ and $T_2 = 108$ s) states (Li et al., 2008). Although equivalent measurements have not been documented for neutrophils, their cell shape changes had typical time scale of 8 s (Hartman et al., 1994) and the persistence time during chemotaxis was 103 s (Itakura et al., 2013; Haastert, 2021). From the MSD measurement, the persistent time of *Dictyostelium* and neutrophil-like HL60 were 151 s and 278 s, respectively (Imoto et al., 2021). Interestingly, VAC of Human keratinocyte-like cells (HeCaT) whose speed was much slower (0.18 μm/min) could also be fit with the sum of two exponential functions [$T_1 = 76$ s and $T_2 = 860$ s; (Selmeczi et al., 2005)]. The characteristic time scale of around 10 s was attributed to the time scale of actin polymerization in the protruding pseudopodia (Haastert, 2021). However, the pseudopod lifetime in *N. gruberi* was rather long; about 15–50 s. The discrepancy may be attributed to the sister pseudopods that formed from the main pseudopods which were not analyzed in our manual tracking. In some cases, the pseudopod itself also appeared to bend in one direction. In support of this notion, the autocorrelation of C_{-3} and C_4 had decay time of 7–10 s which matched well with the first decay time of VAC.

On the other hand, the second decay time of VAC (90 s; Figure 3D) was close to the timescale of directional persistence i.e. "run" phase estimated from the curvature wave dynamics (142 s; Figure 6F). As for the average cell speed, we found strong correlation between the centroid velocity with the coupling of deformation modes C_{-3} and C_4, instead of C_{-2} and C_3. This suggests that the orientation of *N. gruberi* cells depends not on the primary membrane protrusions but on their sister sub-structures. A further pseudopod-level analysis at finer time-scale is required to clarify the relation between the deformation modes and the branching pseudopods. The rare cells with high persistency did not take high $PC1_{fourier}$ value (Figure 7D) which was opposite of *Dictyostelium* (Tweedy et al., 2013). This likely stems from the fact that, in *N. gruberi,* the elongated form was usually dumbbell-shaped which occurred when the cells stalled and reoriented.

The splitting pseudopod may entail a mechanism similar to those found in amoebozoan and metazoan cells where dendritic actin meshworks are regulated by excitable and oscillatory dynamics (Huang et al., 2013). The presence of local inhibitor of pseudopod formation in neutrophils and *Dictyostelium* (Xu et al., 2017) and potential lack of such in *Naegleria* may underlie the difference in the number of pseudopods. Alternatively, there may be local reduction in the actin cortex that are stochastic in nature. Although protrusions observed under our culture conditions did not appear as blebs, marked flow of cytosol towards the membrane observed during extension of a protrusion suggests local pressure release. Protruding form triggered by the pressure difference at a fluid-fluid interface is known as viscous fingering. The movement speed of *N. gruberi* was 5 times as large as that of neutrophils and *Dictysotelium*, but closer to that known for fragments of *Physarum* which also exhibit marked cytoplasmic streaming (Rieu et al., 2015) and persistent random walk (Rodiek and Hauser, 2015). Such high velocity and potential interface instability may underlie the observed branching of pseudopods. Another unique shape feature was the dumbbell-like cell shape. According to a recent theoretical model of lamellipodia-based dynamics, a similar "two-arc shape" appeared when the protrusive force was high (Sadhu et al., 2023). The dumbbell-shape may thus be a prevalent shape feature that was heretofore overlooked due to peculiarity of the model cells. Indeed, a similar dumbbell-shape has been reported in fragmented *Physarum polycephalum* (Rieu et al., 2015).

In the *E. coli* run-and-tumble, the underlying biochemical network has been proposed to be optimally designed to extract binary information in a noisy environment (Nakamura and Kobayashi, 2021). Some bacterial species make use of multiple run modes that differ in how they are modulated in the presence of chemoattractants (Alirezaeizanjani et al., 2020) suggesting diversity and depth at which random walk strategies are likely employed in prokaryotes. In *Dictyostelium* amoebae, the run length increases under starvation (Haastert and Bosgraaf, 2009) which may be related to their foraging strategy. In immune cells, high correlation between cell speed and persistence is thought to underlie their search efficiency *in vivo* (Shaebani et al., 2020; Shaebani et al., 2022). Cancer cells show persistent random walk in the metastatic state while weakly persistent in non-metastatic state (Huda et al., 2018). Although chemoattractants for *N. gruberi* are so far unknown, in *Naegleria fowleri*, formylated peptides are known to act as chemokine (Marciano-Cabral and Cline, 1987) meaning that it enhances cell polarity and movement in the absence of gradient. Cell-cell variability in such response may explain how a minority of *N. gruberi* cells under our experimental condition showed persistent monopolarity. *Naegleria fowleri* are one of several known "brain-eating" amoebae that cause fatal central nervous system infection called amebic meningoencephalitis. Their pathogenicity is thought to be related to their capacity to enter brain by penetrating nasopharygeal mucosa and migrate along olfactory nerves (Thong and Ferrante, 1986). In future works, it should be informative to study how the properties quantified in this work are modulated by chemotactic and chemokinetic factors and how they are related to exploratory and invasive strategies.

4 Materials and methods

4.1 Cell culture

Naegleria gruberi strain NEG-M was obtained from American Type Culture Collection (ATCC 30224). For routine cell propagation, small bits of frozen stock were scraped off using a sharp needle onto a fresh lawn of *Klebsilella aerogenes* on a NM agar

plate (Peptone, Dextrose, K_2HPO_4, KH_2PO4, 2% bactoagar) (Fulton, 1970). The two-member culture plate was incubated at 30°C for a few days until cleared plaques appeared. To start axenic culture, growing cells were picked from the edge of a plaque and suspended in Milli-Q water. 10 µL of the cell suspension was added to 25 mL modified HL5 media (Fulton, 1970) supplemented with 40 ng/mL vitamin B12 and 80 ng/mL folic acid, 10% fetal bovine serum (FBS, Sigma 172,012) and 1% Penicillin-Streptomycin (Gibco) in a 75 cm^2 canted-neck plastic flask (Corning 431464U). Cells were allowed to attach to the bottom of the flask and incubated at 30°C for 3 days before harvesting for imaging.

4.2 Time-lapse imaging

Axenic growing cells were dislodged from the flask bottom by gentle agitation. Cells were pelleted by centrifugation at 7×10^2 G for 3 min and resuspended in fresh HL5 media. The medium contains 5 mM KH_2PO_4/Na_2HPO buffer and thus provides required electrolytes (King et al., 1979) for optimal migration. The cell density was adjusted to 3.3×10^2 cells/mL for the observations. 3 mL of the cell suspension was plated on a 35 mm glass bottom dish (No. 0 20 mm hole diameter, MatTek). The plate was set to the stage of an inverted microscope (IX81, Olympus) equipped with either a thermal plate or a closed stage-top incubator set to 30°C and left still for 30 min before starting time-lapse image acquisition. All image acquisition was performed at 30°C.

Phase contrast images were obtained by ×40 (LUCPLFLN) objective lens and a sCMOS camera (Prime 95B, Photometrics). To track target cells at multiple non-overlapping fields of view, Micromanager software with a custom written plugin was employed. Timelapse images were obtained from 2 or 3 positions at an interval of 1 s for up to 1 h. Each position was chosen so that initially only a single cell at the center existed in the entire field of view. In between each image acquisition, the cell centroid was calculated from a mask obtained by applying the "Make Binary" function in ImageJ to the most recent image. The automated stage was then recentered to cancel out the centroid displacement.

4.3 Analysis

4.3.1 Characteristics of cellular trajectories

Binary masks from timelapse images were prepared using LABKIT (Arzt et al., 2022). Trajectories of cell centroid were extracted from the mask images using the ImageJ plugin TrackMate (Ershov et al., 2022). The generalized Langevin equation (Eqs 4–6a, b) was numerically solved using the Euler-Maruyama method at 2-milisecond interval with the TorchSDE library (Li et al., 2020; Kidger et al., 2021). Simulated data were sampled at 1 s interval. Velocity $\hat{\vec{v}}$ and acceleration $\hat{\vec{a}}$ were calculated from the difference in the sampled positions $\hat{\vec{r}}$ at time $t_n = n\delta t$ with an interval δt:

$$\hat{\vec{v}}(t_n) = \frac{\left(\hat{\vec{r}}(t_{n+1}) - \hat{\vec{r}}(t_n)\right)}{\delta t} \tag{6a}$$

$$\hat{\vec{a}}(t_n) = \frac{\left(\hat{\vec{v}}(t_{n+1}) - \hat{\vec{v}}(t_n)\right)}{\delta t}. \tag{6b}$$

MSD $msd(m\delta t)$, probability distribution of speed $p(v)$, velocity autocorrelation $vac(m\delta t)$, mean and standard deviation of acceleration conditional on speed $(\hat{a}_\parallel(v'), \hat{a}_\perp(v'), \sigma_{\hat{a}_\parallel}(v'), \sigma_{\hat{a}_\perp}(v'))$, and conditional-averaged strength of turning $\langle\cos\theta\rangle(v')$ were calculated from the trajectories for both the experiment and simulation data according to following equations:

$$msd(m\delta t) = \left\langle \left(\hat{\vec{r}}(t_{n+m}) - \hat{\vec{r}}(t_n)\right)^2 \right\rangle_n \tag{7a}$$

$$\kappa(v') = \left\{ (i,n) \middle| v' \le \left|\hat{\vec{v}}_i(t_n)\right| < v' + \delta v \right\} \tag{7b}$$

$$p(v') = \frac{\#\kappa(v')}{\#\{(i,n)\}\,\delta v} \tag{7c}$$

$$vac(m\delta t) = \left\langle \hat{\vec{v}}_i(t_n) \cdot \hat{\vec{v}}_i(t_{n+m}) \right\rangle_{(i,n)} \tag{7d}$$

$$\hat{a}_\parallel(v') = \left\langle \hat{a}_{i,\parallel}(t_n) \right\rangle_{(i,n)\in\kappa(v')}, \quad \hat{a}_\perp(v') = \left\langle \hat{a}_{i,\perp}(t_n) \right\rangle_{(i,n)\in\kappa(v')} \tag{7e}$$

$$\sigma_{\hat{a}_\parallel}(v') = std\left(\hat{a}_{i,\parallel}(t_n)\right)_{(i,n)\in\kappa(v')}, \quad \sigma_{\hat{a}_\perp}(v') = std\left(\hat{a}_{i,\perp}(t_n)\right)_{(i,n)\in\kappa(v')} \tag{7f}$$

$$\hat{a}_{i,\parallel}(t_n) = \hat{\vec{a}}_i(t_n) \cdot \frac{\hat{\vec{v}}_i(t_n)}{\left|\hat{\vec{v}}_i(t_n)\right|}, \quad \hat{a}_{i,\perp}(t_n) = \hat{\vec{a}}_i(t_n) \times \frac{\hat{\vec{v}}_i(t_n)}{\left|\hat{\vec{v}}_i(t_n)\right|} \tag{7g}$$

$$\langle\cos\theta\rangle(v') = \left\langle \frac{\hat{\vec{v}}_i(t_n)}{\left|\hat{\vec{v}}_i(t_n)\right|} \cdot \frac{\hat{\vec{v}}_i(t_{n+1})}{\left|\hat{\vec{v}}_i(t_{n+1})\right|} \right\rangle_{(i,n)\in\kappa(v')} \tag{7h}$$

where $\langle\,\rangle_X$ is the average over X, subscript i indicates the i-th trajectory, # is the number of items in the following set {}, std denotes the unbiased standard deviation, and $\delta v = 0.1$ µm/s is the bin width. Additionally, we checked the detail of the time evolution of velocity by calculating the autocorrelation of the magnitude and the angle:

$$\left|\hat{\vec{v}}\right| autocorrelation\,(m\delta t) = \left\langle \left(\left|\hat{\vec{v}}_i\right|(t_n) - \left\langle\left|\hat{\vec{v}}_{i'}\right|(t_{n'})\right\rangle_{(i',n')}\right)\left(\left|\hat{\vec{v}}_i\right|(t_{n+m}) - \left\langle\left|\hat{\vec{v}}_{i'}\right|(t_{n'})\right\rangle_{(i',n')}\right)\right\rangle_{(i,n)} \tag{8a}$$

$$arg\left(\hat{\vec{v}}\right) autocorrelation\,(m\delta t) = \left\langle \frac{\hat{\vec{v}}_i(t_n)}{\left|\hat{\vec{v}}_i(t_n)\right|} \cdot \frac{\hat{\vec{v}}_i(t_{n+m})}{\left|\hat{\vec{v}}_i(t_{n+m})\right|} \right\rangle_{(i,n)}. \tag{8b}$$

4.3.2 Velocity distribution

We fit a Gaussian distribution to both v_x and v_y to determine the standard deviation σ_G. For $\hat{\vec{v}}$ that follows 2-dimensional Gaussian distribution, the distribution of $|\hat{\vec{v}}|$ is readily derived from the chi-square distribution with 2 degrees of freedom where the square of $|\hat{\vec{v}}|/\sigma_G$ follows:

$$p\left(\frac{\left|\hat{\vec{v}}\right|^2}{\sigma_G^2} \in [v^{sq}, v^{sq} + dv^{sq}]\right) = \frac{1}{2} exp\left(-\frac{v^{sq}}{2}\right) dv^{sq}$$

$$\therefore p\left(\left|\hat{\vec{v}}\right| \in [v', v' + dv']\right) = \frac{1}{2} exp\left(-\frac{v'^2}{2\sigma_G^2}\right) \left.\frac{d\left(\left|\hat{\vec{v}}\right|^2 / \sigma_G^2\right)}{d\left|\hat{\vec{v}}\right|}\right|_{\left|\hat{\vec{v}}\right| = v'} dv'$$

$$= \frac{v'}{\sigma_G^2} exp\left(-\frac{v'^2}{2\sigma_G^2}\right) dv'. \tag{9}$$

To note, the peak of the above distribution is located at $|\hat{\vec{v}}| = \sigma_G$.

4.3.3 Fitting VAC

To fit the experimental data with the generalized Langevin equation (Eqs 5a, b), we employed the analytical solution for the velocity autocorrelation vac^{ss}. For the observed velocity $\widehat{\vec{v}}(t_n) = \delta t^{-1}\int_{t_n}^{t_{n+1}} \vec{v}(t)dt$, the autocorrelation is:

$$vac^{ss}(m\delta t) \equiv \langle \widehat{\vec{v}}(t_{n+m}) \cdot \widehat{\vec{v}}(t_n) \rangle_n^{ss}$$
$$= \phi_+ e^{-(m-1)\lambda_+\delta t}\left(\frac{1-e^{-\lambda_+\delta t}}{\lambda_+\delta t}\right)^2 + \phi_- e^{-(m-1)\lambda_-\delta t}\left(\frac{1-e^{-\lambda_-\delta t}}{\lambda_-\delta t}\right)^2 \quad (10a)$$

$$\lambda_\pm = \frac{(\beta+\gamma) \pm \sqrt{(\beta-\gamma)^2+4\alpha^2}}{2} \quad (10b)$$

$$\phi_\pm = \sigma^2 \frac{1 \pm (\beta-\gamma)}{(\beta-\gamma)^2+4\alpha^2}\left(\frac{1 \pm (\beta-\gamma)}{4\lambda_\pm} + \frac{1 \mp (\beta-\gamma)}{(\beta+\gamma)}\right). \quad (10c)$$

Optimal values of $\alpha, \beta, \gamma, \sigma$ were obtained by minimizing the mean square error between $vac^{ss}(m\delta t)$ and $vac^{exp}(m\delta t)$.

4.3.4 Positional uncertainty

Parameters in Table 1 were obtained by fitting VAC at $\tau \geq 2\,sec$. As for the simulation only with generalized Langevin equations (Eqs 5a, b), VAC matched poorly for the shortest time interval of our data (τ = 0 and 1 s) due to measurement uncertainty arising from finite time step and spatial resolution of the observation. Because acceleration was also defined as the velocity difference in this time interval, the magnitude of acceleration in the simulations was off by one order of magnitude from the real cell data. We emulated these effects in the simulations by including white Gaussian noise with the observed standard deviation σ_X (see *Methods*, Table 1). The value of VAC changed only at the shortest time window of $\tau = 0$ and 1 s by this correction.

To represent positional uncertainty, we incorporated additive noise in the model so that

$$\widehat{\vec{r}}(t_n) = \vec{r}(t_n) + \sigma_X \vec{\xi}_n^{(X)} \quad (11)$$

where $\vec{\xi}_n^{(X)}$ is white gaussian noise which satisfies $\langle \vec{\xi}_n^{(X)} \rangle = \overrightarrow{0}, \langle \vec{\xi}_n^{(X)} \vec{\xi}_m^{(X)^T} \rangle = \begin{pmatrix} 1 & 0 \\ 0 & 1 \end{pmatrix} \delta_{nm}$ where δ_{nm} is the Kronecker delta, and thus independent of all the other variables. σ_X is the strength of the positional noise, $\vec{r}(t_n)$ is the position sampled at time t_n, calculated by integrating $\vec{v}(t)$ in time according to Eqs 5a, b. The observed velocity $\widehat{\vec{v}}'(t)$ used in the analysis is defined as follows:

$$\widehat{\vec{v}}'^{(t_n)} = \frac{\widehat{\vec{r}}(t_{n+1}) - \widehat{\vec{r}}(t_n)}{\delta t}. \quad (12)$$

Due to the positional noise, the analytical solution of the velocity autocorrelation at steady state becomes

$$vac^{ssX}(m\delta t) \equiv \langle \widehat{\vec{v}}'(t_{n+m}) \cdot \widehat{\vec{v}}'(t_n) \rangle_n^{ss} = \begin{cases} vac^{ss}(0) + \dfrac{2\sigma_X^2}{\delta t^2} & (m=0) \\ vac^{ss}(\delta t) - \dfrac{\sigma_X^2}{\delta t^2} & (m=1) \\ vac^{ss}(m\delta t) & (m \geq 2) \end{cases}. \quad (13)$$

The optimal values of $\alpha, \beta, \gamma, \sigma, \sigma_X$ were obtained by minimizing mean square error between $vac^{ssX}(m\delta t)$ and $vac^{exp}(m\delta t)$.

4.3.5 Cell boundary analysis

A MATLAB code for the active contour method (Driscoll et al., 2012)—BoundaryTrack (Nakajima et al., 2016; Fujimori et al., 2019) was used to plot kymographs of the curvature and protrusion velocity of the cell binary mask contour. In brief, the kymographs show time-evolution of curvature or normal vector-projected velocity on the contour. The angle of normal vector was also obtained using this code.

4.3.5.1 Boundary point tracking by BoundaryTrack

Initially, BoundaryTrack detects the sequence of boundary pixels of the mask starting clockwise from the upper-left most point (Supplementary Figure S4A left). At each frame, the boundary was divided into equally spaced 500 points, where the upper-left most point was assigned index 1 (Supplementary Figure S4A center). The boundary points in two consecutive frames were linked so that the mean square of the distance between the linked points was minimized (Supplementary Figure S4A right). As for the latter frame, the index of the point linked with the first point in the previous frame was reset to 1. From the assigned boundary points, the curvature and the velocity were calculated. In particular, the velocity was obtained by calculating the displacement of the points assigned with the same index over time.

4.3.5.2 Comparing the protrusion velocity and the cell centroid velocity

To detect the forward region of the cell, the i-th boundary point at time t in the velocity kymograph $\{u_i(t)\}_{i=1,\ldots,500}$ were smoothed by fitting the velocity values at boundary points in each time with the following joint function:

$$u_i(t) = \begin{cases} A_1(t)\cos\left(\dfrac{\pi}{L\{I(t)\}} min(|i - C\{I(t)\}|, |i - C\{I(t)\} \pm 500|)\right) & (i \in I(t)) \\ -A_2(t)\cos\left(\dfrac{\pi}{500 - L\{I(t)\}} min\left(\left|i - \bar{C}\{I(t)\}\right|, \left|i - \bar{C}\{I(t)\} \pm 500\right|\right)\right) & (i \notin I(t)) \end{cases}$$

$$I(t) = \begin{cases} \{i \mid i_1 \leq i \leq i_2\} & (i_1 \leq i_2) \\ \{i \mid i \leq i_2 \leq i_1\} \cup \{i \mid i_2 \leq i_1 \leq i\} & (i_2 < i_1) \end{cases}$$

where $A_1, A_2 \geq 0$, $I(t)$ is a continuous front region bounded by two ends $i_1(t)$ and $i_2(t)$. The center $\{I(t)\}$, length $L\{I(t)\}$, the center of rear region $\bar{C}\{I(t)\}$ were defined in the coordinate with the periodic boundary condition, as follows:

$$C\{I(t)\} = \begin{cases} (i_1+i_2)/2 & (i_1 \leq i_2) \\ (i_1+i_2+500)/2 & (i_2 < i_1 \wedge i_1+i_2 \leq 500) \\ (i_1+i_2-500)/2 & (i_2 < i_1 \wedge i_1+i_2 > 500) \end{cases}$$

$$\bar{C}\{I(t)\} = \begin{cases} (i_1+i_2)/2 & (i_2 < i_1) \\ (i_1+i_2+500)/2 & (i_1 \leq i_2 \wedge i_1+i_2 \leq 500) \\ (i_1+i_2-500)/2 & (i_1 \leq i_2 \wedge i_1+i_2 > 500) \end{cases}$$

$$L\{I(t)\} = \begin{cases} i_2 - i_1 & (i_1 \leq i_2) \\ 500 - (i_1 - i_2) & (i_2 < i_1) \end{cases}.$$

To investigate the relation of front or rear region with the direction of cell centroid velocity, we calculated the angle difference between the normal vector at the center of front or rear region and the centroid velocity.

4.3.5.3 Curvature wave tracking and the leading edge detection

To track the curvature waves, we first detected protrusive regions as follows. Depending on the curvature $\{c_i(t)\}_{i=1,\ldots,500}$, position #i in the curvature kymograph were classified as either "protrusive" $(c_i(t) > c^{(2)})$, "flat" $(c^{(1)} < c_i(t) \le c^{(2)})$ or "caved" $(c_i(t) \le c^{(1)})$ where the thresholds $c^{(1)}, c^{(2)}$ were obtained by the Otsu's method. At each time point t, continuous protrusive regions (j = 1, 2, 3 . . .) were defined as set $I^c_{j,t}$ of neighboring protrusive boundary points i between two ends $(i^L_{j,t}, i^R_{j,t}) \in I^{LR}(t)$:

$$I^{LR}(t) = \left\{ \left(i^L_{j,t}, i^R_{j,t}\right) \in \mathbb{Z}^2 \middle| \left(c_{i^L_{j,t}-1}(t) \le c^{(2)}\right) \wedge \left(c_{i^R_{j,t}+1}(t) \le c^{(2)}\right) \wedge \left(\forall i\, s.t. \left(i^L_{j,t} \le i \le i^R_{j,t} \vee i \le i^R_{j,t} \le i^L_{j,t} \vee i^R_{j,t} \le i^L_{j,t} \le i\right), c_i(t) > c^{(2)}\right)\right\}$$

$$I^c_{j,t} = \begin{cases} \left\{ i \mid i^L_{j,t} \le i \le i^R_{j,t} \right\} & \left(i^L_{j,t} \le i^R_{j,t}\right) \\ \left\{ i \mid i \le i^R_{j,t} \le i^L_{j,t} \right\} \cup \left\{ i \mid i^R_{j,t} \le i^L_{j,t} \le i \right\} & \left(i^R_{j,t} < i^L_{j,t}\right) \end{cases}$$

$$C\left\{I^c_{j,t}\right\} = \begin{cases} \left(i^L_{j,t} + i^R_{j,t}\right)/2 & \left(i^L_{j,t} \le i^R_{j,t}\right) \\ \left(i^L_{j,t} + i^R_{j,t} + 500\right)/2 & \left(i^R_{j,t} < i^L_{j,t} \wedge i^L_{j,t} + i^R_{j,t} \le 500\right) \\ \left(i^L_{j,t} + i^R_{j,t} - 500\right)/2 & \left(i^R_{j,t} < i^L_{j,t} \wedge i^L_{j,t} + i^R_{j,t} > 500\right) \end{cases}$$

where $C\left\{I^c_{j,t}\right\}$ is the center of j-th protrusive region.

Next, we traced the curvature waves by linking the j-th fragment at frame t and the j'-th fragment at frame $t+1$ if $I^c_{j,t}$ and $I^c_{j',t+1}$ have overlapping points. Thus, the set of linked fragments J^c was defined as follows:

$$J^c = \left\{ (j, j', t) \middle| \exists i \in I^c_{j',t+1}, i \in I^c_{j,t} \right\}.$$

From each pair of the linked fragments $(j, j', t) \in J^c$, we obtained the angular velocity $\omega^c_{j,j'}(t)$ of a protruding region as follows:

$$\omega^c_{j,j'}(t) = \left(\varphi_{C\left\{I^c_{j',t+1}\right\}}(t+1) - \varphi_{C\left\{I^c_{j,t}\right\}}(t) \right) \Big/ \Delta t$$

where $\varphi_i(t)$ is the angle of the normal vector at point i at time t. The representative angular velocity ω^c were obtained by fitting the histogram of $|\omega^c_{j,j'}(t)|$ to an exponential distribution for all the linked fragments.

To investigate the relation between the curvature wave and the centroid velocity angle, we selected a single dominant wave $j^d(t)$ whose angle of normal vector $\varphi_{C\left\{I^c_{j^d(t),t}\right\}}(t)$ was closest to that of the centroid velocity at time t. The lifetime $\{\tau^d_k\}$ of the leading edge was measured by calculating the time window during which the leading edge was assigned to a particular curvature wave. To this end, we computed the time interval between the time points $t^d_k \in T^d$ at which $j^d(t^d_k)$ become un-linked to the dominant wave at the next time frame $j^d(t^d_k + 1)$:

$$T^d = \left\{ t^d_k \middle| \left(j^d\left(t^d_k\right), j^d\left(t^d_k + 1\right), t^d_k \right) \notin J^c \right\}$$
$$\tau^d_k = \left(t^d_{k+1} - t^d_k - 1\right)\Delta t$$

where the index k is given so that t^d_k is listed in the ascending order, i.e., $t^d_k < t^d_{k+1}$ for all integer k. We fit a histogram of τ^d_k for all the linked fragments with exponential distribution to obtain the typical duration time of driving wave τ^d.

4.3.5.4 Estimating the time scale of centroid velocity autocorrelation

The angular velocity ω^c and the duration time τ^d obtained above were used to estimate the autocorrelation of the angle of cell centroid velocity $\psi(t)$. The time evolution of $\psi(t)$ was modeled as 1D persistent random walk with time scale τ^d and step size $\omega^c\tau^d$. Then the probability distribution of the angle difference $\Delta\psi \in (-\infty, \infty)$ is:

$$p(\psi(t) - \psi(0) = \Delta\psi) = \frac{1}{\sqrt{\pi(\omega^c)^2\tau^d t}} exp\left(-\frac{\Delta\psi^2}{(\omega^c)^2\tau^d t}\right).$$

Therefore, the autocorrelation AC(t) is:

$$\begin{aligned} \mathrm{AC(t)} &= \int_{-\infty}^{\infty} p(\psi(t) - \psi(0) = \Delta\psi) \cos\Delta\psi \, d\Delta\psi \\ &= Re\left(\int_{-\infty}^{\infty} \frac{1}{\sqrt{\pi(\omega^c)^2\tau^d t}} exp\left(-\frac{\Delta\psi^2}{(\omega^c)^2\tau^d t} + i\Delta\psi\right) d\Delta\psi \right) \\ &= exp\left(-\frac{(\omega^c)^2\tau^d}{4} t\right). \end{aligned}$$

Thus, the estimated decay time of the autocorrelation is $T^{est} = 4/(\omega^c)^2\tau^d$.

4.3.6 Cell morphology analysis

4.3.6.1 Fourier-based shape analysis

To quantify cell shape, we calculated the elliptic Fourier descriptor (Kuhl and Giardina, 1982). First, we extracted the outline of cell binary mask with a homemade code according to (Nakajima et al., 2016; Fujimori et al., 2019). The periphery of a cell mask Γ was defined as a folded line parametrized with length $0 \le \ell < L$ connecting the pixels $\vec{q}_i$ on the edge, where each pixel i has pixel $i-1$ and $i+1$ in its 4 nearest neighbor pixels:

$$\Gamma = \left\{ \vec{q}(\ell) \middle| 0 \le \ell < L, \vec{q}(\ell) = \begin{cases} \vec{q}_i + (\ell - i)(\vec{q}_i - \vec{q}_{i+1}) & (i \le \ell < i+1) \\ \vec{q}_{L-1} + (\ell - (L-1))(\vec{q}_{L-1} - \vec{q}_0) & (L-1 \le \ell < L) \end{cases} \right\}. \quad (14)$$

Next, the polygonal outline was converted to 160 equally spaced points $\left\{\widehat{\vec{q}}_i\right\}_{i=0}^{159}$ on a relative position on Γ:

$$\vec{q}_i' = \sqrt{\frac{3000}{A}} \vec{q}\left(\frac{i}{160} L\right) \quad (15a)$$

$$\widehat{\vec{q}}_i = \vec{q}_i' - \frac{1}{160} \sum_{j=0}^{159} \vec{q}_j'\left(\frac{j}{160} L\right) \quad (15b)$$

which is rescaled according to the total number of pixels A in the mask, and the coordinate was set so that the origin is at the cell centroid.

The elliptic Fourier descriptor was calculated by taking the discrete Fourier transformation of $\widehat{\vec{r}}_i$ with wave number k:

$$\widetilde{\vec{q}}_k = \sum_{i=0}^{159} \mathcal{R}\left(-2\pi k \frac{i}{160}\right) \widehat{\vec{q}}_i, k = 0, 1, \ldots, 159 \quad (16)$$

where $\mathcal{R}(\cdot)$ is a rotational matrix. Its power spectrum $S_k = |\widetilde{\vec{q}}_k|^2$ was calculated. C_n and C_{-n} are complex number equivalents of $\widetilde{\vec{q}}_{n-1}$ and $\widetilde{\vec{q}}_{161-n}$.

4.3.6.2 Fourier descriptor PCA

We calculated principal component vectors from the representative dataset containing 63 snapshots. From the power spectrum vector $\vec{S} \equiv (S_0, S_1, \ldots S_{159})$ for each mask in the representative dataset, averaged power spectrum vector $\bar{\vec{S}}$ and the covariance matrix $\eta = (\eta_{kl})_{k,l=0,1,\ldots,159}$

$$\bar{\vec{S}} = \langle \vec{S} \rangle \tag{17}$$

$$\eta_{kl} = \begin{cases} var(S_k) & k = l \\ cov(S_k, S_l) & k \neq l \end{cases} \tag{18}$$

were calculated, where *var* and *cov* denotes the variance and covariance. The m-th eigenvalue and eigenvector $(\lambda_m, \vec{e}_m)$ of matrix η were defined so that the conditions $\lambda_1 \geq \lambda_2 \geq \cdots \geq \lambda_{160}$ and $\vec{e}_m \cdot \vec{e}_{m'} = \delta_{mm'}$ are met. To note, thus obtained values of $\bar{\vec{S}}$, λ_m, and $\vec{e}_m$ were used to analyze all the data. Using the eigenvectors, the m-th principal component

$$PCm = \left(\vec{S} - \bar{\vec{S}}\right) \cdot \vec{e}_m \tag{19}$$

was calculated for each power spectrum vector of mask.

To characterize cell shape change dynamics, we calculated autocorrelation AC^{PC} of PC1 and PC2 values. Using the PC values of cell i at time t_n, AC^{PC} is:

$$\widetilde{PC1}_i(t_n) = PC1_i(t_n) - \langle PC1_i(t_{n'}) \rangle_{n'}$$
$$\widetilde{PC2}_i(t_n) = PC2_i(t_n) - \langle PC2_i(t_{n'}) \rangle_{n'}$$
$$AC^{PC}(m\delta t) = \frac{1}{2} \langle \widetilde{PC1}_i(t_n) \widetilde{PC1}_i(t_{n+m}) + \widetilde{PC2}_i(t_n) \widetilde{PC2}_i(t_{n+m}) \rangle_{(i,n)}.$$

To restore the shape of cell from a set of principal components $(PC1, PC2, \ldots, PC160)$, $\vec{S}$ and $\hat{\vec{q}}_i$ were sequentially calculated:

$$\vec{S} = \bar{\vec{S}} + \sum_{m=1}^{160} PCm\, \vec{e}_m \tag{20}$$

$$\hat{\vec{q}}_i = \frac{1}{160} \sum_{k=0}^{159} \mathcal{R}\left(2\pi k \frac{i}{160}\right) \begin{pmatrix} \sqrt{S_k} \\ 0 \end{pmatrix}. \tag{21}$$

The pixels $\vec{q}_i$ included in the edge were obtained by rounding off $\hat{\vec{q}}_i$. To show the recovered edge as an image, we made a binary image which has white color only on the pixels $\vec{q}_i$.

4.3.6.3 CNN-based shape analysis

CNN-based PCA and classification were performed based on the morphometry obtained previously (Imoto et al., 2021). In brief, each snapshot image of *N. gruberi* was input to the pre-trained CNN, and the morphology features were obtained as output. The principal components of these features were calculated using the PCA parameters obtained in (Imoto et al., 2021). The time average of the principal components was taken from all the frames in each time series. According to the morphology features, each snapshot was classified into three morphology classes: *Dictyostelium-like*, HL60-like, and fish keratocyte-like. Since only two snapshots were classified as keratocyte-like, we conducted the further analysis on *Dictyostelium-like*, HL60-like classes. The HL60 class ratio was calculated for each timeseries, as the number of snapshots classified as HL60 divided by the total number of snapshots in the timeseries.

4.3.7 Analytical solution of VAC at steady state without positional noise

First, we define VAC as an ensemble-averaged inner product of true velocities at two timepoints:

$$vac(\Delta t; t) = \langle \vec{v}(t) \cdot \vec{v}(t + \Delta t) \rangle. \tag{22}$$

To obtain the dynamics of thus defined VAC, $\vec{v}(t)$ can be obtained as itô-integral of generalized Langevin equation with 2-dimensional Brownian motion $\vec{B}_t = (B_{x,t}, B_{y,t})^T$:

$$d\begin{pmatrix} v_x(t) \\ V_x(t) \\ v_y(t) \\ V_y(t) \end{pmatrix} = \begin{pmatrix} -\beta & \alpha & 0 & 0 \\ \alpha & -\gamma & 0 & 0 \\ 0 & 0 & -\beta & \alpha \\ 0 & 0 & \alpha & -\gamma \end{pmatrix} \begin{pmatrix} v_x(t) \\ V_x(t) \\ v_y(t) \\ V_y(t) \end{pmatrix} dt + \sigma \begin{pmatrix} dB_{x,t} \\ 0 \\ dB_{y,t} \\ 0 \end{pmatrix} \tag{23}$$

$$d\left[e^{Ct} \begin{pmatrix} v_x(t) \\ V_x(t) \end{pmatrix} \right] = \sigma e^{Ct} \begin{pmatrix} dB_{x,t} \\ 0 \end{pmatrix}, C = \begin{pmatrix} \beta & -\alpha \\ -\alpha & \gamma \end{pmatrix} \tag{24a}$$

$$d\left[e^{Ct} \begin{pmatrix} v_y(t) \\ V_y(t) \end{pmatrix} \right] = \sigma e^{Ct} \begin{pmatrix} dB_{y,t} \\ 0 \end{pmatrix} \tag{24b}$$

$$\therefore \begin{pmatrix} v_x(t) \\ V_x(t) \end{pmatrix} = e^{-Ct} \left[\begin{pmatrix} v_x(0) \\ V_x(0) \end{pmatrix} + \sigma \int_0^t e^{Ct'} \begin{pmatrix} dB_{x,t'} \\ 0 \end{pmatrix} dt' \right] \tag{25a}$$

$$\begin{pmatrix} v_y(t) \\ V_y(t) \end{pmatrix} = e^{-Ct} \left[\begin{pmatrix} v_y(0) \\ V_y(0) \end{pmatrix} + \sigma \int_0^t e^{Ct'} \begin{pmatrix} dB_{y,t'} \\ 0 \end{pmatrix} dt' \right]. \tag{25b}$$

Especially, the velocity can be calculated from the eigenvalues $\lambda_\pm$ defined above and corresponding eigenvectors $\vec{e}_\pm \equiv \begin{pmatrix} e_{x,\pm} \\ e_{y,\pm} \end{pmatrix}$ of C with $e^{Ct} = \begin{pmatrix} \vec{e}_+ & \vec{e}_- \end{pmatrix} \begin{pmatrix} e^{\lambda_+ t} & 0 \\ 0 & e^{\lambda_- t} \end{pmatrix} \begin{pmatrix} \vec{e}_+^T \\ \vec{e}_-^T \end{pmatrix}$:

$$v_x(t) = \begin{pmatrix} e_{x,+} \\ e_{x,-} \end{pmatrix}^T \left[\begin{pmatrix} e^{-\lambda_+ t} \vec{e}_+^T \\ e^{-\lambda_- t} \vec{e}_-^T \end{pmatrix} \begin{pmatrix} v_x(0) \\ V_x(0) \end{pmatrix} + \sigma \int_0^t \begin{pmatrix} e^{\lambda_+ (t'-t)} e_{x,+} \\ e^{\lambda_- (t'-t)} e_{x,-} \end{pmatrix} dB_{x,t'} \right] \tag{26a}$$

$$v_y(t) = \begin{pmatrix} e_{x,+} \\ e_{x,-} \end{pmatrix}^T \left[\begin{pmatrix} e^{-\lambda_+ t} \vec{e}_+^T \\ e^{-\lambda_- t} \vec{e}_-^T \end{pmatrix} \begin{pmatrix} v_y(0) \\ V_y(0) \end{pmatrix} + \sigma \int_0^t \begin{pmatrix} e^{\lambda_+ (t'-t)} e_{x,+} \\ e^{\lambda_- (t'-t)} e_{x,-} \end{pmatrix} dB_{y,t'} \right] \tag{26b}$$

$$\vec{e}_\pm = \begin{pmatrix} \cos\theta_\pm \\ \sin\theta_\pm \end{pmatrix}, \tan\theta_\pm = \frac{\beta - \gamma \mp \sqrt{(\beta - \gamma)^2 + 4\alpha^2}}{2\alpha}. \tag{26c}$$

Using the representation of $\vec{v}(t)$ above and the property of Brownian motion $\int f(t) d\vec{B}_t = \vec{0}, d\vec{B}_t d\vec{B}_{t'}^T = \delta(t - t') \begin{pmatrix} dt & 0 \\ 0 & dt \end{pmatrix}$, VAC is:

$$vac(\Delta t; t_0) =$$
$$\left\langle \sum_{\chi=x,y} \left\{ \left[\begin{pmatrix} e_{x,+} \\ e_{x,-} \end{pmatrix}^T \begin{pmatrix} e^{-\lambda_+ t_0} \vec{e}_+^T \\ e^{-\lambda_- t_0} \vec{e}_-^T \end{pmatrix} \begin{pmatrix} v_\chi(0) \\ V_\chi(0) \end{pmatrix} \right] \left[\begin{pmatrix} e_{x,+} \\ e_{x,-} \end{pmatrix}^T \begin{pmatrix} e^{-\lambda_+ (t_0 + \Delta t)} \vec{e}_+^T \\ e^{-\lambda_- (t_0 + \Delta t)} \vec{e}_-^T \end{pmatrix} \begin{pmatrix} v_\chi(0) \\ V_\chi(0) \end{pmatrix} \right] \right\}$$
$$+ 2\sigma^2 \int_0^{t_0} \left[\begin{pmatrix} e_{x,+} \\ e_{x,-} \end{pmatrix}^T \begin{pmatrix} e^{\lambda_+ (t'-t_0)} e_{x,+} \\ e^{\lambda_- (t'-t_0)} e_{x,-} \end{pmatrix} \right] \left[\begin{pmatrix} e_{x,+} \\ e_{x,-} \end{pmatrix}^T \begin{pmatrix} e^{\lambda_+ (t'-(t_0+\Delta t))} e_{x,+} \\ e^{\lambda_- (t'-(t_0+\Delta t))} e_{x,-} \end{pmatrix} \right] dt' \Bigg\rangle. \tag{27}$$

Since $\lambda_\pm$ is always positive when $\alpha, \beta, \gamma > 0$, the first term of VAC disappears with time at the rate of $e^{-2\lambda_- t_0}$. The lower limit of integration also disappears at the same rate. The only time-independent term comes from the upper limit of integration and is the steady state solution of VAC:

$$vac(\Delta t; t) \overset{t \to \infty}{\longrightarrow} \phi_+ e^{-\lambda_+ \Delta t} + \phi_- e^{-\lambda_- \Delta t} \tag{28a}$$

$$\phi_{\pm} = 2\sigma^2\left(\frac{e_{x,\pm}^4}{2\lambda_{\pm}} + \frac{e_{x,+}^2 e_{x,-}^2}{\lambda_+ + \lambda_-}\right) \tag{28b}$$

where the second line is another representation of $\phi_{\pm}$ defined above. Finally, considering the sampling procedure where the velocity is observed as the difference of discretely sampled positions, the representation of vac^{ss} is obtained by time integration of VAC:

$$\begin{aligned} vac^{ss}(k\delta t) &= \frac{1}{\delta t^2}\langle(\vec{r}(t_{n+k+1}) - \vec{r}(t_{n+k}))\cdot(\vec{r}(t_{n+1}) - \vec{r}(t_n))\rangle_n \\ &= \frac{1}{\delta t^2}\langle\left(\int_{t_{n+k}}^{t_{n+k+1}}\vec{v}(t')dt'\right)\cdot\left(\int_{t_n}^{t_{n+1}}\vec{v}(t'')dt''\right)\rangle_n \\ &= \frac{1}{\delta t^2}\int_{k\delta t}^{(k+1)\delta t}dt'\int_0^{\delta t}dt''\,\langle vac(t'-t'';t_n)\rangle_n \\ &= \phi_+ e^{-(k-1)\lambda_+\delta t}\left(\frac{1-e^{-\lambda_+\delta t}}{\lambda_+\delta t}\right)^2 + \phi_- e^{-(k-1)\lambda_-\delta t}\left(\frac{1-e^{-\lambda_-\delta t}}{\lambda_-\delta t}\right)^2. \end{aligned} \tag{29}$$

In the third raw, we used the relation $\langle vac(t'-t'';t_n)\rangle_n = \lim_{n\to\infty} vac(t'-t'';t_n) = \lim_{t\to\infty} vac(t'-t'';t)$ because time average should converge to the steady state solution if the VAC itself converges.

Data availability statement

The raw data supporting the conclusion of this article will be made available by the authors, without undue reservation.

Author contributions

MU: Data curation, Formal Analysis, Investigation, Methodology, Software, Supervision, Validation, Visualization, Writing–original draft, Funding acquisition. YM: Data curation, Formal Analysis, Investigation, Writing–review and editing, Software. AK: Data curation, Writing–review and editing. DI: Writing–review and editing, Data curation, Investigation, Software, Visualization. SS: Conceptualization, Funding acquisition, Methodology, Project administration, Resources, Supervision, Writing–original draft.

Funding

The author(s) declare financial support was received for the research, authorship, and/or publication of this article. This was work was supported by JSPS KAKENHI Grant Number JP19H05801 to SS, JP22H05673 to MU, JST CREST JPMJCR1923 to SS and partly by HFSP Research Grant RGP0051/2021 to SS.

Acknowledgments

The authors thank the present and the past members of the SS lab for experimental supports and discussion.

Conflict of interest

The authors declare that the research was conducted in the absence of any commercial or financial relationships that could be construed as a potential conflict of interest.

The author(s) declared that they were an editorial board member of Frontiers, at the time of submission. This had no impact on the peer review process and the final decision.

Publisher's note

Supplementary material

The Supplementary Material for this article can be found online at: https://www.frontiersin.org/articles/10.3389/fcell.2023.1274127/full#supplementary-material

References

Alirezaeizanjani, Z., Großmann, R., Pfeifer, V., Hintsche, M., and Beta, C. (2020). Chemotaxis strategies of bacteria with multiple run modes. *Sci. Adv.* 6, eaaz6153. doi:10.1126/sciadv.aaz6153

Ariel, G., Rabani, A., Benisty, S., Partridge, J. D., Harshey, R. M., and Be'er, A. (2015). Swarming bacteria migrate by Lévy Walk. *Nat. Commun.* 6, 8396. doi:10.1038/ncomms9396

Arzt, M., Deschamps, J., Schmied, C., Pietzsch, T., Schmidt, D., Tomancak, P., et al. (2022). LABKIT: labeling and segmentation toolkit for big image data. *Front. Comput. Sci.* 4. doi:10.3389/fcomp.2022.777728

Bartumeus, F., Catalan, J., Fulco, U. L., Lyra, M. L., and Viswanathan, G. M. (2002). Optimizing the encounter rate in biological interactions: Lévy versus brownian strategies. *Phys. Rev. Lett.* 88, 097901. doi:10.1103/physrevlett.88.097901

Brown, M. W., Silberman, J. D., and Spiegel, F. W. (2012). A contemporary evaluation of the acrasids (Acrasidae, Heterolobosea, Excavata). *Eur. J. Protistol.* 48, 103–123. doi:10.1016/j.ejop.2011.10.001

Chi, Q., Yin, T., Gregersen, H., Deng, X., Fan, Y., Zhao, J., et al. (2014). Rear actomyosin contractility-driven directional cell migration in three-dimensional matrices: a mechano-chemical coupling mechanism. *J. Roy. Soc. Interface* 11, 20131072. doi:10.1098/rsif.2013.1072

Dieterich, P., Klages, R., Preuss, R., and Schwab, A. (2008). Anomalous dynamics of cell migration. *Proc. Natl. Acad. Sci. U. S. A.* 105, 459–463. doi:10.1073/pnas.0707603105

Driscoll, M. K., McCann, C., Kopace, R., Homan, T., Fourkas, J. T., Parent, C., et al. (2012). Cell shape dynamics: from waves to migration. *Plos Comput. Biol.* 8, e1002392. doi:10.1371/journal.pcbi.1002392

Dunn, G. A., and Brown, A. F. (1987). A unified approach to analysing cell motility. *J. Cell Sci.* 8, 81–102. doi:10.1242/jcs.1987.supplement_8.5

Ebata, H., Yamamoto, A., Tsuji, Y., Sasaki, S., Moriyama, K., Kuboki, T., et al. (2018). Persistent random deformation model of cells crawling on a gel surface. *Sci. Rep.* 8, 5153. doi:10.1038/s41598-018-23540-x

Ershov, D., Phan, M.-S., Pylvänäinen, J. W., Rigaud, S. U., Blanc, L. L., Charles-Orszag, A., et al. (2022). TrackMate 7: integrating state-of-the-art segmentation algorithms into tracking pipelines. *Nat. Methods* 19, 829–832. doi:10.1038/s41592-022-01507-1

Fritz-Laylin, L. K., Lord, S. J., and Mullins, R. D. (2017). WASP and SCAR are evolutionarily conserved in actin-filled pseudopod-based motility. *J. Cell Biol.* 216, 1673–1688. doi:10.1083/jcb.201701074

Fritz-Laylin, L. K., Prochnik, S. E., Ginger, M. L., Dacks, J. B., Carpenter, M. L., Field, M. C., et al. (2010). The genome of Naegleria gruberi illuminates early eukaryotic versatility. *Cell* 140, 631–642. doi:10.1016/j.cell.2010.01.032

Fujimori, T., Nakajima, A., Shimada, N., and Sawai, S. (2019). Tissue self-organization based on collective cell migration by contact activation of locomotion and chemotaxis. *Proc. Natl. Acad. Sci. U. S. A.* 116, 4291–4296. doi:10.1073/pnas.1815063116

Fulton, C. (1970). Amebo-flagellates as research partners: the laboratory biology of Naegleria and Tetramitus. *Methods Cell Physiology* 4, 341–476. doi:10.1016/S0091-679X(08)61759-8

Gail, M. H., and Boone, C. W. (1970). The locomotion of mouse fibroblasts in tissue culture. *Biophys. J.* 10, 980–993. doi:10.1016/s0006-3495(70)86347-0

Haastert, P. J. M. V. (2021). Short- and long-term memory of moving amoeboid cells. *Plos One* 16, e0246345. doi:10.1371/journal.pone.0246345

Haastert, P. J. M. V., and Bosgraaf, L. (2009). Food searching strategy of amoeboid cells by starvation induced run length extension. *Plos One* 4, e6814. doi:10.1371/journal.pone.0006814

Harris, T. H., Banigan, E. J., Christian, D. A., Konradt, C., Wojno, E. D. T., Norose, K., et al. (2012). Generalized Lévy walks and the role of chemokines in migration of effector CD8+ T cells. *Nature* 486, 545–548. doi:10.1038/nature11098

Hartman, R., Lau, K., Chou, W., and Coates, T. D. (1994). The fundamental motor of the human neutrophil is not random: evidence for local non-Markov movement in neutrophils. *Biophys. J.* 67, 2535–2545. doi:10.1016/S0006-3495(94)80743-X

Huang, C. -H., Tang, M., Shi, C., Lglesias, P. A., and Devreotes, P. N. (2013). An excitable signal integrator couples to an idling cytoskeletal oscillator to drive cell migration. *Nat. Cell Biol.* 15, 1307–1316. doi:10.1038/ncb2859

Huda, S., Weigelin, B., Wolf, K., Tretiakov, K. V., Polev, K., Wilk, G., et al. (2018). Lévy-like movement patterns of metastatic cancer cells revealed in microfabricated systems and implicated *in vivo*. *Nat. Commun.* 9, 4539. doi:10.1038/s41467-018-06563-w

Huo, H., He, R., Zhang, R., and Yuan, J. (2021). Swimming Escherichia coli cells explore the environment by Lévy walk. *Appl. Environ. Microb.* 87, 024299–e2520. doi:10.1128/aem.02429-20

Imoto, D., Saito, N., Nakajima, A., Honda, G., Ishida, M., Sugita, T., et al. (2021). Comparative mapping of crawling-cell morphodynamics in deep learning-based feature space. *Plos Comput. Biol.* 17, e1009237. doi:10.1371/journal.pcbi.1009237

Itakura, A., Aslan, J. E., Kusanto, B. T., Phillips, K. G., Porter, J. E., Newton, P. K., et al. (2013). p21-Activated kinase (PAK) regulates cytoskeletal reorganization and directional migration in human neutrophils. *Plos One* 8, e73063. doi:10.1371/journal.pone.0073063

Jerison, E. R., and Quake, S. R. (2020). Heterogeneous T cell motility behaviors emerge from a coupling between speed and turning *in vivo*. *Elife* 9, e53933. doi:10.7554/elife.53933

Kidger, P., Foster, J., Li, X., Oberhauser, H., and Lyons, T. (2021). Neural SDEs as infinite-dimensional GANs. Available from: https://arxiv.org/abs/2102.03657.

King, C. A., Davies, A. H., and Preston, T. M. (1981). Lack of substrate specificity on the speed of amoeboid locomotion inNaegleria gruberi. *Experientia* 37, 709–710. doi:10.1007/bf01967936

King, C. A., Westwood, R., Cooper, L., and Preston, T. M. (1979). Speed of locomotion of the soil amoebaNaegleria gruberi in media of different ionic compositions with special reference to interactions with the substratum. *Protoplasma* 99, 323–334. doi:10.1007/bf01275804

Kuhl, F. P., and Giardina, C. R. (1982). Elliptic Fourier features of a closed contour. *Comput. Vis. Graph* 18, 236–258. doi:10.1016/0146-664x(82)90034-x

Kwon, T., Kwon, O.-S., Cha, H.-J., and Sung, B. J. (2019). Stochastic and heterogeneous cancer cell migration: experiment and theory. *Sci. Rep.* 9, 16297. doi:10.1038/s41598-019-52480-3

Li, L., Cox, E. C., and Flyvbjerg, H. (2011). "Dicty dynamics": dictyostelium motility as persistent random motion. *Phys. Biol.* 8, 046006. doi:10.1088/1478-3975/8/4/046006

Li, L., Nørrelykke, S. F., and Cox, E. C. (2008). Persistent cell motion in the absence of external signals: a search strategy for eukaryotic cells. *Plos One* 3, e2093. doi:10.1371/journal.pone.0002093

Li, X., Wong, T.-K. L., Chen, R. T. Q., and Duvenaud, D. (2020). Scalable gradients for stochastic differential equations. Available from: https://arxiv.org/abs/2001.01328.

Marciano-Cabral, F., and Cline, M. (1987). Chemotaxis by Naegleria fowleri for bacteria. *J. Protozool.* 34, 127–131. doi:10.1111/j.1550-7408.1987.tb03147.x

Morales, J. C. F., Xue, Q., and Roh-Johnson, M. (2022). An evolutionary and physiological perspective on cell-substrate adhesion machinery for cell migration. *Front. Cell Dev. Biol.* 10, 943606. doi:10.3389/fcell.2022.943606

Nakajima, A., Ishida, M., Fujimori, T., Wakamoto, Y., and Sawai, S. (2016). The microfluidic lighthouse: an omnidirectional gradient generator. *Lab. Chip* 16, 4382–4394. doi:10.1039/c6lc00898d

Nakamura, K., and Kobayashi, T. J. (2021). Connection between the bacterial chemotactic network and optimal filtering. *Phys. Rev. Lett.* 126, 128102. doi:10.1103/physrevlett.126.128102

Ohta, T., Tarama, M., and Sano, M. (2016). Simple model of cell crawling. *Physica D.* 318–319, 3–11. doi:10.1016/j.physd.2015.10.007

Parfrey, L. W., Lahr, D. J. G., Knoll, A. H., and Katz, L. A. (2011). Estimating the timing of early eukaryotic diversification with multigene molecular clocks. *Proc. Natl. Acad. Sci. U. S. A.* 108, 13624–13629. doi:10.1073/pnas.1110633108

Partridge, B., Anton, S. G., Khorshed, R., Adams, G., Pospori, C., Celso, C. L., et al. (2022). Heterogeneous run-and-tumble motion accounts for transient non-Gaussian super-diffusion in haematopoietic multi-potent progenitor cells. *Plos One* 17, e0272587. doi:10.1371/journal.pone.0272587

Passucci, G., Brasch, M. E., Henderson, J. H., Zaburdaev, V., and Manning, M. L. (2019). Identifying the mechanism for superdiffusivity in mouse fibroblast motility. *Plos Comput. Biol.* 15, e1006732. doi:10.1371/journal.pcbi.1006732

Pollard, T. D. (2007). Regulation of actin filament assembly by Arp2/3 complex and formins. *Annu. Rev. Bioph. Biom.* 36, 451–477. doi:10.1146/annurev.biophys.35.040405.101936

Preston, T. M., and King, C. A. (1978). An experimental study of the interaction between the soil amoeba Naegleria gruberi and a glass substrate during amoeboid locomotion. *J. Cell Sci.* 34, 145–158. doi:10.1242/jcs.34.1.145

Prostak, S. M., Robinson, K. A., Titus, M. A., and Fritz-Laylin, L. K. (2021). The actin networks of chytrid fungi reveal evolutionary loss of cytoskeletal complexity in the fungal kingdom. *Curr. Biol.* 31, 1192–1205.e6. doi:10.1016/j.cub.2021.01.001

Reynolds, A. M. (2010). Can spontaneous cell movements be modelled as Lévy walks? *Phys. Stat. Mech. Appl.* 389, 273–277. doi:10.1016/j.physa.2009.09.027

Reynolds, A. M., and Ouellette, N. T. (2016). Swarm dynamics may give rise to Lévy flights. *Sci. Rep.* 6, 30515. doi:10.1038/srep30515

Rieu, J.-P., Delanoë-Ayari, H., Takagi, S., Tanaka, Y., and Nakagaki, T. (2015). Periodic traction in migrating large amoeba of Physarum polycephalum. *J. Roy. Soc. Interface* 12, 20150099. doi:10.1098/rsif.2015.0099

Rodiek, B., and Hauser, M. J. B. (2015). Migratory behaviour of Physarum polycephalum microplasmodia. *Eur. Phys. J. Spec. Top.* 224, 1199–1214. doi:10.1140/epjst/e2015-02455-2

Sadhu, R. K., Iglič, A., and Gov, N. S. (2023). A minimal cell model for lamellipodia-based cellular dynamics and migration. *J. Cell Sci.* 136, jcs260744. doi:10.1242/jcs.260744

Schwarz, G. (1978). Estimating the dimension of a model. *Ann. Stat.* 6. doi:10.1214/aos/1176344136

Sebé-Pedrós, A., Grau-Bové, X., Richards, T. A., and Ruiz-Trillo, I. (2014). Evolution and classification of myosins, a paneukaryotic whole-genome approach. *Genome Biol. Evol.* 6, 290–305. doi:10.1093/gbe/evu013

Selmeczi, D., Li, L., Pedersen, L. I. I., Nrrelykke, S. F., Hagedorn, P. H., Mosler, S., et al. (2008). Cell motility as random motion: a review. *Eur. Phys. J. Spec. Top.* 157, 1–15. doi:10.1140/epjst/e2008-00626-x

Selmeczi, D., Mosler, S., Hagedorn, P. H., Larsen, N. B., and Flyvbjerg, H. (2005). Cell motility as persistent random motion: theories from experiments. *Biophys. J.* 89, 912–931. doi:10.1529/biophysj.105.061150

Shaebani, M. R., Jose, R., Santen, L., Stankevicins, L., and Lautenschläger, F. (2020). Persistence-speed coupling enhances the search efficiency of migrating immune cells. *Phys. Rev. Lett.* 125, 268102. doi:10.1103/physrevlett.125.268102

Shaebani, M. R., Piel, M., and Lautenschläger, F. (2022). Distinct speed and direction memories of migrating dendritic cells diversify their search strategies. *Biophys. J.* 121, 4099–4108. doi:10.1016/j.bpj.2022.09.033

Stokes, C. L., Lauffenburger, D. A., and Williams, S. K. (1991). Migration of individual microvessel endothelial cells: stochastic model and parameter measurement. *J. Cell Sci.* 99, 419–430. doi:10.1242/jcs.99.2.419

Takagi, H., Sato, M. J., Yanagida, T., and Ueda, M. (2008). Functional analysis of spontaneous cell movement under different physiological conditions. *Plos One* 3, e2648. doi:10.1371/journal.pone.0002648

Taktikos, J., Stark, H., and Zaburdaev, V. (2013). How the motility pattern of bacteria affects their dispersal and chemotaxis. *Plos One* 8, e81936. doi:10.1371/journal.pone.0081936

Thong, Y. H., and Ferrante, A. (1986). Migration patterns of pathogenic and nonpathogenic Naegleria spp. *Infect. Immun.* 51, 177–180. doi:10.1128/IAI.51.1.177-180.1986

Tweedy, L., Meier, B., Stephan, J., Heinrich, D., and Endres, R. G. (2013). Distinct cell shapes determine accurate chemotaxis. *Sci. Rep.* 3, 2606. doi:10.1038/srep02606

Velle, K. B., and Fritz-Laylin, L. K. (2020). Conserved actin machinery drives microtubule-independent motility and phagocytosis in Naegleria. *J. Cell Biol.* 219, e202007158. doi:10.1083/jcb.202007158

Velle, K. B., and Fritz-Laylin, L. K. (2019). Diversity and evolution of actin-dependent phenotypes. *Curr. Opin. Genet. Dev.* 58, 40–48. doi:10.1016/j.gde.2019.07.016

Viswanathan, G. M., Buldyrev, S. V., Havlin, S., Luz, M. G. E. D., Raposo, E. P., and Stanley, H. E. (1999). Optimizing the success of random searches. *Nature* 401, 911–914. doi:10.1038/44831

Walsh, C. J. (2007). The role of actin, actomyosin and microtubules in defining cell shape during the differentiation of Naegleria amebae into flagellates. *Eur. J. Cell Biol.* 86, 85–98. doi:10.1016/j.ejcb.2006.10.003

Welf, E. S., Ahmed, S., Johnson, H. E., Melvin, A. T., and Haugh, J. M. (2012). Migrating fibroblasts reorient directionality by a metastable, PI3K-dependent mechanism. *J. Cell Biol.* 197, 105–114. doi:10.1083/jcb.201108152

Xu, X., Wen, X., Veltman, D. M., Keizer-Gunnink, I., Pots, H., Kortholt, A., et al. (2017). GPCR-controlled membrane recruitment of negative regulator C2GAP1 locally inhibits Ras signaling for adaptation and long-range chemotaxis. *Proc. Natl. Acad. Sci. U. S. A.* 114, E10092–E10101. doi:10.1073/pnas.1703208114

frontiers | Frontiers in Cell and Developmental Biology

TYPE Original Research
PUBLISHED 02 November 2023
DOI 10.3389/fcell.2023.1136537

OPEN ACCESS

EDITED BY
Takuji Ishikawa,
Tohoku University, Japan

REVIEWED BY
Kyosuke Shinohara,
Tokyo University of Agriculture and Technology, Japan
Toshihiro Omori,
Tohoku University, Japan

*CORRESPONDENCE
Manabu Yoshida,
yoshida@mmbs.s.u-tokyo.ac.jp

†PRESENT ADDRESS
Satoe Aratake, Department of Urology, St Marianna University School of Medicine, Kawasaki, Japan

RECEIVED 03 January 2023
ACCEPTED 03 October 2023
PUBLISHED 02 November 2023

CITATION
Kijima T, Kurokawa D, Sasakura Y, Ogasawara M, Aratake S, Yoshida K and Yoshida M (2023), CatSper mediates not only chemotactic behavior but also the motility of ascidian sperm.
Front. Cell Dev. Biol. 11:1136537.
doi: 10.3389/fcell.2023.1136537

CatSper mediates not only chemotactic behavior but also the motility of ascidian sperm

Taiga Kijima[1], Daisuke Kurokawa[1], Yasunori Sasakura[2], Michio Ogasawara[3], Satoe Aratake[1†], Kaoru Yoshida[4] and Manabu Yoshida[1*]

[1]Misaki Marine Biological Station, School of Science, The University of Tokyo, Miura, Kanagawa, Japan, [2]Shimoda Marine Research Center, University of Tsukuba, Shimoda, Japan, [3]Department of Biology, Graduate School of Science, Chiba University, Chiba, Japan, [4]Faculty of Biomedical Engineering, Toin University of Yokohama, Yokohama, Kanagawa, Japan

Introduction: Sperm motility, including chemotactic behavior, is regulated by changes in the intracellular Ca^{2+} concentration, and the sperm-specific Ca^{2+} channel CatSper has been shown to play an important role in the regulation of intracellular Ca^{2+}. In particular, in mammals, CatSper is the only functional Ca^{2+} channel in the sperm, and mice deficient in the genes comprising the pore region of the Ca^{2+} channel are infertile due to the inhibition of sperm hyperactivation. CatSper is also thought to be involved in sea urchin chemotaxis. In contrast, in ascidian *Ciona intestinalis*, SAAF, a sperm attractant, interacts with Ca^{2+}/ATPase, a Ca^{2+} pump. Although the existence of *CatSper* genes has been reported, it is not clear whether CatSper is a functional Ca^{2+} channel in sperm.

Results: We showed that CatSper is present in the sperm flagella of *C. intestinalis* as in mammalian species, although a small level of gene expression was found in other tissues. The spermatozoa of *CatSper3* KO animals were significantly less motile, and some motile sperms did not show any chemotactic behavior. These results suggest that CatSper plays an important role in ascidians and mammals, and is involved in spermatogenesis and basic motility mechanisms.

KEYWORDS

sperm motility, chemotaxis, Ca^{2+} channel, CatSper, spermatogenesis, CRISPR/Cas9, *Ciona intestinalis*

1 Introduction

The regulation of sperm motility, including chemotactic behavior, is a well-organized single-cell behavior in complex field environments, and Ca^{2+} is indispensable for controlling sperm behavior (Yoshida and Yoshida, 2011; Yoshida and Yoshida, 2018). In particular, Ca^{2+} regulates flagellar beating patterns (Brokaw et al., 1974; Brokaw, 1979) and the direction of sperm swimming (Shiba et al., 2008). The concentration of intracellular Ca^{2+} ($[Ca^{2+}]_i$) is regulated by Ca^{2+} influx via Ca^{2+} channels and Ca^{2+} efflux driven by Ca^{2+} exchangers or Ca^{2+} pumps; thus, both Ca^{2+} channels and Ca^{2+} pumps play a role in sperm function.

In ascidians, an increase in $[Ca^{2+}]_i$ is also involved in sperm motility and chemotactic behavior toward the egg (Yoshida et al., 1994; Yoshida et al., 2003; Shiba et al., 2008). The sulfate-conjugated hydroxysteroid, SAAF, acts as a sperm activator and attractant in ascidians (Yoshida et al., 2002; Oishi et al., 2004). Spermatozoa with chemotactic behavior undergo transient increases in $[Ca^{2+}]_i$ in the flagellum (Ca^{2+} bursts) when the

concentration of SAAF decreases to a maximum, forming an asymmetric flagellar waveform of the sperm and inducing a series of sperm movements, including turning and straight swimming (Yoshida et al., 2003; Shiba et al., 2008; Miyashiro et al., 2015). The regulation of $[Ca^{2+}]_i$ is mainly carried out by SAAF, which controls the Ca^{2+} efflux, and SAAF binds to and activates Ca^{2+}/ATPase on the sperm plasma membrane (PMCA), thus causing Ca^{2+} efflux (Yoshida et al., 2018). However, the molecules involved in Ca^{2+} influx remain unknown, although the involvement of store-operated Ca^{2+} channels has been suggested pharmacologically (Yoshida et al., 2003).

Among many Ca^{2+}-regulating systems, the Ca^{2+} channel on the plasma membrane is an important player in Ca^{2+} influx. In mammalian sperm, CatSper, which is a sperm-specific Ca^{2+} channel, plays a crucial role in the regulation of sperm function. CatSper is homologous to a voltage-gated Ca^{2+} channel (Ren et al., 2001) and consists of four pore-forming subunits (CatSper 1, 2, 3, and 4) (Qi et al., 2007; Lishko et al., 2012; Bystroff, 2018) and several auxiliary subunits (CatSper β, γ, δ, ε, ζ, η, and EFCAB9) (Liu et al., 2007; Chung et al., 2011; Chung et al., 2017; Hwang et al., 2019). CatSper is located in the sperm flagella and mediates hyperactivation (Quill et al., 2001; Ren et al., 2001; Carlson et al., 2003; Qi et al., 2007). Furthermore, CatSper seems to be the only functional Ca^{2+} channel in mammalian sperm (Zeng et al., 2013); thus, CatSper is implicated in not only mediating hyperactivation but also flagellar beating and swimming patterns.

In contrast to its crucial role in mammals, CatSper is absent in many animals, including birds, amphibians, and teleostean fishes (Cai and Clapham, 2008). Furthermore, the expression and function of CatSper proteins in animals other than mammals have been poorly investigated, although CatSper appears to regulate sperm chemotaxis in sea urchins (Seifert et al., 2015). In the genome database of the ascidian *Ciona intestinalis*, all CatSper pore-forming isoforms (CatSper 1–4) are present, similar to mammals (Cai and Clapham, 2008).

Because CatSper is a complex protein with many subunits, it has not been successfully expressed functionally in cultured cells (Chung et al., 2017). There is only one study in which the voltage sensor domain of CatSper3 was expressed in HEK293T cells and *Xenopus* oocytes (Arima et al., 2018). Therefore, functional analyses of CatSper have been performed using spermatozoa from genetically deficient animals, and until now, most studies have been conducted using mice. Thus, we examined the role of CatSper in ascidians to identify the effectors of Ca^{2+} influx during sperm chemotaxis. Interestingly, CatSper expression in the ascidian was not restricted to the sperm flagellum but was also observed in other cells. Furthermore, we developed the *CatSper3*-deficient ascidian using the CRISPR/Cas9 system and found that CatSper is an indispensable Ca^{2+} channel in ascidian sperm. However, it plays a role not only in sperm chemotaxis but also in fundamental sperm motility.

2 Materials and methods

2.1 Materials

The ascidian *C. intestinalis* (type A; also called *Ciona robusta*) was obtained from the National BioResource Project for *Ciona* (http://marinebio.nbrp.jp/). Ascidian sperm were obtained as previously described (Yoshida et al., 1993). Artificial seawater (ASW) contained 462 mM NaCl, 9 mM KCl, 10 mM $CaCl_2$, 48 mM $MgCl_2$, and 10 mM HEPES-NaOH (pH 8.2). SAAF and its derivatives were synthesized, as described previously (Oishi et al., 2003; Oishi et al., 2004). Juveniles were developed by artificial insemination using mature eggs and sperm obtained from the dissected gonoducts. Whole-mount juveniles and dissected adult specimens were prepared for *in situ* hybridization, as described by Nakayama and Ogasawara (2017).

2.2 RNA isolation and cDNA synthesis

Tissue samples were collected from the testes, ovaries, muscles, gills, and hearts of adult individuals (n = 5) of *C. intestinalis*. Whole juveniles 1 week (100 individuals), 3 weeks (30 individuals), and 4 weeks (15 individuals) after fertilization were used in one batch (n = 3). Total RNA was extracted from each specimen using an RNeasy Plant Mini Kit (QIAGEN, Hilden, Germany), according to the manufacturer's instructions. The total RNA concentration was determined using the Qubit RNA HS Assay (Thermo Fisher Scientific, Waltham, MA, United States). RNA quality was analyzed using a Bioanalyzer 2000 system (Agilent, Santa Clara, CA, United States) with an RNA 6000 Nano Kit (Agilent). The results of the RNA quality check are shown in Supplementary Material (Supplementary Figure S2). According to the MIQE guidelines, only RNA samples with an RIN value of eight or higher were used for qPCR analysis. Total RNA (150 ng) was reverse-transcribed to cDNA using oligo $d(T)_{20}$ primers or random hexamers and the SuperScript IV First-Strand Synthesis System Kit (Thermo Fisher Scientific), according to the manufacturer's instructions. Individually synthesized cDNA using oligo $d(T)_{20}$ primers and random hexamers was combined and used for quantitative real-time polymerase chain reaction (qRT-PCR) analyses.

2.3 Quantitative real-time PCR (qRT-PCR)

Equal amounts of cDNA from each tissue sample were used for the qRT-PCR analysis. Quantitative polymerase chain reactions were performed using the PowerUp SYBR Green Master Mix (Thermo Fisher Scientific), according to the manufacturer's instructions. Briefly, 1 µL of cDNA was used in a final volume of 20 µL, containing 10 µL of PowerUp SYBR Green Master Mix and 500 nM of each primer for *CatSper1*, *CatSper2*, *CatSper3*, *CatSper4*, and *GAPDH*. Predicted *CatSper* and *GAPDH* genes were identified from the genome database of *C. intestinalis* type A (*C. robusta*) (Ghost: http://ghost.zool.kyoto-u.ac.jp/default_ht.html) (Satou et al., 2022). The gene IDs are as follows: *CatSper1*, KH.C10.377; *CatSper2*, KH.S391.7; *CatSper3*, KH. C2.323; and *CatSper4*, KH.C2.993. Real-time PCR was performed using a StepOnePlus Real-Time PCR System (Thermo Fisher Scientific), and 40 PCR cycles were performed. Prior to the cycling and DNA denaturation steps,

polymerase activation was achieved at 95°C for 20 s. The cycling conditions consisted of denaturation at 95°C for 3 s, annealing and extension at 60°C for 30 s, and plate reading at 50°C for 2 min. A melt-curve analysis of 15 s at 95°C and 1 min at 60°C, increasing 0.2°C per second to 95°C, was performed at the end. qPCR data were analyzed using StepOne software for calculating Cp values, and the standard curve method was used to determine the expression of *CatSper1*, *CatSper2*, *CatSper3*, and *CatSper4* relative to *GAPDH*, which was used as a housekeeping gene. The primers used for qPCR are listed in Supplementary Table S1.

2.4 Whole-mount *in situ* hybridization

Digoxigenin-labeled antisense RNA probes for the *Ciona* CatSper genes were synthesized from T7-RNA polymerase promoter-attached amplified cDNA, and the probes were purified by centrifugal ultrafiltration, as previously described by Ogasawara et al. (2001). Whole-mount *in situ* hybridization (WISH) of the *Ciona* specimens was performed using "*InSitu* Chip," as described by Ogasawara et al. (2006). Gene expression signals were visualized using nitroblue tetrazolium/5-bromo-4-chloro-3-indolylphosphate (NBT/BCIP) solutions using a standard method (Thermo Fisher Scientific). Whole-mount and sectioned specimens of *Ciona* were observed using an SZX12 stereomicroscope (Olympus, Tokyo, Japan).

2.5 Gene knockdown by the CRISPR/Cas9 system

The CRISPR/Cas9 method (Cong et al., 2013; Hwang et al., 2013) was used for genome editing in *C. intestinalis*, as previously described by Sasaki et al. (2014). We designed target sequences of gRNA that are specific for *CatSper3* as 5′-CGAAAGCGAAGT TTTTAATGGTCT-3′ at exon 5 using ZiFiT (http://zifit.partners.org/ZiFiT) (Sander et al., 2007; Sander et al., 2010). The target DNAs were inserted into the BsaI site of pDR274 (Addgene; Hwang et al., 2013) as vectors for the *in vitro* transcription of gRNAs. The Cas9 gene, a gift from George Church (hCas9) (Addgene plasmid #41815; http://n2t.net/addgene:41815; RRID:Addgene_41815) (Mali et al., 2013), was sub-cloned into pCS2+ as a vector for *in vitro* transcription of mRNAs. Cas9 gRNAs and mRNAs were synthesized using the MEGAshortscript T7 and MEGAshortscript SP6 Transcription Kits (Thermo Fisher Scientific), respectively.

We injected approximately 30–100 pL of the RNA solution containing 400 ng/μL gRNA, 800 ng/μL Cas9 mRNA, and 10% phenol red into unfertilized eggs, and reared embryos and animals in aquariums.

We extracted DNA from juveniles or muscles of adults and performed PCR to check the genome editing efficiency using the heteroduplex mobility assay (Ota et al., 2013). The primers used for PCR are 5′-TTGACTGCTCTCATAGACACGATG-3′ and 5′-TTA CCGTAACGAAGCTGAAGAGC-3′. After purifying the PCR bands by electrophoresis, the products were sub-cloned into pGEM-T Easy (Promega, Madison, WI, United States) for sequencing analysis using a Genetic Analyzer (ABI 3130, Applied Biosystems).

2.6 Histochemistry

The testes were dissected and fixed in Bouin's fixative consisting of 71.4% saturated picric acid, 23.8% formalin, and 4.7% acetic acid for 2 h at room temperature. The tissues were embedded in paraffin and cut into 4-μm-thick sections. Some sections were stained with hematoxylin and eosin for morphological observation and made into permanent specimens.

2.7 Western blotting

Samples were directly solubilized in the NuPAGE LDS sample buffer (Thermo Fisher Scientific). The solubilized samples were treated with benzonase (Novagen, Billerica, MA, United States). Proteins were separated on a NuPAGE SDS-PAGE Gel System using 4%–12% Bis–Tris gels (Thermo Fisher Scientific) and transferred onto PVDF membranes. The anti-CatSper3 antibody (ab197924; Abcam, Cambridge, UK), horseradish peroxidase (HRP)-conjugated anti-rabbit IgG (GE Healthcare), and ECL Prime (GE Healthcare) were used to detect CatSper. Luminescence was imaged using a C-DiGit Blot Scanner (LI-COR Biosciences, Lincoln, NE, United States). Images were processed using Adobe Photoshop and Adobe Illustrator (Adobe, San Jose, CA, United States).

2.8 Indirect immunofluorescence

Sperm suspension was put onto a coverslip, fixed with 4% paraformaldehyde for 10 min, and washed twice with ASW for 5 min. To visualize, the sperm suspension was incubated with 1 μM MitoBright IM Red (Dojindo, Kumamoto, Japan) for 30 min before fixation. The fixed sperms were permeabilized with 0.1% NP-40 for 15 min, blocked with 1% BSA for 1 h, and incubated with 0.6 μg/mL anti-α tubulin monochronal antibody (#236-10501: Invitrogen) or 4.3 μg/mL anti-CatSper3 antibody (ab197924, Abcam) with 1% BSA in PBS for 1 h. Sperms were washed three times with PBS and incubated with x1/2000 Alexa 488-conjugated anti-rabbit IgG (ab150077, Abcam) or x1/2000 Alexa 568-conjugated anti-mouse IgG (ab175473, Abcam) for 1 h. After washing twice with PBS, the stained sperms were mounted with ProLong Glass Antifade Mountant with NucBlue Stain (Thermo Fisher Scientific) and observed by confocal laser-scanning microscopy (FV3000; Olympus, Tokyo, Japan). For control experiments, the samples were stained only with Alexa 488-conjugated anti-rabbit IgG.

2.9 Analysis of sperm motility and chemotaxis

Sperm chemotaxis was examined, as previously described by Shiba et al. (2008). Briefly, semen was diluted 10^4–10^5 times in ASW with 1 mM theophylline (Sigma-Aldrich, Tokyo, Japan) to

activate motility (Yoshida et al., 1994). The activated sperm suspension was placed in the observation chamber, and the sperm movement around the micropipette tip containing SAAF was recorded. The position of the sperm head was analyzed using Bohboh (BohbohSoft, Tokyo, Japan) (Shiba et al., 2002). The motility and chemotactic activity parameters (trajectory, distance between the capillary tip and sperm, and linear-equation-based chemotaxis index (LECI)) were calculated, as previously described by Yoshida et al. (2002). LECI is an index of the slope of a linear approximation of the time course of the distance between the sperm head and the attraction source, which indicates the average speed at which the sperms approach the attraction source (Yoshida et al., 2002).

2.10 Statistical analysis

All experiments were repeated at least three times for different specimens. Data are expressed as mean ± SD. Statistical significance in Figure 1 was calculated using Tukey's test; $p < 0.05$ was considered significant. Statistical significance in Figures 6, 8 was calculated using the Student's t-test; $p < 0.01$ was considered significant. Tukey's analyses were performed using EZR (Saitama Medical Center, Jichi Medical University, Saitama, Japan), a graphical user interface for R (The R Foundation for Statistical Computing, Vienna, Austria).

3 Results

3.1 CatSper expression in the ascidian

Initially, we examined CatSper expression in the ascidian *C. intestinalis* using RT-PCR. In adults, all *CatSper* subtypes (*CatSper1*, *2*, *3*, and *4*) were mainly expressed in the testis, but weak expression was also observed in other organs: the ovary, heart, gill, and muscle (Figure 1). Although the expression levels of *CatSper* genes in organs other than the testes varied because quantities of mRNA were

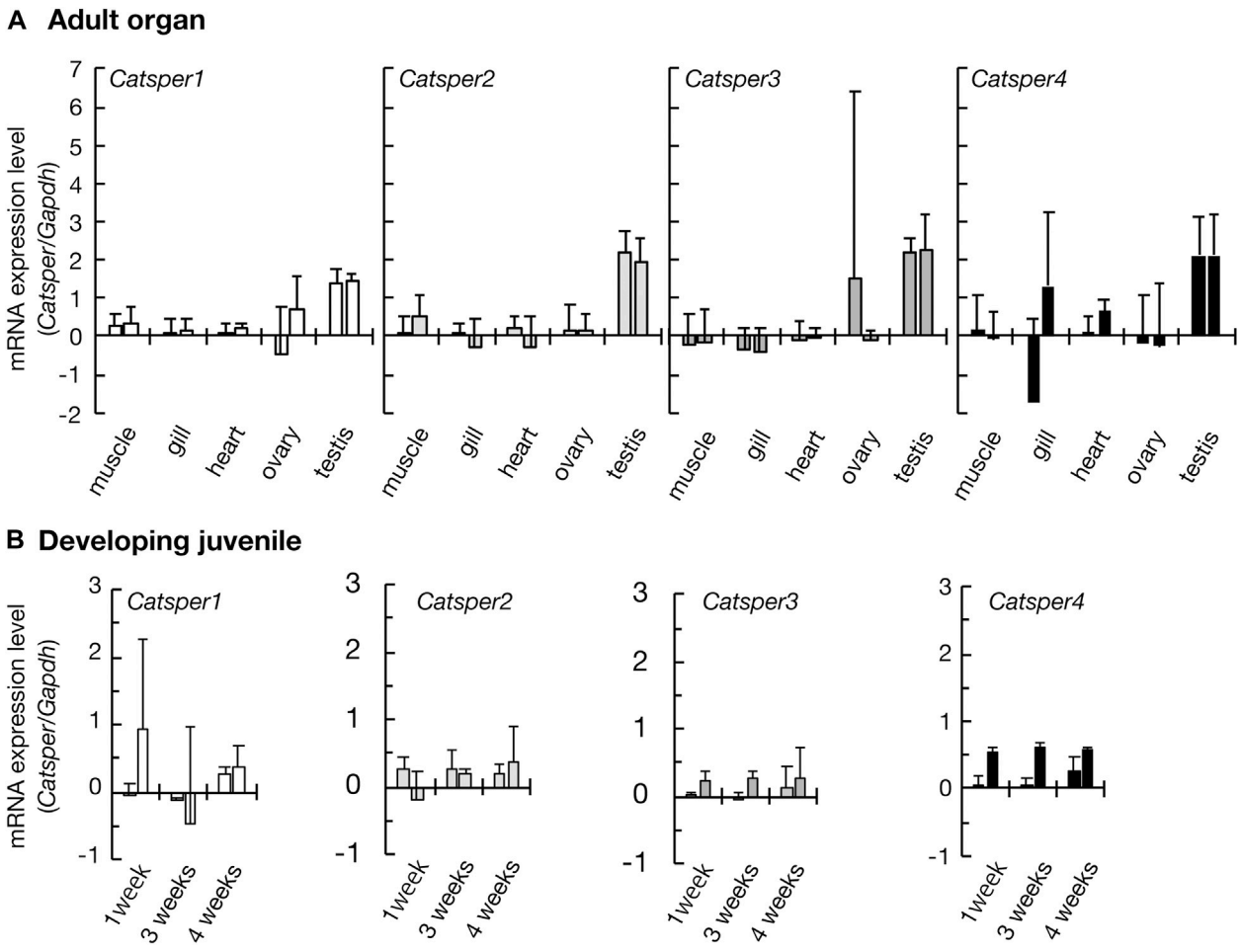

FIGURE 1
Expression of *CatSper* genes in the ascidian *C. intestinalis*. Gene expression was examined by quantitative real-time PCR. **(A)** Gene expression in the adult organs. **(B)** Gene expression in the developing juveniles. Two different primer pairs were used for the quantification of each gene (see Supplementary Table S1). Gene expression levels were normalized to the household gene glyceraldehyde-3-phosphate dehydrogenase (*GAPDH*). Values are expressed as mean ± S.D. (n = 3–5). There is a significant difference between the testis and some other organs (Tukey's HSD-test: $*p < 0.05$). All raw data on qPCR are shown in Supplementary Figure S3 in Supplementary Material.

10.3389/fcell.2023.1136537

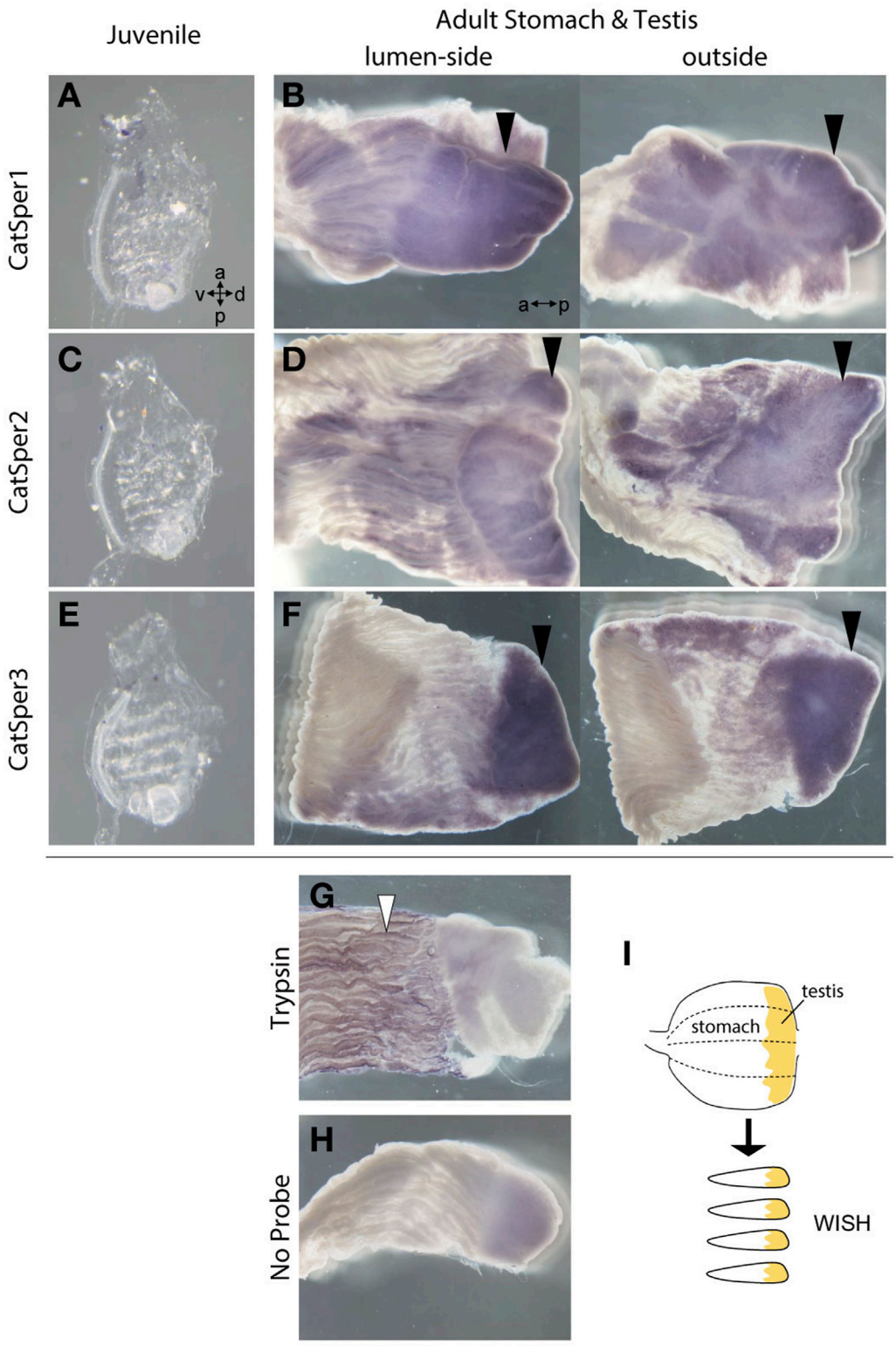

FIGURE 2
The WISH method was used to analyze the expression of *CatSper1*, *CatSper2*, and *CatSper3* in the ascidian juveniles and adult stomach with testis. **(A, B)** Typical expression of *CatSper1* in the juvenile **(A)** and the adult stomach with testis **(B)**. **(C, D)** Typical expression of *CatSper2* in the juvenile **(C)** and the adult stomach with testis **(D)**. **(E, F)** Typical expression of *CatSper3* in the juvenile **(E)** and the adult stomach with testis **(F)**. None of the *CatSper* subtypes were expressed in juveniles but only in adult testes (black arrowhead). a, anterior side; p, posterior side; v, ventral side; d, dorsal side. **(G, H)** Control of WISH: the probe of *trypsin-like* (XP_002126930.1) for positive control **(G)** and no probe for negative control **(H)**. Positive signal is denoted by a white arrowhead. **(I)** Schematic drawing of stomach preparations.

adjusted to the heart in the qPCR process, which has the lowest amount of obtained total RNA, in most cases, the expression levels in the testes were still significantly higher than those in the other organs. In contrast, for the *CatSper4* gene, no significant differences in expression levels between the heart and testes were observed for either of the two primer sets used. The expression of *CatSper* genes in organs other than the testes was also confirmed using semi-quantitative RT-PCR (Supplementary Figure S1). When the expression of *CatSper* was examined in developmental juveniles, all *CatSper* genes were expressed in juveniles aged 1–4 weeks, although the expression was weak (Figure 1, Supplementary Figure S1). The 1- and 2.5-week-old juveniles were still immature, and their testes had not developed at this stage (Okada and Yamamoto, 1999). Thus, the expression of *CatSper* in ascidians is not restricted to the testis. On the other hand, using WISH, the expression of *CatSper* was observed in adult testis but not detected in juveniles (Figure 2). These results indicate that ascidian *CatSper* genes are mainly expressed in the testis, similar to those of mammalian species, but are weakly expressed in places other than the testis.

3.2 CatSper3 was localized around the ascidian sperm flagella

Next, we examined the presence of CatSper proteins. As previously described, the ascidian *CatSper* genes were mainly expressed in the testis but were also weakly expressed in the heart, muscles, and gills. Therefore, we examined whether CatSper proteins were seen in these tissues. In mammals, CatSper proteins were seen only in sperm flagella. In ascidians, Western blotting with an anti-human CatSper3 antibody in each ascidian tissue showed that a band of 50 kDa, the molecular weight of the CatSper3 protein, existed only in the sperm (Figure 3A). Precise observation by immunocytochemistry showed that CatSper3 was localized in the flagella, similar to that in mammalian sperm (Figure 4). Staining with the anti-CatSper3 antibody was also observed in the head region, where mitochondria were located; however, the difference from the control experiment was unclear (Figure 4B), and its presence could not be concluded.

3.3 CatSper3-knockout animals delay their development

To examine the function of the CatSper channel in ascidian sperm, we tried to produce the *CatSper*-deficient ascidian using the CRISPR/Cas9 system. We selected exon 5 of *CatSper3* as the target gene of the CRISPR/Cas9 system (Figure 5A) because we could not find an effective target site for the other ascidian *CatSper* genes. The mutation frequency on the *CatSper3* gene using the CRISPR/Cas9 system was 94.7% (n = 38) when checked at the juvenile stage.

Unfortunately, F_0 animals in which the *CatSper3* gene was edited by the CRISPR/Cas9 system (CatSper3 KO animals) tended to die when their tadpole larvae settled and metamorphosed into juveniles. Furthermore, the growth rate of *CatSper3* KO animals was much slower than that of the control; the body size of the two-month-old individuals was significantly smaller than that of the wildtype animals (Figure 6). Finally, we obtained nine KO animals that

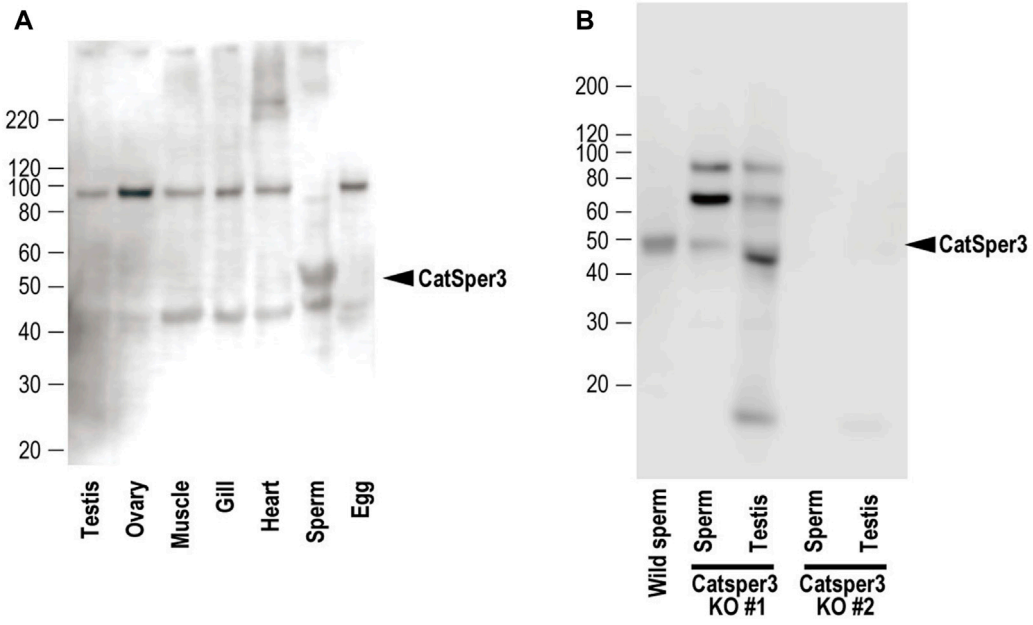

FIGURE 3
Representative results of Western blotting with the anti-CatSper3 antibody of **(A)** each tissue of mature adults, and **(B)** sperm and testis from the two *CatSper3* KO animals. The ascidian CatSper3 protein showed a 50-kDa band (arrowhead), whereas the predicted size from the deduced amino acid sequence is 49809 Da. Control data (without the anti-CatSper3 antibody) on the Western blotting are shown in Supplementary Figure S4 in Supplementary Material.

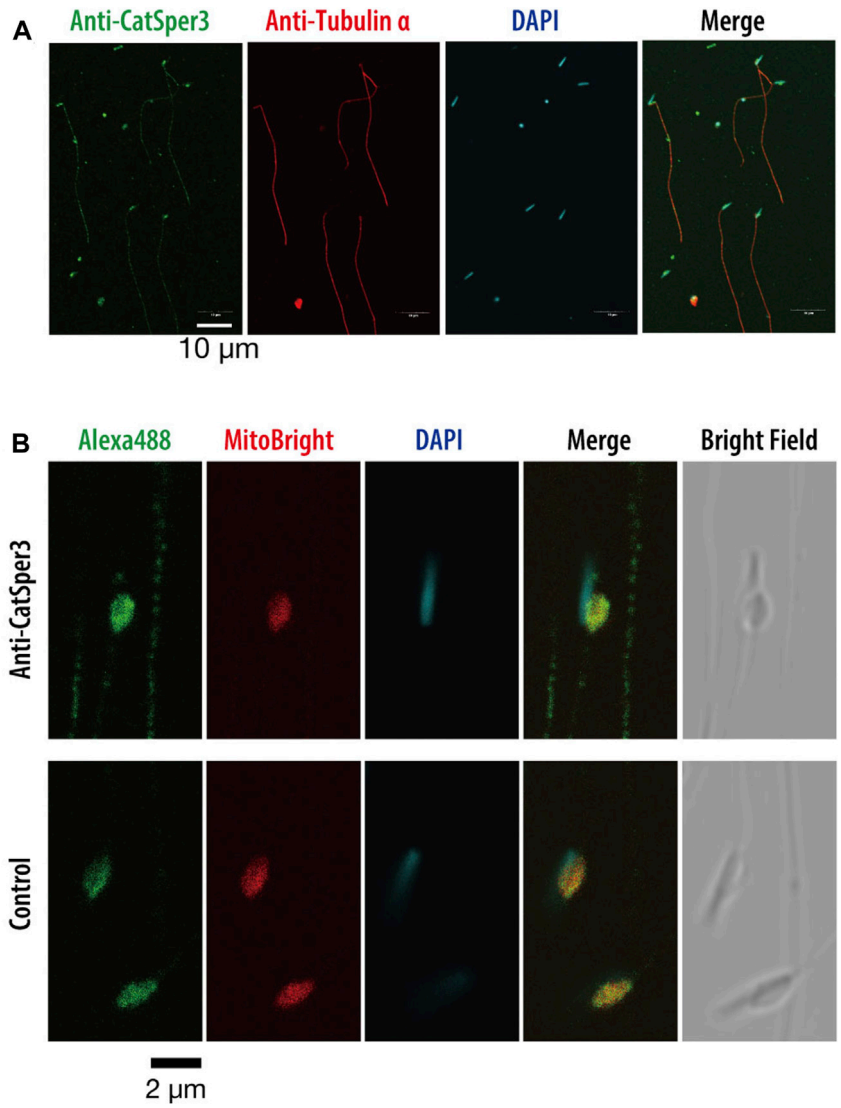

FIGURE 4
Indirect immunofluorescence assay with the anti-CatSper3 antibody in the ascidian sperm. **(A)** Nuclei of the sperm are shown with DAPI staining, and flagella are shown with anti-tubulin antibody staining. Scale bar = 10 μm. **(B)** Enlarged view of the head area. The nucleus and mitochondrion of the sperm were stained with DAPI and MitoBright IM Red, respectively. Control experiments were stained without a primary antibody (lower row). Scale bar = 2 μm.

reached the mature reproductive stage (Figure 5B). Because gametes from the KO animals could not be fertilized, we used the KO animals for the following analyses.

3.4 Spermatogenesis of the CatSper3-knockout animals

In the sperm obtained from CatSper3 KO animals, the 50-kDa CatSper3 protein was reduced or completely lost (Figure 3B). The antibody-reacted band in the Western blotting was seen at 90 kDa and 70 kDa, which was higher than the wildtype CatSper3 protein, and 42 kDa, which was lower than the wildtype CatSper3 protein in some KO sperms and testes (Figure 3B).

The testes of CatSper3 KO animals were smaller than those of wildtype animals at the same age, which was consistent with the poor development of the individuals. Spermatogenesis appeared to occur normally in the KO animals (Figures 7B, D), which yielded mature spermatozoa whose shape appeared normal. However, spermatozoa from KO animals were fragile; headless or broken-flagellar spermatozoa were often observed by microscopy (Figure 7F).

3.5 Sperm motility and chemotactic behavior of the CatSper3-knockdown animals

The sperm appeared normal in shape, but many of the sperms had no motility, even in the presence of theophylline, which is an activating agent for ascidian sperm motility (Figure 8, Supplementary Movies S1, S2). A few

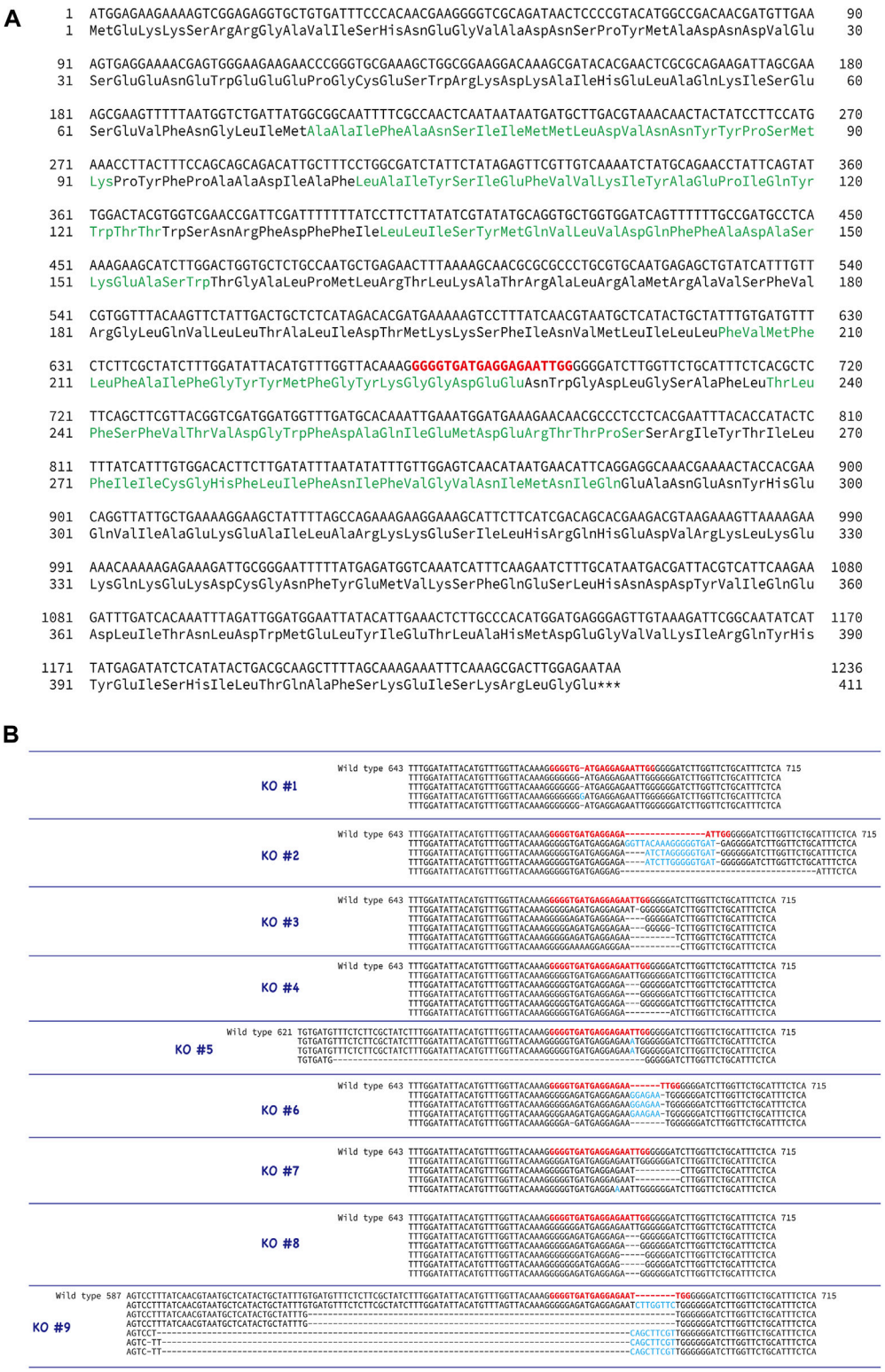

FIGURE 5
Generation of *CatSper3* KO ascidians. **(A)** DNA and amino acid sequences of *CatSper3*. Target sequence for the CRISPR/Cas9 system is shown in red bold letters. **(B)** Representative DNA sequences around the target sequence of the *CatSper3* KO ascidians with the CRISPR/Cas9 system. The DNA sequence of the un-muted wildtype *CatSper3* is shown in the upper row (wildtype). Bold red letters show the target sequence for the CRISPR/Cas9 system. Deleted and inserted nucleotides are denoted by dashes and blue letters, respectively.

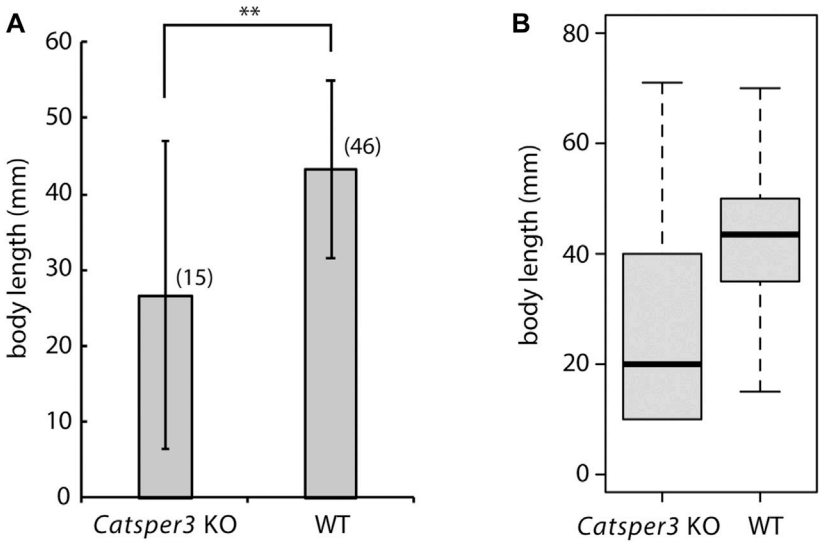

FIGURE 6
Average **(A)** and box plot **(B)** of body sizes of the *CatSper3* KO and wildtype (WT) animals. The examined KO and WT animals are 60–74 days old and 47–75 days old, respectively. Values are expressed as mean ± S.D. The number in the parenthesis represents the number of examined animals. There is a significant difference between wildtype and KO animals (Student's *t*-test: $^{**}p < 0.01$).

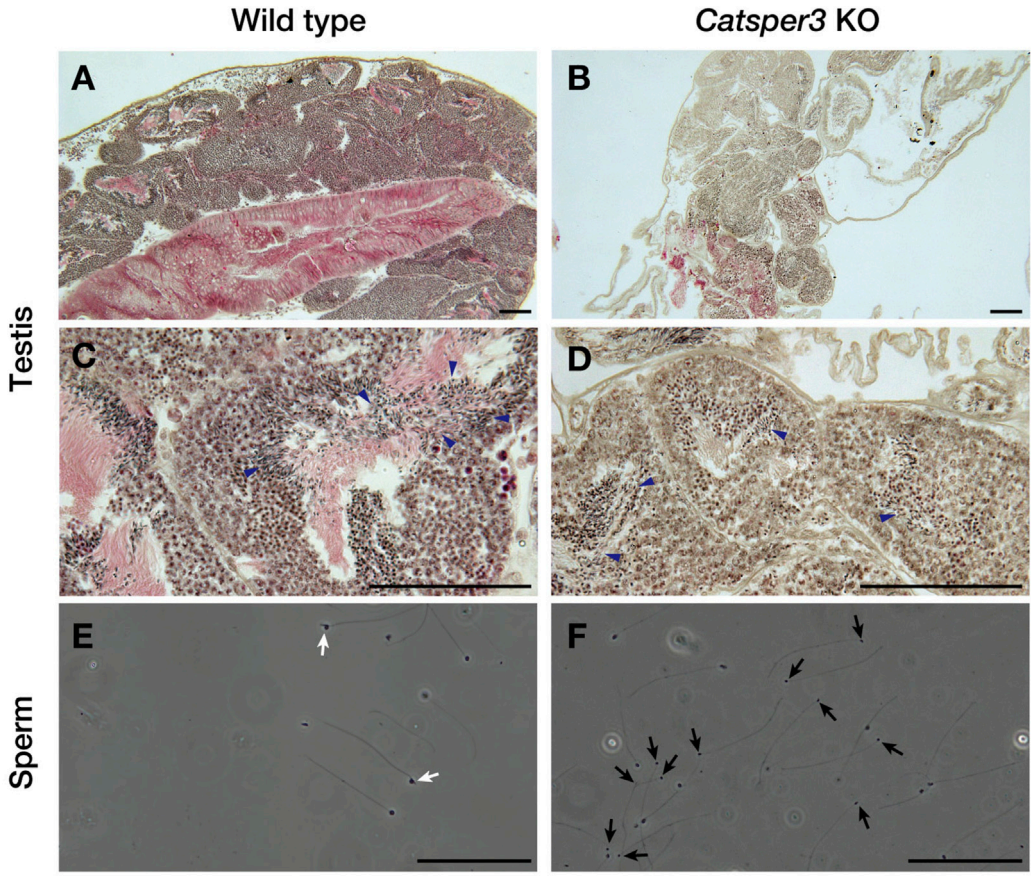

FIGURE 7
Histological assessment of testes and sperm of the *CatSper3* KO ascidians. **(A–D)** Lower **(A, B)** and higher **(C, D)** magnification of testicular sections stained with hematoxylin and eosin taken from the wildtype **(A, C)** and *CatSper3* KO **(B, D)** ascidians. Arrowheads denote sperm produced in the testis. **(E, F)** Spermatozoa obtained from the spermiduct of the wildtype **(E)** and *CatSper3* KO **(F)** ascidians. Some sperm of the KO animal lost head or have broken flagella (black arrows). The typical head of the wildtype sperm is indicated by white arrows. Scale bar = 50 μm.

10.3389/fcell.2023.1136537

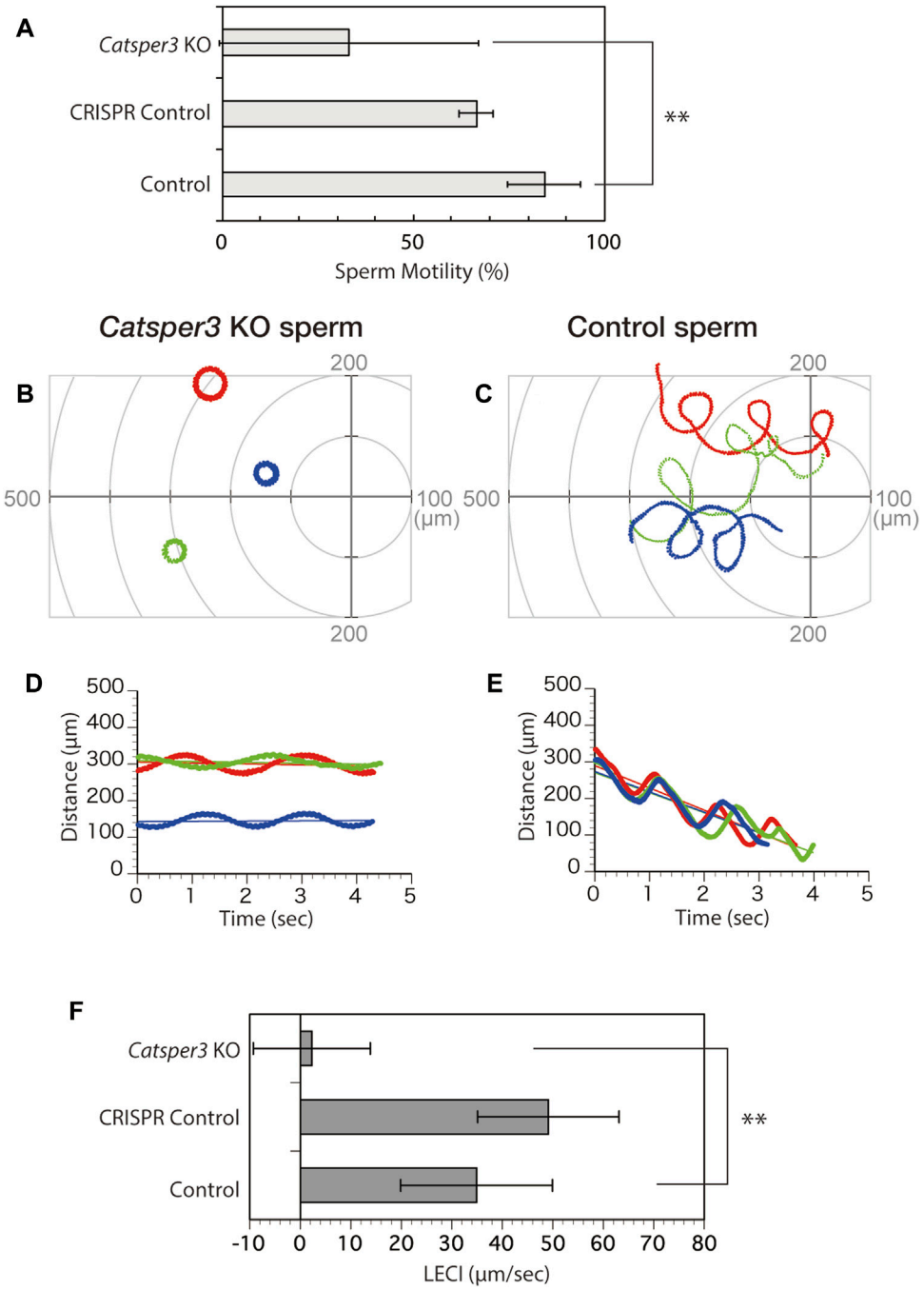

FIGURE 8
Chemotactic behavior of the CatSper3-knockout sperm. **(A)** Rate of *CatSper3* KO and wildtype spermatozoa with forward motility. *CatSper3* KO, five individuals; control, four individuals. CRISPR control comprises the data on sperm from an animal that was injected with Cas9 and gRNA but did not show any genetic mutation (one individual). Values are expressed as mean ± S.D. Statistical significance was shown with $^{**}p < 0.01$ (Student's *t*-test). **(B, C)** Typical three sperm trajectories of *CatSper3* KO **(B)** and wildtype **(C)** animals suspended in seawater around the tip of a capillary containing 5 μM SAAF. The origin of the coordinates indicates the capillary tip. **(D, E)** Changes in the distance between the capillary tip and the head of the swimming sperm of *CatSper3* KO **(D)** and wildtype **(E)** animals shown in **(B)** and **(C)**, respectively. The colors shown in **(B)** and **(C)**, and that shown in **(D)** and **(E)** represent the same sperm. The lines represent the linear equation of time vs. distance. The chemotaxis index (LECI) is calculated as negative values of the coefficients in the equation. **(F)** Chemotaxis indexes of sperm. *CatSper3* KO, $n = 32$ from five individuals; control, $n = 12$ from four individuals. CRISPR control, $n = 8$ from one individual. Values are expressed as mean ± S.D. Statistical significance is shown with $^{**}p < 0.01$ (Student's *t*-test).

spermatozoa showed forward motility, and those seemed to have a large lateral amplitude of the head (Supplementary Movie S2, Figure 8), similar to sperm movement in the presence of a PMCA inhibitor (Yoshida et al., 2018). None of the spermatozoa exhibited chemotactic responses (Figure 8).

4 Discussion

In the 20 years since the discovery of CatSper as a sperm-specific Ca^{2+} channel (Ren et al., 2001), several studies have shown that CatSper is the only important functional Ca^{2+} channel in mammalian sperm (Lishko and Mannowetz, 2018). CatSper is localized at linear quadrilateral nanodomains along the flagellum in the mammalian sperm, and it mediates rheotactic behavior in the female reproductive tract (Chung et al., 2014; Chung et al., 2017). However, many animals, including birds and amphibians, lack the CatSper genes (Cai and Clapham, 2008), and it is not known whether CatSper has the same functions in the sperm of animals other than mammals, although only in the sea urchin does CatSper seem to mediate chemotactic behavior according to pharmacological studies (Rennhack et al., 2018). The ascidian *C. intestinalis* is a chordate and has four CatSper isoforms (CatSper 1–4), as in mammals. Interestingly, CatSper does not seem to be restricted to sperm, and our study shows that ascidian CatSper expression was not restricted to the testis but was also observed in the heart, gills, ovary, and muscles, even though normal CatSper protein was only observed in sperm. CatSper in ascidian sperm appeared to be localized in the flagellum, similar to that in mammalian sperm (Figure 4). Furthermore, most *CatSper3*-KO ascidians died within a month because of stunted growth, and the body size of mature *CatSper3*-KO ascidians was significantly small. These data suggest that CatSper plays a role in development and/or nutrient uptake. Although the expression area of CatSper3 in organs other than the testes has not been examined, the cilia seemed to be immunoreactive to the anti-CatSper3 antibody. Thus, CatSper might be expressed in the cilia and flagella, not only in the sperm but also in the whole body, and play some role in the movement of the cilia/flagella.

The shape of the sperm obtained from the *CatSper3*-KO ascidians was almost normal, but they were fragile; the head was easily disconnected from the flagellum (Figure 7). Furthermore, the spermatozoa were almost quiescent and never activated by any stimulation. Some sperm were motile but did not show chemotactic behavior. In the mouse, there are no morphological differences between the wildtype and the *CatSper*-KO sperm in any subunits (Ren et al., 2001; Quill et al., 2003; Liu et al., 2007; Qi et al., 2007; Chung et al., 2011; Chung et al., 2017; Hwang et al., 2019). In contrast, spermatogenesis in the *CatSper3*-KO male individual did not appear to differ from that in the wildtype, although the testes in KO animals were smaller than those in the wildtype (Figure 7). Whether morphological abnormalities in spermatozoa are due to abnormal spermatogenesis or low nutrition caused by eating disorders requires further detailed analysis.

CatSper3-KO sperm did not show any response to SAAF, and no chemotactic behavior was observed. This result is consistent with the pharmacological findings on sperm chemotaxis in the sea urchin, *Arbacia punctulata* (Seifert et al., 2015). In mammals, the sperm lacking CatSper are motile but cannot show hyperactivation, resulting in infertility (Ren et al., 2001; Qi et al., 2007). Therefore, CatSper may be involved in the regulation of flagellar motility in ascidians, sea urchins, and mammals. In mammals, CatSper is assumed to be a direct or indirect target of various chemicals and is involved in chemotaxis (Brenker et al., 2012). In humans, progesterone, which is a putative sperm attractant, has been shown to activate CatSper through binding to α/β hydrolase domain-containing protein 2 (Miller et al., 2016). Furthermore, subunits of CatSper, EFCAB9 and Catsperζ, regulate the opening of CatSper channels in response to changes in intracellular Ca^{2+} and pH (Hwang et al., 2019). On the other hand, in ascidians, the sperm attractant SAAF directly binds to PMCA and seems to induce the Ca^{2+} efflux from the sperm (Yoshida et al., 2018). Furthermore, the *CatSper3*-KO sperm not only lacked chemotactic behavior but also had significant effects on motility itself, with many sperms failing to initiate movement. In mammals, sperms lacking any pore-forming CatSper subunits have similar initial velocities, as their wildtype counterparts (Qi et al., 2007), and CatSperζ-null and EFCAB9-null spermatozoa are also motile, although they show abnormal flagellar waveforms (Chung et al., 2017; Hwang et al., 2019). On the other hand, as for the ascidian auxiliary subunits of CatSper, *ß* (KH.C9.522), γ (KH.C11.410), EFCAB9 (KY21. Chr7.569), and ABHD2 (KY21. Chr3.1310) have been found in the *Ciona* genome database; however, *δ*, *ε*, *ζ*, and *η* have not been found and do not appear to exist. Thus, the system regulating sperm flagellar beating, including the CatSper channel, seems to differ from that in mammals, even though it is mainly regulated by $[Ca^{2+}]_i$: CatSper is also an indispensable Ca^{2+} channel in ascidian sperm, but it plays roles not only in sperm flagellar beatings but also in fundamental sperm motility.

In addition, although an increase in pH is necessary for the activation of ascidian sperm, sperm chemotaxis itself is observed even under low pH conditions (Sensui et al., 2023). This suggests that ascidian CatSper is involved in motility activation rather than chemotaxis.

In conclusion, this study indicates that CatSper plays an important role in ascidian sperm development. However, unlike in mammals, CatSper seems to be involved not only in the regulation of sperm flagellar beatings but also in sperm motility. Therefore, CatSper may play a role in development and spermatogenesis. Notably, although the role of CatSper in ascidians appears to be more important than that in mammals, this may only be due to impaired spermatogenesis, and more detailed studies are needed. We would like to identify the differences in CatSper roles.

Data availability statement

The datasets presented in this study can be found in online repositories. The names of the repository/repositories and accession number(s) can be found in the article/Supplementary Material.

Ethics statement

Ethical approval was not required for the studies on humans in accordance with the local legislation and institutional requirements because only commercially available established cell lines were used. The requirement of ethical approval was waived by Office for Life Science Research Ethics and Safety, the University of Tokyo, for the studies involving animals because our research is focused on ascidians, which are invertebrates. At the university, research conducted on invertebrates is not subject to ethical review. The studies were conducted in accordance with the local legislation and institutional requirements.

Author contributions

Conceptualization: MY; methodology: DK, MO, YS, KY, and MY; research: TK, DK, YS, MO, SA, KY, and MY; resources: DK, MO, YS, KY, and MY; writing and original draft: MY; visualization: MO, YS, KY, and MY; supervision: MY; funding acquisition: MY. All authors contributed to the article and approved the submitted version.

Funding

This work was supported partly by JSPS KAKENHI (grant number 21H05304).

Acknowledgments

The authors would like to thank Prof. T. Miura for allowing them to use the CLSM. They thank Mr. H. Kohtsuka, Ms. M Kawabata, Ms. M. Kohtsuka, Mr. M Nozawa, and Dr. H Kakizaki (MMBS, Univ. of Tokyo, Japan) for their technical assistance. They also thank Mr. S. Nakayama for his technical assistance of *in situ* hybridization. They also thank the National Bio-Resource Project of MEXT, Japan, for supplying materials. The content of this manuscript has previously appeared, as in a preprint in bioRxiv (https://www.biorxiv.org/content/10.1101/2021.07.06.451356).

Conflict of interest

The authors declare that the research was conducted in the absence of any commercial or financial relationships that could be construed as a potential conflict of interest.

Publisher's note

Supplementary material

The Supplementary Material for this article can be found online at: https://www.frontiersin.org/articles/10.3389/fcell.2023.1136537/full#supplementary-material

References

Arima, H., Tsutsui, H., Sakamoto, A., Yoshida, M., and Okamura, Y. (2018). Induction of divalent cation permeability by heterologous expression of a voltage sensor domain. *Biochim. Biophys. Acta* 1860 (5), 981–990. doi:10.1016/j.bbamem.2018.01.004

Brenker, C., Goodwin, N., Weyand, I., Kashikar, N. D., Naruse, M., Krahling, M., et al. (2012). The CatSper channel: a polymodal chemosensor in human sperm. *EMBO J.* 31 (7), 1654–1665. doi:10.1038/emboj.2012.30

Brokaw, C. J. (1979). Calcium-induced asymmetrical beating of triton-demembranated sea urchin sperm flagella. *J. Cell Biol.* 82 (2), 401–411. doi:10.1083/jcb.82.2.401

Brokaw, C. J., Josslin, R., and Bobrow, L. (1974). Calcium ion regulation of flagellar beat symmetry in reactivated sea urchin spermatozoa. *Biochem. Biophys. Res. Commun.* 58 (3), 795–800. doi:10.1016/s0006-291x(74)80487-0

Bystroff, C. (2018). Intramembranal disulfide cross-linking elucidates the super-quaternary structure of mammalian CatSpers. *Reprod. Biol.* 18 (1), 76–82. doi:10.1016/j.repbio.2018.01.005

Cai, X., and Clapham, D. E. (2008). Evolutionary genomics reveals lineage-specific gene loss and rapid evolution of a sperm-specific ion channel complex: catSpers and CatSperbeta. *PLoS One* 3 (10), e3569. doi:10.1371/journal.pone.0003569

Carlson, A. E., Westenbroek, R. E., Quill, T., Ren, D., Clapham, D. E., Hille, B., et al. (2003). CatSper1 required for evoked Ca^{2+} entry and control of flagellar function in sperm. *Proc. Natl. Acad. Sci. U. S. A.* 100 (25), 14864–14868. doi:10.1073/pnas.2536658100

Chung, J. J., Miki, K., Kim, D., Shim, S. H., Shi, H. F., Hwang, J. Y., et al. (2017). CatSperζ regulates the structural continuity of sperm Ca^{2+} signaling domains and is required for normal fertility. *Elife* 6, e23082. doi:10.7554/eLife.23082

Chung, J. J., Navarro, B., Krapivinsky, G., Krapivinsky, L., and Clapham, D. E. (2011). A novel gene required for male fertility and functional CATSPER channel formation in spermatozoa. *Nat. Commun.* 2, 153. doi:10.1038/ncomms1153

Chung, J. J., Shim, S. H., Everley, R. A., Gygi, S. P., Zhuang, X., and Clapham, D. E. (2014). Structurally distinct Ca^{2+} signaling domains of sperm flagella orchestrate tyrosine phosphorylation and motility. *Cell* 157 (4), 808–822. doi:10.1016/j.cell.2014.02.056

Cong, L., Ran, F. A., Cox, D., Lin, S., Barretto, R., Habib, N., et al. (2013). Multiplex genome engineering using CRISPR/Cas systems. *Science* 339 (6121), 819–823. doi:10.1126/science.1231143

Hwang, J. Y., Mannowetz, N., Zhang, Y., Everley, R. A., Gygi, S. P., Bewersdorf, J., et al. (2019). Dual sensing of physiologic pH and calcium by EFCAB9 regulates sperm motility. *Cell* 177 (6), 1480–1494. doi:10.1016/j.cell.2019.03.047

Hwang, W. Y., Fu, Y., Reyon, D., Maeder, M. L., Tsai, S. Q., Sander, J. D., et al. (2013). Efficient genome editing in zebrafish using a CRISPR-Cas system. *Nat. Biotechnol.* 31 (3), 227–229. doi:10.1038/nbt.2501

Lishko, P. V., Kirichok, Y., Ren, D., Navarro, B., Chung, J. J., and Clapham, D. E. (2012). The control of male fertility by spermatozoan ion channels. *Annu. Rev. Physiol.* 74, 453–475. doi:10.1146/annurev-physiol-020911-153258

Lishko, P. V., and Mannowetz, N. (2018). CatSper: a unique calcium channel of the sperm flagellum. *Curr. Opin. Physiol.* 2, 109–113. doi:10.1016/j.cophys.2018.02.004

Liu, J., Xia, J., Cho, K. H., Clapham, D. E., and Ren, D. (2007). CatSperbeta, a novel transmembrane protein in the CatSper channel complex. *J. Biol. Chem.* 282 (26), 18945–18952. doi:10.1074/jbc.M701083200

Mali, P., Yang, L., Esvelt, K. M., Aach, J., Guell, M., DiCarlo, J. E., et al. (2013). RNA-guided human genome engineering via Cas9. *Science* 339 (6121), 823–826. doi:10.1126/science.1232033

Miller, M. R., Mannowetz, N., Iavarone, A. T., Safavi, R., Gracheva, E. O., Smith, J. F., et al. (2016). Unconventional endocannabinoid signaling governs sperm activation via the sex hormone progesterone. *Science* 352 (6285), 555–559. doi:10.1126/science.aad6887

Miyashiro, D., Shiba, K., Miyashita, T., Baba, S. A., Yoshida, M., and Kamimura, S. (2015). Chemotactic response with a constant delay-time mechanism in Ciona spermatozoa revealed by a high time resolution analysis of flagellar motility. *Biol. Open* 4 (2), 109–118. doi:10.1242/bio.20137351

Nakayama, S., and Ogasawara, M. (2017). Compartmentalized expression patterns of pancreatic- and gastric-related genes in the alimentary canal of the ascidian *Ciona intestinalis*: evolutionary insights into the functional regionality of the gastrointestinal tract in Olfactores. *Cell Tissue Res.* 370 (1), 113–128. doi:10.1007/s00441-017-2627-7

Ogasawara, M., Minokawa, T., Sasakura, Y., Nishida, H., and Makabe, K. W. (2001). A large-scale whole-mount *in situ* hybridization system: rapid one-tube preparation of DIG-labeled RNA probes and high throughput hybridization using 96-well silent screen plates. *Zool. Sci.* 18 (2), 187–193. doi:10.2108/zsj.18.187

Ogasawara, M., Satoh, N., Shimada, Y., Wang, Z., Tanaka, T., and Noji, S. (2006). Rapid and stable buffer exchange system using InSitu Chip suitable for multicolor and large-scale whole-mount analyses. *Dev. Genes Evol.* 216 (2), 100–104. doi:10.1007/s00427-005-0031-x

Oishi, T., Tsuchikawa, H., Murata, M., Yoshida, M., and Morisawa, M. (2004). Synthesis and identification of an endogenous sperm activating and attracting factor isolated from eggs of the ascidian *Ciona intestinalis*; an example of nanomolar-level structure elucidation of novel natural compound. *Tetrahedron* 60 (33), 6971–6980. doi:10.1016/J.Tet.2004.02.075

Oishi, T., Tuchikawa, H., Murata, M., Yoshida, M., and Morisawa, M. (2003). Synthesis of endogenous sperm-activating and attracting factor isolated from ascidian *Ciona intestinalis*. *Tetrahedron Lett.* 44 (34), 6387–6389. doi:10.1016/S0040-4039(03)01598-3

Okada, T., and Yamamoto, M. (1999). Differentiation of the gonad rudiment into ovary and testis in the solitary ascidian, *Ciona intestinalis*. *Dev. Growth Differ.* 41 (6), 759–768. doi:10.1046/j.1440-169x.1999.00471.x

Ota, S., Hisano, Y., Muraki, M., Hoshijima, K., Dahlem, T. J., Grunwald, D. J., et al. (2013). Efficient identification of TALEN-mediated genome modifications using heteroduplex mobility assays. *Genes Cells.* 18 (6), 450–458. doi:10.1111/gtc.12050

Qi, H., Moran, M. M., Navarro, B., Chong, J. A., Krapivinsky, G., Krapivinsky, L., et al. (2007). All four CatSper ion channel proteins are required for male fertility and sperm cell hyperactivated motility. *Proc. Natl. Acad. Sci. U. S. A.* 104 (4), 1219–1223. doi:10.1073/pnas.0610286104

Quill, T. A., Ren, D., Clapham, D. E., and Garbers, D. L. (2001). A voltage-gated ion channel expressed specifically in spermatozoa. *Proc. Natl. Acad. Sci. U. S. A.* 98 (22), 12527–12531. doi:10.1073/pnas.221454998

Quill, T. A., Sugden, S. A., Rossi, K. L., Doolittle, L. K., Hammer, R. E., and Garbers, D. L. (2003). Hyperactivated sperm motility driven by CatSper2 is required for fertilization. *Proc. Natl. Acad. Sci. U. S. A.* 100 (25), 14869–14874. doi:10.1073/pnas.2136654100

Ren, D., Navarro, B., Perez, G., Jackson, A. C., Hsu, S., Shi, Q., et al. (2001). A sperm ion channel required for sperm motility and male fertility. *Nature* 413 (6856), 603–609. doi:10.1038/35098027

Rennhack, A., Schiffer, C., Brenker, C., Fridman, D., Nitao, E. T., Cheng, Y. M., et al. (2018). A novel cross-species inhibitor to study the function of CatSper Ca^{2+} channels in sperm. *Br. J. Pharmacol.* 175 (15), 3144–3161. doi:10.1111/bph.14355

Sander, J. D., Maeder, M. L., Reyon, D., Voytas, D. F., Joung, J. K., and Dobbs, D. (2010). ZiFiT (Zinc Finger Targeter): an updated zinc finger engineering tool. *Nucleic Acids Res.* 38, W462–W468. doi:10.1093/nar/gkq319

Sander, J. D., Zaback, P., Joung, J. K., Voytas, D. F., and Dobbs, D. (2007). Zinc Finger Targeter (ZiFiT): an engineered zinc finger/target site design tool. *Nucleic Acids Res.* 35, W599–W605. doi:10.1093/nar/gkm349

Sasaki, H., Yoshida, K., Hozumi, A., and Sasakura, Y. (2014). CRISPR/Cas9-mediated gene knockout in the ascidian *Ciona intestinalis*. *Dev. Growth Differ.* 56 (7), 499–510. doi:10.1111/dgd.12149

Satou, Y., Tokuoka, M., Oda-Ishii, I., Tokuhiro, S., Ishida, T., Liu, B., et al. (2022). A manually curated gene model set for an ascidian, *Ciona robusta* (*Ciona intestinalis* type A). *Zool. Sci.* 39 (3), 253–260. doi:10.2108/zs210102

Seifert, R., Flick, M., Bonigk, W., Alvarez, L., Trotschel, C., Poetsch, A., et al. (2015). The CatSper channel controls chemosensation in sea urchin sperm. *EMBO J.* 34 (3), 379–392. doi:10.15252/embj.201489376

Sensui, N., Itoh, Y., Okura, N., Shiba, K., Baba, S. A., Inaba, K., et al. (2023). Spawning-Induced pH increase activates sperm attraction and fertilization abilities in eggs of the ascidian, *Phallusia philippinensis* and *Ciona intestinalis*. *Int. J. Mol. Sci.* 24 (3), 2666. doi:10.3390/ijms24032666

Shiba, K., Baba, S. A., Inoue, T., and Yoshida, M. (2008). Ca^{2+} bursts occur around a local minimal concentration of attractant and trigger sperm chemotactic response. *Proc. Natl. Acad. Sci. U. S. A.* 105 (49), 19312–19317. doi:10.1073/pnas.0808580105

Shiba, K., Mogami, Y., and Baba, S. A. (2002). Ciliary movement of sea-urchin embryos. *Nat. Sci. Rep. Ochanomizu Univ.* 53 (1), 49–54.

Yoshida, K., Shiba, K., Sakamoto, A., Ikenaga, J., Matsunaga, S., Inaba, K., et al. (2018). Ca^{2+} efflux via plasma membrane Ca^{2+}-ATPase mediates chemotaxis in ascidian sperm. *Sci. Rep.* 8 (1), 16622. doi:10.1038/s41598-018-35013-2

Yoshida, M., Inaba, K., Ishida, K., and Morisawa, M. (1994). Calcium and cyclic-AMP mediate sperm activation, but Ca^{2+} alone contributes sperm chemotaxis in the ascidian, *Ciona savignyi*. *Dev. Growth and Differ.* 36 (6), 589–595. doi:10.1111/j.1440-169X.1994.00589.x

Yoshida, M., Inaba, K., and Morisawa, M. (1993). Sperm chemotaxis during the process of fertilization in the ascidians *Ciona savignyi* and *Ciona intestinalis*. *Dev. Biol.* 157 (2), 497–506. doi:10.1006/dbio.1993.1152

Yoshida, M., Ishikawa, M., Izumi, H., De Santis, R., and Morisawa, M. (2003). Store-operated calcium channel regulates the chemotactic behavior of ascidian sperm. *Proc. Natl. Acad. Sci. U. S. A.* 100 (1), 149–154. doi:10.1073/pnas.0135565100

Yoshida, M., Murata, M., Inaba, K., and Morisawa, M. (2002). A chemoattractant for ascidian spermatozoa is a sulfated steroid. *Proc. Natl. Acad. Sci. U. S. A.* 99 (23), 14831–14836. doi:10.1073/pnas.242470599

Yoshida, M., and Yoshida, K. (2018). "Modulation of sperm motility and function prior to fertilization," in *Reproductive and developmental strategies. Diversity and commonality in animals*. Editors K. Kobayashi, T. Kitano, Y. Iwao, and M. Kondo (Tokyo: Springer), 437–462.

Yoshida, M., and Yoshida, K. (2011). Sperm chemotaxis and regulation of flagellar movement by Ca^{2+}. *Mol. Hum. Reprod.* 17 (8), 457–465. doi:10.1093/molehr/gar041

Zeng, X. H., Navarro, B., Xia, X. M., Clapham, D. E., and Lingle, C. J. (2013). Simultaneous knockout of Slo3 and CatSper1 abolishes all alkalization- and voltage-activated current in mouse spermatozoa. *J. Gen. Physiol.* 142 (3), 305–313. doi:10.1085/jgp.201311011

frontiers | Frontiers in Cell and Developmental Biology

TYPE Original Research
PUBLISHED 10 November 2023
DOI 10.3389/fcell.2023.1249165

OPEN ACCESS

EDITED BY
Toshiyuki Nakagaki,
Hokkaido University, Japan

REVIEWED BY
Kentaro Ito,
Hosei University, Japan
Nobuhiko J. Suematsu,
Meiji University, Japan
Hanh Tran,
National University of Ho Chi Minh,
International University, Vietnam
Itsuki Kunita,
University of the Ryukyus, Japan

*CORRESPONDENCE
Atsuko Takamatsu,
atsuko_ta@waseda.jp

RECEIVED 28 June 2023
ACCEPTED 30 October 2023
PUBLISHED 10 November 2023

CITATION
Yoneoka E and Takamatsu A (2023), Relation between learning process and morphology of transport tube network in plasmodium of *Physarum polycephalum*. *Front. Cell Dev. Biol.* 11:1249165. doi: 10.3389/fcell.2023.1249165

Relation between learning process and morphology of transport tube network in plasmodium of *Physarum polycephalum*

Emiri Yoneoka and Atsuko Takamatsu*

Department of Electrical Engineering and Bioscience, Waseda University, Tokyo, Japan

The question of whether a single-celled organism without a brain could have functions such as learning and memory has been the subject of much debate in recent years. The plasmodium of the true slime mold, *Physarum polycephalum*, is an ideal model organism for such a question. The plasmodium exhibits behaviors that resemble intelligence, including solving mazes, mimicking optimal rail transportation networks, predicting the weather, and solving traveling salesman problems. In addition, the plasmodium has recently been shown to have the simplest form of learning: habituation. In the experiments in which plasmodia were repeatedly allowed to cross bridges containing aversive chemicals, the habituation behavior has been confirmed. It has been shown that the habituation process involves chemicals that are stored internally. However, it is not clear how these chemicals result in change in the behavior of plasmodium during habituation learning. This study focused on the transport tube network formed in plasmodium during the above experiments. Then, the role of the network morphology in the habituation learning process was investigated. The results showed that the network morphology changes from tree to mesh type during habituation learning, and disrupting the learned network reduces habituation behavior. In addition, it was shown that the thickness oscillation frequency depends on the network morphology. The study found that in the plasmodium of *P. polycephalum*, a primitive organism without a brain, transport tube networks, instead of neuronal networks, play an important role in habituation learning and the resulting decision making.

KEYWORDS

slime mold, memory, habituation, transport tube, network, *Physarum polycephalum*

1 Introduction

The question of whether single-celled organisms without brains have functions such as learning and memory has been much debated in recent years, and the importance of this question has been widely recognized (Dussutour, 2021; Gunawardena, 2022; Wright et al., 2023). Although the definition of learning has long been discussed for animals with brains and nervous systems, it can be extended to single-celled organisms as follows: "learning" is a change in the internal state of a system in response to external stimuli, followed by an appropriate change in the behavior in response to the same stimuli (Barron et al., 2015). From this perspective, the learning function has been reported in a variety of single-celled

organisms; examples include *E. coli* (Yi et al., 2000), *Stentor* (Rajan et al., 2023), *Spirostomum* (Eisenstein et al., 1982), and *Paramecium* (French, 1940; Hanzel and Rucker, 1972).

In this context, the plasmodium of the true slime mold, *Physarum polycephalum*, is an ideal model organism. Although it is a single-celled organism, it behaves as if it has "intelligence" in a diorama environment artificially constructed in a laboratory (Nakagaki, 2021). After Nakagaki et al. demonstrated in 2000 that the plasmodium of *P. polycephalum* can solve mazes (Nakagaki et al., 2000a), a variety of important studies relating to their "intelligence" have been conducted. The slime mold can find the shortest path (Nakagaki et al., 2004), optimize railway networks (Tero et al., 2010; Watanabe et al., 2011), predict weather (Saigusa et al., 2008), solve traveling salesman problems (Zhu et al., 2013; Zhu et al., 2018), and more.

The plasmodium is a vegetative form of the true slime mold of *P. polycephalum*. It is a very large amoeboid cell, ranging in size from a few millimeters to several meters. It crawls around in the environment while changing its shape (William et al., 1986). Because the plasmodium has many nuclei within its single-cell body, it can survive even if part of it is separated from the rest of the cell. Then, the separate parts behave as individuals. Meanwhile, there is a network structure of transport tubes, i.e., veins, inside the cell body (Takamatsu et al., 2017). These tubes are responsible for transporting the contents of the cell, cytoplasm (including the nucleus, nutrients, and oxygen), throughout the body. This is an essential structure for the plasmodium that must maintain a large cell body. The outer part of the transport tube is a harder structure consisting of gel, while the inner part consists of a softer material, cytosol. As the plasmodium crawls and spreads through the environment, the hard and soft parts can change their states with each other through sol-gel transformation (Kamiya, 1959). This allows the transport tube network to change shape easily, resulting in an efficient network that responds to the surrounding environment (Takamatsu et al., 2009; Tero et al., 2010; Ito et al., 2011; Takamatsu et al., 2017). For example, in an environment with aversive chemicals or under starvation, the network forms a dendritic or tree structure; in a nutrient-rich environment, it forms a mesh structure with a thin sheet-like structure at the front (Takamatsu et al., 2009).

Recently, studies have directly examined the learning function in plasmodium of *P. polycephalum* (Boisseau et al., 2016; Vogel and Dussutour, 2016; Boussard et al., 2019). These studies have focused on the simplest form of learning, habituation. Habituation, classified as non-associative learning, is a phenomenon in which the response to repeated stimuli decreases. To determine this phenomenon as a form of learning, nine criteria were initially established (Thompson and Spencer, 1966), and later, a tenth was added (Rankin et al., 2009). In the above studies, seven criteria were met: decreased response to repeated stimuli, sensory recovery, dependence on stimulus frequency, dependence on stimulus intensity, stimulus specificity, and dishabituation (Boisseau et al., 2016; Vogel and Dussutour, 2016) or long-term habituation (Boussard et al., 2019). This learning memory is found to be closely related to the cellular uptake and retention of stimulus chemical substances given during learning (Boussard et al., 2019), but it is not known how exactly the chemicals from the environment act on the internal system of the plasmodium, nor how the information is stored and how they cause changes in the behavior of plasmodium.

This study focused on the transport tube network formed in plasmodium. The transport tubes of plasmodium adaptively change in thickness in response to the flow rate of the cytoplasm (Tero et al., 2007). The thickening follows nonlinear dynamics and then generates bipolar states, such as thick or thin; this property is analogous to the phenomenon of neuronal firing. Furthermore, it was shown by a combination of experimental analysis and mathematical modeling that information applied locally can be retained in the spatial gradient of transport tube thickness, and it was suggested that a single transport tube itself could have a memory function (Kramar and Alim, 2021). It is expected that networks composed of transport tubes with such properties will provide plasmodium with more advanced information processing functions beyond that of a mere single cell.

Inspired by the habituation experiments of Boisseau et al. (2016) on plasmodium , this study examined the relationship of transport tube network morphology to the learning process and memory of habituation, and we discuss how memory information is read out and output to plasmodium behavior.

2 Materials and method

2.1 Preparation of organism for experiments, plasmodium of *Physarum polycephalum*

Prior to the following procedure, plasmodia of *P. polycephalum* are cultured on 1.5 w/v% agar medium (FUJIFILM Wako pure chemical industries), fed oat flakes (Premium Pure Oats, Nippon food manufacture), and incubated for approximately 1 day at 25°C in the dark.

2.2 Experimental setup

The basic experimental setup consists of a start block, bridge block, and goal block, as shown in Figure 1. The start and goal blocks are food blocks made of 1.0 w/v% agar containing 10 g w/v% oat-flake-grind extract (Takamatsu et al., 2009). They are circular in shape, 18 mm in diameter and 3–4 mm thick. The bridge block is made of 1.0 w/v% agar with or without containing 0.5 mM Quinine hydrochloride dihydrate (FUJIFILM Wako pure chemical industries), which are used for Quinine experiments or control experiments, respectively. Quinine was used to inhibit the plasmodium from crossing bridges for habituation training in the same manner as in the experiments of Boisseau et al. (2016). Quinine is an alkaloid and an aversive chemical substance for the plasmodium. It was reported that application of this substance slowed the flow of cytoplasm (Kamiya, 1959), and temporarily inhibited the progress of the plasmodium on agar medium containing this substance (Takagi et al., 2007). The bridge blocks are rectangular, 18 × 18 mm in size, and 3–4 mm thick. The bridge blocks are placed between the start and goal, as shown in Figure 1B.

Thirty setups shown in Figure 1B (almost half of them were for Quinine experiments, while the rest were for control experiments) were placed on two large plastic plates (square bio assay dish, 245 ×

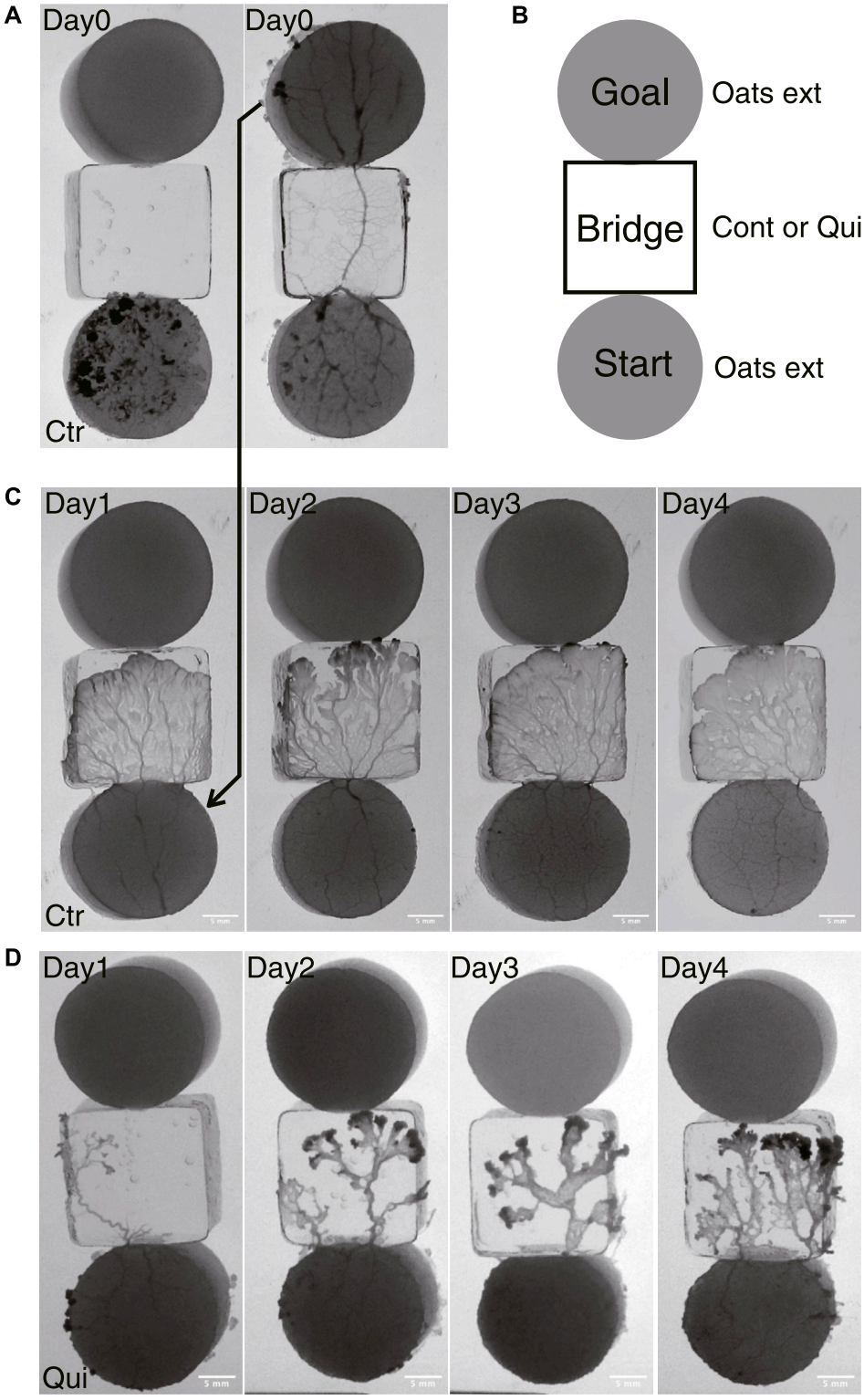

FIGURE 1
Experimental setup and typical results of Days 1–4. **(A)** An example of an experimental setup on Day 0. At t = 0 min, the plasmodium spread only on the start area and then begin to cross the bridge (left panel). At t = 905 min, the plasmodium spread toward the goal and finished crossing the bridge (right panel). The sample is a control sample. **(B)** Illustration of experimental setup. Start and goal blocks are a 1.0 w/v % agar plate containing 10 w/v %oat-flak-grind extract. The bridge is a 1.0 w/v % agar plate containing 0.5 mM Quinine for test bridges (Qui) and without chemicals for control bridges (Ctr). **(C, D)** Typical results of control and Quinine experiments on Days 1–4, respectively. The images represent the ones at the time t_e when the plasmodia reached the upper edge of the bridge block, which is in contact with the goal block. See also Supplementary Movie S1 (control) and Supplementary Movie S2 (Quinine) for descriptions of how the plasmodia progress across the bridges to reach the goal blocks. **(C)** Control: t_e = 110, 80,120,110 min. **(D)** Quinine: t_e = 285, 280, 210, 150 min.

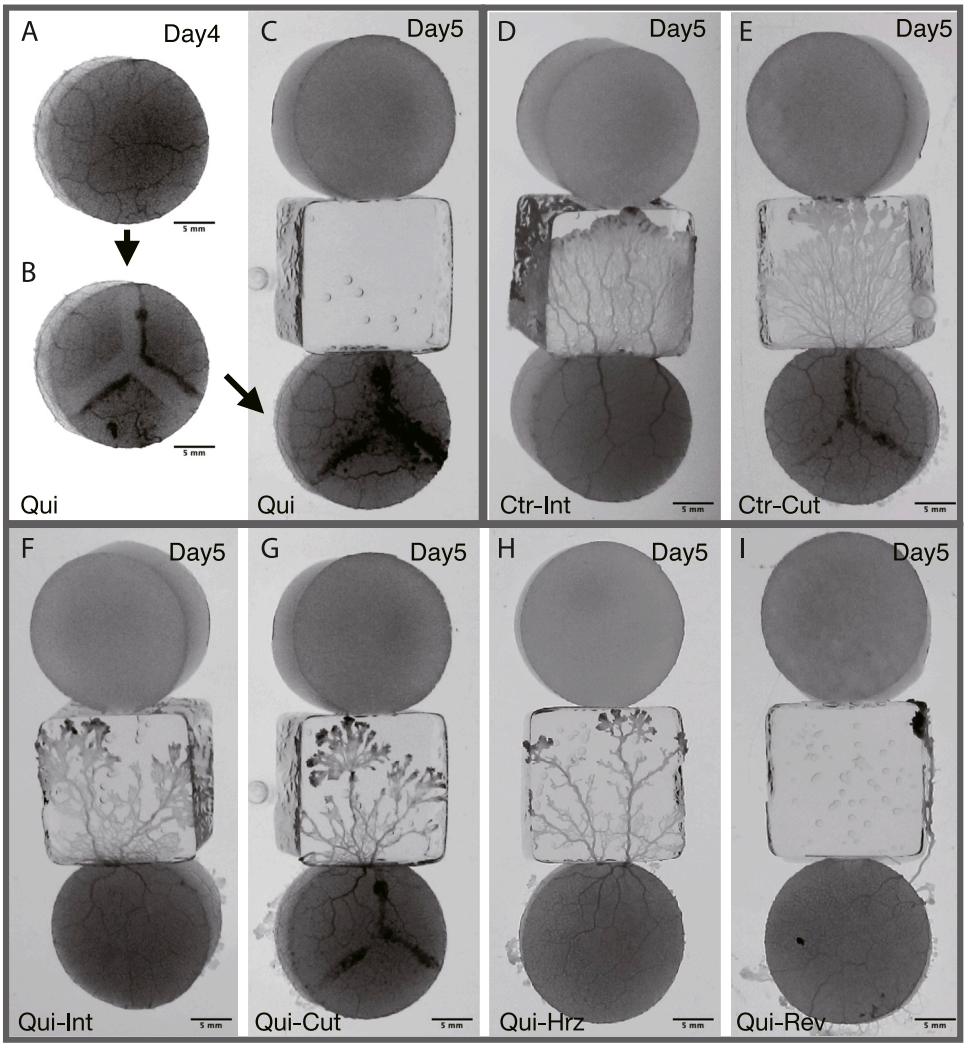

FIGURE 2
Typical results of Day 5. **(A–C)** Preparation of cutoff network. The same sample as that of the panel **(G)** **(A)** Plasmodium covering goal on Day 4 is used as the start sample on Day 5. t = −230 min in stage time on Day 5 (see Figure 3 for definition of time). **(B)** Before the Day 5 experiment, the tube network of **(A)** is cutoff in a Y-shape. t = −220 min. **(C)** Once the cutoff wound has healed, the sample is placed at the starting position on Day 5. t = −40 min. **(D, E)** Typical result of Control. See also Supplementary Movie S5. **(F–I)** Typical result of Quinine. See also Supplementary Movie S6. **(D)** Intact. t = 105 min. **(E)** Cutoff. t = 85 min. **(F)** Intact. t = 130 min. **(G)** Cutoff. t = 185 min. **(H)** Horizontal: Horizontally placed at the starting position. t = 155 min. **(I)** Reverse: Reversely placed at the starting position. t = 165 min. All results presented here are from experiments conducted on the same day. The images in **(D–I)** represent the ones at the time t_e when the plasmodia reached the upper edge of the bridge block, which is in contact with the goal block.

245 mm, Corning Inc.) for a single experiment set. To avoid systematic effects, Quinine and control setups were alternately placed on the large plates. In total, eight sets of experiments were performed on different days in different seasons (October and November 2019; July, August, October, and November 2020; and February and March 2021) in Shinjuku, Tokyo. The samples were illuminated with transmitted light by yellow-LED illumination plate (around 580 nm; LM8C 311X455-35Y AItec) to avoid light and thermal response of plasmodia (Ueda et al., 1988). The experiments were performed in a thermostatic and humidistatic chamber at 25 ± 0.3°C, with a relative humidity of 85% ± 3% (PR2KT; ESPEC Corp, Japan).

The transmitted light images were recorded with a digital camera (body: EOS RP; lens: EF24 mm F2.8 IS USM, Canon Inc.) at 5 min intervals for approximately 24 h. Image resolutions were 0.06–0.08 mm/pixels. For the analysis of thickness oscillations, the images were captured at 5 s intervals for 10 min. The original raw images were converted linearly to 8-bit gray scale images using image processing software [Photoshop, Adobe Inc; Fiji (Schindelin et al., 2012)]. The images in the figures have been linearly adjusted in brightness and contrast according to their purpose, so that any description can be easily understood. In Figure 1A, Figure 3A, and Figure 9, the treatment focuses on the entire plasmodium on the three blocks. In Figures 1C, D, Figures 2D–I, the treatment focuses on the plasmodium on the bridge. In Figures 2A, B, Figure 3C, Figure 6 and Figure 7, the treatment focuses on the network formed by the plasmodium on the goal block.

Eight datasets were used for behavior analysis, including measuring area and speed. Six datasets were used for network

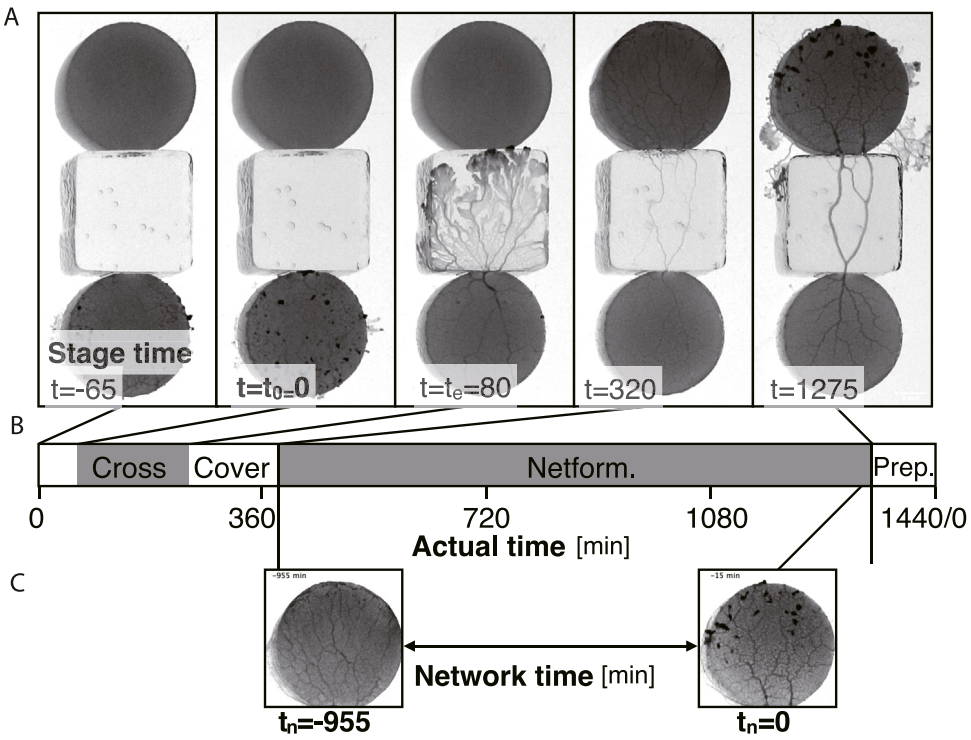

FIGURE 3
Definition of the times in a day. Time units are in minutes. **(A)** Examples of each stage at time t. **(B)** Time chart of each stage indicated using actual time in a day. At actual time 0 min (t = −65 min in stage time in this example), the start block is placed. Crossing: the plasmodium begins to cross the bridge at stage time $t = t_0 = 0$ and finishes at stage time $t = t_e$. Covering: the goal block is being covered with the plasmodium (t = 80–320). Network formation (Netform.): The transport tube network at the goal is formed (t = 320–1275). Preparation (Prep.): Preparation period for the next day's experiment. **(C)** Network time t_n. The time $t_n = 0$ is defined as the last time of the network formation phase. t_n is defined backward from $t_n = 0$. The image examples are taken from the same sample of Figure 1C Day 2.

analysis. Three datasets were used for connection analysis. One dataset was used for thickness oscillation analysis.

2.3 Procedure

A single set of experiments lasted for 6 days, from Day 0 to Day 5. For these experiments, plasmodia are cut from the fan-shaped frontal part of the cultured plasmodium (§2.1) so that the total amount is 0.085 g. As the wounds of the freshly collected plasmodia are not sufficiently healed, the Day 0 procedure is performed before the test experiments of Day 1–5 are begun. The fresh plasmodia are transferred to the start block on Day 0 (Figure 1A). The plasmodium begins to spread on the bridge block, then reaches the goal block, and finally covers it. The goal block covered by the plasmodium is detached from this setup, and then used for Day 1's experiment (Figure 1C). On Day 1, the plasmodium at start position begins to spread on the new test bridge, then reaches and covers the new goal. These procedures are repeated until Day 4.

On Day 5, the goal plasmodia of Day 4 are divided into 4 groups named intact, cutoff, horizontal, and reverse, respectively as shown in Figure 2. The first group (intact) of the goal plasmodia are placed intact at the start of the Day 5 experiment, the same as the experiments of Days 1–4 (Figures 2D, F). The second group (cutoff) of the goal plasmodia are placed at the start after being cut in a Y-shape so that the transport tube network becomes disconnected (Figures 2B, C, G). In this procedure, the plasmodium are scratched 2–3 mm wide by gently sliding a spatula over the agar surface. Care is taken not to damage the agar surface. This procedure divides the single plasmodium into three parts as shown in Figure 2B. Note that the block are placed at starting position after their wound has healed and the three separate parts become a single body. The third and fourth groups (horizontal and reverse) of the goal plasmodia of Day 4 are placed after rotating their orientations by 90° and 180° from the original direction at the start positions of Day 5, respectively (Figures 2H, I).

2.4 Definition of times in a day

The procedure of placing the start block of Day N is performed at almost the same time in 1 day, which is defined as time 0 in actual time (Figure 3). Then, the experiment day finishes at actual time = 1440 min, including preparation time for the next-day experiment (Figure 3B).

Two different time definitions are introduced: stage time (Figures 3A, B) and network time (Figure 3C). The stage time $t = t_0 = 0$ is defined when the plasmodium on the start block

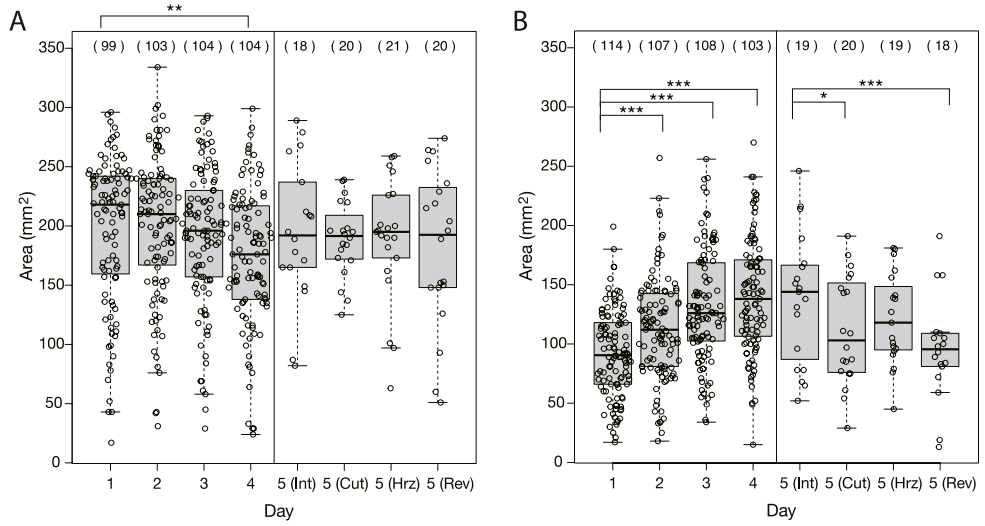

FIGURE 4
Area of plasmodia on bridges at the moment when they finished crossing bridges. **(A)** Control experiment. **(B)** Quinine experiment. The abbreviations in parentheses shown in Day 5 represent Int: intact, Cut: cutoff, Hrz: horizontally placed, Rev: reversely placed. Open circles represent data of a single sample. Thick bars in box plots are the median of each dataset; Upper and lower edges of boxes are upper and lower quantiles, respectively; Upper and lower thin bars are the largest/smallest value less/greater than upper/lower quantile plus/minus 1.5 times interquartile range, respectively; See R manual for details. The numbers in parentheses above the boxes indicate the number of data in each dataset. Asterisks represent the degree of p-value calculated as a result of appropriate statistical tests for each dataset as follows: * $p < 0.1$, ** $p < 0.05$, *** $p < 0.01$, and unlabeled $p > 0.1$. See Supplementary Table S1 for details. As reference data in the multiple comparison test, the Day 1 dataset was used for Days 1–4 of analysis, and the intact Day 5 dataset was used for Day 5 of analysis.

begins to cross the test bridge (Figure 3A). Then, at time t_e, the plasmodium reaches the upper edge of the bridge block, which is in contact with the goal block. The plasmodium then enters the goal block followed by the covering state. The goal block has finished being covered by the plasmodium at $t = 320$ in this example. Through this event, the transport tube network is formed on the goal block. This network formation is observed until the time for preparation of the next day's experiment begins, which is defined as network time $t_n = 0$ (Figure 3C). Therefore the value of the network time t_n is negative during covering state, whose definitions are used in Figures 6A–H and Figures 7A–H.

2.5 Estimation of area on the bridge

Areas of plasmodium on the bridges were estimated using Fiji (Schindelin et al., 2012). The background image, which is the image at t_0 (second part of Figure 3A) was subtracted from the image at t_e (third part of Figure 3A; Supplementary Figure S1A). Only the part of plasmodium on the bridge was extracted by thresholding the image (Supplementary Figure S1B) so that it is binarized (Supplementary Figure S1C). Then, the pixels were counted.

2.6 Estimation of speed on the bridge

The speed of the plasmodium on the bridge was estimated as [bridge length (mm)]/[$t_e - t_0$ (min)]. The speed of progression strongly depends on the environment of the day (wind exposure in the thermostatic and humidistatic chamber, season, and parentage of the plasmodium). To compensate for such effects, the speed data were normalized with the mean speed of the samples of a control experiment performed on the same day.

2.7 Characterization of tube network at goal

The tube networks at goals were characterized by two-dimensional Fourier transform analysis that captures the spatio-periodic structure. The goal image at time t_n was cropped into a square for Fast Fourier transform (FFT) analysis using the Fiji plugin (Supplementary Figure S2A), and then the power spectrum was obtained (Supplementary Figure S2B), which includes direction angles and power values. The angle values were weighted by power value, and then the distribution of tube orientation was obtained (Supplementary Figure S2C). Note that the 180° – 360° data were not included in the analysis because the spectrum is point symmetric. Finally, the major orientation angles of transport tubes in a goal network at time t_n were estimated as the mode of the distribution, as shown Supplementary Figure S2C, which was obtained by density estimation using the R software (R Core Team, 2023). Note that the estimated angle values are orthogonal to the orientation direction of the tube, as shown in Supplementary Figure S2D.

2.8 Characterization of daily change of network morphology

Characteristic angles of the day were estimated from the time course of the orientation angles. The characteristic angles were

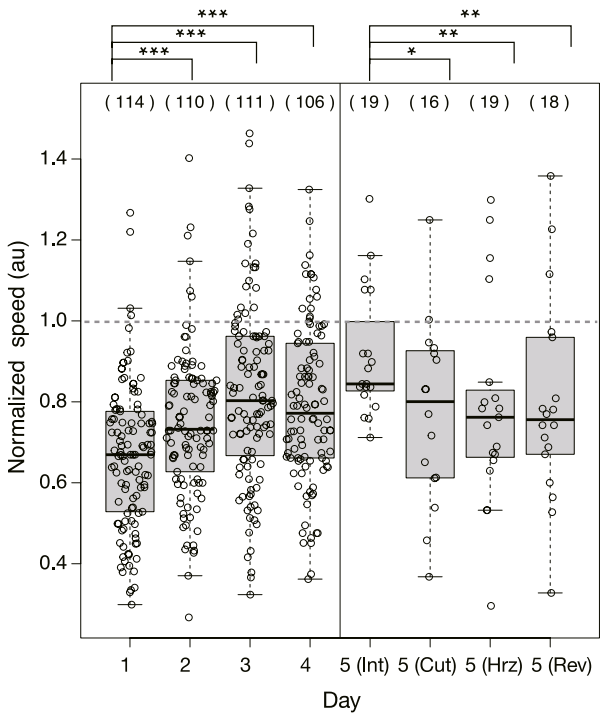

FIGURE 5
Normalized speed of plasmodium crossing the bridge in Quinine experiment. The speeds were normalized by the mean speed of samples of control experiment performed on the same day. Dashed horizontal line denotes 1.0 in normalized speed, which means the mean speed in the control experiment. Other notations are the same as those in Figure 4.

plotted in terms of daily change. These plots were manually classified from Type 0 to Type 4 with the conditions blindfolded. See §3.1.3 for details.

2.9 Analysis of thickness oscillation

The thickness oscillations of plasmodia on the start block during the 10 min before they begin to cross the bridge were analyzed (Supplementary Figure S3). The area of 320 × 320 pixels (about 20 × 20 mm^2) was divided into smaller areas of 10 × 10 pixels, and then the transmitted light intensity of the plasmodium of this area was averaged for each smaller area to obtain the time series data, as shown in Supplementary Figure S3A. The time series data were smoothed by locally-weighted polynomial regression using the R "lowess" function to remove noise. The oscillation periods were estimated as the times between two successive peaks of this waveform. Then, the mode of the period distribution was used as the measure of period T of the small area, and the value was converted into angular frequency as $2\pi/T$. Supplementary Figure S3B shows the spatial distribution of the angular frequencies. Supplementary Figure S3C shows a histogram of the angular frequency obtained from the data of Supplementary Figure S3B. Note that the data above half (more strict threshold than usual) of the Nyquist frequency ($2\pi \cdot [f_n/2]$, where the Nyquist frequency $f_n = 0.1$) were omitted as noise. The median of this distribution was taken as the representative value of the oscillation frequency of the plasmodium on the start block, whose value was used in §3.4.

2.10 Statistical analysis

To determine the significance of the data, the normality and equal variance of the data groups were first subjected to the Shapiro and Bartlett tests, respectively. For data groups for which the normal distribution and equal variance were not rejected, the Dunnett test was applied as a multiple test, and for the other data groups, the Steel test was applied. The results of statistical analysis are summarized in Supplementary Table S1. These statistical analyses were performed using R.

3 Results

The experimental process is divided into two phases. The first phase is the process of learning "habituation" in Day 1–4, and second phase is the process of deletion of "learning memory". It should be noted that the terms such as "habituation" are used here according to the findings by reports on plasmodium of *P. polycephalum* (Boisseau et al., 2016; Vogel and Dussutour, 2016; Boussard et al., 2019), not in the original psychological sense. Control and Quinine experiments were always simultaneously performed.

3.1 Learning process of "habituation"

The habituation experiments were performed from Days 1–4. On each day, the start block, which is the goal block of the previous day's experiment and is covered with the plasmodium, was placed in contact with the bridge, as shown in Figures 1B–D. The plasmodium began to spread on the bridge ($t = t_0$ in Figure 3A) after 10 min to several hours (Supplementary Figures S4A, B), irrespective of control or Quinine experiments. The tip portion of the plasmodium finish the bridge crossing at $t = t_e$ (Figure 3A). It took 1–2.5 h for the control and 1.5–3.5 h for the Quinine experiments to finish the bridge crossing (Supplementary Figures S4C, D), whose details are discussed in §3.1.2. Then, the plasmodium covered the goal block over a 3–10 h period (Supplementary Figures S4E, F). The time for covering took longer with the passage of days in both the control and Quinine experiments. Finally, the tube network of plasmodium was formed over the start, bridge, and goal blocks, as shown in the final panel of Figure 3A ($t = 1275$; details are discussed in §3.3). The above behaviors can be seen in Supplementary Movie S1 for control experiments and Supplementary Movie S2 for Quinine experiments. The difference in characteristics of control and Quinine experiments appeared in the area on the bridges (§3.1.1) and speed of crossing them (§3.1.2), as Boisseau et al. (2016) reported.

3.1.1 Area on the bridges

As seen in Figure 1, the shape and area of the plasmodia on the bridges over the Day 1–4 experiments were quite different between control and Quinine experiments. In the control experiments, the plasmodium spread in thin sheets over the bridge, with little daily variation in shape (Figure 1C). The area on the bridge also changed little over the days, but tended to decrease slightly on Day 4, as

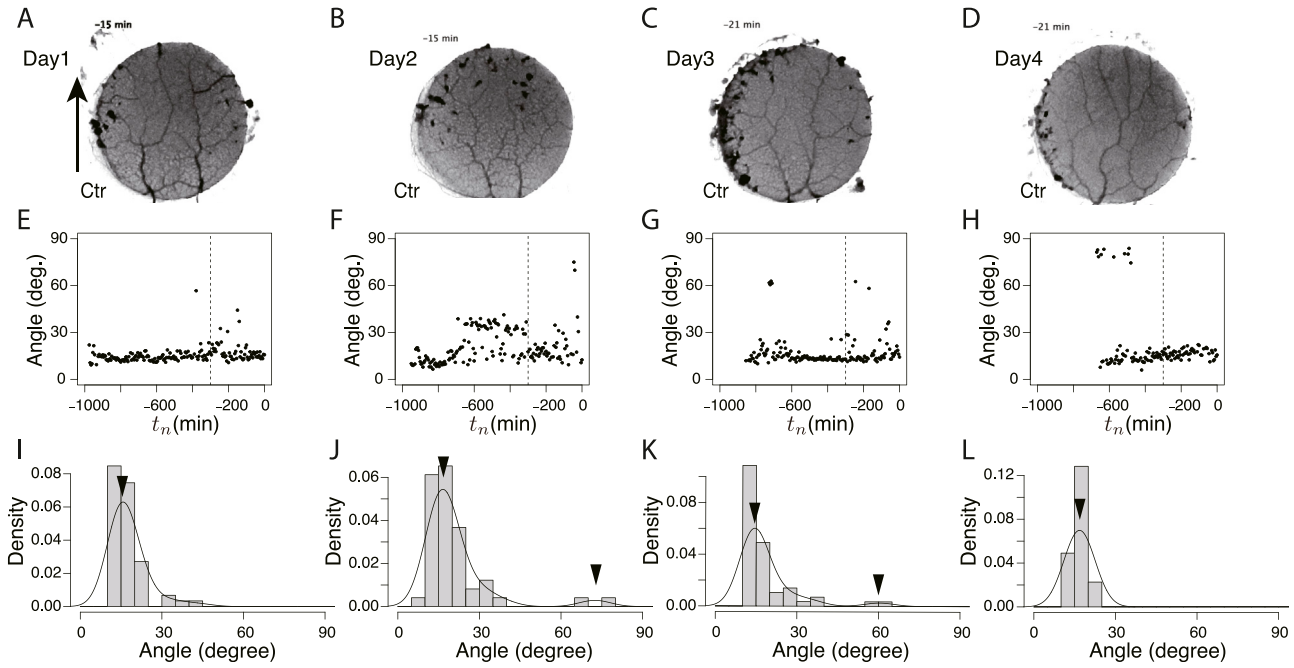

FIGURE 6
Orientation angle of transport tubes in control experiment. **(A–D)** Examples of final tube network morphology. The arrows indicate the direction in which the tip portion of the plasmodium moves. **(E–H)** Time course of major orientation angle of tube network. The angle is from the direction of the arrow shown in Figure **(A)**. The vertical dashed line is at $t_n = -300$. **(I–L)** Distribution of final major orientation angle taken from $t_n = -300$ to $t_n = 0$. The curve is a density plot in which peak angles (denoted by arrowheads) are estimated as characteristic angles of the day. These examples of the peak angles and their density values were used for Figure 8B. **(A, E, I)** Day 1, **(B, F, J)** Day 2, **(C, G, K)** Day 3, **(D, H, L)** Day 4.

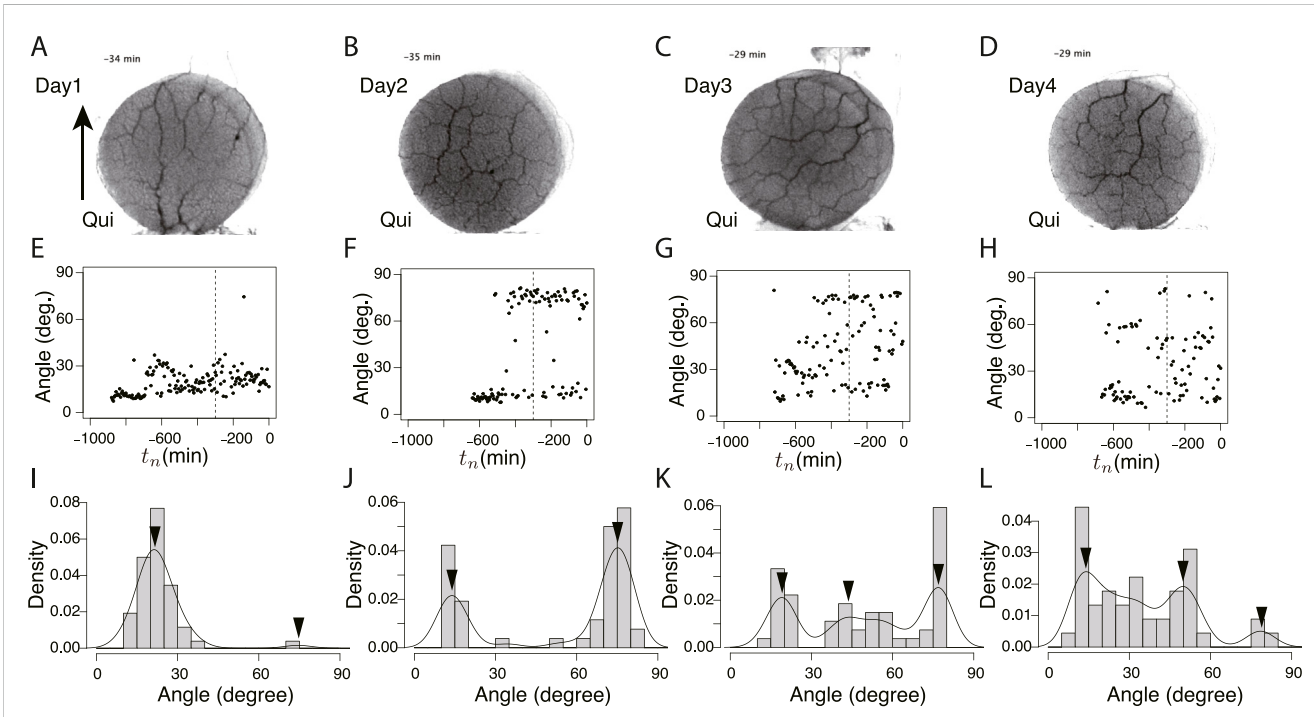

FIGURE 7
Orientation angle of transport tubes in Quinine experiment. **(A–D)** Examples of final tube network morphology. **(E–H)** Time course of major orientation angle of tube network. **(I–L)** Distribution of final major orientation angle taken from $t_n = -300 - 0$. These examples of peak angles and their density values are used for Figure 8E. **(A, E, I)** Day 1, **(B, F, J)** Day 2, **(C, G, K)** Day 3, **(D, H, L)** Day 4. Other notations are the same as those in Figure 6.

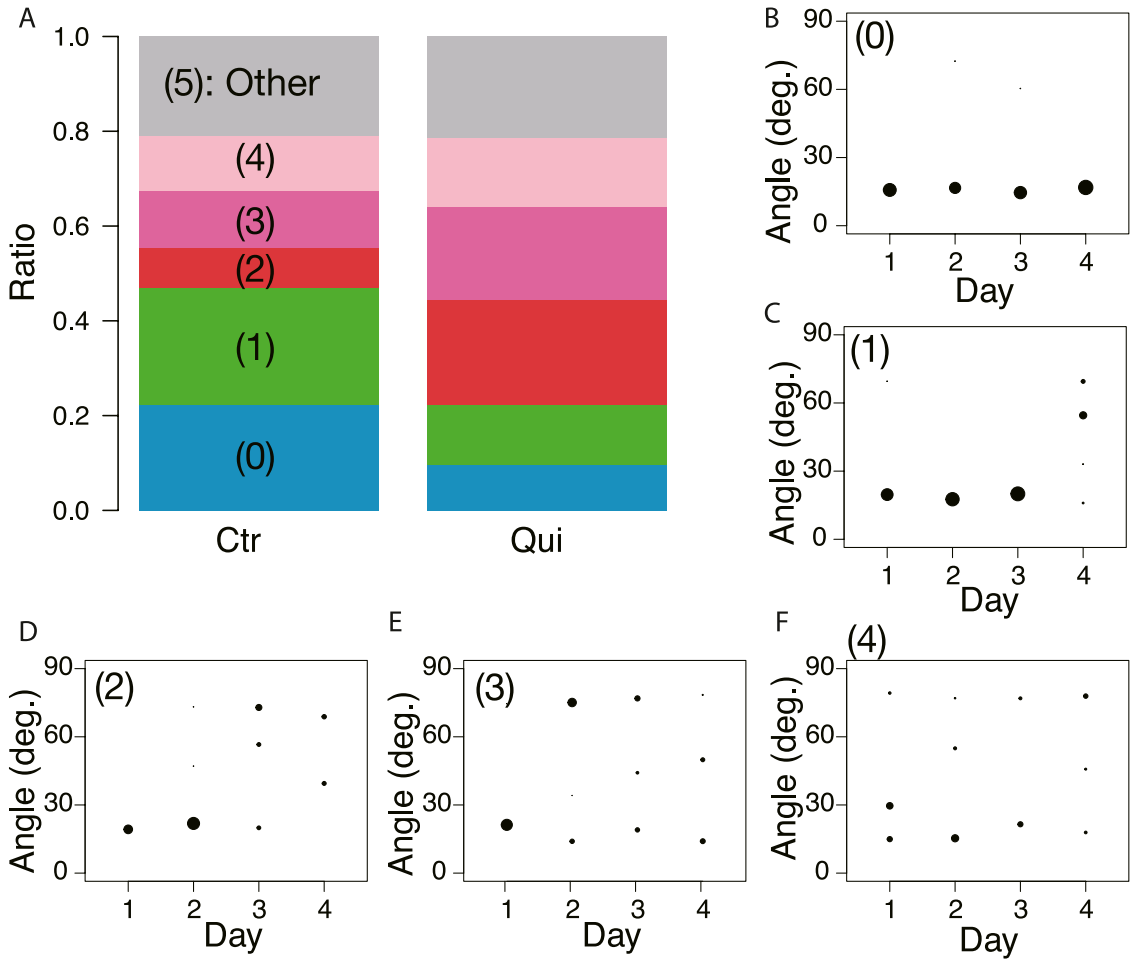

FIGURE 8
Daily change of orientation angles of tubes in the final transport networks. **(A)** Classification of daily change is shown as a ratio to the number of observations. Numbers in parentheses indicate type number. The numbers of observation data are 83 and 79 for the control and Quinine experiments, respectively. **(B)** Type 0: major tube orientations are always parallel to the direction in which the tip of the plasmodium was advancing (angle $< 45°$). **(C)** Type 1: tube orientation changes to multidirection on Day 4. **(D)** Type 2: tube orientation changes to multidirection on Day 3. **(E)** Type 3: tube orientation changes to multidirection on Day 2. **(F)** Type 4: tube orientation is always multidirection. Type 5 is classified as other changes.

shown in Figure 4A. On the contrary, in the Quinine experiments, the shape (Figure 1D) and area (Figure 4B) changed markedly over the days. On Day 1, the shape is string-like and the area is very small. Each day thereafter, the shape changed to a branch-like shape with the sheet area increased (Figure 1D), and the area increased significantly (Figure 4B). These trends are consistent with the results of Boisseau et al. (2016).

3.1.2 Speed of crossing the bridges

With respect to the raw data of speed of the plasmodium crossing the bridge, the results differed slightly from those of Boisseau et al. (2016). As shown in Supplementary Figure S5A, the speed in the control experiment decreased over days, whereas the results of Boisseau et al. showed no change. In the Quinine experiment, the speed seemed to increase slightly over days but not statistically significantly, whereas the results of Boisseau et al. showed a significant increase.

The difference between Boisseau et al.'s experimental setup and ours is in the preparation method of the start and goal blocks and in the concentration of Quinine in the bridge. The start and goal blocks contained 10% blended oat flakes in their setup, whereas ours contained 10 g w/v% oat-flake-grind extract because it was needed to increase the light transparency of the blocks for observation of the transport tube network. The latter is less attractive as nutrition than the former. This would affect the result of speed reduction in the control experiment. In addition to this, the tendency of reduction was not always observed: half of the eight sets of experiments showed a different tendency. As mentioned in §2.6, the speed would be affected by the environment condition of the day of experiment. Therefore, speed was evaluated using values normalized by those of the control experiment of the same date.

Figure 5 shows the speed of the Quinine experiment normalized with the mean speed of the control samples performed on the same day. Then, it is concluded that the normalized speed increases statistically significantly over days.

Together with the results of §3.1.1 and §3.1.2 and compared with the results of Boisseau et al., it can be concluded that the

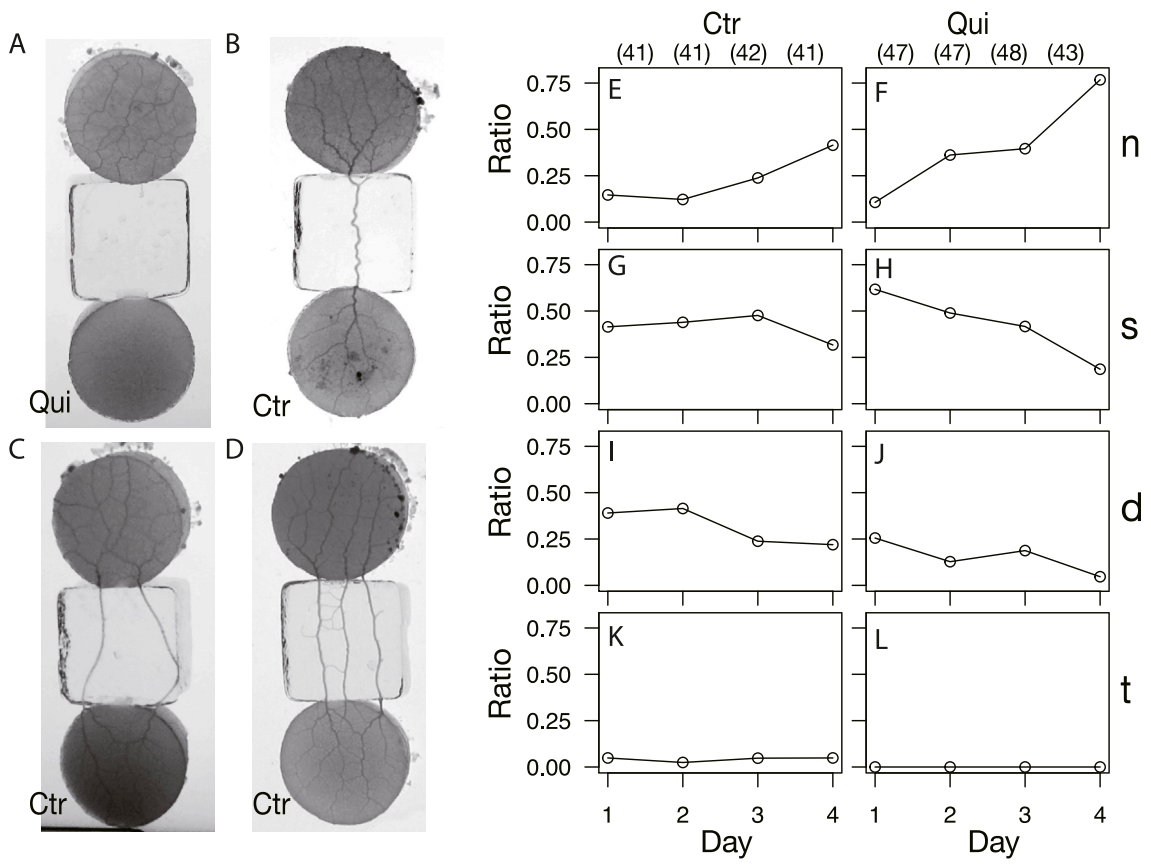

FIGURE 9
Types of start and goal connections after network formation. **(A, E, F)** No-connection (*n*). **(B, G, H)** Single tube (*s*). **(C, I, J)** Double tube (*d*). **(D, K, L)** Triple tube (*t*); the connections with more than three tubes are also included in this category. **(A–D)** Images are those of almost final phase of network formation. **(A)** Quinine experiment on Day 3. **(B, C)** Control experiment on Day 3. **(D)** Control experiment on Day 1. **(E–L)** Daily change of observation ratio of each connection type. The denominator of the ratio is the number of data in the same conditions on the same day, which are shown in parentheses placed at the top of Figures **(E)** and **(F)**.

plasmodium learnt to overcome the danger of the bridge under repeated experiences, thus learning of "habituation" was established.

3.1.3 Network formation during "learning" process

To study the state of the learning memory in the plasmodium, we focused on the network of transport tubes that form over the goal block. Figure 6 and Figure 7 show the typical results of network formation on the goal blocks after crossing control and Quinine bridges, respectively. In the control experiments, the branching network (tree) was formed, and there was little day-to-day change in the network morphology (Figures 6A–D). On the contrary, in the Quinine experiments, the network morphology changed from a tree structure to a mesh structure over the course of days (Figures 7A–D).

These typical images of the networks were obtained from the final states of the network formation process, which lasts from the covering stage to the end of the observation of the day (Supplementary Movie S3 for control experiment and Supplementary Movie S4 for Quinine experiment). To quantify the process of network formation, the orientation angles of transport tubes were examined. Figures 6E–H and Figures 7E–H show the time course of the orientation angles. For example, in Figures 6E, G, H (control, Day 1, 3, and 4), and Figure 7E (Quinine, Day 1), the orientation angles of tubes were always approximately parallel (approximately 10–30°) to a direction denoted by arrows in Figures 6A, 7B, which is the direction of the plasmodium advancing during network formation. This characterizes the tree network. Meanwhile, in Figures 7F–H (Quinine, Day 2–4), the orientation angles were initially only parallel, but later, vertical angles (about 70–80°) were added to the end. This final state characterizes the mesh network. This correspondence between orientation angle and network formation was later used to automatically determine the classification of network shapes for a large number of samples.

The angle data from $t_n = -300$ to $t_n = 0$ of Figures 6E–H and Figure 7E–H were used to determine the final states. Figures 6I–L and Figures 7I–L show the distributions of the above data. The peak angles obtained from the distribution were used as the characteristic angle of the day for the following statistical analysis of the daily change.

Figure 8 shows the classification of network formation according to the daily change in characteristic angle. The typical daily changes are shown in Figures 8B–F. In Figure 8B, the major tube orientations are always parallel to the direction in which the tip of the plasmodium was advancing (Type 0). This indicates that the network is always a tree. In Figures 8C–F, the orientation of

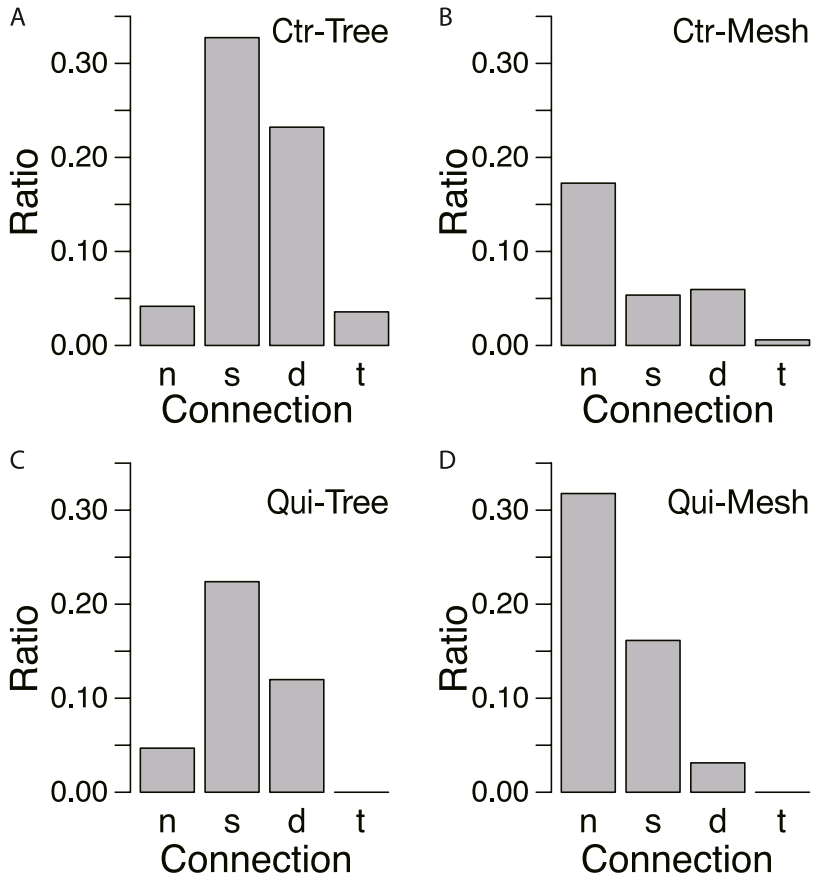

FIGURE 10
Relation between connections and network morphology. **(A, B)** Control experiment. *N* = 165. **(C, D)** Quinine experiment. *N* = 185. Denominator of ratio is the number of data in the same conditions. The meanings of symbols of connection types are as follows: no-connection (*n*), single tube (*s*), double tube (*d*), triple tube (*t*). The data from Days 1–4 are combined. Network morphologies are tree in A and C and mesh in B and D, which were determined based on whether the characteristic angle is small (tree network) or multiple (mesh network) from the data of Figure 8.

tubes changes to multidirectional on Day 4–1, respectively (named type 1–4, respectively). Here, the multidirectional tubes indicate that the network is mesh type. As shown in Figure 8A, Type 0 and 1 are the majority in the control experiment, while Type 2–4 are the majority in the Quinine experiment. This quantitative analysis supports the observations of the typical case described at the beginning of this section.

3.2 Deletion of "learning memory"

As shown in §3.1.3, it was confirmed that the network morphology changed during the learning process of "habituation" in the Quinine experiment. This indicates that the network morphology relates to the state of the learning memory of the plasmodium. To verify this hypothesis, Day 5 experiments were performed to see whether memory status changes when the network of the start blocks is artificially disrupted or when the start blocks are placed at different orientations. Figure 2 shows a typical view of plasmodium spreading on bridges after these manipulations. In the control experiment, there is not much change in the area after cutting the network (Figure 2E; Supplementary Movie S5) compared to the intact case (Figure 2D). On the contrary, in the Quinine experiment, after cutting or changing direction of the network, the area is smaller than in the intact case (Figures 2F–I; Supplementary Movie S6). These results can be statistically confirmed through the quantitative analysis of the area, as shown in Figure 4. In addition, in the Quinine experiment, when the network is manipulated, the speed of crossing the bridge becomes smaller than for the intact case, as shown in Figure 5. Taken together, these results suggest that there is a strong relationship between learning memory and the maintenance of network morphology.

3.3 Relation of network formation with the types of connections between the start and goal blocks

As shown in §3.1.3, the network formation differed between the control and Quinine experiments. To investigate how these different networks are formed, the type of tube connection between the start and goal blocks was examined (Figure 9). There are four types of connections: there is no connection between the start block and the goal block, as shown in Figure 9A (Type *n*); the number of connection tubes is single, double, and triple, as shown in Figures 9B–D (Type *s*, *d*, and *t*), respectively. Note that type *t*

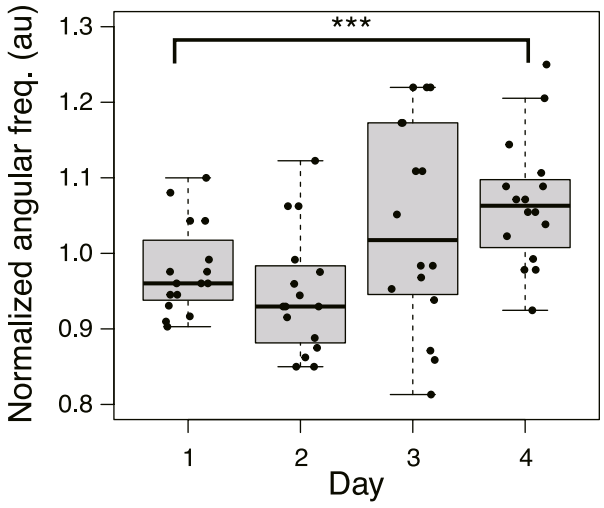

FIGURE 11
Angular frequency of thickness oscillation on start block in Quinine experiment. N = 16 for all daily data. Data are normalized by the median of the control data on the same day. See Supplementary Figure S6 for details. Asterisks represent the degree of p-value calculated as a result of appropriate statistical tests for each data set as follows: *** $p < 0.01$, and unlabeled $p > 0.1$. As reference data in the multiple comparison test, the Day 1 dataset was used. See Supplementary Table S1 for details.

also categorizes the case where the number of connection tubes is greater than three. The observation ratio of Type *n* increases with the passage of days, regardless of whether the experiment is control or Quinine (Figures 9E, F). It should be noted that the values grow much larger in the Quinine experiments, especially on Days 2–4. On the contrary, the ratios of Types *s* and *d* significantly decrease with the days in the Quinine experiments, while they are almost constant in the control experiments (Figures 9G–J). Finally, on Day 4, the case that the start and goal blocks are strongly connected is dominant in the control experiments, whereas the case of no-connection is dominant in the Quinine experiments. This suggests that the strength of connection affects network formation on the goal block.

To confirm this assumption, the ratio of connecting types was examined for each type of network formed in the goal, as shown in Figure 10. In the control, tree networks are very common, and the results are concentrated in the cases of strong connections (Type *s*, *d*, and *t*; Figure 10A). A small number of mesh networks can also be observed in the control experiments, but they are more common in the absence of connections (Type *n*; Figure 10B). In contrast, in the Quinine experiments, Type *n* connection is the most frequently observed in the mesh networks, as shown in Figure 10D.

To summarize the above results, a tree-type network is formed when start and goal blocks are connected through transport tubes. Conversely, if plasmodia on both blocks are separated by bridges containing repellent materials, the network will be formed only within the goal block, resulting in a mesh-type network. In the control experiment environment, the plasmodium on the start and goal blocks remained strongly connected via tubes developed on the bridges (Figures 9B–D). In this dumbbell-shaped morphology of the plasmodium, the cytoplasm of the plasmodium frequently moves back and forth between the start and goal, autocatalytically strengthening the connection between the two portions (Nakagaki et al., 2000b; Takamatsu et al., 2000). Thus, the reciprocal flow of protoplasm from the start to goal direction (arrow direction shown in Figure 6A) may have led to the development of transport tubes parallel to this direction, resulting in the formation of a tree-shaped network. Meanwhile, in the Quinine experiment environment, the start and goal blocks became separated as the number of experimental days passed, and the networks were formed only on the goal block (Figure 9A). Of course, plasmodia sometimes remain in the start block as well; however, we will ignore them here because they will not be used in the next day's experiment. The reason for the division of the two blocks is supposed to be due to the tendency of the plasmodium to escape from aversive chemicals contained in the bridge blocks. Within a limited area on the goal block, no cross-sectional cytoplasmic flow over the goal block is observed. In addition, the goal contains nutrition, on which it is known that a mesh-type network is formed (Takamatsu et al., 2009; Ito et al., 2011). Due to both above effects, a mesh network would be formed in the later days of the Quinine experiment.

3.4 Relation between frequency of thickness oscillation and network morphology

Based on the above results, after crossing a Quinine bridge, a tree network is formed in the goal block on Day 1 or 2 in most cases, and a mesh network is formed on Day 3 or 4. Meanwhile, the area of plasmodium on a bridge increases with the passage of days, and the relative crossing speed also increases. To investigate how these different morphologies of networks affect the bridge-crossing behavior of the plasmodium, the thickness oscillation of the plasmodium at the start blocks was investigated. Figure 11 shows the oscillation frequency in the Quinine experiments normalized by the median of the control data on the same day (see Supplementary Figure S6 for the original data). The frequencies are lower on Days 1 and 2 compared to the control data (denoted by 1.0 of the normalized angular frequency) and then become higher on Days 3 and 4. The results suggest that higher frequency of thickness oscillation assists the plasmodium to pass through the Quinine bridge, increasing its speed and spreading area. To confirm this hypothesis, the relations between oscillation frequency and the quantitative indices of behavior of the plasmodium on the bridges, such as area and speed, were analyzed. However, it was difficult to find direct correlations between the frequency and the behavioral indices (Supplementary Figure S7), which might be due to the wide dispersion of the data.

Then, the oscillation frequency data were analyzed separately for each network morphology to clarify what causes the oscillation frequency to rise on the later days, as shown in Figures 12A, B. Regardless of whether it was a control or Quinine experiment, the frequency of plasmodium oscillations in the mesh networks was always higher than in the tree networks. This indicates that the network morphology is a factor in controlling the oscillation frequency.

Similarly, the effect of network morphology on behavioral indices was investigated, as shown in Figures 12C–F. Both area and speed were found to be greater when the plasmodium placed at the start formed a mesh network than a tree network in the Quinine experiment, while there was no significant difference in network morphology in the control experiment.

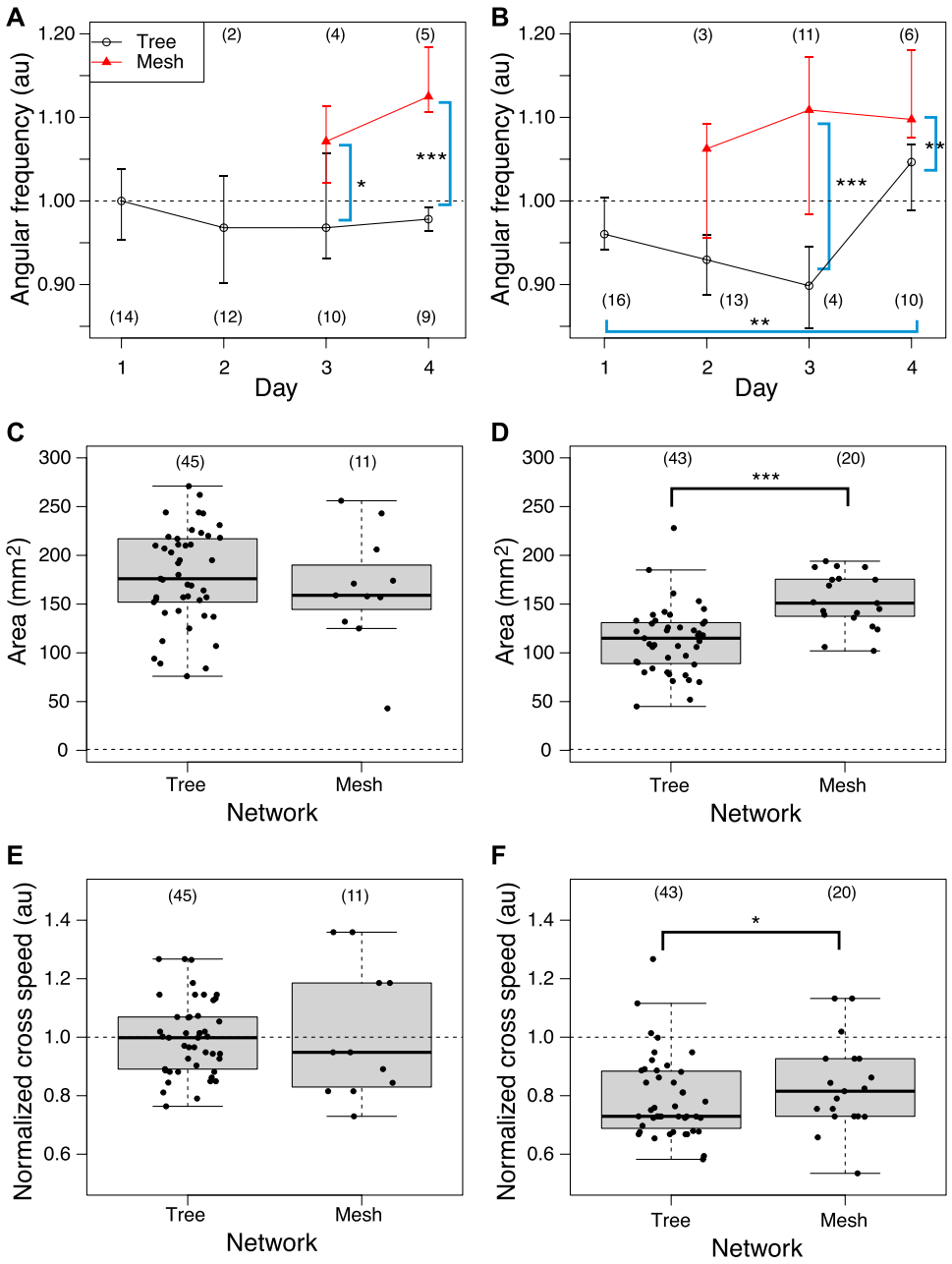

FIGURE 12
Relation between network morphology and quantitative indices of habituation behavior. **(A, B)** Angular frequency of thickness oscillation at start block. Angular frequencies are normalized by the median of the control data on the same day. Network morphologies are classified using those of the previous day's goal. **(C, D)** Area. **(E, F)** Crossing speed. **(A, C, E)** Control experiment. **(B, D, F)** Quinine experiment. Numbers in parentheses indicate number of data in each dataset. Asterisks represent the degree of p-value calculated as a result of appropriate statistical tests for each dataset as follows: *** $p < 0.01$, and unlabeled $p > 0.1$. Steel tests (one sided; greater) were applied to test daily changes using the Day 1 dataset as reference data (or earlier date if the number of data is less than 3) for multiple comparison in Figures **(A)** and **(B)**. Mann-Whitney tests (one sided) were applied to test for differences by network morphology. See Supplementary Table S1 for details.

4 Discussion

We trained plasmodium of true slime mold *P. polycephalum* to cross a bridge containing Quinine, an aversive substance, in accordance with the procedure of Boisseau et al. (2016). As shown in the results of §3.1.1 and §3.1.2, we confirmed that "habituation learning" was established after 4 days of training in Quinine experiment, which agreed with the results of Boisseau et al. (2016), who conducted the first habituation experiment with plasmodium. The experiments performed by Boussard et al. (2019) showed that the uptake and retention of the stimulants given during the learning process are deeply involved in the mechanism of habituation. However, it is unclear how the uptake chemicals act on the plasmodia themselves to bring the memory

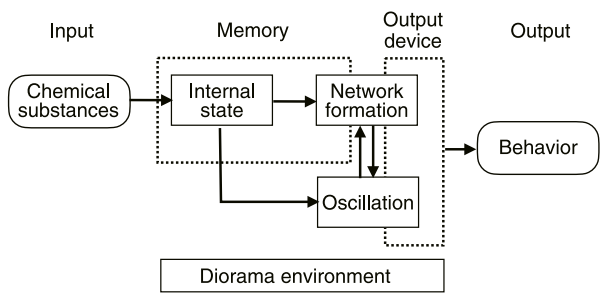

FIGURE 13
Conceptual diagram of memory in plasmodium of true slime mold.

function and how this memory results in changes in the behavior of the plasmodia.

We hypothesized that the key to the answer lies in the transport tube network of plasmodium, and we quantitatively examined the network morphology formed in the goal, as shown in §3.1.3. In the Quinine experiment, most formed a tree network in the goal on the first day, and their morphology changed to a mesh network over the course of daily repetitive stimulation (Figure 7; Figure 8). If the retention of the aversive chemical taken into the cell is the only factor important for memory retention, then disrupting the network should not result in a change in habituation behavior (memory deletion). However, when the network formed after learning was disrupted or redirected, the behavior changed as if the memory had been deleted (§3.2). Therefore, it is reasonable to hypothesize that not only the uptake of the chemical, but also the morphology of the transport tube network would assist the habituation behavior in some manner.

In fact, it has already been shown that the morphology of the network depends on the chemical substances in the environment (Takamatsu et al., 2009). From this, it can be deduced that the uptake of chemicals from the environment changes the internal state of the plasmodium, namely, the physical properties of the intracellular sol and/or outer gel, which leads to a change in the network morphology. For "habituation memory", the uptake of chemicals into the cell would be necessary to rewrite the internal state, and the change in network morphology would be necessary as a gateway to the output (Figure 13).

The learning mechanism connecting from network morphology to habituation behavior has not been elucidated. As a candidate mechanism, we expected that the thickness oscillation of plasmodium would act as a pump because of the following reports: it is known that different network morphologies produce different spatio-temporal oscillation patterns (Takamatsu et al., 2001); it has been reported that the oscillation frequency of plasmodium is high in the attractive environment and low in the aversive environment (Takahashi et al., 1997). Our experiment results confirmed that the oscillation frequency is higher when a mesh network is formed (§3.4; Figure 12B). Meanwhile, the behavioral indices of habituation, the area and speed of plasmodium spreading on the Quinine bridges, were higher when a mesh network was formed than when a tree network was formed, (Figure 12D, F). The results of these two quantitative analyses lead to the inference that the formation of the mesh network may assist the action of crossing the Quinine bridge by increasing the oscillation frequency. However, no direct evidence was found to support the hypothesis that thickness oscillations act as a pump to support the bridge cross. Further investigation is needed on this.

The following questions also remain. In the Quinine experiments, as discussed previously, the relationship between habituation behavior and network morphology was clear: the plasmodium was inactive in crossing the Quinine bridge when the network was a tree, and it was active when it was a mesh. In contrast, in the control experiment, there was little change in behavior whether the network was a tree or mesh. This does not lead to the conclusion that the morphology of the network simply causes changes in behavior. Actually, the environment for the plasmodia of the goal blocks is complicated in this experimental setup: the goal block contains a nutrient medium, while the learned plasmodium additionally uptakes an aversive chemical substance. These complex factors need to be investigated in future studies.

5 Conclusion

In this paper, from the memory deletion experiment, we have shown that transport tube network in addition to the retention of the chemicals plays an important role in habituation behavior in plasmodium. There would be advantages for the system where information input from the outside is not only stored internally in the form of concentration of chemical substance, but also converted into transport tube network morphology. This is because external stimuli can take various forms, such as thermal and mechanical stimuli in addition to stimuli by chemical substances. It was mentioned in the Introduction section that the transport tubes of plasmodium have neuron-like properties. Moreover, the thickness of transport tubes can be strengthened or weakened by the relationship between the oscillations of the parts (phase difference of the oscillation), resulting in the formation of different morphologies of transport tube networks. This reminds us of strengthening synapses in neurons and the formation of neural networks. Although learning functions in various single-celled organisms are widely reported, plasmodium may be the closest single-celled organism to a neural network because of the transport tube network. It would be important to study such primitive networks to hypothesize their evolution into more sophisticated neural networks.

Data availability statement

The original contributions presented in the study are included in the article/Supplementary Material, further inquiries can be directed to the corresponding author.

Ethics statement

The manuscript presents research on animals that do not require ethical approval for their study.

Author contributions

AT contributed to conception and design of the study. EY developed the experimental system and performed the experiments. EY and AT performed the data analysis of the results. EY wrote the first draft of the manuscript in Japanese. AT rewrote the manuscript. All authors contributed to the article and approved the submitted version.

Funding

This work was supported by the MEXT KAKENHI Grant-in-Aid for Transformative Research Areas (A) 22H05693 for AT and JSPS KAKENHI Grant-in-Aid for Scientific Research (C) 19K03774 for AT.

Acknowledgments

We thank all members of "Ethological dynamics in diorama environment", Grant-in-Aid for Transformative Research Areas (A), MEXT, Japan for their useful discussion.

Conflict of interest

The authors declare that the research was conducted in the absence of any commercial or financial relationships that could be construed as a potential conflict of interest.

Publisher's note

Supplementary material

The Supplementary Material for this article can be found online at: https://www.frontiersin.org/articles/10.3389/fcell.2023.1249165/full#supplementary-material

References

Barron, A. B., Hebets, E. A., Cleland, T. A., Fitzpatrick, C. L., Hauber, M. E., and Stevens, J. R. (2015). Embracing multiple definitions of learning. *Trends Neurosci.* 38, 405–407. doi:10.1016/j.tins.2015.04.008

Boisseau, R. P., Vogel, D., and Dussutour, A. (2016). Habituation in non-neural organisms: evidence from slime moulds. *Proc. R. Soc. Lond. Ser. B Biol. Sci.* 283, 20160446–20160447. doi:10.1098/rspb.2016.0446

Boussard, A., Delescluse, J., Pérez-Escudero, A., and Dussutour, A. (2019). Memory inception and preservation in slime moulds: the quest for a common mechanism. *Philosophical Trans. R. Soc. B Biol. Sci.* 374, 20180368. doi:10.1098/rstb.2018.0368

Dussutour, A. (2021). Learning in single cell organisms. *Biochem. Biophysical Res. Commun.* 564, 92–102. doi:10.1016/j.bbrc.2021.02.018

Eisenstein, E., Brunder, D., and Blair, H. (1982). Habituation and sensitization in an aneural cell: some comparative and theoretical considerations. *Neurosci. Biobehav. Rev.* 6, 183–194. doi:10.1016/0149-7634(82)90054-9

F. D. William, J. Dee, S. Hatano, F. B. Haugli, and K.-E. Wohlfarth-Bottermann (Editors) (1986). "The molecular Biology of physarum polycephalum," *NATO ASI series* (Berlin, Germany: Springer). doi:10.1007/978-1-4613-2203-0

French, J. W. (1940). Trial and error learning in paramecium. *J. Exp. Psychol.* 26, 609–613. doi:10.1037/h0059015

Gunawardena, J. (2022). Learning outside the brain: integrating cognitive science and systems Biology. *Proc. IEEE* 110, 590–612. doi:10.1109/jproc.2022.3162791

Hanzel, T. E., and Rucker, W. B. (1972). Trial and error learning in paramecium: a replication. *Behav. Biol.* 7, 873–880. doi:10.1016/S0091-6773(72)80180-9

Ito, M., Okamoto, R., and Takamatsu, A. (2011). Characterization of adaptation by morphology in a planar biological network of plasmodial slime mold. *J. Phys. Soc. Jpn.* 80, 074801. doi:10.1143/jpsj.80.074801

Kamiya, N. (1959). *Protoplasmic streaming*. Wien: Springer-Verlag. doi:10.1007/978-3-7091-5750-3

Kramar, M., and Alim, K. (2021). Encoding memory in tube diameter hierarchy of living flow network. *Proc. Natl. Acad. Sci.* 118, e2007815118. doi:10.1073/pnas.2007815118

Nakagaki, T. (2021). *Ethological dynamics in diorama environments*. Available at: https://diorama-ethology.jp/eng/greeting.html.

Nakagaki, T., Kobayashi, R., Nishiura, Y., and Ueda, T. (2004). Obtaining multiple separate food sources: behavioural intelligence in the Physarum plasmodium. *Proc. R. Soc. Lond. Ser. B Biol. Sci.* 271, 2305–2310. doi:10.1098/rspb.2004.2856

Nakagaki, T., Yamada, H., and Tóth, A. (2000a). Maze-solving by an amoeboid organism. *Nature* 407, 470. doi:10.1038/35035159

Nakagaki, T., Yamada, H., and Ueda, T. (2000b). Interaction between cell shape and contraction pattern in the Physarum plasmodium. *Biophys. Chem.* 84, 195–204. doi:10.1016/s0301-4622(00)00108-3

Rajan, D., Makushok, T., Kalish, A., Acuna, L., Bonville, A., Almanza, K. C., et al. (2023). Single-cell analysis of habituation in Stentor coeruleus. *Curr. Biol.* 33, 241–251.e4. doi:10.1016/j.cub.2022.11.010

Rankin, C. H., Abrams, T., Barry, R. J., Bhatnagar, S., Clayton, D. F., Colombo, J., et al. (2009). Habituation revisited: an updated and revised description of the behavioral characteristics of habituation. *Neurobiol. Learn. Mem.* 92, 135–138. doi:10.1016/j.nlm.2008.09.012

R Core Team (2023). *R: a language and environment for statistical computing*. Vienna, Austria: R Foundation for Statistical Computing.

Saigusa, T., Tero, A., Nakagaki, T., and Kuramoto, Y. (2008). Amoebae anticipate periodic events. *Phys. Rev. Lett.* 100, 4, 018101. doi:10.1103/physrevlett.100.018101

Schindelin, J., Arganda-Carreras, I., Frise, E., Kaynig, V., Longair, M., Pietzsch, T., et al. (2012). Fiji: an open-source platform for biological-image analysis. *Nat. Methods* 9, 676–682. doi:10.1038/nmeth.2019

Takagi, S., Nishiura, Y., Nakagaki, T., Ueda, T., and Ueda, K.-I. (2007). Indecisive behavior of amoeba crossing an environmental barrier. *Topol. Aspects Crit. Syst. Netw.* 2007, 86–93. doi:10.1142/9789812708687_0011

Takahashi, K., Takamatsu, A., Hu, Z. S., and Tsuchiya, Y. (1997). Asymmetry in the self-sustained oscillation ofPhysarum plasmodial strands. *Protoplasma* 197, 132–135. doi:10.1007/bf01279891

Takamatsu, A., Fujii, T., and Endo, I. (2000). Time delay effect in a living coupled oscillator system with the plasmodium of physarum polycephalum. *Phys. Rev. Lett.* 85, 2026–2029. doi:10.1103/physrevlett.85.2026

Takamatsu, A., Gomi, T., Endo, T., Hirai, T., and Sasaki, T. (2017). Energy-saving with low dimensional network in Physarum plasmodium. *J. Phys. D Appl. Phys.* 50, 154003. doi:10.1088/1361-6463/aa635a

Takamatsu, A., Takaba, E., and Takizawa, G. (2009). Environment-dependent morphology in plasmodium of true slime mold *Physarum polycephalum* and a network growth model. *J. Theor. Biol.* 256, 29–44. doi:10.1016/j.jtbi.2008.09.010

Takamatsu, A., Tanaka, R., Yamada, H., Nakagaki, T., Fujii, T., and Endo, I. (2001). Spatiotemporal symmetry in rings of coupled biological oscillators of physarum plasmodial slime mold. *Phys. Rev. Lett.* 87, 078102. doi:10.1103/physrevlett.87.078102

Tero, A., Kobayashi, R., and Nakagaki, T. (2007). A mathematical model for adaptive transport network in path finding by true slime mold. *J. Theor. Biol.* 244, 553–564. doi:10.1016/j.jtbi.2006.07.015

Tero, A., Takagi, S., Saigusa, T., Ito, K., Bebber, D. P., Fricker, M. D., et al. (2010). Rules for biologically inspired adaptive network design. *Science* 327, 439–442. doi:10.1126/science.1177894

Thompson, R. F., and Spencer, W. A. (1966). Habituation: a model phenomenon for the study of neuronal substrates of behavior. *Psychol. Rev.* 73, 16–43. doi:10.1037/h0022681

Ueda, T., Mori, Y., Nakagaki, T., and Kobatake, Y. (1988). Action spectra for superoxide generation and uv and visible light photoavoidance in plasmodia of *physarum polycephalum*. *Photochem. Photobiol.* 48, 705–709. doi:10.1111/j.1751-1097.1988.tb02884.x

Vogel, D., and Dussutour, A. (2016). Direct transfer of learned behaviour via cell fusion in non-neural organisms. *Proc. R. Soc. Lond. Ser. B Biol. Sci.* 283, 20162382–20162386. doi:10.1098/rspb.2016.2382

Watanabe, S., Tero, A., Takamatsu, A., and Nakagaki, T. (2011). Traffic optimization in railroad networks using an algorithm mimicking an amoeba-like organism, Physarum plasmodium. *Biosystems* 105, 225–232. doi:10.1016/j.biosystems.2011.05.001

Wright, C. S., Joshi, K., and Iyer-Biswas, S. (2023). Cellular learning: habituation sans neurons in a unicellular organism. *Curr. Biol.* 33, R61–R63. doi:10.1016/j.cub.2022.12.008

Yi, T.-M., Huang, Y., Simon, M. I., and Doyle, J. (2000). Robust perfect adaptation in bacterial chemotaxis through integral feedback control. *Proc. Natl. Acad. Sci.* 97, 4649–4653. doi:10.1073/pnas.97.9.4649

Zhu, L., Aono, M., Kim, S.-J., and Hara, M. (2013). Amoeba-based computing for traveling salesman problem: long-term correlations between spatially separated individual cells of Physarum polycephalum. *Biosystems* 112, 1–10. doi:10.1016/j.biosystems.2013.01.008

Zhu, L., Kim, S.-J., Hara, M., and Aono, M. (2018). Remarkable problem-solving ability of unicellular amoeboid organism and its mechanism. *R. Soc. Open Sci.* 5, 180396. doi:10.1098/rsos.180396

Frontiers in
Cell and Developmental Biology

Explores the fundamental biological processes of life, covering intracellular and extracellular dynamics.

The world's most cited developmental biology journal, advancing our understanding of the fundamental processes of life. It explores a wide spectrum of cell and developmental biology, covering intracellular and extracellular dynamics.

Discover the latest Research Topics

See more →

Frontiers

Avenue du Tribunal-Fédéral 34
1005 Lausanne, Switzerland
frontiersin.org

Contact us

+41 (0)21 510 17 00
frontiersin.org/about/contact